

# **Design and Implementation of a Piezoelectric Servo-Flap Actuation System for Helicopter Rotor Individual Blade Control**

by

Eric Frederick Prechtel

B.S., Penn State University (1991)

S.M., Massachusetts Institute of Technology (1994)

Submitted to the Department of Aeronautics and Astronautics  
in partial fulfillment of the requirements for the degree of  
Doctor of Philosophy

at the

MASSACHUSETTS INSTITUTE OF TECHNOLOGY

February 2000

© Massachusetts Institute of Technology 2000. All rights reserved.

Author .....  
Department of Aeronautics and Astronautics  
January 14, 2000

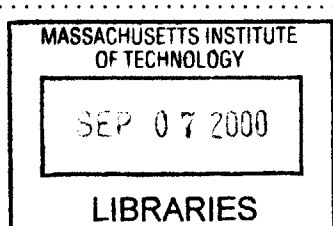
Certified by .....  
Professor Steven R. Hall  
Thesis Committee Chairman, Department of Aeronautics and Astronautics

Certified by .....  
Professor Edward F. Crawley  
Department of Aeronautics and Astronautics

Certified by .....  
Professor Nesbitt W. Hagood IV  
Department of Aeronautics and Astronautics

Certified by .....  
Professor Terrence A. Weisshaar  
Department of Aeronautics and Astronautics, Purdue University

Accepted by .....  
Professor Nesbitt W. Hagood IV  
Chairman, Department Graduate Committee



Aero



**Design and Implementation of a Piezoelectric Servo-Flap  
Actuation System for Helicopter Rotor Individual Blade  
Control**

by

Eric Frederick Prechtl

Submitted to the Department of Aeronautics and Astronautics  
on January 14, 2000, in partial fulfillment of the  
requirements for the degree of  
Doctor of Philosophy

**Abstract**

A novel new actuator for helicopter rotor control, the *X-Frame Actuator*, was developed, demonstrating superior performance for applications requiring compact, fast acting, large stroke actuation. The detailed experimental characterization of this actuator is described, including bench-top output energy measurements and transverse shake test performance. A Mach scaled rotor blade utilizing the X-Frame actuator to power a trailing edge servo-flap near the tip was also designed, manufactured and tested. A description of the design and composite manufacturing of the rotor blade and servo-flap is presented. Preliminary bench tests of the active blade actuation system are also presented. The hover tests of the active blade provided transfer function identification of the performance of the actuator in producing flap deflections, and the response of the rotor from deflections of the servo-flap. At the highest field level of 60 V/mil P-P the actuation system produces 7.75 degrees of quasi-static peak-to-peak flap deflection in hover. The servo-flap produces significant control authority, especially near the 3/rev frequency that would be important for the CH-47. Scaled to a full-sized CH-47, the rotor can produce over 16,000 lb peak-to-peak thrust variation at 3/rev, which is 32% of the aircraft's gross weight. Closed-loop feedback control was experimentally applied to the model rotor system. Both single frequency and combined frequency controllers were successfully implemented on the rotor. Most significantly, simultaneous control of 1/rev, 3/rev, 4/rev, 5/rev, and 6/rev harmonic vibration has been successfully demonstrated. The peak vibrations were eliminated at each frequency, as well as the vibrations over a small bandwidth surrounding each peak. Experimental comparison of continuous time versus discrete time control has shown the former to be a more effective approach for vibration reduction.

Thesis Committee:

**Professor Steven R. Hall**

Associate Professor of Aeronautics and Astronautics

**Professor Edward F. Crawley**

Professor of Aeronautics and Astronautics

**Professor Nesbitt W. Hagood IV**

Associate Professor of Aeronautics and Astronautics

**Professor Terrence A. Weisshaar**

Professor of Aeronautics and Astronautics

## Acknowledgments

If I took the space to properly thank everyone who has assisted me in this project, I would end up with a document almost as long as this thesis (perhaps without as many appendices). Consequently, I am sure that these words of acknowledgment will fall short in expressing how grateful I am to all the people who have supported me.

I would first like to thank my advisor, Professor Steven R. Hall, for his tremendous support and his ability to guide me around the technical problems that, at first, appeared insurmountable. His high standards of excellence have made me into a better engineer. I must express my gratitude to all of my colleagues in the Active Materials and Structures Laboratory and the Space Systems Laboratory. Special thanks go to John Rodgers for all his help and for giving freely of his time to assist me in the lab, even after he had graduated and left MIT. I also want to thank Professor Nesbitt Hagood for making the laboratory facilities available so that I could complete this research; Paul Bauer for teaching me all those intangible lessons in the lab that you cannot learn from a book or in a classroom; Mauro Atalla for his immeasurable assistance in almost every facet of this project; Mads Schmidt for his invaluable contributions toward the manufacturing of the active blade; Seward Pulitzer III and Sangjoon Shin for solving a number of spinstand instrumentation issues; Theodora Tzianetopoulou for her help in strength testing the active blade; Alex Pizzochero for his support in the laboratory; and Chris Dunn for administering the laboratory computers. I also gratefully acknowledge the laboratory secretaries and administrators, Sharon Leah Brown, Mai Cleary, Paula Peche, Jennifer Donaldson, and Mary Jones.

I want to thank my UROPs, Ben Erwin, Corinne Ilvedson, Winston Fan, Dan Paluska, Will Nielson, Margaret Pan, Sam Towell, Dan Frisk, and Terry Fong, for their contributions to this research. Special thanks goes to Aaron Julin who provided invaluable assistance in designing the spinstand rotating frame components and the actuator shake testing apparatus.

I gratefully acknowledge Robert Derham, Douglas Weems, Dan Podgurski, and

especially Richard Bussom at Boeing Helicopters for their support and rapid response to my endless stream of questions. I would also like to thank Professor Mark Drela for providing me with the aerodynamic analysis software, MSES, and the code used to generate the machining commands for the rotor blade and servo-flap molds. Also, thanks goes to Jerry Wentworth for assisting me in machining these molds.

Manufacturing an active blade with integrated actuator components is like building a ship in a bottle. Therefore, it is only fair that I thank my shipbuilders, the machinists at Advanced Machining and Tooling in San Diego. I would especially like to acknowledge Terry Deane and Dave Belt for their assistance and invaluable feedback regarding the machining of the actuator components.

I was fortunate to have a number of very good friends who provided me with a great deal of moral support throughout this project. I especially want to thank Brian Bingham, Laila Elias, Kamyar Ghandi, Timothy Glenn, Charrissa Lin, Alex Makarenko, Greg Mallory, Donald O'Sullivan, Jennifer Rochlis, Raymond Sedwick, Patrick Trapa, Heidi Westerlund, and Jeremy Yung. In addition, two friends who have been extraordinarily supportive over the past five years are Brian Wardle and Yool Kim. I am indebted to them for listening to me complain and for straightening me out ... when necessary.

Lastly, I would like to thank my family: my three brothers, Russ, Brian and Glenn and my parents, James and Carmela Prechtl. They have been the foundation upon which I have built all my accomplishments and the shelter in which I have weathered the storms.

This research was supported by DARPA under Contract Number F49620-95-2-0097 and MDA972-98-3-0001, monitored by Bob Crowe, Bill Coblenz, and Ephrahim Garcia. Additional support was provided by the Army Research Office, under contract DAAH04-95-0104, monitored by Gary Anderson.

*This thesis is dedicated  
to the memory of*

*Lee Ann Ranieri,  
Frederick R. Colombo,  
and Christine R. Legere*



# Contents

<b>1</b>	<b>Introduction</b>	<b>19</b>
1.1	Rotor Blade Vibration and Noise . . . . .	20
1.2	Rotor Control . . . . .	21
1.3	Advantages of Blade Mounted Actuation . . . . .	23
1.4	Previous Blade Mounted Actuation Approaches . . . . .	26
1.4.1	Integral Rotor Blade Actuation . . . . .	27
1.4.2	Discrete Rotor Blade Actuation . . . . .	27
1.5	Thesis Overview . . . . .	31
<b>2</b>	<b>The X-Frame Actuator</b>	<b>33</b>
2.1	Actuator Requirements . . . . .	33
2.2	Mass Efficiency . . . . .	34
2.3	Actuator Design Axioms . . . . .	35
2.4	X-Frame Actuator Operational Principles . . . . .	37
2.5	Model Scale X-Frame Actuator Design . . . . .	40
2.6	Actuator Validation Experiments . . . . .	44
2.6.1	Quasi-Static Actuator Testing . . . . .	44
2.6.2	Dynamic Actuator Testing . . . . .	49
<b>3</b>	<b>Active Rotor Blade Design, Manufacture and Bench-Test</b>	<b>55</b>
3.1	Active Rotor Blade Design . . . . .	55
3.1.1	Active Rotor Blade Design Requirements . . . . .	56
3.1.2	Actuation System Design . . . . .	57

3.1.3	Aerodynamic Predictions . . . . .	63
3.1.4	Actuation System Compliance and Strength Modeling . . . . .	68
3.1.5	Estimate of System Performance . . . . .	72
3.1.6	Active Blade Instrumentation . . . . .	73
3.2	Blade Manufacture . . . . .	74
3.3	Active Rotor Blade Properties . . . . .	77
3.4	Rotor Blade Validation Tests . . . . .	78
3.4.1	Active Blade Actuation System Bench Tests . . . . .	78
3.4.2	Actuator Bay Strength Testing . . . . .	82
<b>4</b>	<b>Hover-Test System Identification and Performance</b>	<b>85</b>
4.1	Aeroelastic Scaling . . . . .	86
4.2	The MIT Hover Test Facility . . . . .	92
4.2.1	Hardware . . . . .	93
4.2.2	Instrumentation . . . . .	101
4.2.3	Hover Test Facility Data Collection and Analysis Techniques .	104
4.2.4	Blade Tracking . . . . .	111
4.3	Hover-Test Results . . . . .	112
4.3.1	Active Blade Modal Identification . . . . .	114
4.3.2	Actuation System Performance . . . . .	120
4.3.3	Rotor Transfer Functions . . . . .	130
4.3.4	Strength and Thermal Data . . . . .	138
<b>5</b>	<b>Closed-Loop Rotor Vibration Control</b>	<b>143</b>
5.1	Vibrational Disturbance Spectrum . . . . .	144
5.2	Single Harmonic Continuous-Time Control . . . . .	146
5.3	Multiple Harmonic Continuous-Time Control . . . . .	160
5.4	Single Harmonic Discrete-Time Control . . . . .	164
<b>6</b>	<b>Summary</b>	<b>169</b>
6.1	Major Results and Conclusions . . . . .	169

6.2 Contributions . . . . .	171
6.3 Recommendations for Future Work . . . . .	173
<b>A Material Survey</b>	<b>187</b>
A.1 The Case for Active Materials . . . . .	187
A.2 General Active Material Characteristic Definitions . . . . .	188
A.3 Specific Active Material Comparison . . . . .	190
A.4 Compressive Depolarization of EC-98 . . . . .	193
<b>B Discrete Actuator Background Analysis and Design</b>	<b>195</b>
B.1 Actuator Design Comparisons . . . . .	195
B.1.1 The Piezoelectric Bender Actuator . . . . .	196
B.1.2 Coupling mechanisms . . . . .	197
B.1.3 Stack/Inert Frame Actuators . . . . .	202
B.2 Proof-of-Concept X-Frame Actuator . . . . .	207
B.2.1 Prototype Manufacture . . . . .	208
B.2.2 Prototype Experimental Performance . . . . .	209
<b>C Hover Data Transfer Function Plots</b>	<b>223</b>
<b>D Closed-Loop Rotor Control Plots</b>	<b>269</b>
<b>E Active Rotor Blade Fabrication</b>	<b>307</b>
E.1 X-Frame Actuator Drawings . . . . .	307
E.2 Manufacturing Steps . . . . .	316
E.2.1 Main Blade Manufacture . . . . .	316
E.2.2 Servo-Flap Manufacture . . . . .	360
E.2.3 Active Rotor Blade Assembly . . . . .	366

# Notation

$A$	Rotor disk area
$A_e$	Cross-sectional area of an active element
$A_f$	Cross-sectional area of an actuator support frame
BS	“Blade Station”; Distance from center of rotation
$C_{D_\delta}$	Servo-flap sectional drag curve slope with flap deflection
$C_{D_{0f}}$	Servo-flap sectional steady coefficient of drag
$C_{H_\delta}$	Servo-flap sectional hinge moment curve slope with flap deflection
$C_{H_{0f}}$	Servo-flap sectional steady coefficient of hinge moment
$C_L$	Rotor blade sectional coefficient of lift
$C_{L_\alpha}$	Rotor blade sectional lift curve slope with angle of attack
$C_{L_\delta}$	Servo-flap sectional lift curve slope with flap deflection
$C_{L_{0f}}$	Servo-flap sectional steady coefficient of lift
$C_M$	Rotor blade sectional coefficient of moment
$C_{M_\delta}$	Rotor blade sectional moment curve slope with flap deflection
$C_P$	Rotor blade sectional coefficient of pressure
$C_{P_i}$	Induced power loss from rotor operation
$C_{SI}$	Non-dimensional ratio of blade stiffness to mass
$C_T$	Rotor coefficient of thrust
$\frac{C_T}{\sigma}$	Blade loading
$C_{ps}$	Compliance of the pre-stress wire inboard length due to flexing
$D_s$	Stack diameter
$E$	Applied electric field
$EI_1, EI_2$	Rotor blade bending stiffness about thickness and chordline axes
$E_e$	Young's modulus of an active material
$E_f$	Young's modulus of an actuator support frame material

$E_{ps}$	Young's modulus of the pre-stress wire material
$F_f$	Frictional force on the actuator
$F_x$	Rotating frame hub force component perpendicular to active blade
$F_y$	Rotating frame hub force component in the direction of active blade
$F_z$	Rotating frame hub force component normal to the tip path plane
$\mathbf{G}(s)$	Plant transfer function
$\overline{G_i}(f)$	Average transfer function from U to Y
$GJ$	Rotor blade torsional stiffness per unit length
$G_{ps}$	Shear modulus of the pre-stress wire material
$I_b$	Flapwise mass moment of inertia of rotor blade about center or rotation
$I_F$	Mass moment of inertia of servo-flap about its axis of rotation
$I_{in}$	Bending moment of inertia of inboard section of pre-stress wire
$J_{ps}$	Polar moment of inertia of the pre-stress wire
$\mathbf{K}$	Stiffness matrix of a generic coupling mechanism
$\mathbf{K}(s)$	Controller transfer function
$K_L$	Linear stiffness of the load
$K_{L_{rot}}$	Rotational stiffness of the load
$K_{aero}$	Effective stiffness due to servo-flap deflection in air in hover
$K_a$	Output stiffness of a generic actuator (or flexible mechanism)
$K_{cf}$	Parallel stiffness due to deformation of the cross-flexures
$K_c$	Stiffness of a generic coupler
$K_e$	Stiffness of a generic expansive element
$K_f$	Frame stiffness located in a generic actuator (or flexible mechanism)
$K_s$	Stiffness of a stack
$\overline{K}_{12}$	Non-dimensional coupling coefficient
$L_f$	Total lift on flap
$L_{tot}$	Total thrust generated by the rotor blades

$M_e$	Mass of the active material
$M_{\text{tot}}$	Total mass of an actuator
$M_x$	Rotating frame hub moment around the x-axis (defined by $F_x$ , above)
$M_y$	Rotating frame hub moment around the y-axis (defined by $F_y$ , above)
$M_z$	Rotor torque
$N$	Number of blades in rotor
$N_{\text{ps}}$	Normal force due to actuator pre-stress
$\mathbf{P}$	Controller gain/phase adjustment matrix
$P_{\text{motor}}$	Power required by motor to operate rotor
$P_{xx}$	Power spectral density of the signal $x(t)$
$Q_L$	Force applied to a load
$Q_{ab}$	Blocked force capability of an actuator
$Q_{cb}$	Blocked force capability of a generic coupler
$Q_e$	Force reacted by a generic expansive element
$Q_{eb}$	Blocked force capability of a generic expansive element
$Q_1, Q_2$	Generalized forces of a generic coupling mechanism
$R$	Rotor radius
$R_i$	Inboard spanwise position of the servo-flap
$R_{\text{in}}$	Radius of the inboard section of the pre-stress wire
$R_o$	Outboard spanwise position of the servo-flap
$Re$	Reynolds number
$\mathbf{T}$	Control response matrix
$T$	Tension in rotor blade due to centrifugal force
$U$	Free stream air velocity
$U_a$	Energy density of an actuator
$U_e$	Energy density of an active material
$V$	Applied voltage

$V_e$	Active material volume
$W_L$	Work done on a load
$W_a$	Internal mechanical energy of an actuator
$W_c$	Work extracted from an expansive element/coupler combination
$W_e$	Energy available from a generic expansive element
$a_{fm}$	Stroke amplification ratio of an actuator
$c$	Rotor blade chord length
$c_f$	Servo-flap chord length
$c_s$	Chord length at the slotted rotor blade sections
$d(t)$	Thrust disturbance in the time domain
$d_{31}$	Transverse piezoelectric strain coefficient
$d_{33}$	Longitudinal piezoelectric strain coefficient
$h_b(f)$	Bartlett window in frequency domain
$h_{\text{nom}}$	Distance between stack end-points at pivot end of the X-Frame actuator
$k$	Controller gain
$k_A$	“Radius of moment of inertia” of rotor blade section
$k_{\text{fix}}$	Scalar adjustment to gain of closed-loop controller
$k_{ps}$	Parallel rotational stiffness of the pre-stress wire
$k_{sm}$	Normalization parameter to set Bartlett window characteristics
$k_{m_1}, k_{m_2}$	Radii of gyration of the blade section around sectional axes
$l_e$	Length of an active element
$l_f$	Length of frame member
$l_{\text{in}}$	Effective length of inboard section of pre-stress wire
$l_{ps}$	Effective length (in torsion) of the pre-stress wire
$l_s$	Stack length
$m$	Rotor blade mass per unit length
$q_L$	Displacement of a load

$q_a$	Actuator displacement
$q_e$	Displacement of a generic expansive element
$q_f$	Actuator free displacement
$q_1, q_2$	Generalized displacements of a generic coupling mechanism
$r$	Radial position along the rotor blade
$r_c$	Radius of clevis spherical bearing
$r_{co}$	Radius of rotor root cut-out
$r_{ifh}$	Radius of main flap spherical bearing at inboard side of pre-stress wire
$s$	Actuator lever arm length
$u(t)$	Control signal in the time domain
$v$	Chordwise rotor blade deformation
$w$	Flapwise bending deformation of rotor blade
$x$	Distance along the rotor blade
$y(t)$	Rotor thrust signal in the time domain
$z(t)$	Total thrust signal in the time domain
$\Lambda$	Non-dimensional rotor disk inflow
$\Omega$	Rotor speed
$\alpha$	Rotor blade sectional angle of attack
$\alpha_{fm}$	Ratio of active material to actuator frame specific moduli
$\beta$	Total angle of rotor blade flapwise deformation
$\gamma$	Blade Lock number
$\gamma_s$	Smoothing parameter for a Bartlett window
$\delta$	Servo-flap deflection angle
$\epsilon$	Induced strain from an active material
$\eta_c$	Mechanical efficiency of a generic coupler
$\eta_{im}$	Impedance matching efficiency
$\eta_{mass}$	Mass efficiency of an actuator

$\eta_{\text{mech}}$	Mechanical efficiency of an actuator
$\theta$	Rotor blade built in angle of attack
$\theta_a$	X-Frame actuator amplification angle
$\mu$	Coefficient of viscosity of air
$\mu_k$	Kinetic coefficient of friction
$\rho$	Density of air
$\rho_e$	Density of an active material
$\rho_f$	Density of an actuator support frame material
$\sigma$	Rotor solidity
$\sigma_x, \tau_{xy}, \tau_{xz}$	Components of stress on pre-stress wire inboard segment
$\sigma_{I,II}$	Principal stress components
$\phi$	Torsional deformation of the rotor blade
$\phi_{xx}$	Autocorrelation of the signal $x(t)$
$\widehat{\phi}_{uu}$	Averaged auto-spectrum of signal $U(f)$
$\widehat{\phi}_{yu}$	Averaged cross-spectrum of $Y(f)$ and $U(f)$ signals
$\widetilde{\phi}_{uu}$	Smoothed and averaged auto-spectrum of signal $U(f)$
$\widetilde{\phi}_{yu}$	Smoothed and averaged cross-spectrum of $Y(f)$ and $U(f)$ signals

## Subscripts

f	Full scale parameter
m	Model scale parameter
p-p	“Peak-to-peak”

## Superscripts

( )*	Optimum quantity or complex conjugate
(̄)	Non-dimensional parameter



# Chapter 1

## Introduction

The normal operation of a helicopter rotor in forward flight can result in vibration, noise, and aerodynamic inefficiencies. The source of these problems is the unsteady aerodynamic environment associated with rotor operation, due mostly to interactions between vortices in the rotor wake and the rotor blades. Many passive and active techniques have been suggested to improve the response of the rotor under these conditions, but there is much room for improvement. This thesis presents the development of a new technology, utilizing a rotor blade-mounted actuator to actively control a trailing edge servo-flap, designed to address these problems.

In this chapter, a review of the literature on rotor vibration and noise control is given. This chapter is organized as follows: Section 1.1 presents a discussion about the cause of rotor blade vibration and noise and Section 1.2 reviews the strategies that have been applied to reduce these problems. Section 1.3 discusses how the use of blade mounted actuators can more effectively attack the rotor noise and vibration problem and Section 1.4 presents the blade mounted actuator designs that have been proposed. Within this section, the two most commonly suggested blade mounted actuation schemes, integral and discrete actuation, are defined and discussed. The chapter concludes with an overview of the rest of the thesis.

## 1.1 Rotor Blade Vibration and Noise

There are a number of sources of rotor vibration and noise which ultimately are due to unsteady aerodynamic effects on the rotor blades. These include atmospheric turbulence, retreating blade stall, blade/vortex interaction and blade/fuselage interaction, as well as blade and rotor instabilities (ground/air resonances) [39]. These forces are then transmitted through to the hub, and are felt as vibration in the fuselage. Generally, the forces on the blades are harmonics of the rotor frequency, since the rotor aerodynamics are (nearly) periodic. Of these harmonics, only those which are multiples of the blade passage frequency ( $N\Omega$ ) are transmitted to the fixed frame due to the symmetry of the rotor. In contrast, there is no such filtering of the noise generated by the rotor blades. Thus, the entire spectrum of rotor noise must be considered when addressing the noise control problem.

Rotor noise of greatest concern (in terms of human annoyance) is concentrated in the frequency range between 100 Hz and a few kHz. George divides rotor noise into discrete frequency, impulsive, and broadband noise [48]. Discrete frequency noise occurs naturally due to blade rotation and forward flight of the helicopter. For the main rotor, discrete frequency noise for the first dozen or so harmonics lie below 100 Hz. However, many of the tail rotor harmonics do exceed 100 Hz, and are therefore of concern.

Impulsive noise is typically caused by blade vortex interactions (BVI) and local transonic events on the blades. George remarks that aeroacoustic rotor blade design can be applied to provide improvements in impulsive noise generation [48]. However, Splettstoesser *et al.* state that such aeroacoustic design can only provide minor improvements [73].

George also presents an excellent study of the make-up of broadband noise generation for rotor blades [48]. In it, the three main sources of broadband noise are identified as inflow turbulence, trailing edge noise and tip vortex formation noise. Comparisons between theoretical predictions and experimental results show that inflow turbulence noise dominates at low frequencies (near 100 Hz) and trailing edge

and tip vortex noise become more important at higher frequencies [48]. Inflow turbulence may in fact be a major cause of noise from the tail rotor because much of its inflow consists of the highly turbulent main rotor wake.

To reduce the vibration and noise generated by helicopter rotor operation, various techniques from the field of control theory have been implemented. These are outlined in the next section.

## 1.2 Rotor Control

Helicopter rotor control can be used to reduce noise and vibration. Many devices have been implemented on helicopters to improve performance in these areas. Both passive and active control techniques have been studied extensively.

Passive control can provide moderate reduction of vibration with a low risk of instability. Passive devices are used in many operational helicopters by tuning their characteristics to filter out specific vibrational frequencies. Most are used in the helicopter cabin, but a few studies have investigated the use of passive devices on the rotor blades themselves [52, 5, 82, 12].

Because of the random nature of the helicopter aerodynamics in flight, it is expected that active feedback control will lead to greater performance benefits in comparison to passive control. Two general methods have been developed to implement active rotor control; higher harmonic control (HHC), and individual blade control (IBC). The difference between these two types of rotor control is in what each treats as the *plant*. Higher harmonic control applies inputs to the rotor system, treating the group of  $N$  blades as the plant. Individual blade control differs in that it treats each blade as a separate plant with independent feedback loops applied in the rotating frame [46, 39].

Note that individual blade control may be used for a number of purposes not suitable for HHC. In addition to attacking the problems addressed by HHC, using IBC, the designer may address additional problems such as gust alleviation, attitude stabilization, lag damping augmentation, flapping stability at high advance ratios and

individual blade tracking [39].

A number of experimental studies have been performed demonstrating the benefits of applying higher harmonic and individual blade control. One of the first studies in higher harmonic (or multicyclic) control was done by Kaman with their Controllable Twist Rotor (CTR) (discussed in more detail in Section 1.4.2). Full-scale wind tunnel tests of this rotor by Lemnios *et al.* [53] and McCloud and Weisbrich [57] showed that a mechanically controlled servo-flap in combination with a torsionally soft rotor blade could be used to redistribute the lift on the rotor disk and, through HHC, reduce the root flapwise bending loads.

Shaw *et al.* [69] applied higher harmonic control in a comprehensive wind tunnel study of a 1/6 scale CH-47D rotor demonstrating the possibilities of HHC. Using a swashplate controlled by electro-hydraulic actuators, with the ability to produce  $\pm 3^\circ$  of blade pitch motion at the 3/rev frequency (69 Hz), they were able to demonstrate a 90% decrease in vibratory shears at the hub (at the cost of a 20% increase in hub moments) or performance improvements of 4% and 6% less power at advanced ratios of 0.37 and 0.31, respectively. Nguyen and Chopra [61] performed an analytical study of the same rotor and confirmed many of these results.

The vibration control results of Shaw *et al.* were all obtained using fixed gain (as opposed to adaptive) controllers. The helicopter dynamics were well-behaved with changes in flight condition, so that the same fixed gain controllers could be used in many different flight regimes [69].

A number of rotor vibration and noise experiments have been performed in the German-Dutch Wind-Tunnel (DNW) by various European and U.S. researchers at DLR, NASA, MBB, and Aerospatiale. Kube performed HHC tests on a four bladed rotor with blade root actuators [49]. An important observation from this study was that 3/rev actuation was more effective than 4/rev or 5/rev actuation in reducing the 4/rev fixed frame vertical shear. This effectiveness was attributed to the fact that the 3/rev actuation excites the 1st and 2nd flapwise bending modes more than 4/rev or 5/rev excitation, significantly altering the rotor hub loads [49, 51].

In a follow-on study, Kube also compared fixed gain and adaptive controllers

and showed that a fixed gain controller has the robustness to remain stable over the entire flight envelope [50], which agrees with the results of Shaw *et al.* discussed above. Use of such a fixed gain controller will lead to faster controller response times in comparison to an adaptive controller, providing better helicopter maneuverability.

Rotor control studies were also performed in controlling impulsive rotor noise caused by BVI. Splettstoesser *et al.* conclude that blade vortex interactions represent a major proportion of rotor noise and vibration, where vortex strength, local blade lift and blade vortex separation distance all play a role in the level of noise/vibration created [73]. The results from this study, as well as follow on studies by Splettstoesser *et al.* [74], and Kube and Schultz [51] highlight a number of important conclusions regarding rotor noise control. First, BVI noise is most intense when the vortex impinges parallel to the blade leading edge. This tends to occur mostly in the first quadrant when the vortex generated near the 130° and 230° azimuthal positions impinge on the blade at the 35° azimuthal position. Control results show that by increasing the lift near the 100° and 260° azimuths, the increased downwash there pushes these critical vortices farther down, increasing the blade/vortex miss distance and thus reducing the noise generated [74, 51].

Simultaneous reduction of noise and vibration proved to be difficult. Part of the reason for this is that rotor noise seems to be mostly dependent on vortex miss-distance, while vibration is more dependent on blade deformation. Nevertheless, Kube and Schultz were able to simultaneously reduce BVI noise by 6 dB and vibration by 30% using 2/rev actuation [51].

### 1.3 Advantages of Blade Mounted Actuation

Both methods of active rotor control (HHC and IBC) use some type of actuator to affect the aeroelastic behavior of the rotor blades. Traditionally, active rotor control is achieved by using actuators mounted either at the swash-plate or on the pitch links to superimpose high frequency actuation signals on top of the primary collective and cyclic commands. This results in rigid-body pitch actuation of the blades. There are

a great number of benefits associated with placing actuators closer to the blade tip to produce spanwise varying blade displacements, summarized below.

**Vibration Control.** An analysis performed almost 30 years ago by Lemnios *et al.* addressed the effect of the built-in twist of a rotor blade on its aerodynamics [54]. They noted that the vibratory loads of a helicopter are a strong function of the blade twist. To minimize vibratory loads, a decreased negative twist is necessary on the advancing side while a simultaneous increased negative twist should be present on the retreating side. A torsionally flexible blade along with moment control inputs at the blade tip and root would accommodate such a twist schedule, significantly improving the vibration reduction ability of a rotor system. More recently, at MIT, Garcia and Hall [29] performed a linear state space analysis of an H-34 helicopter rotor equipped with blade mounted servo-flaps. The model included rigid blade flapping and elastic torsion. The results predicted control loads much less than those necessary for root pitch control in hover and forward flight. In parallel, a study by Millott and Friedmann [60] also reported that the power requirements necessary to twist a flexible blade and perform rotor vibration control are lower than those needed to perform full blade feathering control at the root.

**Noise Control.** The mechanisms behind rotor noise were described in Section 1.1. The majority of the rotor noise is caused by aerodynamic events on or near the blades. It is therefore plausible to expect that some sort of blade mounted actuation would be most effective in controlling noise. In particular, by definition, broadband noise is non-periodic in nature. Thus, such noise sources cannot be addressed via swashplate control and individual actuators on each blade are needed to address these types of non-harmonic control problems.

**Performance Control.** A study at MIT by Hall *et al.* [38] determined that actual rotor systems operate with induced power losses 14% greater than would exist given a maximum coefficient of lift,  $C_L$ , of 1.5 and the ability to prescribe a specific lift pattern over the entire rotor area. A spanwise varying pitch command could be used in this context to improve the efficiency of the rotor.

**Degrees of Freedom.** Ham [39] studied individual blade control at length. These studies showed that all of the benefits of individual blade control mentioned in Section 1.2 could be achieved to some degree using the conventional swashplate. However, since the swashplate only provides a maximum of three degrees of freedom, for rotors with four or more blades, less improvement is obtained by applying IBC with just the swashplate.

Placing one actuator on each rotor blade provides the necessary degrees of freedom to take full advantage of IBC algorithms. Of course, this could easily be achieved by using blade root actuators on the pitch links. However, the implementation of blade mounted actuators near the tip, by definition, would provide the additional facility to take full advantage of IBC algorithms.

Independent of this issue, the implementation of separate actuators on each blade could eliminate the need for the swashplate, according to Kretz *et al.* [46, 47]. This is desired because the swashplate is a coupling path between blades that leads to monocyclic pitch variations.

**Maintenance and Independence.** Finally, implementation of blade mounted active control would reduce the loads encountered by the hub components, lowering the maintenance costs of the rotor. Furthermore, if used purely for HHC or IBC, blade mounted actuation would not be considered a flight critical system. Actuator failure would not catastrophically affect the robustness of the flight vehicle.

In the past, using blade mounted actuators added either a substantial amount of weight or complexity to the rotor system design. Nevertheless, because there are so many benefits from placing an actuator in the rotating frame, the problem has been the subject of a number of studies. The next section provides a brief review of the actuation concepts that have been proposed and applied to this problem.

## 1.4 Previous Blade Mounted Actuation Approaches

In 1950 Carpenter and Paulnock first used blade mounted actuation via a trailing edge servo-flap driven by a hub mounted pitch link system [9]. Since then, numerous other rotor blade mounted actuation concepts have been proposed and implemented. Some very good surveys of these techniques have been presented by Straub [76], Strehlow and Rapp [81], and Friedmann [24].

Active materials were first suggested for active rotor blade control in 1989 [71, 72, 35]. The use of active materials for blade mounted actuation provides two additional advantages to those described in the previous section. First, the high bandwidth characteristics of the active material will improve closed-loop performance. Second, active materials are powered electrically. Electric actuation is preferred to hydraulic or pneumatic actuation because standard slippings and wiring could be used, simplifying the problem and reducing manufacturing and maintenance costs.

A number of concepts have been proposed for using active materials in rotor blade control. Two fundamentally different actuation concepts have emerged from the literature. These are termed *integral* and *discrete* rotor blade actuation.

The concepts of integral and discrete rotor blade actuation are described in the following sections. However, it should first be noted that the research in this thesis was performed as part of the Smart Structures for Rotorcraft Consortium (SSRC), which was a DARPA funded study investigating the development of blade mounted actuation. It was a collaboration between researchers from Boeing Helicopters, Penn State and MIT. One of the goals of this project was to address the question of whether integral or discrete actuation was better suited for rotor control by experimentally comparing state of the art versions of these two actuation concepts on identical rotor blade systems. The research in this thesis represents the discrete rotor blade portion of this project. The project described by Rodgers and Hagood [66] represents the sister study on integral rotor blade actuation. A brief comparison of these two concepts is given in Section 4.3.3.

### **1.4.1 Integral Rotor Blade Actuation**

In integral rotor blade actuation, active materials are either bonded to the surface of the rotor blade or integrated directly into the blade skin. Actuation forces are generated at  $\pm 45^\circ$  orientations to induce a torsional moment on the rotor blade. Typically, the actuators are distributed over the entire span of the blade, resulting in an effective torsional moment near the blade tip. This type of control has also been referred to in the literature as the Actively Twisted Rotor (ATR) concept [24]. Research on this type of rotor blade actuation has been performed at the University of Maryland by Chen and Chopra [11] and by Hagood at MIT and his collaborators [66, 84].

Hagood's approach is to embed active fiber composites (AFCs) in the rotor blade structure. The AFCs consist of piezoelectric fibers embedded in an epoxy matrix. They are integrated into the composite lay-up in a manner identical to that for the passive composite skin plies. Results from 1/6th Mach scaled hover tests of a CH-47D rotor blade incorporating these materials demonstrated a maximum tip twist of  $\pm 0.4$  degrees in hover [66]. Predictions from Boeing Helicopters and the results from other rotor control experiments indicate that tip rotations on the order of  $\pm 2^\circ$  are needed to perform adequate rotor control [69, 74, 68, 62]. Some problems in the manufacturing process of this blade limited the performance of the system. Research is ongoing at MIT and Boeing Helicopters to improve the actuation authority of this AFC rotor blade concept.

### **1.4.2 Discrete Rotor Blade Actuation**

In discrete rotor blade actuation, referred to in the literature as the Actively Controlled Trailing Edge Flap (ACF) [24], an actuator is embedded in the rotor blade structure and connected to a trailing edge servo-flap, located near the blade tip. The actuator is typically powered by a high bandwidth active material. High frequency deflections of the servo-flap induce aerodynamic lift and moment forces on the blade, which result in changes in rotor hub reactions.

There is some uncertainty whether the flap is best used to induce more of an aerodynamic moment, an aerodynamic lift, or a specific combination of the two to optimally excite the blade. Early uses of servo-flaps for rotor control combined torsionally soft blades with flaps operating in reversal. The aerodynamic moments from the servo-flap deflections lead to linear blade pitch variations [54, 53, 57]. Other researchers have relied more on the primary induced lift of the servo-flap for rotor control [40]. In fact, there has been some experimental evidence that the excitation of the elastic flapwise bending mode of the rotor blades is quite effective in controlling vertical hub shear [49, 51].

A great deal of research has been performed over the past ten years in developing an effective discrete rotor blade actuation system. The greatest challenge has been the development of a discrete actuator to adequately perform the servo-flap control. Appendix B provides a more detailed survey of actuator technology, but a brief introduction will be provided here.

Spangler and Hall first proposed trailing edge servo-flap actuation using a piezoelectric bender actuator [71, 72, 35]. The bender was used because it was an expedient method to amplify the active material stroke. Spangler and Hall demonstrated the feasibility of this actuation method through wind tunnel testing of an airfoil typical section. While they obtained appreciable flap deflections and force authority ( $\pm 6$  deg at 18.7 m/s test velocity), they found their design did not work entirely as expected due to hinge friction and backlash. Later work by Prechtl and Hall [64, 33] improved on this actuation concept by implementing a tapered bender and a flexural connection between the bender and the flap. Benchtop tests were performed on this actuation system demonstrating  $\pm 11.5^\circ$  flap deflections in still air [33]. Chopra *et al.* [83, 2, 45] have also investigated the use of piezoelectric bender actuators on Froude-scaled model rotors, and have begun testing of a Mach-scaled model rotor with these actuators.

Unfortunately, bender actuators have a number of limitations. Their placement in the rear of the airfoil imposes a severe weight penalty on the blade, since the bender mass must be counter-balanced with weight at the leading edge for aeroelastic

stability. More importantly, the energy density of current piezoelectric materials, using the  $d_{31}$  effect, required for bending actuation, is too low for effective flap-actuation in full scale or Mach-scale blades.

In contrast, the energy density of piezoelectric materials using the  $d_{33}$  effect is about sufficient for rotor control. The challenge has been in developing an efficient amplification mechanism to convert the small strains these materials produce (1000–2000  $\mu$ strain peak-to-peak) into usable motion. A number of researchers have developed actuators that amplify the motion of piezoelectric or magnetostrictive stacks.

Bothwell *et al.* used an extension-torsion coupling mechanism to amplify longitudinal motion to produce rotary motion [8]. Fenn *et al.* have also proposed a discrete actuator that uses two magnetostrictive expansive elements oriented at a shallow angle for geometric amplification [22]. Large stroke actuators based on amplifying active element stroke are also available commercially, *e.g.*, Physik Instrumente sells such a large stroke actuator [63]. The performance of each of these actuators is considered in Section B.1. Other researchers have developed actuators not specifically addressed in this thesis. For example, Giurgiutiu *et al.* have built an actuator using hydraulics to amplify active material motion [32]. Jänker *et al.* are developing two new actuator concepts, a planar Disc Actuator and a Hybrid Actuator using a piezoelectric stack and an inert frame amplification mechanism [43]. And, finally, Straub *et al.* have developed an actuator that is also designed for helicopter rotor control utilizing a mechanical amplification of the active material stroke [78].

Another challenge in developing a successful discrete rotor blade actuation system is in the design and experimental evaluation of a model scale active rotor. At the University of Maryland, a number of experimental investigations have been performed into ACF rotor blade research. Koratkar and Chopra, using the bender actuator, have performed Mach scaled tests of a rotor blade in hover [13]. Their results showed between  $\pm 6$  and  $\pm 9$  deg flap deflections at 2100 RPM for a 5% of span servo-flap. In addition, Lee and Chopra have developed a double-lever discrete actuator that uses a lever and fulcrum arrangement to amplify piezoelectric stack stroke. The output is connected to a trailing edge servo-flap for rotor control. Vacuum tests of

the actuator have shown that performance does not degrade appreciably at speeds up to 900 RPM, and wind-tunnel tests of an airfoil section incorporating the actuator show flap deflections of  $\pm 6$  at 120 ft/sec airspeeds for a 25% of chord and 4 inch long flap [13]. However, the compliance of the mechanism is very high resulting in a low actuator energy density.

Straub *et al.* have done a great deal of analysis and experiments relating to developing an active rotor blade controlled via a discrete actuator/trailing edge flap combination [80, 76, 79]. These studies identify the force/deflection predictions that are needed for primary and active rotor control using a trailing edge servo-flap.

In a related study, Straub describes a wind tunnel experiment of a rotor with cam-driven trailing edge servo-flaps in NASA Langley's 14  $\times$  22 Foot Subsonic Wind Tunnel. Using hub mounted cams of varying shapes, noise and vibration controls were addressed with peak to peak flap deflection inputs of up to 20 deg and 9 deg, respectively. The results highlighted the fact that the trailing edge flaps can significantly affect rotor noise and vibration [77]. An excellent comparison between analytical predictions and the experimental data from this rotor test is provided by Milgram *et al.* [59]. Comparisons of a comprehensive rotor model with actual wind-tunnel data provides an excellent method to analyze the effect of various parameters on system performance. This study highlighted that the effects of blade torsional flexibility and a free wake model were important in predicting performance.

Fulton and Ormiston have also performed some hover and forward flight open loop tests recently where a piezoelectric bender was used to control 10% of chord elevons on scaled rotor blades operating at reduced speeds [26, 27, 28]. For simplicity, an existing set of rotor blades was altered to incorporate the bender and modified trailing edge. This research represents a comprehensive investigation of the effects of using a trailing edge flap for rotor control. Elevon deflections in excess of  $\pm 5$  deg were obtained at full speed and the approximately 50% reduction in elevon angle between non-rotating and full speed conditions highlights the behavior of a properly impedance matched actuator. The induced torsional moment due to actuator operation in reversal was lower than usual, possibly because the low Reynolds number conditions led to an

unusually thick boundary layer, reducing actuator effectiveness [26]. Proper phasing of actuator frequency and phase showed large decreases in blade flapping moments in forward flight, indicating the usefulness of this actuation system for closed loop rotor blade control.

## 1.5 Thesis Overview

The fundamental objective of this research was to develop an active rotor blade using a discrete actuator to power a trailing edge servo-flap for rotor vibration control. The central element that was required to achieve this goal was the development of a discrete actuator that could satisfy the specified design requirements. This actuator, the “X-Frame Actuator,” was invented and two scaled versions of this actuator were manufactured and tested. In parallel to the actuator development efforts, requirements governing the design and manufacture of an active blade with a trailing edge flap were developed. Using these requirements, the prototype active blade was designed and manufactured. Finally, the active blade was hover tested to measure the performance of the designed system and closed-loop control tests were performed to evaluate the effectiveness of the actuation system in performing the designed task of vibration reduction. This thesis describes these developments.

Specifically, Chapter 2 describes the design of the X-Frame actuator. Experimental data is presented on the authority and sensitivity of the model scale or second generation actuator. Appendices A and B describe the background research performed on active material selection and actuator design that led to the X-Frame design.

Chapter 3 summarizes the design, manufacturing, and bench-testing of the active blade. This chapter presents the design of the blade in the face of the requirements for successful implementation into an operational rotor blade. In addition, the composite manufacturing of the active blade is presented. The chapter concludes by presenting validation data on the blade strength and non-rotating actuator performance.

Chapter 4 describes the Mach scaled hover tests performed on the active rotor

blades to identify the performance of both the actuation system and the entire active blade. The design of the MIT hover test stand is described along with the data collection techniques. A detailed analysis of the measured performance is presented, focusing on the frequency response of both the actuator alone and the discrete rotor blade actuation system. The chapter concludes with a presentation of some strength and reliability data for the active blade. Only the pertinent data traces that support the specific discussion are presented in Chapter 4. In support of this chapter, Appendix C contains the full set of transfer function data collected for the active rotor as a function of speed and angle of attack.

Chapter 5 presents the results from the closed-loop control applied to the active rotor. The development of the control algorithm as well as the development of the single harmonic and multiple harmonic controllers is presented. Specific results are given for the 4/rev controller and one multiharmonic controller. A comparison of the performance achieved for discrete and continuous time control is also presented. Appendix D contains the full set of data plots for all of the controllers implemented in this research.

Finally, Chapter 6 summarizes the results of this research. The contributions of this doctoral research are collected and recommendations for future work are given.

# Chapter 2

## The X-Frame Actuator

A new actuator, called the *X-Frame actuator*, has been invented to provide efficient amplification of active material stroke [34]. While it was developed for operation in a rotor blade, it is ideal for any engineering application requiring fast acting, large stroke actuation. The design and experimental characterization of this actuator is discussed in this chapter. Background information regarding its development is provided in Appendices A and B.

### 2.1 Actuator Requirements

The actuator was developed in consideration of the requirements associated with the operation of a trailing edge servo-flap on a helicopter rotor blade. In support of this study, Boeing Helicopters, through the use of their TECH-01 rotor analysis tool, identified the requirements that any actuator for servo-flap control must satisfy. They are collected here:

**Force:** The actuator must be able to react operational hinge moments.

**Stroke:** The actuator must be capable of  $\pm 5$  deg of flap motion.

**Mass:** The actuator should be light, with the actuation adding less than 20% to the blade weight.

**Bandwidth:** The actuator must have a bandwidth appropriate for higher harmonic control ( $> 4/\text{rev}$ ).

**Integration:** The actuator must fit within the blade spar for acceptable mass balance.

**Lifetime:** The actuator fatigue life must exceed 200,000,000 cycles.

**Environment:** The actuator must be able to perform in the operational load, vibration, and thermal environment.

The characteristics of the active material used to power an actuator play a significant role in its ability to satisfy these requirements. A survey of active materials was performed to identify the active material that best satisfies these requirements. The details of that survey are presented in Appendix A. This study led to the selection of piezoelectric ceramic, operating in the direct mode (*i.e.*, 33 actuation), for the blade mounted actuation experiments.

## 2.2 Mass Efficiency

To succeed in performing the required control task, the available output energy must exceed the energy needed as defined by the force and stroke requirements. Once the active material for a device is selected, it is the efficiency with which the material strain energy is transformed into useful work that determines the output energy. In this research a strong emphasis was placed on finding efficient stroke amplification strategies. In particular, because of the mass requirements intrinsic to rotor blade design and, indeed, to most aerospace applications, the standard definition of device efficiency was extended to reflect the trade-off in mechanism design between low weight and high efficiency.

In general, an amplification mechanism consists of an active element (or active elements), which provides the actuator force and displacement, and a support structure, which reacts the loads. Compliance in the support structure leads to mechanical inefficiencies in the actuator. The impact of frame compliance on actuator performance

is measured by the *mechanical efficiency* of the actuator, defined as

$$\eta_{\text{mech}} = \frac{\frac{1}{2}K_a q_f^2}{\frac{1}{2}E_e \epsilon^2 V_e} \quad (2.1)$$

which is the ratio of the actuation output energy to the active element energy. Here  $K_a$  is the stiffness measured at the actuator output,  $q_f$  is the free (unloaded) displacement corresponding to the induced strain,  $\epsilon$ , in the active element.  $E_e$  and  $V_e$  are the Young's modulus and volume of the active material element, respectively.

A straightforward way to increase the mechanical efficiency is to incorporate a very stiff frame. But such a frame would also be very massive. In applications where weight is important, it is preferable to sacrifice some mechanical efficiency in order to minimize weight. This tradeoff can be quantified by the *mass efficiency* of the actuator, defined as

$$\eta_{\text{mass}} = \eta_{\text{mech}} \frac{M_e}{M_{\text{tot}}} \quad (2.2)$$

Augmenting the mechanical efficiency with the ratio of active element mass,  $M_e$ , to total mass,  $M_{\text{tot}}$ , makes the mass efficiency a useful design metric reflecting the trade between frame compliance and frame mass. The mass efficiency can be thought of as the ratio of the specific work delivered by the actuator to the specific energy available in the active element.

Combining the required energy for a control task with the actuator mass efficiency and active material energy density gives an accurate estimate of the required actuation system mass. Optimum actuator design is largely focused on maximizing the product of actuator mass efficiency and material energy density.

## 2.3 Actuator Design Axioms

The mass efficiency metric was used to compare different active material actuation mechanisms that have been proposed in the literature. A survey of this field is presented in Appendix B. From this study a number of axioms were developed that can be used in consideration of the performance of a potential actuator. A successful

actuator will usually incorporate many, if not all, of them. They are collected here:

**Planar Actuators.** Planar actuators, such as the piezoelectric bender, do not offer a significant energy advantage over optimally designed stack/inert frame actuators, have manufacturing difficulties and lead to poor sectional CG characteristics.

**Coupling Mechanisms.** The use of coupling mechanisms is a deceptively inefficient amplification strategy.

**Flexures.** The use of flexures at the ends of high load active elements is an inefficient method of obtaining rotational degrees of freedom

**Bending.** Bending is a highly compliant method of carrying loads, such as in a lever and fulcrum design. Actuator designs where loads are transferred through components in bending should be avoided.

**Compressive Pre-Load.** To prolong active element lifetimes, it is imperative they stay in compression. Typically, this is done through a pre-load mechanism. Optimally, the pre-stress mechanism is placed in the actuation load path, performing the additional task of removing slop in load path joints and interfaces. Of course, compressive pre-stress values must be limited, in order to avoid compressively depoling the active material and to limit bearing stresses on articulating components.

**Self-Reacting Actuators.** By replacing the inert frame material that is used to react active material forces with other active material, larger mass efficiencies than those of stack/inert frame type actuators are theoretically possible. Such a design was pursued but later abandoned for a number of reasons, such as the fact that large stress concentrations occur at the interface between reacting elements, leading to actuator compliance. Furthermore, to keep the active material under compression, a complex pre-stress mechanism, outside the load path, is required for these actuators. Self reacting actuator designs, while theoretically efficient, do not offer much improvement over stack/inert frame designs and are complex to realize.

**Simplicity.** The actuator must be functional, meaning that the mechanism must be simple, for easy construction and to make it easier to debug. A complicated mechanism, while theoretically efficient, is often practically impossible to realize.

**Form Factor.** The actuator should be compact or take up minimal space. In addition, it should actuate displacements in a desired direction.

**Thermal Stability.** The actuator should be thermally stable. Its performance should not vary greatly with temperature. Actuators need to operate over wide temperature ranges. A helicopter rotor blade, for example, has a thermal survival range that spans 185 deg F.

**Linearity.** Linear operation is desired so that the actuator can be modeled with standard linear techniques and easily incorporated into linear feedback control systems.

## 2.4 X-Frame Actuator Operational Principles

The lessons learned from the actuator trade study led to the development of the X-Frame discrete actuator. An isometric drawing of the actuator is shown in Figure 2-1. This section presents the operational principles of the actuator.

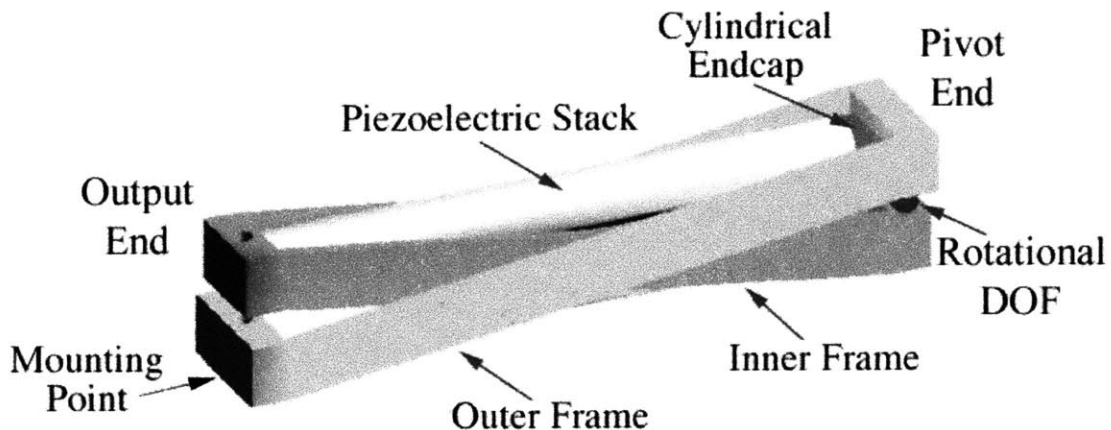


Figure 2-1: Isometric view of the X-Frame actuator concept

The actuator consists of two active elements simultaneously extending against two

frames. In this research piezoelectric stacks were used for the active elements and the frames were machined out of steel. Each frame consists of two end plates connected by two side members, running adjacent to the active elements. The frames are denoted as the inner and outer frames. The width of the inner frame is small enough to fit within the outer frame. At one end of the actuator, referred to as the *pivot end*, a rotational degree of freedom allows for the two frames to pivot with respect to each other while maintaining the distance between the frame end-plates. This rotational degree of freedom can be accomplished with a dowel pin or a flexure. Stack extension and resultant frame rotation creates relative linear displacement between the frames at the opposite end of the actuator, referred to as the *output end*. As the stacks expand, the frames pivot about the rotating degree of freedom and pinch together at the output end. By fixing the output end of the outer frame, all of the displacement is realized at the output end of the inner frame. The small angle of the frame side members relative to the stack axes leads to a geometric stroke amplification. For the actuator used in this research, this angle was designed to be 7.1 degrees, leading to an amplification factor of 16.

The operational characteristics of the actuator are easily understood through the use of a simple truss model, as shown in Figure 2-2. In this figure, the solid line

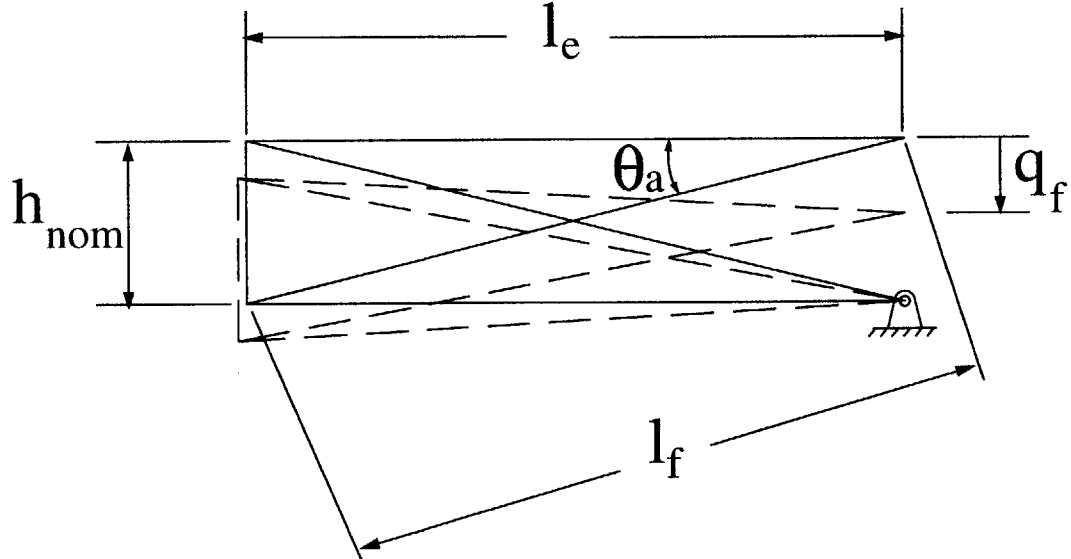


Figure 2-2: Simple truss model of X-Frame actuator

represents the undeformed actuator configuration and the dashed line represents the displaced position of the truss members due to elongation of the stacks. The stacks are represented as horizontal members of length  $l_e$ , and the frames as diagonal members of length  $l_f$ . The two frames are coupled by a vertical member at the pivot side of the actuator, of length  $h_{\text{nom}}$ . The linearity of the device is due to the fact that the length of this horizontal member and, therefore, the angle  $\theta_a$  in Figure 2-2, does not change appreciably during operation. The free amplification of the X-Frame actuator is found by solving, geometrically, for the displaced equilibrium of the truss given an induced stack extension. The exact free displacement is given as

$$q_f = -\frac{2l_e}{h_{\text{nom}}} \left(1 + \frac{\epsilon}{2}\right) (\epsilon l_e) \quad (2.3)$$

Note that the derivation assumes that no stack end-caps are present. Equation (2.3) is an exact relationship and quantifies the linearity of the device, due to the weak dependence of the amplification on the induced strain.

Using the principle of virtual work [7], the output compliance of the truss in Figure 2-2 is

$$\frac{1}{K_a} = \frac{2l_e}{(\tan^2 \theta_a) E_e A_e} + \frac{2l_f}{(\sin^2 \theta_a) E_f A_f} \quad (2.4)$$

Note that only the compliance of the stacks and the adjacent frame side-members are included in this expression; the contribution of the horizontal member,  $h_{\text{nom}}$ , was neglected. In practice, this member as well as various other components add compliance to the system.

The X-Frame actuator design successfully integrates many of the optimal discrete actuator design axioms outlined in Section 2.3. First of all, the actuator design is uncomplicated. No flexures are used and the loads are predominantly transferred through axial loads in the frames and stacks. Because of this, the actuator retains a relatively high mass efficiency. Numerical optimization of this design, assuming perfect rolling contacts between stack and frame, yields a maximum achievable mass efficiency of 50%, matching that predicted by Equation (B.24) for steel frames and piezoelectric stacks.

The form factor of the actuator is very good, such that a large stroke amplification is obtained with a relatively compact structure. In fact, the entire package is naturally suited for placement inside a rectangular cavity, such as a rotor blade spar. This compact design also allows for large amplifications without substantial risk of buckling the stacks. Furthermore, because the amplified motion occurs transverse to the stack axes, the actuator is also ideally suited for the rotor blade application. The stacks are aligned with and kept in compression under the centrifugal field in the rotor blades while the output motion occurs naturally in the chordwise direction.

The actuator is easily scaled for different applications. The amplification of the actuator is solely dependent on the angle the frames make with the stacks at the output end of the actuator. Upon scaling, as long as this angle remains constant, *i.e.*, as long as all dimensions scale proportionally (geometric scaling), the amplification will remain constant. For example, micro-machining techniques could be developed to construct a miniature X-Frame actuator. Or, conversely, the actuator can be scaled for larger applications, *e.g.*, incorporation into a full-scale CH-47D rotor blade for servo-flap control.

## 2.5 Model Scale X-Frame Actuator Design

The actuator has been developed through two generations of design and testing. The testing and analysis of the first generation actuator, referred to as the “proof-of-concept” actuator, is given in Appendix B. The second generation actuator was designed specifically to operate in the 1/6 Mach scaled CH-47D rotor blades. The design of this actuator is described in this section.

A drawing of the model scale actuator is shown in Figure 2-3. Two lead magnesium niobate - lead titanate (PMN-PT) stacks are used to power the X-Frame actuator. The stacks were purchased from the EDO Corporation. The exact material configuration is designated as EC-98 by EDO. PMN-PT is an electrostrictive material (PMN) doped with enough lead-titanate (PT) to give the material a dominate piezoelectric (sign dependent) strain characteristic. The specific material characteristics for the

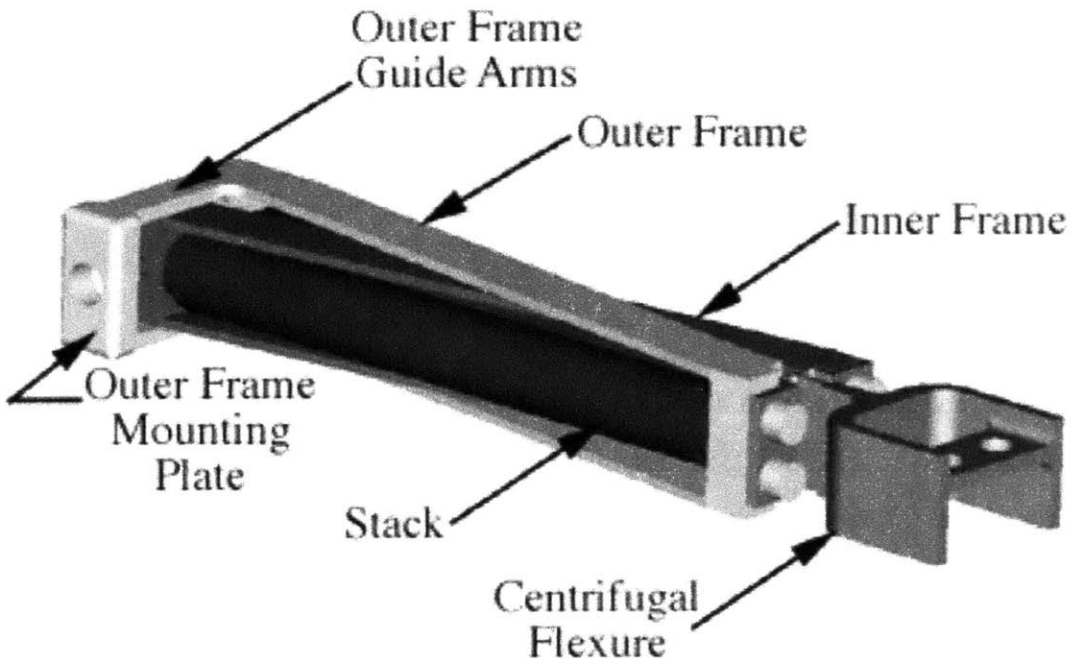


Figure 2-3: The model Scale X-Frame actuator

bulk EC-98 material and for the model scale stacks are given in Table 2.1 and 2.2.

Table 2.1: Bulk properties of EC-98

Catalog $d_{33}$	$730 \times 10^{-12} \text{ m/V}$
Density	$7850 \text{ kg/m}^3$
Modulus	$6.87 \times 10^6 \text{ psi}$

The stacks consists of 90 layers that are nominally 0.0221" thick. Each layer consists of a thin disk of piezoelectric material that is 0.0208" thick, an electrode that is 0.001" thick and two bond layers that are each 0.00015" thick. According to EDO, the compliance from the bond layers reduces the modulus of the stacks to approximated 70% of the bulk material [14].

The  $d_{33}$  constant for EC-98 material is  $2.874 \times 10^{-5} \text{ mil/V}$  ( $730 \text{ pm/V}$ ). Thus, a 57.4 V/mil electric field will induce a 1650 microstrain in the active material. Because large negative fields can cause heating and/or depole the EC-98 material [14], a DC offset was used to achieve this electric field level. Thus, the maximum operational

Table 2.2: Properties of manufactured EC-98 stacks

Serial Number	S/N 004	S/N 005
$d_{33}$	$736 \times 10^{-12} \text{ m/V}$	$706 \times 10^{-12} \text{ m/V}$
Mass	10.02 g	9.94 g
Modulus	$4.81 \times 10^6 \text{ psi}$	$4.81 \times 10^6 \text{ psi}$
Diameter	0.200 in	0.200 in
Length	2.096 in	2.094 in
Capacitance	113.6 nF	112.1 nF

voltage signal consisted of a  $400V_{DC}$  bias with a  $\pm 600V_{AC}$  sinusoidal excitation. (This will be referred to as  $1200V_{pp}$  actuation) The EDO recommended maximum operating voltage signal for these stacks consists of a  $400V_{DC}$  bias with a  $\pm 400V_{AC}$  sinusoidal excitation (referred to as  $800V_{pp}$  actuation). Larger than recommended applied voltages were used in order to meet the energy requirements of the application. Previous experience with piezoelectric ceramics indicated that the extended operational voltage range could be achieved with minimal risk.

Spherical endcaps are used at the ends of each stack to keep loads aligned predominantly with the axis of the stacks. To avoid excessive losses due to Hertzian contact effects, the radius of each endcap was set relatively large at 1 inch. Small holes were bored into the center of each stack to allow for tapered steel alignment pins to interface with the stacks. These pins are used for alignment but also help retain the stacks in high transverse acceleration environments, such as in rotor blades.

The outer frame differs slightly from the shape of the inner frame, in that it includes guide arms and a mounting plate at its output end. The output end of the inner frame slides between these guide arms during operation. These guides both keep the two frames aligned with each other and react transverse forces on the inner frame.

At the pivot end both frames are bolted to a part called the *Centrifugal Flexure*. This part consists of three flexures, as shown in Figure 2-4. Two of the flexures, labeled *Pivot Flexures*, simply provide the rotational degree of freedom discussed above for actuator operation. The third flexure, labeled *CF Flexure*, provides a

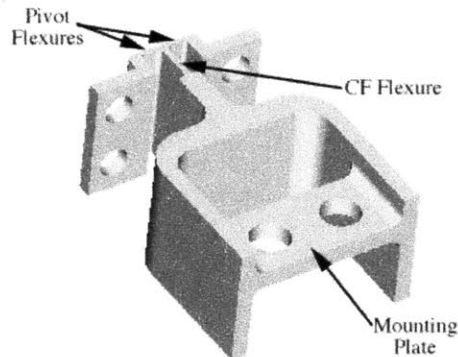


Figure 2-4: Detailed view of centrifugal flexure

rotational balance point for the entire actuator in the centrifugal field. This balance point acts like the center of a see-saw, equilibrating the load on the two stacks. Maintaining approximately equal loads on the stacks will minimize the possibility of compressively depoling a stack due to mis-alignments in the centrifugal field.

All frame components were machined out of steel using wire electron discharge machining (EDM). Picture of the actuator components in an exploded and assembled configuration are shown in Figures 2-5 and 2-6, respectively.

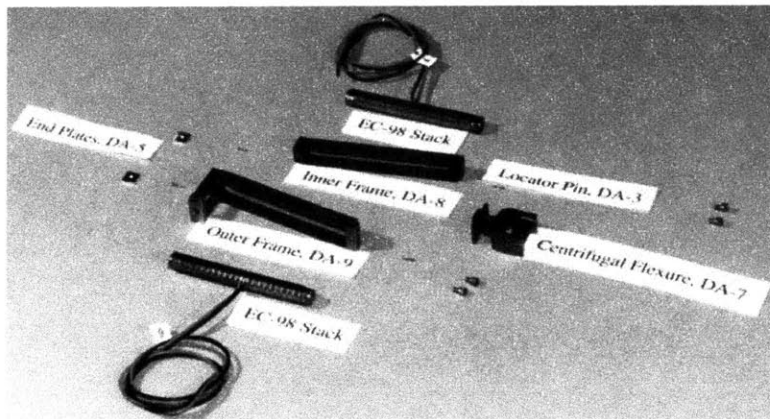


Figure 2-5: Exploded view of the model scale X-Frame actuator

## 2.6 Actuator Validation Experiments

The performance of the actuator was measured under varying conditions. Three tests are presented. First, the quasi-static operation of the actuator was measured. Actuator performance is monitored by studying the deflection versus voltage characteristic and the actuator characteristic load lines. Second, the actuator was tested on a shake table, to simulate the out-of-plane loads that would be encountered by a blade-mounted actuator due to unsteady aerodynamic loads. Finally, the actuator was tested to determine its frequency response. The experimental setup and results are described below.

### 2.6.1 Quasi-Static Actuator Testing

To test the quasi-static performance, the actuator was mounted on the bench top. A picture of the experimental set-up is shown in Figure 2-7. The outer frame mounting plate butts up against a large steel truss. A clearance hole allows for a control rod to pass through the steel truss and screw into the inner frame. The control rod is attached to a piano wire which runs approximately 5 feet down the bench top and over a pulley to a 19 lb mass, providing a constant pre-stress on the actuator. Two dowel pins are placed under the steel truss to support its weight and ensure all actuation loads are transferred back to a load cell. By clamping the piano wire at a number of locations along the table, loads of varying impedance are simulated at the output of the actuator.



Figure 2-6: Assembled model scale X-Frame actuator

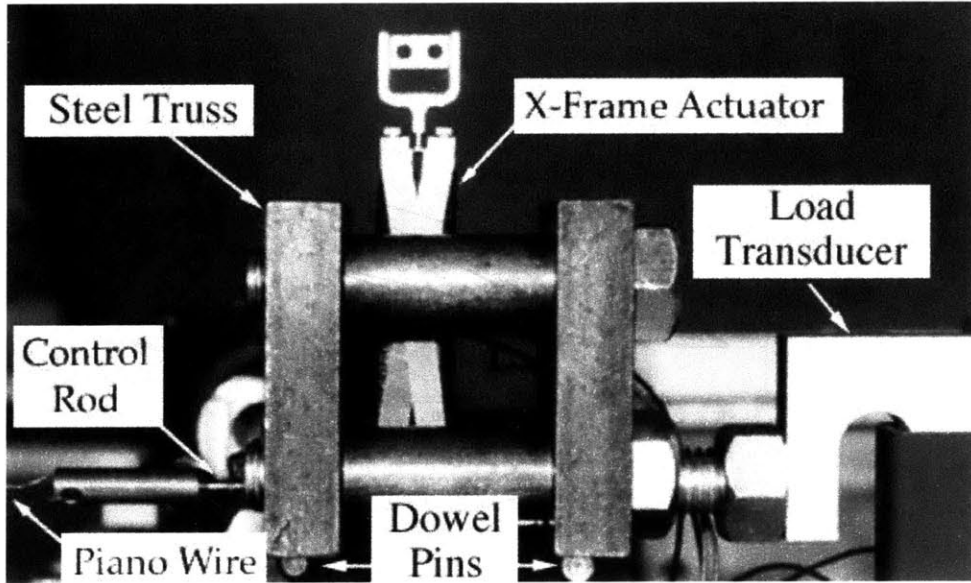


Figure 2-7: X-Frame actuator bench test set-up

The actuator is driven using a Kepco Bipolar Operational Power Supply Amplifier, Model BOP1000M. The deflection of the actuator was measured by interferometry using a Zygo Axiom 2/20 laser. The load transducer was an SM-100 Interface 100 lb Load Transducer. Both these measurements and the voltage into the stacks were monitored using a Labview Data Acquisition system. The actuator was run quasi-statically with a sine wave at 1 Hz. A  $50 \text{ Hz} \pm 15 \text{ V}$  dither signal was superimposed on the stack input voltage to alleviate slight frictional effects due to the sliding interface between the inner frame and outer frame guide arms. At each operating point 3 seconds of data was stored, containing 200 data points with 10 point oversampling.

Figure 2-8 shows the time response of the actuator in the free and near impedance matched configurations at two different field levels. Two important operational characteristics are highlighted from this data. The first noticeable characteristic is the non-trivial level of hysteresis. From the data, the hysteresis appears to be directly related to the deflection of the material. Thus, the hysteresis is much smaller when driving an elastic load, such as in the servo-flap control application. Hysteresis is undesirable because it can cause substantial heating in the material, adds phase lag to the dynamic characteristics and can lead to problems in static applications, such as blade tracking for helicopter rotor systems. The latter two problems can be overcome

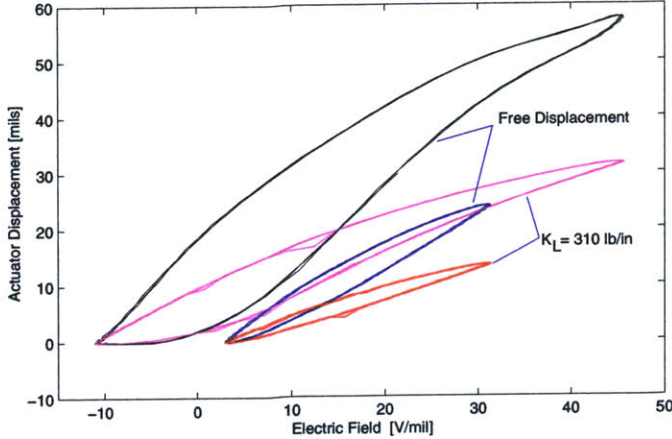


Figure 2-8: Quasi-static time response

by closing simple feedback loops around the active materials; but the heating due to this phenomenon would still be present [16].

The second trend to notice from the data in Figure 2-8 is that the maximum deflection more than doubles for both the free and loaded case upon doubling the applied peak-to-peak electric field. This behavior is related to the field-dependent nonlinear strain behavior of the EC-98. This nonlinear behavior is discussed at length in Section B.2.2.

Section B.2.2 presents a discussion on the load dependent behavior of actuators and on the impedance matching concept. Characteristic actuator load lines, such as those described by Equation (B.27), are found by measuring the actuator deflections while driving loads of varying elastic stiffness. How close this data approaches the linear model of Equation (B.27) gives a good measure of the actuator's linearity and stiffness properties. Varying stiffness loads were simulated by clamping the piano wire, shown in Figure 2-7, at different locations along its length. The actuator was operated at each of these clamping conditions at 12 different applied field levels. The characteristic load lines from this data are shown in Figure 2-9. Each line corresponds to a different driving field level, noted on the left side of the plot.

Over most of the operating range each force/stroke characteristic follows a linear trend, as shown by fitting the dashed line to the outermost actuator characteristic. This linearity is especially important at the center of the operating range ( $\frac{1}{2}Q_{ab}$ ,  $\frac{1}{2}q_f$ ),

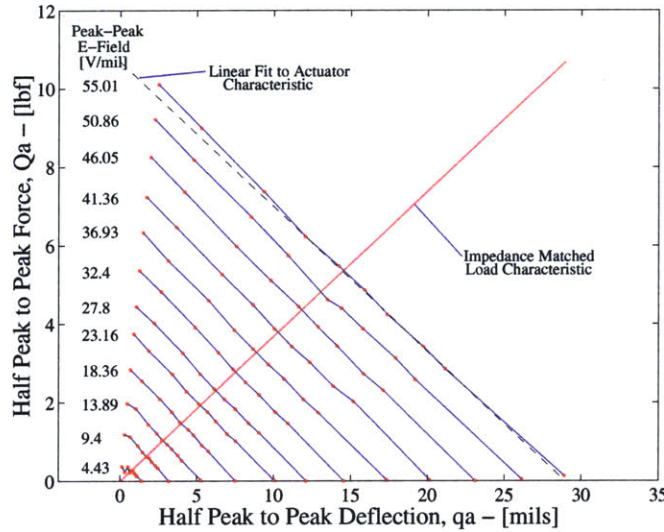


Figure 2-9: Quasi-static experimental load-lines

where an impedance matched load would operate having a force characteristic similar to the solid line noted in Figure 2-9 as the “Impedance Matched Load Characteristic”. The intersection of the load characteristic with the actuator characteristic determines the actuator operating point. Notice that the two intersect within the substantially linear range of the actuator.

Comparing the fit of the outermost force/deflection characteristic to the “linear fit” highlights two nonlinear operating regimes for the actuator near the free (zero force) and blocked (zero deflection) boundaries. Larger deflections than predicted are realized at the blocked boundary condition because the stacks are under their largest compressive force at that point. The compressive force hardens the bond layers in the stacks, stiffening the actuator, leading to larger actuator deflections. The nonlinearity at the free boundary condition is a result of the field dependent nonlinear characteristic of piezoelectric ceramics, discussed above.

Because the designed operating point is located away from these two nonlinear regimes, they should not significantly affect the performance. However, it is important to realize this nonlinear effect (especially at the free stroke operating point) when trying to extrapolate performance of systems incorporating piezoelectric ceramics.

The actuator energy is found by taking the area under the dashed line fit to the

outermost load line. This dashed line intersects the axes indicating a linear peak-to-peak blocked force of 21.4 lbf and free peak-to-peak deflection of 57.9 mil, yielding a peak-to-peak output energy of

$$W_a = 0.618 \text{ in-lb} \quad (2.5)$$

The mass of the entire actuator prototype is 0.0027 slug (39 g), giving the actuator output energy density as

$$U_a = 19.3 \frac{\text{ft-lb}}{\text{slug}} \quad (2.6)$$

In order to get good estimates of the mechanical and mass efficiency of the device, load lines, similar to those in Figure 2-9, must be obtained for the individual stacks. Then a direct ratio of the areas under lines of comparable electric field for the actuator and the stacks would yield the mechanical efficiency of the device. Unfortunately, at the time of these experiments, no reliable method existed to collect this type of stack data. Recently, a component tester has been developed at MIT by Lutz and Hagood that would allow for exactly such a measurement to be made [56] and future work should focus on performing this measurement.

Because of the uncertainty with the performance of the raw stacks, at best, a range of efficiencies can be provided for the actuator, depending on what value is used for  $d_{33}$ , and how we account for stack bond layer losses and additional mass. The detailed steps for calculating the upper and lower bounds for the “proof-of-concept” actuator efficiency bounds are presented in Section B.2.2. For the model scale actuator, these upper and lower efficiency bounds are given in Table 2.3. The values predicted using

Table 2.3: Comparison of efficiency bounds for model scale X-Frame actuator

Method #	$\eta_{\text{mass}}$	$\eta_{\text{mech}}$
1	23.8%	61.2%
2	44.8%	87.4%

the second method, where all losses due to the stacks are excluded, are very close

to the theoretical optimum. The reason for this is most likely that the stacks are providing more strain than predicted and bond layer losses in the stacks may not be as great as predicted. Therefore, until independent load line data for the stacks is obtained, we cannot put a great deal of confidence on these efficiency calculations.

The blocked force and free deflection above imply a model scale actuator stiffness of 369 lb/in. Using the geometric properties of the actuator given in Section 2.5, Equation (2.4) yields an expected actuator stiffness of 400 lb/in. The experimental stiffness is expected to be lower due to additional compliance in the device from unmodeled Hertzian losses, end-plate flexing, and slight bending of the stacks. Of course, because we have no independent stack data, it is difficult to narrow down the distribution of compliance from these various components.

### **2.6.2 Dynamic Actuator Testing**

To perform dynamic actuator tests, an apparatus was constructed that allowed the actuator to be operated at high frequencies and on a shake table, while simulating as much as possible the conditions that the actuator experiences in the blade. A picture of this testing apparatus is shown in Figure 2-10. In particular, inboard and outboard actuator restraints were manufactured identical to those designed for the active blade, except for flanges necessary to mount them to the apparatus. These restraints will be discussed again in Chapter 3 but, briefly, the outboard restraint provides a platform to which the actuator centrifugal flexure is bolted and the inboard restraint provides a sliding restraint for the actuator. To simulate the load of the flap, a pushrod is connected between the inner frame output and a steel load flexure with stiffness matching the expected aerodynamic hinge stiffness of the flap. Note that the inertia of the flap was not incorporated into the apparatus, which has implications for the frequency response testing later.

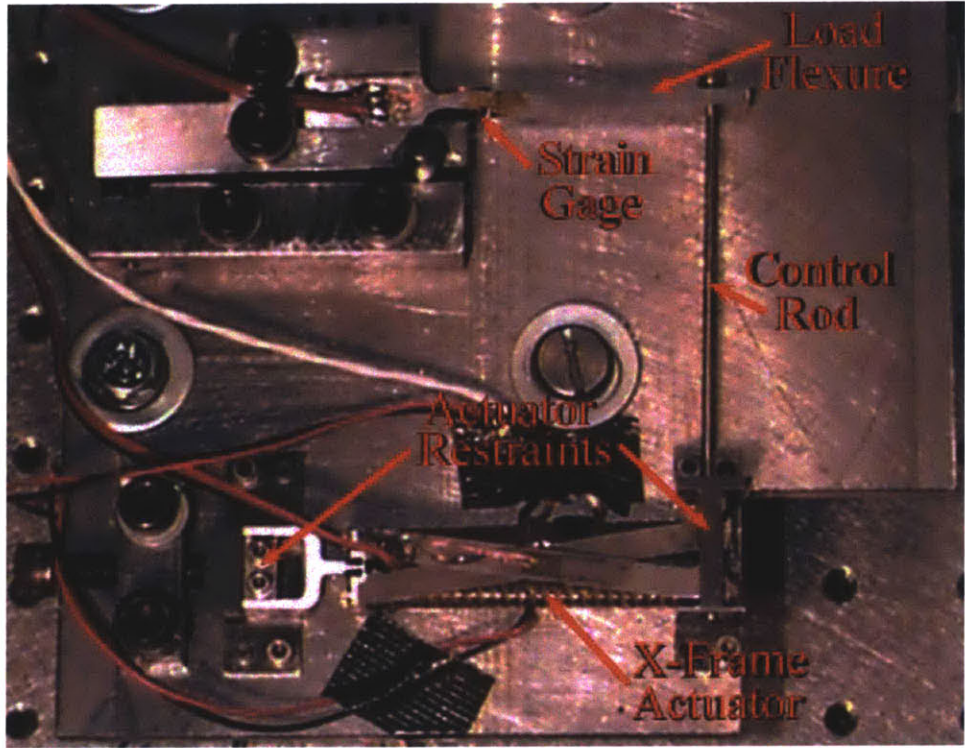


Figure 2-10: X-Frame actuator dynamic testing apparatus

### Transverse Vibration Testing

One issue of concern is whether a blade-mounted actuator is sensitive to blade accelerations. Such a sensitivity can take two forms. First, the actuator may have induced deflections due to acceleration, which would produce an undesirable (perhaps even destabilizing) coupling between blade motion and flap deflection. Second, blade accelerations may cause the actuator to have reduced performance. For example, increased friction due to inertial forces might reduce the output deflection. In a typical rotor, the highest (unsteady) accelerations by far occur in the out-of-plane direction. Therefore, the X-Frame actuator was tested for acceleration sensitivity by simultaneously operating the actuator while shaking in the out-of-plane direction at the frequencies and amplitudes that would occur in forward flight, appropriately scaled to the model rotor. A picture of the actuator mounted to the shake table is shown in Figure 2-11.

The actuator was operated under four different rms acceleration amplitudes (7.1g, 14.5g, 43g, and 69g); four different acceleration frequencies (22.5 Hz, 45 Hz, 67.5 Hz,

and 135 Hz); and four different actuation frequencies (3 Hz, 22.5 Hz, 45 Hz, and 67.5 Hz). In addition, the actuator was operated prior to and after shake testing with no acceleration. In all, 48 test runs were performed.

Figure 2-12 shows the results from two of the tests, which are roughly the two extreme cases. The plot on the left shows actuator excitation at 3 Hz, with no shaking. The plot on the right shows the result with the same excitation and acceleration at 69g rms amplitude and 45 Hz frequency. In the two cases, the time responses of the actuator are nearly identical. The peak-to-peak amplitude of motion is the same, as is the amount of hysteresis due to material properties. The only slight difference visible is that in the case with shaking there is a very small ripple visible, apparently at 90 Hz. We believe that this is due to the side members of the frames bending at 45 Hz, which produces foreshortening with fundamental frequency at 90 Hz. In any event, the ripple is small and is only noticeable in the highest acceleration cases.

The results in Figure 2-12 are typical. That is, all 48 cases have similar time traces, except for a slight frequency-dependent amplitude variation, probably due to material properties. The results of all test cases are shown in Table 2.4.

## Frequency Response

Finally, the transfer function of the actuator was determined. Figure 2-13 shows the frequency response for the actuator in the shake test apparatus. The deflection of the actuator was measured using a strain gage attached to the load flexure, which had been calibrated using a laser interferometer.

In addition to the frequency response due to random excitation, the data points from the shake test actuation at varying frequencies are plotted by the circles in Figure 2-13. Note that these individual frequency tests match the frequency response, as expected.

The frequency response is very nearly second order, with natural frequency at about 650 Hz, and lightly damped. There is slightly increased phase lag in comparison to a second-order system, due to material hysteresis. Of course, in the rotor blade, because of the inertia of the servo-flap, the first mode of the rotor blade actuation

Table 2.4: Shake Test Data. All cases were performed with stack voltage amplitudes between 390.5 V and 396.5 V amplitude. The deflection data in this table is linearly scaled to obtain the deflection at 400V amplitude.

Shake Amplitude (g)	Shake Frequency (Hz)	Actuation Frequency (Hz)			
		3	22.5	45	67
0	0	15.30	14.65	14.50	14.51
7.1	22.5	15.05	14.44	14.30	14.28
	45.0	15.11	14.48	14.33	14.28
	67.5	15.12	14.51	14.33	14.29
14.5	22.5	15.05	14.44	14.27	14.22
	45.0	15.13	14.55	14.30	14.29
	67.5	15.16	14.56	14.34	14.31
	135.5	15.18	14.55	14.37	14.39
43.0	45.0	15.09	14.50	14.19	14.12
	67.5	15.09	14.52	14.31	14.31
69.0	45.0	15.08	7.01 <sup>a</sup>	7.09 <sup>a</sup>	6.95 <sup>a</sup>
0	0	15.10	14.48	14.33	14.28

<sup>a</sup>For these cases, the leads to one of the two stacks in the actuator were inadvertently disconnected. As a result, the amplitude of the response is approximately one-half that of the other cases.

system will be significantly lower than 650 Hz; but these results demonstrate the high bandwidth characteristics of the raw actuator.

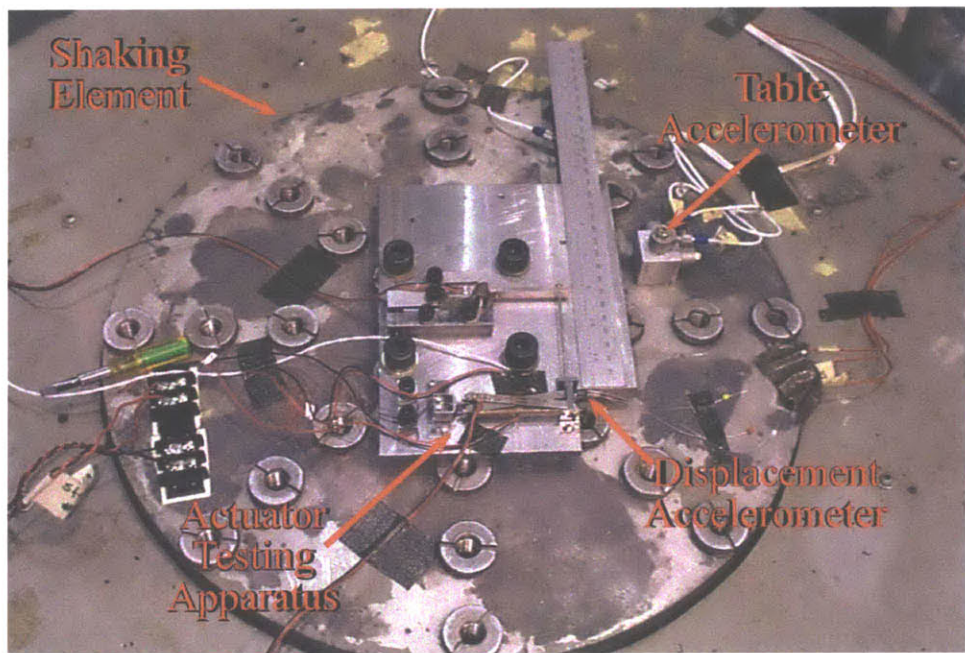


Figure 2-11: X-Frame actuator testing apparatus mounted to shake table

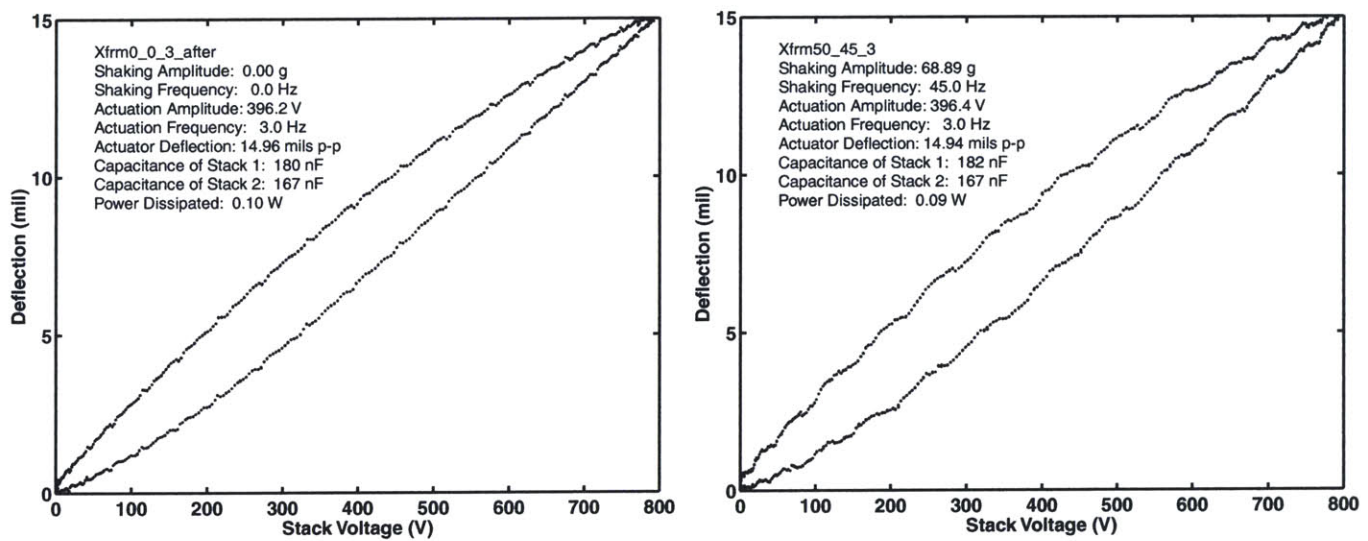


Figure 2-12: Shake Data

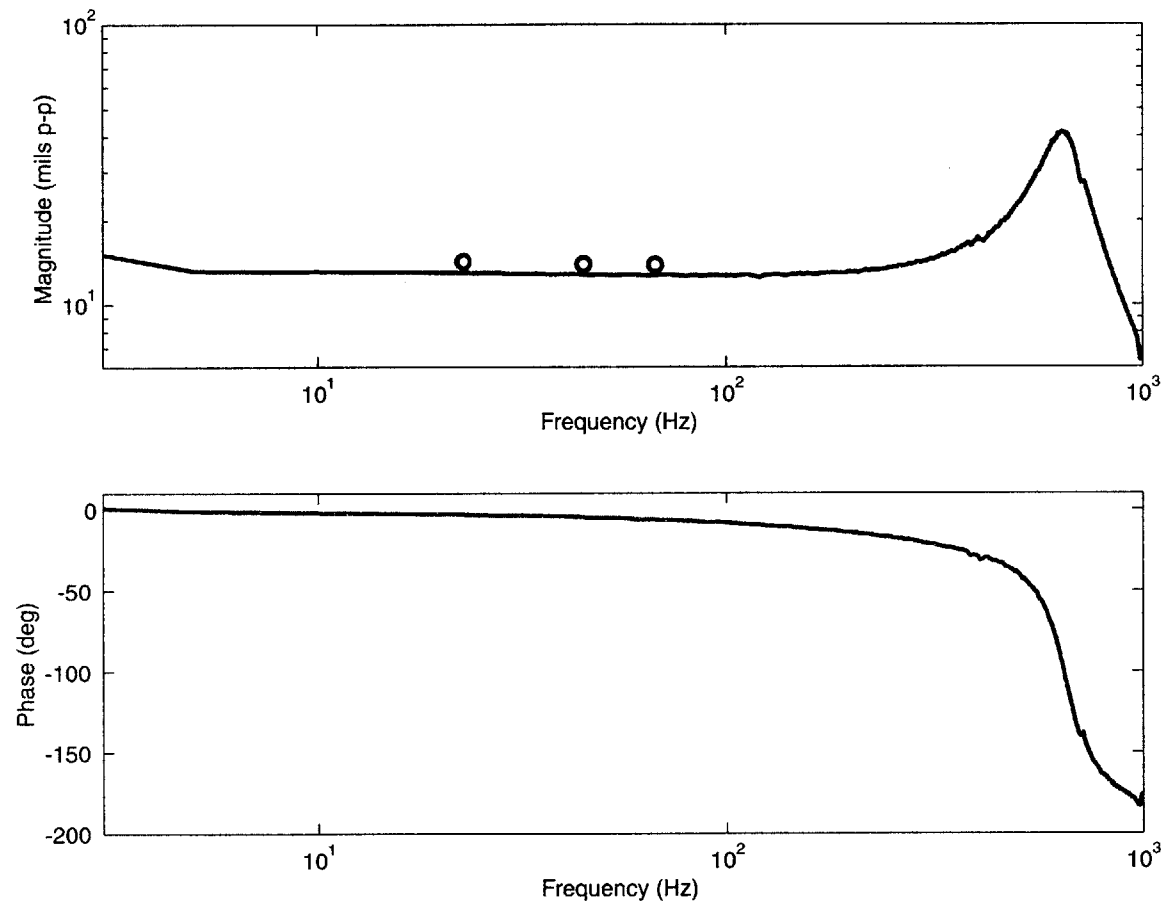


Figure 2-13: Frequency response of actuator in shake-test apparatus, with random excitation.

# **Chapter 3**

## **Active Rotor Blade Design, Manufacture and Bench-Test**

A 1/6<sup>th</sup>, Mach scaled CH-47D rotor blade has been built that incorporates an X-Frame actuator to control a trailing edge servo-flap. This chapter addresses the design, manufacturing, and bench-tests of this active blade.

### **3.1 Active Rotor Blade Design**

The base design of the rotor blade was provided by Boeing Helicopters. Modifications were made to the blade design and manufacturing procedure to incorporate the actuator and servo-flap while satisfying a number of system requirements. One of the most important goals in setting these requirements was to keep the actuation system largely decoupled from the overall blade structure. In doing so, the majority of the design effort was expended on the actuation system and this section is focused primarily on describing this design. The design modifications made to the overall blade structure are addressed in Appendix E.

This section begins by listing the design requirements. Then the final system design is described to introduce the name and function of the various system components. This section is followed by a presentation of the method used to estimate the various aerodynamic coefficients and an overview of the compliance and strength

modeling used for the system. Using an estimate of the actuation system stiffness parameters, an estimate is provided of the expected quasi-static servo-flap actuation performance. The section concludes with a description of the blade instrumentation used to measure actuator and blade response for the hover tests.

### 3.1.1 Active Rotor Blade Design Requirements

To guide the active blade design process, a number of requirements were established for the active rotor blades. These requirements are:

- Separable** The actuator must be inserted in a nearly complete blade. Laying up the rotor blade around a discrete actuator would unnecessarily complicate the blade manufacturing procedure.
- Accessible** The actuator must be accessible in case of failure to allow for periodic upgrades and repairs to the actuator. If the actuator fails, it can be replaced independent of the rotor blade.
- Pre-load** There must be a pre-load mechanism for two reasons. The first is to keep the active material in compression at all times for longevity. The second is to remove backlash from the actuation system.
- Adjustment** There must be an adjustment mechanism so that the servo-flap can be trimmed upon installing the discrete actuator.
- Independence** The actuator should not rely heavily on the rotor blade to carry actuation loads. If a compliant member in the blade is used to carry loads, such as the blade fairing, much of the actuation energy will be lost there. If a stiff member of the blade is used to mount the actuator in two or more separate locations, vibration of that member will tend to *actuate* the actuator.
- Mass** All components included in the design should be light, designed in a mass efficient sense.

- Integrity** The actuator centrifugal loads must be reacted.
- Balance** The centripetal loads on the actuator must be evenly distributed between active material elements to avoid compressive depolarization.
- Vibration** The actuator must be constrained in out-of-plane and lead-lag directions.

These requirements embody the active rotor blade design constraints. By satisfying the requirements, a successful actuation system that is minimally dependent on the blade structure will result.

### 3.1.2 Actuation System Design

The design of the entire system assembly was done through the use of the solid modeling software program, ProEngineer (ProE). Multiple iterations were performed to design the system components to operate within the aerodynamic, centrifugal, and actuation loading environment associated with rotor operation. This section provides a full description of the final design of these actuation system components.

A rendering of the ProE model of the actuator and trailing edge control system is shown in Figure 3-1. Note that the skin of the servo-flap is rendered with a slight transparency to highlight the presence of the flap horn, keymount, and pre-stress wire in the interior of the flap. Additional views of the Active Rotor Blade are given in Appendix E.1.

Two restraints are used to mount the actuator within the rotor blade spar. Figure 3-2 provides a detailed view of the interface between the actuator and the spar restraints. The tip end of the actuator is bolted to the *outboard spar restraint*, constraining that end in the flapwise, chordwise and spanwise directions. At the root side, the actuator is restrained in the chordwise and flapwise directions via a sliding interface between the outer frame and the *inboard spar restraint*. A sliding degree of freedom is allowed in the spanwise direction so that both stacks are allowed to

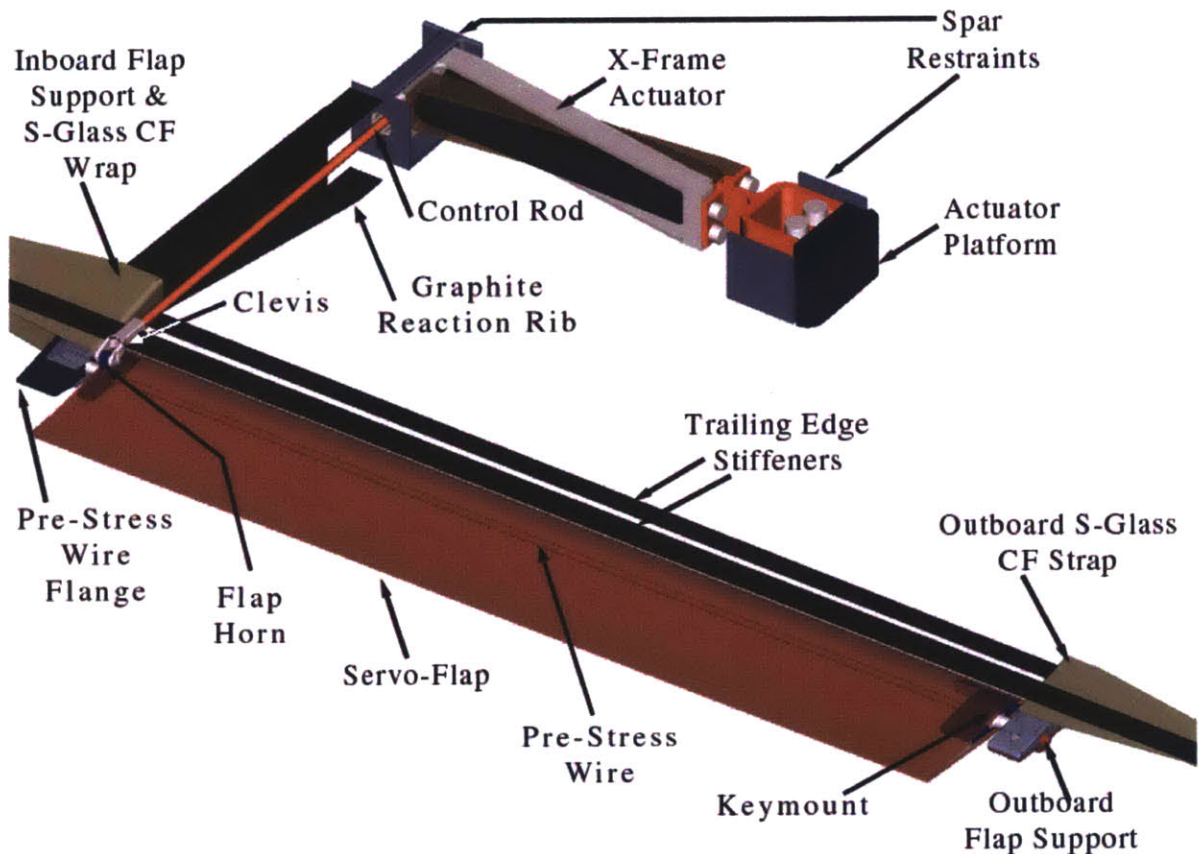


Figure 3-1: Rendering of rotor blade servo-flap actuation system

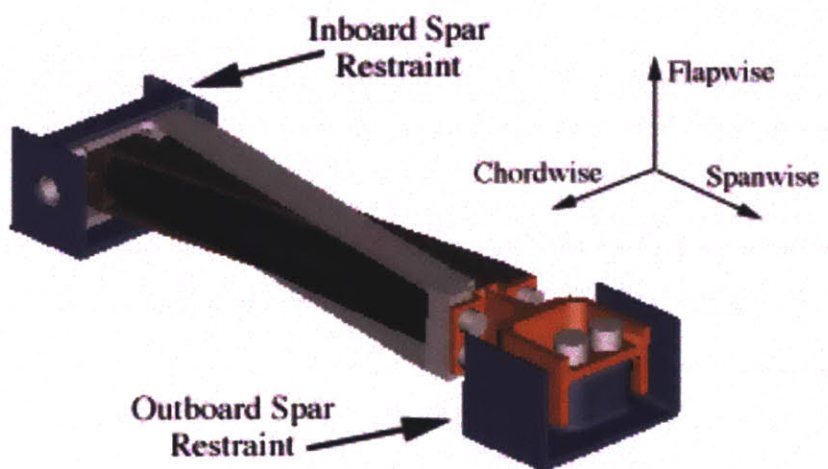


Figure 3-2: Actuator spar restraints

actuate freely and the inner frame is allowed the necessary kinematic degrees of freedom to operate unimpeded. To facilitate this sliding connection and to minimize the transmission of external spar forces into the actuator, a layer of 0.005 inch thick Guaranteed Non-Porous Teflon (GNPT) tape is placed between this outer frame/inboard spar restraint interface.

All of the centrifugal loads on the actuator frames and stacks are carried by a spanwise flexure integrated into the centrifugal flexure part. This flexure is used to enforce a zero-moment boundary condition at its center. By doing so, in case of slight mis-alignments of the stacks with respect to the centrifugal force, the flexure compensates to keep the load on both stacks approximately equal. This satisfies the “Balance” requirement stated in Section 3.1.1, minimizing the chance of compressively depoling a stack during rotor operation.

An actuator platform, shown in Figure 3-1, is placed between the outboard ends of the centrifugal flexure and the bay. Its purpose is to transfer all centrifugal actuator loads to the main blade structure, so that the two outboard restraint bolts carry predominantly chordwise and flapwise loads.

Unidirectional S-Glass composite is used to transfer the centrifugal actuator loads from the Actuator Platform to the top and bottom surfaces of the blade. This is done by using three 0° plies that make a U-shape along the front, outboard, and aft walls of the bay and one ply each of +45° and -45° S-Glass on the front and aft walls to transfer the loads.

The actuator forces and deflections are transferred to the servo-flap via a *control rod*. 0-80 threads at either end of the control rod are used to connect it to the inner frame and a *clevis* at the trailing edge. The threaded engagement between the control rod and clevis acts as the adjustment/trimming mechanism for the servo-flap. Integer turns of the clevis with respect to the control rod changes the relative position of the clevis by 0.0125 inch increments, and, through a 0.120 inch lever arm between the clevis and flap rotational axis, changes the servo-flap trimmed position by 5.97 deg increments.

The servo-flap consists of a foam core with a composite skin. The aerodynamic

design of the servo-flap is described in Section 3.1.3. A *flap horn* is bonded to the inboard side of the flap. The horn is connected to the clevis using a small *clevis pin*. The engineering drawing of this pin is shown in Figure 3-3. The pin has a spherical protrusion in the center, where it interfaces with the *horn* to allow for small relative flapwise and chordwise rotations between the clevis and the horn.

At the outboard end of the flap, a part called the *keymount* is bonded to the flap. This part contains two symmetric key-ways to provide an interface between the servo-flap and the *pre-stress wire*, which is described below. All of the centrifugal loads on the flap are transferred to the pre-stress wire at this location. The keymount is relatively wide (0.25 inches) to provide adequate surface area to transfer these loads.

A small Neodymium-Iron-Boron magnet is located just inboard of the keymount and at the very leading edge of the flap. A *magnet housing* is used to hold the magnet in place in the servo-flap. This magnet was designed to be used in conjunction with a hall effect transducer mounted at the trailing edge of the main blade structure to provide a measurement of the servo-flap deflection.

The servo-flap is supported at the inboard and outboard ends by the *inboard flap support* and *outboard flap support*. S-Glass composite is added in the manufacturing procedure to support these two restraints in the centrifugal environment.

A graphite *reaction rib* is laid up in the composite rotor blade, oriented in the chordwise direction. This rib serves to react actuation forces back towards the blade spar because the blade fairing has considerable compliance.

A *pre-stress wire* runs through the entire length of the servo-flap. It interfaces with the keymount at the outboard side of the flap through two keys and is welded to the *pre-stress wire flange* at the inboard side. The pre-stress wire performs the three primary functions of servo-flap rotational shaft, servo-flap thrust bearing, and actuator pre-stress element. It is described in the context of these three functions here:

**Servo-Flap Shaft.** The pre-stress wire acts as the shaft about which the flap rotates. Two spherical protrusions at each end of the wire are the rotational contact surfaces. The outboard protrusion rotates within a bore

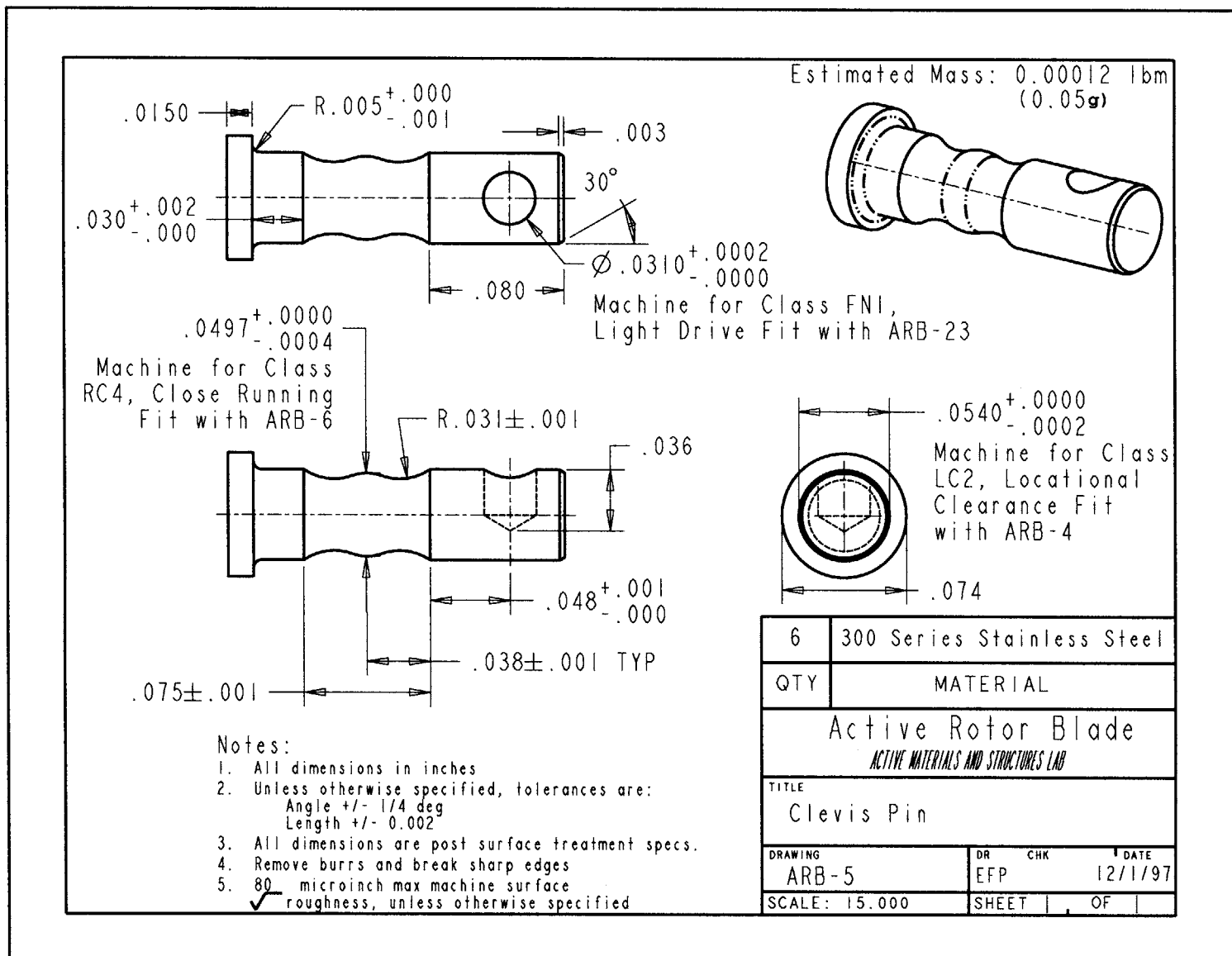


Figure 3-3: Clevis Pin

formed by the interface of the outboard flap support and the *outboard flap support Clamp*. The inboard protrusion rotates within a bore at the center of the flap horn. As with the clevis pin, discussed above, the spherical protrusions allow for small flapwise and chordwise rotations between the flap and main blade section. The wire also transfers the lift, drag and actuation loads on the servo-flap back to the main rotor blade structure.

**Flap Thrust Bearing.** The keys on the pre-stress wire engage the key-mount at the outboard end of the servo-flap. All of the centrifugal force (CF) on the servo-flap and embedded components are transferred to the pre-stress wire at this point. These forces are reacted back to the rotor blade structure through the pre-stress wire flange that is welded to the inboard end of the wire and which butts up against the inboard side of the inboard flap support. Additional composite at the trailing edge provides a lap joint to the inboard flap support to transfer these CF loads to the main rotor blade composite structure.

**Actuator pre-stress element.** As the name suggests, the pre-stress wire is also used to create a pre-stress on the actuator. This is done by placing a bias torsional load on the pre-stress wire (and servo-flap). The flap is then attached to the clevis with this bias torsional load applied. The effect is a tensile force on the control rod and a compressive force on both piezoelectric stacks. This also effectively takes out any backlash in the system between the servo-flap and the actuator.

The actuation load path can be described with reference to Figure 3-1. A linear chordwise force is applied through the control rod to the flap horn, which results in angular flap deflections. These actuation forces are transferred to the inboard flap support and back to the spar through the reaction Rib. This closed actuation load path is virtually independent of the rotor blade structure, which was one of the major design requirements discussed in Section 3.1.1.

### 3.1.3 Aerodynamic Predictions

The energy (stroke and force) required to deflect the trailing edge flap drive the sizing of the discrete actuator. This section describes the design of the servo-flap and the method used to predict the force required for operation.

A slotted flap was used for the servo-flap design. A cross-section of the modified blade section incorporating the slotted flap section is shown in Figure 3-4. The

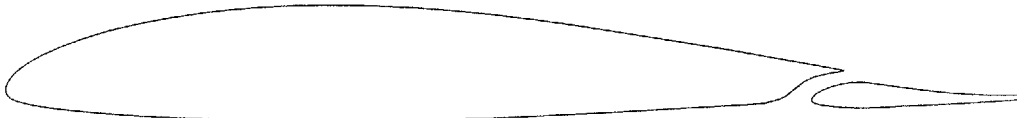


Figure 3-4: Aerodynamic cross-section of slotted flap blade stations

airfoil/flap contour was designed using MSES, a multi-element, viscous, compressible airfoil analysis code. MSES is a derivative of the single element code, ISES [30, 19, 17].

A slotted flap design was selected mostly because it requires substantially lower control forces than a similarly sized plain flap. The slotted flap provides two additional benefits. First, it pivots about an axis very close to its centroid, resulting in lower inertia and therefore increased actuation bandwidth. Second, weights can be added to the leading edge of the flap in case the dynamic aeroelastic characteristics of the flap must be altered. The one drawback of using a slotted flap is that it provides a slight increment in the drag on the blade.

The hinge moment on a slotted servo-flap is directly related to the position of the flap axis. If hinged at the leading edge, the control forces approach those of a plain flap. By moving the pivot point back, the required control forces drop. MSES simulations were used to predict this trend and select a hinge position.

To use MSES, the 2-D profiles of the main blade section and the slotted flap are specified. Viscous effects were neglected but compressibility effects were accounted for and a Mach number of 0.5382 (the Mach number at the 86% spanwise location in hover) was used. For each case, the servo-flap chordwise axis position, servo-flap rotational deflection and blade angle of attack were specified. Table 3.1 contains the

three dimensional matrix describing the range of parameter values over which these simulations were performed. At each operating point, the coefficients of lift, drag,

Table 3.1: Three dimensional array of parameter values used for aerodynamic simulations of slotted flap profile

$\alpha$ [deg]	-4	0	4	8	12
$c_f$ [%]	0	5	10	15	20
$\delta$ [deg]	-10	-8	-6	-4	-2

and moment were recorded. A sample of the pressure distribution calculated using a panel solver from the MSES analysis software package for one particular case is shown in Figure 3-5.

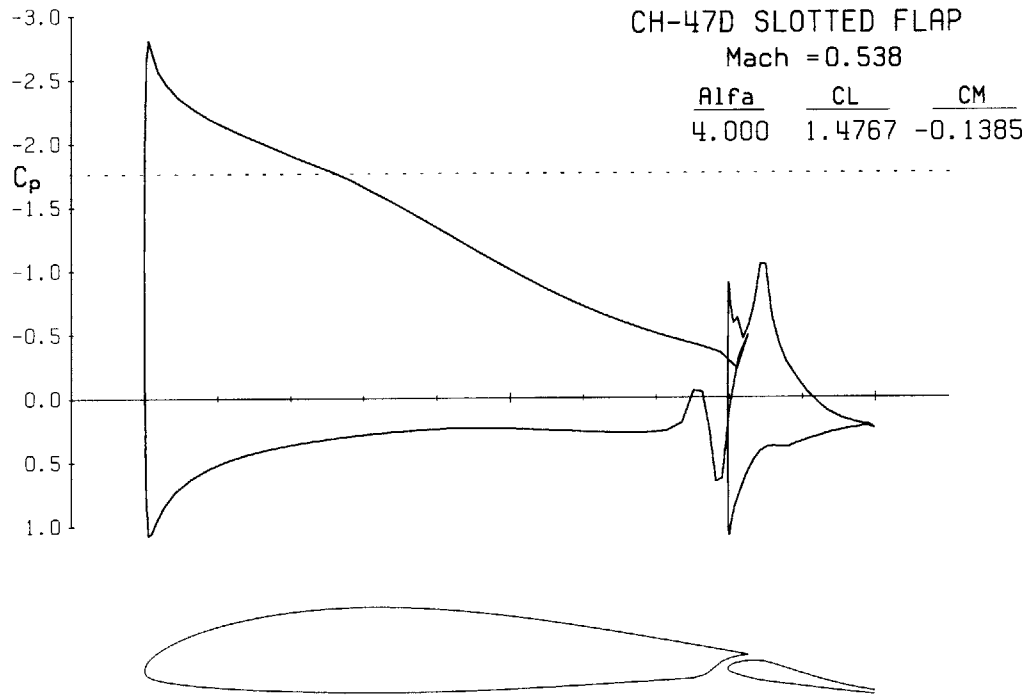


Figure 3-5: Calculated pressure distribution using a panel solver from the MSES analysis software package

From this data, a linear least squares fit to the data was used to estimate the hinge moment curve slope,  $C_{H\delta}$ , for various angles of attack at each axis position. This trend is plotted in Figure 3-6. As expected, the hinge moment curve slope decreases as the axis position moves aft. The blade angle of attack does have an

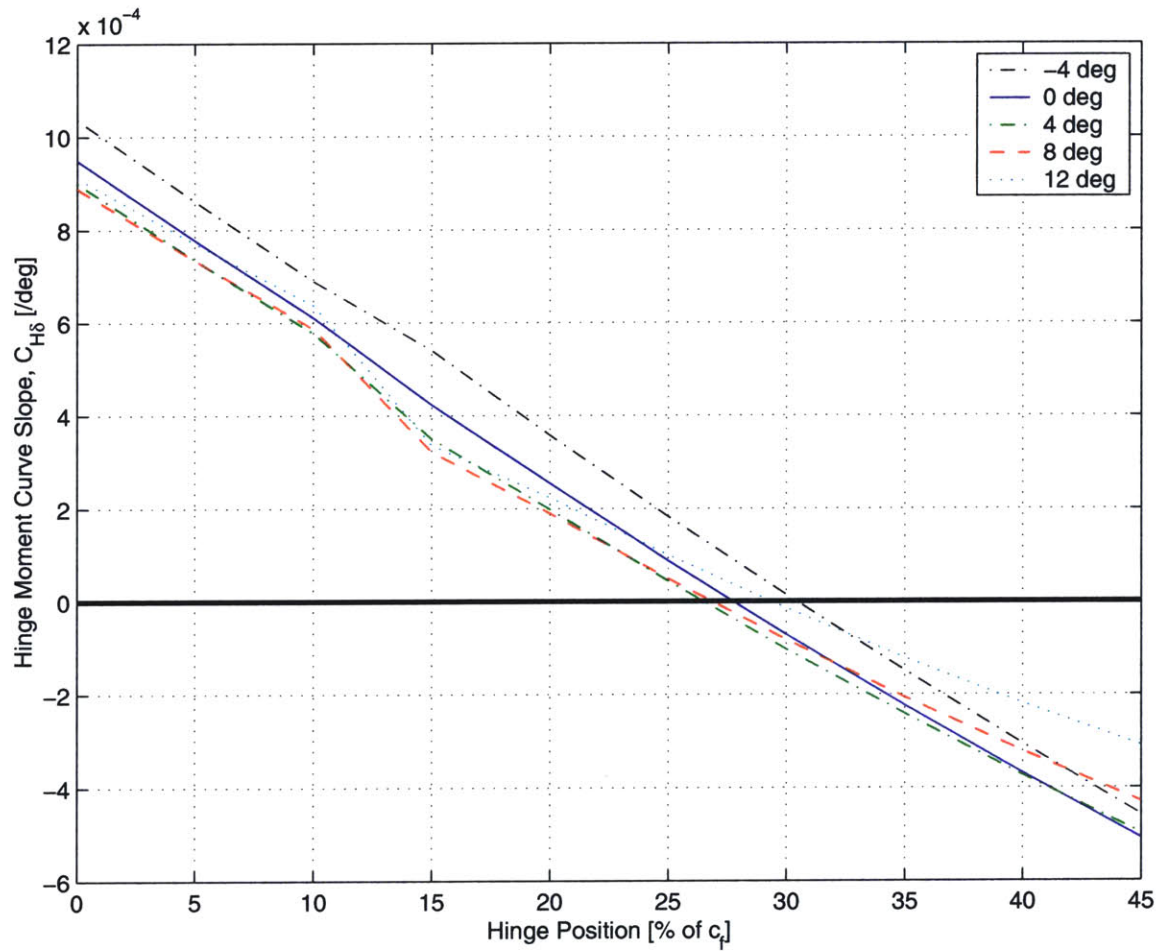


Figure 3-6: Variation in predicted hinge moment curve slope with flap axis position

effect on the required forces, but there is no apparent monotonic trend. Negative hinge moment curve slopes imply an unstable configuration. A flap axis position at 27.5% of flap chord was chosen because it represented a good trade-off between low required control forces and system stability at all angles of attack. As a reference, a similar analysis was performed for a 20% of chord plain flap configuration. This analysis led to a predicted hinge moment curve slope of  $C_{H\delta} = 11.0 \times 10^{-4}$ , more than an order of magnitude greater than the slotted flap.

The same analysis was used to calculate the lift and drag coefficients for the servo-flap. For example, the lift per unit span on the servo-flap can be expressed as

$$dL_f = \frac{1}{2} \rho U^2 c_s C_{L_f} dr \quad (3.1)$$

where  $c_s$  is the chord at the slotted blade section, which is 5.493 inches because the flap extends 0.105 inches farther aft than the trailing edge of the regular blade section. The coefficient of lift in Equation (3.1) is given by

$$C_{L_f} = C_{L_{f\delta}} \delta + C_{L_{0f}} \quad (3.2)$$

Similar relationships are used for the servo-flap drag and hinge moment.

Values for the steady and deflection dependent aerodynamic coefficients were collected for each angle of attack. The maximum value for each of these occurred at different angles of attack. A conservative approach to designing the system is to assume that the components will encounter the maximum steady and alternating loads during operation. Therefore, the maximum value for each coefficient was chosen for design purposes, even though they correspond to different blade angles of attack. These aerodynamic coefficients are collected in Table 3.2. The last column of this table contains the angle of attack condition at which the particular values were calculated.

The above aerodynamic coefficient analysis was done without including the effects of viscosity, so the boundary layer effects were neglected. Because of this, certain phenomenon are not accounted for in the analysis. Of particular importance is whether

Table 3.2: Predicted Aerodynamic Curve Slopes.

Parameter	Value	$\alpha$
$C_{L_{f\delta}}$	0.0170 /deg	-4°
$C_{L_{of}}$	0.0518	12°
$C_{D_{f\delta}}$	-0.00266 /deg	-4°
$C_{D_{of}}$	0.0122	12°
$C_{H_\delta}$	$0.977 \times 10^{-4}$ /deg	-4°
$C_{H_{of}}$	-0.00282	-4°

the servo-flap is more effective in deflecting upward or downward. To test this, an analysis was done using MSES, including the compressibility and viscous effects to calculate the coefficient of lift and moment generated by servo-flap deflections of -5, 0, and +5 degrees. Note that positive angles correspond to downward flap deflections. A Mach number of 0.5382 and the model scale Reynolds number of  $1.768 \times 10^6$  were used. A blade angle of attack of 5 degrees was used. The calculated coefficients of total lift and moment at the blade quarter chord are shown in Table 3.3. The ef-

Table 3.3: This table shows the change in coefficient of lift and moment for upward and downward flap deflections of equal magnitude. The induced moment appears to be independent of flap deflection sign but there is a slight dependence in the induced lift.

Flap Angle [deg]	$C_L$ [-]	$C_M$ [-]
-5	0.668	0.0416
0	0.986	-0.0164
+5	1.180	-0.0732

fectiveness of the servo-flap in inducing a moment at the blade 1/4 chord is nearly equivalent for the two cases. However, the induced lift is 64% more sensitive to upward flap deflections. At full scale, the Reynolds number will be six times larger and the boundary layer will be thinner. Because of this, this nonlinear behavior should be reduced [18].

### 3.1.4 Actuation System Compliance and Strength Modeling

The components of the actuation system were sized to maximize system mass efficiency, while ensuring adequate fatigue life of the most critically loaded components. An optimization script was developed to aid in this process. A full description of the detailed calculations in this script is beyond the depth of this discussion. However, the design of one of the most critical components in the design, the pre-stress wire, will be presented as an example of the type of modeling that was done.

The impact of each component on the system model was considered in three contexts. If the component deforms elastically in parallel with the servo-flap deflections, it is said to add *parallel stiffness* to the total load driven by the actuator. If the component acts as part of the actuation load path, it is said to add *series compliance* to the actuation system. The parallel stiffness and series compliance of each component was considered in the model. In addition, the strength of each part was modeled to ensure an infinite fatigue life given the steady and alternating loads from rotor operation. The pre-stress wire provides a useful illustration of the approach used because it contributes to the model in all three of these contexts.

The outboard end of the pre-stress wire is constrained through the keymount to match the rotational servo-flap deflections. This represents a parallel stiffness on the actuation of the form

$$k_{ps} = \frac{G_{ps} J_{ps}}{l_{ps}} \quad (3.3)$$

The pre-stress wire is made of high tensile strength steel. It is composed of a long, thin cylindrical section, 6.640 inches in length and 0.054 inches in diameter, with two larger diameter end-pieces that act as the inboard and outboard flap axes. Assuming that most of the torsional compliance is determined by the center section, application of Equation (3.3) yields a parallel stiffness of  $k_{ps} = 1.402$  in-lbf/rad. This stiffness adds directly to the servo-flap aerodynamic stiffness to give an aggregate load on the actuator.

Actuation forces are transferred from the horn to the inboard flap support through the inboard section of the pre-stress wire. Flexing of this short member will add series

compliance to the actuation system. The compliance from the inboard section is given as

$$C_{ps} = \frac{l_{in}^3}{3E_{ps}I_{in}} \quad (3.4)$$

For the manufactured blade, the inboard pre-stress wire segment has a radius of 0.043 inches and a length of 0.149 inches. Thus, the inboard segment of the pre-stress wire represents a stiffness of 70600 lb/in in series with the actuation load path.

The modeled compliance of all components sums to give an overall actuation system compliance. As discussed in Section 2.6.1, the actuator alone has a stiffness of 369 lb/in. Thus, the inboard section of the pre-stress wire does not significantly affect the stiffness of the actuation system, lowering it to 367 lb/in. However, adding the compliance of all the components in the actuation load path (*i.e.*, axial strain in the control rod, bending of the servo-flap horn, torsion of the flap skin, *etc.*), the predicted system stiffness is 323 lb/in.

The most critical location with regards to the strength of the pre-stress wire is the very inboard edge, at the transition into the pre-stress wire flange, because of the combined torsion, bending, and axial loads there. The torsional loads are due to actuation and the bias loads applied to the pre-stress wire. The bending loads are due to actuation and the steady and alternating lift and drag on the servo-flap. The axial forces are due to the centrifugal loads on all the servo-flap components carried by the pre-stress wire.

A diagram of the forces applied to the inboard end of the pre-stress wire at the flap horn is shown in Figure 3-7. Because there is a spherical interface at the point of contact with the horn, no moments are applied. The forces are calculated using the aerodynamic coefficients predicted in Section 3.1.3, an estimate of the mass of the components in the acceleration field of the blade, and the applied actuation forces.

The stress at any point at the root of the pre-stress wire is represented using these forces as

$$\sigma_x = \frac{F_{x_{ps}}}{A_{ps}} + \frac{F_{y_{ps}}l_{ps}y}{I_{in}} - \frac{F_{z_{ps}}l_{ps}z}{I_{in}} \quad (3.5)$$

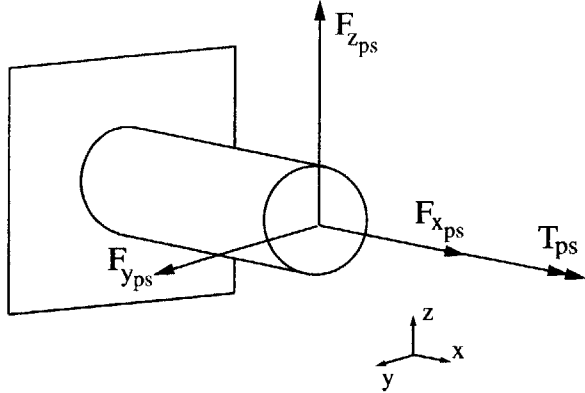


Figure 3-7: Distribution of forces on the inboard section of the pre-stress wire

$$\tau_{xy} = \frac{4F_{y_{ps}}(R_{in}^2 - y^2)}{3\pi R_{in}^4} + \frac{T_{ps}z}{J_{in}} \quad (3.6)$$

$$\tau_{xz} = \frac{4F_{z_{ps}}(R_{in}^2 - z^2)}{3\pi R_{in}^4} + \frac{T_{ps}y}{J_{in}} \quad (3.7)$$

The components of normal stress in the  $y$  and  $z$  directions as well as the shear stress,  $\tau_{yz}$ , are assumed to be zero. The principal stresses are expressed using the three non-zero stress components as

$$\sigma_{I,II} = \frac{1}{2} \left( \sigma_x \pm \sqrt{\sigma_x^2 + 4(\tau_{xy}^2 + \tau_{xz}^2)} \right) \quad (3.8)$$

Using the estimate of the aerodynamic coefficients given in Table 3.2, and the mass and accelerations of all components, values for the steady and maximum principal stresses were identified. A Goodman diagram for the pre-stress wire material was used to ensure that the estimated stress levels were low enough to ensure an infinite (*i.e.*,  $200 \times 10^6$  cycles) fatigue life.

A similar analysis is performed for all of the critically loaded points in the actuation system design. The strength and compliance analyses of the components in the actuation system were combined into a series of Matlab script files. Simulations optimizing component geometries were performed to maximize system performance.

The simulations that were performed showed that there was an optimum flap length leading to a maximum level of flap deflections. The reason for this optimum is related to the fact that the pre-stress wire was designed to run the full length of the

servo-flap. For exceptionally long flaps, the parallel stiffness of the wire became very small, but the aerodynamic loads dominated. Conversely, for very short flap lengths, the parallel stiffness of the wire dominated. At both extreme cases, the actuated deflections were driven to zero (even with impedance matched lever arm lengths). The variation in predicted displacement with flap length is shown in Figure 3-8, which shows an optimum flap length of seven inches. Of course, smaller deflections

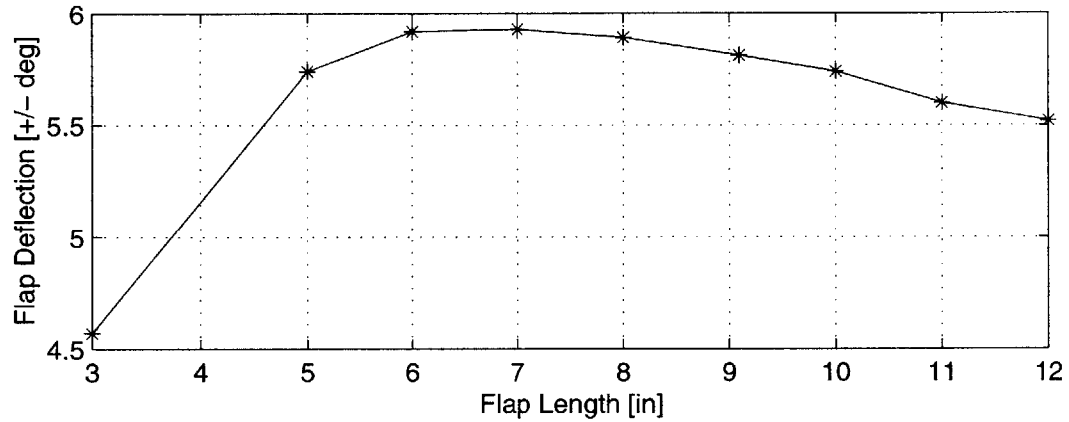


Figure 3-8: Predicted flap deflection vs spanwise flap length

of longer flaps may lead to greater effectiveness in controlling hub forces, but the capability to predict this effect was beyond the scope of the design code. Therefore, a seven inch long flap length was chosen as a good compromise of all considerations.

Because the rotor blade molds provided by Boeing for this research taper linearly from a 12% to an 8% thick airfoil over the outer 15% of the blade span, the outboard edge of the outer flap support was placed at 0.85R. This was done to minimize manufacturing complexity for the prototype active blade. A ProEngineer drawing of the entire rotor blade showing the designed location of the servo-flap and actuator bay is shown in Figure 3-9.

The modeling used for the prototype component design is limited because it is a superposition of a number of one-dimensional models. Inaccuracies can be expected between the predicted and actual loads and great conservatism was accordingly used in the design process. For a prototype, this approach is warranted. Future generations should combine detailed rotor and finite element modeling to maximize actuation and

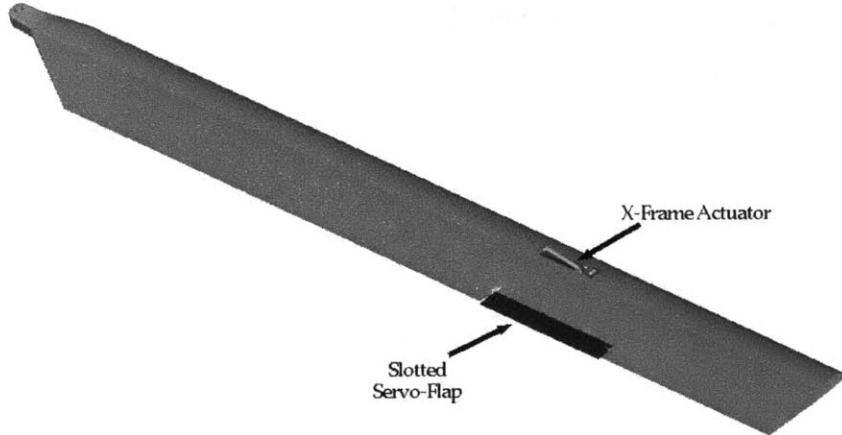


Figure 3-9: Active rotor blade configuration.

rotor control efficiency as well as ensuring proper strength margins.

### 3.1.5 Estimate of System Performance

Use of the compliance and strength model described in the previous section predicted an actuation system stiffness of 322.3 lb/in. Parallel stiffness is contributed by the pre-stress wire and the cross-flexures of the centrifugal flexure part. The values for these parallel stiffnesses are 1.402 in-lb/rad and 0.1519 in-lb/rad. The aerodynamic stiffness of the servo-flap is estimated as

$$K_{\text{aero}} = \frac{1}{6} \rho \Omega^2 c_s^2 (R_o^3 - R_i^3) C_{H_\delta} \quad (3.9)$$

Using the value for  $C_{H_\delta}$  in Table 3.2 and considering that the inboard and outboard spanwise locations of the servo-flap are 44.174 and 51.174 inches, the aerodynamic stiffness is predicted to be  $K_{\text{aero}} = 3.024$  in-lb/rad. The lever arm length is set to impedance match the actuation system to the total load as

$$K_a = \frac{K_{L_{\text{rot}}}}{s^2} = \frac{(K_{\text{aero}} + K_{\text{ps}} + K_{\text{cf}})}{s^2} \quad (3.10)$$

$$s = \sqrt{\frac{K_{\text{aero}} + K_{\text{ps}} + K_{\text{cf}}}{K_a}} = 0.12 \text{ inches} \quad (3.11)$$

The lever arm length, *i.e.*, the distance from the center of the pre-stress wire bore to the clevis pin bore in the flap horn, was set at 0.120 inches for the prototype blade.

The predicted servo-flap deflection is given by Equation (B.34). Using the data in Figure 2-9, showing a free displacement of 0.056", the predicted flap deflection is  $\pm 6.7^\circ$ . The associated actuator force is  $\pm 4.5$  lbf.

### 3.1.6 Active Blade Instrumentation

The active blade was instrumented with a collection of strain gage sensors to measure blade response, two hall effect transducers, used for flap deflection measurement, and one RTD to monitor the thermal environment inside the bay. The list of sensors used is given in Table 3.4.

Table 3.4: List of sensors integrated into the active blade.

Sensor Number	Sensor Description	Bridge Type	Blade Station [%]	Blade Station [in]
5	Flapwise Bending Strain	Full	18.9	11.457
6	Torsional Strain	Full	20.7	12.548
7	Chordwise Bending Strain	Full	23.5	14.245
8	Flapwise Bending Strain	Full	42.5	25.763
9	Torsional Strain	Full	63.0	38.190
10	Torsional Strain	Full	87.0	52.739
11	TE Stiffener Axial Strain	Half	66.1	40.072
12	Top Inboard/Forward Bay Axial Strain	Half	73.0	44.249
13	Top Inboard/Aft Bay Axial Strain	Half	73.0	44.249
14	Top Inboard Bay Shear Strain	Half	70.8	42.949
15	Top Outboard Bay Shear Strain	Half	79.8	48.372
16	Actuator Outer Frame Axial Strain	Full	74.8	45.322
17	HET Displacement of Actuator Inner Frame	N/A	72.6	44.024
18	HET Displacement of Servo-Flap	N/A	83.7	50.714
20	RTD Bay Thermal Measurement	Quarter	74.8	45.322

Strain gages were used in the blade to both measure the blade response and ensure the health of the blade near the actuator bay. These are differentiated as far-field and near-field gages, respectively. The near field gages include shear strain sensors on the top surface, inboard and outboard of the actuator bay axial strain sensors on

the top surface, fore and aft of the inboard edges of the actuator bay, axial strain of the trailing edge stiffener inboard of the servo-flap components, and axial strain on the actuator outer frame. These near field gage locations are shown in Figure 3-10.

The far-field gages include three torsion gages, two flapwise bending gages and one chordwise bending gage. The location of these gages were chosen to maximize the observability of the targeted modes while avoiding blade stations corresponding to changes in composite ply or leading edge weight distribution and any area within four inches of the servo-flap. These far-field gage locations are shown in Figure 3-11. Note that during testing we lost two of the wires to the flapwise bending gage at the 42% spanwise position. So that we could continue to use this sensor, it was re-wired as a quarter bridge. The drawback in doing this was that a quarter bridge sensor is sensitive to both blade tension as well as bending. However, since most of the vibratory response of the blade is due to bending, this sensor performs well enough to provide transfer function identification.

## 3.2 Blade Manufacture

One prototype active rotor blade was manufactured at MIT. The blade was fabricated using a procedure very similar to that used by Boeing Helicopters to manufacture their model scale rotor blades. Some of the details of the blade manufacturing process, which are proprietary to Boeing Helicopters, have been omitted from this document. This section provides a general discussion of the blade manufacturing process. A more detailed description of the steps used to make the blade are given in Appendix E.

The rotor blade consists of a Rohacell foam core with an external composite skin. The main body of the rotor blade is manufactured in two cures, a spar cure and then a fairing cure. Each cure is performed by wrapping composite plies around the foam core and curing the laminate in an aluminum blade mold.

The spar cure is performed first. Most of the structural material in the blade is contained in the spar. Thus, the spar determines the dominant strength and stiffness properties of the blade. This active blade was designed to keep the structural

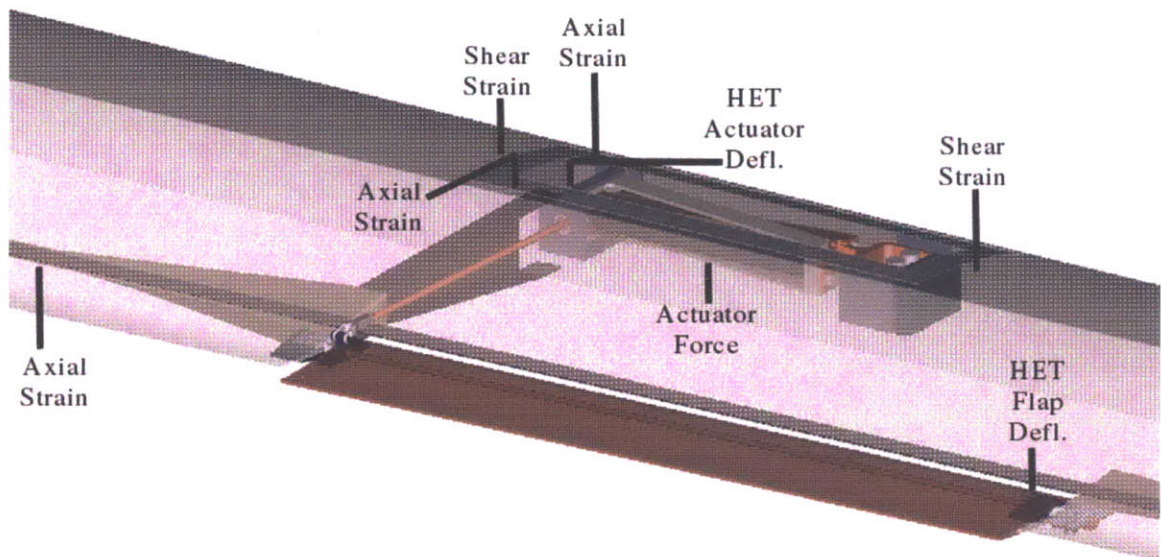


Figure 3-10: Near-field sensor placement

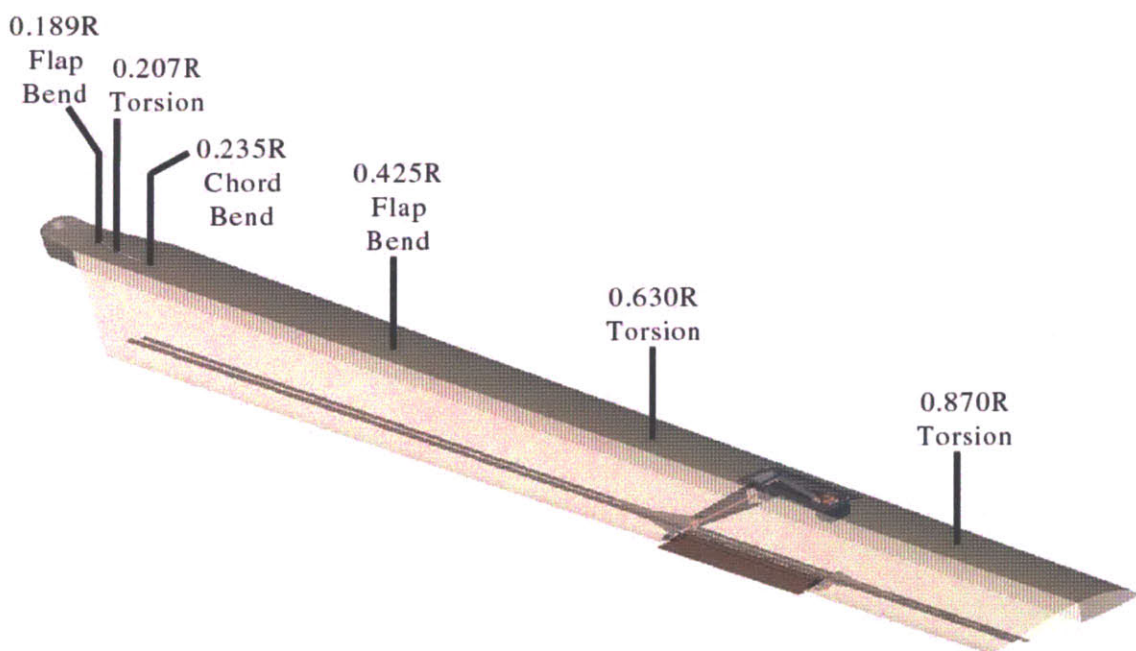


Figure 3-11: Far-field strain gage placement

properties nearly identical to those of a standard Mach-scaled passive blade. The two major differences were the additional concentrated inertia near the blade tip due to the actuator components and servo-flap and a reduction in torsional stiffness of the active blade by a factor of two. The torsional stiffness of the active blade was reduced to make the flap more effective in inducing torsional rotor blade deformations.

The spar was manufactured in a standard fashion. However, to properly locate the actuator spar restraints, a three piece spar mandrel assembly was used during the spar cure. As discussed above, post-cure access to the actuator was necessary. This was achieved in the prototype blade by placing a hatch (or hole) on the top surface of the spar. The actuator hatch is incorporated into the top surface because as the blade reaches a steady pre-cone angle, the centrifugal force tends to push the actuator back into the blade, against the bottom skin. The use of the mandrel assembly and the composite lay-up techniques used to create the actuator hatch are described in detail in Appendix E.

The fairing was attached in the second cure. The positioning of the flap supports and the incorporation of the slotted trailing edge profile at the servo-flap blade stations was achieved using a trailing edge mandrel, which was fixtured at the back of the blade mold during the fairing cure. The use of this mandrel is also described in Appendix E.

The servo-flap was manufactured using a similar procedure to that used for the rotor blade. Servo-flap molds were designed and numerically controlled (NC) machined in-house. This flap was composed of two layers of E-Glass fabric, oriented at  $\pm 45^\circ$  and one layer of IM7 uni-directional composite over the front 55% of the flap to give it some flapwise bending stiffness. The detailed manufacturing of this flap is also described in Appendix E.

After all components were manufactured, the blade was assembled and bench and rotor hover tests were performed. These tests are described in Section 3.4.1 and Chapter 4. The next section gives some of the structural properties of the prototype active blade.

### 3.3 Active Rotor Blade Properties

The predicted and manufactured properties of the active blade are collected in Table 3.5. The predicted blade properties were obtained through a combination of the ProEngineer model of the active blade and from input from Boeing Helicopters on the blade design. Center of gravity measurements of the manufactured active blade were not performed.

It is useful to separate the mass of the components supporting the actuator and servo-flap from the total mass. These components are identified as those drawn in Figure 3-1, and will be referred to as the “actuation system” components. Because these components represent a prototype design, it is expected that through future design iterations, their mass can be reduced. Also note that the mass of the leading edge weights used to balance the actuation system components about the blade quarter chord is also called out as “Actuation System LE Weight Mass”. Again, through better redesign, the CG of the system could easily be moved forward, reducing or eliminating the need for these weights.

Table 3.5: Properties of active rotor blade. Note that entries where there is no experimental data are labeled as “NED”.

Property	Measured	Predicted
Total Blade Mass	1.96 lbm	2.01 lbm
Actuation System Mass <sup>a</sup>	0.165 lbm	0.157 lbm
Actuation System LE Weight Mass	0.088 lbm	0.088 lbm
Actuation System Radial CG	NED	BS 45.950
Actuation System Chordwise CG <sup>a</sup>	NED	2.003" from LE
Blade $I_b^b$	NED	0.511 slug ft <sup>2</sup>
Average blade mass per span <sup>c</sup>	NED	0.0303 lbm/in
Blade Pre-Twist	NED	-12 deg

<sup>a</sup>Without leading edge weights

<sup>b</sup>About flapping hinge line, excluding pitch shaft assembly mass

<sup>c</sup>Away from actuator/flap locations

## 3.4 Rotor Blade Validation Tests

### 3.4.1 Active Blade Actuation System Bench Tests

#### Quasistatic Response

Typically, active materials such as piezoelectric ceramics exhibit nonlinear behavior, such as hysteresis, as well as voltage-dependent nonlinearities (increasing or decreasing  $d_{33}$ ). In addition, there can be other sources of nonlinear behavior, such as binding or friction in the actuator mechanism, or nonlinear gain. Thus, it is important to characterize the quasistatic response of the active blade actuation system on the bench top before performing hover tests.

Figure 3-12 shows the quasistatic responses of the actuator on the bench top driving a light load (to match that of the pre-stress wire in the blade), and in the rotor blade. The blade flap deflection was determined by measuring the actuation deflection using the primary Hall effect sensor, which was calibrated by comparing the Hall effect sensor output voltage to flap angle measured using a laser light lever. The data in Figure 3-12a is normalized to yield equivalent flap deflection, so that it can be compared directly to Figure 3-12b. In Figure 3-12a, the hysteresis is moderate, and is primarily due to material effects. In contrast, friction in the flap hinge (*i.e.*, the pre-stress wire) and clevis increase the hysteresis significantly, reducing the free deflection by about 4 deg.

The flap was actuated at several frequencies, and videotaped while illuminated with a strobe light, in order to visualize the flap motion. Interested readers can view the video at <http://web.mit.edu/srhall/www/blade.html>. Note that this web address should remain active until December, 2005.

The friction problem is largely a result of the difficulties associated with building at model scale. In particular, because we were unable to locate suitable bearings for the hinge line, we were forced to use the metal-to-metal spherical flap and clevis “bearings” described in Section 3.1.2. Also, the friction problem could be reduced significantly in a configuration where the actuator preload is not applied through the

flap itself.

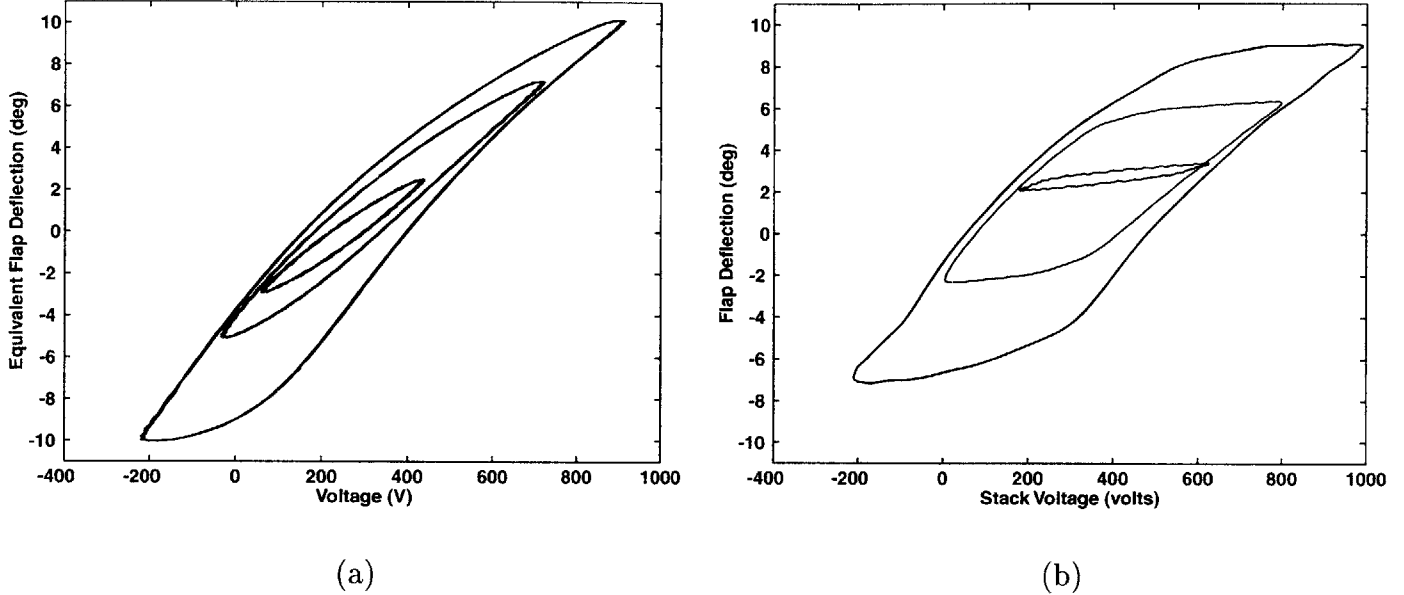


Figure 3-12: Actuator Hysteresis. (a) Actuator displacement vs. voltage for the actuator in the bench-top apparatus, at 3 Hz. The displacement is converted to equivalent flap deflection by dividing the actuator displacement by the flap horn length. (b) Flap displacement vs. voltage for the actuator in the blade, with flap attached.

Using the quasistatic bench data and a simple friction model, a coefficient of kinetic friction can be identified for the system. Figure 3-13 shows a simple model of the actuator driving a load with associated friction. A free body diagram at node A yields the relationship

$$K_a q_a = K_L q_L + F_f \quad (3.12)$$

The free deflection of the actuator equals the sum of the actuator and load displacements, thus, the actuated displacement is

$$q_L = \frac{K_a \left( q_f - \frac{F_f}{K_a} \right)}{K_a + K_L} \quad (3.13)$$

Equation (3.13) can be interpreted as the characteristic of a modified actuator with identical stiffness, but whose achievable blocked force and free deflection are reduced by the friction.

Assuming the friction is due entirely to hinge friction in the clevis and inboard

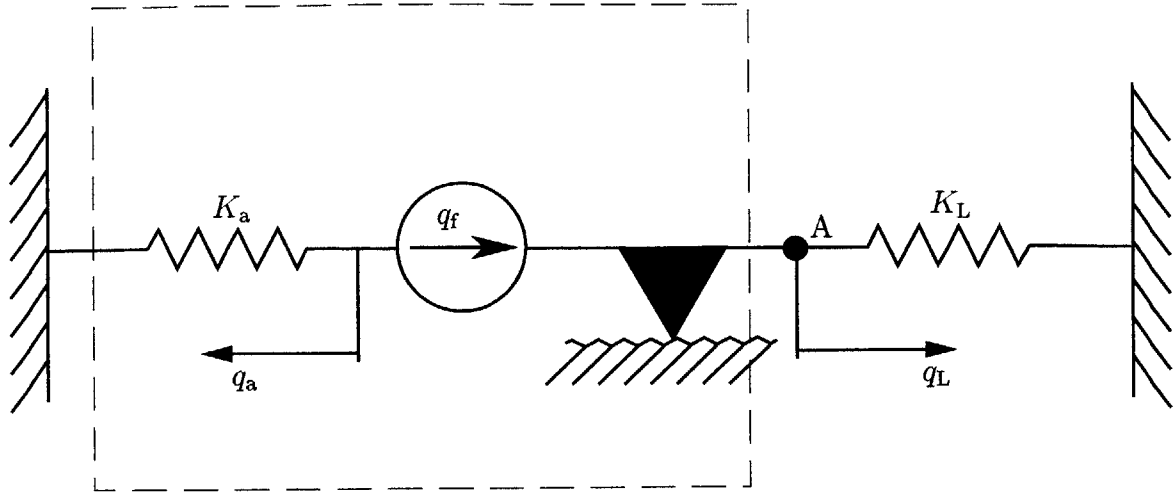


Figure 3-13: Model of actuator driving load with friction.

servo-flap bearings, a simple model of the frictional force generated during the peak-to-peak motion of the actuator is

$$F_f = 2 \frac{N_{ps}\mu_k (r_{ifh} + r_c)}{s} \quad (3.14)$$

where the factor of 2 is included to account for peak-to-peak motion. Using Equations 3.12–3.14 yields an expression for the kinetic coefficient of friction as

$$\mu_k = \frac{s (K_a q_f - (K_a + K_L) q_L)}{2 N_{ps} (r_{ifh} + r_c)} \quad (3.15)$$

The following parameters are easily substituted into the above expression.

$$K_a = 323.1 \text{ lb/in}$$

$$s = 0.120 \text{ in}$$

$$N_{ps} = 18.6 \text{ lbf}$$

$$r_{ifh} = 0.043 \text{ in}$$

$$r_c = 0.0249 \text{ in}$$

The actuator load on the bench top is a sum of the parallel stiffness from the pre-stress wire and actuator centrifugal flexures. These stiffnesses were estimated in

Section 3.1.5 as

$$K_{ps} = 97.36 \text{ lb/in}$$

$$K_{cf} = 10.55 \text{ lb/in}$$

$$K_L = K_{ps} + K_{cf} = 107.9 \text{ lb/in}$$

From the bench top data for the active blade, the actuated displacements at 400, 800, 1000, and 1200 Volt actuation are identified. Similarly, free displacements for the same actuation levels are identified from the actuator bench-top tests presented in Section 2.6.1. These displacements are

$$q_f = \begin{Bmatrix} 0.0579'' \\ 0.0470'' \\ 0.0340'' \\ 0.0150'' \end{Bmatrix} \quad q_L = \begin{Bmatrix} 0.0306'' \\ 0.0253'' \\ 0.0170'' \\ 0.0025'' \end{Bmatrix}$$

Substituting the above values into Equation (3.15) gives the estimated coefficients of friction at the four actuation levels as

$$\mu_k = \begin{Bmatrix} 0.245 \\ 0.189 \\ 0.163 \\ 0.169 \end{Bmatrix}$$

All four predicted coefficients of friction are within reason for steel on steel friction. The difference between the coefficients at high voltage may be due to dependence of the friction on amplitude and/or nonlinearities in the modulus of the active material with applied voltage. Regardless, using the above friction model will allow us to make a first order estimate of the breakdown of loads on the actuator, especially in identifying various aerodynamic parameters from the hover tests discussed in the next chapter.

### 3.4.2 Actuator Bay Strength Testing

Because of the diversion of the unidirectional plies around the actuator bay, the blade had to be tested to ensure that it would be strong enough to react the centrifugal loads that the actuator itself would impose on the blade. To test this, a shortened, 1/2 span blade was built. The manufacturing procedure was similar to the active blade spar, but the blade length was limited to 30" so that it could fit within the tensile testing machine.

To test the strength of this modified blade configuration in reacting the centrifugal force (CF) of the actuator on the blade, a modified spar section was placed into an Instron 8501 testing machine, as shown in Figure 3-14. The hole in the spar specimen

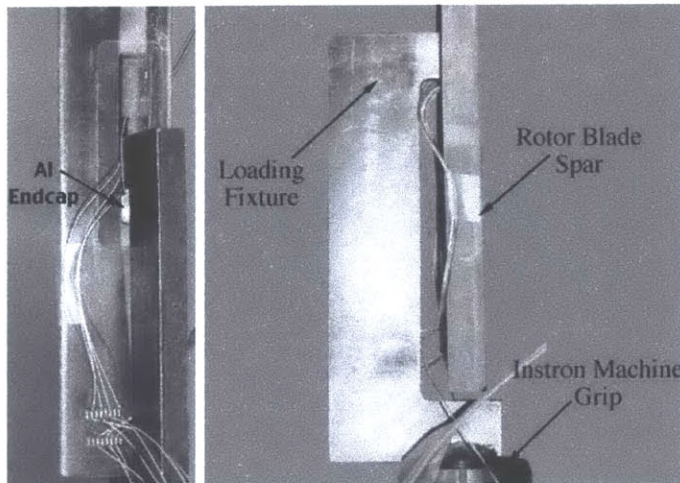


Figure 3-14: Tensile test set-up for modified blade section (a) Front view (b) Side view

was located on the bottom surface of the blade. A standard root-end pinned boundary condition was used and a special loading fixture was used to apply the simulated actuator CF to the outboard end of the bay. The blade section was loaded up to 563 lbf, which is a load 2.2 times larger than that expected in hover. Loads on the specimen were resolved to within  $\pm 1$  lbf using an Instron 5 kN load cell, placed in series with the specimen. This load level was applied quasi-statically in both 0.01 Hz sine wave input and 1 lbf/sec ramp input tests.

Strain gages were used to monitor how the loads were carried by the spar section.

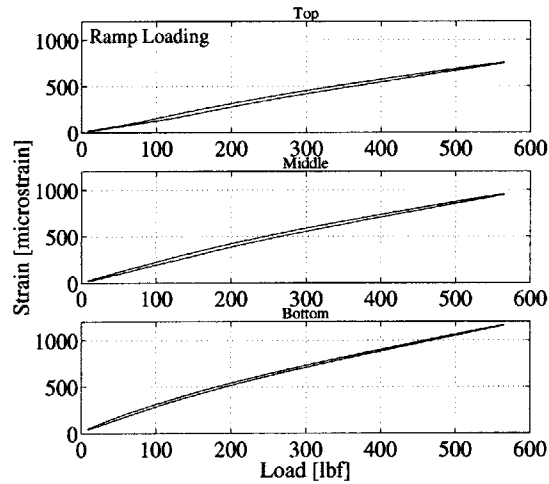


Figure 3-15: Measured strain on actuator bay wall vs applied load

All gages were in quarter bridge configurations for the test. Thirteen strain gages were placed throughout the rotor blade section. Two gages were placed in the far field, near the root of the blade while the other eleven gages were placed in and around the actuator bay. A characteristic set of strain measurements as a function of loading is shown in Figure 3-15. The strain measurements presented in this figure correspond to the aft side of the bay at the top, middle, and bottom positions. Note that the strain in the bottom gage is the largest. This is expected since the hole in this particular rotor blade section is on the bottom side. In the active blade, the bay hatch is on the top surface, so the strains shown in Figure 3-15 may reverse.

The strains measured in all gages during the test were well below the static allowables for the materials, indicating that the modified blade section has adequate strength to react the anticipated loads. The results from this test also indicate that the simulated actuator CF loads are being transferred from the actuator bay wall to the upper and lower blade skin, as designed.



# Chapter 4

## Hover-Test System Identification and Performance

After building the active blade and successfully testing it in a non-rotating bench-top setting, it became necessary to evaluate its performance in a more realistic environment. Two major requirements had to be satisfied in order to create a realistic testing environment. First, to address longevity concerns, it was important to subject the actuator and rotor blade to a stress environment representative of a full-scale helicopter. Second, to ensure that these tests could be used to predict full-scale performance, it was necessary to test the actuation system such that the model scale measurements could be scaled directly to full scale. To satisfy these requirements, Mach scaled hover tests of the active blade were performed. These tests are described in this chapter.

The two primary performance objectives of the hover tests were to measure the effectiveness of the actuator in controlling the servo-flap, and the resulting effectiveness in controlling vertical shear at the rotor hub. The performance of the system was measured at typical operating conditions with respect to rotor speed, blade angle of attack and stack applied voltage. In addition, to give a measure of the sensitivity of the system to parametric changes to these operating conditions, the performance was also measured as these conditions were varied.

A large quantity of data was collected during these tests. While all of the data was used in evaluating the system response, this chapter contains only those data plots

that best illustrate the primary objectives mentioned above. A detailed discussion of the effect of the actuation on the general response of the blade (*e.g.*, strain gage response to servo-flap deflection), while important, is beyond the scope of this study. For completeness, a full set of transfer functions for all of the blade sensors is included in Appendix C.

This chapter is organized as follows. We begin with a derivation of the aeroelastic scaling laws to determine the important non-dimensional parameters for rotor control using active material actuators. Next, a description of the MIT Hover Test Facility is provided. Some focus is provided on the instrumentation of the facility and an explanation of the system identification process is given. In the second half of the chapter, the hover data for the active blade is presented, addressing the performance of the actuator in driving the trailing edge servo-flap and the effectiveness of the servo-flap in controlling rotor hub vertical shear. A comparison is made between this rotor blade and a similar integral rotor blade. Finally, strain data from gages near the actuator bay and trailing edge components is presented to address the reliability issue; and thermal data from a sensor placed inside the actuator bay is presented to demonstrate the amount of heating that occurs due to actuator operation while in the enclosed spar cavity.

## 4.1 Aeroelastic Scaling

The purpose of this section is to address the validity of scaling the results from the model helicopter rotor to the full scale case. By non-dimensionalizing the governing equations of the phenomenon being studied, the most important parameters to keep constant between model and full scale can be identified. Below, a very simplified version of the rotor blade aeroelastic equations will be non-dimensionalized to identify these parameters. The nomenclature may be found in the front-matter of this thesis. Because of the simplified nature of the equations considered, many of the second order and non-linear effects are neglected. Nevertheless, this approach will yield a realistic set of parameters to provide a first order application of these results to a full-

scale helicopter. Friedmann provides a detailed treatment of the rotor blade scaling problem in [24]. There, he maintains that proper scaling laws must be developed using a combination of computer simulation and traditional dimensional analysis. While such a comprehensive treatment may be necessary for exact scaling of the model tests, it is felt that acceptable accuracy will be obtained by applying the scaling laws developed below.

Houbolt and Brooks provide a detailed derivation of the aeroelastic equations describing the torsion, flapping and lagging of a rotor blade with zero steady pre-cone angle [41]. Assuming coincident elastic axis, center of gravity and modulus weighted centroid, no built in pre-twist, zero offset between the elastic axis and center of rotation, only sectional aerodynamic servo-flap forcing on the rotor blade, and neglecting chordwise motion, the torsion equation (Equation 22 from [41]) becomes

$$\begin{aligned} -\left\{\left[GJ + Tk_A^2\right]\phi'\right\}' + \Omega^2 m \left(k_{m_2}^2 - k_{m_1}^2\right) \cos(2\beta)\phi + mk_m^2 \ddot{\phi} \\ = \frac{1}{2}\rho r^2 \Omega^2 c^2 C_{M_\delta} \delta - m\Omega^2 \left(k_{m_2}^2 - k_{m_1}^2\right) \sin \beta \cos \beta \end{aligned} \quad (4.1)$$

Similarly, the flapping equation (Equation 23 from [41]) becomes

$$\left[\left(EI_1 \cos^2 \beta + EI_2 \sin^2 \beta\right) w''\right]'' - (Tw')' + m\ddot{w} = \frac{1}{2}\rho r^2 \Omega^2 c C_{L_\delta} \delta \quad (4.2)$$

We define the following non-dimensional parameters

$$\begin{aligned} \overline{GJ} &= \frac{GJ}{EI_0}, & \overline{EI_i} &= \frac{EI_i}{EI_0}, & \overline{k_A} &= \frac{k_A}{k_{A_0}} \\ \overline{C_{M_\delta}} &= \frac{C_{M_\delta}}{C_{L_\alpha}}, & \overline{T} &= \frac{T}{m_0 \Omega^2 R^2}, & \overline{c} &= \frac{c}{c_0} \\ \overline{C_{L_\delta}} &= \frac{C_{L_\delta}}{C_{L_\alpha}}, & \overline{t} &= t\Omega, & \overline{x} &= \frac{x}{R} \\ \overline{k}_{m_i}^2 &= \frac{k_{m_i}^2 m_0 R}{I_b}, & \overline{m} &= \frac{m}{m_0} \end{aligned}$$

where the subscript  $i$  represents a 1 or 2, depending on which blade cross-sectional

axis the property is taken about. In addition, the subscript 0 represents a reference quantity taken at one particular blade location. Inserting these parameters into Equations 4.1 and 4.2 and simplifying yields

$$\begin{aligned} & -\frac{\partial}{\partial \bar{x}} \left\{ \left[ \left( \frac{EI_0}{I_b R \Omega^2} \right) \overline{GJ} + \left( \frac{m_0 R^3}{I_b} \right) \left( \frac{k_{A_0}}{R} \right)^2 \overline{T k_A^2} \right] \frac{\partial \phi}{\partial \bar{x}} \right\} \\ & + \overline{m k_m^2} \frac{\partial^2 \phi}{\partial \bar{t}^2} + \overline{m} (\overline{k}_{m_2}^2 - \overline{k}_{m_1}^2) \cos(2\beta) \phi \\ = & -\overline{m} (\overline{k}_{m_2}^2 - \overline{k}_{m_1}^2) \sin \beta \cos \beta + \left( \frac{\rho C_{L_\alpha} c_0 R^4}{I_b} \right) \left( \frac{c_0}{R} \right) \frac{1}{2} \bar{r}^2 \bar{c}^2 \overline{C_{M_\delta}} \delta \end{aligned} \quad (4.3)$$

$$\begin{aligned} & \left( \frac{EI_0}{I_b R \Omega^2} \right) \frac{\partial^2}{\partial \bar{x}^2} \left[ (\overline{EI_1} \cos^2 \beta + \overline{EI_2} \sin^2 \beta) \frac{\partial^2 \bar{w}}{\partial \bar{x}^2} \right] \\ & + \left( \frac{m_0 R^3}{I_b} \right) \overline{m} \frac{\partial^2 \bar{w}}{\partial \bar{t}^2} - \left( \frac{m_0 R^3}{I_b} \right) \frac{\partial}{\partial \bar{x}} \left( \overline{T} \frac{\partial^2 \bar{w}}{\partial \bar{x}^2} \right) \\ = & \left( \frac{\rho C_{L_\alpha} c_0 R^4}{I_b} \right) \frac{1}{2} \bar{r}^2 \bar{c} \overline{C_{L_\delta}} \delta \end{aligned} \quad (4.4)$$

A simple estimate of the hub thrust is given by

$$L_{\text{tot}} = N \int_{r_{\text{co}}}^R \frac{1}{2} \rho r^2 \Omega^2 c \{ C_{L_\delta} \delta + C_{L_\alpha} \alpha \} dr \quad (4.5)$$

Non-dimensionalizing this equation using the previously defined non-dimensional parameters, and the additional parameter

$$\bar{L} = \frac{L_{\text{tot}}}{m_0 R^2 \Omega^2}$$

yields

$$\bar{L} = \left( \frac{\rho C_{L_\alpha} c_0 R^4}{I_b} \right) \left( \frac{I_b}{m_0 R^3} \right) N \int_{\bar{r}_{\text{co}}}^1 \frac{1}{2} \bar{r}^2 \bar{c} \{ \overline{C_{L_\delta}} \delta + \alpha \} d\bar{r} \quad (4.6)$$

The supposition is that the servo-flap excites the flapping and torsion modes of the blade, as governed by Equations 4.3 and 4.4, which affect the angle of attack,  $\alpha$ , in Equation (4.6). What remains is to model the contribution of the servo-flap actuation system.

The servo-flap actuation system can be modeled as shown in Figure 4-1.

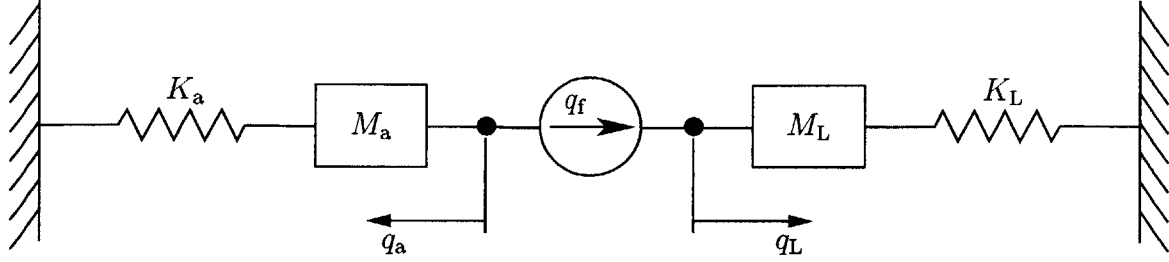


Figure 4-1: Mass-spring model of the servo-flap actuation system.

$$K_a q_f + M_a \ddot{q}_f = (K_L + K_a) q_a + (M_L + M_a) \ddot{q}_a \quad (4.7)$$

The stiffness of the actuator is modified from Equation (2.4) to be

$$K_a = \left( \frac{1}{2 \left( \frac{1}{\tan^2 \theta_a} + \frac{K_s}{K_f \sin^2 \theta_a} \right)} \right) K_s = f_K K_s = f_K \frac{E_e A_e}{l_e} \quad (4.8)$$

The mass of the actuator is

$$\begin{aligned} M_{\text{tot}} &= 2\rho_e A_e l_e + 2\rho_f A_f l_f \\ &= 2 \left( 1 + \frac{\rho_f A_f l_f}{\rho_e A_e l_e} \right) \rho_e A_e l_e \\ &= f_M \rho_e A_e l_e \end{aligned} \quad (4.9)$$

Defining the stroke gain of the actuator as  $g_a$  permits us to write the free displacement of the actuator as

$$q_f = g_a l_e \epsilon \quad (4.10)$$

The load that the actuator drives is the sum of the aerodynamic servo-flap hinge moment and the torsional stiffness of the pre-stress wire,

$$K_L = \frac{G J_{\text{ps}}}{s^2 l_{\text{ps}}} + \frac{\frac{1}{2} \rho r_{\text{eff}}^2 \Omega^2 c^2 C_{H_\delta} l_{\text{eff}}}{s^2} \quad (4.11)$$

where  $l_{\text{eff}}$  is the effective spanwise length of the flap given a reference flap location of  $r_{\text{eff}}$ . The mass of the load is dominated by the rotational inertia of the servo-flap, such

that the pre-stress wire inertia is considered negligible. Substituting Equations (4.8)–(4.11) into Equation (4.7) and non-dimensionalizing yields

$$\begin{aligned}
& \left( \frac{EI_0}{I_b R \Omega^2} \right) f_K g_a \overline{EA_s} \epsilon + \left( \frac{m_0 R^3}{I_b} \right) f_M g_a \rho \overline{A_e l_e}^2 \frac{\partial^2 \epsilon}{\partial t^2} \\
&= \left\{ \left( \frac{EI_0}{I_b R \Omega^2} \right) \frac{\overline{GJ_{ps}}}{\bar{s}^2 \bar{l}_{ps}} + \left( \frac{\rho C_{L_\alpha} c_0 R^4}{I_b} \right) \left( \frac{c_0}{R} \right) \frac{\frac{1}{2} \bar{r}^2 \bar{c}^2 C_{H_\delta} l_{eff}}{\bar{s}^2} \right. \\
&\quad \left. + \left( \frac{EI_0}{I_b R \Omega^2} \right) f_K \frac{\overline{EA_e}}{\bar{l}_e} \right\} \overline{q_a} + \left\{ \frac{\overline{I_F}}{\bar{s}^2} + \left( \frac{m_0 R^3}{I_b} \right) f_M \rho \overline{A_e l_e} \right\} \frac{\partial^2 \overline{q_a}}{\partial t^2} \tag{4.12}
\end{aligned}$$

where the following non-dimensional parameters are used:

$$\overline{GJ_{ps}} = \frac{GJ_{ps}}{EI_0}, \quad \overline{I_F} = \frac{I_F}{I_b}, \quad \overline{\rho_e A_e} = \frac{\rho_e A_e}{m_0}$$

$$\overline{EA_e} = \frac{E_e A_e R^2}{EI_0}, \quad \overline{C_{H_\delta}} = \frac{C_{H_\delta}}{C_{L_\alpha}}, \quad \bar{l}_e = \frac{l_e}{R}$$

Equations (4.3), (4.4), (4.6), and (4.12) are the governing equations for the phenomenon under study in this research.

In order to apply the model scale experimental results to a full scale helicopter, all of the non-dimensional parameters identified above should remain constant between model and full scale. It is natural to geometrically scale the model being tested. This implies that all dimensions scale by an identical factor. In doing this, the following non-dimensional parameters are assured of remaining constant:

$$\bar{x}, \bar{c}, \bar{l}_e, \bar{l}_{ps}, \overline{C_{M_\delta}}, \overline{C_{L_\delta}}, \overline{C_{H_\delta}}$$

In addition, as long as the blade is constructed from materials with similar stiffnesses and densities, the following non-dimensional parameters will also remain constant between model and full scale:

$$\overline{EI_i}, \left( \frac{m_0 R^3}{I_b} \right), \overline{I_F}, \overline{GJ}, \overline{GJ_{ps}}, \overline{k_A}, \overline{k_{m_i}^2}$$

If, in addition, the model scale tests are run in air, the Lock number,

$$\gamma = \frac{\rho C_{L\alpha} c_0 R^4}{I_b}$$

will remain equal between tests. (Note that in the present model scale tests the Lock number of the model scale blades is a bit lower than a regular helicopter blade because of the concentrated mass of the actuation system components near the tip of the blade, and, to a lesser extent, because the scaled mass of the pitch shaft assemblies used on the MIT Hover Test Facility are greater than that of similar parts on a full-scale helicopter. See Table 4.1 for more details.)

Another important non-dimensional quantity is the ratio of blade stiffness to rotary inertia,

$$C_{SI} = \frac{EI_0}{I_b R \Omega^2} \quad (4.13)$$

Accepting the above stipulations that the model blade is geometrically scaled and constructed with materials similar to those of the full-scale blade, the following relations can be used

$$E_m = E_f \quad I_0 = k_1 R^4 \quad I_b = k_2 R^5$$

where  $k_1$  and  $k_2$  are constant factors. Using these definitions and enforcing the requirement that  $C_{SI}$  be equal between the model and full scale gives

$$R_f \Omega_f = R_m \Omega_m \quad (4.14)$$

This implies that, in order to extract useful information from the model scale tests, the model rotor should have the same tip speed as the full scale rotor. Enforcing this requirement is referred to as Mach scaling.

Performing Mach scaled tests provides a number of additional scaling advantages. For example, the aerodynamic model assumed in Equations 4.1 and 4.2 is exceedingly simple. Performing Mach scaled tests also assures that compressibility effects as well as the unsteady aerodynamics, governed by the reduced frequency  $k = \frac{\omega b}{r \Omega}$ , are satisfied in such rotor tests.

The one parameter of considerable importance that is not held constant between the model and full scale tests is the Reynolds number,  $\text{Re} = \frac{\rho U c_0}{\mu}$ . It is not possible, given the above geometric and manufacturing constraints, to keep both the Mach number and Reynolds number constant for a scaled test in air. Proper Reynolds number scaling ensures that the effects of viscosity, especially in the formation of the airfoil boundary layer, are captured in the model test. Because these model scale tests will be at a much lower Reynolds number than the full-scale tests, the boundary layer in which the servo-flap operates will be larger than in the full-scale blade. This will have two major effects. First, because the boundary layer represents a dead-band for the flap in affecting the aerodynamics, the flap will be slightly less effective in creating hub shear in the model scale tests. Second, the contribution of the additional drag from the servo-flap components will not be properly represented. Thus, the model scale tests will be a conservative evaluation of servo-flap authority in controlling the rotor but will underestimate the extra power needed to operate a rotor with blade mounted servo-flaps.

Froude scaling was not addressed in these experiments. Froude scaling is typically used when the effects of gravity on the deformation of the structure are important. Because the steady centrifugal acceleration at the tip of the blades is approximately 3000 g's and scaled flapwise vibratory accelerations of up to 70 g's are typically encountered, the 1 g acceleration due to gravity is considered unimportant in evaluating blade mounted actuation authority.

## 4.2 The MIT Hover Test Facility

The active rotor blade was tested in air at the MIT Hover Test Facility. This facility was developed as part of this overall research effort in order to provide a test-bed to evaluate the effectiveness of blade mounted actuation schemes at Mach scaled rotor speeds. The facility is described in this section. An excellent description of this facility is also given by Rodgers [67] (See esp. Appendix B in [67]).

### 4.2.1 Hardware

The hover stand was sized for 1/6 scale CH-47 (Chinook) rotor blades. The design of the facility was based on the hover test facilities used at Boeing Helicopters in Philadelphia. The properties of the rotor and support structure are given in Table 4.1. Because of the concentrated actuator mass located near the tip of the rotor blades,

Table 4.1: Properties of MIT Hover Test Facility hardware.

Property	Value
Radius	60.619 in (5.05 ft)
Hover Speed	1336 RPM
Max Motor Power	150 hp
Lowest Stand Elastic Mode	> 150 Hz
Number of Blades	2
Flap Articulation	BS 1.734 (0.0286R)
Feathering Degree of Freedom	Clamped at BS 4.078 (0.0673R)
Lag Articulation	BS 9.093 (0.15R)
$I_b$ of Pitch Shaft Assemblies	0.0213 slug ft <sup>2</sup>
Mass of Pitch Shaft Assemblies	6.437 lbm
Lock Number of Blade/PSA Structure	7.49
Blade Chord (nominal)	5.388
Full Scale to Model Scale Geometric Factor	5.939:1

the inertia of this active blade was much higher than that of a blade with a more uniform cross-section. For example, the Lock number of a full-scale CH-47 blade is 9.37. The difference between these Lock numbers is due solely to the difference in the blade mass moments of inertia.

The motor was sized to be capable of driving a three bladed rotor ( $c = 5.388$  in) at a maximum blade loading of  $\frac{C_T}{\sigma} = 0.11$ . The induced power, which represents about 60% of the total power loss in rotor operation [44], is related to the blade loading by

$$C_{P_i} = \frac{1.15}{\sqrt{2}} \left( \frac{C_T}{\sigma} \right)^{3/2} \sigma^{3/2} \quad (4.15)$$

Thus, the relation used to size the motor to a target blade loading is given by

$$P_{\text{motor}} = \frac{1}{0.60} \frac{1.15}{\sqrt{2}} \left( \frac{C_T}{\sigma} \right)^{3/2} \sigma^{3/2} \rho A (\Omega R)^3 \quad (4.16)$$

The motor drives the rotor via a 3 inch diameter steel shaft that is about four feet long. A thrust bearing is used at the top of the shaft to transfer both radial and rotor thrust loads to the pyramid support structure. A standard cylindrical bearing, transferring only radial loads, is used at the bottom of the shaft, just above the motor. A 162 channel sliring is sandwiched between the two shaft bearings. 138 of the sliring channels are rated for low voltage sensor signals. 24 of the sliring channels are rated for high voltage actuation of up to  $\pm 4000$  Volts.

The support structure was designed using a finite element package to ensure the structural resonances were outside of the bandwidth of rotor testing, which is nominally from 10 to 150 Hz.

To isolate the stand from building vibrations, during operation of the rotor, the entire structure is supported by pneumatic isolation pads. Four shock absorbers are used to add damping to the soft suspension modes to minimize the possibility of dynamic instability. A picture of the isolation system for the stand is shown in Figure 4-2.

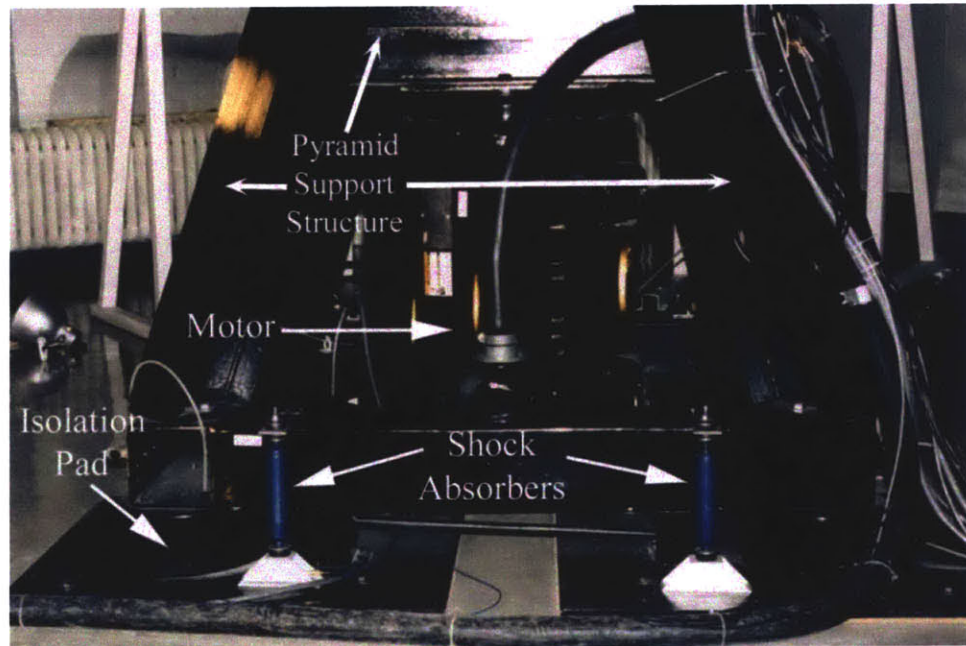


Figure 4-2: Test stand isolation pads and dampers.

The top of the shaft interfaces with a 6-axis load transducer through a 2 inch thick coupling flange. The load transducer is described in Section 4.2.2. Another 2

inch thick flange sits on top of the load transducer, and the rotor hub is mounted to the top of that flange. The load transducer is sandwiched between two stiff flanges to ensure that the loads sensed by the transducer are true hub loads, and are not due to local deformations of the surface of the sensor casing.

The blades are connected to the hub via pitch shaft assemblies. The assemblies allow for free articulation of the flap and lag degrees of freedom. To allow for angle of attack adjustments, the pitch shaft assemblies were manufactured with separate inboard and outboard sections that are keyed together. The keys transfer centrifugal force but allow for free rotation between the two sections. A swashplate is not used to control blade angle of attack on this rotor. Instead, the blade angle is set by using a worm and gear mechanism attached to the inboard and outboard sections of the pitch shaft assemblies. Once the blades are at a desired angle of attack, the inboard and outboard pitch shaft assembly sections are clamped together at a mating surface, defined by the pitch plates (see Figure 4-9). The split clamps used to retain the keys also provide some torsional clamping force due to friction. This arrangement allows for testing of actuation authority at specific angles of attack.

The pitch shaft assemblies used for these rotor tests were heavier than comparable parts on other operational rotor stands. The extra mass was incorporated into the design of these components to bolster their fatigue strength, for safety. The extra mass slightly lowers the blade Lock number and the natural frequencies of the flapwise bending modes of the rotor blades. The implications of this are pointed out, where appropriate, in Section 4.2.3. The flapwise moment of inertia of just the pitch shaft assemblies about the center of rotation as well as the Lock number of the entire blade and pitch shaft assembly structure are given in Table 4.1.

A passive rotor blade was supplied by Boeing Helicopters to balance the active blade during hover testing. The passive blade has the same planform as the active blade, except that its chord tapers linearly to 1.625 inches from blade station 54.557 inches out to the tip. Before spinning it was necessary to balance the blades so that the sum of the centrifugal force transferred from the blades to the hub was close to zero. The mass of the passive blade is 734 grams. The mass of the active blade (excluding

root electrical connectors) is 889 grams, 21% higher than the passive blade weight. As discussed in Section 3.3, the extra weight in the active blade is due primarily to the actuator and balance weights, which are centered at the 75.8% spanwise location.

The blades were balanced by using a large steel split clamp to retain the keys on the passive pitch shaft assembly and a small aluminum split clamp on the active pitch shaft assembly. As shown in Figure 4-3, before mounting the blades to the stand, a teeter mechanism was used on the bench top to ensure the blades were balanced in the spanwise direction. The heavier electrical connectors for the active blade rested on

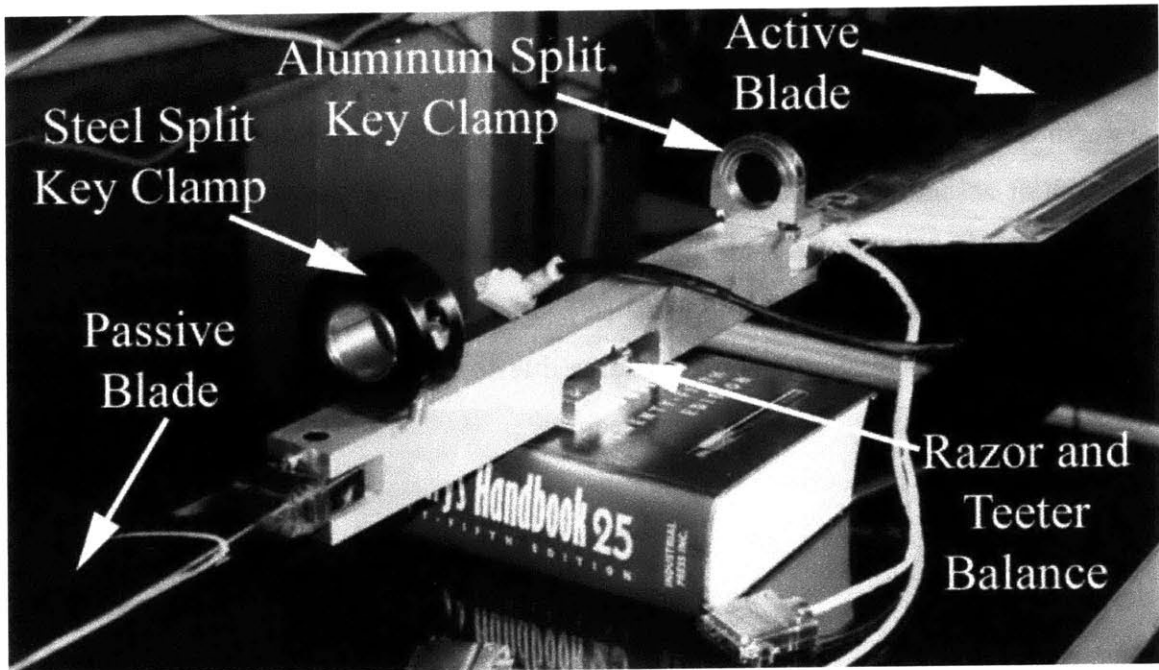


Figure 4-3: Rotor blade balancing.

the table because their centrifugal force is transferred to the hub mostly independent of the pitch shaft assemblies. After balancing, the blades are attached to the lag hinge of the pitch shaft assemblies via a 0.5 inch diameter steel pin. Pictures of the blades mounted to the spin stand are shown in Figures 4-4 and 4-5.

A containment ring surrounds the rotor to protect personnel and equipment in case a blade is lost during testing. The ring is 14 feet in diameter. Plywood is bolted to the interior of the ring to prevent ricochets. In addition, 1/8 inch steel plate covers the wall between the spin stand and control room, to protect the operators from any

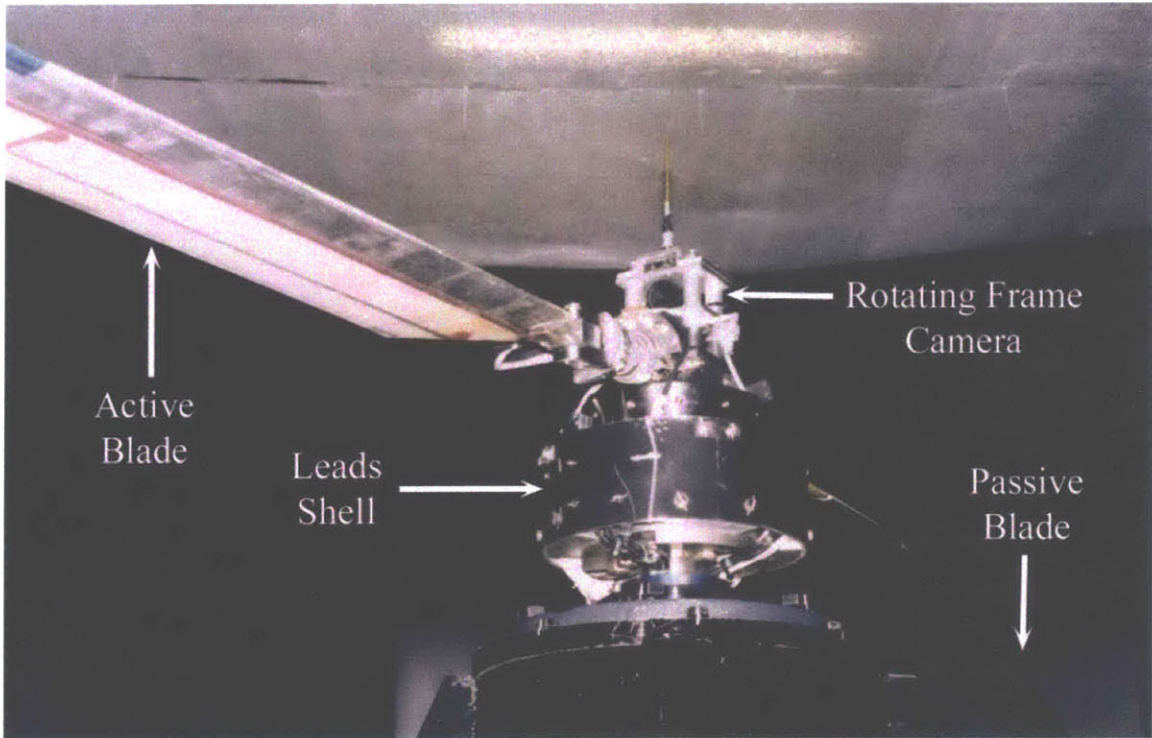


Figure 4-4: Rotor blades mounted on test stand.

debris not stopped by the containment ring.

The MIT Hover Test Facility is in a relatively small room. For example, the total height of the test stand room is approximately 14 feet, and the nominal tip-path plane of the rotor blades is approximately 7 feet, 11 inches from the floor, placing the rotor within ground effect. Furthermore, the walls of the room place additional constraints on the airflow. The lateral room dimensions measure approximately 26 feet wide by 52 feet long, and there are also a large number of overhanging pipes in the room. Figure 4-6 shows the arrangement of the test stand and containment ring with respect to the room boundaries. Left untreated, the walls, floor, ceiling and overhanging pipes disrupt the normal flow of air, creating a large amount of inflow turbulence into the rotor. To reduce this problem, an aerodynamic mesh was placed on top of the containment ring. The mesh serves to smooth out regions with a large amount of turbulence, creating a uniform stream of air into the rotor. To ensure that all (or most) of the air flowing through the rotor disk flows first through the mesh, a bellmouth was also added around the rotor. Figure 4-7 is a close-up of the test

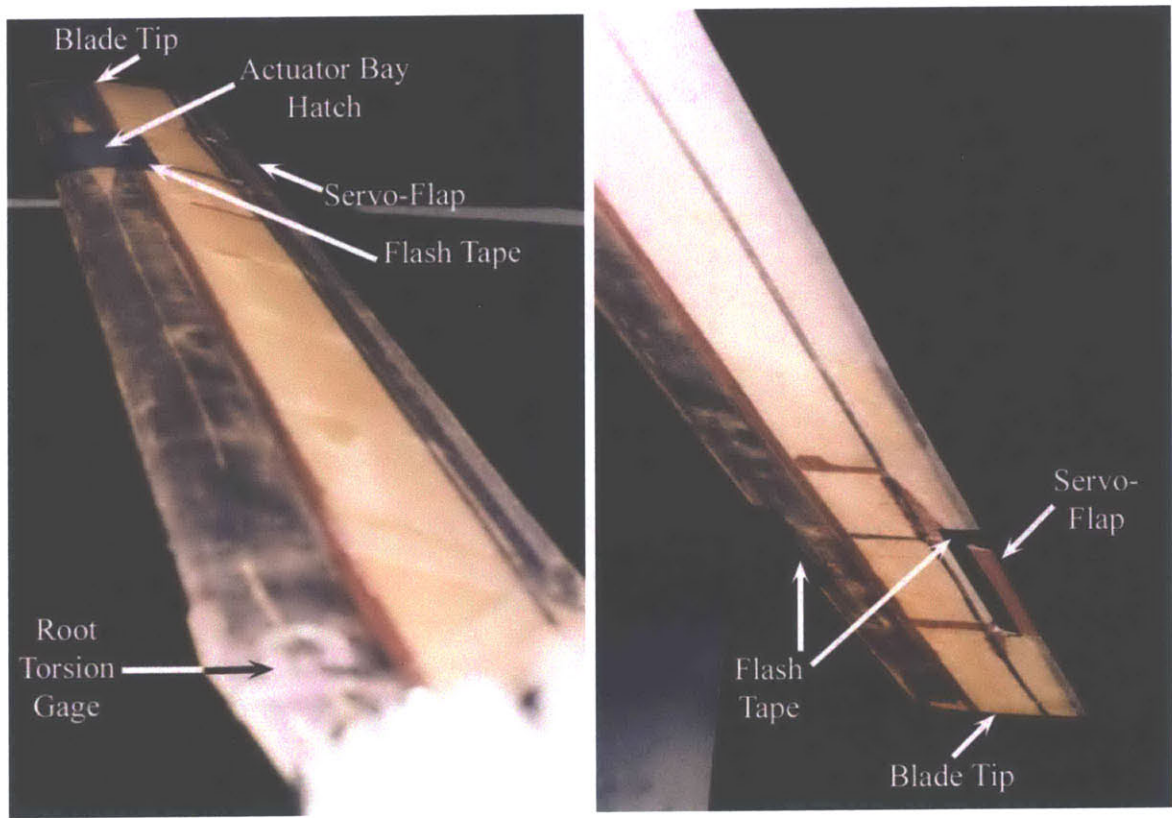


Figure 4-5: Active blade on test stand, looking outboard. a) View from above. b) View from below.

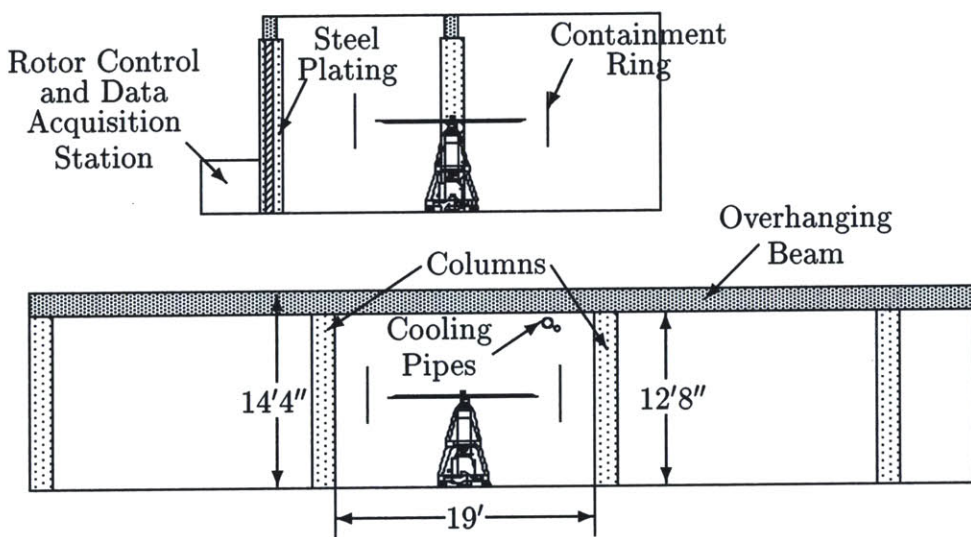


Figure 4-6: Arrangement of test stand room.

stand (with no rotor blades), including a section of the containment ring, mesh and bellmouth in the background.

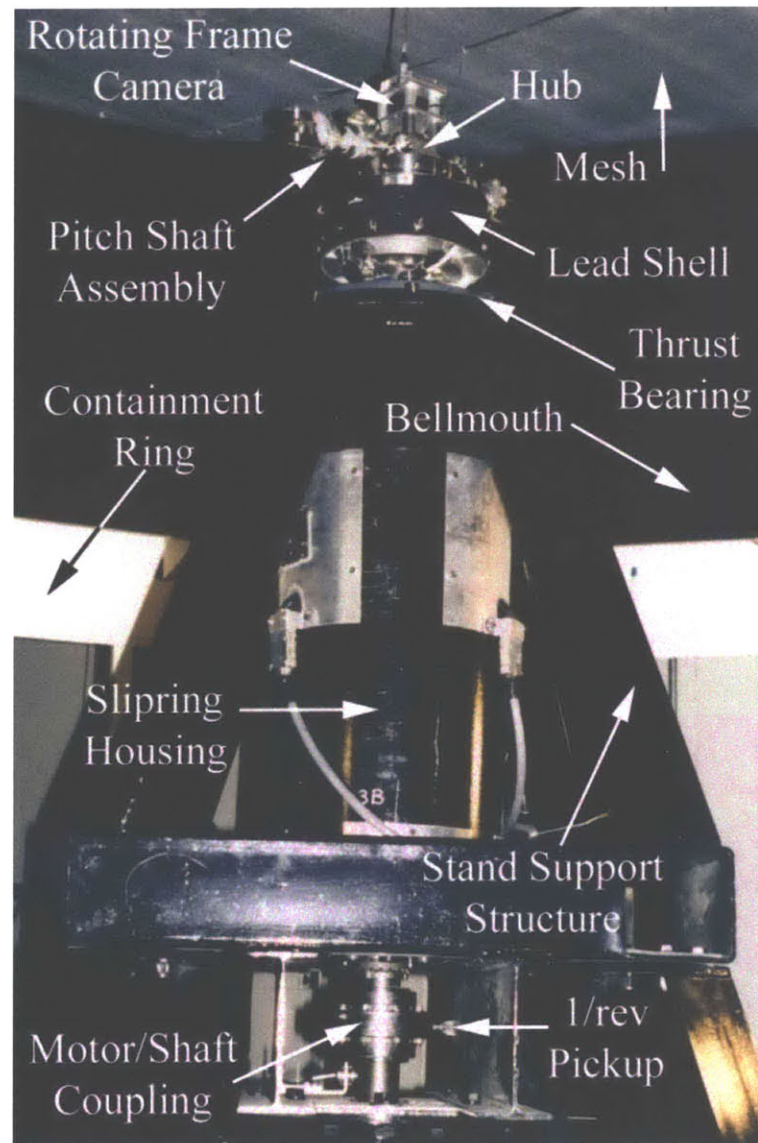


Figure 4-7: Test stand, containment ring, bellmouth, and aerodynamic mesh.

The use of the aerodynamic mesh and bellmouth was very effective. Figure 4-8a shows a typical thrust spectrum of the rotor with just the containment ring in place. A 2/rev vibration that is  $\pm 49\%$  of the steady thrust is present. By adding the aerodynamic mesh and bellmouth, this vibrational component is reduced by nearly an order of magnitude, as shown in Figure 4-8b.

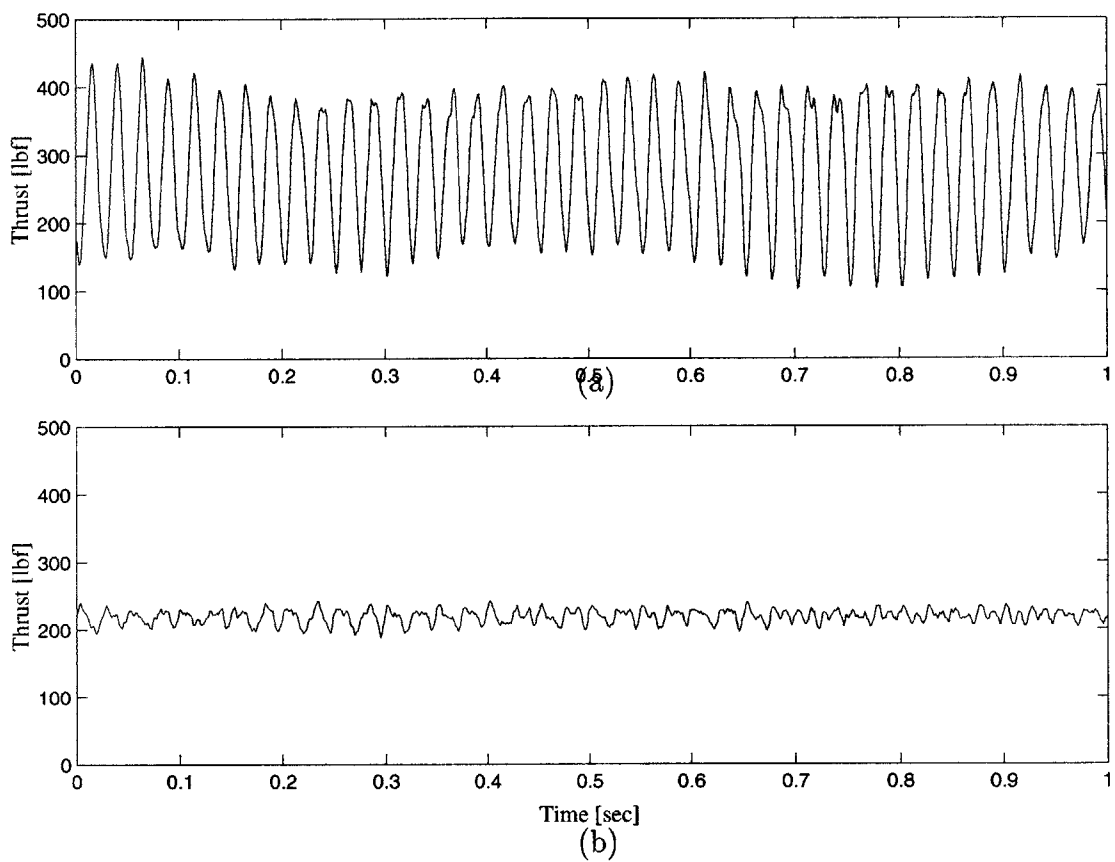


Figure 4-8: Thrust response (a) without aerodynamic treatment, and (b) with bell-mouth and mesh.

#### 4.2.2 Instrumentation

In addition to the strain gages and Hall effect transducers in the active blade, there are a number of sensors used outside of the blade. The most important sensor for identifying rotor vibrational control performance is the six axis load transducer mounted at the center of rotation, 3.7 inches below the blade flapping hinge plane. The transducer is cylindrical, 7.5 inches in diameter and 3 inches tall, and was manufactured by JR3 Inc. It provides measurements of the three forces and three moments in the rotating frame at the center of rotation. The sensor is oriented such that the positive y-axis points along the active rotor blade, and the positive z-axis points upward along the rotor shaft (*i.e.*, positive thrust is in the +z direction). The designed maximum load and resolution of the six channels are shown in Table 4.2. Of course, the resolution

Table 4.2: Properties of JR3 load transducer.

Load Component	Max Load	Accuracy	Resolution
$F_x$	$\pm 300$ lbf	1.5 lbf	0.08 lbf
$F_y$	$\pm 300$ lbf	1.5 lbf	0.08 lbf
$F_z$	+2000/-500 lbf	6.2 lbf	0.25 lbf
$M_x$	$\pm 250$ ft-lbf	1.2 ft-lbf	0.06 ft-lbf
$M_y$	$\pm 250$ ft-lbf	1.2 ft-lbf	0.06 ft-lbf
$M_z$	+200/-800 ft-lbf	2.5 ft-lbf	0.05 ft-lbf

achieved during testing may not be at the levels noted in Table 4.2, due to factors such as additional electrical noise and limitations in the data acquisition resolution. The bandwidth of the transducer exceeds 500 Hz on all channels.

The flapping angle of the active blade was also measured using a Hall effect transducer. This transducer was mounted in a housing located at the end of the flapping pin. The transducer sensed changes in the field of a magnet, fixed to the end of the flapping pin, as the blades flapped.

All of the rotating frame signals were transferred to the non-rotating frame via a slipring. The rotating frame leads of the slipring are attached to a number of connectors that are fixed along the inside wall of the “lead shell”. This aluminum shell is mounted concentrically around the load transducer, with an inner diameter of

10.2 inches. A picture of the hub with the various components is shown in Figure 4-9. After connecting the blade to the pitch shaft assemblies, the signal and high voltage

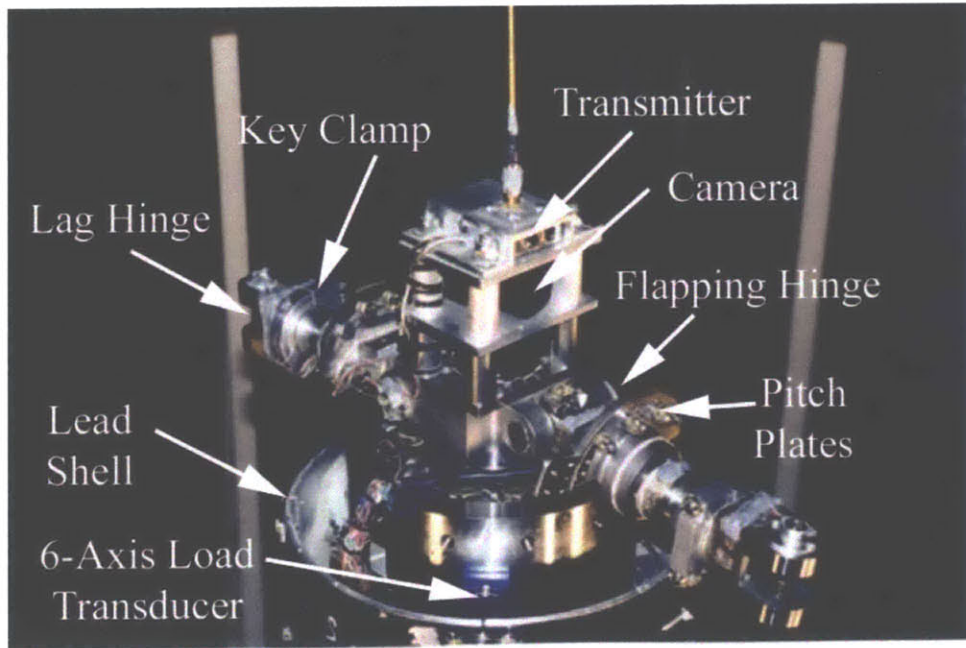


Figure 4-9: Test stand hub components.

blade connectors are attached to the sliring connectors inside the lead shell. The blade wire bundles are then tie-wrapped at a number of strategic locations to the pitch shaft assemblies and other hub components. Additional views of the hub components and the wire bundle logistics of the active blade are shown in Figure 4-10.

Additional sensors were used in the non-rotating frame. A non-contacting magnetic proximity sensor was used at the base of the rotor shaft to provide a pulse signal once per revolution. This 1/rev pick-up is shown in Figure 4-7. The voltage and current on the actuator were stored during actuation. Finally, when closed-loop control was applied, the feedback control signal was also stored.

Two cameras were used to record all rotor tests. One non-rotating frame camera was mounted near the floor pointing up at the stand and rotor. It served primarily as a safety of flight monitor of the stand during testing. A second camera was mounted in the rotating frame above the hub, pointed along the active blade. It is shown in Figures 4-4, 4-7, 4-9, and 4-10. The signal from this camera was transmitted via radio frequency to a receiver mounted between the bellmouth and containment ring. This

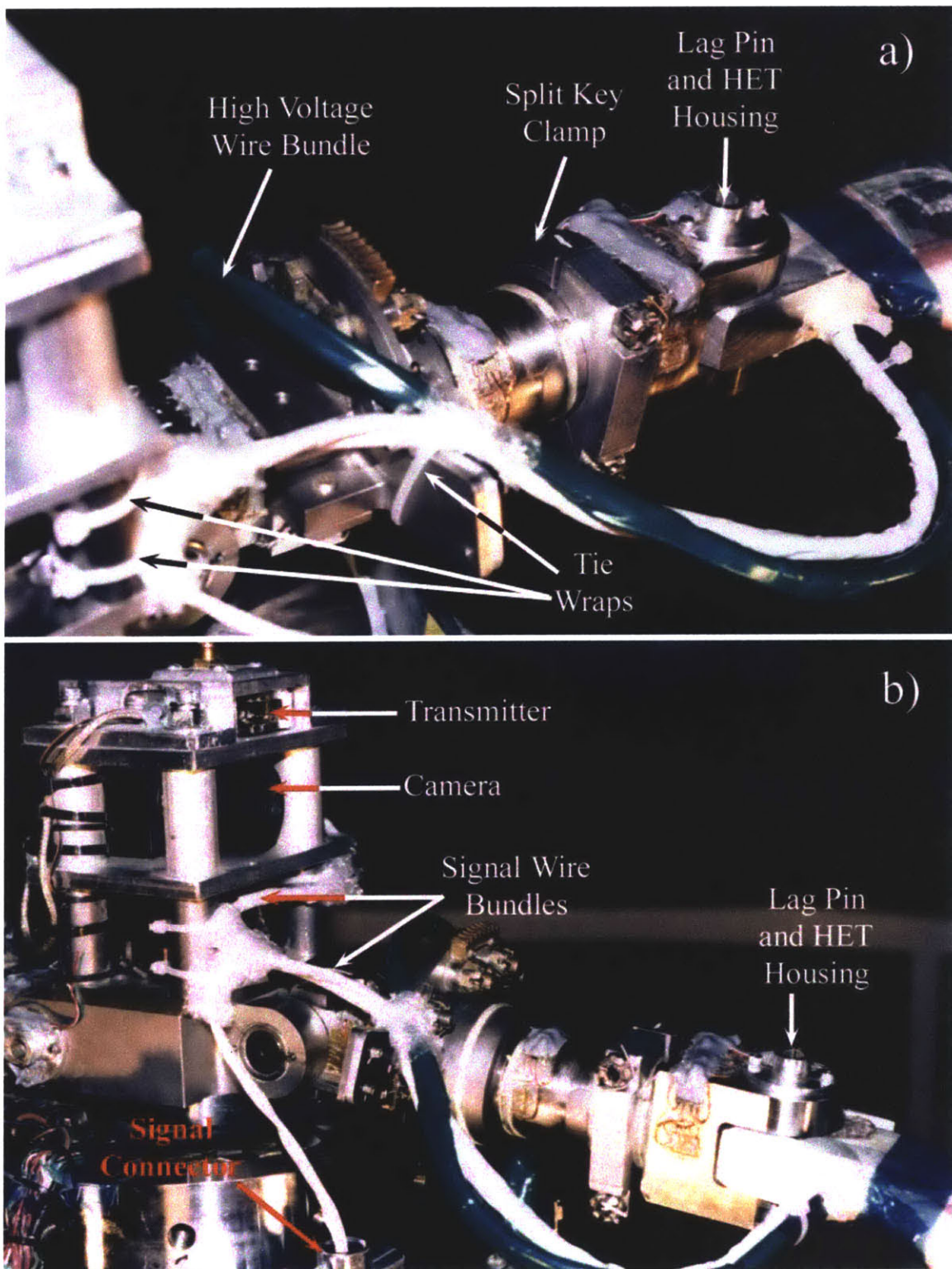


Figure 4-10: Blade wiring at hub, (a) looking outboard, and (b) looking from just aft of lead-lag pin.

camera picked up blade and servo-flap motion during testing. Images from each of these cameras during testing are shown in Figure 4-11.

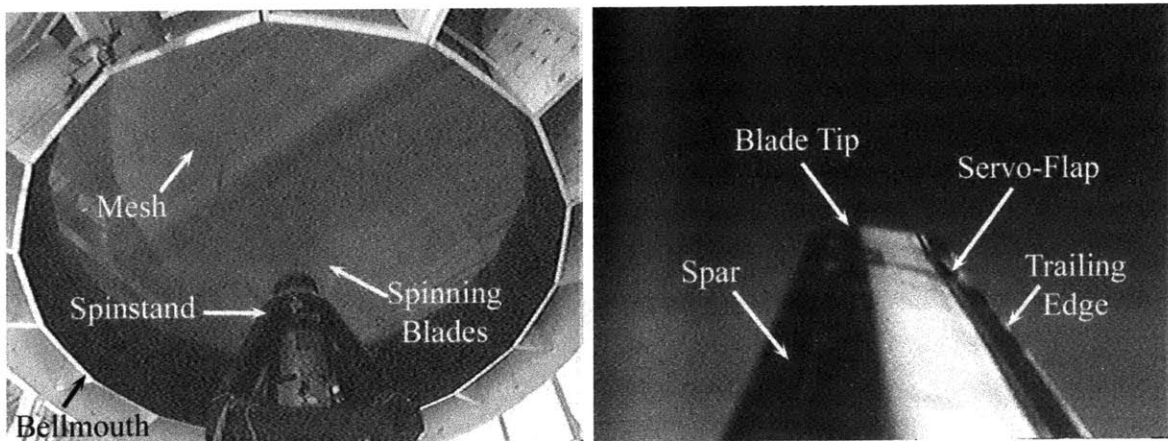


Figure 4-11: Camera images during hover test. (a) Non-rotating frame camera. (b) Rotating frame camera.

All sensor signals were run to an instrumentation break-out panel in the rotor control room. On this panel dummy resistors were used to complete the quarter and half strain gage bridges used in the blades. In addition, capacitors were used to filter out high frequency noise. All of the sensor signals were stored to the computer through a National Instruments SCXI-1001 data acquisition box using 1120/1320 modules to store direct analog signals and 1121/1321 modules to provide strain gage excitation and conditioning. An analog circuit was built to provide current excitation and differential amplification for the Hall effect transducer sensors.

Figure 4-12 shows a block diagram of the entire hover test data acquisition set-up. Figure 4-13 shows a picture of the rotor control station and data acquisition electronics used during all the rotor tests.

#### 4.2.3 Hover Test Facility Data Collection and Analysis Techniques

A LabView data acquisition system running on a 450 MHz, Pentium II computer was used to store all signals during the hover tests. The signals were transferred from the National Instruments SCXI Data Acquisition box through a multiplexing connection

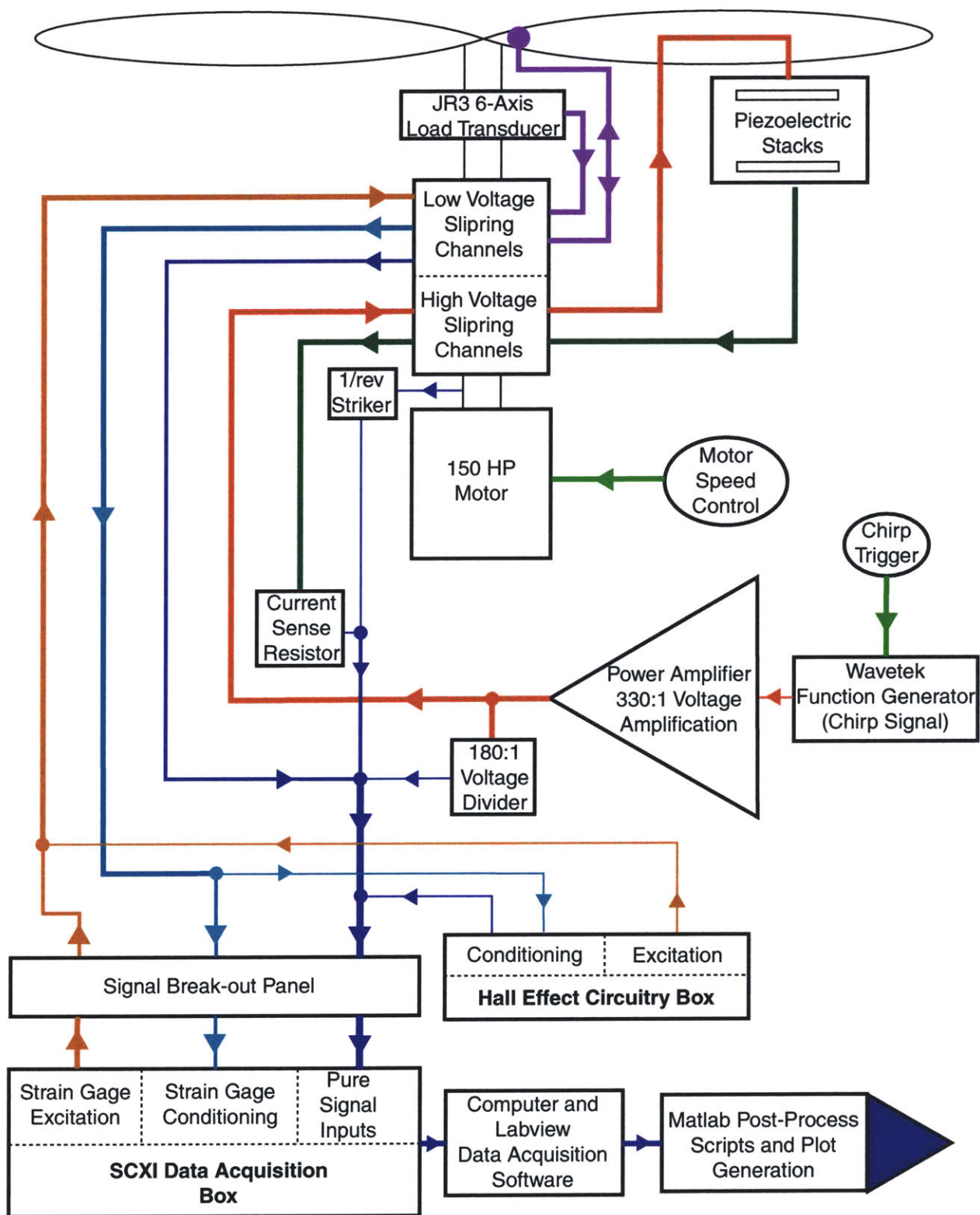


Figure 4-12: Block diagram of the hover test instrumentation.

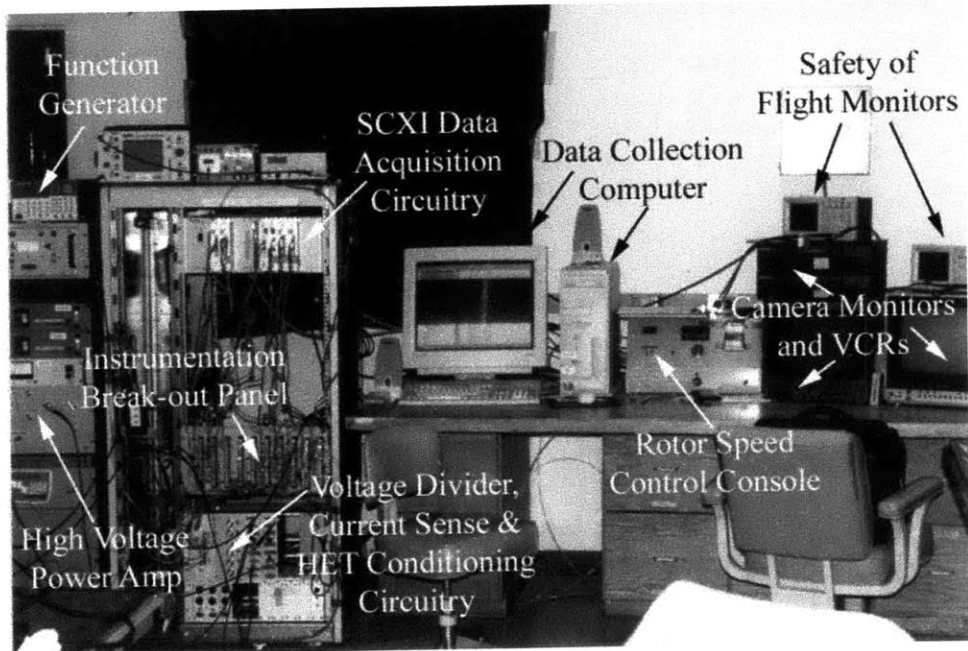


Figure 4-13: Rotor control station and data acquisition electronics.

operating at speeds of up to 100 kHz, with an interchannel delay of  $2.5 \mu\text{s}$ . 25 signals in all were stored during the test. They are listed, in the order stored, in Table 4.3.

A nominal scan rate of 1000 points per second on all channels was used for all rotor tests. A “stream-to-disk” LabView virtual instrument was developed so that, while acquiring data during a test, all 25 signal channels were stored directly to the computer hard drive. Signal processing techniques, described below, were applied after the test was completed to identify transfer functions and evaluate performance. A second virtual instrument (VI) based on transfer function identification using sine dwell techniques was applied in a few instances to validate the transfer function identification techniques described below. This VI is based on identifying a transfer function to within a set accuracy with a certain level of confidence. The theory behind the development of this VI is described in depth by Rodgers [67] (pps 280-281).

To identify the transfer functions during rotor testing, a swept sine signal, or “chirp”, is input into the servo-flap actuator. This swept sine consists of a constant amplitude voltage sine wave signal increasing in frequency linearly with time over a ten second period between two frequency bounds. After a two second delay, the chirp is repeated. The sweeps are repeated multiple times, as desired. For example,

Table 4.3: Data signals stored during rotor tests.

Signal Number	Description
1	Primary Actuator Deflection
2	Secondary Actuator Deflection
3	Active Blade Flapping Angle
4	Feedback Control Signal (closed-loop data cases)
5	Actuator Voltage
6	Actuator Current
7	Hub Force, $F_x$
8	Hub Force, $F_y$
9	Hub Force, $F_z$
10	Hub Moment, $M_x$
11	Hub Moment, $M_y$
12	Hub Moment, $M_z$
13	1/rev Striker
14	0.19R Flapwise Bending Strain
15	0.42R Flapwise Bending Strain
16	0.66R TE Stiffener Axial Strain
17	0.71R Shear Strain Inboard of Actuator Bay
18	0.75R Bay Temperature Measurement
19	0.75R Strain on Actuator Frames
20	0.63R Torsional Strain
21	0.87R Torsional Strain
22	0.73R Axial Strain just Forward of Actuator Bay
23	0.73R Axial Strain just Aft of Actuator Bay
24	0.80R Shear Strain Outboard of Actuator Bay
25	0.21R Torsional Strain

a typical test consists of 10 chirps from 10 Hz to 200 Hz. The frequency range was narrowed for some tests to zoom in on areas of interest. All data signals are stored to disk during the entire chirp testing period.

An empirical transfer function estimate (ETFE) is obtained from the data by taking a ratio of the FFT of the output and input signals directly. This ratio tends to be dominated by noise, and is not very accurate. The collection of chirps was averaged in the frequency domain using the cross- and auto-spectra, to eliminate some of the noise. For example, if the Fourier transform of the output and input signals are given by  $Y(f)$  and  $U(f)$ , respectively, the averaged cross-spectrum is

$$\widehat{\phi_{yu}} = \frac{1}{N} \sum_{i=1}^N Y_i(f) U_i^*(f) \quad (4.17)$$

where  $U_i^*(f)$  is the complex conjugate of the control signal,  $i$  is the index of a particular chirp, and  $N$  is the total number of chirps. Similarly, the auto-spectrum of the input is given by

$$\widehat{\phi_{uu}} = \frac{1}{N} \sum_{i=1}^N U_i(f) U_i^*(f) \quad (4.18)$$

An average transfer function is given by

$$\overline{G_1}(f) = \frac{\widehat{\phi_{yu}}}{\widehat{\phi_{uu}}} \quad (4.19)$$

Smoothing is then applied to the averaged cross- and auto spectra by convolving these signals in the frequency domain with a smoothing window. A Bartlett window gave the best results in terms of smoothing the transfer function while picking up the details of the transfer functions. The smoothed cross- and auto spectra are given by

$$\begin{aligned}\widehat{\widehat{\phi_{yu}}} &= \widehat{\phi_{yu}} * h_b(f) \\ \widehat{\widehat{\phi_{uu}}} &= \widehat{\phi_{uu}} * h_b(f)\end{aligned}$$

where  $h_b(f)$  is the Bartlett window. The form of the Bartlett window used here is

$$h_b(f) = \frac{1}{\gamma_s} \left( \frac{\sin \frac{\gamma_s}{2k_s} f}{\sin \frac{1}{2k_s} f} \right)^2 \quad (4.20)$$

where the constant  $k$  was used to normalize the frequency values in the argument of the sines. The actual Bartlett window used to reduce most of the rotor data in this thesis is shown Figure 4-14. The smoothed transfer function is obtained by taking

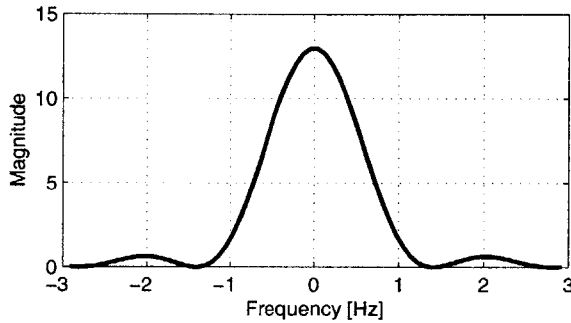


Figure 4-14: Typical Bartlett window used to smooth data.

the ratio of the smoothed cross- and auto spectra as

$$\widehat{\widehat{G}}_1(f) = \frac{\overline{\overline{\phi_{yu}}}}{\overline{\overline{\phi_{uu}}}} \quad (4.21)$$

As an example, Figure 4-15 shows the transfer function data from flap actuation to blade root torsional strain. The ETFE, the averaged transfer function and the smoothed transfer function are all plotted in this figure. Note: For all of the transfer functions in this document, the frequency axis is labeled in units of Hz. In addition, vertical grid lines are placed at frequencies corresponding to harmonics of the rotor speed to aid in identifying harmonic behavior of the system.

Averaging the data will always lead to a more accurate estimate of the transfer function and can be done without limit. In contrast, smoothing must be done carefully – too much smoothing can lead to an overestimate of the system damping. The parameters defining the shape of the Bartlett window used were chosen to give a smooth transfer function while capturing the predominant details of the transfer

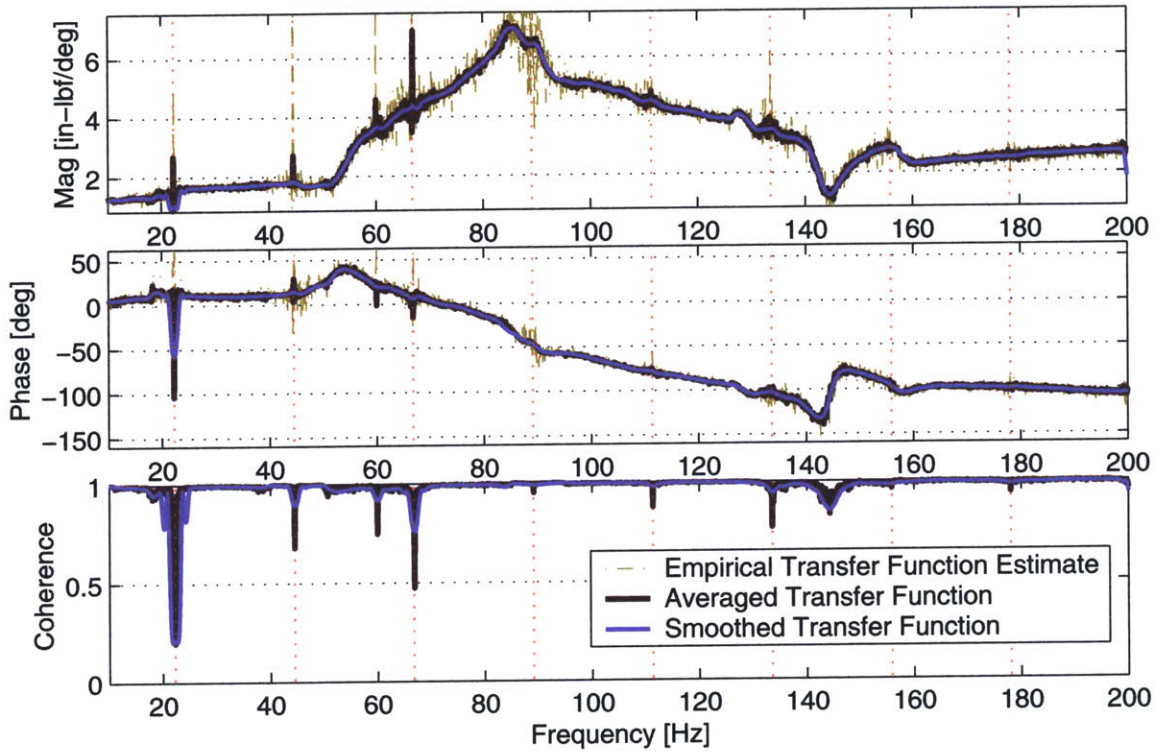


Figure 4-15: Comparison of ETFE, averaged and smoothed transfer functions.

function, as indicated by the averaged transfer function. Engineering judgement was used in applying this smoothing. All transfer functions presented in the rest of this thesis have been averaged and smoothed using the above techniques.

A complementary estimate of the transfer function is obtained by calculating

$$G_2(f) = \frac{\overline{\overline{\phi_{yy}}}}{\overline{\overline{\phi_{uy}}}} \quad (4.22)$$

The ratio of  $\widehat{G}_1(f)$  to  $\widehat{G}_2(f)$  defines the coherence of a transfer function. The coherence varies between zero and one. The coherence of a transfer function will be low if there is excessive noise in the system or if the system is non-linear. Except for some friction and material nonlinearities in the actuation system, the rotor blade experimental system can be considered linear. However, because of the poor aerodynamic environment in the test, there is a large amount of aerodynamic noise present at the harmonics of the rotor speed. Thus we tend to see poor coherence at these harmonic

frequencies, as shown in Figure 4-15. Because the data is from a two-bladed rotor, the noise at the 2/rev (22.27 Hz) and 4/rev (44.53 Hz) frequencies dominates in all transfer functions from flap deflection to hub forces.

During a standard chirp identification, the noise at some harmonics led to very poor estimates of the transfer functions at these frequencies. To remedy this, chirps over small frequency ranges around these harmonics were used to zoom-in and get a better transfer function estimate there. The improved transfer function estimate was spliced into the original transfer function data in place of the poor data regions.

For the remainder of the transfer functions in the main body of the thesis, the coherence will not be included. The identification led to an acceptable amount of coherence in the identification of all transfer functions.

#### 4.2.4 Blade Tracking

After attaching the blades to the stand, the collective angle of attack of the blades was set at a desired orientation. The angle was checked using a digital level at the 75% spanwise section of the blade. To ensure an accurate blade track, a thin piece of reflective tape was applied to the blades, spanwise, near the tip. A laser was pointed upwards at the rotor plane at a 45 deg angle, and the non-rotating camera was mounted on the floor and oriented directly upward to view the spinning rotor blades. Once in hover, as the blades passed the camera, the laser dot would jump from side to side in the camera view, depending on the track of the two blades. The blades were considered tracked (*i.e.*, rotating with the same steady pre-cone angle) when the laser dot reflecting off of both blades did not move appreciably between blade passes. Figure 4-16 shows an illustration of the blade tracking procedure.

During the blade tracking at 8 deg angle of attack, blade tracking measurements showed that the active blade untwisted by about 3.2° with respect to the passive blade between 0 and 1336 RPM. This untwisting was most likely due to a combination of the reduced torsional stiffness of the active blade, and the propeller moment on the components of the actuation system.

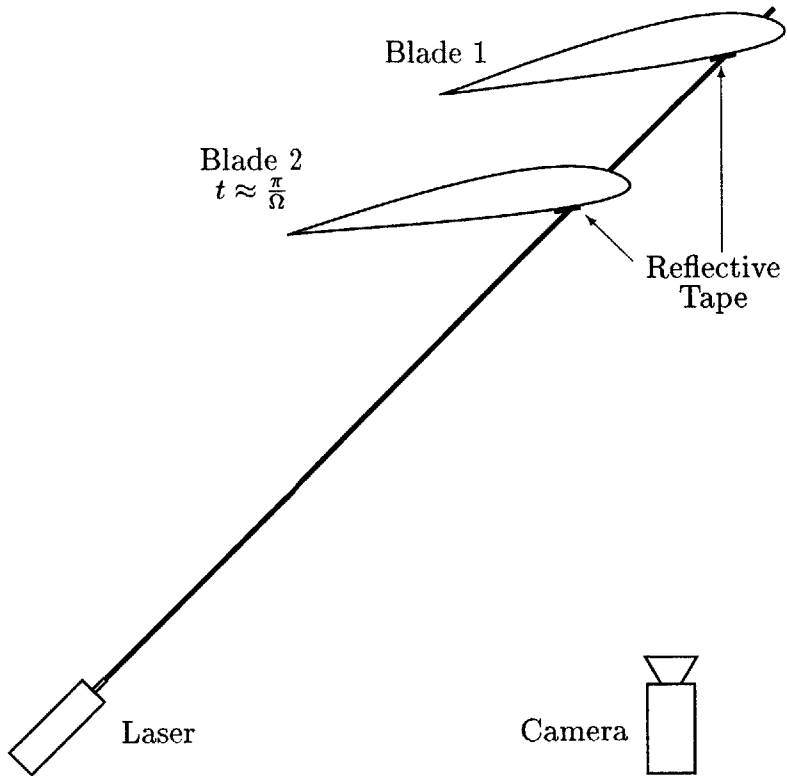


Figure 4-16: Illustration of the blade tracking procedure.

### 4.3 Hover-Test Results

After mounting the rotor blades on the test stand, the hover performance was evaluated. Most of the rotor data was collected at a blade angle of attack of 8 deg. This included tests where the rotor speed and actuation voltage was varied to study the effects of parametric changes to operating conditions. A full set of four deg angle of attack data was collected at 1336 RPM and  $800V_{p-p}$  actuation to help understand the sensitivity of the performance to blade angle. Table 4.4 shows the nominal thrust, coefficient of thrust, blade loading, and maximum torque measured at the 6-axis load transducer while in hover (1336 RPM) for the two angles of attack. The following

Table 4.4: Thrust, blade loading and rotor torque for angle of attack tests.

Angle of Attack (deg)	Thrust (lbf)	$C_T$	$\frac{C_T}{\sigma}$	$M_z$ (ft-lbf)
4	153.6	0.00161	0.0285	-59.38
8	317.6	0.00333	0.0589	-111.34

coefficient of thrust and solidity are given by

$$C_T = \frac{F_z}{\rho A(\Omega R)^2} \quad (4.23)$$

$$\sigma = \frac{Nc}{\pi R}, \quad (4.24)$$

respectively.

Because the active blade is a coupled elastic system, the modal structure has a strong effect on performance. Therefore, before discussing system performance, this section begins by examining the modal structure of the blade, leading to a presentation of the experimental Campbell diagram, or fan plot. The performance of both the actuation system (*i.e.*, the effectiveness of the X-Frame actuator in producing flap deflections) and the rotor control system (*i.e.*, the effectiveness of the flap deflections in producing rotor thrust) are then explained in light of the dynamic make-up of the rotor blade. This section concludes by presenting the strain and temperature data from the sensors in and around the actuator bay to verify system strength and thermal properties.

A large quantity of data was collected during the rotor tests. In this chapter, however, only those measurements that most significantly demonstrate the effectiveness of the designed systems are discussed. A full set of the rotor data, in transfer function form (including signal coherence), is included in Appendix C.

A note on terminology is needed here. Firstly, in the following, the term *flapwise bending* or *flapwise motion* will be used to denote motion of the blade out of the plane defined by the flapping hinge line and a line perpendicular to the rotor shaft. Similarly, the term *chordwise* or *lag bending/motion* will be used to denote motion of the blade out of the plane defined by the lag hinge line and a line perpendicular to the rotor shaft. Because the blade is pre-twisted and at a non-zero angle of attack in the various cases discussed below, the strain gage bridges designated previously as *flapwise bending gages* will tend to pick up both flapwise and chordwise blade bending. Secondly, the first *flapwise* (or chordwise) *mode* will be a pinned-free rigid body mode and will be referred to as the *rigid body flap mode* (or *rigid body lag mode*).

The second *flapwise* (or chordwise) *mode* will be an elastic pinned-free bending mode and will be referred to as the *first flapwise bending mode* (or *first chordwise bending mode*). The next two flapwise modes will then be designated as *second* and *third* flapwise bending modes in the sequel.

#### 4.3.1 Active Blade Modal Identification

The response of the individual rotor blades and the entire rotor system to servo-flap actuation is strongly related to the dynamic modes of the blade. The modes are identified by examining the transfer functions from flap deflection to the various bending and torsion gages in the rotor blade. Studying these modes in hover and how they change as a function of rotor speed helps to identify the nature of and coupling between the modes. The modes of the rotor blade are a function of speed because the increased centrifugal force effectively stiffens the various modes of the blade. Flapwise bending modes are the most sensitive to this “centrifugal stiffening.”

As an example, Figure 4-17 shows the transfer function from flap deflection to the bending gage at the 42% spanwise location for varying rotor speeds. All transfer functions in this figure were taken at an 8 deg blade angle of attack and  $800V_{p-p}$  actuation.

There are a number of peaks in these data traces below 44 Hz. Because the signal to noise ratio there was low, we have little confidence in the accuracy of those peaks. Therefore, these data points should be disregarded. Because of the low frequency inaccuracies, however, the phase calculation differs between the various data traces by multiples of 360 degrees.

Because the 42% flapwise bending gage was wired as a quarter bridge (see Section 3.1.6), it has similar sensitivity to both flapwise and chordwise bending. The first and third flapwise bending modes are seen in this figure, with peaks at 55 Hz and 142 Hz at 1336 RPM, respectively. In addition, the first lag bending mode dominates the response with a peak at 157 Hz at 1336 RPM. The second flapwise bending mode is not observable with this sensor, most likely because its node is near the 42% spanwise location. As expected, in all modes increasing rotor speed stiffens the various modes,

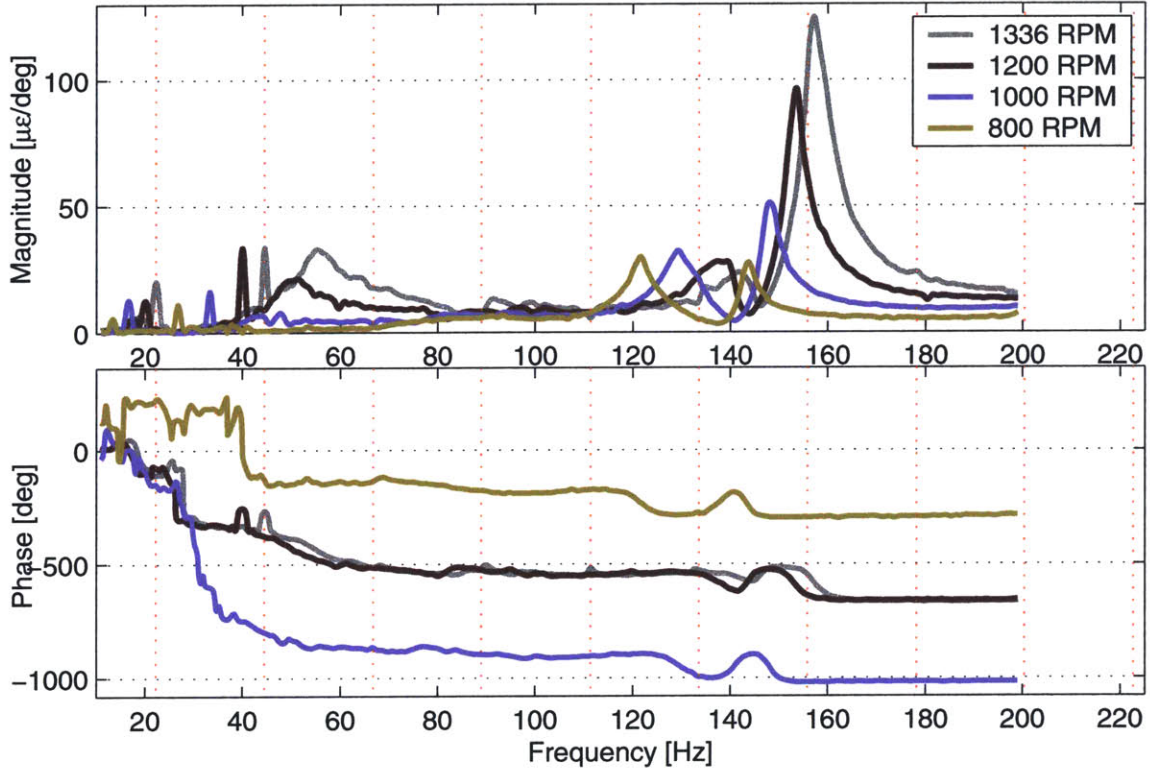


Figure 4-17: Flap to 0.42R flapwise bending transfer functions at various speeds.

leading to higher resonant frequencies.

The damping in the various modes can be estimated by finding the half power frequencies of each mode [58]. Using this method, the damping of the first flapwise bending mode is estimated to be about 8%, while it is 2-3% for the higher modes. Structural damping can account for about 1-2% of this damping. The extra damping is most likely due to aerodynamics. If this is true, the aerodynamic damping seems to be more dominant at lower frequencies.

The data in this figure shows that the servo-flap becomes more effective in exciting the first flapwise and first chordwise bending modes with dynamic pressure. Greater effectiveness with dynamic pressure indicates that the excitation of these modes is dependent on the aerodynamic effects associated with servo-flap motion. In particular, the lag mode is highly controllable by the servo-flap, probably due to drag forces generated from the servo-flap deflections.

In contrast, the effectiveness of the servo-flap in exciting the third flapwise bending

mode stays constant (or degrades slightly) with dynamic pressure. One explanation for this behavior is that at higher frequencies the inertial effects due to the servo-flap motion dominate the forcing of the flapwise bending mode. Thus, the servo-flap may be acting more like a proof mass than an aerodynamic surface to this particular mode.

Figure 4-18 shows the transfer function from flap deflection to torsional strain at the 21% spanwise location for varying rotor speeds. These transfer functions were

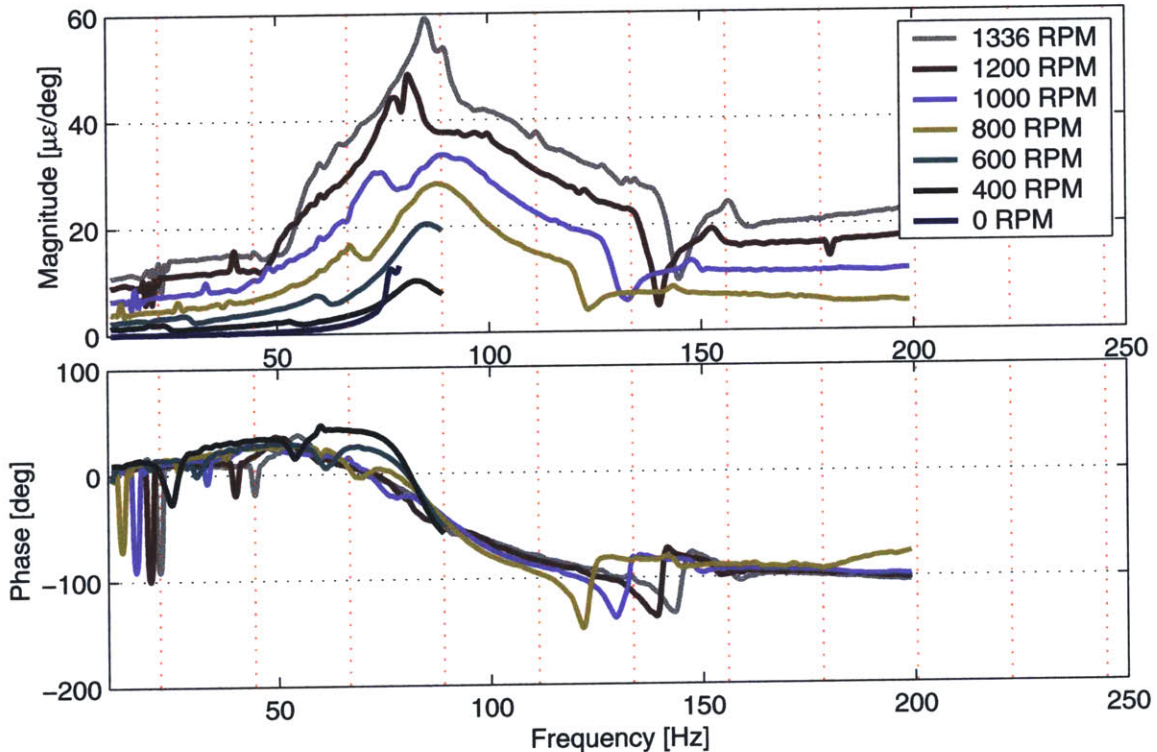


Figure 4-18: Flap to root torsion transfer function at various rotor speeds.

also taken during the same tests as those in Figure 4-17.

Three blade modes are identified by examining the magnitude and phase of this transfer function. The second flapwise bending mode and the first torsion mode are closely coupled near 4/rev, at 1336 RPM, with a zero separating the two. In addition, the third flapwise bending mode has some contribution at approximately 139 Hz (at 1336 RPM).

The fact that the torsion gage can sense contributions from flapwise bending is unexpected. The proximity of the second flapwise bending mode to the first torsion mode implies that these two modes are coupled to some degree, which probably leads

to the observability. The observability of the third flapwise bending mode may be due to the generation of blade moments due to the flapwise motion. (A proposed mechanism by which flapwise motion leads to blade lift [and moment] is presented later, in Section 4.3.3.) However, the presence of a zero in close proximity, at 144 Hz, highlights the fact that this mode and this effect are nearly unobservable.

The effects of rotor speed on the modal natural frequencies is clearly evident in Figure 4-18. As in Figure 4-17, the flapwise modal frequencies are more sensitive to rotor speed due to centrifugal effects. In contrast, the torsion mode is only slightly sensitive to rotor speed. The torsion mode is seen clearly in all seven data traces with a natural frequency very close to 4/rev. One exception is that the peak corresponding to the torsion mode at 1200 RPM seems to be at a lower frequency than expected from the trend. This may be due to some coupled dynamics with the second flapwise bending mode and the zero at that particular speed. In fact, the phase response there seems to support this conclusion.

The aerodynamic damping of the torsion mode is difficult to estimate, due to the presence of the second flapwise bending mode. However, the half power estimate puts an upper bound on the damping of approximately 14%. This substantial level of damping is, again, possibly due to aerodynamics.

Just as in the flapwise bending case, the servo-flap becomes more effective in exciting the second flapwise bending mode and the first torsion mode with dynamic pressure. Of particular interest is the broad nature of these two modes with frequency. The resonant effects cover a range from 60-140 Hz. As will be shown in Section 4.3.3, it is the combination of the response of these two modes along with the first flapwise bending mode at 56 Hz that gives the active blade such good authority in affecting hub vertical shear over the range of frequencies between 50-100 Hz.

While the third elastic bending mode is slightly observable, it is highly damped. In addition, it also seems that there is no sensitivity of this mode to rotor speed. (The different magnitude levels of the four data traces near 6/rev are due to the residues of the 1st torsion/2nd flapwise bending modes.) This again indicates that the excitation of this mode is due to inertial effects of the servo-flap, as opposed to aerodynamics

at the higher frequencies.

Appendix C contains a complete set of transfer function plots of the various sensors as a function of rotor speed. By analyzing all of these plots in a manner similar to that applied to Figures 4-17 and 4-18 above, the variation in the natural frequencies of all the modes with rotor speed were identified. Plotting these natural frequencies as a function of rotor speed gives the rotor blade Campbell diagram, as shown in Figure 4-19. In addition, predictions of the blade modal behavior using Boeing's TECH-01 rotor code, along with lines corresponding to harmonics of the rotor speed, are also plotted in Figure 4-19. The rigid flap and lag modes of the blade are not included in this plot. Table 4.5 lists the mode type and frequencies of the various blade modes within the testing bandwidth.

Table 4.5: Rotor modes in hover (1336 RPM).

Mode Type	Frequency	
	(Hz)	(per rev)
1st Flap Bending	55.2	2.48
2nd Flap Bending	86.5	3.88
1st Torsion	94.3	4.24
3rd Flap Bending	143.1	6.43
1st Lag Bending	157.0	7.05

The agreement between model and experiment is fairly good. The predicted and achieved torsional frequencies are closely correlated. In addition, the sensitivity to rotor speed of all of the bending modes is similar to that predicted. However, the natural frequencies of the bending modes are off slightly. All of the flapwise bending modal frequencies were lower than predicted. This is most likely due to the extra mass of the pitch shaft assemblies. (See Section 4.2.1.) The effect of this extra mass is more dominant in the higher modes, because the mass near the root contributes more to the modal energy in these modes. The chordwise bending frequency is also higher than predicted. This is most likely due to extra un-modeled composite embedded near the trailing edge to support the servo-flap components.

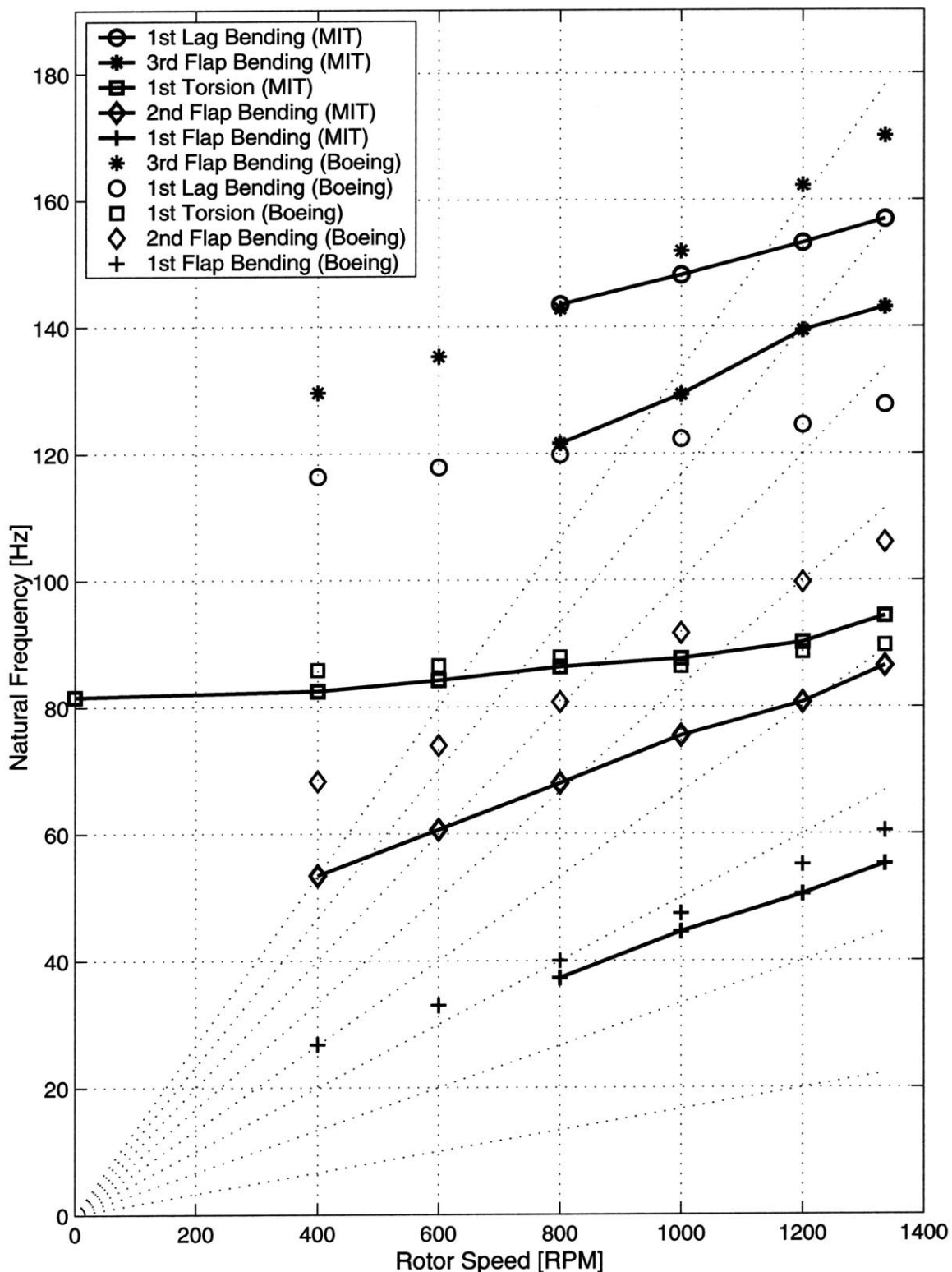


Figure 4-19: Campbell diagram of the active blade.

### 4.3.2 Actuation System Performance

The majority of the effort in this research project has been focused on developing a discrete actuator capable of producing servo-flap deflections on a rotor blade operating at Mach-scaled speeds. This section contains a presentation and analysis of the experimental hover test results showing the effectiveness of the actuator in performing this designed function and the degree to which the aerodynamic loads encountered match the predicted levels.

The large amount of friction in the servo-flap hinges required the application of a combination of molybdenum di-sulfide and bearing grease to each bearing. (See Section 3.4.1 for a detailed discussion of the friction.) The same treatment was applied to the bearings for the hover tests but, because of the centrifugal force, this lubricant was thrown off of the blade while spinning. If the actuator was run in hover for extended periods of time, most of the lubricant was eventually lost, and the hinges heated and began to bind up. To avoid this occurrence testing times were limited to 1-2 minutes per run and lubricant was re-applied between each test. This reduced the effects of friction to a level which allowed for adequate system identification.

The obvious difference between the bench tests and the hover tests is the addition of centrifugal force and aerodynamics as the rotor spins. Figure 4-20 shows a direct comparison of the 10 Hz deflection versus applied voltage of the actuator between hover and 0 RPM (non-spinning) operating conditions while at the 8 deg angle of attack. The non-spinning deflection data is very similar to the data presented in Figure 3-12b, as expected. As discussed in Section 3.4.1, the hysteresis is due to the friction and material nonlinearities. As the rotor blades spin, the amount of hysteresis, of course, decreases with the flap deflection but the percentage hysteresis remains the same between the two operating conditions. This indicates that the effect of friction on the quasistatic performance of the actuator is relatively constant with rotor speed.

Figure 4-21 shows the frequency response of the servo-flap deflection while operating the rotor at hover, with an 8 deg collective angle of attack (AOA), and three

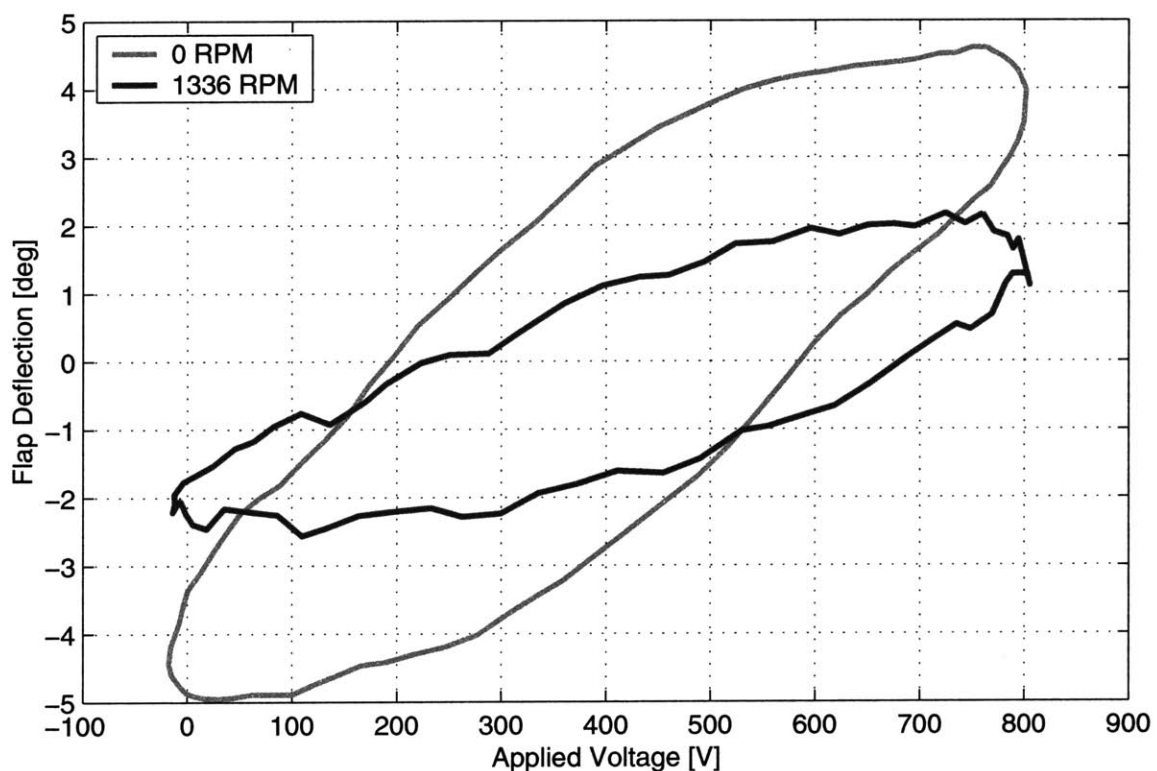


Figure 4-20: Comparison of servo-flap deflection in hover and non-rotating operating conditions.

voltage excitation levels. The magnitude response of the actuation system is relatively

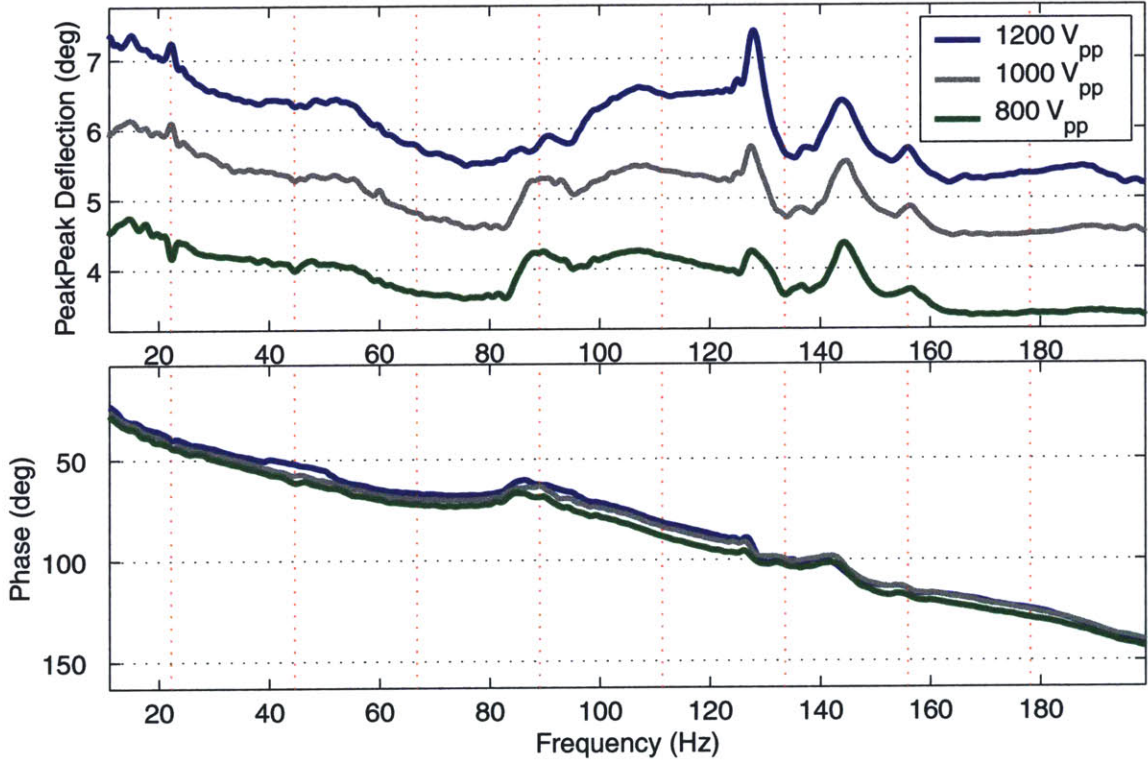


Figure 4-21: Servo-flap deflection frequency response for varying actuation levels.

constant over the testing bandwidth. There is some reduction in deflection, which is mostly due to the frequency dependent characteristics of the active material and the slight interactions of the actuator with the elastic blade modes. At the maximum voltage the actuator is producing between 5-7 deg (peak-to-peak) flap deflections well past 6/rev (133.6 Hz). Of course, the hinge friction reduced the achievable servo-flap deflections. An estimate of this degradation due to friction is presented later in this section.

There is substantial phase loss in the frequency response of the actuator. Some of this is due to the nonlinear behavior of the active material. (See Figure 2-13 for a typical actuator transfer function sans friction.) However, a large portion of the phase loss is due to the friction in the flap hinges.

The friction also has the effect of damping the fundamental actuator resonance to the point that it is difficult to identify the location of this mode. The non-spinning

fundamental mode of the actuator is at about 165 Hz. The peak in the actuator magnitude response is broad and clipped at the resonance due to the friction. The effects of spinning the blade on the actuation system are two-fold. First, the stiffness due to the aerodynamics increases the natural frequency of the system and second, the aerodynamic damping flattens the magnitude response further. Because of these effects and the interaction of the actuation system with the flexible blade structure, it is difficult to identify the resonant frequency for the system at hover. Additional rotor testing (possibly on a system with lower hinge friction) is needed in order to satisfactorily identify the sensitivity of this mode with rotor speed.

Changes in operating conditions affect the actuator performance. Figure 4-22 shows the frequency response from voltage to flap deflection for a series of rotor speeds. The phase roll-off does not change appreciably with speed. There is a slight

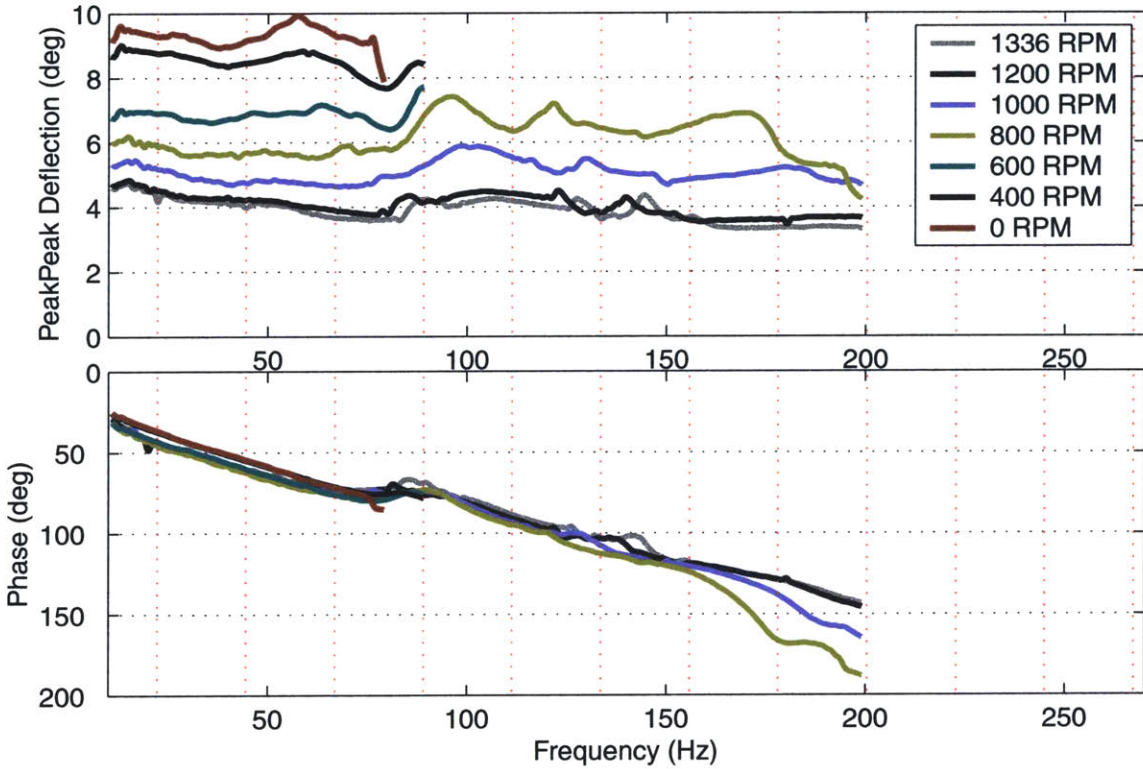


Figure 4-22: Frequency response of servo-flap deflection at different rotor speeds.

decrease in phase with rotor speed at frequencies above 7/rev. The cause for this may be due to boundary layer effects or some other aerodynamic lag.

The shape of the magnitude response is very similar between all speeds. Slight shifts in blade and actuator modes due to centrifugal stiffening are present. The major difference in the response is the change in magnitude between cases. The quasistatic hover deflection is about one-half that in the low speed case. The difference in deflection between the cases is due to the increased aerodynamic stiffness of the servo-flap hinge moment with speed. Below, an analysis of these hinge moments is presented.

The actuated deflection also changes as a function of blade angle of attack. Figure 4-23 shows the frequency response of the servo-flap deflections at  $800V_{p-p}$  actuation at 4 and 8 deg angle of attack. At quasi-steady frequencies, the actuated flap

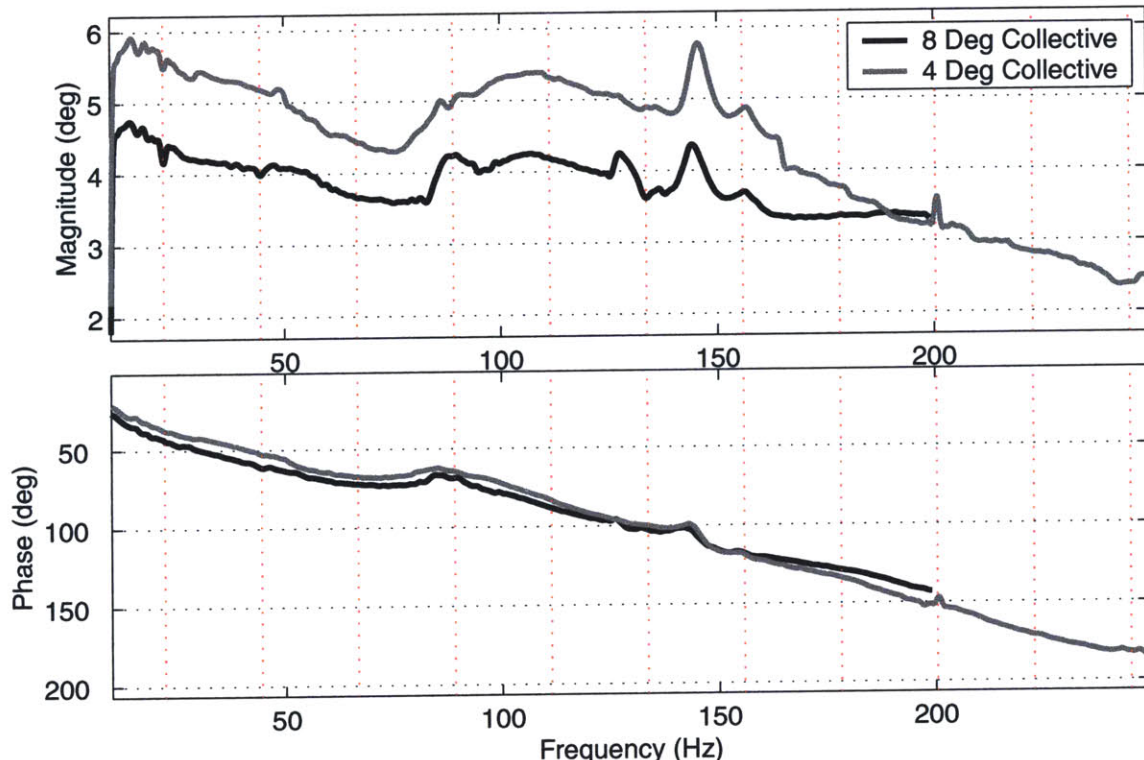


Figure 4-23: Frequency response of flap deflection at 4 and 8 deg angles of attack.

deflections at 8 deg is about 81% of that at 4 deg. The difference in the deflection between these two cases is due to two effects. First, the airspeed over the flap is greater in the 8 deg case due to a larger inflow velocity. Second, the hinge moment curve slope is slightly higher at 8 degrees angle of attack, as was shown in Figure 3-6.

Table 4.6 gives the quasistatic deflection and force under the various rotor operating conditions encountered in these experiments. Quasi-static actuator performance

Table 4.6: Quasi-static (10 Hz) actuator performance under various operating conditions.

$\Omega$ (RPM)	$V_{p-p}$ (V)	$\alpha$ (deg)	$q_{L_{p-p}}$ (in)	$F_{p-p}$ (lbf)
400	800	8	0.0181	5.756
600	800	8	0.0148	6.765
800	800	8	0.0132	7.220
1000	800	8	0.0121	7.876
1200	800	8	0.0099	8.179
1336	800	8	0.0101	8.583
1336	1000	8	0.0119	9.795
1336	1200	8	0.0155	12.975
1336	800	4	0.0122	7.927
1200	800	4	0.0128	7.270

metrics are used in this discussion to simplify the analysis and to allow for comparison with bench top data presented for the actuator in previous chapters.

A plot of the deflection versus force entries in this table is shown by the blue symbols in Figure 4-24. All of the 800 Volt data falls very close to the straight line fit, as expected, since this data should closely follow the bench-top actuator load line data presented in Section 2.6.1. Of course, the 1000 Volt and 1200 Volt data points are located further from the origin, due to the increased actuation energy for those cases. The spacing of the higher voltage data points from the 800 Volt data does not follow a linear trend, due to a combination of friction and material effects.

Using the coefficients of kinetic friction estimated from the bench top data, presented in Section 3.4.1, the frictional force seen by the actuator under the various operating conditions can be estimated using Equation (3.14). This friction reduces the force acting to deflect the servo-flap in the airstream. The red symbols in Figure 4-24 are a plot of the data in Table 4.6, where the forces have been reduced by the predicted friction acting at the actuator output. The difference between the red and blue data points gives a quantitative indication of the impact of friction on the applied servo-flap hinge moments.

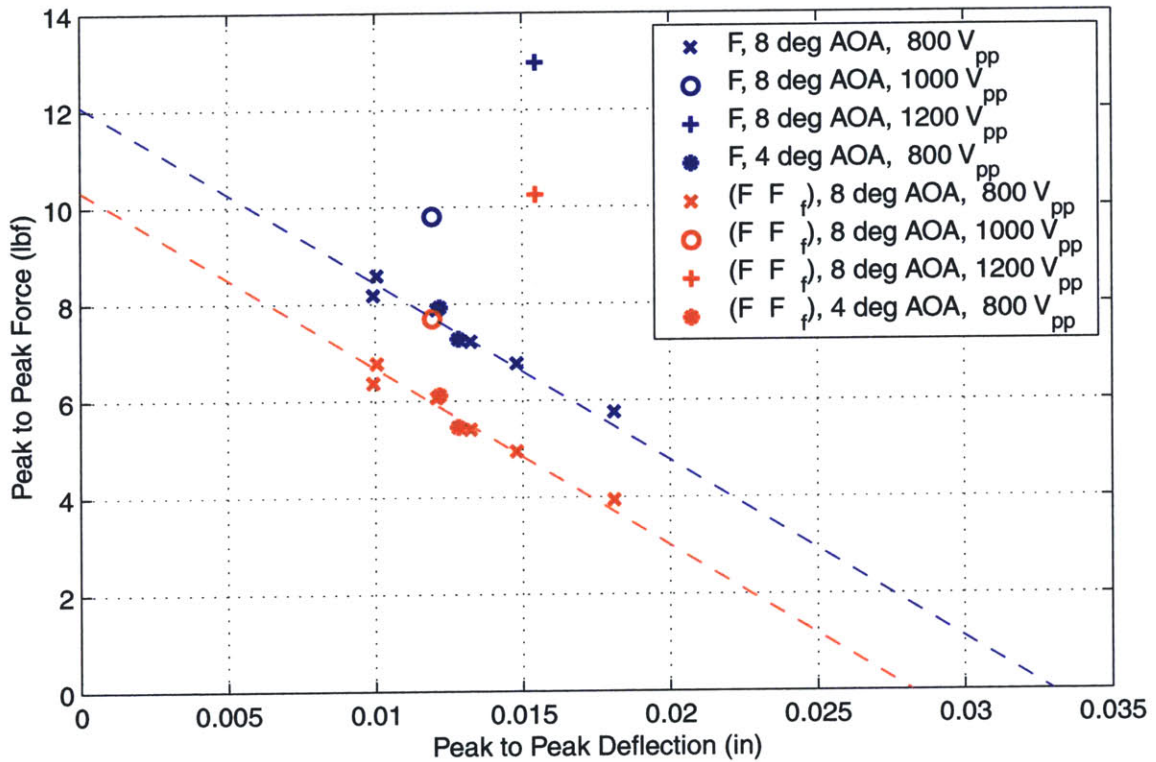


Figure 4-24: Experimental load-lines of actuation system in hover.

The experimental servo-flap deflections are lower than expected, even taking into account the contribution of friction. The reduced performance is due to a greater than expected aerodynamic hinge moment stiffness. Below, two methods will be used to estimate the quasi-static experimental hinge moment curve slope,  $C_{H_\delta}$ , under the various operating conditions in Table 4.6.

The first method used to estimate  $C_{H_\delta}$  simply uses the X-Frame strain gage data in conjunction with the actuator deflection data to give the hinge moment curve slope directly. Using force equilibrium at node A in Figure 3-13 gives

$$F_{\text{out}} = (K_{L_{\text{set}}} + K_{\text{aero}}) q_L + F_f \quad (4.25)$$

where  $K_{L_{\text{set}}}$  is the combined parallel stiffness of the pre-stress wire and centrifugal flexure,  $F_{\text{out}}$  is the force at the output of the actuator obtained by normalizing the data from the strain gage bonded to the actuator outer frame.  $K_{\text{aero}}$  represents the aerodynamic stiffness associated with the hinge moment. Using sectional aerodynam-

ics, this is given by

$$K_{\text{aero}} = \frac{1}{s^2} \int_{r_i}^{r_o} \frac{1}{2} \rho U^2 c_s^2 C_{H_\delta} dr \quad (4.26)$$

The airspeed is a function of both rotor speed and inflow, as is given by

$$U = \Omega r + \lambda(r) \Omega R \quad (4.27)$$

Putting this expression for airspeed into Equation (4.26) yields

$$K_{\text{aero}} = \frac{\frac{1}{2} \rho \Omega^2 c_s^2 C_{H_\delta}}{s^2} \int_{r_i}^{r_o} (r + \lambda R)^2 dr \quad (4.28)$$

Combining Equations 4.28 and 4.25 and solving for the hinge moment curve slope gives

$$C_{H_\delta} = \frac{s^2 \left\{ \frac{F_{\text{out}} - F_f}{q_L} - K_{L_{\text{set}}} \right\}}{\frac{1}{2} \rho \Omega^2 c_s^2 \int_{r_i}^{r_o} (r + \lambda R)^2 dr} \quad (4.29)$$

Using combined blade element and moment theory, Johnson gives an expression for the inflow as ([44], pg 57)

$$\lambda = \frac{\sigma C_{L_\alpha}}{16} \left[ \sqrt{1 + \frac{32}{\sigma a} \theta \frac{r}{R}} - 1 \right] \quad (4.30)$$

For the model scale rotor blades, the built in angle of attack is

$$\theta = \theta_{.75R} + 8.96^\circ - (0.197 \frac{\text{deg}}{\text{in}}) r \quad (4.31)$$

Use of these two relations and the data presented in Table 4.6 leads to an estimate of  $C_{H_\delta}$ . These estimates are plotted as the blue symbols in Figure 4-25 (they are labeled as “Force”, to indicate that they were estimated using the actuator force data). In addition to the estimated hinge moment curve slope, also plotted in this figure is the hinge moment curve slope that was predicted from the aerodynamic simulations in Section 3.1.3.

The second method used to estimate  $C_{H_\delta}$  considers the aerodynamics as a linear spring, in parallel with the pre-stress wire load. The actuated displacement is

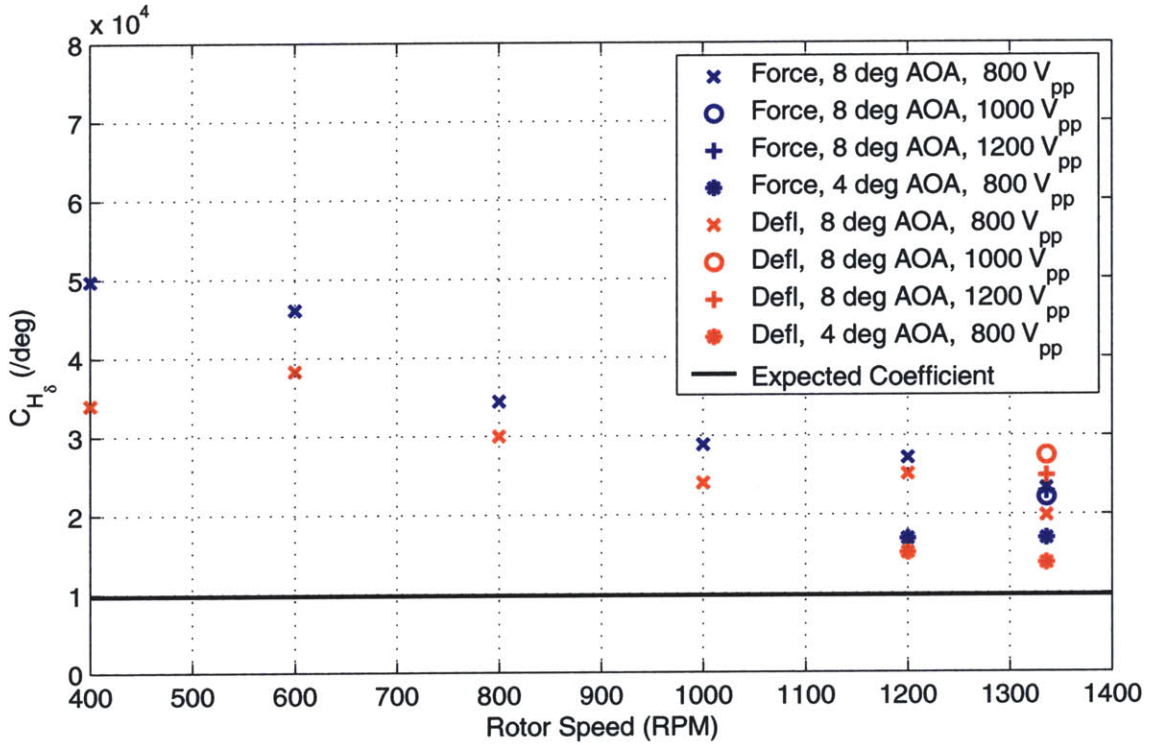


Figure 4-25: Estimated hinge moment curve slope at various operating conditions and with different models.

calculated using a relation similar to Equation (3.13), as

$$q_L = \frac{K_a \left( q_f - \frac{F_f}{K_a} \right)}{K_a + K_{L_{set}} + K_{aero}} \quad (4.32)$$

Using the various expressions given above,  $C_{H_\delta}$  may be expressed as

$$C_{H_\delta} = \frac{s^2 \left\{ \frac{K_a \left( q_f - \frac{F_f}{K_a} \right)}{q_L} - K_a - K_{L_{set}} \right\}}{\frac{1}{2} \rho \Omega^2 c_s^2 \int_{r_i}^{r_o} (r + \lambda R)^2 dr} \quad (4.33)$$

This estimate of the hinge moment curve slope uses just the deflection data and the estimate of hinge friction. The estimates of  $C_{H_\delta}$ , using this model, are plotted in Figure 4-25 as the red symbols. (They are labeled as “Defl”, to indicate that they were estimated using only the actuator deflection data.)

In studying Figure 4-25, a number of observations can be made. The estimated hinge moment curve slope decreases with rotor speed. This may indicate that, as the

Mach number increases, the compressibility effects reduce the required hinge moment coefficient. The hinge moment curve slope increases with angle of attack, which was expected. (See Figure 3-6 in Section 3.1.3.)

In all of the 800 Volt cases the hinge moment curve slope predicted by the second (deflection) model is lower than that predicted using the force data. This may indicate that the actuation system stiffness is higher than expected. An exception to this trend occurs in the high voltage data points. This variation may be due to non-linearities in the aerodynamics at higher servo-flap deflection amplitudes or a field dependent modulus of the active material, as discussed in Section B.2.2.

The estimates of  $C_{H_\delta}$  can be used to calculate the aerodynamic hinge moment stiffness, as given by Equation (4.28). These are plotted with rotor speed in Figure 4-26. This difference between the two models in this figure reinforces the suspicion that the

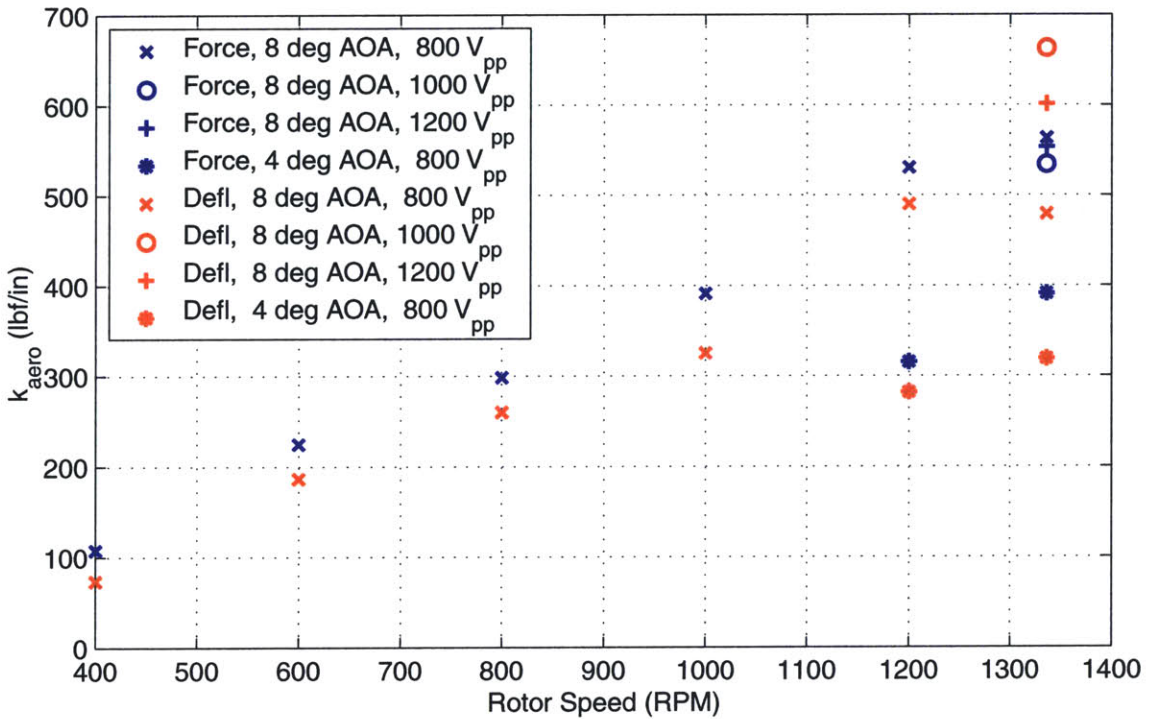


Figure 4-26: Estimated aerodynamic hinge moment stiffness at various operating conditions and with different models.

estimated actuation system stiffness of 323 lb/in may be inaccurate. This is especially evident in considering the difference in scatter between the two models at 1336 RPM.

The impedance matching efficiency at the design point (1336 RPM) can be cal-

culated as

$$\eta_{\text{im}} = \frac{(K_{L_{\text{set}}} + K_{\text{aero}})/K_a}{(1 + (K_{L_{\text{set}}} + K_{\text{aero}})/K_a)^2} \quad (4.34)$$

Using an estimated aerodynamic stiffness of 550 lbf/in, a set actuator load stiffness of 110 lbf/in, and an actuator stiffness of 323 lbf/in yields an impedance matching efficiency of 22.1%. The optimum efficiency is 25%.

It would be advantageous to present frequency response data for the aerodynamic stiffness and hinge moment curve slope. However, because of the large non-linear contribution of hinge friction to the force measurements, all such estimate have very poor coherence levels. Therefore, no dynamic data on these coefficients is presented in the body of this thesis.

### 4.3.3 Rotor Transfer Functions

#### Control Transfer Functions

The flap to hub thrust transfer function is shown in Figure 4-27, with the peaks due to the various structural blade modes identified. This transfer function response was obtained at hover, for 8 deg angle of attack and  $1200V_{p-p}$  actuation.

Both the phase and magnitude of this transfer function are important for rotor control. There is a significant amount of phase roll-off with frequency in the transfer function. The explanation for this is related to the fact that the servo-flap to hub shear transfer function is a non-collocated actuator/sensor pair. This will have implications for the controllability of the system, as discussed in Chapter 5. In terms of the magnitude, at low frequencies the flap has little effect on rotor thrust. This is unexpected because the servo-flap was designed to operate primarily in reversal, creating twisting moments on the rotor blade near the tip, leading to changes in lift. Quasi-statically, the flap should act like the trim tab on a conventional helicopter blade. The ineffectiveness of the flap at low frequencies indicates that, in hover, the flap is very close to the aileron reversal point, *i.e.*, where the change in lift due to the flap deflections is exactly canceled by the cumulative change in lift caused by the servo-flap induced twisting of the rotor blade.

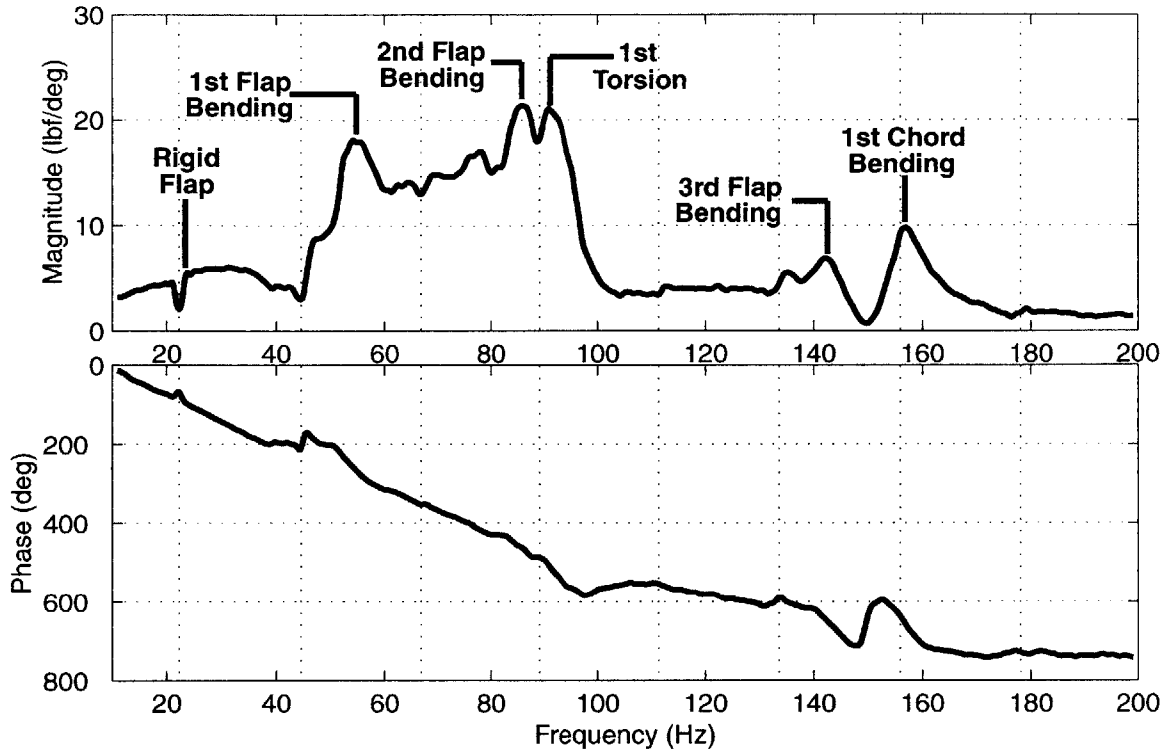


Figure 4-27: Flap to hub vertical shear (thrust) transfer function.

As the actuation frequency increases, the servo-flap begins to excite the dynamic modes of the rotor blade. These modes are labeled in the figure. As may be seen, the mechanism governing the effectiveness of the servo-flap in controlling hub thrust is based on aeroelastic excitation of the blade modes by the servo-flap. The resultant deformations of the rotor blade affect the lift generated.

From the response it is clear that the servo-flap is most effective in creating hub shear through the excitation of the first torsion mode and the first two flapwise bending modes between 50 Hz and 90 Hz. The physics governing how the excitation of the torsion mode leads to changes in hub thrust are relatively straightforward: the servo-flap induces a twisting moment near the tip that leads to an overall twist, changing the angle of attack of the blade over its entire length, which has a substantial effect on the lift generated. The mechanism through which excitation of the flapwise bending modes leads to changes in rotor thrust is more complicated. The thrust generated is nearly proportional to the flapwise angle of the blade at the horizontal pin. Therefore, excitation of the flap modes through the direct lift effect of the flap

will lead to changes in rotor thrust. When acting alone, as in the case of the third flap bending mode in Figure 4-27, the flapwise modes have a small effect on the thrust generated. However, when acting in concert with the first torsion mode of the blade, as is the case for the first and second bending modes, the modes interact to provide a great deal of authority. It is uncertain just what combination of torsional and bending excitation of the rotor blade will maximize the authority of the system in controlling hub shear. Adjusting flap position, *e.g.*, moving it towards the tip and using a smaller chord flap, will trade the amount to which the flap excites blade torsion versus blade bending. Optimizations of the entire rotor system over such variables should be done in future active blade designs to maximize the effectiveness of the system in performing the designed task.

The active blade is most effective in controlling hub shear between 50-100 Hz. By coincidence, this is an ideal range to have maximum effectiveness because the highest level of vibration for a 3-bladed CH-47 is at 3/rev, which corresponds to 66.8 Hz. The servo-flap has a great deal of authority in affecting hub vertical shear at three per rev. At 1200 V actuation (see Figure 4-30) the system is producing vibratory hub shear of  $\pm 39$  lbf and  $\pm 50$  lbf at these frequencies. If these results are scaled to a full-sized Chinook with six identical active blades, this represents an induced vibration of  $\pm 8400$  lbf at three per rev. The maximum take-off gross weight of the Chinook is 50,000 lbf; so this prototype actuation system is capable of inducing vibratory hub shear that represents a large proportion of the vehicle weight. Redesign and refinement of the system should lead to even greater authority.

A zero in the transfer function occurs near the 2/rev frequency, 44.5 Hz. Zeros show up in structural transfer functions between modes that interact with each other, causing a cancellation effect at the zero. The zero near 2/rev is most likely due to an interaction between the rigid flap mode and the first elastic bending mode of the rotor blade. Fortunately, for rotors with three or more blades, the effectiveness at 2/rev is not very important for vibration control. In fact, 2/rev control is ideal for improving rotor induced power losses, so one can imagine a controller designed for vibration control at higher harmonics and induced power control at 2/rev.

## Effects of Parameter Variations

Comparing measured performance while making changes to the operating conditions identify sensitivities of the system to these parameters. This section addresses the changes that occur in the performance of the system in inducing hub vertical shear as the rotor speed, angle of attack, and applied voltage are varied.

Because the servo-flap relies on aeroelastic excitation of the blade to affect hub shear, the flap to thrust transfer function of the rotor blade is obviously dependent on airspeed. Figure 4-28 shows the transfer function for a number of different rotor speeds while operating at  $800V_{p-p}$  and 8 deg collective angle of attack. As expected,

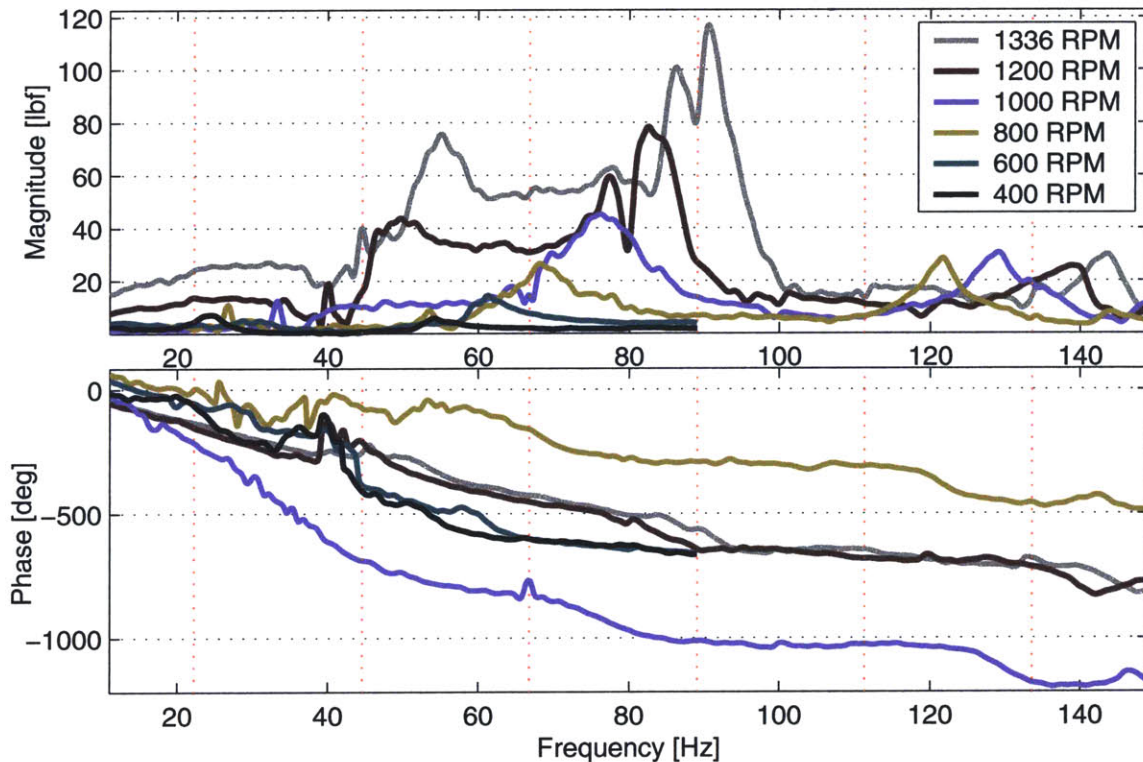


Figure 4-28: Flap to hub thrust for varying rotor speeds.

the effectiveness increases dramatically with dynamic pressure. As in Section 4.3.1 for the bending and torsion gages, the gains due to increasing dynamic pressure far outweigh the effects of aerodynamic damping.

Figure 4-29 shows the comparison of the flap to thrust transfer function at 8 deg and 4 deg collective angles of attack. The magnitude of the response is similar in

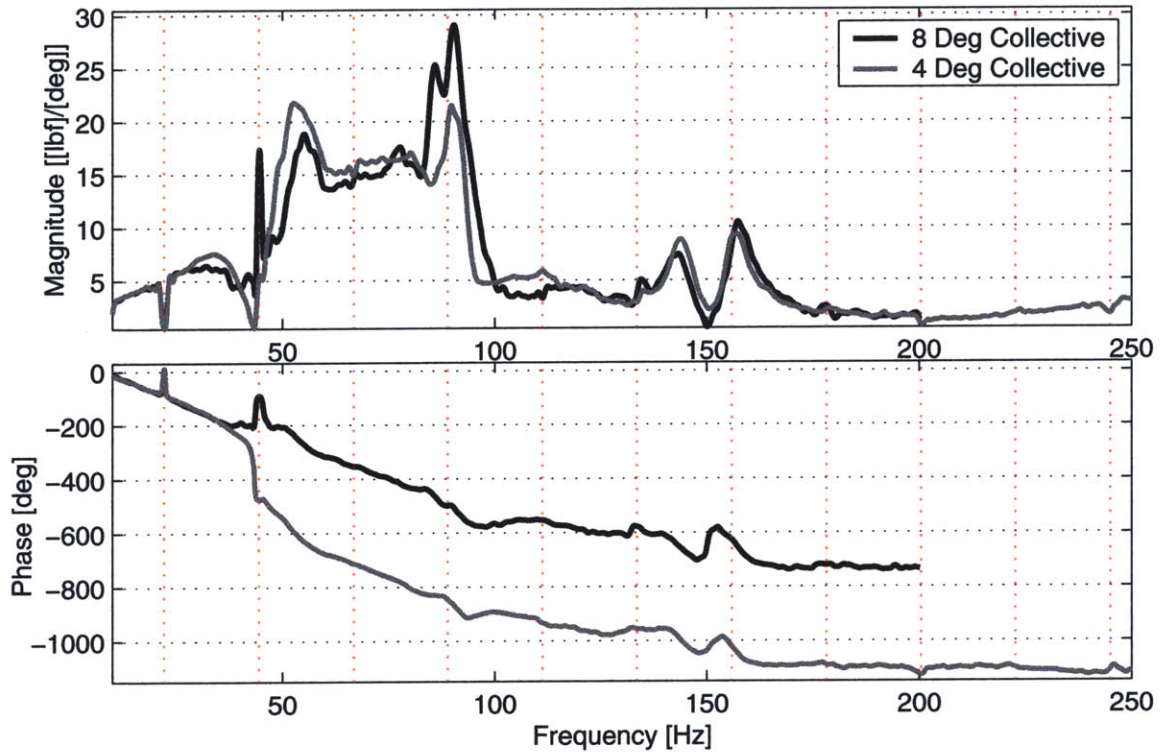


Figure 4-29: Flap to hub thrust transfer function for two blade angle of attacks.

the two cases. Slight variations are present due to the difference in blade orientation between the two cases. A considerable change in the transfer function is evident upon examining the phase responses. Specifically, the phase due to the zero at 2/rev is very different. At 8 deg the zero has almost no phase loss associated with it. This is contrasted by the four deg case, where the phase drops rapidly by 360 deg at the zero. This indicates that the zero is non-minimum phase at the 4 deg angle of attack but becomes minimum phase as the angle of attack increases to 8 deg. The fact that the zero is non-minimum phase at a lower angle of attack is most likely a result of how the rigid flap and first flapwise bending modes interact to affect the overall blade angle of attack and rotor lift. Since the flapwise bending has more of an effect at the lower angle of attack, this interaction is intensified, leading to the deep notch and non-minimum phase characteristic there. The implication of having a non-minimum phase zero in a given frequency range is that it is impossible to close a feedback control loop over the frequencies corresponding to that phase drop. Thus, this highlights that small changes in the rotor plant can have significant implications

on controllability.

Figure 4-30 shows the total thrust frequency response while actuating at three different voltage levels in hover at the 8 deg angle of attack. As expected, the re-

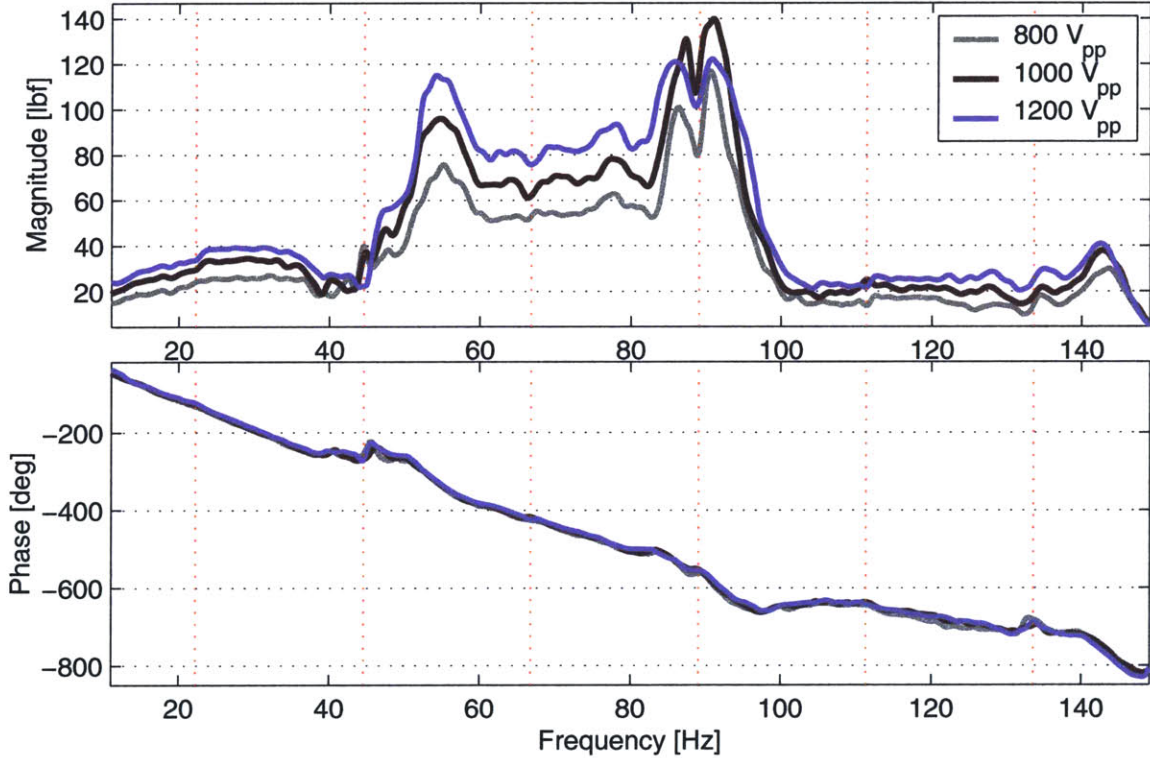


Figure 4-30: Frequency response of the thrust induced from flap deflections at varying applied voltages.

sults differ only by the magnitude of the flap deflection at the three actuation levels. The phase is identical between cases. However, there are some small differences between the total thrust generated near 4/rev. This is evidently due to changes in the actuation system frequency response between the days when the various data sets were collected. These differences are likely an artifact of the non-linear frictional and material characteristics of the actuation system.

### Integral versus Discrete Actuation

Finally, we compare the frequency response of the servo-flap actuated active blade to the integral blade developed in a related study at MIT by Rodgers and Hagood [66]. Figure 4-31 shows a comparison of the induced hub thrust of the two actuation

systems while operating in hover at maximum actuation, at approximately the same blade angle of attack. Note that the discrete data presented in this figure is identical

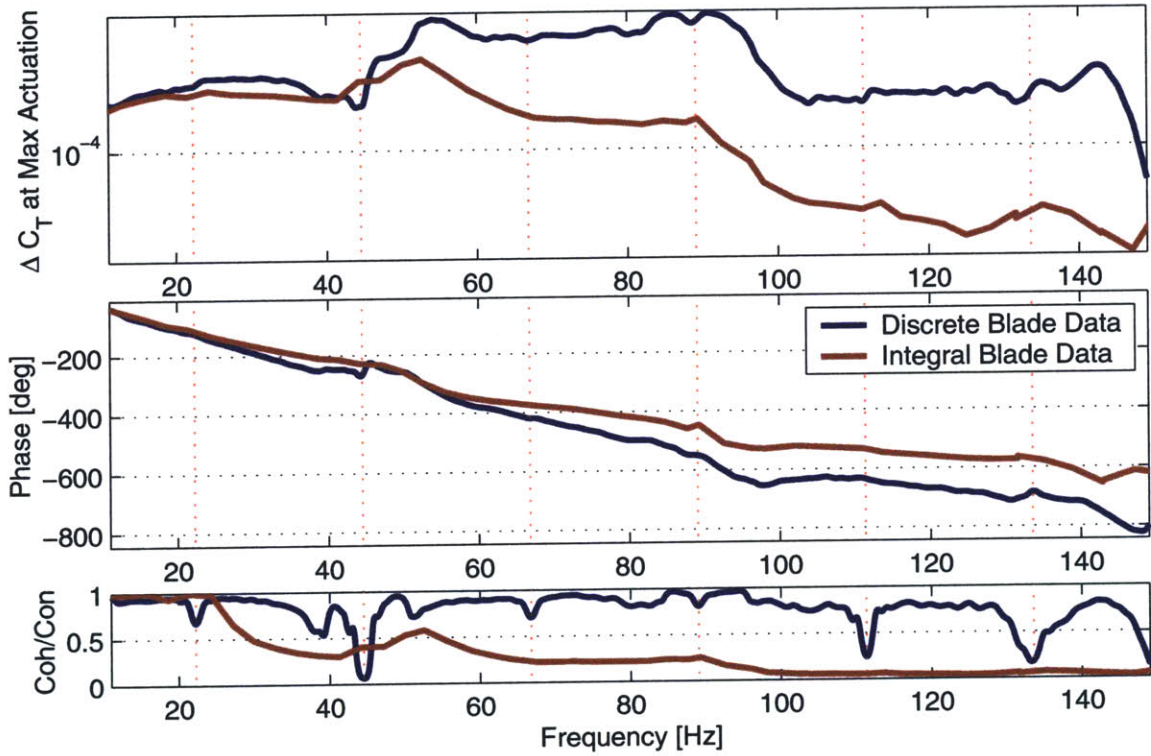


Figure 4-31: Integral versus discrete blade actuation effectiveness comparison.

to Figure 4-30 (for the 1200 V case), but the magnitude has been non-dimensionalized as a coefficient of thrust, as defined in Equation (4.23), to match the presentation used by Rodgers and Hagood. In addition to the magnitude and phase, the coherence of the discrete data is plotted along with the confidence of the integral data in the bottom plot. These data traces give an indication of the accuracy of the experimental data traces.

A direct comparison of the actual data obtained for both experiments shows that the discrete actuation is more effective in inducing hub shear than the integral concept, especially at the frequencies of interest for rotor control, which are greater than 3/rev.

The integral blade was constructed of 42 separate active fiber composite (AFC) packs that were embedded within the composite laminate of the blade spar. The designed maximum voltage level for the integral blade is 4000 V. Unfortunately, during the experimental hover tests of the integral blade, there were a large number of pack

failures in the blade before maximum actuation could be achieved. (See Chapter 8 of [67] for a detailed discussion.) The actual integral data plotted in Figure 4-31 correspond to 18 of 42 packs operating at an excitation of 2000 Volts. If the problems associated with this active blade could be corrected, the authority of the integral blade could increase by a factor of 4.67. If the integral data in Figure 4-31 is scaled by this factor, it is clear that the integral actuation concept has greater authority at low frequencies. However, at frequencies of interest for rotor control, the discrete servo-flap actuation still out-performs the integral concept.

A note is warranted regarding redesign and expected future performance of the two systems. It is clear that the authority of the discrete actuation concept is dependent on the aeroservoelastic excitation of the blade dynamics by the servo-flap deflections. Thus, optimization of the flap size and location in controlling these modes will lead to greater performance of the discrete blade. In particular, by moving the flap towards the tip and possibly using a shorter chord flap, located closer to the trailing edge, the discrete concept will have more authority in reversal to control the low frequency (steady) hub thrust - thus making it viable for blade tracking. In general, studies must be done on whether greater induced hub shear is achieved by maximizing the servo-flap reversal to excite the blade torsion or to rely on the direct lift effect to excite the flapwise bending modes of the blade or to use a combination of the two, as was achieved in this research. Independent of the flap size and location, redesign of some of the trailing edge components can be done to eliminate the friction effects on the servo-flap hinges, which should lead to 25% greater induced hub shears.

The performance of the integral blade has the potential of improving by a factor of 4.67, if the pack failure problem can be solved, allowing for 4000 Volt actuation. In addition, optimizations have been performed on a next generation integral blade (currently being co-designed by MIT and Boeing Helicopters), which predict a 15% increase in the performance of the actuation by adjusting blade ply orientations to reduce the blade torsional stiffness.

As a side note, an issue that may limit the usefulness of the integral technology for rotor blade control is that the greatest load encountered by the active material is the

rotor blade structure itself. A study of the Rodgers and Hagood's data shows that the aerodynamics have little effect on the performance of the system [66]. Therefore, integral actuation does not profit from the aeroservoelastic interaction with the blade dynamics to the same extent as servo-flap control.

The conclusion is that both actuation systems produce substantial induced vertical hub shear. However, the servo-flap actuation system out-performs the integral concept over much of the frequency range and especially at frequencies important for the designed application, control of higher harmonic rotor vibration. In addition, the servo-flap actuation system does this at a much lower cost than the integral blade, with a minor modification to the blade design and construction.

#### 4.3.4 Strength and Thermal Data

The actuator bay and trailing edge flap box cut-out create stress concentrations on the surrounding blade structure. A number of strain gages were placed around the actuator bay and inboard of the servo-flap to measure the level to which the strain rose at these points. These data are presented in this section. In addition, the temperature rise in the actuator bay due to actuation is also presented here.

##### Bay Strains

Figure 4-32(a) and (b) show the strain forward and aft of the actuator bay during a 12 second sine sweep chirp actuation at  $1200V_{p-p}$  actuation, in hover at 8 deg angle of attack. The strain on the forward side of the bay is slightly higher, but both strain levels are at an acceptable level for operation, considering the minimum failure strain of any of the composite used in the spar is  $13,000\mu\epsilon$ . Comparing these strain levels to those in the Instron test results presented in Section 3.4.2 shows the blade strain levels are a bit higher than those encountered in the Instron test. The mean stress in the blade is about  $1000 \mu\epsilon$ . In the Instron test, at a 565 lbf load, the maximum strain on a gage placed in a similar location was  $800 \mu\epsilon$ . The difference, of course, is that the extra load from the centrifugal force on the blade sections outboard of the

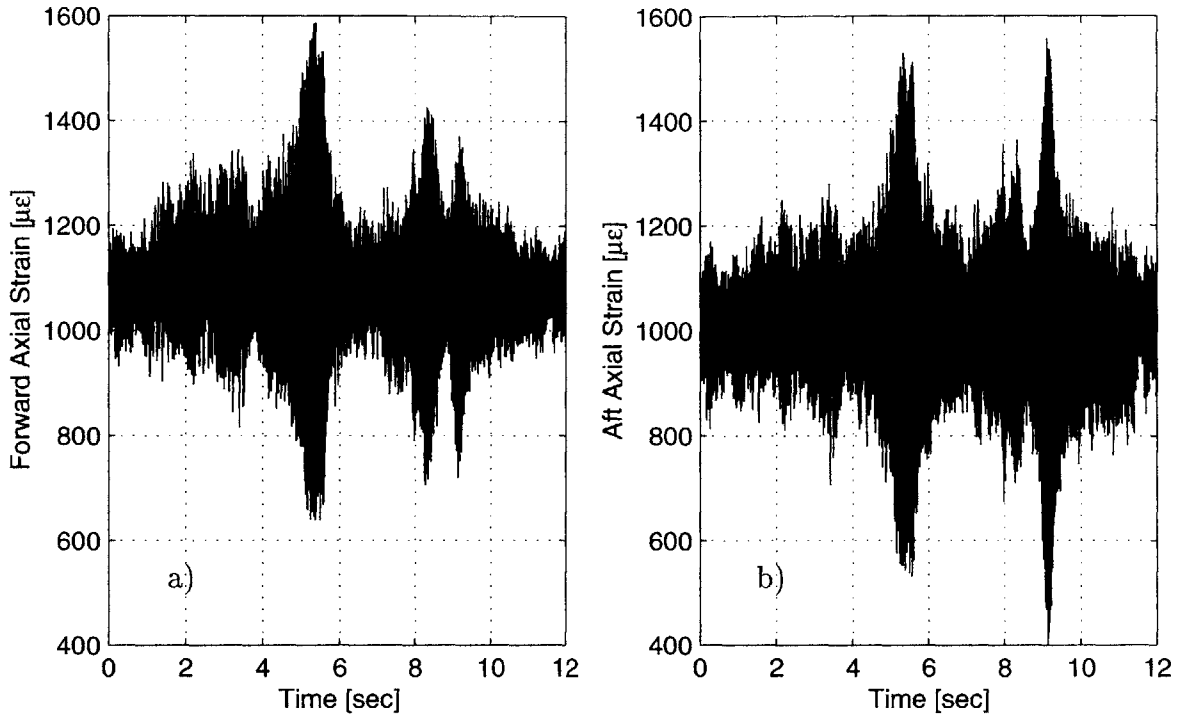


Figure 4-32: Axial strain on top, inboard surface adjacent to actuator bay (a) Forward edge (b) Aft edge.

gage location was not taken into account in the 565 lbf load of the Instron test. In any case, the strain levels around the actuator bay are below the failure strain by at least an order of magnitude.

Similarly, Figure 4-33 shows the shear strain both inboard and outboard of the actuator bay for the same actuation case. These shear strains are also far below the failure strain. The shear on the inboard side is also appreciably larger, due to higher centrifugal tension acting on that blade section. In addition, the peak-to-peak response is probably larger because the servo-flap may be exciting the blade stations inboard of the flap more.

### Trailing Edge Centrifugal Forces

There is one strain gage attached to the trailing edge stiffener, inboard of the servo-flap components. The time trace of this strain gage during the same actuation case presented above for the bay strains is shown in Figure 4-34. The strain and centrifugal

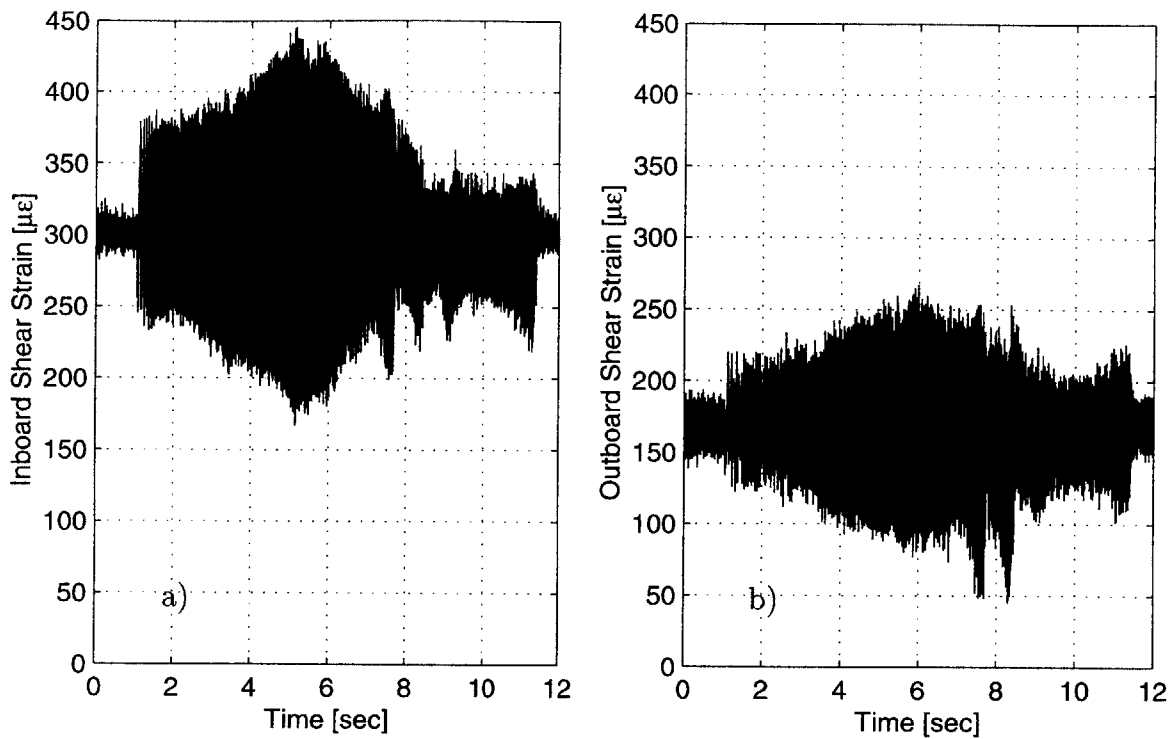


Figure 4-33: Shear strain on the top surface adjacent to actuator bay (a) Inboard side (b) Outboard side.

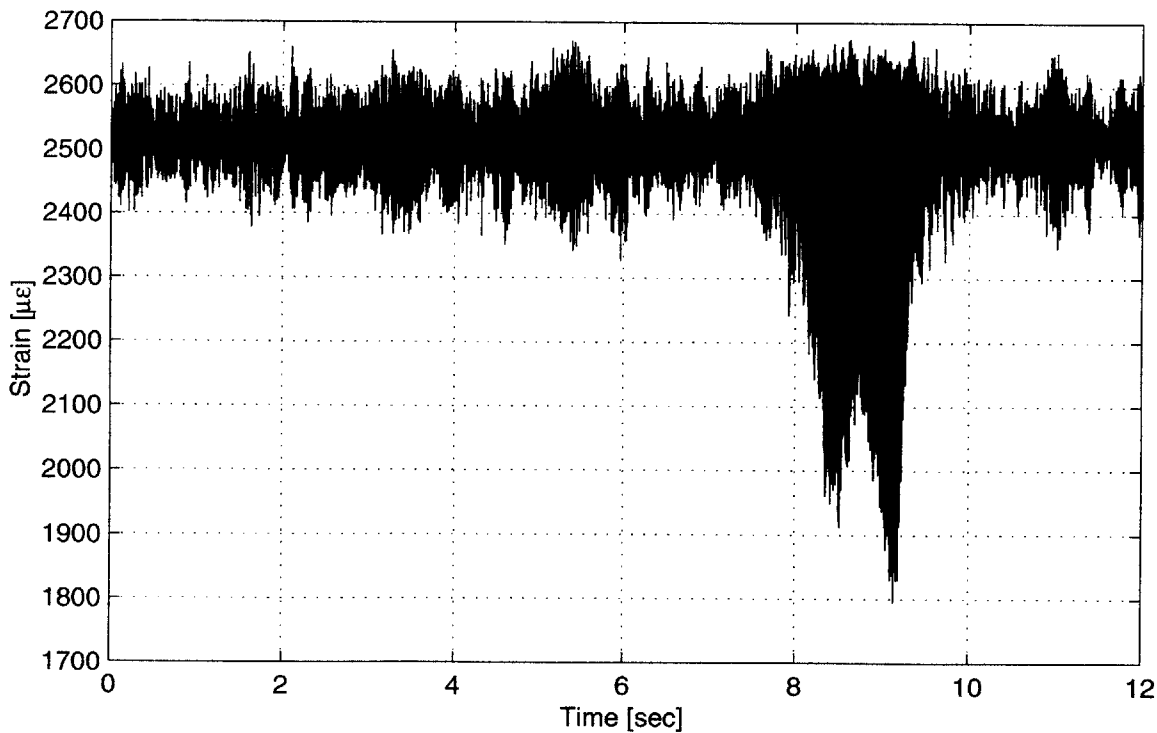


Figure 4-34: Axial strain in trailing edge stiffener during a 10 second chirp.

force levels are both acceptable for blade operation. The peak in the response between 8-9 seconds corresponds to the excitation of the chordwise mode of the blade, which has an obvious effect on this trailing edge strain gage bridge.

### Thermal Properties

Active material tend to possess a non-trivial hysteretic response. This hysteresis leads to heating of the active material and the surrounding environment. To measure the heat generated by the operation of the stacks inside the enclosed bay cavity, a resistive thermal device (RTD) sensor was bonded to the front bay wall, adjacent to the spanwise center of the stacks. The rise in bay temperature during a two-minute long actuation test consisting of 10 chirps over frequencies from 10-200 Hz, is shown in Figure 4-35. The RTD sensor reports a temperature reading 25 Fahrenheit

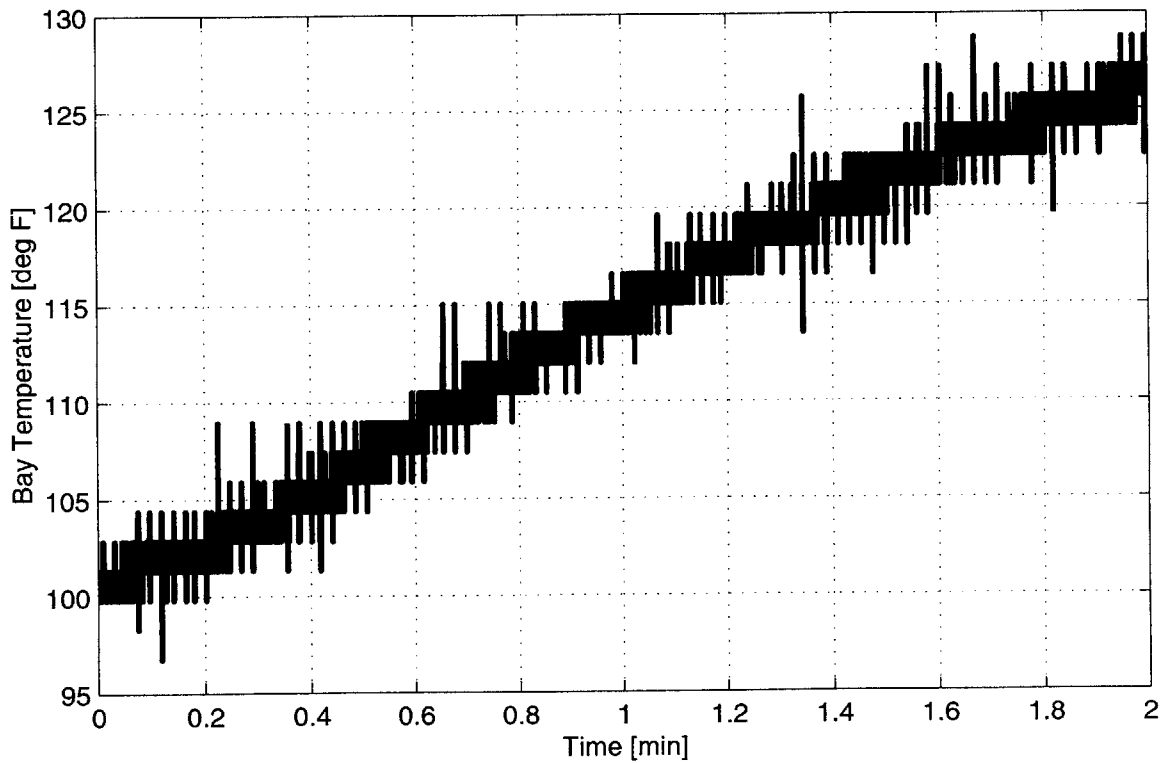


Figure 4-35: Temperature rise in actuator bay during two minute actuation test.

degrees greater than the actual temperature due to lead-wire resistance errors in the bridge circuitry. Therefore, while the absolute temperature measurements reported

are incorrect, the relative measurements should be accurate.

As shown, the actuator causes a steady state rise in temperature of approximately 25 degrees Fahrenheit over the 2 minute test period. This is a sizeable change and could affect actuator performance somewhat, due to the sensitivity of the active material to temperature changes. This will have to be addressed in future active blade design systems either by compensating for the extra heating or adding a heat sink to the design.

# **Chapter 5**

## **Closed-Loop Rotor Vibration Control**

One of the primary goals of this research was to develop an actuation system that, through the use of closed-loop control, is capable of significantly reducing the vibration transmitted from the rotor blades to the helicopter fuselage. To test the effectiveness of the prototype active rotor blade in achieving this goal, closed-loop rotor tests were performed. This chapter describes the development of the closed-loop controller and the implementation of that control strategy to reduce the rotor vibrations at both single and multiple harmonics.

There were three general classes of controllers implemented in these experiments: single harmonic continuous-time controllers, multiple harmonic continuous-time controllers, and single harmonic discrete-time controllers. Within each class, several controllers were implemented, focusing on different harmonics or combinations of harmonics. In this chapter, only one or two selected controllers from each class will be considered. The implementation and performance described for these particular controllers is considered representative of the controller class. For completeness, Appendix D contains a full set of data plots for each of the controllers implemented in these tests.

## 5.1 Vibrational Disturbance Spectrum

The purpose of the feedback control experiments performed in this research was to demonstrate the effectiveness of the actuation system in canceling the hub vertical shear vibration typically encountered in rotor operation. The aerodynamic disturbances caused by normal rotor operation are due primarily to interactions between the blades and shed vortices in the rotor wake, while the helicopter is in forward flight. Because of the periodic nature of rotor operation, these interactions result in disturbances at frequencies very close to the harmonics of rotor speed.

For the current hover tests, while there was an aerodynamic disturbance present, it differed slightly from that associated with normal helicopter operation. The difference is related to the fact that the disturbances generated in these tests were caused by the aerodynamic turbulence within the rotor inflow due to the asymmetry of the testing room and not from interactions with the vortices in the rotor wake. (Section 4.2.1 provides a discussion of the cause of these disturbances.) The disturbances in these tests do occur at frequencies close to harmonics of rotor speed, but the peaks in vibration are more broad with frequency than that seen in a normal helicopter. The width of these peaks has a major effect on the achievable performance, as will be explained in describing the closed-loop performance results below.

Figure 5-1 shows the specific open-loop power spectral density of the hub vertical shear vibration,  $F_z$ , while operating the rotor in hover at a blade loading of  $\frac{C_T}{\sigma} = 0.0589$ . In this work, the power spectral density (psd) of the signal  $x(t)$  is defined as

$$P_{xx}(f) = 2 \int_{-\infty}^{\infty} \phi_{xx}(\tau) e^{-2\pi j f \tau} d\tau \quad (5.1)$$

The factor of 2 in front of the integral is used so that the psd,  $P_{xx}$ , satisfies

$$\int_0^{\infty} P_{xx} df = \langle x^2 \rangle, \quad (5.2)$$

where the units of frequency are in Hz.

(Note that the power spectral density functions,  $\overline{P_{xx}}$ , calculated using the Matlab

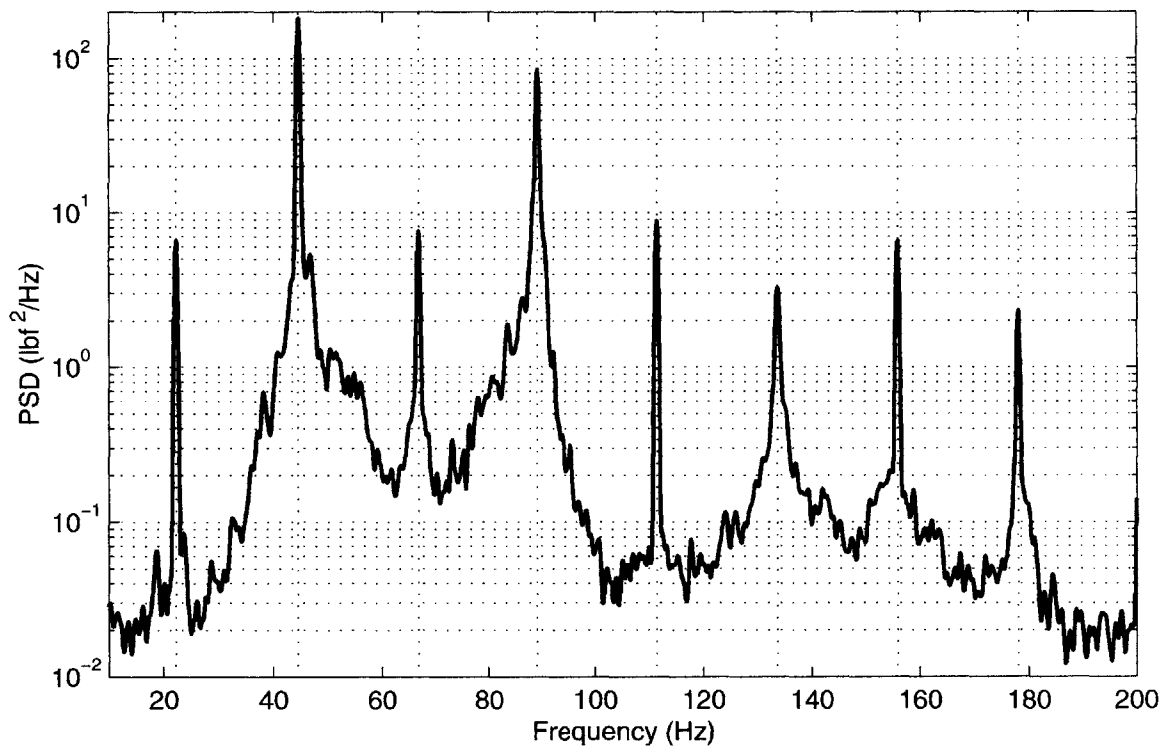


Figure 5-1: Power spectral density of the open-loop hub vertical shear vibration spectrum,  $F_z$ .

(Version 5.3) function `psd`, is related to the functions,  $P_{xx}$ , presented in this chapter by the formula  $P_{xx} = \frac{\overline{P_{xx}}}{N_p \Delta f}$ , where  $N_p$  is the number of points in the calculated power spectral density, and  $\Delta f$  is the change in frequency between points.) For reference, the open-loop rms value of vibration given by integrating under the spectrum of Figure 5-1 is 17.2 lbf. Note that because it is a two bladed rotor, most of the vibration is centered around the 2/rev (44.5 Hz) and 4/rev (89.1 Hz) harmonics.

The goal of higher harmonic control (HHC) is to cancel the vibration at the multiples of rotor speed, where it dominates. In particular, because only those vibrations that are multiples of the blade passage frequency ( $N\Omega$ ) are transmitted to the fixed frame, standard HHC algorithms are usually only concerned with reducing those particular vibrational harmonics. However, to verify the performance of the actuation system over a wide bandwidth, vibration cancellation at each of the first six harmonics of rotor speed was addressed in these tests. The first tests that were performed involved continuous time vibration cancellation at individual rotor harmonics. Follow on tests were performed on simultaneously reducing vibration at multiple rotor harmonics, also using continuous time control. Finally, discrete time control was implemented to highlight the change in performance between using discrete time and continuous time control. The implementation and resulting performance from these tests are discussed in the following three sections.

## 5.2 Single Harmonic Continuous-Time Control

One of the first HHC algorithms was suggested and implemented by Shaw *et al.*, and the results from these tests were described in Section 1.2 [70, 69]. These experiments served to validate this HHC algorithm as an effective vibration reduction approach. Because of the previous experimental success of this algorithm, it was adopted for the present rotor tests.

The block diagram of the controller used for these tests is shown in Figure 5-2. The “plant” represents the active rotor blade system. The input to the plant is the commanded voltage to the high voltage amplifier that drives the X-Frame actuator

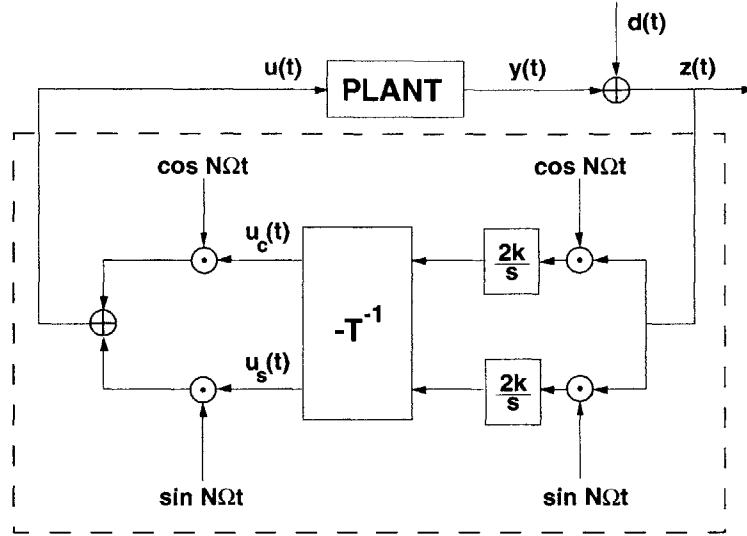


Figure 5-2: Block diagram of the continuous-time feedback controller.

and the output is the vertical hub shear in the rotating frame, *i.e.*, the  $z$ -component of force measured by the 6-axis load transducer at the hub. In the model, quasi-steady, linear time invariant assumptions are made about the rotor dynamics which allows the system to be represented by a control response matrix,  $\mathbf{T}$ . The control response matrix is a  $2 \times 2$  matrix relating the cosine and sine components of the input to the cosine and sine components of the output. Note that this quasi-steady assumption does not hold in reality and the variation in phase and gain of the plant will determine the stability margins and resultant performance of the system. This is discussed in more detail below. The vibratory disturbance, which was described in the previous section, is modeled by adding it at the output of the plant.

The compensator in Figure 5-2 is designed to eliminate disturbances at a specific frequency. The components of the compensator are located within the dashed box of the figure. The cosine and sine components of the performance signal,  $z(t)$ , are identified by multiplying that signal by a cosine and sine at the particular harmonic targeted by the controller and multiplying that signal by an integrator and a gain, given by  $\frac{2k}{s}$ . Multiplying these components by  $-\mathbf{T}^{-1}$  gives the cosine and sine components of the control necessary to cancel the vibration at that particular frequency. These signals are re-modulated by the cosine and sine signals of the appropriate

frequency, added together, and fed back to the amplifier.

Hall and Wereley [36, 37] showed the algorithm in Figure 5-2 to be equivalent to the classical control system shown in Figure 5-3, where

$$K(s) = \frac{2k(as + bN\Omega)}{s^2 + (N\Omega)^2} \quad (5.3)$$

$$a = \operatorname{Re} \left\{ \frac{1}{G(s)} \right\} \quad (5.4)$$

$$b = -\operatorname{Im} \left\{ \frac{1}{G(s)} \right\} \quad (5.5)$$

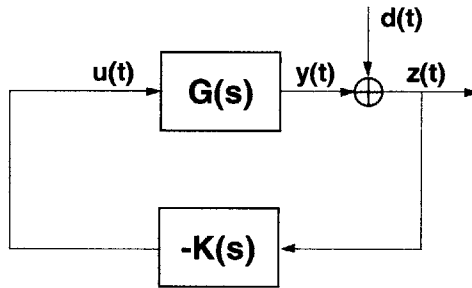


Figure 5-3: Block diagram of classical disturbance rejection model.

The feedback controller was implemented in the MIT Hover Test Facility using Simulink. Figure 5-4 shows the Simulink model of the controller. The components in the dashed box of Figure 5-4 are easily matched with the controller components in the dashed box of Figure 5-2. Some additional features have been added to the Simulink version of the controller. In addition to the hub shear,  $F_z$ , a second switch input was added so that the controller could be activated externally. This “pushbutton counter” turns on both the input and output to the controller, and an output flag is used to indicate the on/off status of the controller. A high pass filter, with a corner frequency of 1 Hz, was placed at the input so that, when switching on the controller, the step increase in measured force did not send out a transient control spike.

A number of safety features were added at the output of the controller. The primary safety was a fuse that would trip and cut off the controller if the commanded voltage exceeded a pre-set threshold. A voltage limiter was also placed downstream

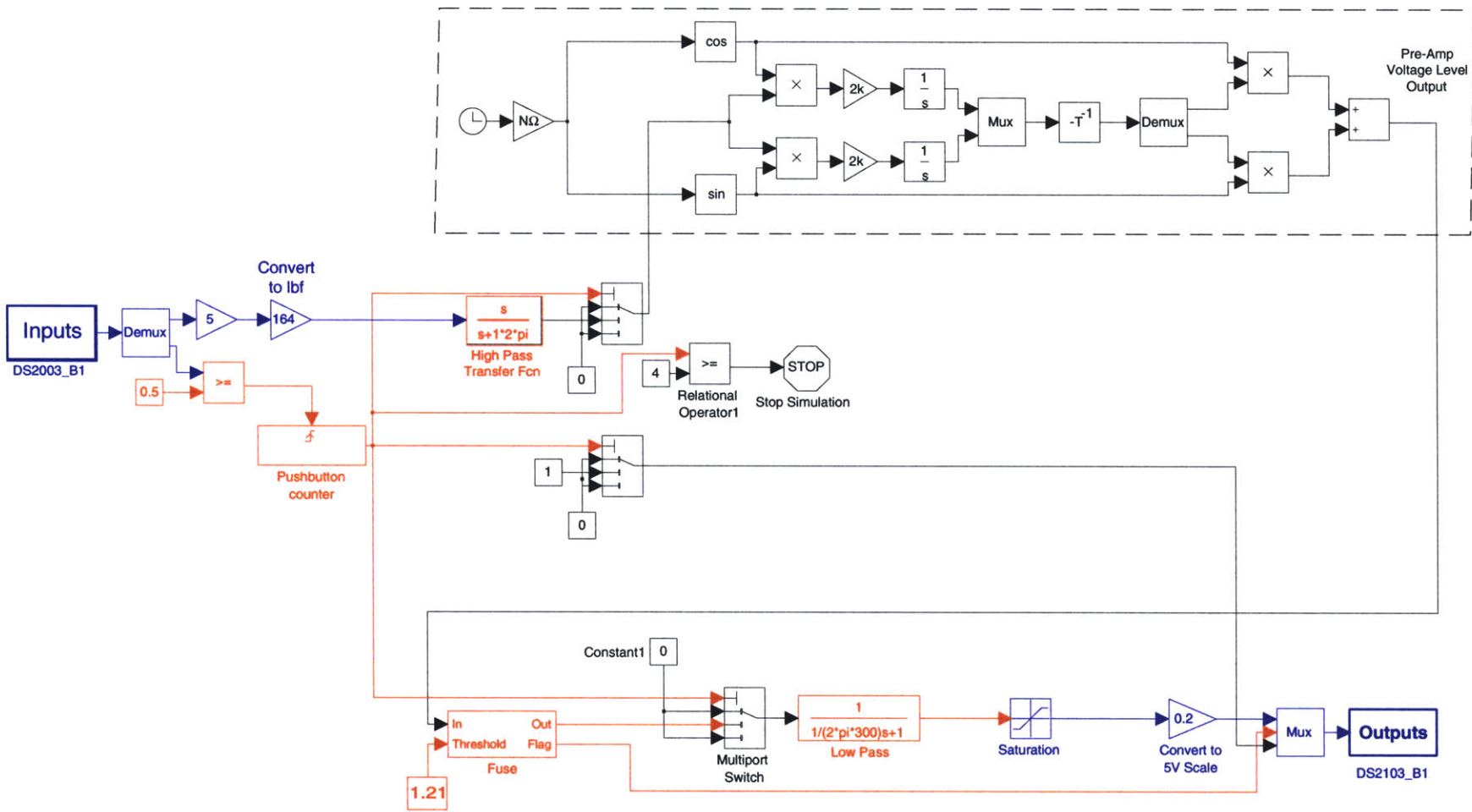


Figure 5-4: Simulink model of a typical single harmonic controller.

of the fuse to restrict the output voltage of the controller. A low-pass filter was used in combination with this limiter to avoid introducing any high frequency artifacts due to the limiting operation.

A dSpace real time control system, based on a TMSC40 Processor from Texas Instruments, was used to convert the Simulink code to C, compile it, and download to the digital signal processor. A/D and D/A cards were used to connect this controller to the (thrust) input and (actuator voltage) output signals. This controller architecture was used for all single harmonic continuous-time tests. Only the cosine and sine frequencies and the gain of the  $\mathbf{T}$  matrix were adjusted between each case. Modifications to this controller were made to implement the multiple harmonic and discrete-time controllers. Those modifications are explained in Sections 5.3 and 5.4.

As was discussed in the previous chapter, there are a number of rotor blade dynamic modes located within the control bandwidth, and the gain and phase of the plant vary greatly between each harmonic. Figure 5-5 shows the transfer function from actuator voltage to hub vertical shear, *i.e.*, the plant that was used for all closed-loop tests in these experiments. Although not included in the plot of Figure 5-5, the gain and phase of the high and low pass filters added into the Simulink model add additional gain and phase to the plant at low and high frequencies, respectively.

It is clear from examining Figure 5-5 that the quasi-steady assumption made in the control law development does not hold. If the quasi-steady assumption did hold, the controller given by Equation (5.3) would have 90 degrees of phase margin and infinite gain margin. However, the variation of plant phase with frequency violates this assumption and lowers the stability margins of the resultant system.

In order to check the system stability margins before implementation, the loop gain, which is the product of the identified plant transfer function (Figure 5-5) and the designed compensator, is examined in the frequency domain. For example, Figure 5-6 shows a Bode plot of the loop gain for the 4/rev controller. There exists a chance for instability at the frequencies where the gain of the loop transfer function exceeds unity. Because this particular controller has an infinite weighting at 4/rev, the gain of the loop transfer function goes to infinity at 89.1 Hz and exceeds unity over a narrow

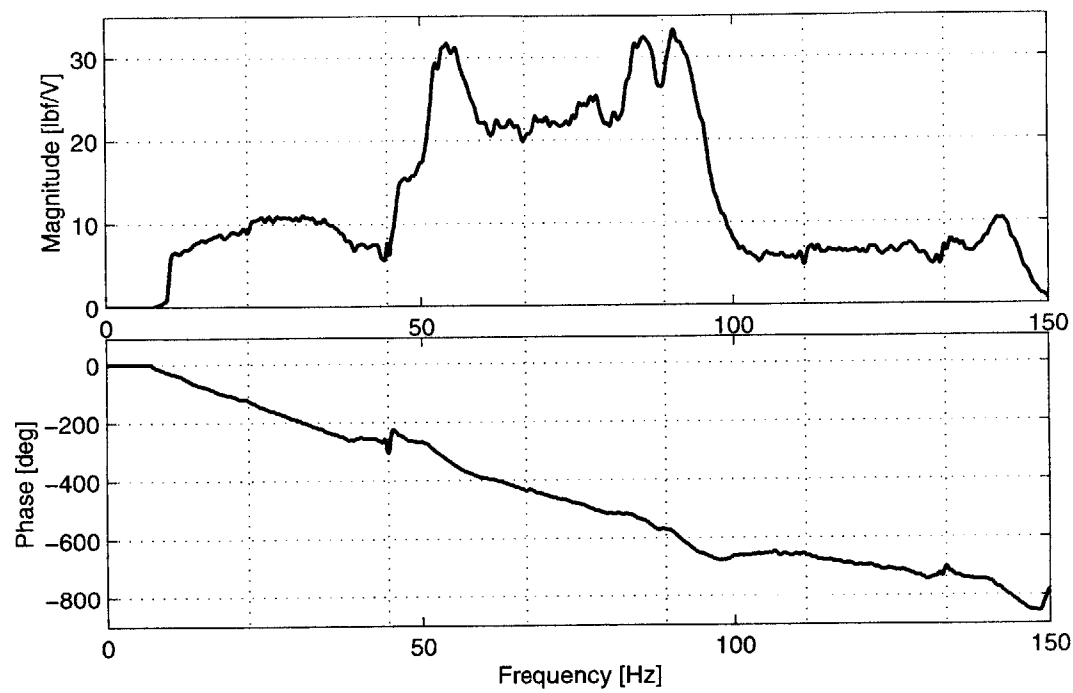


Figure 5-5: Experimentally measured transfer function from pre-amplifier voltage to hub vertical shear, *i.e.*, the plant transfer function,  $G(s)$ .

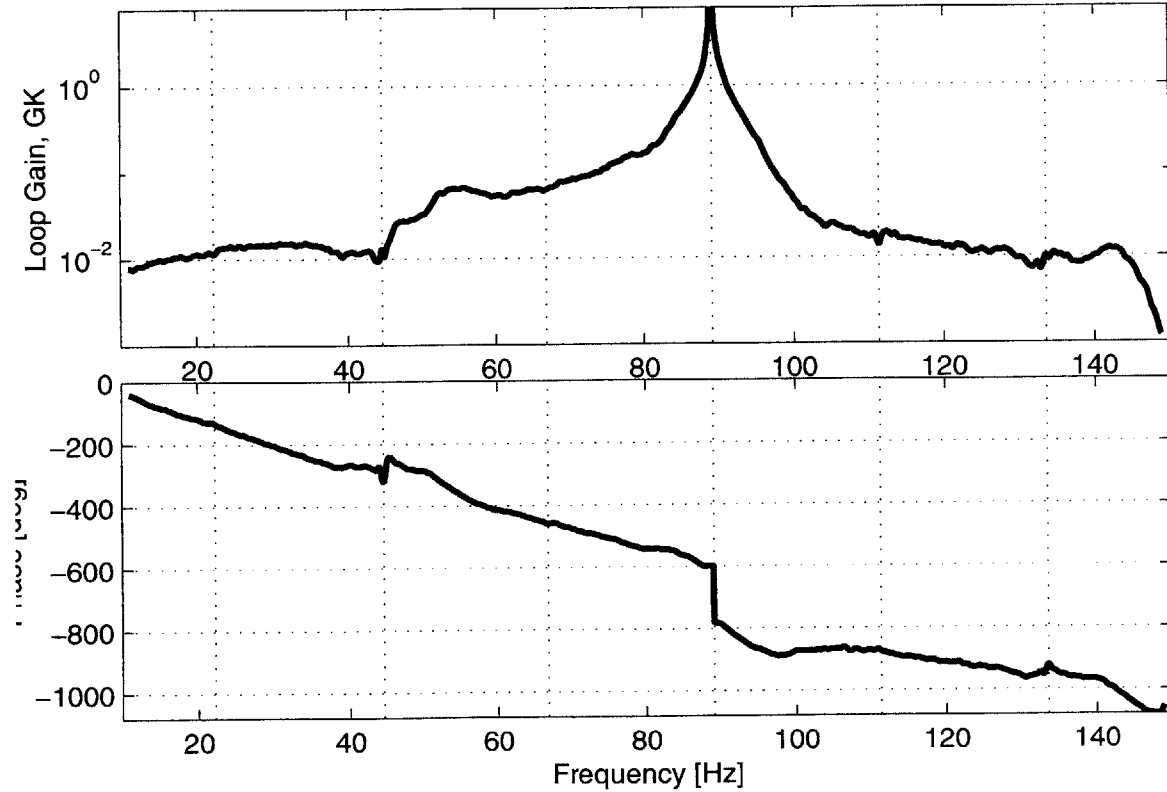


Figure 5-6: Bode plot of loop transfer function for the 4/rev controller.

bandwidth centered about this frequency. The variation of phase within this region determines the stability of the controller.

A useful method for checking controller stability is to look at the Nichols plot of the loop transfer function. A Nichols plot contains the same information as a Bode plot. The difference is that instead of plotting the gain and phase separately as a function of frequency, in the Nichols plot, the gain is plotted against the phase and the frequency information is not displayed explicitly. The data from Figure 5-6 is plotted in such a manner by the thicker, dark curve in Figure 5-7. The stability of the system

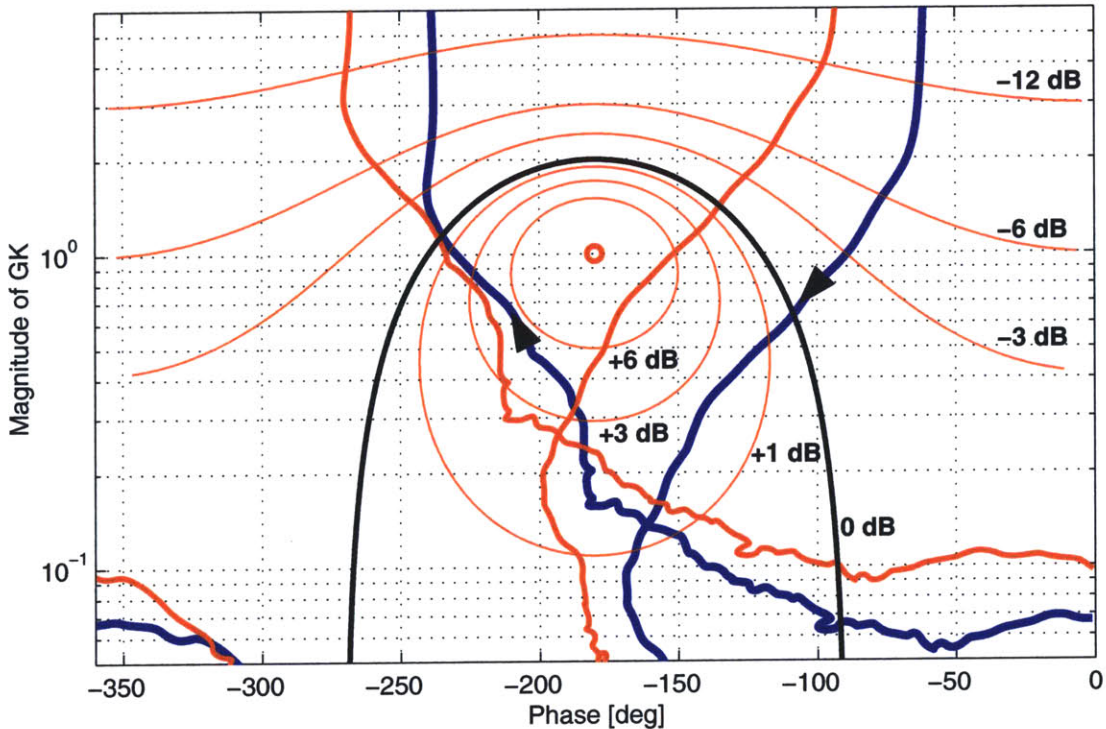


Figure 5-7: Modified Nichols plot of the loop transfer function for the 4/rev controller.

is ensured if there are no encirclements of the critical point (unity magnitude at 180 degrees of phase). This point is shown by the red circle in Figure 5-7. Contours of constant disturbance rejection (or amplification), given by the relation

$$\frac{y}{d} = \frac{1}{1 + GK} \quad (5.6)$$

are also plotted on the Nichols chart. The closed contours around the critical point

represent levels of vibration amplification. The thick, black, U-shaped contour represents the 0 dB boundary, where no vibration rejection or amplification is achieved. The open contours above the critical point represent levels of vibration reduction. The dB values listed next to each contour indicate how much amplification or rejection is caused at the frequency where the loop transfer function intersects the contour.

To aid in interpreting the level of vibration or reduction a particular controller causes at a certain frequency, the magnitude of Equation (5.6) as a function of frequency is plotted in Figure 5-8. As the frequency approaches 4/rev, the gain increases,

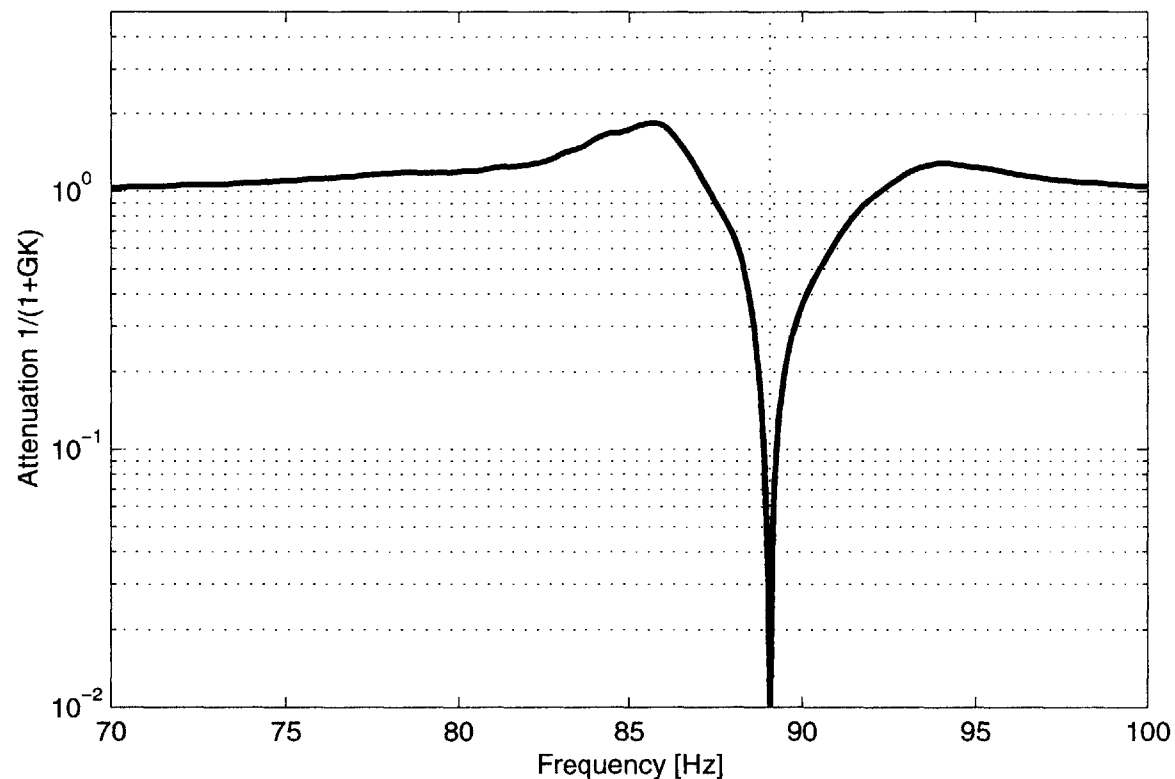


Figure 5-8: Closed-loop sensitivity to an output disturbance with the 4/rev feedback controller.

as does the disturbance rejection. Slight amplifications of the vibration result at the frequencies surrounding the targeted harmonic. The amount of amplification present is related to the stability margins of the control system.

Using the Nichols plot, the gain and phase margins are easily identified by measuring the proximity of the contour to the critical point when the phase equals 180

degrees or the gain equals unity, respectively. The gain margin for this controller is approximately 6.4, and the phase margin is 50 degrees.

Before implementing each controller, its Nichols plot was generated to verify stability. If the margins were not acceptable, the  $-\mathbf{T}^{-1}$  matrix was modified to improve stability as follows:

$$-\mathbf{T}^{-1} = k_{\text{fix}} (-\mathbf{T}_{\text{old}}^{-1}) \mathbf{P} \quad (5.7)$$

where  $k_{\text{fix}}$  is a scalar used to adjust the gain of the controller and the matrix,  $\mathbf{P}$ , is used to modify the controller phase.  $\mathbf{P}$  is expressed as

$$\mathbf{P} = \begin{bmatrix} \cos \phi & -\sin \phi \\ \sin \phi & \cos \phi \end{bmatrix} \quad (5.8)$$

where  $\phi$  is the change in phase angle. The 4/rev controller data given in Figures 5-6 to 5-8 was modified in this way by reducing the gain by a factor of two and adding 30 degrees of phase. These adjustments result in the thicker, blue curve in Figure 5-7. Before making these adjustments, the Nichols plot followed the thinner, red curve in that figure. Adjustments to the gain and phase of the controller are necessary because the change of phase with frequency of the open-loop rotor system leads to reduced stability margins.

Once acceptable stability margins for a controller were achieved through the use of Equation (5.7), it was tested by implementing it in a hover test. All of the closed-loop control tests performed in this research were done at 1336 RPM and at 8 deg angle of attack. Each controller test consisted of spinning the rotor to 1336 RPM, and accumulating at least 2 minutes of data. The first minute was taken with the controller turned on. During the second minute open-loop data was acquired to provide a direct comparison with the closed-loop data. The closed-loop in comparison to the open-loop performance of the 4/rev controller discussed above is shown in Figure 5-9. The data in each case corresponds to an 8192 point power spectral density of one minute of  $F_z$  data, taken at a sampling rate of 1000 points per second. The Matlab `psd` command (using an 8192 point Bartlett window) was used to calculate the power

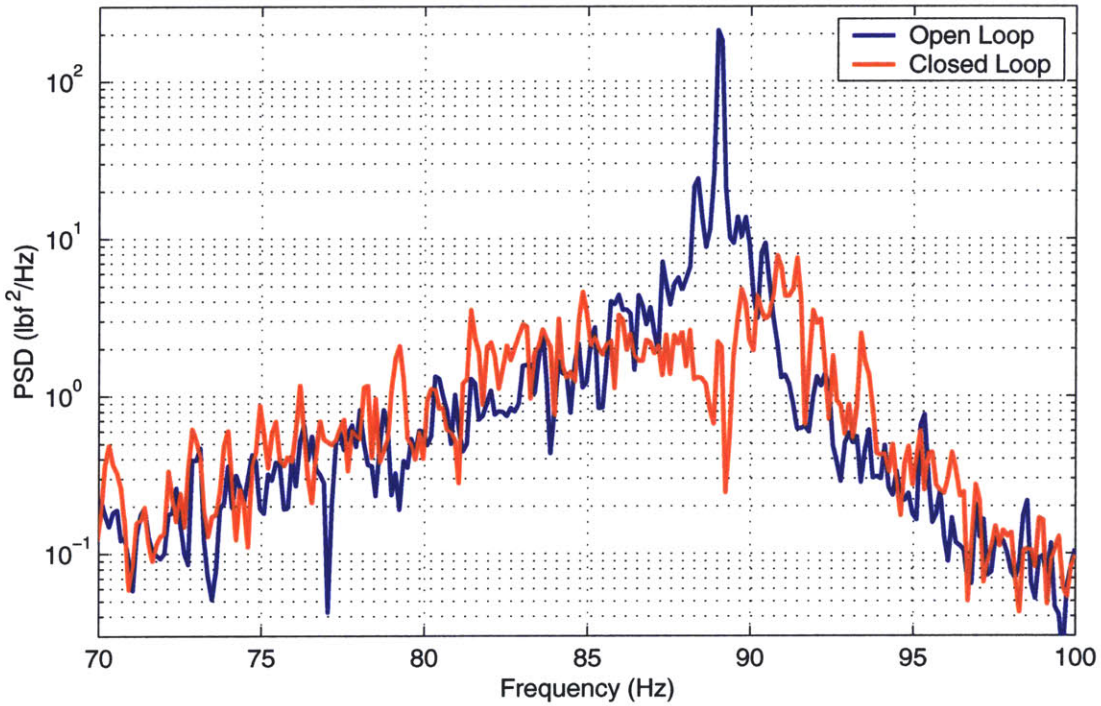


Figure 5-9: Open and closed-loop power spectral densities for the 4/rev controller in hover at 8 degrees angle of attack.

spectral densities.

As shown, because of the infinite controller gain precisely at 4/rev, the vibration there is virtually eliminated. In addition, the vibration over a small bandwidth surrounding the harmonic was also reduced. The change in performance due to the control can be quantified by comparing the open loop and closed loop root mean square values over small frequency bands centered at the controlled harmonic. For example, the change in performance over a 1 Hz window, expressed in decibels, is given by

$$20 \log_{10} \left[ \frac{\sqrt{\int_{f_1}^{f_2} P_{cl} df}}{\sqrt{\int_{f_1}^{f_2} P_{ol} df}} \right], \quad (5.9)$$

where  $P_{cl}$  and  $P_{ol}$  are the closed- and open-loop power spectral densities of the vibration signal,  $F_z$ , and  $f_1 = (89.067 - 0.5)$  Hz and  $f_2 = (89.067 + 0.5)$  Hz. A negative change corresponds to vibration reduction. Similar calculations are made for the performance over windows spanning 3 Hz, 10 Hz, and over the entire spectrum. All of these performance values are shown in Table 5.1. Also shown in Table 5.1 are the con-

Table 5.1: Experimental performance of continuous time single harmonic controllers. This table shows the change in closed-loop performance for each single harmonic controller implemented. Performance was evaluated by taking the ratio of closed- to open-loop rms vibration levels over 1 Hz ( $\pm 0.5$  Hz), 3 Hz ( $\pm 1.5$  Hz), and 10 Hz ( $\pm 5$  Hz) bands as well as over the entire frequency spectrum. Also shown are the open and closed loop rms levels of vibration for the spectrum.

Hrm	$\Delta$ Gain $k_{\text{fix}}$	$\Delta$ Phase $\phi$ (deg)	Change in Performance (dB)				OL rms $F_z$ (lbf)	CL rms $F_z$ (lbf)
			1 Hz	3 Hz	10 Hz	spect		
1	1	0	-5.26	-2.74	0.997	-0.148	15.3	15.1
3	1	0	-11.8	-7.82	-2.99	-0.190	16.0	15.7
4	1/2	30	-15.9	-10.6	-5.95	-0.919	16.9	15.2
5	1/4	0	-6.91	-4.78	-3.05	0.252	17.0	16.5
6	1	60	-15.3	-7.52	-4.56	-1.49	17.5	14.7

troller gain and phase adjustments,  $k_{\text{fix}}$  and  $\phi$ , as specified in Equations 5.7 and 5.8, and the open and closed loop rms value of the vibration,  $F_z$ , over the entire frequency bandwidth. Note that the performance improvement is very good near the rotor harmonic being controlled, but as the width of the frequency band increases to the full spectrum, very little change in performance is seen. As was noted in Section 5.1, the vibrational spectrum present during the current tests is broader with frequency than the spectrum typically seen in an operational helicopter. Because of this, it is expected that better performance over the entire spectrum will be achieved in an operational helicopter.

In Figure 5-9, some amplification is seen at the edges of the bandwidth. These local peaks in vibration are a natural artifact of the controller design. The size of these peaks is related to the stability margins of the controller as discussed above in relation to Figure 5-8. The heights of the peaks can be reduced by lowering the gain of the controller. However, this would also reduce the bandwidth over which vibration reduction is achieved. Therefore, there is a trade-off between the width of vibration reduction achieved and the level of vibration amplification incurred at the edges of the control envelope.

Identical controller development was implemented at each of the first six rotor harmonics. The best performance for each of these continuous-time, single harmonic

controllers is listed in Table 5.1. Appendix D contains the Bode and Nichols plot of each loop transfer function as well as a comparison plot of the open-loop in comparison to the closed-loop performance for each of these controllers.

Successful implementation was achieved at each harmonic except at 2/rev. The presence of a zero in the transfer function near that harmonic reduced the authority of the system there. In addition, a large portion of the disturbance is centered around 2/rev. Because of these two facts, attempts at performing 2/rev feedback control led to actuator saturation. To further complicate the situation, as was discussed in Section 4.3.3, this particular zero becomes non-minimum phase as the angle of attack drops from 8 deg to 4 deg. The presence of a non-minimum phase zero at the frequency of interest severely limits the achievable performance. Fortunately, for helicopters with more than two blades, most of the vibration occurs at frequencies greater than 2/rev, where the actuator has a great deal of control authority.

An interesting case occurred in implementing the 5/rev controller. The Bode plot of its loop transfer function with no modification to the gain or phase is shown in Figure 5-10. The dynamics of the rotor system at approximately 90 Hz nearly destabilize the system. The poor stability margin there is seen clearly in the Nichols plot of the loop transfer function, shown in Figure 5-11. To implement this controller, the gain was reduced by a factor of 4 to ensure proper stability margins at the 4/rev frequency.

The effect of the closed-loop vertical hub shear control on the other five components of force and moment at the rotor hub must be assessed to ensure that the feedback is not adversely increasing those components of vibration. Figure 5-12 shows a comparison of the power spectral densities for these five hub reactions during open-loop and closed-loop implementation of the 4/rev vertical hub shear controller. As shown, there is slight amplification occurring at the edges of the control bandwidth in the force in the direction of the active blade,  $F_y$ , and in the moment around the two in-plane axes. If this additional vibration is unacceptable, higher dimension closed loop controllers designed to reduce these additional hub reactions may need to be implemented. Appendix D contains a similar plot of the closed- and open-loop hub

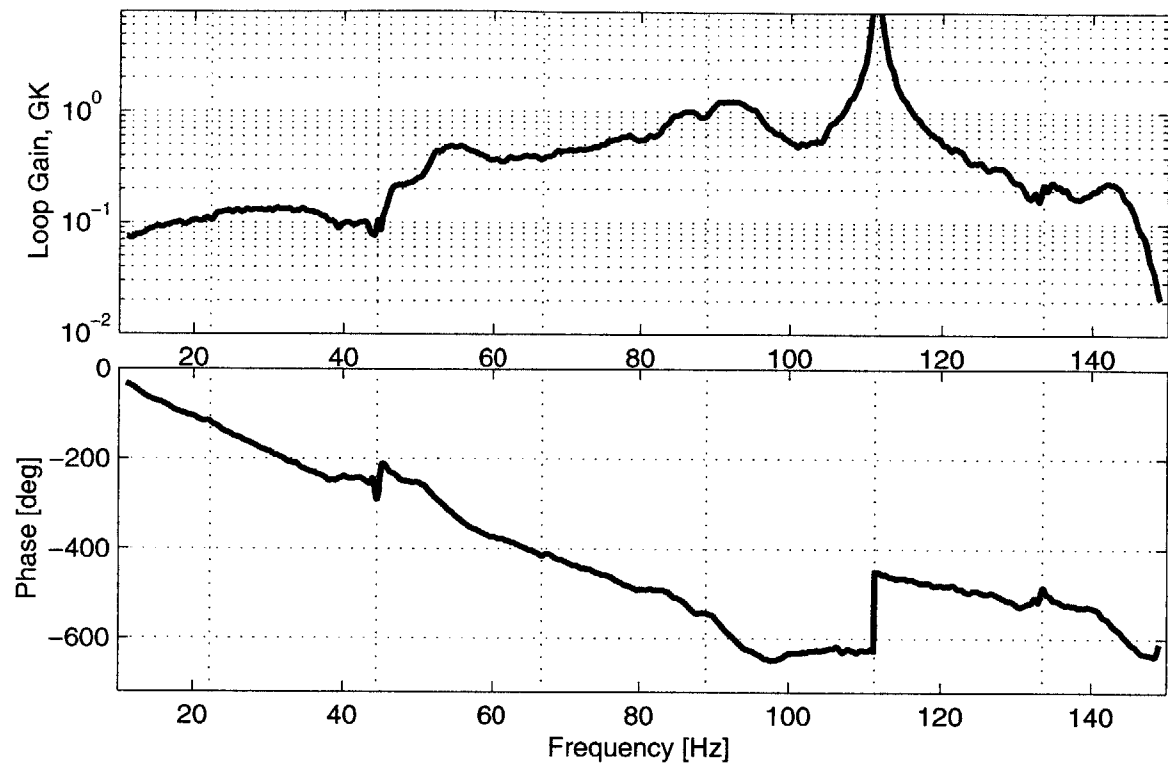


Figure 5-10: Bode plot of loop transfer function for the unmodified 5/rev controller.

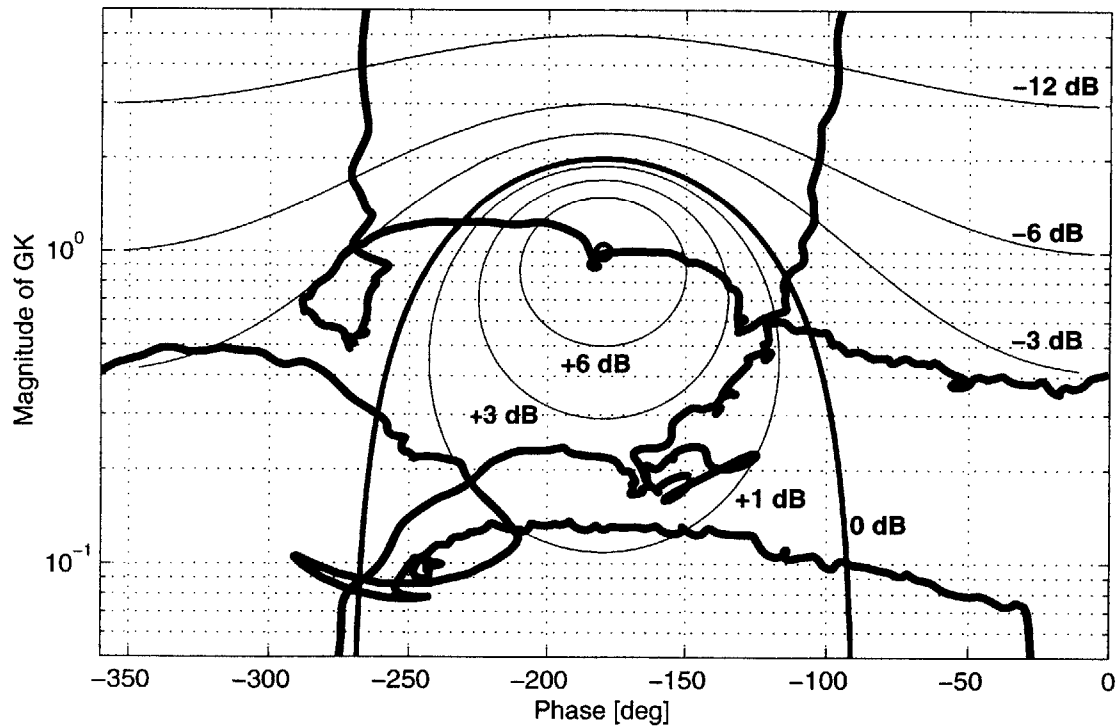


Figure 5-11: Nichols plot of the loop transfer function for the unmodified 5/rev controller.

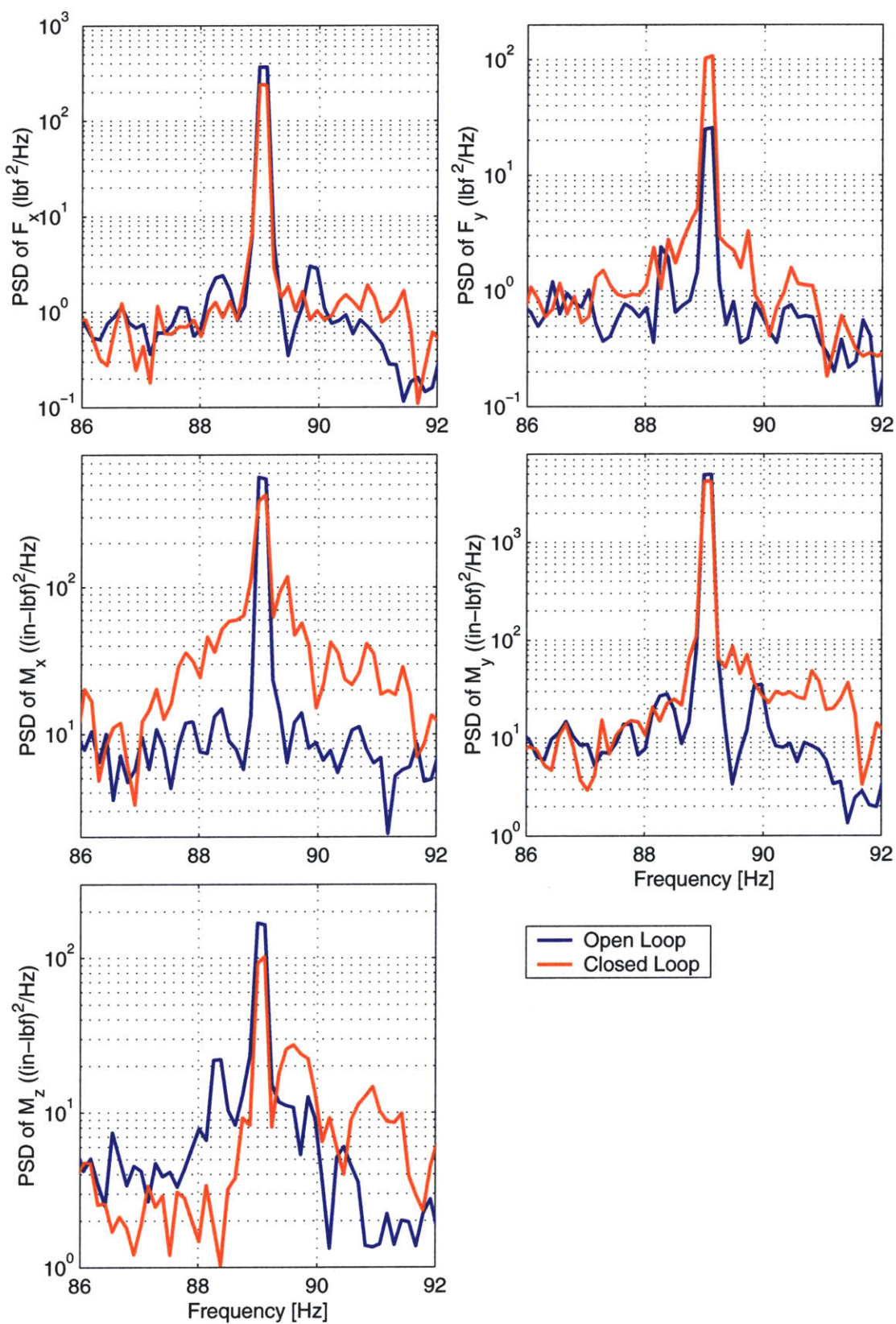


Figure 5-12: Open- and closed-loop components of force and moment at the hub during implementation of 4/rev controller.

reactions for each of the controllers implemented in this research.

### 5.3 Multiple Harmonic Continuous-Time Control

The algorithm used for the single harmonic controllers was extended to test the ability of the actuator in simultaneously reducing multiple harmonics of vibration. Three separate multiple harmonic controllers were implemented in these tests. One controller was designed to simultaneously reduce the vibration at 3, 4, and 5/rev, a second was designed to reduce 4, and 6/rev vibrations, and the last targets the 1, 3, 4, 5, and 6/rev harmonics. These three controllers are referred to below as the multiharmonic I, II, and III controllers, respectively.

The multiharmonic controllers are constructed through a superposition of single harmonic controllers. For example, Figure 5-13 shows the block diagram of the control strategy for the multiharmonic III controller. As in Figure 5-2, the compensator components are drawn inside of the dashed box. In the figure, only the controller components for the 1/rev and 3/rev harmonics are shown explicitly, but the additional three harmonic groups are constructed in an analogous fashion. Separate  $T_i$  matrices are specified for each harmonic. After the compensated signals at each harmonic are generated, they are added together and fed back to the plant, as shown.

In the Simulink realization of the multiple harmonic controller, a similar superposition of the single harmonic model in Figure 5-4 is performed. As in Figure 5-13, multiple copies of the components in the dashed box of Figure 5-4 are copied and wired in parallel for the multiple harmonic controller. In each, only the value of the  $T_i$  matrix and the frequency of the sinusoids are adjusted.

Just as in the single harmonic case, the multiple harmonic controller is subject to the same stability margin concerns. Thus, the Nichols plot of each of these combined controllers were checked to ensure adequate margins before implementation. Figure 5-14 shows the Nichols plot for the multiharmonic III controller. This plot is similar to Figure 5-7 except that now the magnitude of the loop gain exceeds unity in five separate regions, corresponding to the vibration suppression being performed at the

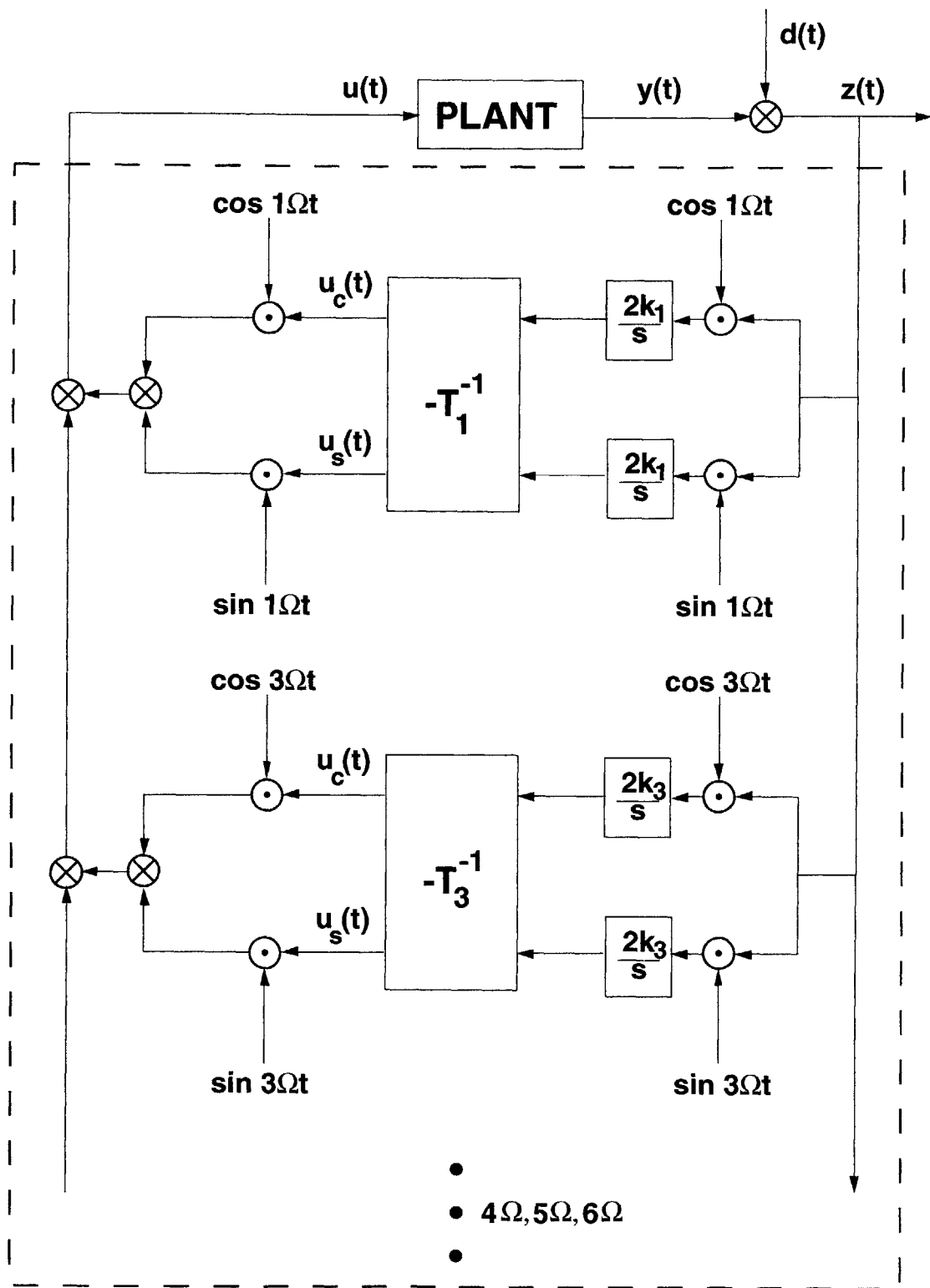


Figure 5-13: Block diagram of the multiple harmonic, continuous-time feedback controller.

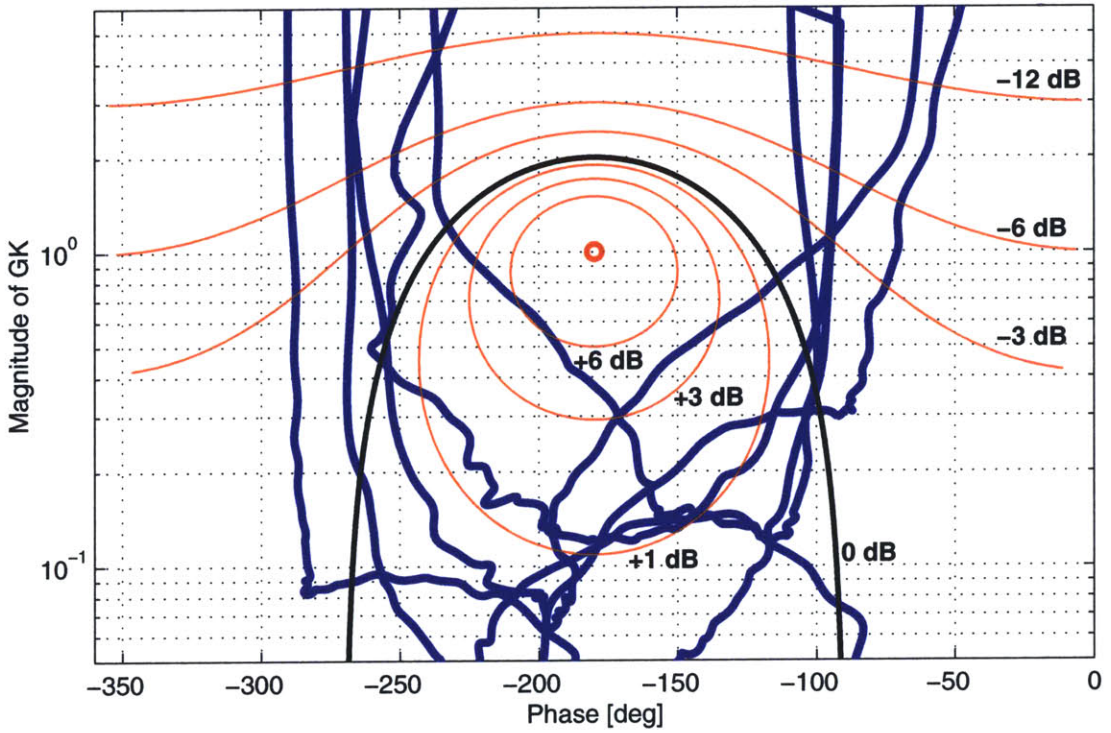


Figure 5-14: Nichols plot of the loop transfer function for the unmodified 5/rev controller.

five different rotor harmonics. The gain and phase margins for this controller can be identified as in Figure 5-7. In this case, we see that the one contour passes within the 6 dB vibration amplification boundary. This contour corresponds to the frequencies near 4/rev and indicates that there will be some amplification of the vibration at the frequencies near that harmonic.

Each of the multiharmonic controllers were implemented as in the single harmonic control experiments. Figure 5-15 shows the open and closed-loop results for the multiharmonic III controller, which is the most sophisticated controller implemented in these tests. As shown, the control system is effective in the simultaneous elimination of the peak vibration at each harmonic. The bandwidth of control around each peak was not as large as in the single harmonic control tests, due to actuator saturation. As expected from examination of the Nichols plot in Figure 5-14, there is some non-trivial amplification of the vibration near the 4/rev frequency in Figure 5-15. This could be reduced by lowering the gain at that particular harmonic, if desired.

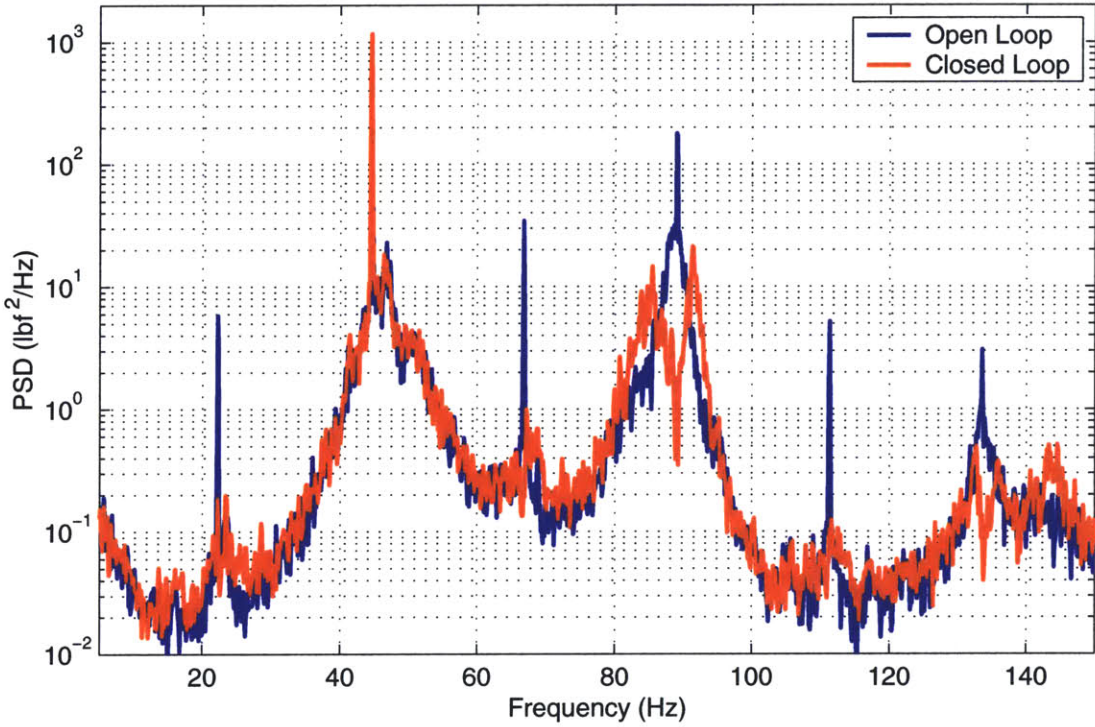


Figure 5-15: Open- and closed-loop power spectral densities for the multi-harmonic controller at 1,3,4,5, and 6/rev frequencies.

The exact performance numbers for all of the multiharmonic controllers are given in Tables 5.2 and 5.3. In addition, Appendix D contains the same plots for the multiharmonic controllers that were included for the single harmonic cases. As in the

Table 5.2: Wide-band experimental performance of continuous time multi-harmonic controllers. For each multiharmonic controller, this table gives the open- and closed-loop rms vibration levels, and their ratio over the entire frequency spectrum.

Multi-Hrm Controller	OL rms $F_z$ (lbf)	CL rms $F_z$ (lbf)	$\Delta$ Perf (dB)
I	15.7	14.3	-0.793
II	15.5	15.4	-0.067
III	20.5	19.3	-0.528

single harmonic control cases, very good performance was achieved in a narrow window around the rotor harmonics, but less improvement is apparent over a broader window. As in the single harmonic case, because of the broad disturbance spec-

Table 5.3: Narrow band experimental performance of continuous time multi-harmonic controllers. This table shows the change in closed-loop performance for each multiple harmonic controller over implemented. Performance was evaluated by taking the ratio of closed- to open-loop rms vibration levels over 1 Hz ( $\pm 0.5$  Hz), 3 Hz ( $\pm 1.5$  Hz), and 10 Hz ( $\pm 5$  Hz) bandwidths.

Hrm	$\Delta$ Gain $k_{\text{fix}}$	$\Delta$ Phase $\phi$ (deg)	Change in Perf (dB)		
			1 Hz	3 Hz	10 Hz
I-3	1/8	-20	-0.461	0.731	0.6685
I-4	1/2	30	-15.3	-8.85	-4.83
I-5	1/16	0	-7.38	-4.32	-2.40
II-4	1/2	30	-15.7	-9.62	-4.78
II-6	1/2	50	-8.68	-4.06	-2.19
III-1	1/10	0	-11.4	-7.50	-4.55
III-3	1/8	-20	-11.9	-7.44	-4.19
III-4	1/2	30	-16.5	-10.7	-3.75
III-5	1/16	0	-10.8	-7.41	-4.08
III-6	1/2	50	-9.43	-5.14	-2.51

trum present for these tests, the improvement should be more dramatic in an actual helicopter.

The open- and close-loop plots of the other 5 components of hub reaction for this multi-harmonic controller are included in Appendix D. As with the single harmonic controller, there is a small effect on the other 5 components of hub reaction. As discussed above, if this additional vibration is unacceptable, higher dimension closed loop controllers may be necessary.

## 5.4 Single Harmonic Discrete-Time Control

The final closed-loop control tests were designed to determine if using discrete-time or continuous-time control is more effective for vibration control. Discrete time implementation of the higher harmonic control algorithm differs from the continuous-time approach by the addition of a sample-and-hold, as shown in Figure 5-16, which operates with a period equal to that of the rotor.

The Simulink model of the discrete-time controller is identical to that shown in

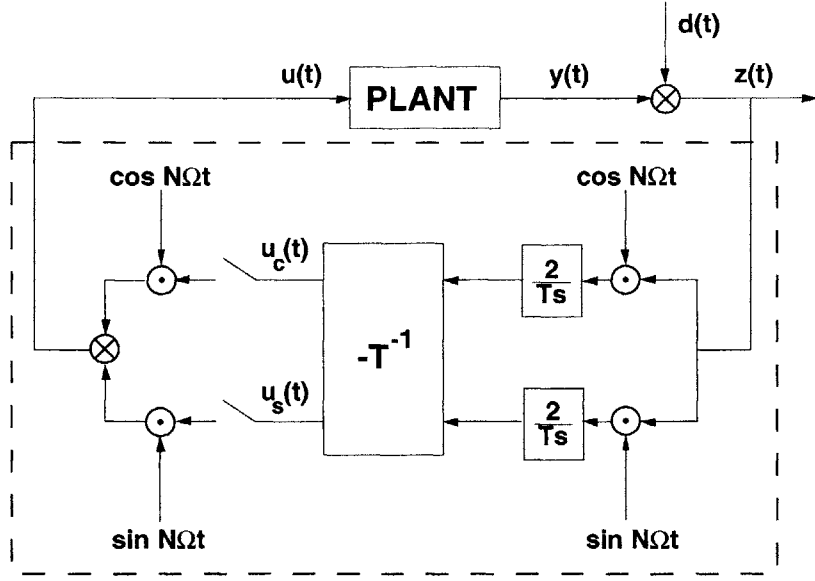


Figure 5-16: Block diagram of the discrete-time feedback controller.

Figure 5-4 except that a sample and hold operator is added at the output of the  $T^{-1}$  multiplier. Another small difference in the implementation of the discrete-time controller is that the controller bandwidth must be chosen equal to an integer number of rotor periods. This is indeed a small difference, however, because the bandwidth of both controller types is far above that of the dynamics being controlled.

The effect the sample and hold on the discrete controller behavior is that the control signal is only updated once per revolution. In contrast, the continuous-time controller updates continuously during operation, thus making use of the entire measured vibratory signal. An example of the fed back control signal for a 4/rev discrete controller is shown in Figure 5-17. The rotor period is 40 ms, and it is clearly evident from the figure how the magnitude of the control signal updates once per rotor period. The predominant 4/rev signal pulse is also easily seen in the figure.

As can be expected, the use of a sample and hold step adds an artificial delay to the performance. It is a well known fact that a sample and hold (or zero-order hold) operation causes a phase delay equal to one half the period of the hold, and is equivalent to multiplying the loop transfer function by  $e^{-jωT/2}$  [23]. This increased phase loss leads to lower stability margins in the controller and thus should worsen the performance of the system. Thus, we expect the continuous-time controller to

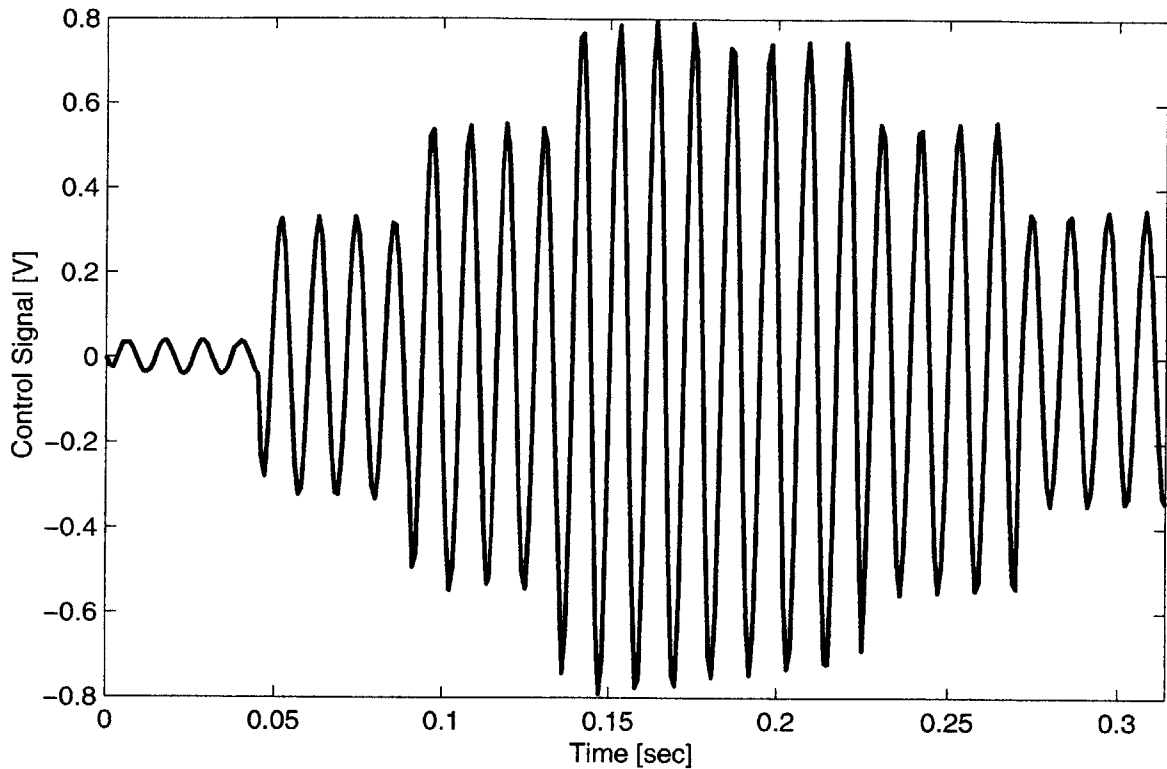


Figure 5-17: Feedback control signal for the 4/rev discrete-time controller.

yield better performance than the discrete-time case [36, 37].

To test this theory, continuous and discrete controllers were implemented with identical  $\mathbf{T}$  matrices and nearly identical controller bandwidths. The open and closed-loop performance for these systems is compared in Figure 5-18. Because of the large controller gain, there is a low gain margin in both cases, leading to large peaks in the response at the edges of the control bandwidth. However, it is clear that, as predicted, the continuous-time controller out-performs the discrete-time controller.

Discrete-time controllers at lower gain levels were also implemented to reduce the amplification at the sides of the rotor harmonics. The performance of these controllers is quantified in Table 5.4 in a manner identical to the single harmonic controllers in Table 5.1. In addition, the comparison of the full gain continuous and discrete 4/rev controllers are also included in this table.

Plots of the open- and close-loop performance of all six components of hub reaction for the two, lower gain discrete controllers are presented in Appendix D.

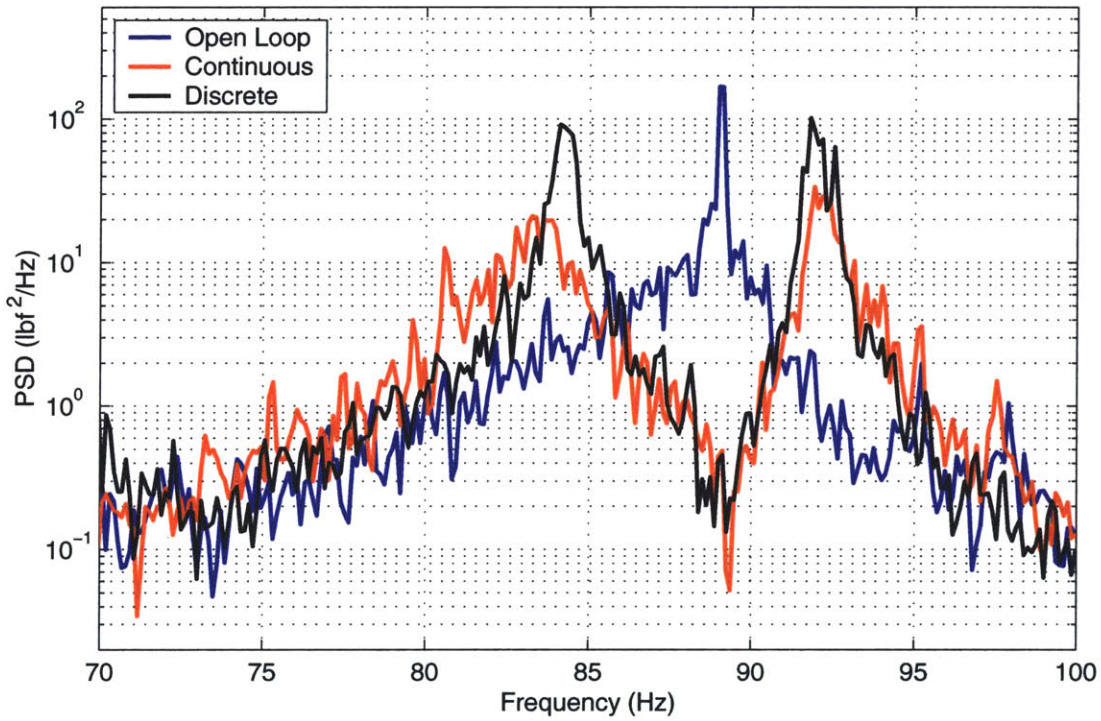


Figure 5-18: Performance comparison of continuous- and discrete-time closed-loop controllers with the open-loop vibration spectrum.

Table 5.4: Experimental performance of discrete time single harmonic controllers.

Hrm	$\Delta$ Gain $k_{\text{fix}}$	$\Delta$ Phase $\phi$ (deg)	Change in Performance (dB)				OL rms $F_z$ (lbf)	CL rms $F_z$ (lbf)
			1 Hz	3 Hz	10 Hz	spect		
3 Dscrt	1	0	-13.1	-7.23	0.438	-0.421	16.7	15.9
4 Dscrt	1/2	30	-16.7	-8.27	1.77	0.633	18.1	16.8
4 Dscrt	1	30	-22.3	-14.9	1.923	1.13	16.8	19.2
4 Cont	1	30	-21.8	-15.2	-2.46	-0.432	15.5	14.7



# Chapter 6

## Summary

### 6.1 Major Results and Conclusions

This thesis presents the successful development of an active rotor blade incorporating a trailing edge servo-flap, that is capable of effective helicopter vibration reduction. A prime element that determined this success was the development of a high performance discrete actuator, the “X-Frame Actuator.” Laboratory tests on this actuator show it to have a mass efficiency approaching the theoretical maximum and greater than other competing actuation technologies. In addition, the performance of the actuator was shown to be robust in the presence of outside disturbances. Most notably, shake tests of the actuator demonstrated it to be insensitive to transverse shaking of up to 69 g’s rms at 45 Hz. All of the test results for this actuator show it to be ideal not only for helicopter rotor control but for most engineering applications requiring compact, high bandwidth, large stroke actuation.

A model scale CH-47D active rotor blade incorporating the X-Frame actuator to power a trailing edge servo-flap was designed and manufactured at MIT. The design of the active blade was performed by adhering to a number of set requirements. Most of the components in the system were designed using ProEngineer and manufactured by wire electron discharge machining (EDM). The basic rotor blade structure was manufactured out of composite using a procedure that was developed at Boeing Helicopters for their model scale rotor blades. Modifications were made to the

manufacturing procedure to allow for the incorporation of the actuator and servo-flap components. Before spinning, the active blade was tested to ensure that it provided acceptable strength and performance levels.

The active blade was hover tested on the MIT Hover Test Facility. Data was collected at 4 and 8 degree angles of attack as a function of rotor speed and applied voltage. The servo-flap actuation system performed as expected with rotor speed. In hover, the deflection drops to about half its non-rotating level, indicating a nearly impedance matched system. The aerodynamic hinge moment is higher than expected, leading to slightly lower than expected flap deflections. Analysis of the test data also shows that the actuation system profits from aeroservoelastic excitation of the blade modes by the servo-flap. This leads to strong actuator authority over frequencies from 50-100 Hz.

Aeroelastic scaling was used to ensure that all experimental results translate directly to full-scale. One exception is that the Reynolds number was not maintained in the model scale tests. Assuming that these viscous effects are not sizeable, if an identical actuation system is implemented in each of the six blades of a CH-47D helicopter, the combined actuation could produce as much as 16,000 lbf at the 3/rev frequency. The CH-47D has a gross-weight of 50,000 lb, so this level of control should be adequate for control of 3/rev vibration. Furthermore, proper next-generation redesign should lead to less friction and better system performance.

Closed-loop feedback control was implemented with a frequency weighted controller used in previous studies on rotor HHC. Controllers were successfully implemented at the individual frequencies of 1/rev, 3/rev, 4/rev, 5/rev, and 6/rev and in various combinations thereof. The most significant result was simultaneous control at all five harmonics. Control at 2/rev was impossible to achieve due to the combination of a zero in the transfer function at that frequency and a large disturbance present at 2/rev. An experimental comparison was made between the achievable performance of continuous time versus discrete time control. The results from these tests verified a hypothesis that continuous time control leads to better closed-loop performance in comparison to discrete time control.

## **6.2 Contributions**

The contributions of this research are grouped into five categories: discrete actuator technology, active rotor blade design and manufacture, the MIT Hover Test Facility, active rotor blade performance identification, and closed-loop helicopter rotor control.

### **Discrete Actuator Technology**

1. The mass efficiency metric was demonstrated as an effective metric to use in optimizing and comparing competing actuation technologies.
2. A number of discrete actuator design axioms were developed that can be used in actuator design and analysis. The use of these axioms was demonstrated by applying them in a survey of the field of discrete actuators.
3. The X-Frame discrete actuator was invented. The performance of this actuator has been extensively characterized in the lab. Bench tests of this actuator have verified that it has a mass efficiency approaching the theoretical maximum. In addition, it has a number of other characteristics that make it ideal for many high bandwidth, large stroke engineering applications, especially rotor blade trailing edge servo-flap control.

### **Active Rotor Blade Design and Manufacture**

1. An active blade has been designed and manufactured that incorporates the X-Frame discrete actuator along with all components needed for proper restraint and operation of the actuation system in the high load environment of a Mach scaled rotor blade. The lessons learned from building this prototype may be used to improve the manufacturing and performance of future active rotor blades.
2. The standard rotor blade manufacturing process was modified to allow for incorporation of the actuator and related components.

## The MIT Hover Test Facility

1. The author was a core member of the design team of the MIT Hover Test Facility. Specifically, the author was responsible for the design and supervised the manufacturing of all rotating frame hub components. These efforts have led to the development of a useful rotor test facility in which blade mounted actuation schemes can be developed.

## Active Blade Performance Identification

1. A data collection process consisting of multiple actuation chirps was developed to collect rotor data. Signal processing techniques were implemented to average and smooth the acquired data traces, leading to accurate identification of the system behavior.
2. The performance of the X-Frame actuator in affecting servo-flap deflections was characterized as a function of angle of attack, rotor speed and applied voltage. These tests have shown the actuator to be very effective in performing its designed function over the entire bandwidth of interest. In addition, the measurements taken have provided an experimental estimate of the servo-flap hinge moment.
3. The transfer function from servo-flap deflection to hub vertical shear (thrust) was identified. This represents the first transfer function of this type ever collected for a Mach scaled rotor blade actuated via a trailing edge servo-flap. This data provides details regarding the aeroservoelastic interactions of the servo-flap with the blade dynamics and the authority of the actuation system in affecting hub vibrational characteristics.
4. The entire set of data from the rotor tests provides an invaluable database that rotor analysts can use to compare and update their rotor analysis codes. This should lead to greater accuracy in rotor modeling and the possibility of optimizing active rotor blade properties to maximize actuation performance.

## Closed-Loop Helicopter Rotor Control

1. Closed loop feedback control was implemented on a Mach scaled rotor in air at both single and multiple rotor harmonics. This represents the first higher harmonic control implemented using a blade mounted actuator under such conditions.
2. An experimental comparison between discrete time and continuous time control was performed. The results from these tests showed that continuous time control is more effective than discrete time control for this problem.
3. A database has been collected demonstrating the achievable performance using this actuation system. This database can be used to predict the improvements one can expect from applying this technology to an operational helicopter.

## 6.3 Recommendations for Future Work

A multi-disciplinary research project such as this touches many different fields of engineering. The applied nature of the project necessarily limits the depth to which some phenomenon can be pursued. In this section, recommendations for possible further research are given.

1. In the experimental evaluation of the mass efficiency of a discrete actuator, an accurate measurement of the existing energy in an active material is needed. For example, in calculating the mass efficiency of the X-Frame actuator, load lines similar to those in Figure B-9 are needed for the stacks alone. Then the ratio of the areas under the load line curves can be used to calculate the mass efficiency of the device. A component tester has recently been developed at MIT by Lutz and Hagood [56] to aid in performing this measurement. Component testers of this type should be used to provide more accurate estimates of device mechanical and mass efficiencies.

In addition, such a component tester can be used to evaluate active material

performance as a function of compressive stress and temperature. Such data would be invaluable in identifying the optimum environment desired for stack operation.

2. Next generation redesign of the active blade should be performed to get closer to a minimum weight design without sacrificing actuator performance. In fact, there now is an experimental measurement of the servo-flap hinge moment so the lever arm length of the servo-flap should be modified to exactly impedance match the actuator to the aerodynamics. A new set of identical CH-47 Mach scaled rotor blades should then be built and tested on the MIT Hover Test Stand and in forward flight wind tunnel tests to verify the measurements made in this research and to continue to address the active control issues important for full-scale rotors.
3. Because of these tests, a large database now exists for a Mach scaled rotor blade operating with trailing edge servo-flaps. This database should be used to validate the accuracy of analytical rotor models. Once a model is developed that can predict active rotor performance to within acceptable accuracy, it should be used to optimize the design of the rotor blade to maximize vibration control authority. These optimizations will most likely include variations in flap dimensions and location as well as rotor blade stiffness and mass properties.
4. As it exists today, this actuation technology is already providing more than adequate control authority. With some redesign to minimize friction, it should be tested in forward flight wind tunnel and flight tests. This area of future work is currently under development by a team of researchers at MIT and Boeing Helicopters. This research group is planning to perform full-scale flight tests in 2001 of a helicopter with active rotor blades utilizing trailing edge servo-flaps, similar to the blade described in this thesis. This will be the first flight test of a helicopter with blade mounted actuators. The actuator that has been selected for these flight tests is a derivative of the X-Frame actuator.

5. A detailed comparison should be made between integral and discrete rotor blade actuation concepts. Comparisons should include factors such as authority, bandwidth, ease in manufacturing, added mass, reliability, aeroelastic impact on blade performance, technological maturity, and cost. This comparison should take into account the fact that advances in active material performance will affect both technologies equally. This comparison will go a long way towards determining the actuation technology best suited for blade mounted control and allow helicopter rotor developers to focus resources on the most appropriate technology.
6. In order to use the closed-loop results obtained in this research to predict the performance improvement on an operational helicopter, a comparison must be made between the disturbance spectra that this model rotor operated within and that of a full-scale helicopter. This data should be obtained for a full-scale helicopter. Note that active rotor blades are not necessary to obtain this open-loop data.
7. In this thesis, simple linear time invariant controllers were used. More sophisticated controllers may have better performance. The use of modern, model-based control techniques should be investigated.



# Bibliography

- [1] M. F. Ashby, *Materials Selection in Mechanical Design*, Pergamon Press, New York, 1993.
- [2] O. Ben-Zeev and I. Chopra, “Development of an improved helicopter rotor model with smart trailing-edge flaps for vibration suppression,” *Journal of Smart Materials and Structures*, 5(1), February 1996.
- [3] A. A. Bent, *Active Fiber Composites for Structural Actuation*, PhD thesis, Massachusetts Institute of Technology, Department of Aeronautics and Astronautics, January 1997.
- [4] A. A. Bent and N. W. Hagood, “Piezoelectric fiber composites with interdigitated electrodes,” *submitted to the Journal of Intelligent Material Systems & Structures*, March 1996.
- [5] R. L. Bielawa, “Analytical investigation of helicopter rotor blade appended aeroelastic devices,” Technical Report CR166525, NASA, 1984.
- [6] R. L. Bisplinghoff and H. Ashley, *Principles of Aeroelasticity*, Dover Publications, Inc., New York, 1975.
- [7] R. L. Bisplinghoff, J. W. Mar, and T. H. H. Pian, *Statics of Deformable Solids*, Dover Publications, Inc., New York, 1990.
- [8] C. M. Bothwell, R. Chandra, and I. Chopra, “Torsional actuation with extens-torsion composite coupling and magnetostrictive actuators,” *Journal of the AIAA*, 33(4), April 1995.

- [9] P. J. Carpenter and S. Paulnock, "Hovering and low-speed performance and control characteristics of an aerodynamic-servocontrolled helicopter rotor system as determined on the Langley helicopter tower," Technical Report TN-2086, NACA, May 1950.
- [10] K. H. Chan, "Nonlinear modeling of high field ferroelectric ceramics for structural actuation," Master's thesis, Massachusetts Institute of Technology, Department of Aeronautics and Astronautics, July 1994.
- [11] P. C. Chen and I. Chopra, "Wind tunnel testing of a smart rotor with induced-strain actuation of blade twist," In *37th Structures, Structural Dynamics and Materials Conference*, pages 76–90, Salt Lake City, UT, April 1996.
- [12] I. Chopra, "Dynamic analysis of constant-lift and free-tip rotors," In AIAA Dynamic Specialists Conference, *Atlanta, GA*, April 1981.
- [13] I. Chopra, "Smart rotor technologies: Progress and future directions," In 8th ARO Workshop on Aeroelasticity of Rotorcraft Systems, State College, PA, October 1999.
- [14] G. Cook, 1995, EDO Corporation, Personal correspondence.
- [15] G. Cook, July 1996, EDO Corporation, Personal correspondence.
- [16] E. F. Crawley and E. H. Anderson, "Detailed models of piezoceramic actuation of beams," *The Journal of Intelligent Material Systems and Structures*, 1(1):4–25, 1990.
- [17] M. Drela, "Newton solution of coupled viscous/inviscid multielement airfoil flows," AIAA 21st Fluid Dyn., Plasma Dyn. and Lasers Conf., Paper AIAA-90-1470, June 1990.
- [18] M. Drela, November 1999, Personal correspondence.
- [19] M. Drela and M.B. Giles, "Viscous-inviscid analysis of transonic and low Reynolds number airfoils," *AIAA Journal*, 25(10):1347–1355, Oct 1987.

- [20] EDO Corporation, Acoustics Division, Ceramic Operations, 2645 South 300 West, Salt Lake City, UT, *Piezoelectric Ceramics, Material Specifications, Typical Applications*.
- [21] ETREMA Products Inc., Ames, IA, *ETREMA Terfenol-D Magnetostrictive Actuators*.
- [22] R. C. Fenn, J. R. Downer, D. A. Bushko, V. Gondhalekar, and N. D. Ham, “Terfenol-D driven flaps for helicopter vibration reduction,” In *SPIE Smart Structures and Intelligent Systems*, volume 1917, pages 407–418, 1993.
- [23] G. F. Franklin and J. D. Powell, *Digital Control of Dynamic Systems, Second Edition*, Addison-Wesley, Reading, MA, 1989.
- [24] P. P. Friedmann, “Rotary-wing aeroelastic scaling and its application to adaptive materials based actuation,” In *39th AIAA Structures, Structural Dynamics, and Materials Conference*, 1998, AIAA Paper 98-2098.
- [25] M. Fripp, “Distributed structural actuation and control with electrostrictors,” Master’s thesis, Massachusetts Institute of Technology, Department of Aeronautics and Astronautics, January 1995.
- [26] M. V. Fulton and R. A. Ormiston, “Hover testing of a small-scale rotor with on-blade elevons,” In *American Helicopter Society 53rd Annual Forum*, Virginia Beach, VA, 1997.
- [27] M. V. Fulton and R. A. Ormiston, “Wind tunnel testing of a small-scale rotor with on-blade elevons,” In *Third ARO Workshop on Smart Structures*, Blacksburg, VA, 1997.
- [28] M. V. Fulton and R. A. Ormiston, “Small-scale rotor experiments with on-blade elevons to reduce blade vibratory loads in forward flight,” In *American Helicopter Society 54th Annual Forum*, Washington, DC, 1998.

- [29] J. C. Garcia, "Active helicopter rotor control using blade-mounted actuators," Master's thesis, Massachusetts Institute of Technology, Department of Mechanical Engineering, February 1994.
- [30] M.B. Giles and M. Drela, "Two-dimensional transonic aerodynamic design method," *AIAA Journal*, 25(9):1199–1206, Sep 1987.
- [31] V. Giurgiutiu, Z. Chaudhry, and C. A. Rogers, "Energy-based comparison of solid-state actuators," Technical Report CIMSS 95-101, Center for Intelligent Material Systems and Structures, September 1995.
- [32] V. Giurgiutiu, Z. Chaudhry, and C. A. Rogers, "Issues in the design and experimentation of induced-strain actuators for rotor blade aeroelastic control," In *Tenth VPI & SU Symposium on Structural Dynamics and Control*, Blacksburg, VA, May 8-10 1995.
- [33] S. R. Hall and E. F. Prechtl, "Development of a piezoelectric servoflap for helicopter rotor control," *Journal of Smart Materials and Structures*, 5(1):26–34, February 1996.
- [34] S. R. Hall and E. F. Prechtl, "High efficiency, large stroke electromechanical actuator," May 1999, U.S. Patent No. 5,907,211.
- [35] S. R. Hall and R. L. Spangler, "Piezoelectric helicopter blade flap actuator," July 1993, U.S. Patent No. 5,244,826.
- [36] S. R. Hall and N. M. Wereley, "Linear control issues in the higher harmonic control of helicopter vibrations," In *45th Annual Forum of the American Helicopter Society*, Boston, MA, May 1989.
- [37] S. R. Hall and N. M. Wereley, "Performance of higher harmonic control algorithms for helicopter vibration reduction," Technical Note 4, American Institute of Aeronautics and Astronautics, July-August 1993.

- [38] S. R. Hall, K. Y. Yang, and K. C. Hall, “Helicopter rotor lift distributions for minimum induced power loss,” In *AHS International Technical Specialists’ Meeting on Rotorcraft Multidisciplinary Design Optimization*, Atlanta, GA, April 1993.
- [39] N. D. Ham, “Helicopter individual-blade-control research at MIT 1977–1985,” *Vertica*, 11(1):109–122, 1987.
- [40] A. A. Hassan and F. K. Straub, “Evaluation of a flapped airfoil configuration for an advanced rotor,” In *Aeromechanics Specialists Conference*, Stratford, CT, October 11-13 1995.
- [41] J. C. Houbolt and G. W. Brooks, “Differential equations of motion for the combined flapwise bending, chordwise bending and torsion of twisted nonuniform rotor blades,” Technical Report 1346, NACA, 1958.
- [42] C. Ilvedson, “Piezoelectric actuator control of a helicopter rotor,” MIT Department of Aeronautics and Astronautics, 16.622 Project Report, Course Advisor: Professor Steven Hall, Fall, 1995.
- [43] Peter Jänker, Frank Hermle, Thomas Lorkowski, Stefan Storm, and Marc Wettemann, “Development of high performance piezoelectric actuators for transport systems,” In *6th International Conference on New Actuators*, June 1998.
- [44] W. Johnson, *Helicopter Theory*, Dover Publications, Inc., New York, 1980.
- [45] N. A. Koratkar and I. Chopra, “Testing and validation of a froude scaled helicopter rotor model with piezo-bimorph actuated trailing edge flaps,” In *SPIE Smart Structures and Integrated Systems*, pages 183–205, San Diego, CA, Mar 1997.
- [46] M. Kretz, “Research in multicyclic and active control of rotary wings,” *Vertica*, 1:95–105, 1976.

- [47] M. Kretz and M. Larche, “Future of helicopter rotor control,” *Vertica*, 4:13–22, 1980.
- [48] A. Krothapalli and C. A. Smith, editors, *Recent Advances in Aeroacoustics*, Chapter: “Analyses of Broadband Noise Mechanisms of Rotors,” pages 87–127, Springer-Verlag, 1986.
- [49] R. Kube, “New aspects of higher harmonic control at a four bladed hingeless model rotor,” In *Fifteenth European Rotorcraft Forum*, Amsterdam, September 12-15 1989.
- [50] R. Kube, “Evaluation of a constant feedback gain for closed loop higher harmonic control,” In *Sixteenth European Rotorcraft Forum*, Glasgow, Scotland, September 18-21 1990.
- [51] R. Kube and K. J. Schultz, “Vibration and BVI noise reduction by active rotor control: HHC compared to IBC,” In *Twentysecond European Rotorcraft Forum*, Brighton, United Kingdom, September 17-19 1996, Paper No. 85.
- [52] A. J. Landgrebe and M. W. Davis, “Analysis of potential helicopter vibration reduction concepts,” In *AHS Decennial Specialists’ Meeting on Rotorcraft Dynamics*, 1984.
- [53] A. Z. Lemnios, W. E. Nettles, and H. E. Howes, “Full scale wind tunnel tests of a controllable twist rotor,” In *32th Annual Forum of the American Helicopter Society*, 1976.
- [54] A. Z. Lemnios, A. F. Smith, and W. E. Nettles, “The controllable twist rotor, performance and blade dynamics,” In *28th Annual Forum of the American Helicopter Society*, 1972.
- [55] M. Lutz, “Piezoelectric actuator control of a helicopter rotor,” MIT Department of Aeronautics and Astronautics, 16.622 Project Report, Course Advisor: Professor Steven Hall, Fall, 1995.

- [56] M. K. Lutz and N. W. Hagood IV, "Study of work flow in piezoelectrically driven linear and non-linear systems," Technical Report 99-1, Active Materials and Structures Laboratory, Rm 37-327, 77 Massachusetts Avenue, Cambridge, MA 02139-4307, 1999.
- [57] J. L. III McCloud and A. L. Weisbrich, "Wind-tunnel results of a full-scale multicyclic controllable twist rotor," In *34th Annual Forum of the American Helicopter Society*, 1978.
- [58] L. Meirovitch, *Analytical Methods in Vibration*, Macmillan Publishing Co., Inc., New York, 1967.
- [59] J. Milgram, I. Chopra, and F. Straub, "A comprehensive rotorcraft aeroelastic analysis with trailing edge flap model: Validation with experimental data," In *American Helicopter Society 52nd Annual Forum*, Washington, DC, 1996.
- [60] T. A. Millot and P. P. Friedmann, "Vibration reduction in helicopter rotors using an actively controlled partial span trailing edge flap located on the blade," Technical Report 4611, NASA, June 1994.
- [61] K. Nguyen and I. Chopra, "Effect of higher harmonic control on rotor performance and control loads," *Journal of Aircraft*, 29(3), 1992.
- [62] M. W. Nixon, R. G. Kvaternik, and T. B. Settle, "Tiltrotor vibration reduction through higher harmonic control," In *American Helicopter Society 53rd Annual Forum*, Virginia Beach, VA, April 29 - May 1 1997.
- [63] Physik Instrumente, Auburn, MA, *Products for Micropositioning, Catalog US-Edition*, 1995.
- [64] E. F. Prechtl, "Development of a piezoelectric servo-flap actuator for helicopter rotor control," Master's thesis, Massachusetts Institute of Technology, Department of Aeronautics and Astronautics, May 1994.

- [65] E. F. Prechtl and S. R. Hall, "Design of a high efficiency, large stroke, electromechanical actuator," *Journal of Smart Materials and Structures*, 8(1):13–30, 1999.
- [66] J. P. Rodgers, *Development of an Integral Twist-Actuated Rotor Blade for Individual Blade Control*, PhD thesis, Massachusetts Institute of Technology, Department of Aeronautics and Astronautics, January 1998.
- [67] J. P. Rodgers and N. W. Hagood, "Preliminary mach-scale hover testing of an integral twist-actuated rotor blade," In *SPIE Smart Structures and Integrated Systems*, Mar 1998.
- [68] J. M. Schmitt, P. V. Bayly, and D. A. Peters, "Stabilization of periodic flap-lag dynamics in rotor blades," In *American Helicopter Society 2nd International Aeromechanics Specialists Conference*, Bridgeport, CT, October 1995.
- [69] J. Shaw, N. Albion, E. J. Hanker, and R.S. Teal, "Higher harmonic control: Wind tunnel demonstration of fully effective vibratory hub force suppression," In *41st Annual Forum of the American Helicopter Society*, Fort Worth, TX, 1985.
- [70] Jr. Shaw, J., "A feasibility study of helicopter vibration reduction by self-optimizing higher harmonic blade pitch control," Master's thesis, Massachusetts Institute of Technology, Department of Aeronautics and Astronautics, 1967.
- [71] R. L. Spangler, "Piezoelectric actuators for helicopter rotor control," Master's thesis, Massachusetts Institute of Technology, Cambridge, MA, June 1989.
- [72] R. L. Spangler and S. R. Hall, "Piezoelectric actuators for helicopter rotor control," In *31st Structures, Structural Dynamics and Materials Conference*, Long Beach, CA, April 1990.
- [73] W. R. Splettstoesser, G. Lehmann, and B. Van der Wall, "Initial results of a model rotor higher harmonic control (HHC) wind tunnel experiment on BVI impulsive noise reduction," In *Fifteenth European Rotorcraft Forum*, Amsterdam, September 12-15 1989.

- [74] W. R. Splettstoesser, K. J. Schultz, R. Kube, T. F. Brooks, Jr. E. R. Booth, G. Niesl, and O. Streby, "BVI impulsive noise reduction by higher harmonic pitch control: Results of a scaled model rotor experiment in the DNW," In *Seventeenth European Rotorcraft Forum*, Berlin, Germany, September 24-26 1991, Paper No. 91-61.
- [75] P. H. Stahlhuth, "Piezoelectric stack motor stroke amplifier," September 1988, U.S. Patent No. 4,769,569.
- [76] F. K. Straub, "A feasibility study of using smart materials for rotor control," In *49th Annual Forum of the American Helicopter Society*, St. Louis, MO, May 1993.
- [77] F. K. Straub, "Active flap control for vibration reduction and performance improvement," In *51st Annual Forum of the American Helicopter Society*, pages 381–392, Fort Worth, TX, 1995.
- [78] F. K. Straub and A. A. Hassan, "Aeromechanic consideration in the design of a rotor with smart material actuated trailing edge flaps," In *52nd Annual Forum of the American Helicopter Society*, Washington D.C., June 1996.
- [79] F. K. Straub and D. J. Merkley, "Design of a smart material actuator for rotor control," In *SPIE ...*, volume 2443, pages 89 – 104, 1995.
- [80] F. K. Straub and L. H. Robinson, "Dynamics of a rotor with nonharmonic control," In *49th Annual Forum of the American Helicopter Society*, St. Louis, MO, May 1993.
- [81] H. Strehlow and H. Rapp, "Smart materials for helicopter rotor active control," *AGARD, Smart Structures for Aircraft and Spacecraft*, 16, April 1993.
- [82] R. H. Stroub, L. Young, M. Cawthorne, and C. Keys, "Helicopter rotor blade with free tip," *NASA Tech Briefs*, 16(8):62, 1992.

- [83] C. Walz and I. Chopra, "Design and testing of a helicopter rotor model with smart trailing edge flaps," In *35th Structures, Structural Dynamics and Materials Conference*, April 1994.
- [84] M. L. Wilbur, W. K. Wilkie, Jr. W. T. Yeager, R. C. Lake, C. W. Langston, C. E. S. Cesnik, and S. Shin, "Hover testing of the NASA/ARL/MIT active twist rotor," In *8th ARO Workshop on Aeroelasticity of Rotorcraft Systems*, State College, PA, October 18-20 1999.

# **Appendix A**

## **Material Survey**

The active material used for a potential actuation application is a critical factor contributing toward its success. The field of active materials was surveyed to identify the configuration best suited for the task of blade mounted actuation. This appendix provides a discussion of the results from this study.

### **A.1 The Case for Active Materials**

There are three primary advantages that make active materials well suited for blade mounted actuation. First, they have high bandwidth characteristics, which will lead to greater closed loop control performance. Second, they are controlled electronically, so that transferring control signals into the rotating frame, via a standard sliring, and along the rotor blade is accomplished easily. Third, active materials are solid state, so that, as long as they are properly supported, they can operate with little difficulty in the high g environment of a rotor blade.

Another useful property of most active materials is that they are capacitive in nature, so that very little current is needed to power the materials. In addition, if the connection to the material is broken, it will retain its position, which may be important if the actuator is used for blade trimming.

The main disadvantages of active materials are that they require high operational voltages and, to avoid damaging the usually brittle ceramic, a constant compressive

pre-stress must be maintained at all times.

The critical factor determining if an active material will succeed is its energy density. Not all materials possess the energy density required for blade mounted actuation. In fact, only through efficient use can the energy of an active material succeed in blade mounted actuation without adding excessive weight to the design.

## A.2 General Active Material Characteristic Definitions

Various active materials were considered. In comparing the various materials, certain criterion were used. Each of these is described here, particularly with respect to its impact on actuator design.

**Energy Density.** The energy density is the specific strain energy an active material can deliver. It is defined as

$$U_e = \frac{\frac{1}{2}E_e\epsilon^2}{\rho_e} \quad (\text{A.1})$$

where  $\rho_e$  is the density of the active material element. The product of the energy density of a material and the mass efficiency of the actuation mechanism gives the specific work a particular actuation/material combination can perform. Thus, for a given actuation mechanism configuration to perform a certain amount of work, use of a larger energy density material implies a lighter actuator.

**Maximum Strain.** A large induced strain is desired because it is directly related to the energy density, through Equation (A.1). More importantly, a large induced strain reduces the required stroke amplification of the discrete actuator. Amplifications on the order of 20:1 are feasible but efficient amplifications greater than that are difficult to obtain.

In this thesis strains are reported as peak-to-peak (PP) values so that materials with induced strains that are linearly dependent on the applied field, like piezoelec-

tric ceramics, can be compared directly against materials with induced strains that are quadratically dependent on the applied field, like magnetostrictive alloys. Maximum strains were estimated by looking at the full, non-linear experimental curves of strain versus applied field. The maximum usable strain was taken as the range of strain without noticeable material saturation. Note that these maximum strains are consistently higher than those specified by most vendors (see *e.g.*, Giurgiutiu *et al.* [31]).

**Bandwidth.** The frequency range over which the actuator will be used defines the required bandwidth. The rotor control objective requires a bandwidth greater than 4/rev. This criterion eliminated some high energy density active materials, like shape memory alloys, from consideration.

**Longevity.** Material lifetime is an important issue because many active materials are inherently brittle ceramics. The concern over the longevity of certain active material systems eliminated them from consideration. For example, the choice between using plate-through or co-fired stacks was based on longevity concerns, as discussed below.

**Technical Maturity.** Technical maturity is a measure of the available knowledge or previous experience that exists with a material. The technical maturity of a material system must be seriously considered in terms of its potential risk before including it in an application.

**Linearity.** All active materials exhibit some nonlinearity. One common example is the nonlinear strain behavior of piezoelectric ceramics. A highly nonlinear material is difficult to integrate into a linear control system.

**Temperature Sensitivity.** Materials with low temperature sensitivity are desired, due to the wide temperature range in which helicopters operate. Unfortunately, most active materials have some temperature dependence.

**Cost.** The use of an expensive material must be weighed against its potential benefit.

### A.3 Specific Active Material Comparison

Four general material types were considered for the present application; piezoelectric ceramics, magnetostrictive (MS) alloys, shape memory (SM) materials, and electrostrictive ceramics. With the exception of magnetostrictive alloys, all of the materials can operate using the strain induced parallel to or transverse to the applied field. These two operational modes are often referred to as the 33 or 31 effect, respectively. Generally, the parallel (or longitudinal) strain is used in stack actuators while the transverse strain is used in planar configurations. In addition to these traditional actuation modes, Active Fiber Composites (AFC) were also considered as a planar actuation alternative [4].

Preliminary material comparison eliminated shape memory alloys and shape memory ceramics from consideration. Shape memory materials boast great energy density levels but have limited bandwidth. Shape memory ceramics have improved bandwidth characteristics but were discarded because they are a relatively immature technology.

The main functional difference between electrostrictive and piezoelectric ceramics is that the induced strain in electrostrictive ceramics is a quadratic function of the applied field, whereas the induced strain in piezoelectric ceramics is a linear function of the applied field. Thus, the induced strain in electrostrictive ceramics is independent of the field polarity. A material that exhibits both electrostrictive and piezoelectric properties is lead magnesium niobate - lead titanate (PMN-PT). The relative amount of PMN and PT determines whether the material exhibits a dominant electrostrictive or piezoelectric character. In fact, both the electrostrictive and piezoelectric materials (longitudinal actuation only) considered in this study are PMN-PT type materials, the difference being their relative amounts of PMN and PT. The data used for the electrostrictive materials was taken from Fripp [25]. The experimental performance

of these materials showed very low energy densities as well as strong electric field dependent and temperature dependent nonlinearities. For these reasons, this particular electrostrictive material was also excluded from consideration.

Commercially available piezoelectric ceramics and magnetostrictive alloys have comparable nonlinearities, durabilities, as well as large voltage and current levels, respectively. Active fiber composites (AFCs) share many of these properties but are more robust to tensile loads. Active fiber composites, however, have the drawback of being a more expensive and immature technology than commercially available piezoelectric and magnetostrictive materials.

The energy density became the criterion used to differentiate between the active material systems. The energy density comparison for these active materials is presented in Table A.1. The Young's modulus and density reported in this table were

Table A.1: Typical linear active material properties

Material	Maximum PP Induced Strain, $\epsilon$ microstrain	Young's Modulus $E_e$ $10^6$ psi	Density $\rho_e$ (slug/ft <sup>3</sup> )	PP Energy Density $U_e$ (ft-lb/slug)
Bulk EC-98 (33)	1650	6.9	15.2	88
EC-98 Stack (33)	1650	4.8	varies	52
Magnetostrictive	1500	4.3	17.9	39
PZT-5H (31)	700	8.8	14.6	21
AFC	1150	4.8	9.3	49

obtained from available literature on the materials. The peak-to-peak strain for the piezoelectric ceramics was estimated from the data in references [3] and [10]. The maximum magnetostrictive strain was estimated from data published by ETREMA [21]. The energy density values in Table A.1 vary from those reported by vendors (see *e.g.*, Giurgiutiu *et al.* [31]) <sup>1</sup> because of the assumed strain ranges. Later, in Section B.2.2, experimental data is presented to support the strain assumption reported in Table A.1 for EC-98 stacks.

<sup>1</sup>Note that the energy densities reported here correspond to the “output energy per active material mass” of Giurgiutiu *et al.* times a factor of four, because Giurgiutiu includes an “impedance matching” factor of 1/4 in his calculation of maximum output energy.

The table is split between longitudinal (33) and planar (31, AFC) actuation materials. In the longitudinal section the properties for bulk piezoelectric and magnetostrictive materials are presented. In practice, it is difficult to attain the energy density of the bulk material. For example, magnetostrictive materials require a heavy solenoid to actuate the material. Accounting for the extra mass of a typical solenoid would substantially reduce the effective energy density of the material. Similarly, piezoelectric stacks have lower energy density than the bulk material, mostly because of compliance losses in the bond layers present between the stack layers. The extra mass of end-caps and the electrode bus also lower the effective energy density of the material. EC-98 stacks supplied by the EDO Corporation are used to power the X-Frame discrete actuator. Assuming a cut-down in the effective stack stiffness of  $0.7 \pm 15\%$  due to bond layer compliance [14], and taking into account the mass of endcaps and the electrode bus, the energy density of the EC-98 stacks is estimated as shown in Table A.1.

Because the mass efficiency of a planar actuator can differ from that of a longitudinal actuator, the product of the achievable mass efficiency of the mechanism and the energy density of the associated material must be used when comparing longitudinal and planar actuation materials. This product represents the specific work such an actuator can perform. While it is possible to come up with planar actuators utilizing PZT-5H material with relatively high mass-efficiencies, *e.g.*, the bender actuator [33], such an actuator would have to be 2.5 times more mass efficient than a stack actuator to be viable. Of course, active fiber composites are a more attractive alternative in this sense, because of their high energy density. Use of AFCs in a bender actuator is discussed further in Section B.1.1.

The only stack design considered in this study was a *plate through* type, *i.e.*, where the electrode between each layer covers the entire cross-section of the stack, as shown in Figure A-1b. However, a different manufacturing technique for piezoelectric stacks uses a co-firing process. Here the electrodes and ceramic material are processed together. This technique yields stacks with much smaller compliance losses between stack layers. Also, because the wafer thickness in these stacks is typically thinner

than plate-through designs, much lower voltage levels are required to create a certain electric field. However, the electrodes in co-fired stacks normally extend only partially through the ceramic, as shown in Figure A-1a. Termination of the electrode within the ceramic leads to a stress concentration at the electrode tip and can limit the lifetimes of these stacks. Plate-through stacks, as shown in Figure A-1b, are used for the rotor control objective because this design presents less risk of failure than co-fired stack designs. The disadvantage in using a plate-through stack design is that extra bond layer compliance will limit the stiffness and force capability of the actuator.

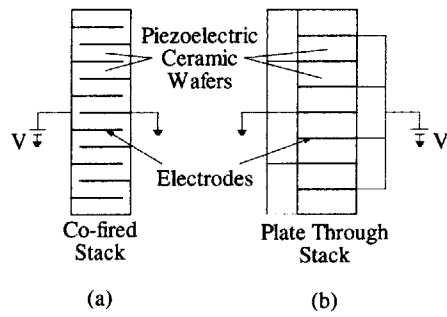


Figure A-1: Co-fired vs plate through stacks

Even with the bond layer losses and additional mass associated with commercially available stacks, their energy density exceeds that of bulk magnetostrictive materials. Thus, piezoelectric stacks are the preferred longitudinal actuation system. Other researchers, such as Strehlow and Rapp [81], have also concluded that piezoelectric ceramics are the active material best suited for rotor control. Of course, in the future, if more capable active material systems, such as single crystal piezoelectric ceramics, become available, they should replace the existing active material elements.

## A.4 Compressive Depolarization of EC-98

In this research the active material used for both the “proof-of-concept” and model scale actuator is a Lead Magnesium Niobate - Lead Titanate (PMN-PT) active material. It is made by the EDO Corporation, who has given it the designation EC-98. The properties of both the bulk material and the EC-98 stacks are discussed in Section 2.5.

Most monolithic active materials are very brittle ceramics. To ensure survival of these materials while being used in a realistic load environment, it is important to pre-stress the material to ensure no tensile stresses are generated. A major concern is that large compressive stresses tend to depole most active materials; and EC-98 is no exception.

Figure A-2 is data provided by EDO regarding the depolarization of EC-98 in the face of compressive stresses. As shown, the material does not show signs of

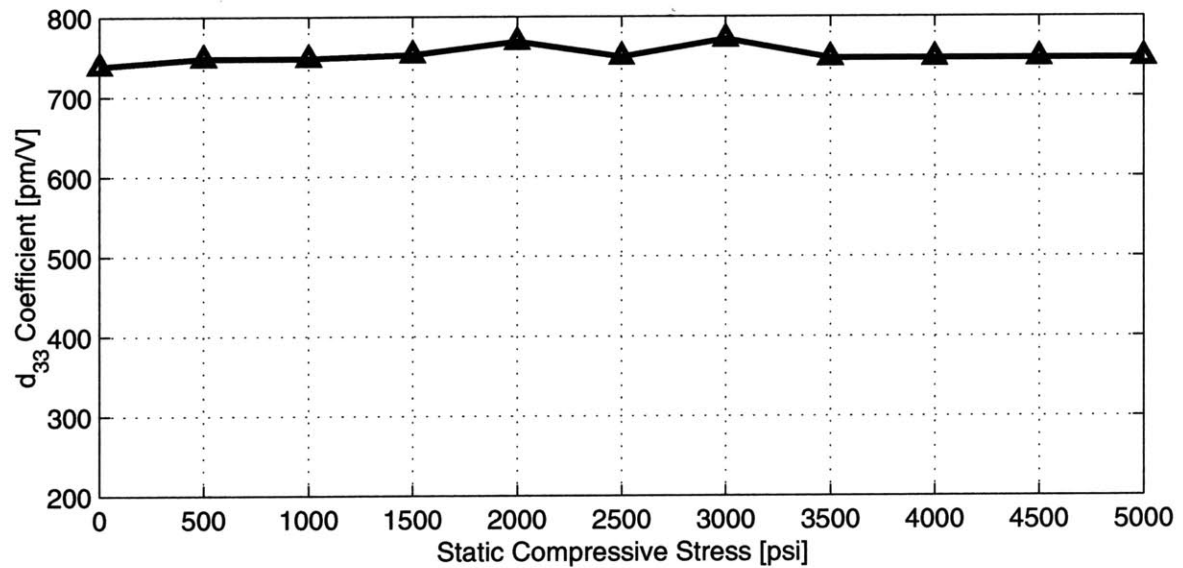


Figure A-2: Compressive depolarization characteristics of EC-98 active material [15]

compressive depolarization at stresses as high as 5000 psi (34 MPa). In the model scale actuator, compressive stresses in the active material were allowed to rise to as high as 6500 psi. However, judging from the data trend in Figure A-2, this should not lead to depolarization problems in the active material.

# **Appendix B**

## **Discrete Actuator Background Analysis and Design**

One drawback of using active materials to control the operation of trailing edge servo-flaps (as well as many other high stroke engineering components) is that these materials tend to be high force / low stroke elements. Therefore, in order to use these materials in high stroke applications, *i.e.*, in order to match the impedance of the intended load, a stroke amplification mechanism is needed. In this appendix the discrete actuator design problem is addressed. This appendix concludes by presenting the design and experimental validation of the “proof-of-concept” X-Frame discrete actuator.

### **B.1 Actuator Design Comparisons**

One drawback of using high bandwidth active materials is that they typically have very small displacements, albeit with high force. Thus, a stroke amplification mechanism must be employed to use these materials for servo-flap control or other applications. The mechanism used to achieve this amplification, the supporting frame components and the active material define the actuator. This section presents the design and analysis of a number of different actuator concepts. This study led to the development of a number of optimal actuator design axioms which were presented in

## Section 2.3.

### B.1.1 The Piezoelectric Bender Actuator

One method of amplifying small strains is by using a bending actuator [71, 72, 35, 33]. Spangler and Hall and Hall and Prechtl developed this actuation concept, as shown in Figure B-1. The bender is connected to the trailing edge flap through a

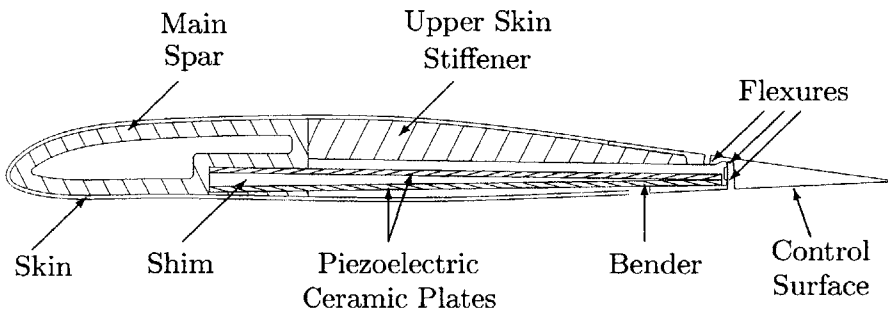


Figure B-1: Concept of a bender actuating a trailing edge flap

mechanism incorporating three flexures. Because the material reacts against itself, the mass efficiency and mechanical efficiency are very high. The nominal mass efficiency of a rectangular cross-section bender is 56%. By tapering the bender, the mass efficiency can be increased to 75%. An experimental bench test of this bender has been performed at MIT demonstrating efficiencies greater than 60% [33].

The high mass efficiency of the bender actuator is mitigated by the fact that the transverse energy density of piezoelectric ceramics is 2.5 times smaller than the longitudinal energy density. Even with high mass efficiencies, benders constructed with monolithic ceramics have output energy densities too low to be competitive with stack actuator designs.

Active fiber composites, on the other hand, yield energy densities approaching longitudinal energy densities. A bender constructed of AFCs should yield output energy densities much greater than a monolithic bender and comparable to existing stack actuator designs. Such an AFC bender was constructed at MIT [55, 42]. Experimental results demonstrated energy densities lower than expected and on the same

order as the monolithic piezoelectric ceramic bender previously tested by Hall and Prechtl [33]. The reason for the lower than expected performance may have been compressive depolarization of the AFC fibers.

The bender actuator also suffers from a number of other problems. One of its main problems for rotor control is the mass of the actuator is behind the 1/4 chord of the airfoil, which can excite aeroelastic instabilities [6]. Leading edge weights can be added to maintain a sectional CG at the 1/4 chord but such weight would lower the overall mass efficiency of the device. Optimizing the properties of such a design results in a maximum mass efficiency of 37%. Another problem with the bender is that it must be mounted in the front of the airfoil and extend back to the trailing edge, requiring significant modification to the existing rotor blade spar.

It is likely that the experimental problems encountered in the AFC bender can be overcome, resulting in a relatively high energy density actuator. However, because of the problems discussed above and because of the immaturity of active fiber composite technology, the risk in using an AFC bender was too high for this project.

### B.1.2 Coupling mechanisms

*The derivation in this section is due to Hall and is published by Prechtl and Hall in [65].*

A possibility for amplifying the small motion available from stack elements is to use elastic structures that couple two types of motion. For example, Bothwell *et al.* [8] proposed using a composite tube with an anisotropic layup, which induces extension-twist coupling. Naturally, it is desirable to design the coupling mechanism to be as efficient as possible. In this section we derive the maximum possible mechanical efficiency of a coupling mechanism amplifier. As will be seen, the efficiency is quite low, unless the coupling is nearly perfect.

To begin, we hypothesize a generic coupling mechanism, with two generalized displacements (*e.g.*, torsion and extension). These degrees of freedom are denoted by  $q_1$  and  $q_2$ . Corresponding to the two degrees of freedom are generalized forces (*e.g.*, torque and force), denoted by  $Q_1$  and  $Q_2$ . The forces and displacements are related

by

$$\mathbf{Q} = \begin{Bmatrix} Q_1 \\ Q_2 \end{Bmatrix} = \begin{bmatrix} K_{11} & K_{12} \\ K_{21} & K_{22} \end{bmatrix} \begin{Bmatrix} q_1 \\ q_2 \end{Bmatrix} = \mathbf{K}\mathbf{q} \quad (\text{B.1})$$

where  $\mathbf{K}$  is a symmetric, positive semidefinite stiffness matrix.

Next we assume that the coupling mechanism is connected to the load at the first degree of freedom ( $q_1$ ) and an expansive element is connected to the coupling mechanism at the second degree of freedom ( $q_2$ ). For example, a typical expansive element could be a piezoelectric stack. The expansive element characteristics are given by

$$Q_e = K_e q_e + Q_{eb} \quad (\text{B.2})$$

where  $Q_e$  is the force on the element,  $K_e$  is the element stiffness,  $q_e$  is the element displacement and  $Q_{eb}$  is the blocked force capability of the element.

By compatibility and equilibrium,

$$q_e = q_2 \quad (\text{B.3})$$

$$Q_e = -Q_2 \quad (\text{B.4})$$

Then

$$Q_2 = -K_e q_2 - Q_{eb} = K_{21} q_1 + K_{22} q_2 \quad (\text{B.5})$$

Solving for  $q_2$  in terms of  $q_1$  and  $Q_{eb}$ , we have that

$$q_2 = -(K_e + K_{22})^{-1} K_{21} q_1 + (K_e + K_{22})^{-1} Q_{eb} \quad (\text{B.6})$$

Finally, we can determine  $Q_1$  as

$$Q_1 = [K_{11} - K_{12}(K_e + K_{22})^{-1} K_{21}] q_1 + K_{12}(K_e + K_{22})^{-1} Q_{eb} \quad (\text{B.7})$$

$$= K_c q_1 + Q_{cb} \quad (\text{B.8})$$

where

$$\begin{aligned} K_c &= K_{11} - K_{12}(K_e + K_{22})^{-1}K_{21} \\ Q_{cb} &= K_{12}(K_e + K_{22})^{-1}Q_{eb} \end{aligned}$$

Note that Equation (B.8) is similar in form to the expansive element characteristic Equation (B.2). Indeed, Equation (B.8) may be viewed as the characteristic of the coupled actuator. The useful work that may be extracted from the element/coupling mechanism combination is

$$W_c = \frac{1}{4} \frac{Q_{cb}^2}{K_c} \quad (B.9)$$

$$= \frac{1}{4} \frac{K_{12}^2(K_e + K_{22})^{-2}Q_{eb}^2}{K_{11} - K_{12}(K_e + K_{22})^{-1}K_{21}} \quad (B.10)$$

The energy available from the expansive element is

$$W_e = \frac{1}{4} \frac{Q_{eb}^2}{K_e} \quad (B.11)$$

The coupling efficiency,  $\eta_c$ , is defined as the ratio of the work delivered at the output of the coupling mechanism to the available expansive element energy, so that

$$\eta_c = \frac{K_{12}^2 K_e}{K_{11}(K_e + K_{22})^2 - K_{12}^2(K_e + K_{22})} \quad (B.12)$$

This equation may be simplified somewhat by dividing both the numerator and denominator by  $K_{11}K_{22}^2$ . Then

$$\eta_c = \frac{\bar{K}_{12}^2 \bar{K}_e}{(\bar{K}_e + 1)^2 - \bar{K}_{12}^2(\bar{K}_e + 1)} \quad (B.13)$$

where  $\bar{K}_e$  and  $\bar{K}_{12}$  are dimensionless parameters, given by

$$\bar{K}_e = \frac{K_e}{K_{22}} \quad (B.14)$$

$$\bar{K}_{12} = \frac{K_{12}}{\sqrt{K_{11}K_{22}}} \quad (\text{B.15})$$

The parameter  $\bar{K}_{12}$  is the coupling coefficient, which describes how close the elastic coupling mechanism is to an ideal coupling mechanism. Since  $\mathbf{K}$  is positive semidefinite, we have that

$$-1 \leq \bar{K}_{12} \leq 1 \quad (\text{B.16})$$

The parameter  $\bar{K}_e$  describes how stiff the expansive element is relative to the stiffness of the coupling mechanism.

When  $|\bar{K}_{12}| = 1$ , the stiffness matrix  $\mathbf{K}$  is singular, and the coupler acts as a flexible mechanism. That is, there is no inherent resistance to motion in the coupler. An example of such a device is a flexible lever on an ideal fulcrum. To get the most efficiency out of the coupled actuator one should make the expansive element stiffness low compared to that of the coupler, *i.e.*,  $\bar{K}_e$  should be small. Indeed, when  $|\bar{K}_{12}| = 1$ ,

$$\eta_c = \frac{1}{\bar{K}_e + 1} \quad (\text{B.17})$$

Hence, the efficiency can be made arbitrarily close to unity by making  $\bar{K}_e$  arbitrarily small.

When  $|\bar{K}_{12}| < 1$ , the coupler is no longer a mechanism, and there is resistance to motion, even when there is no load attached to  $q_1$ . Therefore, there will be a tradeoff between making  $\bar{K}_e$  small, which will produce little motion; and making  $\bar{K}_e$  large, which will result in significant motion, but will also waste energy as elastic deformation of the coupler. Therefore, there will be an optimal matching between the coupler and the expansive element. The optimum efficiency may be found by taking the derivative of  $\eta_c$  with respect to  $\bar{K}_e$ , holding  $\bar{K}_{12}$  fixed, and setting the result to zero. The optimal actuator stiffness is

$$\bar{K}_e^* = \sqrt{1 - \bar{K}_{12}^2} \quad (\text{B.18})$$

For this matched condition the coupling efficiency is

$$\eta_c^* = \frac{\bar{K}_{12}^2}{2 - \bar{K}_{12}^2 + 2\sqrt{1 - \bar{K}_{12}^2}} \quad (\text{B.19})$$

Not surprisingly, when  $\bar{K}_{12} = \pm 1$ , the coupler is a mechanism, and we can achieve  $\eta_c^* = 1$ . Likewise, when  $\bar{K}_{12} = 0$ , the “coupler” has no coupling at all, and  $\eta_c^* = 0$ . For values of  $\bar{K}_{12}$  between 0 and 1, the efficiency  $\eta_c^*$  likewise varies between 0 and 1. The surprising part is how close the coupler must be to a perfect mechanism to achieve reasonable efficiencies, as shown in Table B.1

Table B.1: Efficiencies for various coupling parameters

Coupling parameter, $\bar{K}_{12}$	Optimum coupling efficiency, $\eta_c^*$
0.5	0.0718
0.75	0.2038
0.9	0.3929
0.99	0.7527
0.999	0.9144
0.9999	0.9721

Our conclusion is that, with few exceptions, elastic coupling mechanisms are not feasible. Other researchers have built and tested actuators based on elastic coupling mechanisms. Bothwell *et al.* built and tested an [11]<sub>2</sub> Kevlar-Epoxy extension torsion tube designed according to a parametric ply angle optimization [8]. The coupling parameter for this laminate is calculated using Classical Laminated Plate Theory as  $\bar{K}_{12} = 0.68$ , leading to a maximum theoretical mechanical efficiency of 15%. In practice, it is difficult to reach this optimum efficiency. For example, the data in [8] indicates  $\eta_c = 6.1\%$ . Furthermore, once the extra mass needed to properly fixture and attach the actuators is taken into account, it becomes clear that this is not a mass efficient actuation alternative.

### B.1.3 Stack/Inert Frame Actuators

The considerations in Section B.1.2 led us to investigate flexible mechanisms to amplify active element stroke. The fundamental issue to resolve in the design of such mechanisms is to identify those factors that limit their mass efficiency. This section presents the derivation of an upper bound for flexible mechanisms and presents the performance of two possible actuation mechanisms in light of this optimal mass efficiency argument.

#### Maximum Achievable Mass Efficiency

Consider a simple model of a generic expansive element operating through a 100% efficient stroke amplifier, with amplification ratio  $a_a$ , and reacting against a support frame, as shown in Figure B-2a. Now, assume the end plate at the base of the element

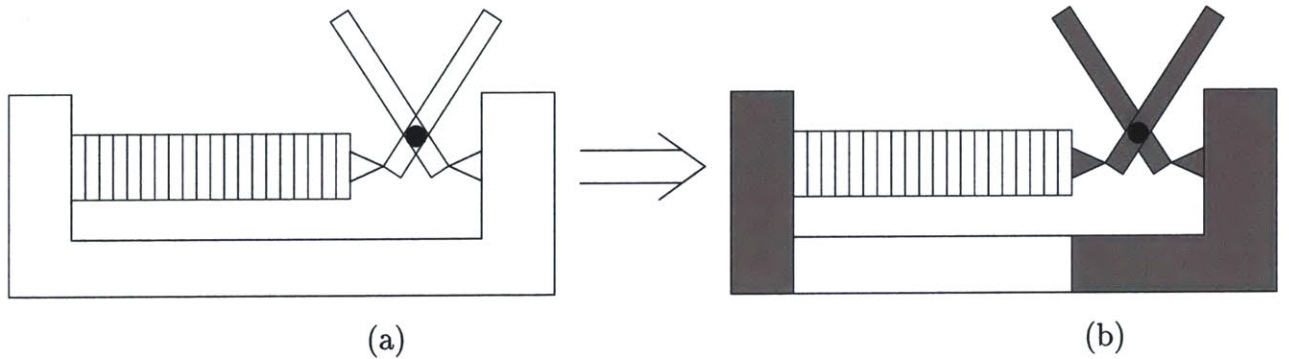


Figure B-2: (a) Concept of generic expansive element/inert frame actuator (b) Idealized concept of generic expansive element/inert frame actuator

and the material supporting the amplification mechanism are ideal, *i.e.*, infinitely stiff with zero mass. These ideal material regions are indicated by the shaded regions in Figure B-2b. Therefore, we consider only the extension of the element and the frame material adjacent to the stack. Let the modulus, density, and cross-sectional areas of the expansive element and frame be denoted as  $E_e$ ,  $E_f$ ,  $\rho_e$ ,  $\rho_f$ ,  $A_e$  and  $A_f$ , respectively. Furthermore, assume the active material and stack have the same length,  $l_e$ . Note that this last assumption does not limit the scope of this analysis. The frame must be at least as long as the element; and unnecessarily long frames result in greater losses.

The output stiffness of this actuator is then given by

$$K_a = \frac{1}{a_a^2} \frac{K_e K_f}{K_e + K_f} \quad (B.20)$$

and the free deflection of the actuator is

$$q_f = \epsilon l_e a_a \quad (B.21)$$

The masses of the element and the total mass of the actuator are

$$\begin{aligned} M_e &= A_e l_e \rho_e \\ M_{\text{tot}} &= (A_f \rho_f + A_e \rho_e) l_e \end{aligned}$$

The mass efficiency of the actuator is

$$\eta_{\text{mass}} = \frac{1}{\left(1 + \frac{E_e A_e}{E_f A_f}\right) \left(1 + \frac{\rho_f A_f}{\rho_e A_e}\right)} = \frac{1}{\left(\overline{1 + EA}\right) \left(1 + \frac{1}{\overline{\rho A}}\right)} \quad (B.22)$$

where the overline represents the element-to-frame ratio, *e.g.*,  $\overline{E} = E_e/E_f$ . Clearly, a tradeoff exists between making  $\overline{A}$  small, which will result in a light but overly flexible actuator, and making  $\overline{A}$  large, resulting in a massive actuator with little compliance. There is an optimum ratio of frame to element cross-sectional area, found by taking the derivative of  $\eta_{\text{mass}}$  with respect to  $\overline{A}$ , holding  $\overline{E}$  and  $\overline{\rho}$  fixed, and setting the result to zero. This optimum area ratio is

$$\overline{A}^* = \frac{1}{\sqrt{\overline{E} \overline{\rho}}} \quad (B.23)$$

For this optimum area ratio, the mass efficiency is

$$\eta_{\text{mass}}^* = \frac{1}{\left(1 + \sqrt{\frac{\overline{E}}{\overline{\rho}}}\right) \left(1 + \sqrt{\frac{\overline{E}}{\overline{\rho}}}\right)} = \frac{1}{\left(1 + \sqrt{\alpha_{\text{fm}}}\right)^2} \quad (B.24)$$

where  $\alpha_{fm}$  is defined as the ratio of active material to frame specific modulus, that is,

$$\alpha_{fm} = \frac{E_e/\rho_e}{E_f/\rho_f} = \frac{\bar{E}}{\bar{\rho}} \quad (B.25)$$

Note that for this optimum mass efficiency condition, the mechanical efficiency is

$$\eta_{mech}^* = \sqrt{\eta_{mass}^*} = \frac{1}{1 + \sqrt{\alpha_{fm}}} \quad (B.26)$$

Equation (B.24) represents an upper bound on the achievable mass efficiency for a stack reacting against an inert frame. Figure B-3a shows the optimum mass efficiency as a function of  $\alpha_{fm}$ . For example, EC-98 stacks reacting against a steel frame has an  $\alpha_{fm}$  parameter of 0.164 and  $\eta_{mass} = 50.6\%$ .

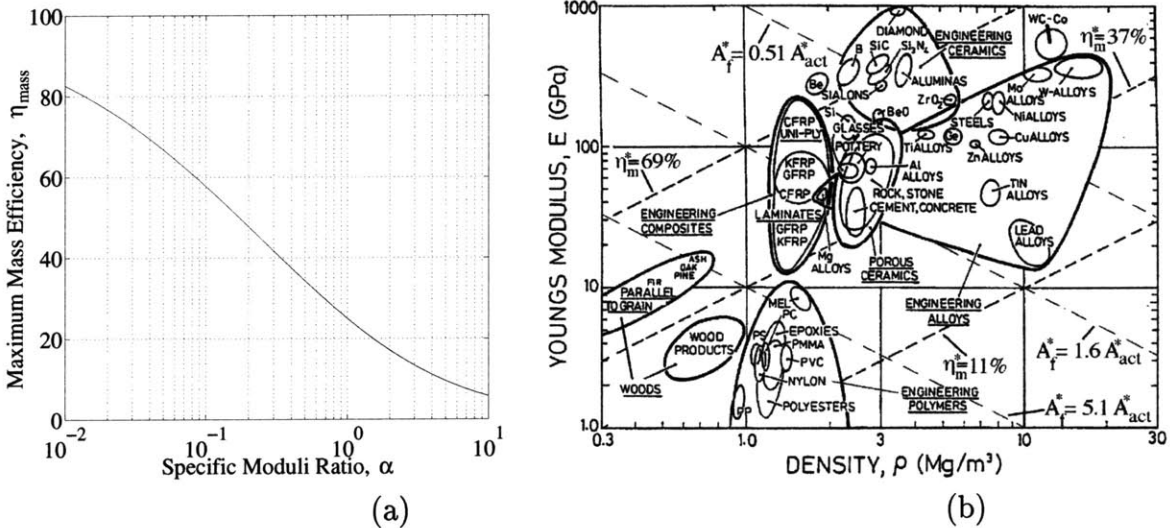


Figure B-3: (a) Maximum theoretical mass efficiencies as a function of  $\alpha_{fm}$  (b) Modulus vs density for possible frame materials [1]

Ideal frame materials are easily found by examining plots of modulus versus density for common engineering materials, such as those given by Ashby [1]. Figure B-3b is a modified version of such a material plot. It is possible to identify lines of constant mass efficiency and constant cross-sectional area in this type a plot by manipulating Equation (B.25) and Equation (B.23). These lines are shown in the figure labeled with optimum mass efficiency and cross-sectional area ratios for frames supporting EC-98 stacks. (Note that, in Figure B-3b,  $\eta_m$  stands for  $\eta_{mass}$  and  $A_{act}^*$  stands for  $A_e^*$ .)

The lines of constant cross-sectional areas are important to consider when actuator size is an issue, such as fitting it within a rotor blade spar.

These material plots can be very effective tools for picking optimum frame materials. Examining the plot shows that exotic frame materials, such as diamond, boron (B) and silicon carbide (SiC), result in very high mass efficiencies. However, other factors, such as cost, longevity, or coefficients of thermal expansion, may make certain frame materials unattractive.

### Lever and Pyramid actuators

A number of stack/inert frame actuators were analyzed. The properties of each design were optimized to maximize the mass efficiency of the device. This maximum mass efficiency was compared to that predicted by Equation (B.24) to rate the performance of the amplification mechanism. This section discusses the conclusions drawn from studying two particular actuator designs.

A simple lever and fulcrum is an obvious method of amplifying stack motion by using an inert frame. Such actuators are available commercially. For example, Physik Instrumente sells such an actuator [63]. The operational concept of the lever actuator is shown in Figure B-4a. This actuator benefits from a simple amplification

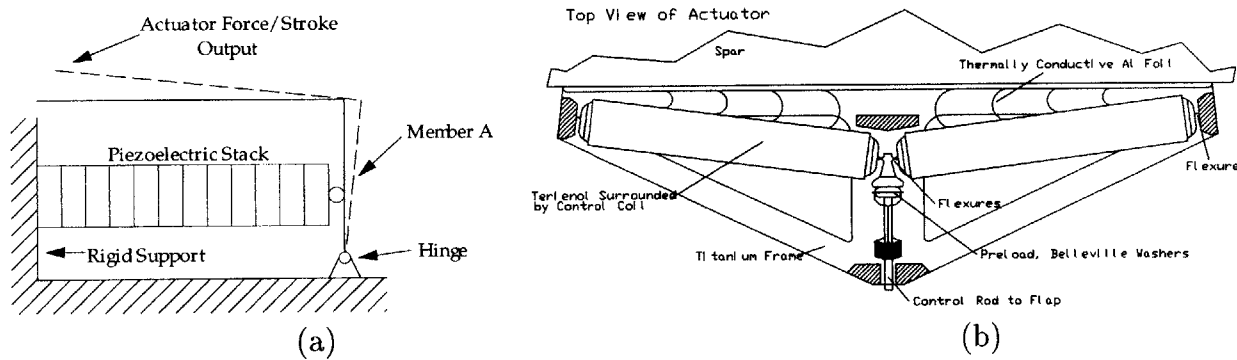


Figure B-4: The lever [63] and the pyramid actuators [22]

mechanism, easy incorporation of a pre-stress mechanism at the actuator output and an ideal form factor for placing the actuator in tight spaces, such as a rotor blade spar for trailing edge flap actuation. However, the design requires that some loads are carried in bending, which is not very efficient. As a result, the mass efficiency

is significantly lower than the theoretical bound. Numerical optimization of this actuation design, assuming perfect rolling contacts between an EC-98 stack and a steel frame, predicts a maximum achievable mass efficiency of 28%.

Another actuator, referred to in this paper as the *pyramid* actuator, is shown in Figure B-4b. It consists of two stacks reacting against each other at a shallow angle, resulting in an amplified displacement. Such an actuator design was invented by Stahlhuth [75] and has also been proposed for the servo-flap actuation concept by Fenn *et al.* Magnetostrictive actuators are used in this particular design, but piezoelectric stacks could easily be substituted. The stacks are supported by a titanium frame, with simple flexures providing rotational degrees of freedom at the stack ends.

Numerical optimization of this design showed that these flexures severely degrade the mass efficiency of the device. The source of this loss is due to the natural trade in the flexure design between axial stiffness and rotational compliance. An acceptable alternative to flexures is to use rolling contacts between the stacks and frames. Such contacts do yield some Hertzian losses, but they are small in comparison to the losses associated with flexures.

Aside from the flexures, this actuator design has a high mass efficiency. Numerical optimization of this design, for EC-98 stacks reacting against steel frames, gives a maximum achievable mass efficiency of 36% for the design with flexures and 51% given perfect rolling contacts at the ends of the stacks. The main drawback of this design is that its amplification is dependent on the shallow angle of the stacks, which changes during operation, resulting in a nonlinear amplification mechanism. For designs yielding a nominal amplification of 15, operational strains can result in a 15% change in the amplification. Furthermore, such a stack arrangement could “snap-through” if, for example, the actuator encounters an impulsive load. In such a case the stacks would bifurcate to an equilibrium position that is a mirror image of that shown in Figure B-4b. Finally, this actuator does not make an efficient use of space, making it less appropriate for compact applications.

## B.2 Proof-of-Concept X-Frame Actuator

The study of discrete actuators presented above led to the invention of the X-Frame actuator. The operational principle of this actuator and the design and testing of the model scale actuator is the focus of Chapter 2. Before the model scale actuator was designed, a “proof-of-concept” actuator was designed, manufactured, and tested to validate the analytical predictions of actuator performance. This first actuator design and related experimental performance is presented here. Note, for this discussion, this proof-of-concept actuator will be referred to as the actuator prototype.

A picture of the prototype in the lab is shown in Figure B-5. Note that the

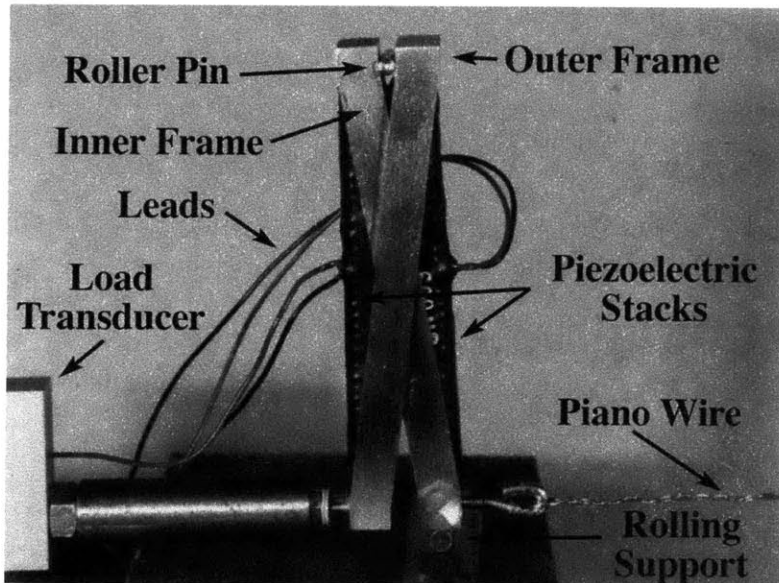


Figure B-5: The X-Frame actuator proof-of-concept prototype in the lab

rotational degree of freedom at the pivot end of the prototype was achieved using a dowel pin. The output end of the outer frame was mounted to a 100 lb Interface load transducer and all the displacement was realized at the output end of the inner frame. A compressive pre-stress on the stacks is required to maintain the stack to frame contact. Such pre-stresses are easy to apply to the X-Frame actuator by placing a tensile load at the output. This pre-stress was accomplished in the prototype by hanging a 25 lb weight off the end of the actuator through a 0.024" diameter piano wire. This piano wire is shown in Figure B-5.

### B.2.1 Prototype Manufacture

The prototype actuator was approximately 50% larger than the model scale actuator. The stacks for this actuator were also manufactured by EDO. They are composed of 140 wafers of piezoelectric ceramic, yielding an active material length of 3.094". Flat and cylindrical steel end-caps were used at the output and pivot ends of these stacks, respectively. Flat end-caps were used at the output end because little relative rotation occurs between the stack and frame at this end, as discussed in Section 2.4. Cylindrical end-caps were used at the pivot end because relative rotation does occur between the stacks and frames there. Rolling contacts are used in lieu of flexures. The cylindrical and flat endcaps are approximately 0.1575" and 0.0225" thick, respectively, yielding an overall stack length of 3.274 inches.

It is important to machine each frame out of one piece of metal, to eliminate the additional compliance associated with using fasteners to connect the frame side members and end-plates. The prototype frames were milled out of stainless steel. The sharp corners inside the frames were made using a broaching process. An alternate method of fabrication is wire electron discharge machining (EDM), which was used in the model scale actuator.

Frames can also be made out of composites to boost the actuator mass efficiency, as discussed in Section B.1.3. In fact, it may be possible to create temperature insensitive actuators by constructing frames out of metal matrix composites with a coefficient of thermal expansion (CTE) matching that of the active material. Preliminary calculations indicate that a frame composed of the metal matrix composite SiC/Ti can yield such a temperature insensitive design, while increasing the theoretical mass efficiency by 36%

Table B.2 gives the geometric properties of the prototype.  $D_s$  is the stack diameter.

Table B.2: Structural properties of the X-Frame actuator prototype

Frames		Stacks	
Material	Steel	Manufacturers	EDO Corporation
Modulus, $E_f$	$29 \times 10^6$ psi	Material	EC-98
$l_f$	3.304 in	Modulus, $E_e$	$4.81 \times 10^6$ psi
$A_f$	0.0377 in <sup>2</sup>	$l_e$	3.094 in
$h_{\text{nom}}$	0.446 in	$D_s$	0.315 in
Amp. Angle, $\theta_a$	7.4°	Capacitance	~ 350 nF

## B.2.2 Prototype Experimental Performance

This section presents the experimental performance of the X-Frame Actuator prototype. Because the performance of a discrete actuator is related to the load it drives, the presentation of the experimental results is prefaced with an impedance matching discussion.

### Impedance matching

A simple linear model for a discrete actuator is

$$Q_a = K_a(q_a - q_f) \quad (\text{B.27})$$

where  $Q_a$  is the output force,  $K_a$  is the output stiffness of the actuator, and  $q_a$  is the actuator displacement. Most active materials have important nonlinear effects that, strictly speaking, make the above model invalid. However, in many cases the materials are nearly linear. In any event, the model above provides a useful framework for determining the capability of a discrete actuator. Alternatively, Equation (B.27) may be written as

$$Q_a = K_a q_a + Q_{ab} \quad (\text{B.28})$$

where  $Q_{ab} = -K_a q_f$  is the *blocked force* capability of the actuator, i.e., the force produced by the actuator when the actuator motion is constrained to be zero.  $Q_{ab}$  may be thought of as an actuated force on the actuator. Now, suppose that the actuator displacement is constrained to be zero and the maximum field is applied to the actua-

tor or, equivalently, that the maximum allowable actuation force is commanded. The actuator then behaves as a spring with spring constant  $K_a$  compressed by an amount  $q_f$ . Therefore, the actuator has internal mechanical energy, when fully actuated, of

$$W_a = \frac{1}{2} K_a q_f^2 \quad (\text{B.29})$$

In principle, all this energy can go into the actuation of a load. In practice, only a fraction of the energy can be converted into useful work. In particular, consider an elastic load with characteristic

$$Q_L = K_L q_L \quad (\text{B.30})$$

where  $Q_L$  is the force applied to the load,  $q_L$  is the load displacement, and  $K_L$  is the load stiffness. If the load is connected directly to the actuator, the actuator and load displacements are equal (compatibility), and the actuator and load forces are equal and opposite (equilibrium), so that

$$q_L = q_a \quad (\text{B.31})$$

$$Q_L = -Q_a \quad (\text{B.32})$$

Substituting in the operating characteristics, Equation (B.27) and Equation (B.30), of the actuator and load yields

$$K_L q_L = -K_a (q_L - q_f) \quad (\text{B.33})$$

solving for the load deflection yields

$$q_L = \frac{K_a}{K_L + K_a} q_f \quad (\text{B.34})$$

The work done on the load is

$$W_L = \frac{1}{2} K_L q_L^2 \quad (\text{B.35})$$

$$= \frac{1}{2} K_L \left( \frac{K_a}{K_L + K_a} q_f \right)^2 \quad (\text{B.36})$$

Of course, the work done on the load is at most equal to the mechanical energy of the stack. Indeed, the maximum of  $W_L$  may be easily found by differentiating Equation (B.36) with respect to  $K_L$  and setting the result to zero. This yields

$$K_L = K_a \quad (\text{B.37})$$

This is known as the *impedance matching condition* [72, 33, 32]. For a load impedance matched to the actuator,

$$q_L = \frac{1}{2} q_f \quad (\text{B.38})$$

and

$$W_L = \frac{1}{4} W_a \quad (\text{B.39})$$

It is theoretically possible to transfer more of the strain energy of the actuator to the load using a mechanism with nonlinear gearing. In practice, however, such a mechanism would be exceedingly difficult to construct and would be undesirable for a number of reasons.

In some cases it may be desirable to operate with the actuator not impedance matched to the load. By using a very stiff actuator, the actuator will not deflect in response to varying load forces. For example, when controlling a helicopter servo flap, changing airloads on the flap may change the flap position, unless the actuator has significantly greater stiffness than the equivalent stiffness produced by the aerodynamics of the flap. Conversely, using a very compliant actuator will effectively command load force, rather than load deflection, which may be useful in some applications. However, changing the actuator stiffness away from the impedance-matched condition will always result in less energy transfer from the actuator to the load. The performance of the X-Frame actuator in driving an impedance matched load is considered below.

## Quasi-static Actuator Performance

A discrete actuator is usually designed for use at frequencies below its first mode. Because of this, the actuator's quasi-static operation gives a good measure of its performance. Of course, at very low frequencies,  $\leq 0.1$  Hz, poling effects exaggerate the achievable strain in the active material. Thus, to capture the quasi-static behavior while minimizing poling effects, all data presented in this section was taken at 1 Hz.

The experimental performance of the actuator was determined by measuring actuator deformations while driving elastic loads of varying stiffness. This section presents the results from these tests.

Figure B-6 presents typical sinusoidal time histories of actuator deflection as a function of electric field for free actuation and while driving an elastic load of 390 lb/in. For each boundary condition the deflection characteristic is shown for two

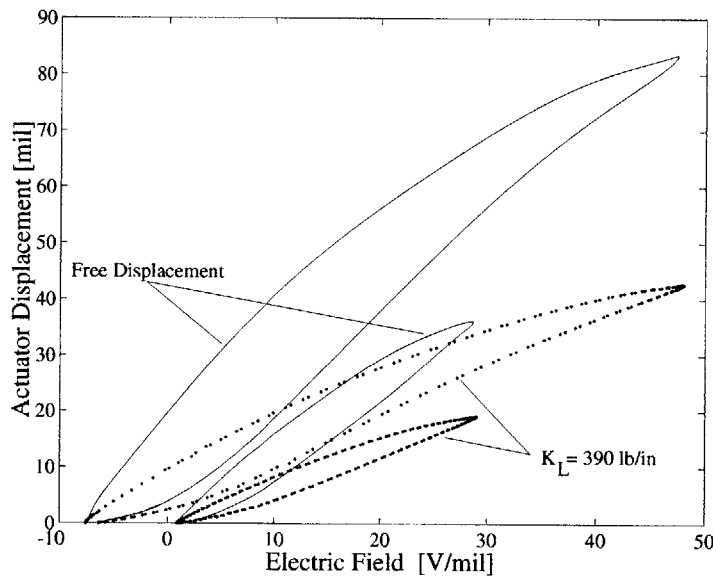


Figure B-6: Voltage vs deflection curves for free and loaded cases

separate peak-to-peak electric field amplitudes. The low voltage case corresponds to a 15 V/mil DC bias applied in conjunction with a 15 V/mil peak amplitude sine wave. The high voltage case corresponds to a 20 V/mil DC bias applied in conjunction with a 30 V/mil peak amplitude sine wave.

The prototype response in Figure B-6 is very similar to that for the model scale

actuator presented in Figure 2-8. The same conclusions can be made regarding the hysteresis and nonlinear behavior of the prototype response.

The induced strain of a piezoelectric ceramic is related to the electric field,  $E$ , through the piezoelectric strain parameter,  $d_{33}$ , as

$$\epsilon = Ed_{33}, \quad (\text{B.40})$$

At high applied fields most active materials exhibit a nonlinear strain characteristic such that these piezoelectric strain “constants” are, in fact, not constant. An excellent discussion of this effect is given by Crawley and Anderson [16].

Crawley and Anderson showed that the  $d_{31}$  parameter for piezoelectric ceramics follows a strain dependent nonlinearity [16]. However, Fripp presents data for PMN-PT material, exhibiting a dominant electrostrictive effect, that shows electric field dependent nonlinearities [25].

EC-98 is a PMN-PT type material, as discussed in Section A.3, and the data in Figure B-6 suggests a nonlinear strain behavior exists for this material as well. To determine the nonlinear characteristics, strain dependent and electric field dependent models were applied separately to predict actuator deflections. In each model the  $d_{33}$  parameter was fit to the experimental free deflection (*i.e.*, no load) data as a function of deflection and field, respectively. The deflection of the actuator driving a load was then predicted using these nonlinear  $d_{33}$  models in conjunction with Equations (2.3), (B.34) and (B.40). Note that an iterative solution was used to find the appropriate  $d_{33}$  in the strain dependent nonlinear model. This approach is very similar to that given by Crawley and Anderson [16].

Comparison of the actuator data to these two models while driving four different loads is shown in Figure B-7. As shown, the EC-98 material exhibits nonlinear behavior closer to the electric field dependent model. This indicates that, while the material does have a linear strain characteristic similar to a piezoelectric material, its nonlinear strain characteristic is closer to that of an electrostrictive ceramic.

The  $d_{33}$  parameter as a function of applied field is backed out from the free de-

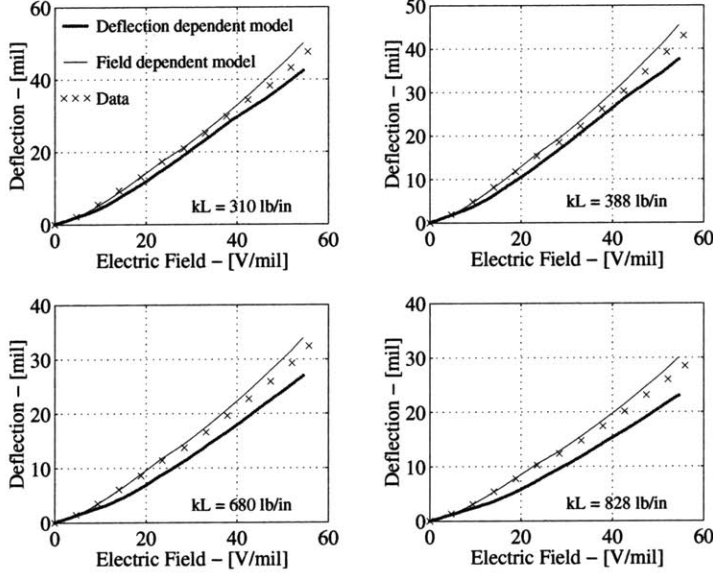


Figure B-7: Comparison of actuator data to strain dependent and electric field dependent nonlinear models.

flection data by using Equations (2.3) and (B.40). It is shown in Figure B-8, along with the  $d_{33}$  value reported by EDO [20]. As shown, this parameter varies by up to 50% from the reported value during operation. The exact mechanism causing this nonlinearity is unknown. It may simply be a field dependence of the  $d_{33}$  parameter or it may be due to a combination of other effects, such as a field dependent Young's modulus. More research is needed to properly characterize this nonlinearity.

The deflection and force generated by the prototype actuator was measured while driving loads of varying impedance to give the prototype load lines shown in Figure B-9. These load lines are very similar to those found for the model scale actuator in Figure 2-9. In fact, the same conclusions can be made regarding the prototype behavior. Only the magnitude of the numbers has changed. However, a few supplementary comments with respect to the actuator load lines are warranted.

The increase in electric field between each electric field line of Figure B-9 is approximately 4.6 V/mil. The nearly even spacing between the lines corresponding to each electric field demonstrates that the stacks are not saturating, even at high applied fields. According to Equation (B.40), a 54.75 V/mil induces 1574 microstrain in the material, using the  $d_{33}$  value reported by EDO for EC-98,  $2.874 \times 10^{-5}$  mil/V

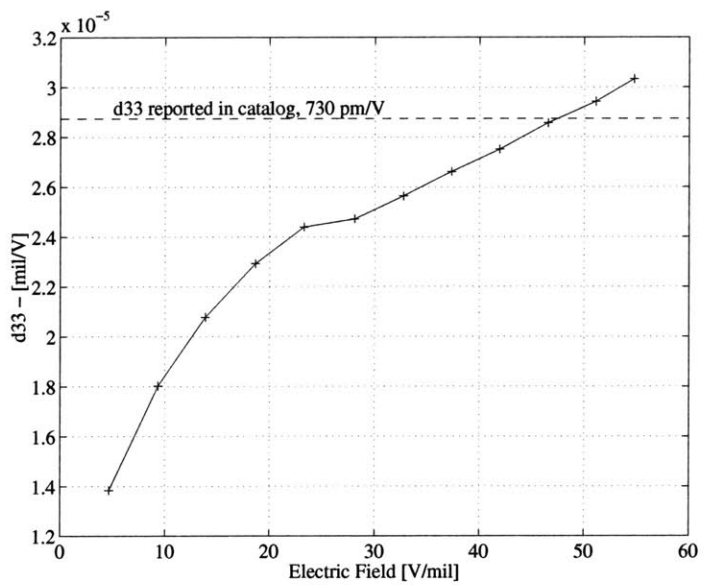


Figure B-8: Strain dependent  $d_{33}$  variation

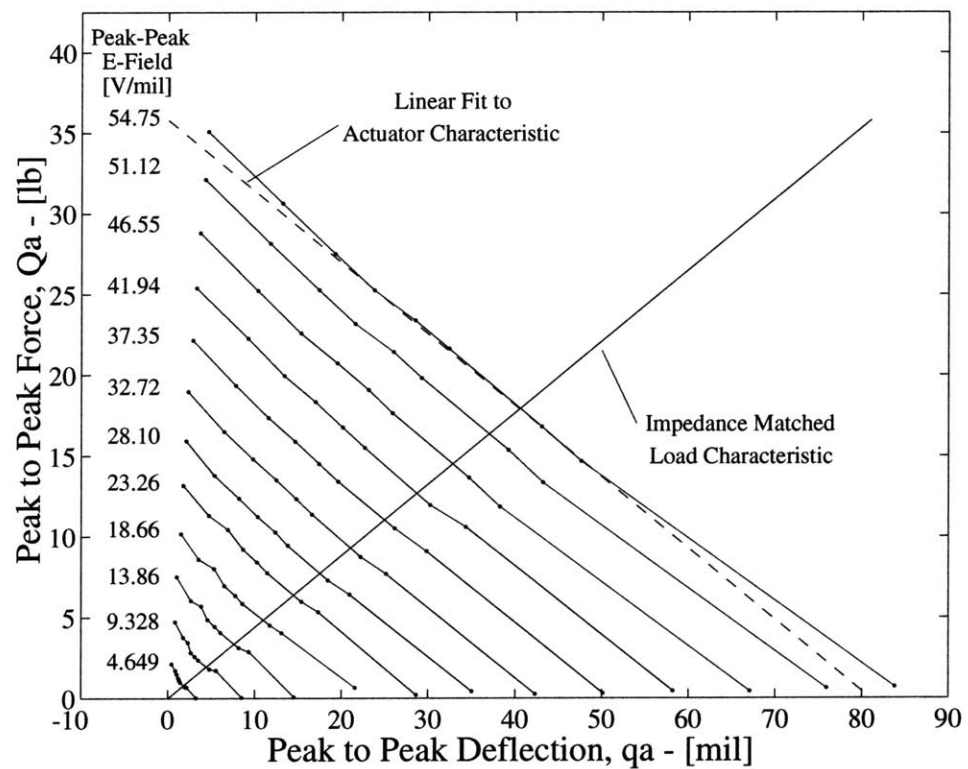


Figure B-9: Experimental prototype load lines for varying electric field levels

[20]. The data indicates that the EC-98 stacks exhibit little saturation at this strain level, supporting the validity of the strain assumption made in Table A.1.

As with the model scale actuator load lines, taking the area under the straight line fit to the outermost actuator characteristic in Figure B-9 gives a good measure of the actuator energy available for linear operation. This dashed line intersects the axes, indicating a linear peak-to-peak blocked force of 35.8 lb and free peak-to-peak deflection of 81.0 mil, yielding an output energy of

$$W_a = 1.45 \text{ in-lb} \quad (\text{B.41})$$

The mass of the entire actuator prototype 0.00830 slug (121 g), giving the actuator output energy density as

$$U_a = 14.6 \frac{\text{ft-lb}}{\text{slug}} \quad (\text{B.42})$$

The mechanical and mass efficiencies of the device are found by normalizing this energy density by the active material strain energy and energy density given by

$$W_e = \frac{1}{2} E_e \epsilon^2 V_e, \quad (\text{B.43})$$

and Equation (A.1), respectively. As discussed in Section 2.6.1, one problem in evaluating these relations is that the  $d_{33}$  parameter (and  $\epsilon$ ) varies as a function of field, as shown in Figure B-8. The cumulative strain energy in the active material could be estimated by integrating Figure B-8 over the appropriate boundary conditions, but this calculation would be an inferential measure of stack performance. For example, it may be that the force/deflection characteristics of the stacks alone could exhibit much larger nonlinear characteristics than those of the actuator shown in Figure B-9. To make an accurate estimate of the available *linear* strain energy in the active material, force/deflection characteristics of the stacks, similar to those of Figure B-9, must be obtained. A linear estimate could be fit to these characteristic lines, as above, and the available linear active material strain energy could be calculated. A component tester designed to acquire this data is currently under development in the Active Materials

and Structures Lab (AMSL) at MIT. In the absence of such active material strain energy data, the catalog  $d_{33}$  value for the PMN-PT stacks is used [20], and an applied field level of 54.75 V/mil is assumed for all calculations in this section.

In addition to determining  $\epsilon$  in Equation (B.43), the calculation of the active material volume,  $V_e$ , and active material mass also affect the efficiency calculations. The mass and mechanical efficiency calculations for the actuator are performed using two different approaches. These two calculations result in upper and lower bounds to the experimental actuator efficiencies. The first method assumes that the “active” material is just the piezoelectric ceramic. Thus, the additional mass from end-caps, electrodes, electrode bus and the additional compliance from the stack bond-layers are accounted for as *actuator* losses. This first method results in a lower, conservative, bound to the actuator efficiency. The second method takes the opposite approach, where all additional mass associated with the stacks is taken as “active material mass”. Furthermore, the bond-layer losses are also taken into account as *stack* losses and not actuator losses. The second method is more realistic but may over-predict the actuator efficiency somewhat. This second method gives an idea of the achievable actuator mass efficiency if 100% mass efficient stacks were used in place of those supplied by EDO. The calculations are as follows.

The active material element volume is the volume of just the piezoelectric material. It is the same in both methods.

$$V_{e_1} = V_{e_2} = 0.454 \text{ in}^3 \quad (\text{B.44})$$

In method 1, the strain energy is assumed to be the strain energy in the bulk material, using Equation (B.43), it is

$$W_{e_1} = 3.86 \text{ in-lb} \quad (\text{B.45})$$

The active material mass for method 1 is just the mass of the piezoelectric material. Multiplying the density for EC-98 material, of 15.23 slug/ft<sup>3</sup>, by the active material

volume, Equation (B.44), yields

$$M_{e_1} = 0.00400 \text{ slug} \quad (\text{B.46})$$

The energy density of the material is found by dividing the strain energy by the mass, giving

$$U_{e_1} = 80.5 \frac{\text{ft-lb}}{\text{slug}} \quad (\text{B.47})$$

Note that this energy density agrees with that reported in Table A.1 for bulk EC-98 material when scaled by the ratio of strains,  $(1650/1574)^2$ .

In method 2 the bond layer losses are accounted for in the strain energy calculation, so

$$W_{e_2} = 2.70 \text{ in-lb} \quad (\text{B.48})$$

The active material mass used is the entire mass of both stacks, including electrode bus and endcaps. The mass of the two stacks was found by weighing them, yielding

$$M_{e_2} = 0.00475 \text{ slug} \quad (\text{B.49})$$

Dividing Equation (B.48) by the mass, Equation (B.49), gives the active material energy density for this method

$$U_{e_2} = 47.4 \frac{\text{ft-lb}}{\text{slug}} \quad (\text{B.50})$$

Again, this energy density also agrees with that given in Table A.1 for EC-98 stacks when scaled by the induced strain.

The mass and mechanical efficiencies are found for each method by dividing the corresponding actuator output energy and energy density by the active material strain energy and energy density, respectively. The results are shown in Table B.3, along with the associated optimal mass efficiency for each case, according to Equation (B.24). Note that because the modulus of the stacks for the two methods is different (bond layer losses are accounted for in Method 2 but not in Method 1), the

Table B.3: Comparison of measured efficiencies calculated using two varying methods

Method #	$W_e$ in-lb	$M_e$ slug	$U_e$ ft-lb slug	$\eta_{\text{mass}}$	$\eta_{\text{mass}}^*$	$\eta_{\text{mech}}$	$\eta_{\text{mech}}^*$
1	3.86	0.00400	80.5	18.1 %	45.2 %	37.5 %	67.2 %
2	2.70	0.00475	47.4	30.7 %	50.5 %	53.6 %	71.0 %

optimal mass efficiency, Equation (B.24), also changes. The important fact is that, because the losses are accounted for differently in the two methods, the calculated efficiencies differ. But the product of the mass efficiency and the energy density in both cases is equal because the energy density of the actuator is a constant, given by Equation (B.42). This range in mass efficiencies is given because it is impossible to discern the true energy output of the active material elements from these tests.

As discussed in Section B.1.3, losses in the stacks and the frame members adjacent to the stacks are expected. However, other compliance losses occur in practice. Furthermore, as a consequence of the mass efficiency definition, even the presence of inert frame material, such as the cylindrical end caps and frame end-plates, lowers the mass efficiency. The following list gives the estimated sources of the additional loss in the X-Frame actuator prototype.

**Eccentric Loading.** Eccentric loading of the stacks introduces bending stresses in the material. As discussed previously, bending stresses are a very compliant way to carry loads. These eccentric losses can severely affect actuator performance. The data presented above was obtained after careful alignment of the stacks within the frames.

Experiments showed that the flat/cylindrical endcap combination in the stack prototypes exacerbated the eccentric loading condition. Spherical end-caps were used in the model scale actuator to minimize this effect.

**Bond Layers.** The bond layers in the piezoelectric stacks reduce the effective stack stiffnesses by at least 70%. This is an active material issue and not at all linked to the X-Frame actuator design. Co-fired stacks may offer lower compliance losses

but there still exist lifetime questions regarding these stack designs.

**Hertzian Losses.** Some Hertzian losses occur at the interface between the stacks and frame end-plates. In the prototype, these losses result in additional compliances (< 10%). These losses are small in comparison to those that would exist if flexures were used to create these rotational degrees of freedom.

**Frame Spanning Losses.** Losses occur at the frame end plates due to bending. These losses are unavoidable because the frames must straddle the stacks. These bending losses are estimated to be about 11%.

An alternate method of viewing the data shown in Figure B-9 is by examining the energy transferred from the actuator into the load. Such a plot is shown in Figure B-10. For each electric field level, the energy delivered to the load, Equation (B.35), is

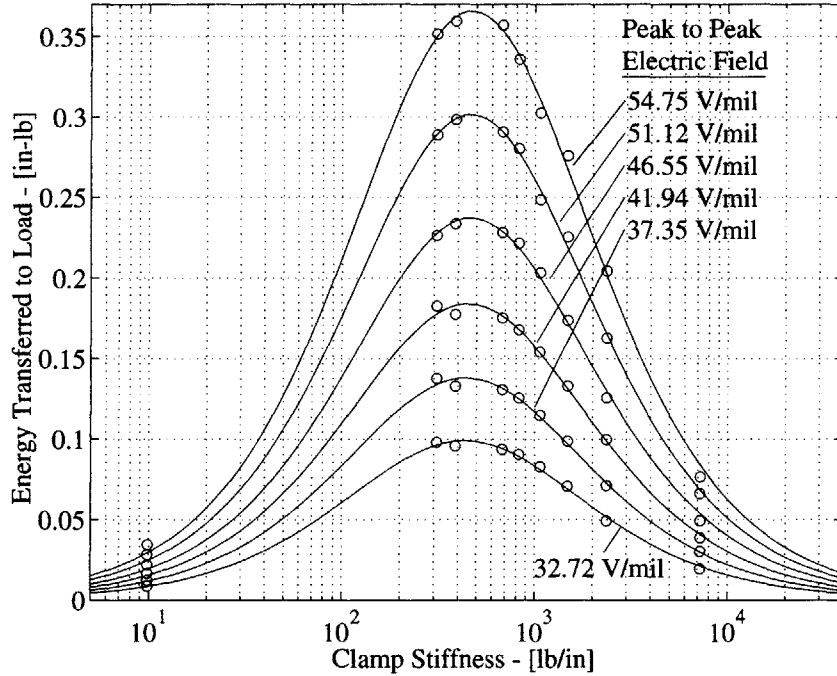


Figure B-10: The impedance matching point for the X-Frame actuator prototype

plotted for each clamp position. For each electric field level the expected impedance matching curve, given by Equation (B.36), is fit to the data by adjusting  $K_a$  and  $q_f$  in a least squares fashion.

As expected and as discussed above, the work transferred to the load is a minimum when the stiffness of the load is much higher or much lower than the actuator stiffness. The optimum transfer of actuator energy to the load occurs at the impedance matching point, where  $K_a = K_L$ .

This procedure gives a least squares actuator stiffness of 467 lb/in. However, direct measurement of the short circuit actuator deflection given an applied external load yields a stiffness of 590 lb/in. The difference between these two measurements may indicate that EC-98 exhibits a field dependent Young's modulus. Further research is needed to identify the cause for this difference.

### **Dynamic actuator characteristic**

The bandwidth of the actuator defines the frequencies over which control can occur. A transfer function of the prototype is shown in Figure B-11. The transfer function

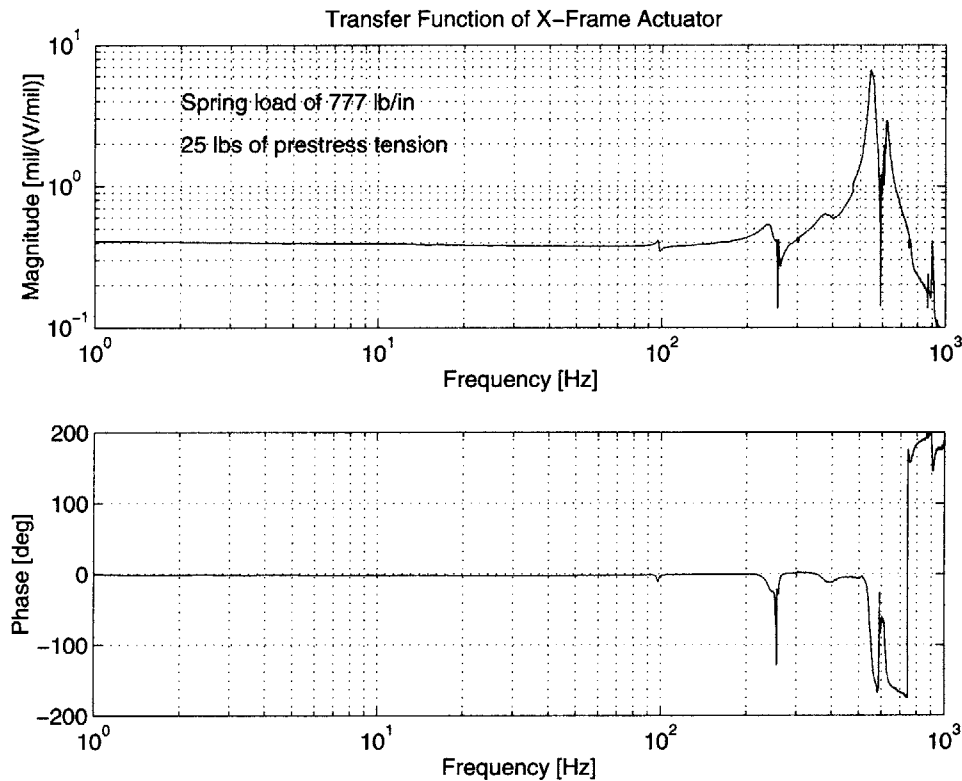


Figure B-11: Transfer function of the X-Frame actuator prototype

was taken with the piano wire clamped such that the actuator drove a 777 lb/in

load at its output. Even with the wire clamped, a number of piano modes were present during the transfer function test and are evident in Figure B-11 by the nearly unobservable modes at approximately 100, 220, and 370 Hz. This transfer function shows the first mode of the actuator at about 543 Hz and it provides nearly constant performance at all frequencies up to this mode.

The magnitude of the transfer function is normalized to give the output stroke [mils] per unit applied electric field [V/mil]. The magnitude for this transfer function data is smaller than expected, upon applying Equation (B.34) to the data in Figure B-6. This is related to the fact that the transfer function data was collected at low field levels and, because of the nonlinear  $d_{33}$  characteristic of the active material shown in Figure B-8, the predicted deflection from the transfer function data is smaller.

# Appendix C

## Hover Data Transfer Function Plots

This appendix contains a full set of transfer function plots for the experimental hover data. It is broken into two sections. The first section contains overlay transfer functions for all pertinent sensors while actuating at  $800V_{p-p}$  in hover (1336 RPM) at 4 and 8 deg collective angles of attack. The second section contains overlay transfer functions of all pertinent sensors while actuating at  $800V_{p-p}$  at an 8 degree collective angle of attack at a number of different rotor speeds. All transfer functions in this appendix include a coherence plot to provide an indication of the accuracy of the transfer function data. As with the transfer function plots in Chapters 4 and 5, the vertical grid lines in all transfer functions correspond to the “per-rev” frequencies while spinning at 1336 RPM.

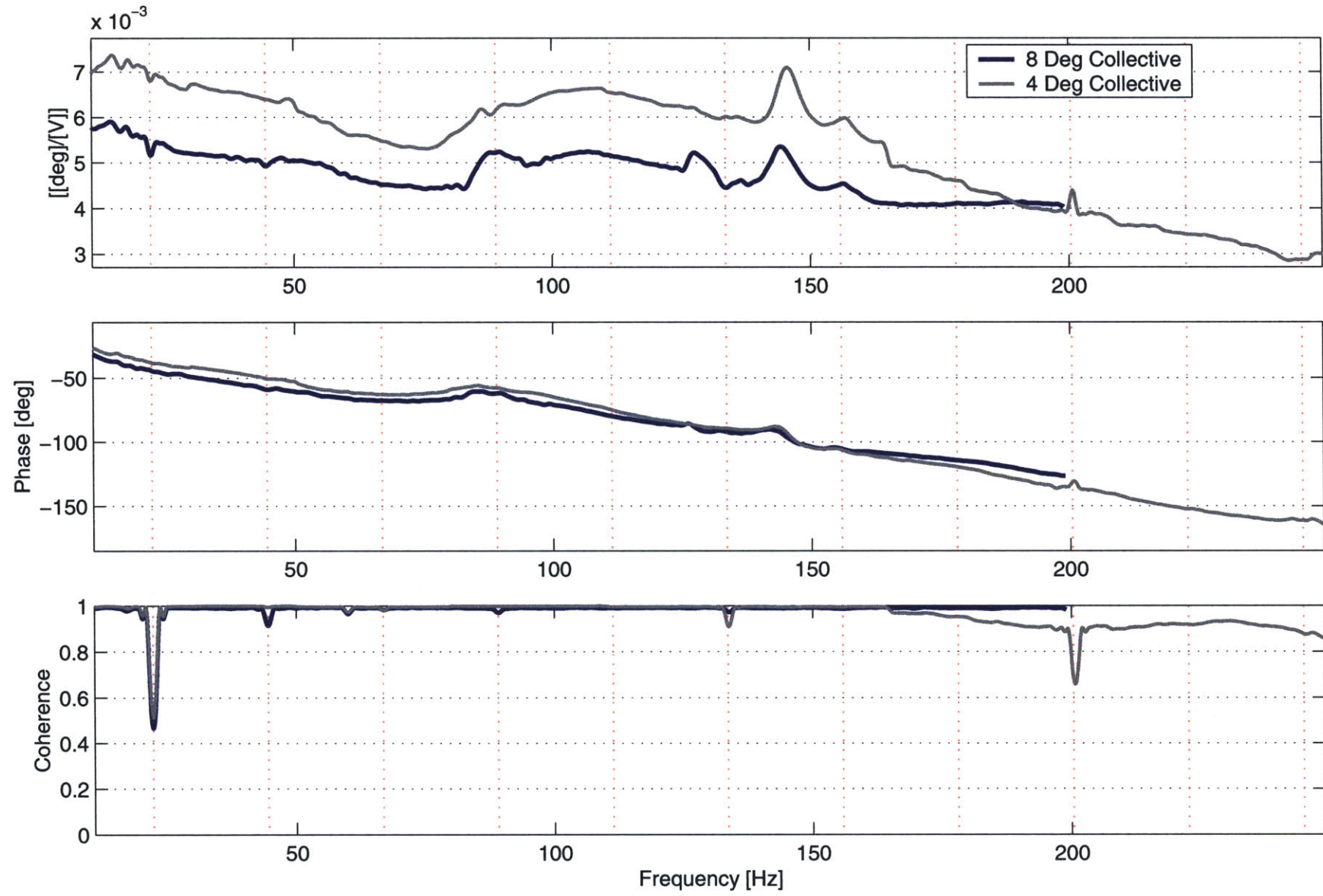


Figure C-1: Transfer function from voltage to flap deflection with angle of attack

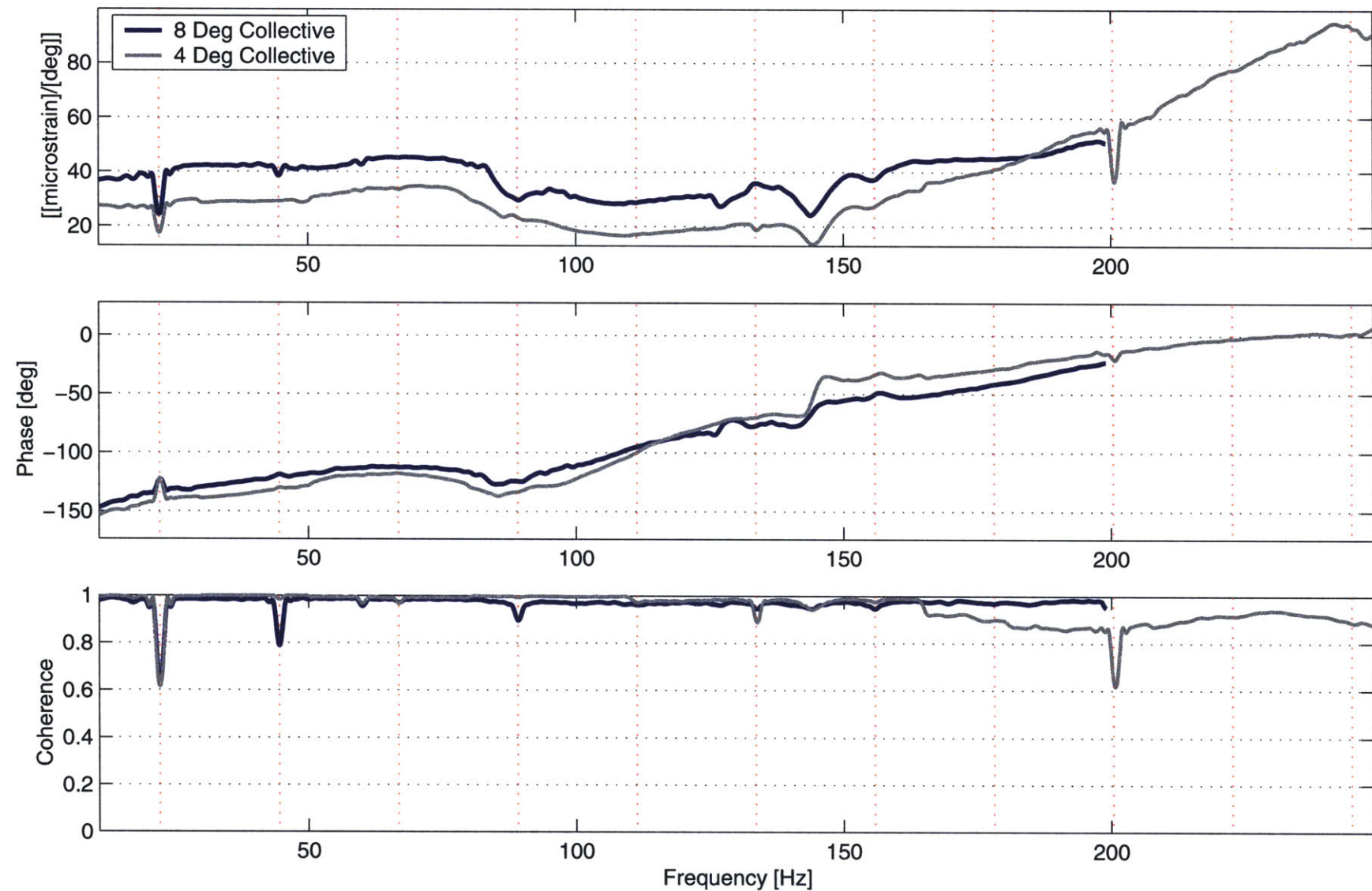


Figure C-2: Transfer function from flap deflection to actuator frame strain with angle of attack

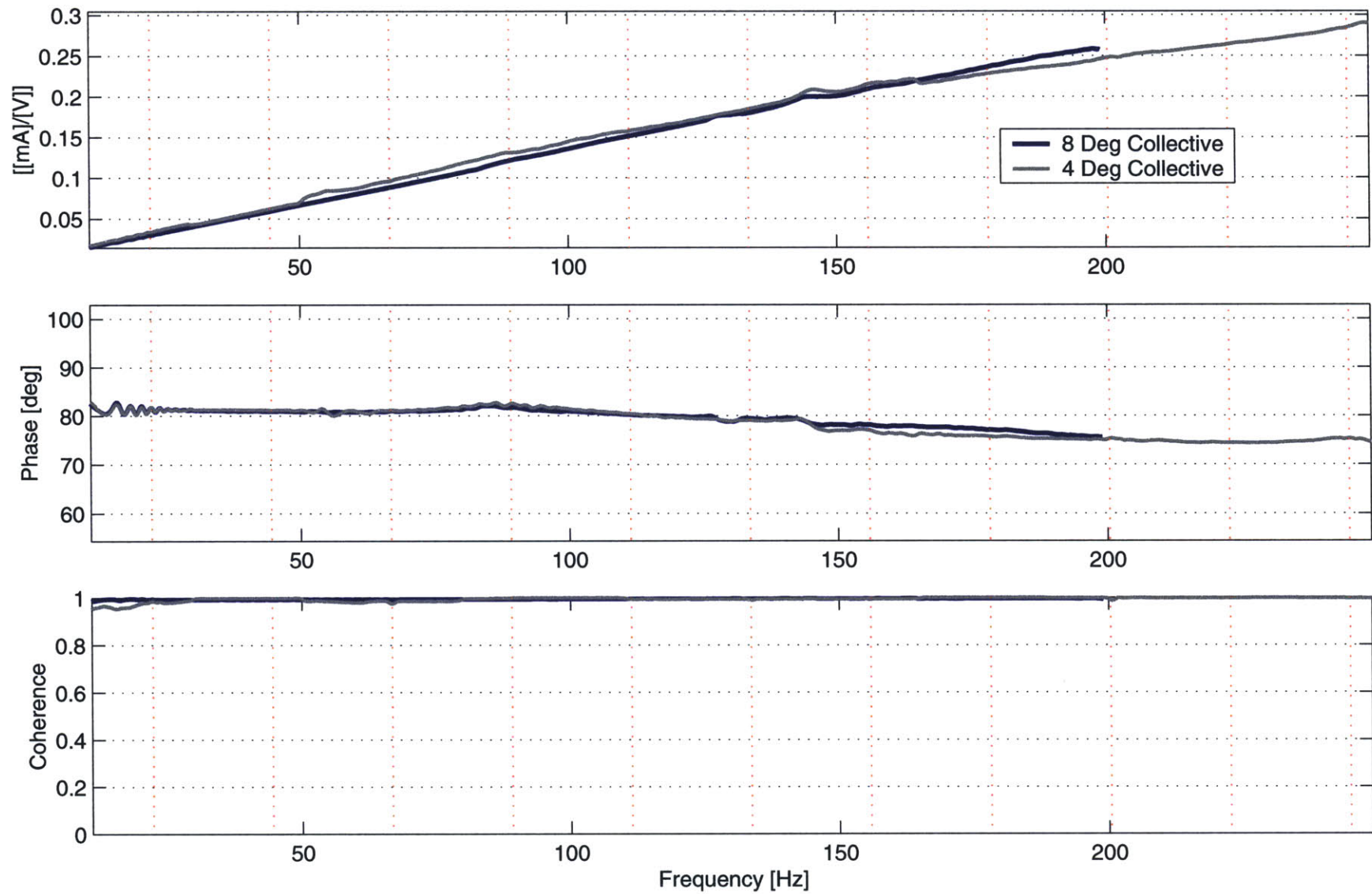


Figure C-3: Transfer function from voltage to piezoelectric stack current with angle of attack

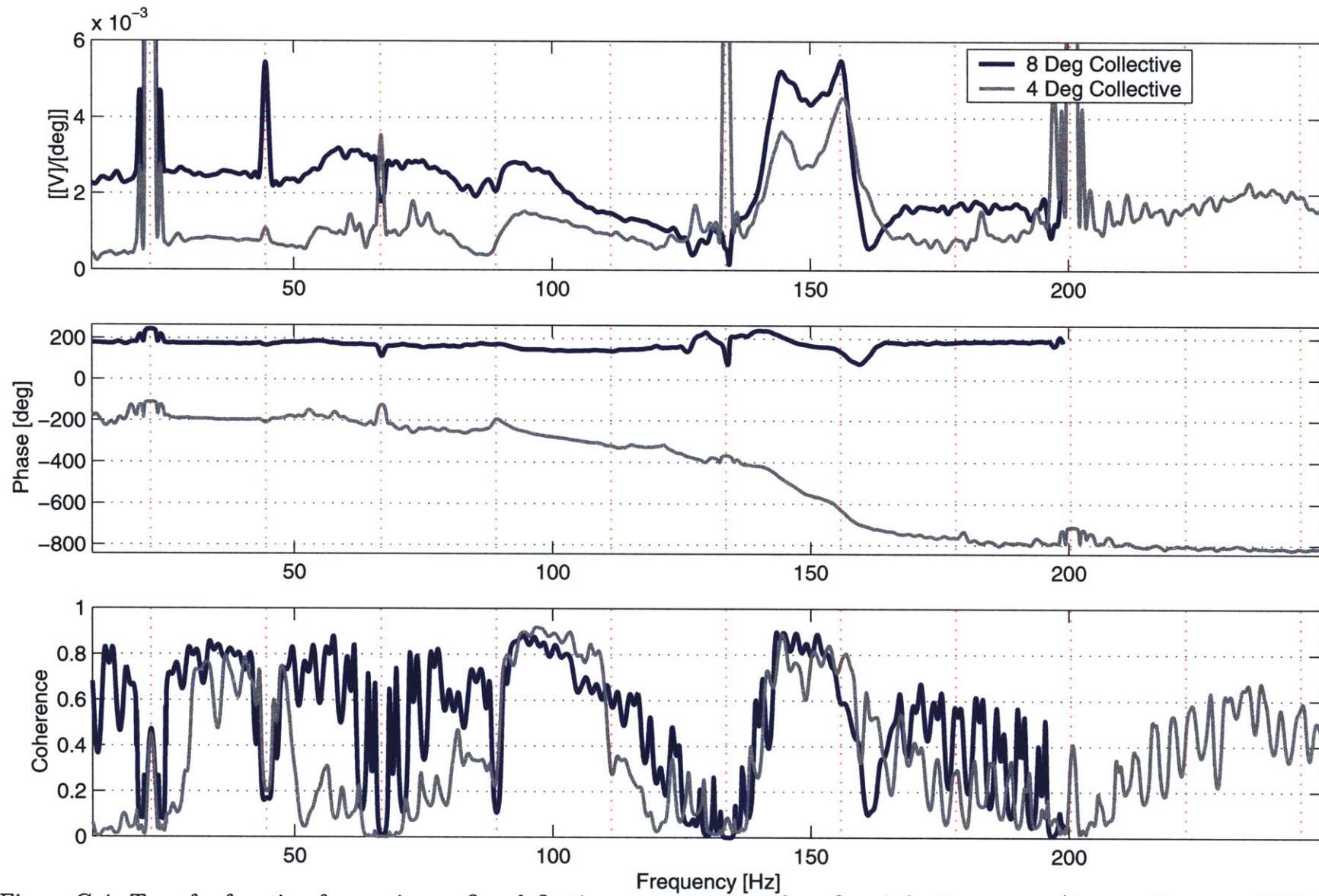


Figure C-4: Transfer function from primary flap deflection sensor to secondary flap deflection sensor (*i.e.*, small magnet/HET pair at outboard side of flap) with angle of attack

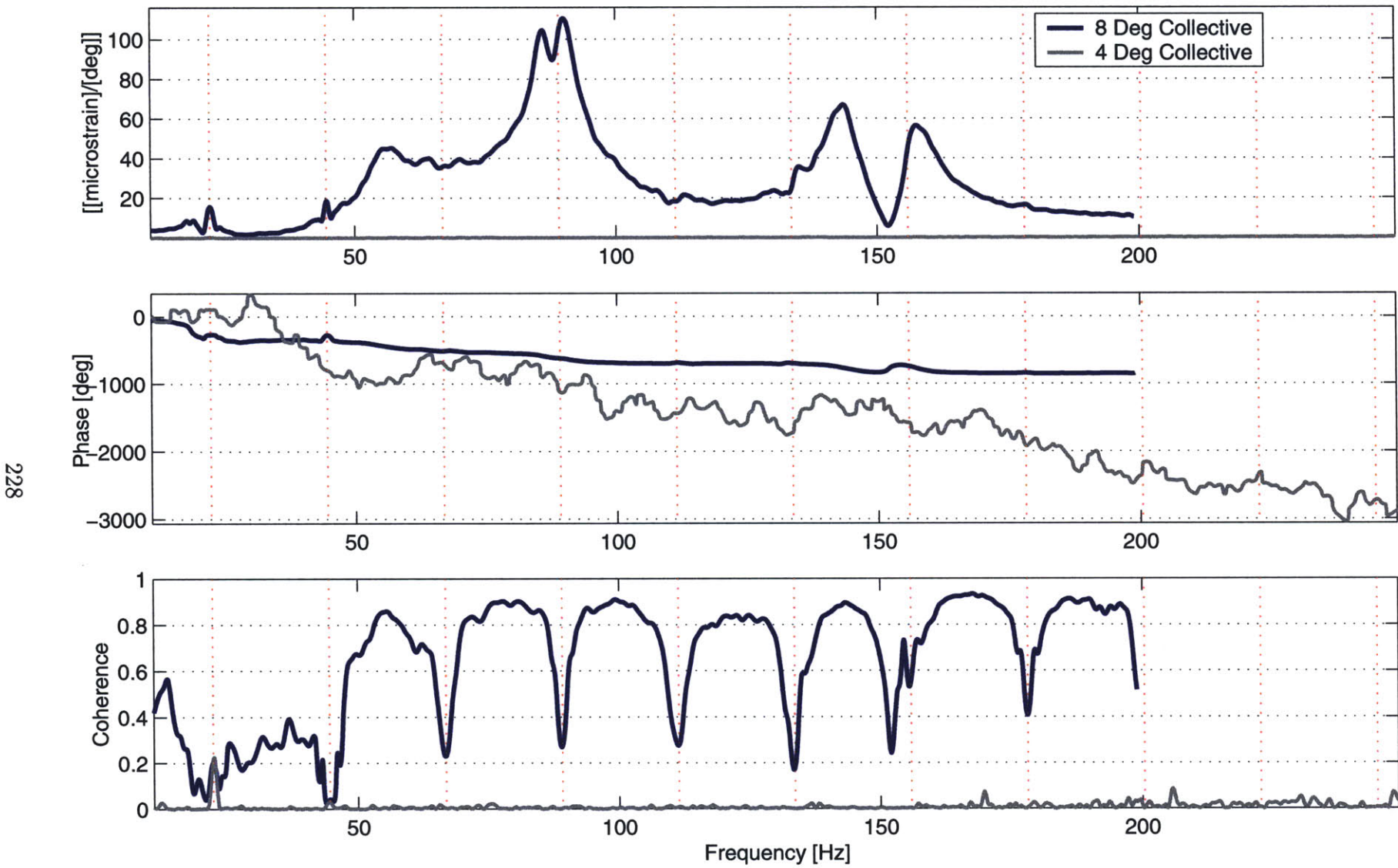


Figure C-5: Transfer function from flap deflection to flapwise bending at 19%R with angle of attack

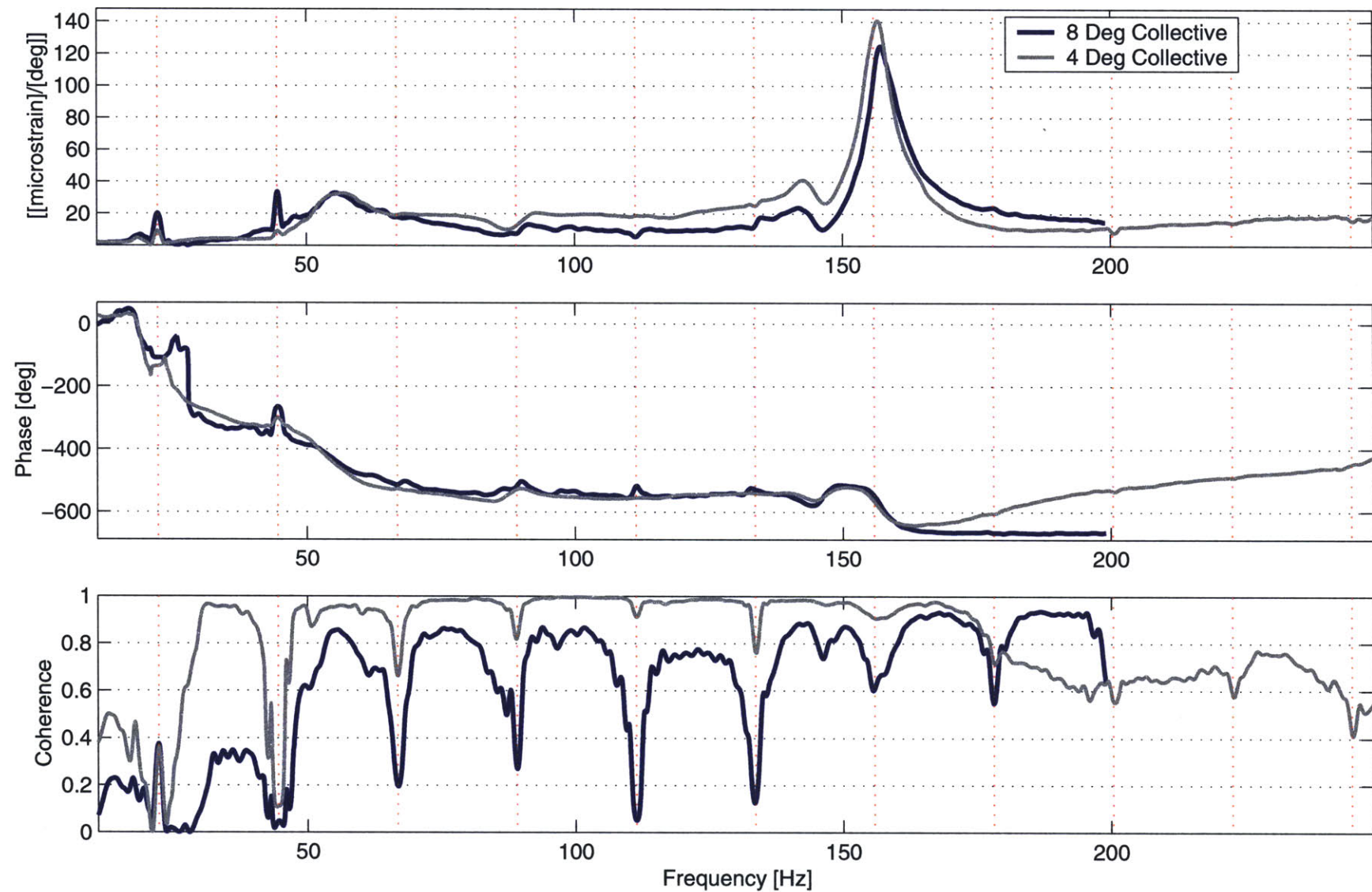


Figure C-6: Transfer function from flap deflection to flapwise bending at 42%R with angle of attack

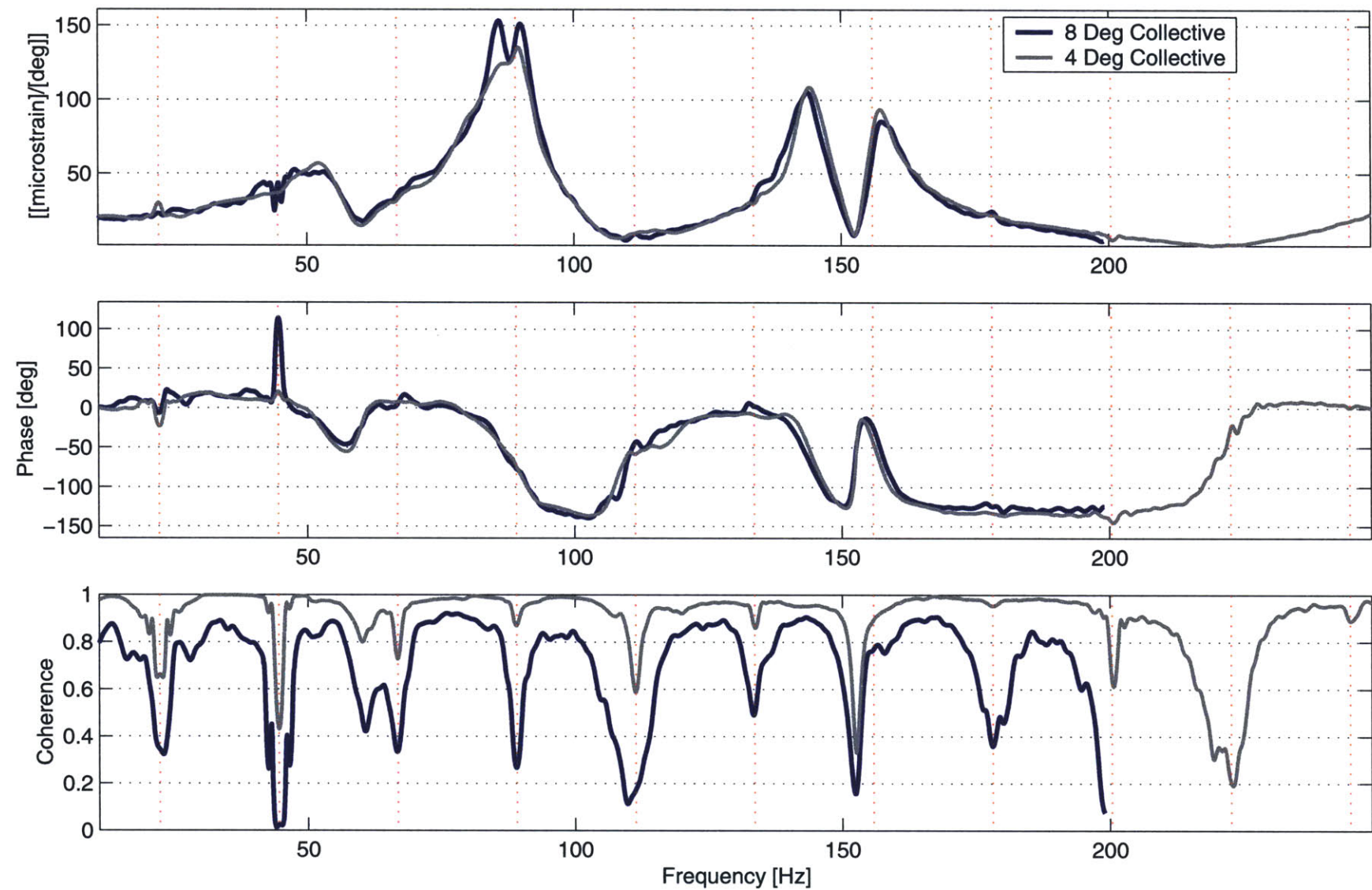


Figure C-7: Transfer function from flap deflection to axial strain at the inboard, forward corner of the actuator bay (top surface) with angle of attack

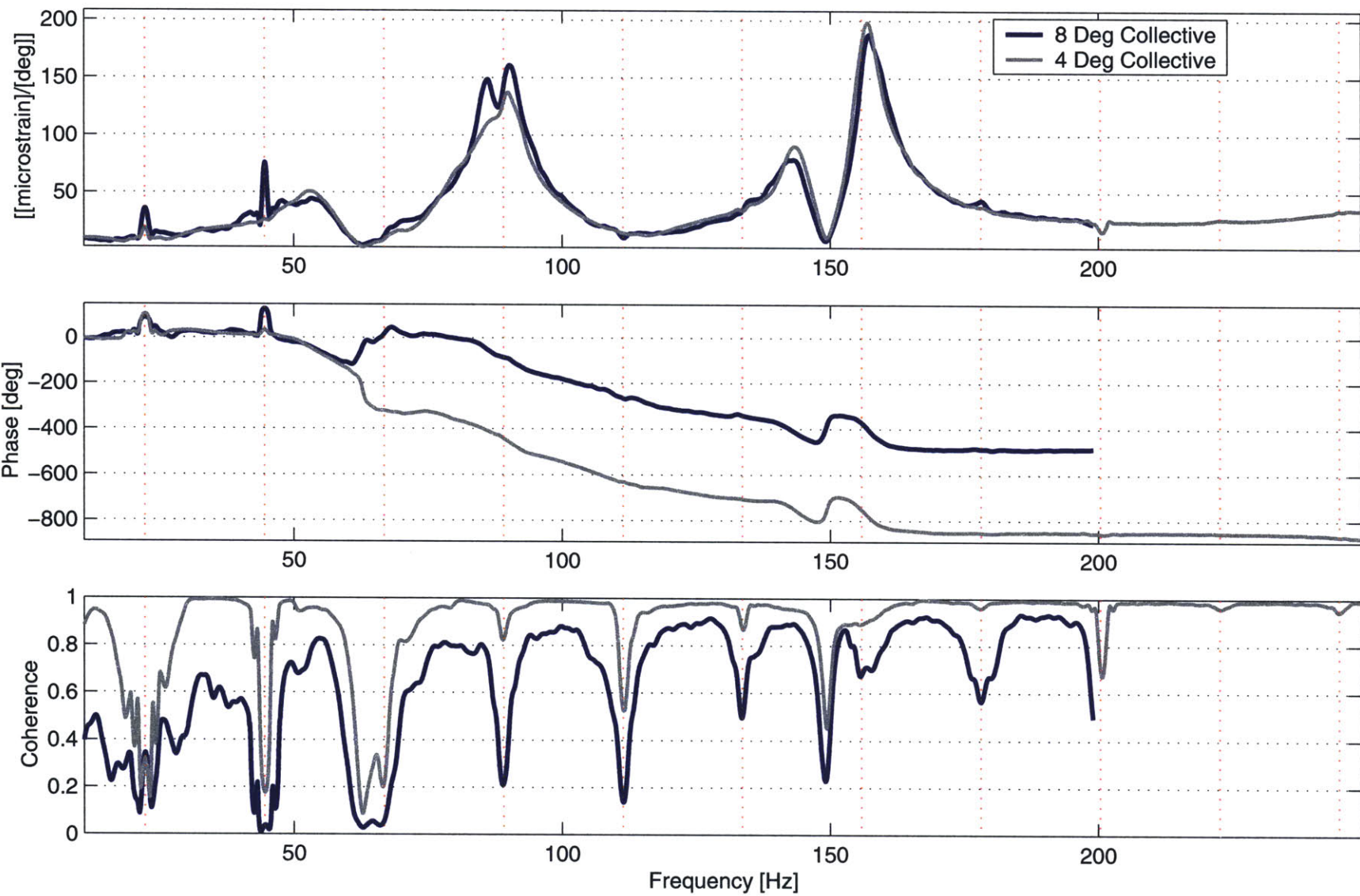


Figure C-8: Transfer function from flap deflection to axial strain at the inboard, aft corner of the actuator bay (top surface) with angle of attack

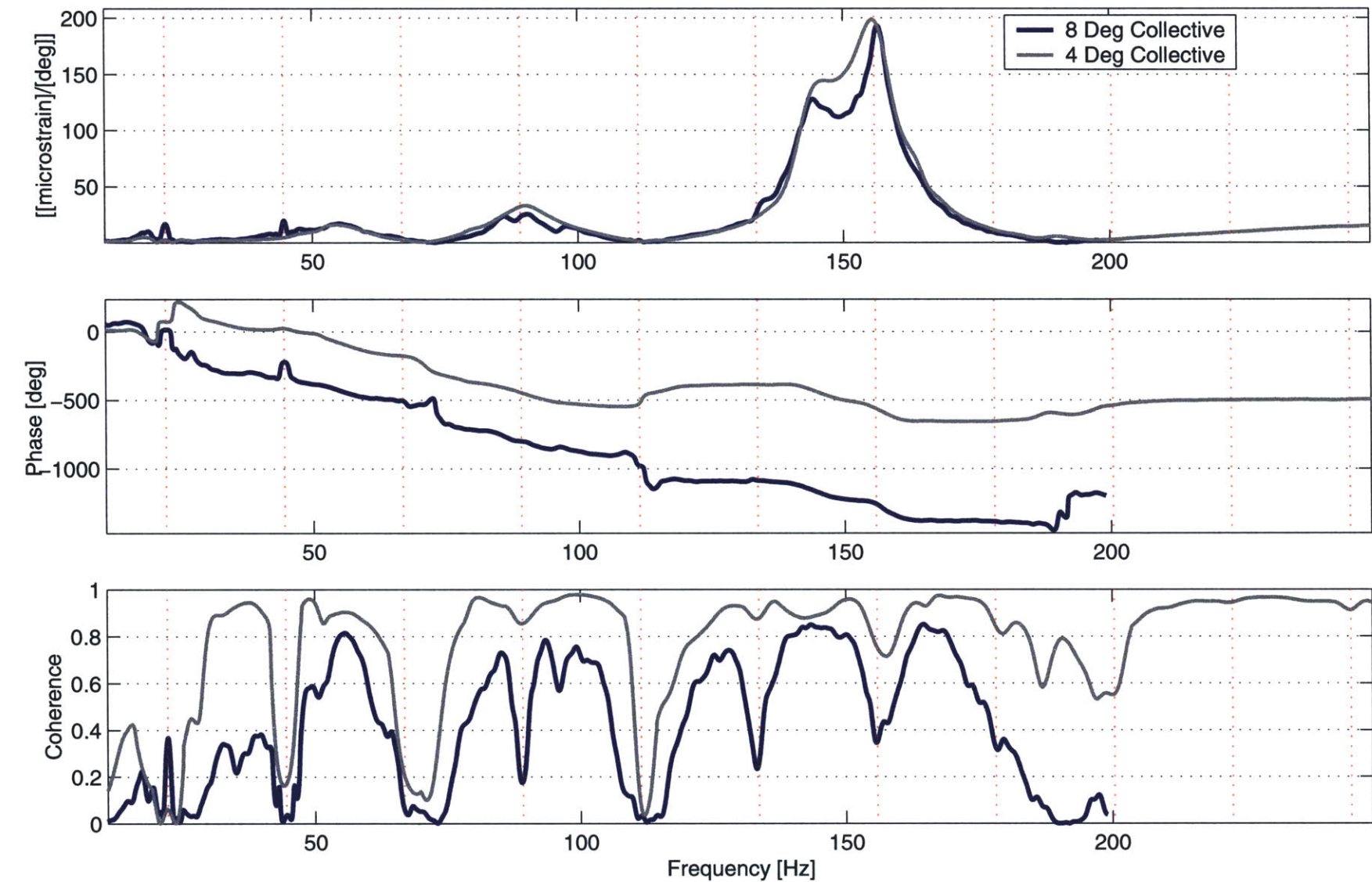


Figure C-9: Transfer function from flap deflection to axial strain in the trailing edge stiffener just inboard of servo-flap components with angle of attack

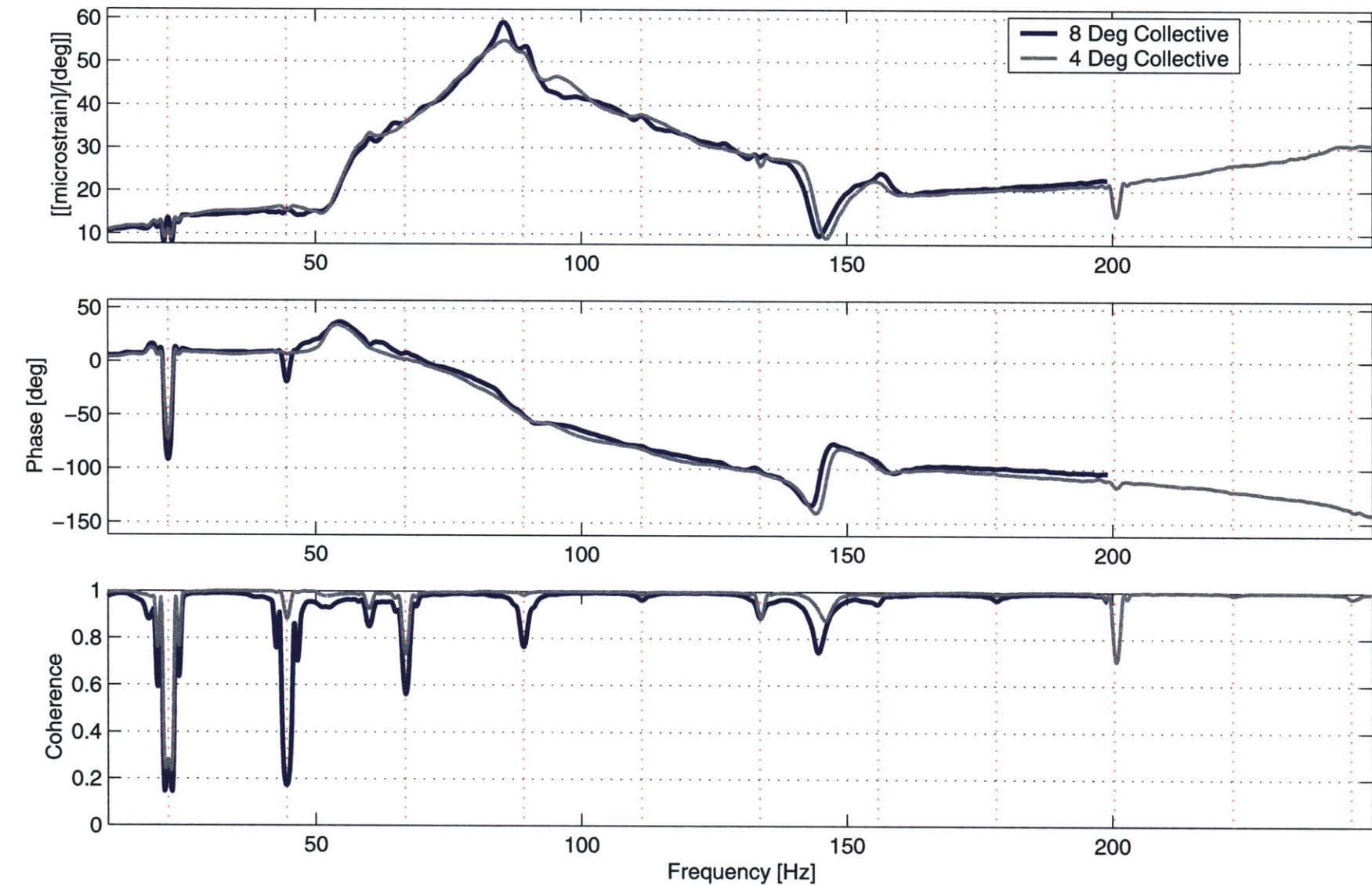


Figure C-10: Transfer function from flap deflection to torsional strain at 21%R with angle of attack

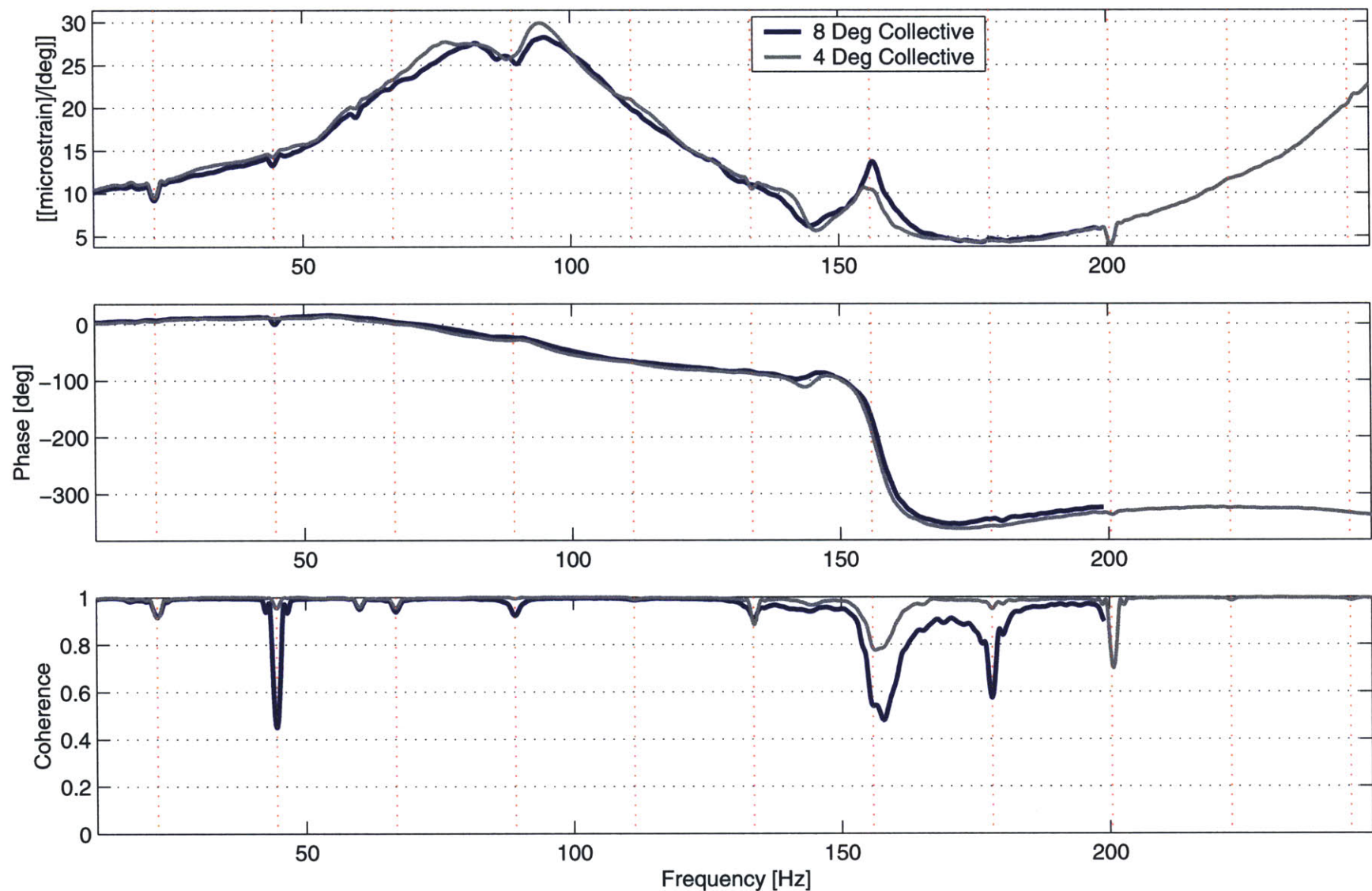


Figure C-11: Transfer function from flap deflection to torsional strain at 63%R with angle of attack

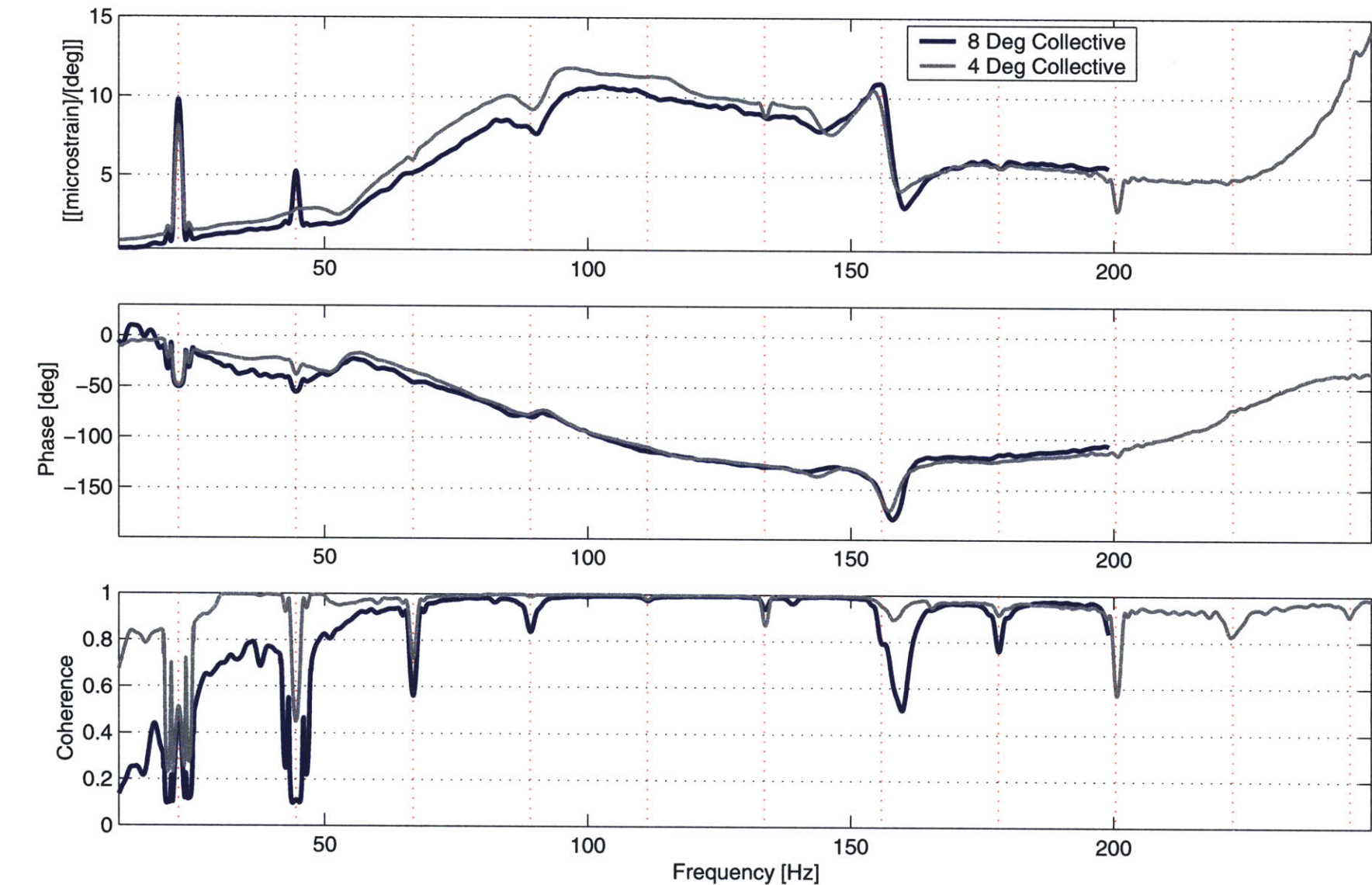


Figure C-12: Transfer function from flap deflection to torsional strain at 87%R with angle of attack

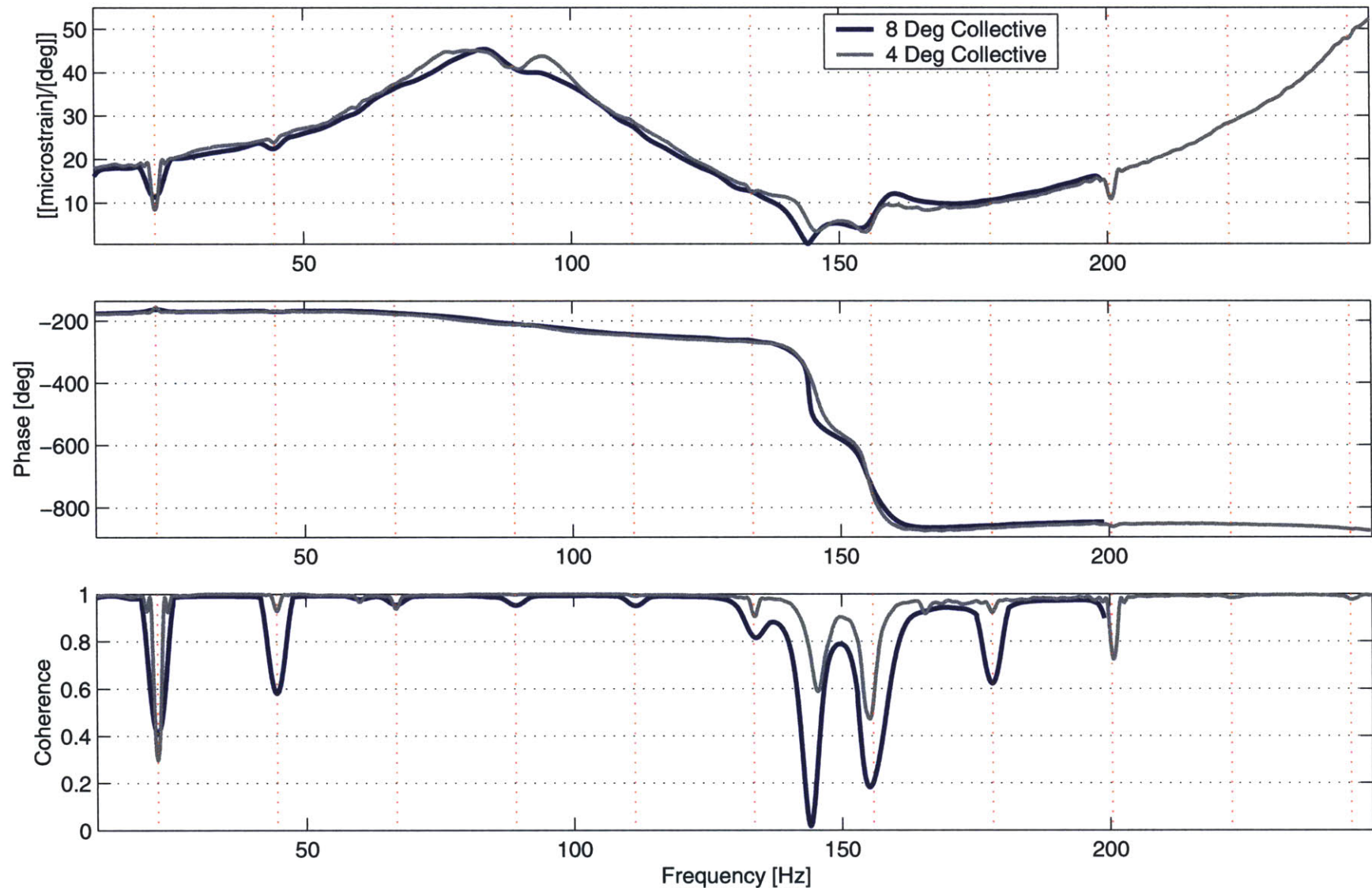


Figure C-13: Transfer function from flap deflection to shear strain just inboard of actuator bay (top surface) with angle of attack

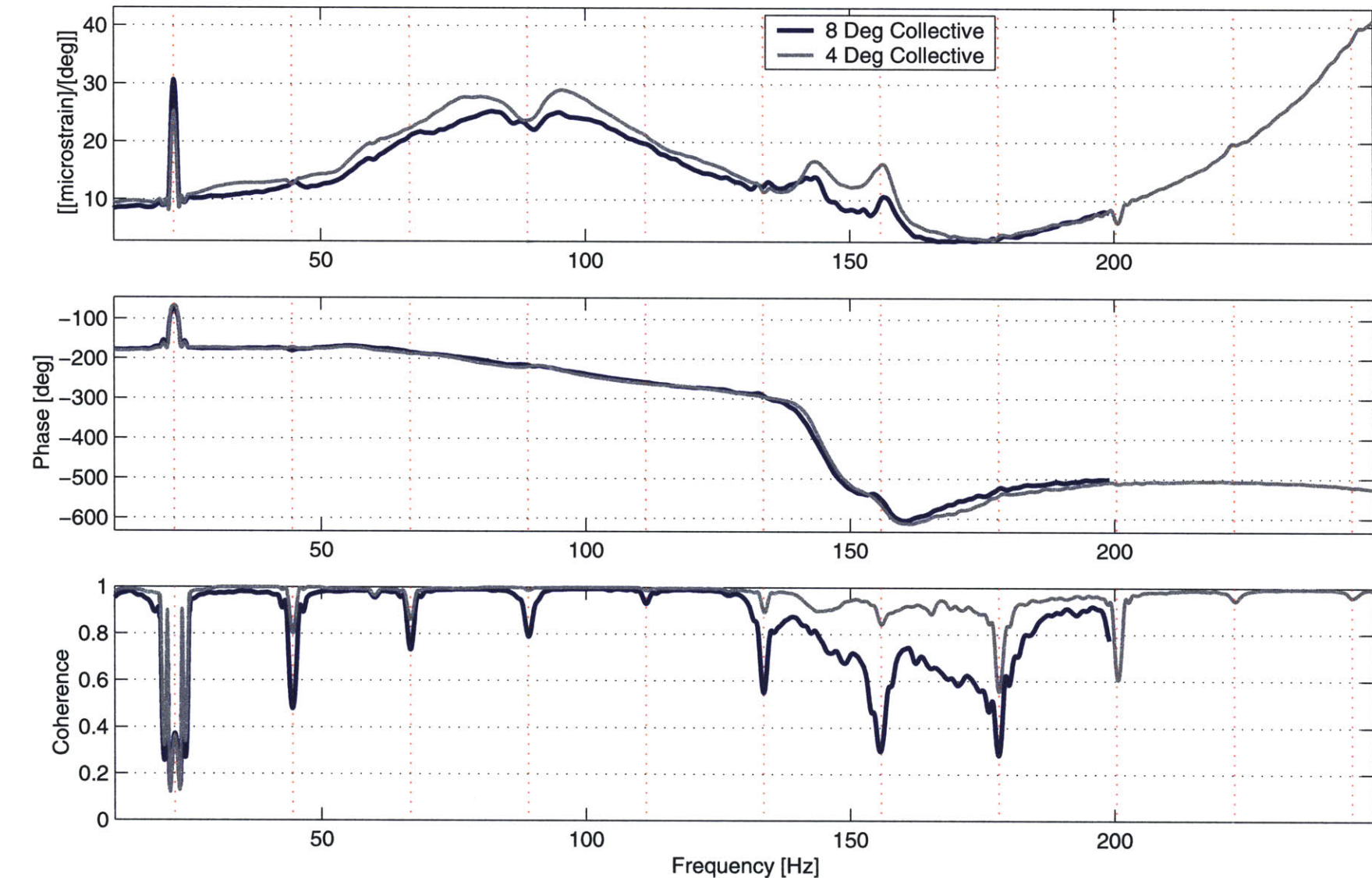


Figure C-14: Transfer function from flap deflection to shear strain just outboard of actuator bay (top surface) with angle of attack

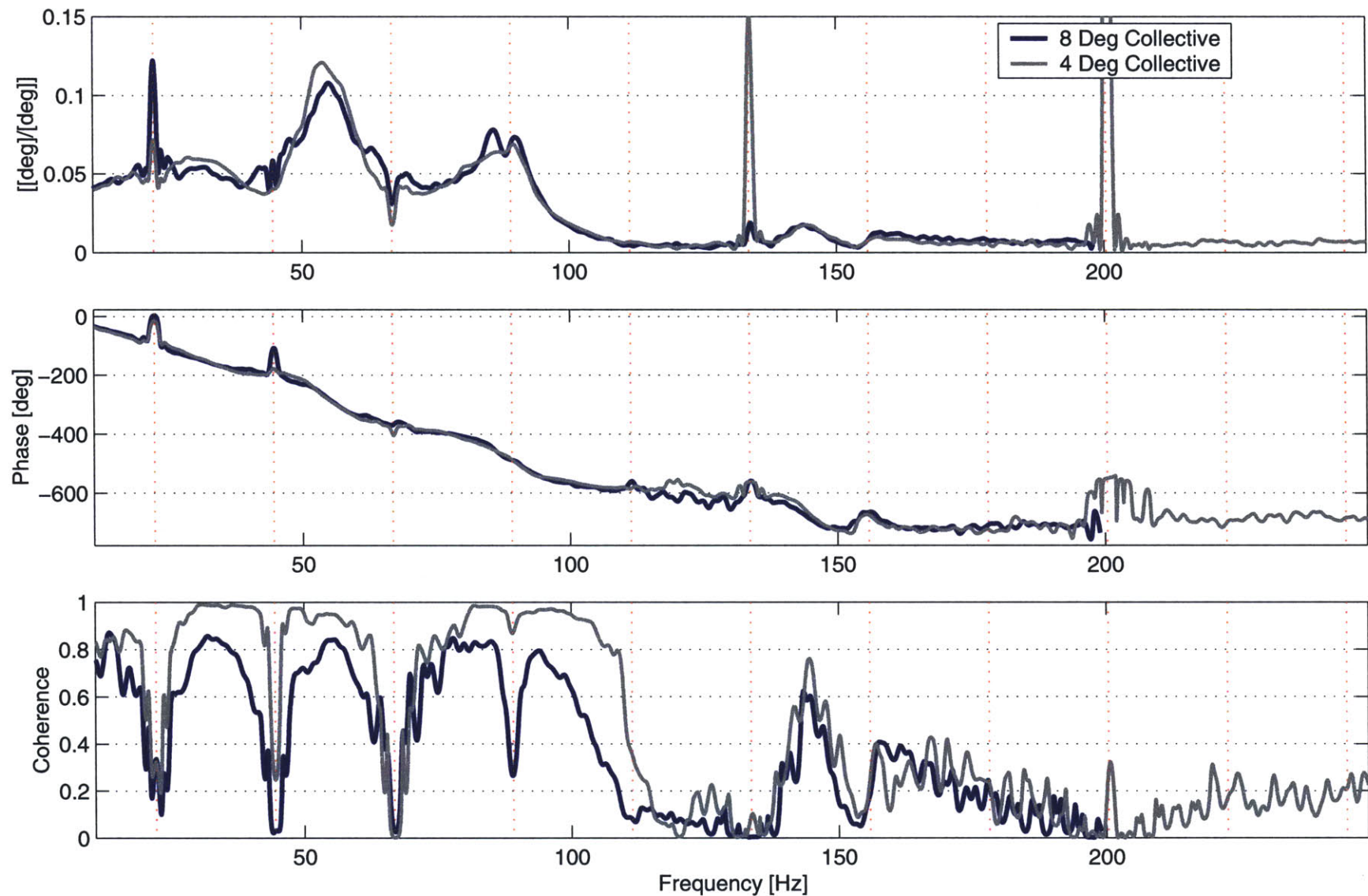


Figure C-15: Transfer function from flap deflection to blade flapping angle with angle of attack

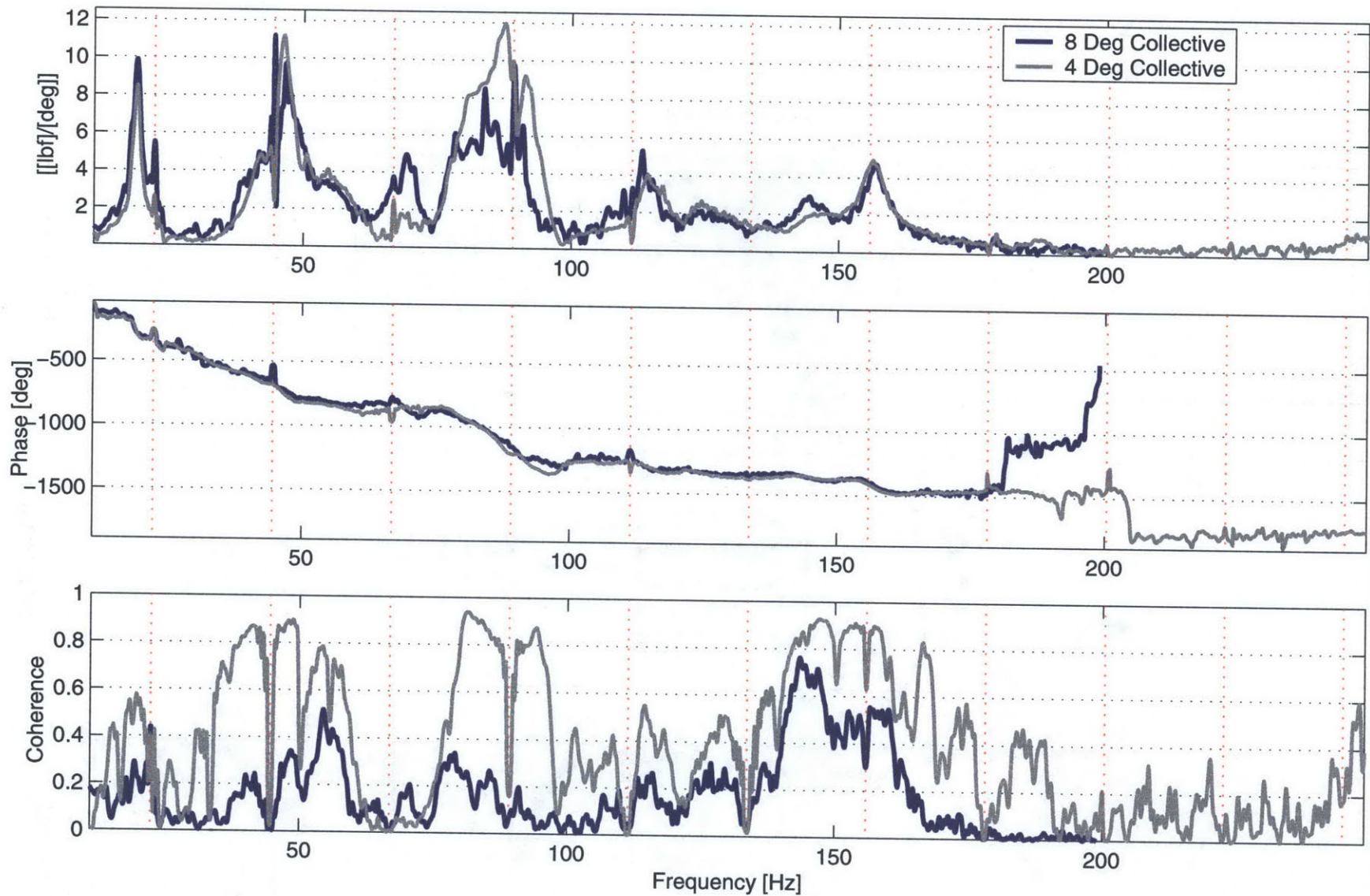


Figure C-16: Transfer function from flap deflection to  $F_x$  at hub with angle of attack

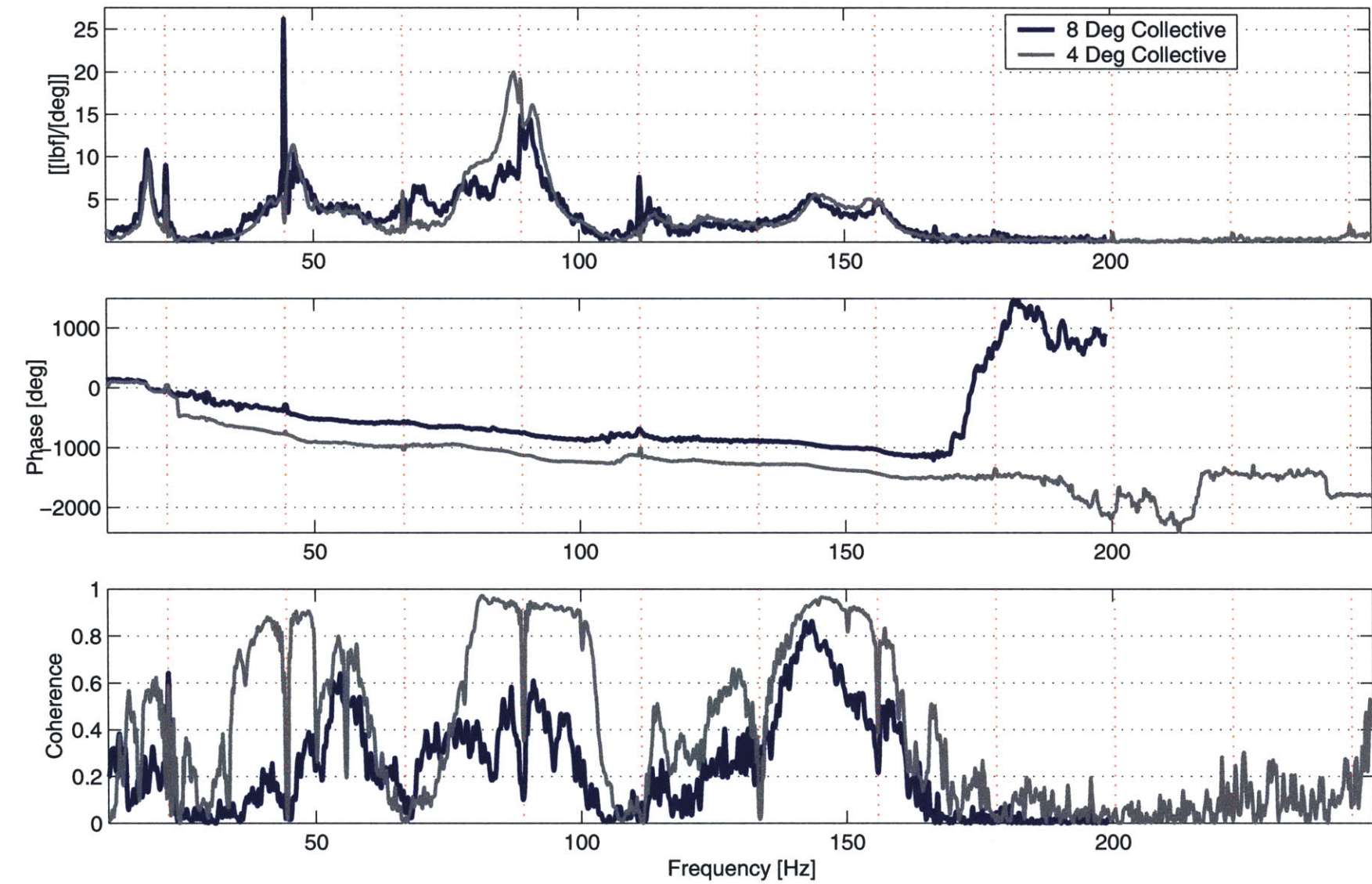


Figure C-17: Transfer function from flap deflection to  $F_y$  at hub with angle of attack

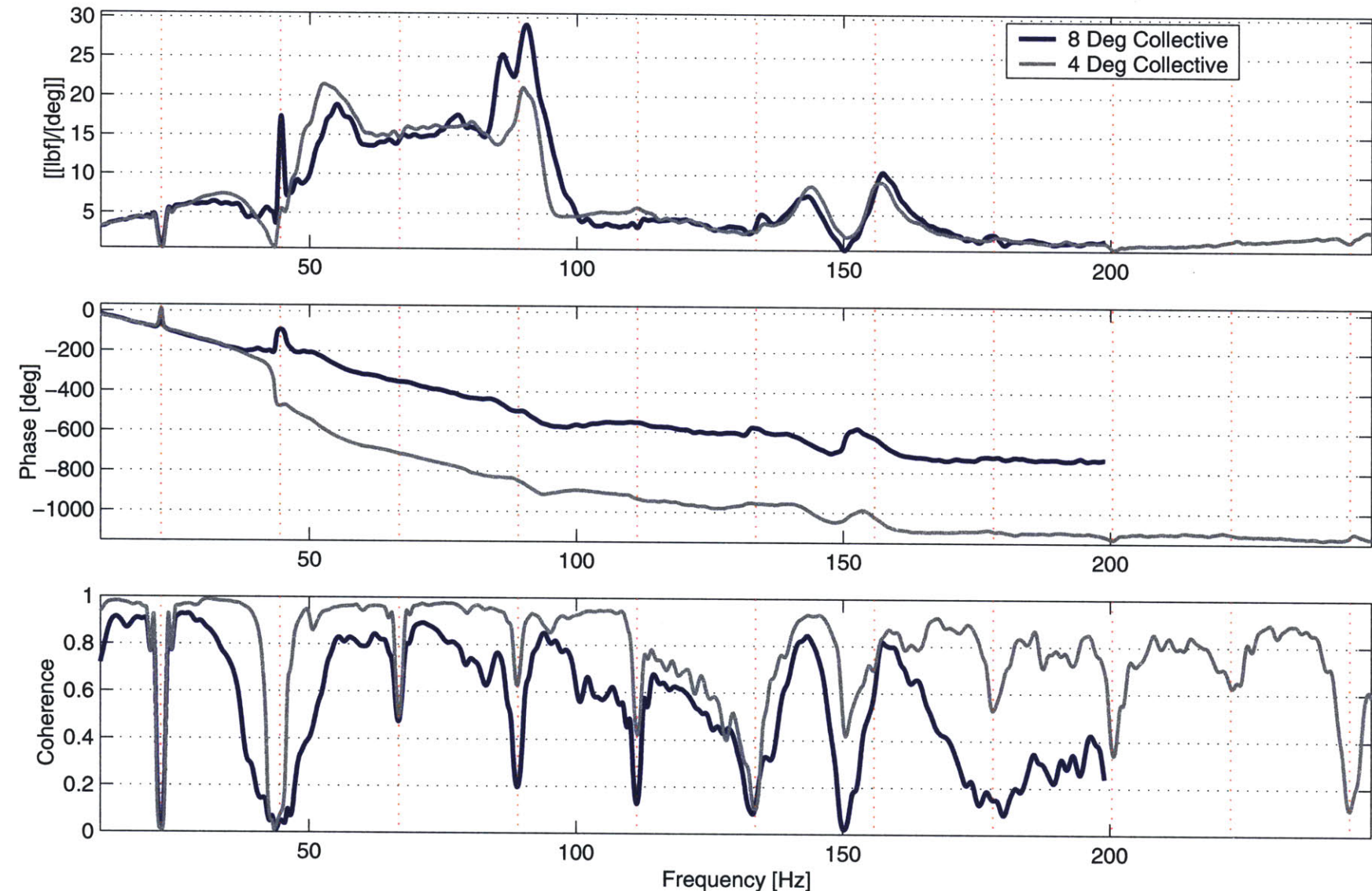


Figure C-18: Transfer function from flap deflection to  $F_z$  at hub with angle of attack

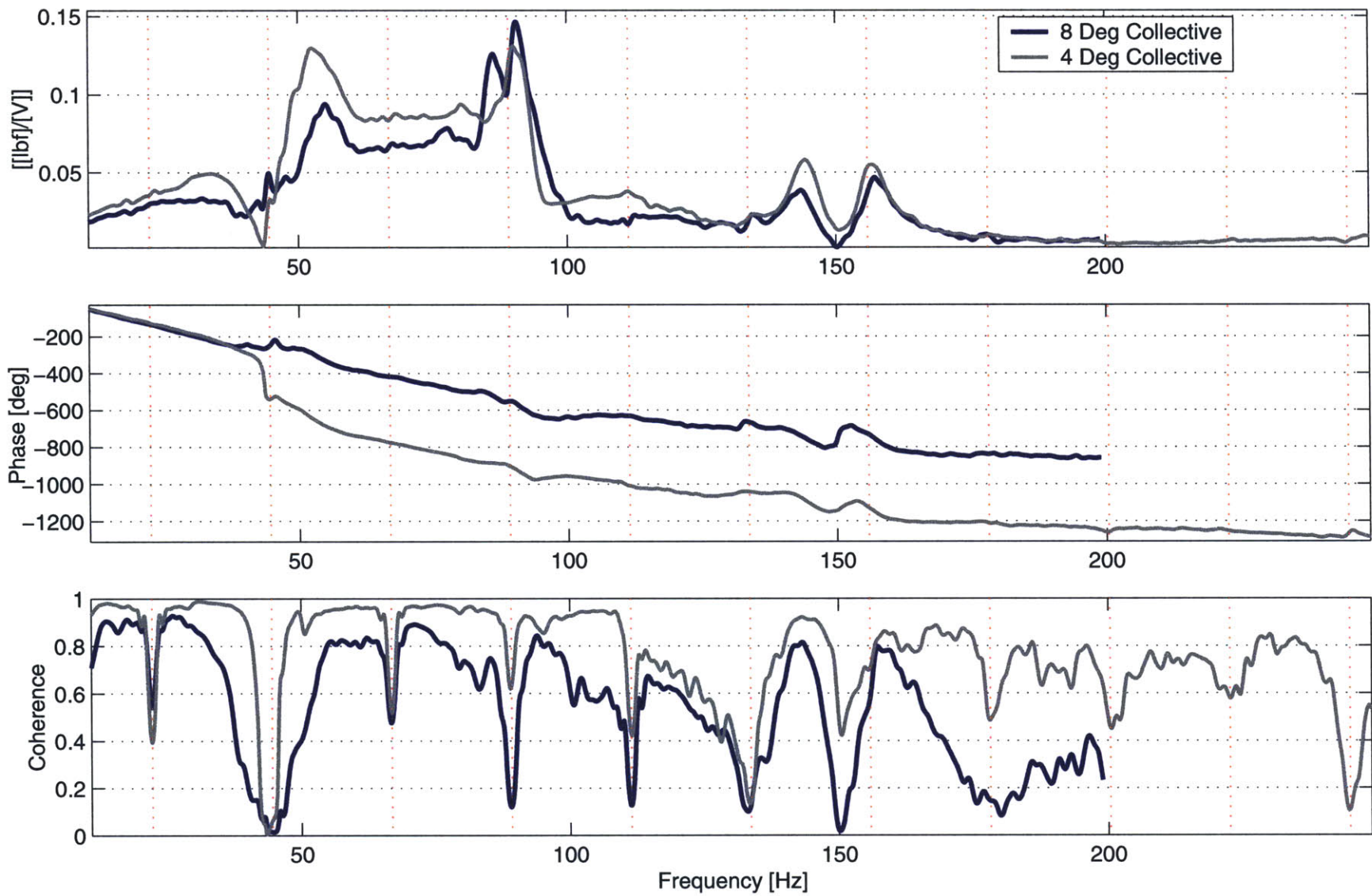


Figure C-19: Transfer function from applied voltage to  $F_z$  at hub with angle of attack

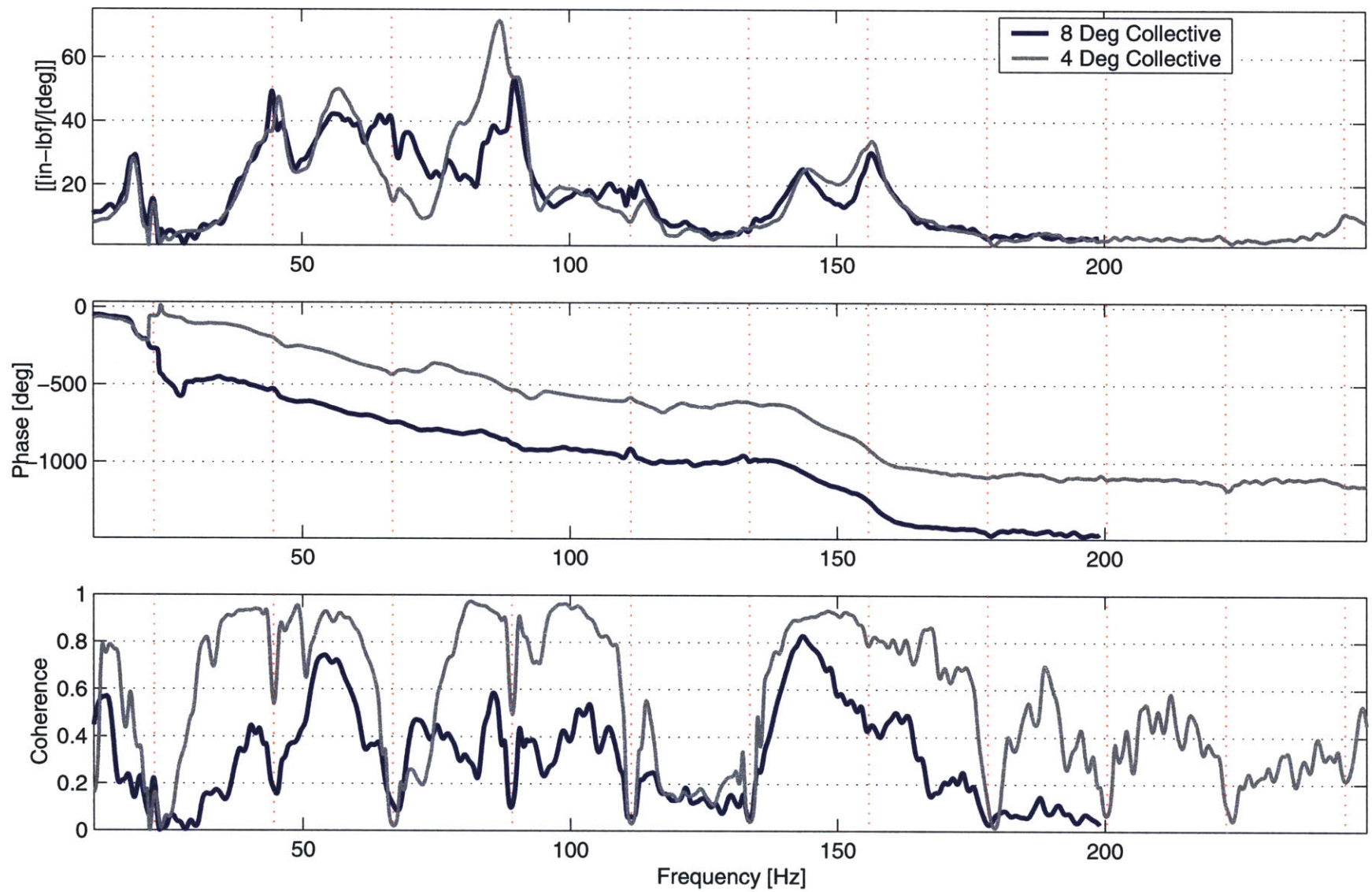


Figure C-20: Transfer function from flap deflection to  $M_x$  at hub with angle of attack

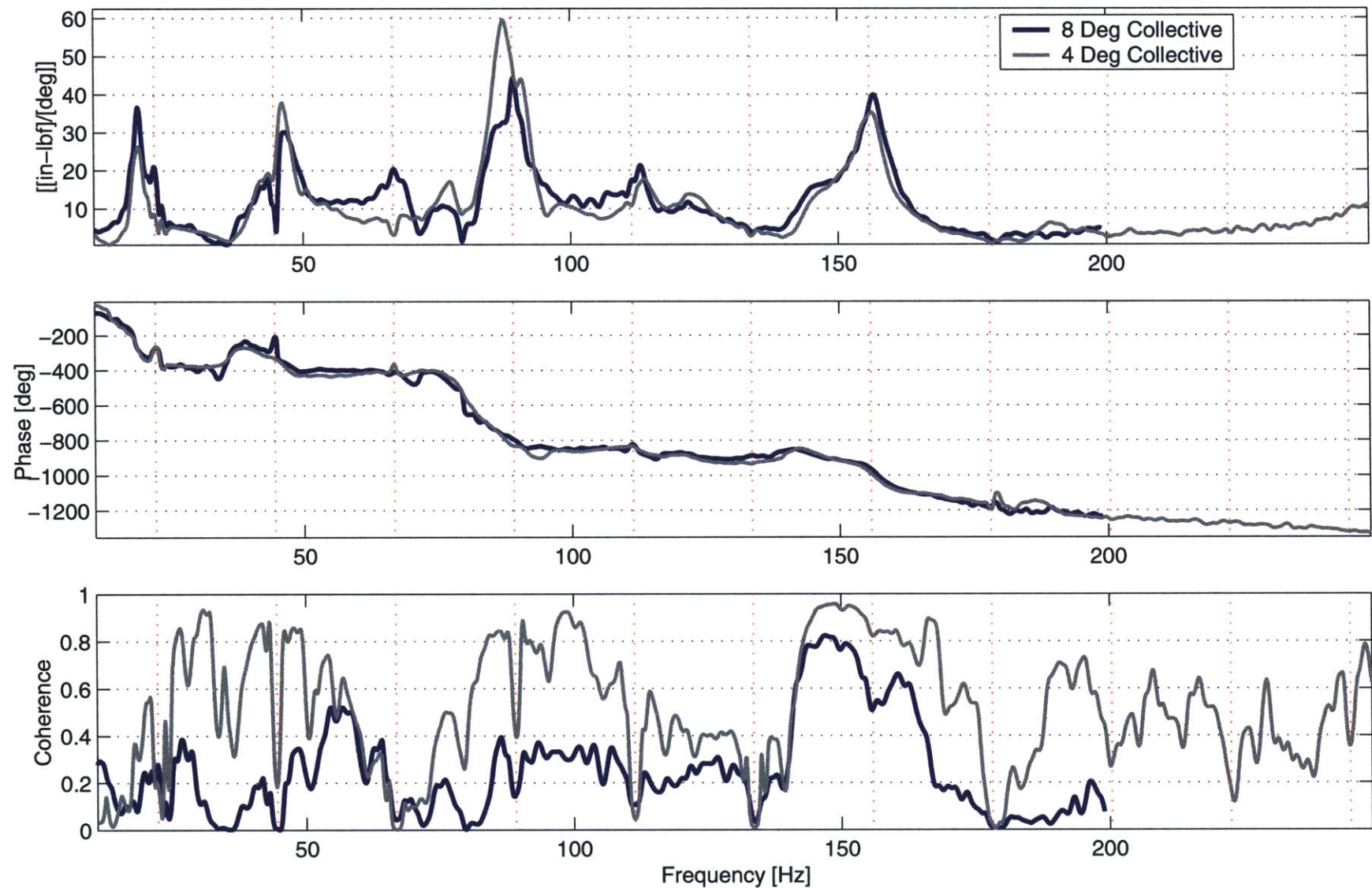


Figure C-21: Transfer function from flap deflection to  $M_y$  at hub with angle of attack

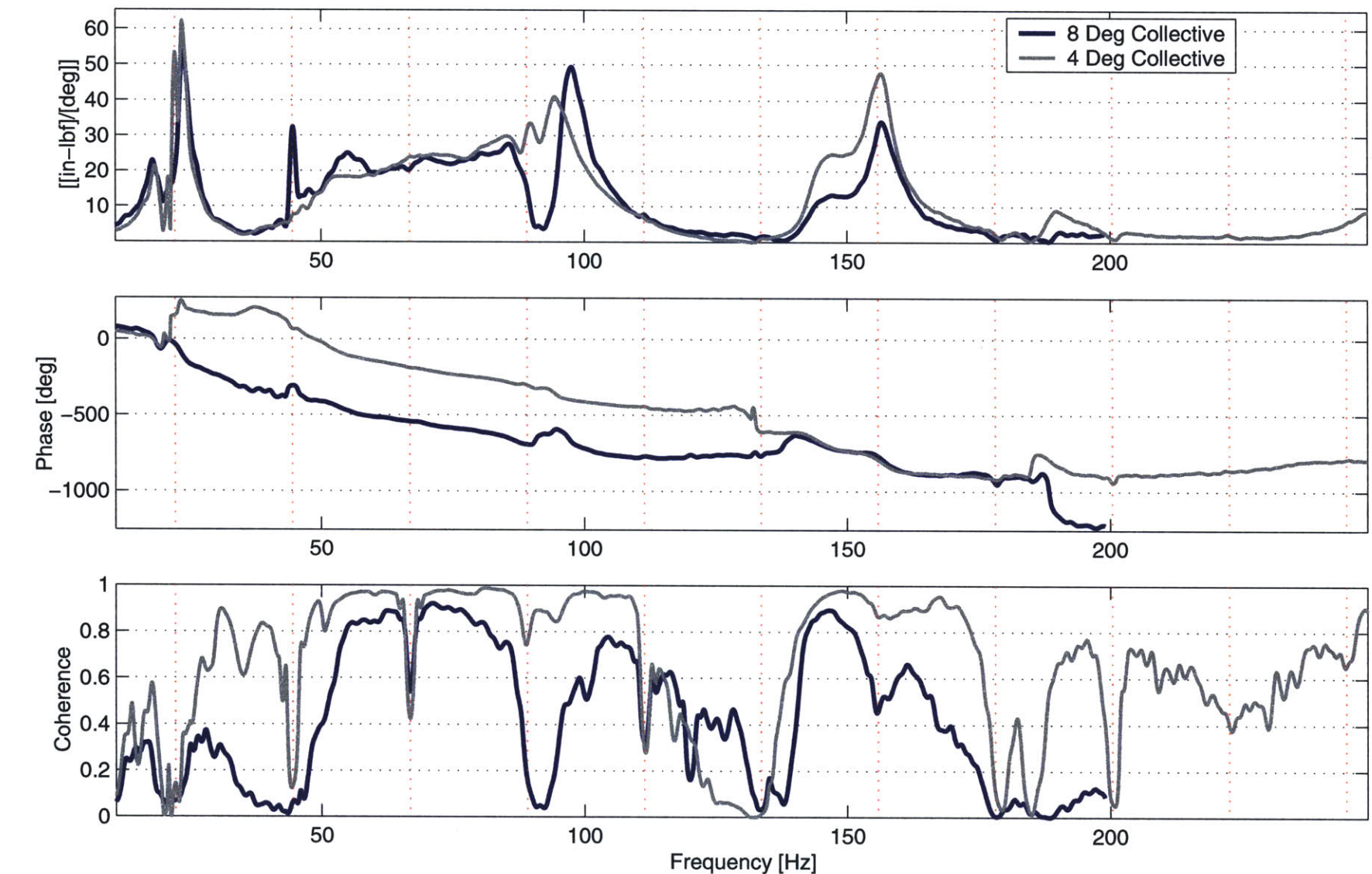


Figure C-22: Transfer function from flap deflection to  $M_z$  at hub with angle of attack

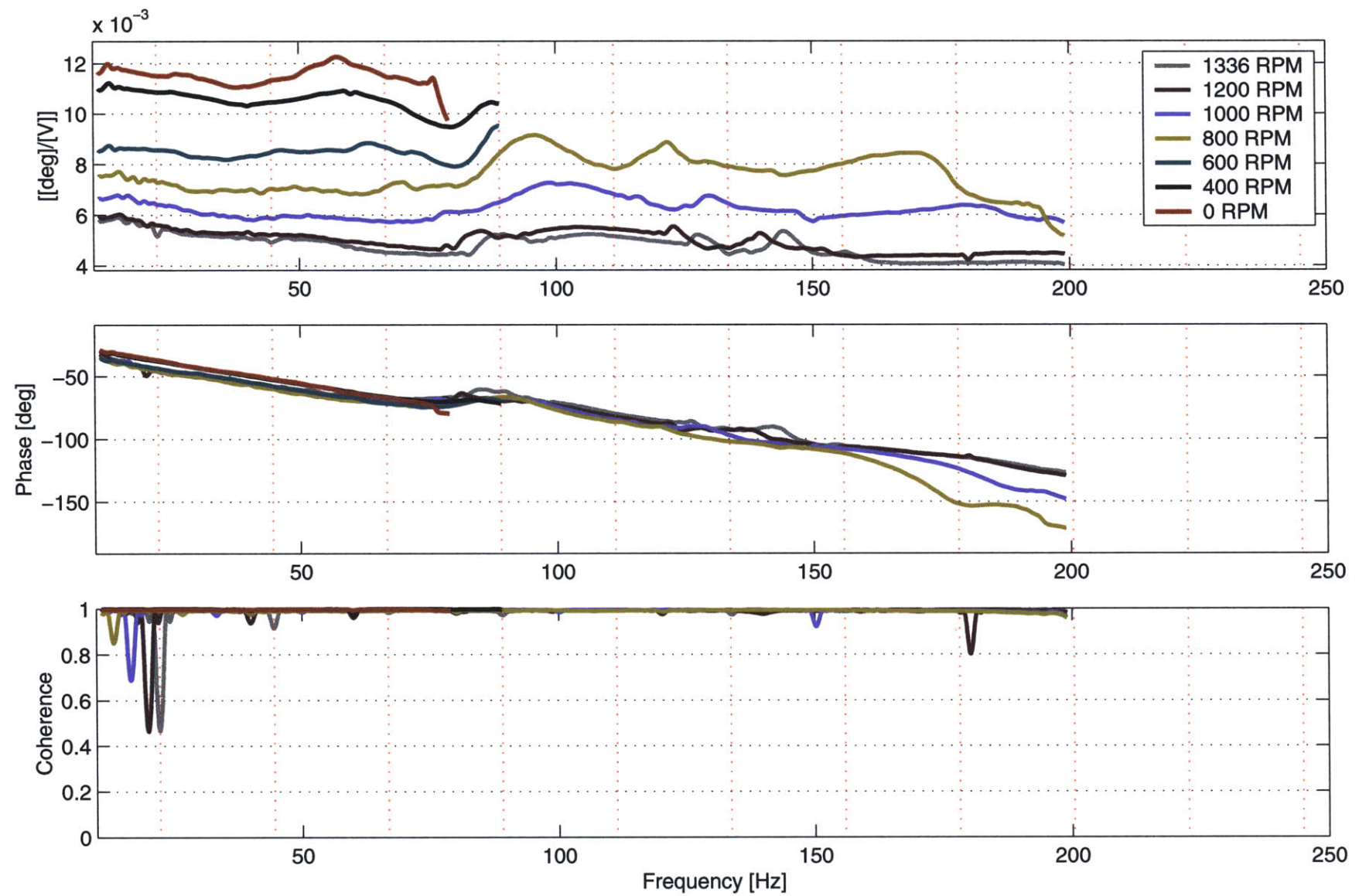


Figure C-23: Transfer function from voltage to flap deflection with rotor speed

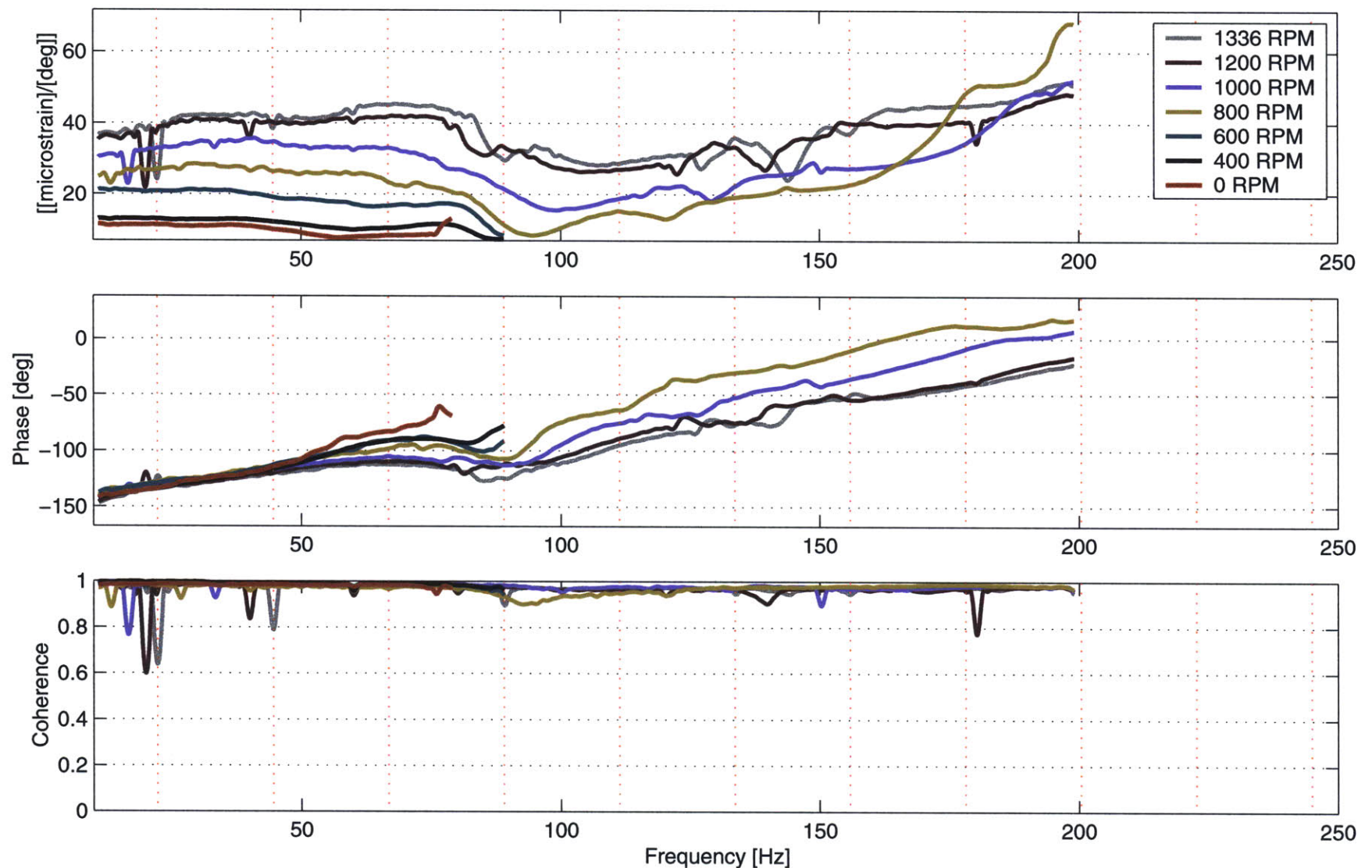


Figure C-24: Transfer function from flap deflection to actuator frame strain with rotor speed

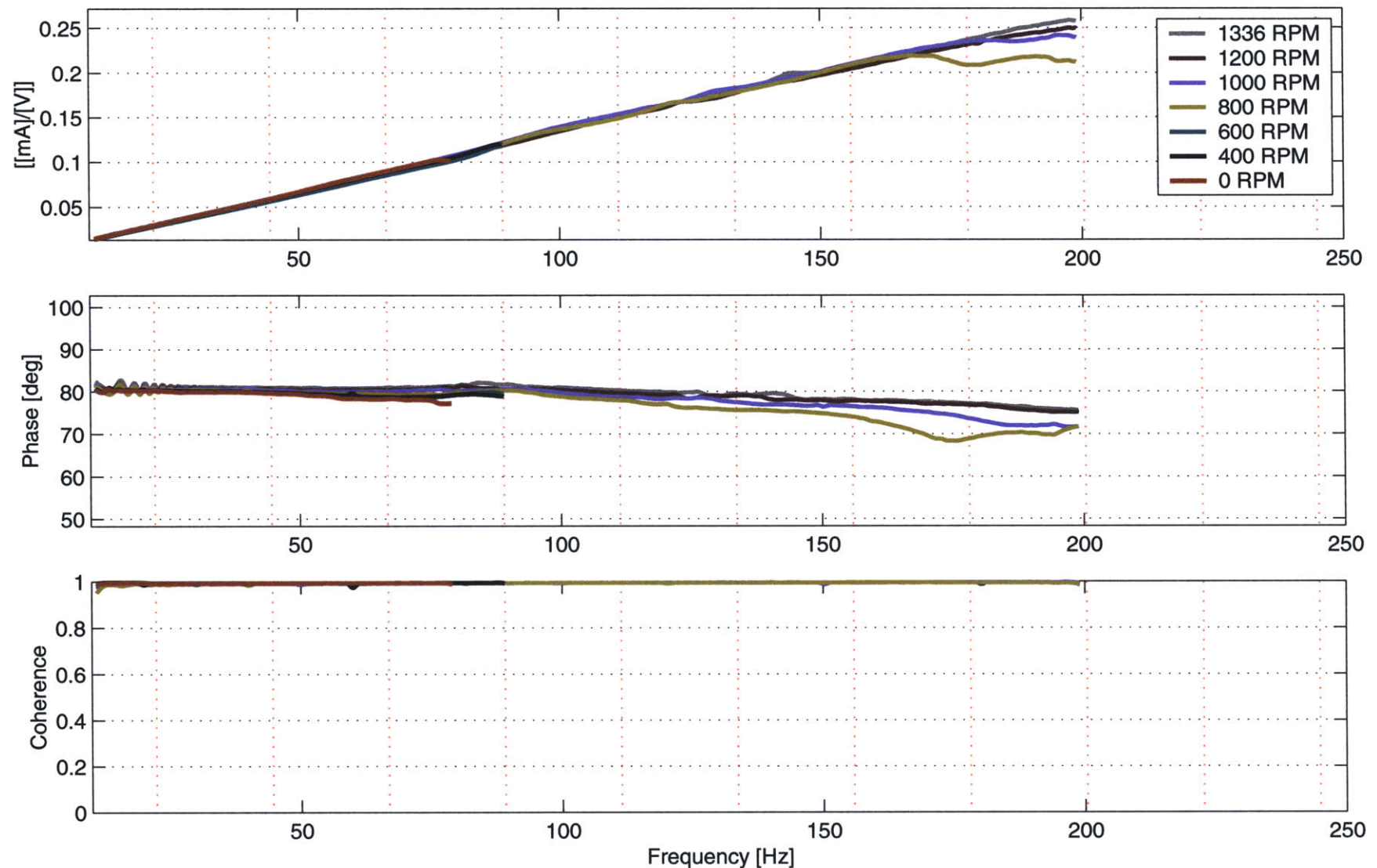


Figure C-25: Transfer function from voltage to piezoelectric stack current with rotor speed

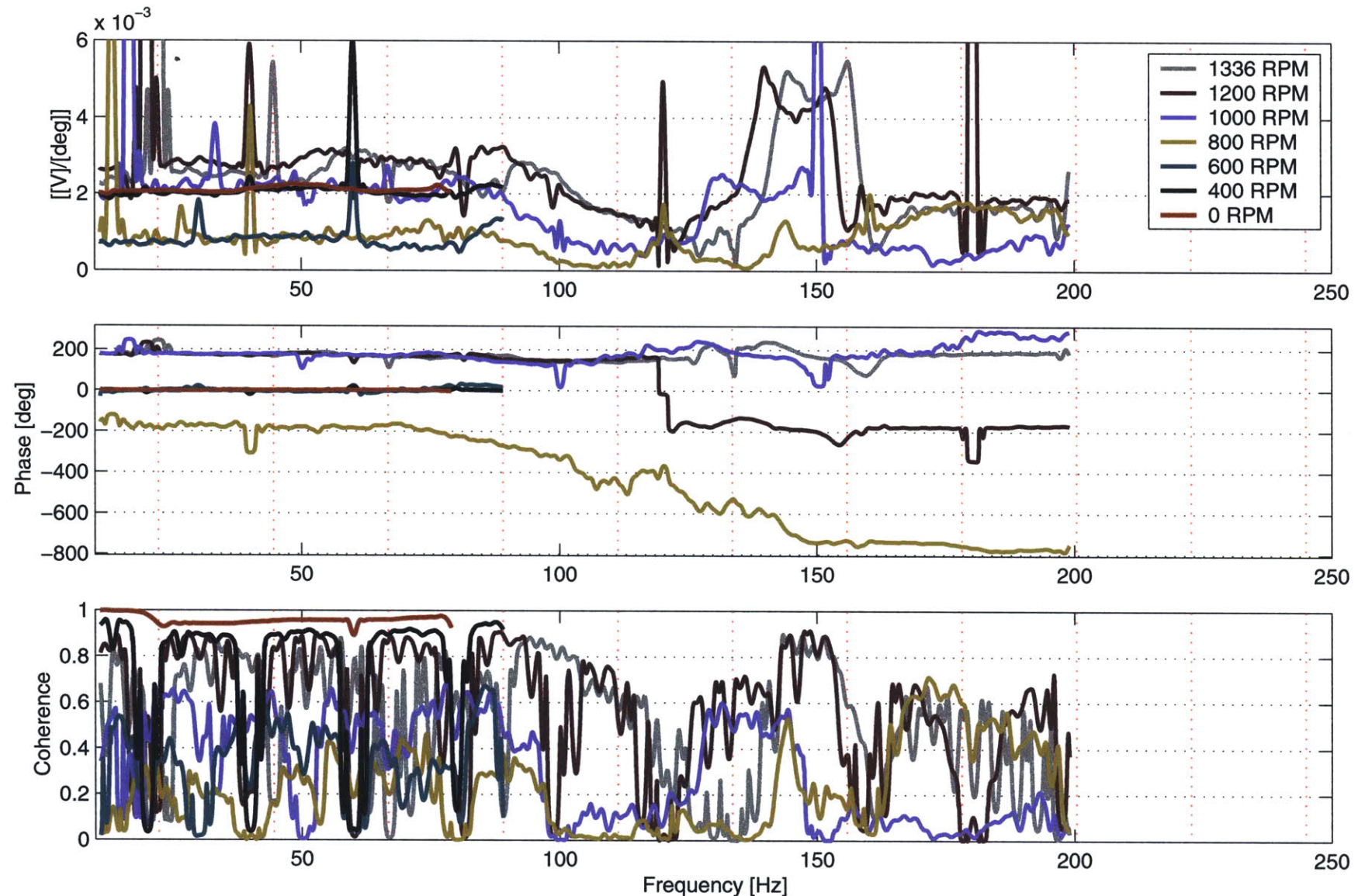


Figure C-26: Transfer function from primary flap deflection sensor to secondary flap deflection sensor (*i.e.*, small magnet/HET pair at outboard side of flap) with rotor speed

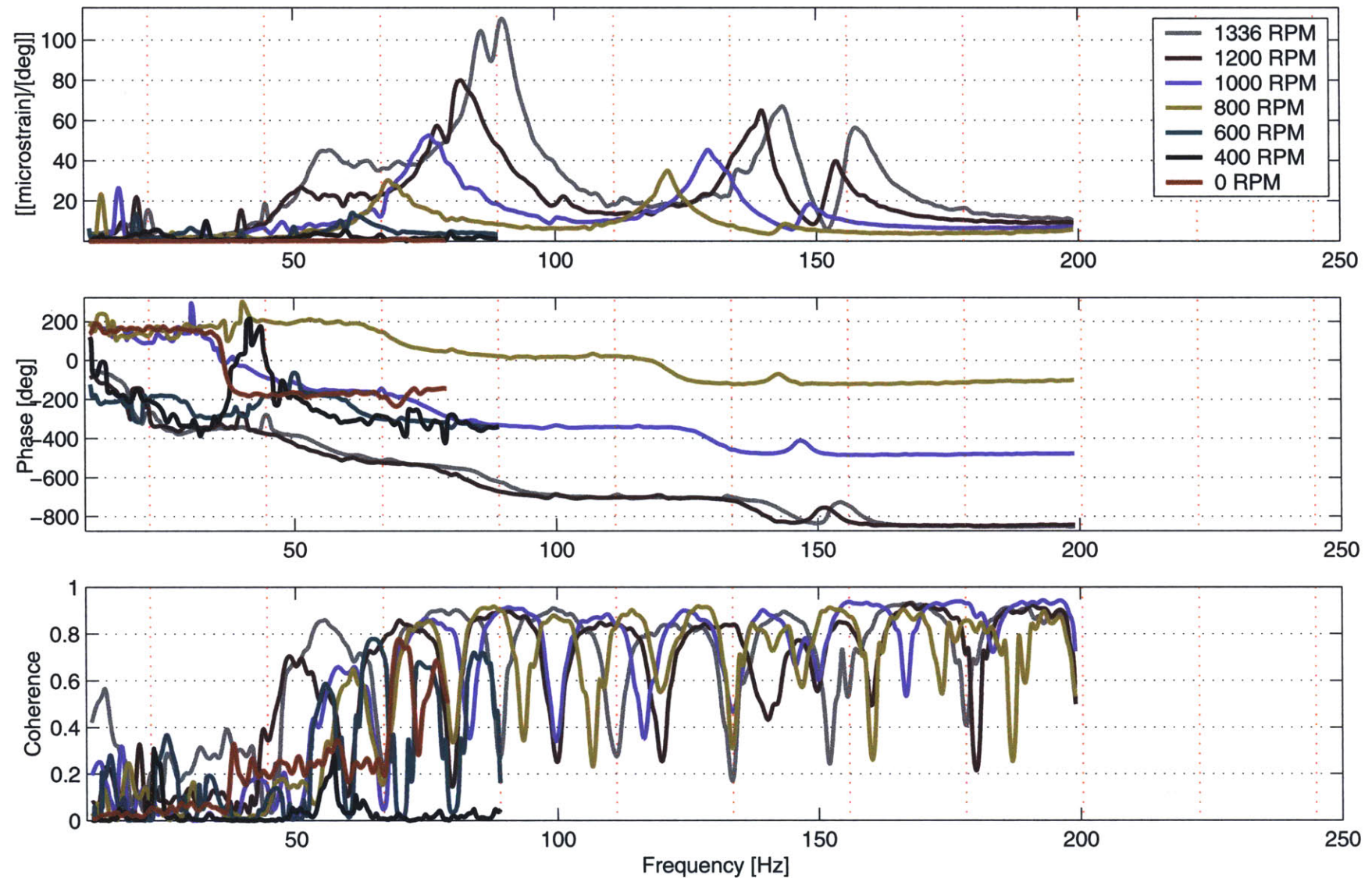


Figure C-27: Transfer function from flap deflection to flapwise bending at 19%R with rotor speed

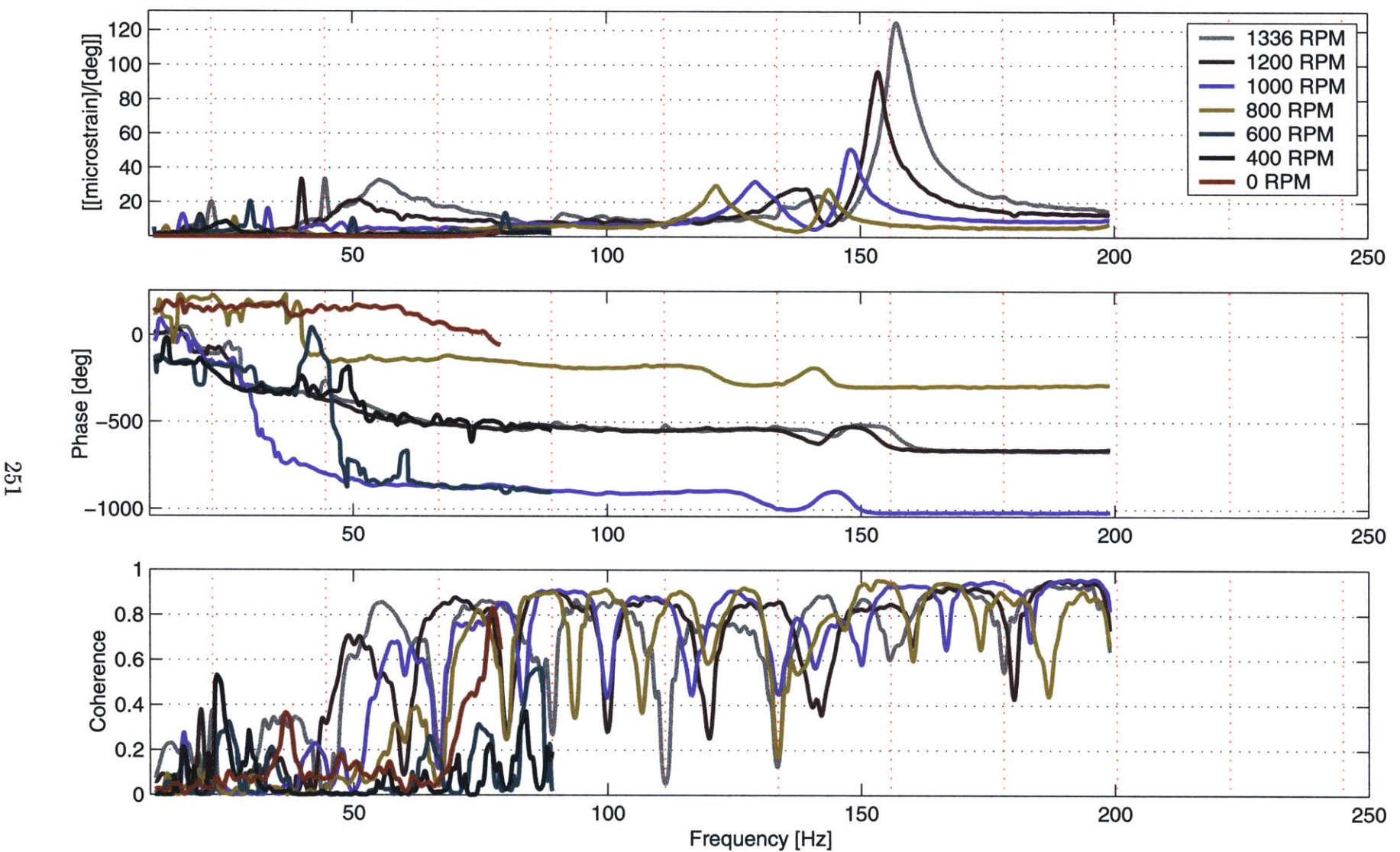


Figure C-28: Transfer function from flap deflection to flapwise bending at 42%R with rotor speed

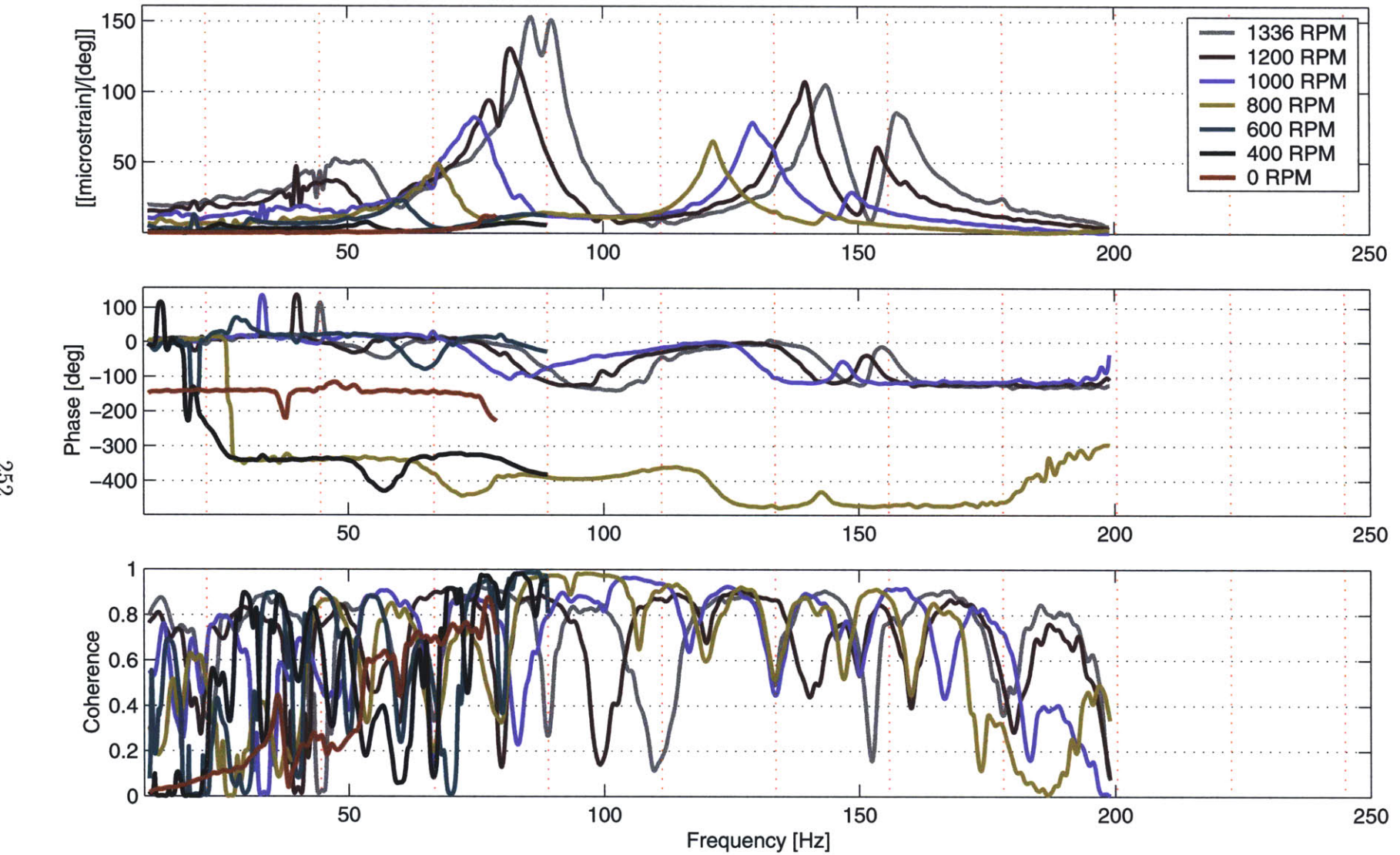


Figure C-29: Transfer function from flap deflection to axial strain at the inboard, forward corner of the actuator bay (top surface) with rotor speed

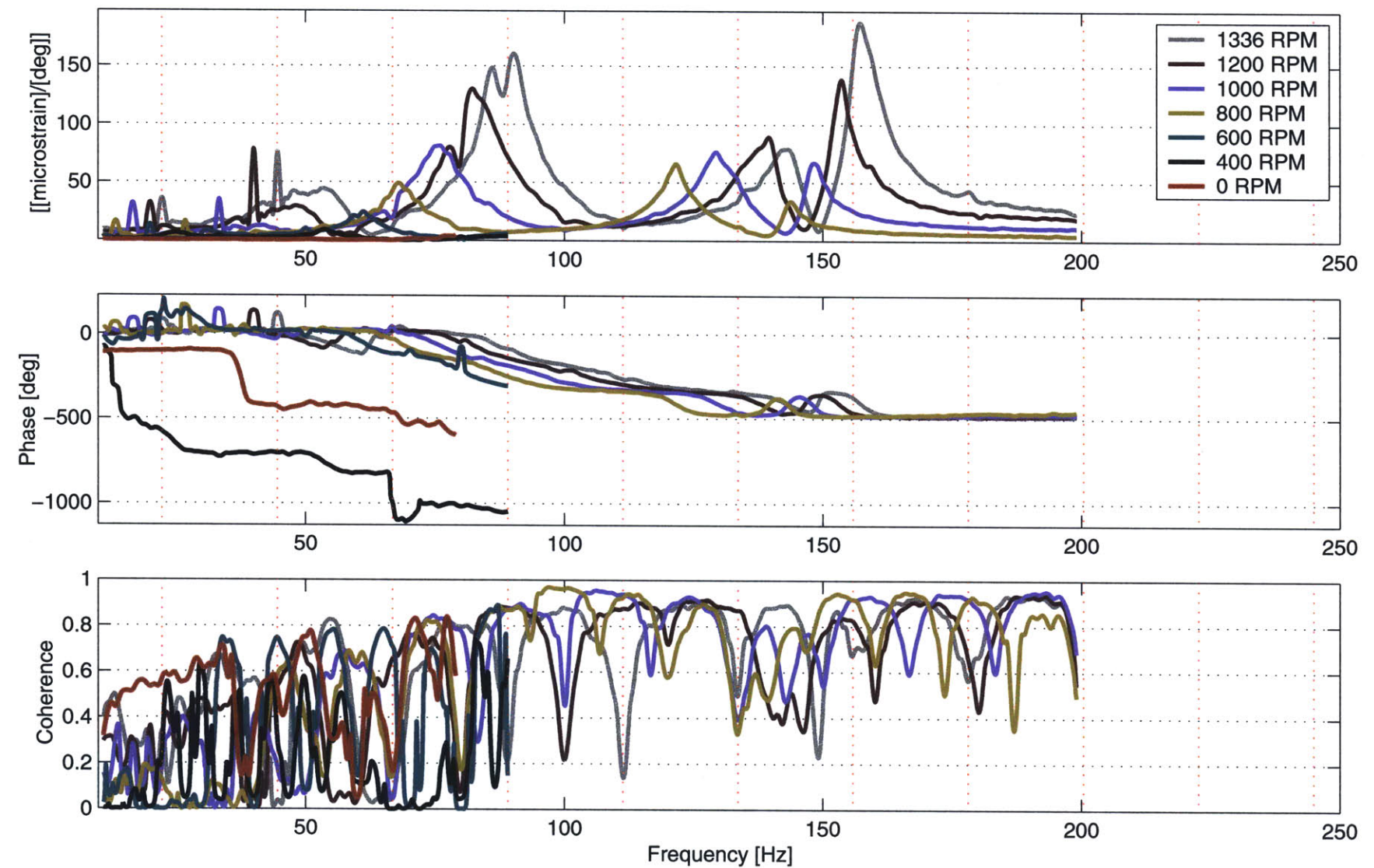


Figure C-30: Transfer function from flap deflection to axial strain at the inboard, aft corner of the actuator bay (top surface) with rotor speed

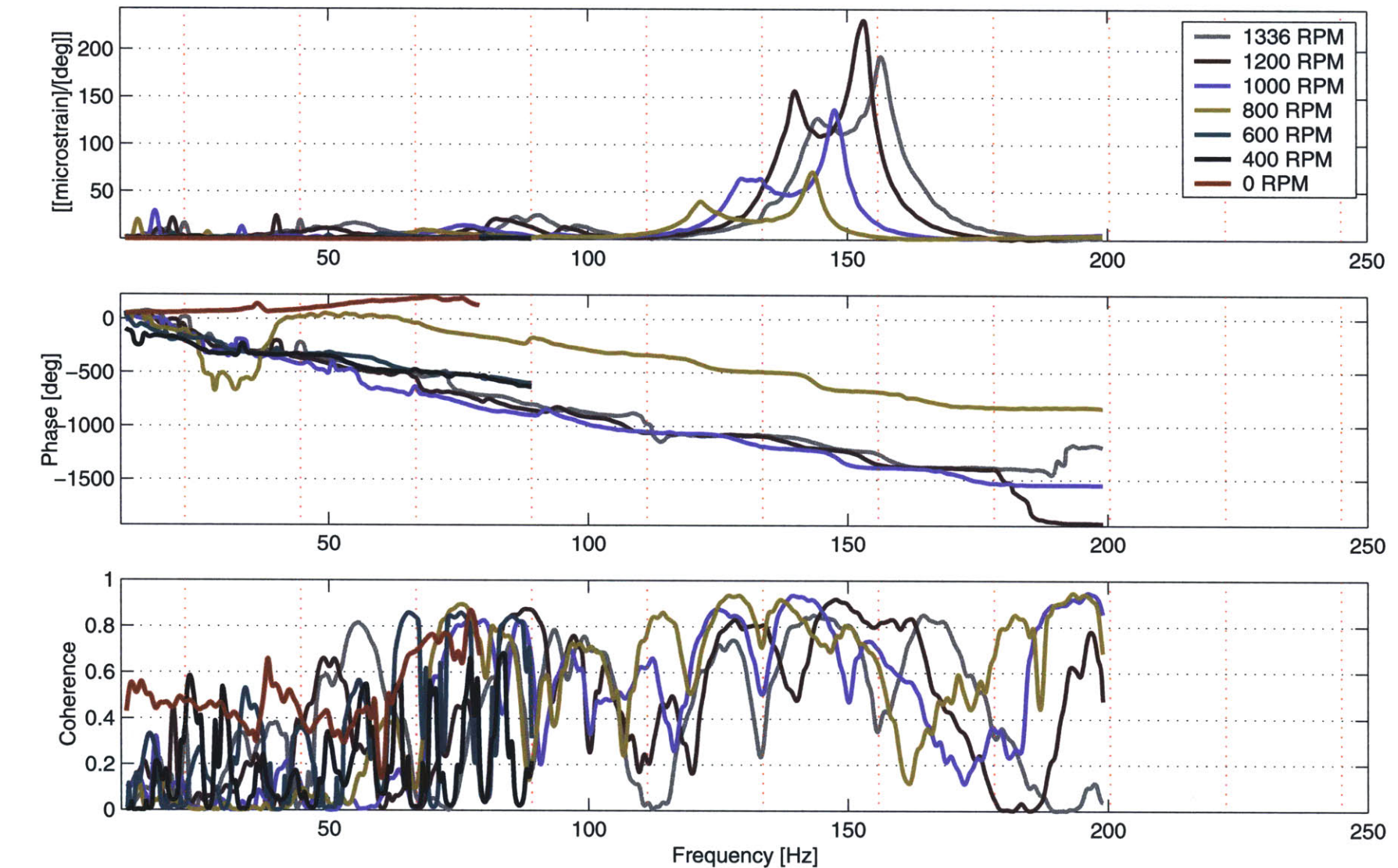


Figure C-31: Transfer function from flap deflection to axial strain in the trailing edge stiffener just inboard of servo-flap components with rotor speed

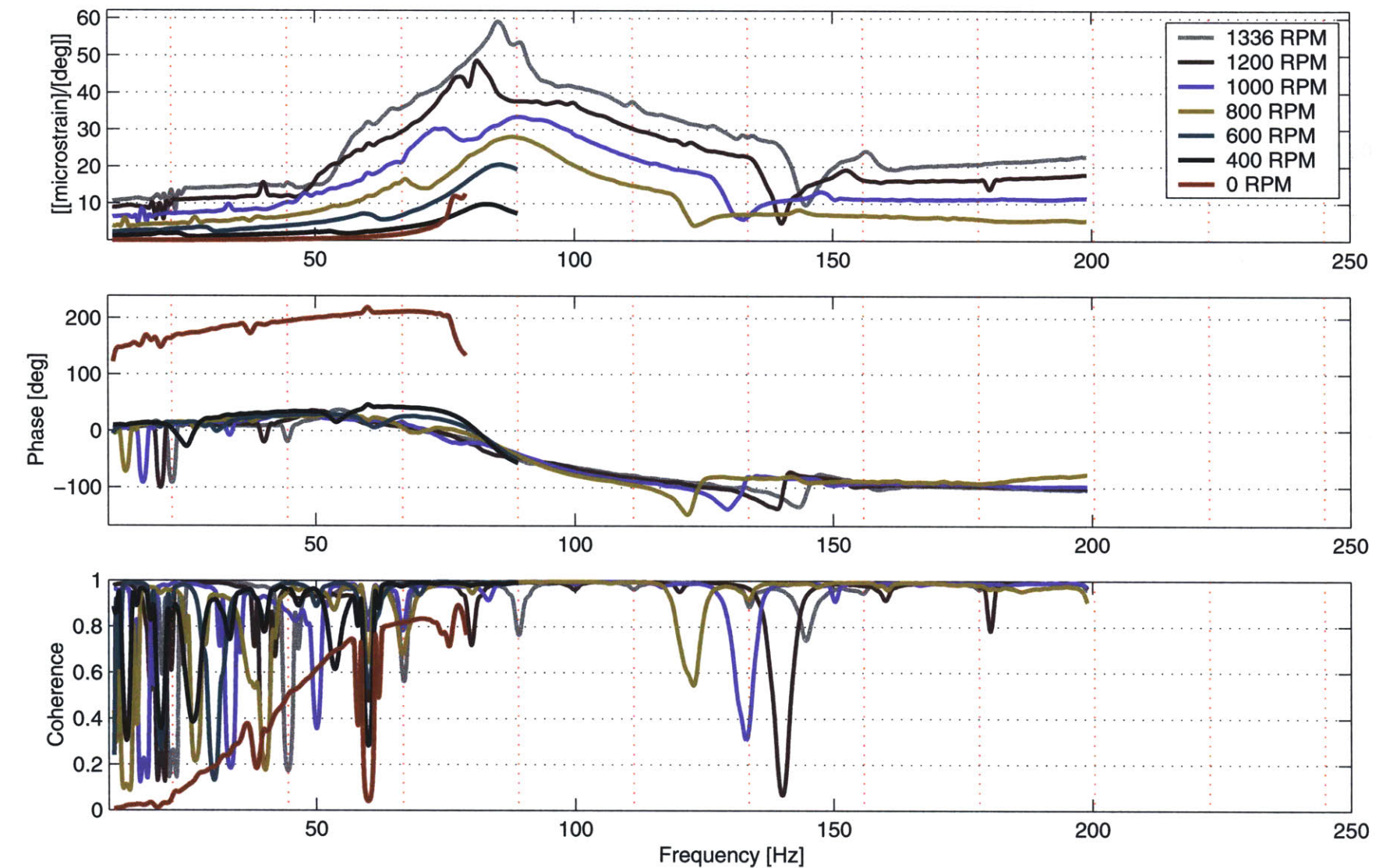


Figure C-32: Transfer function from flap deflection to torsional strain at 21%R with rotor speed

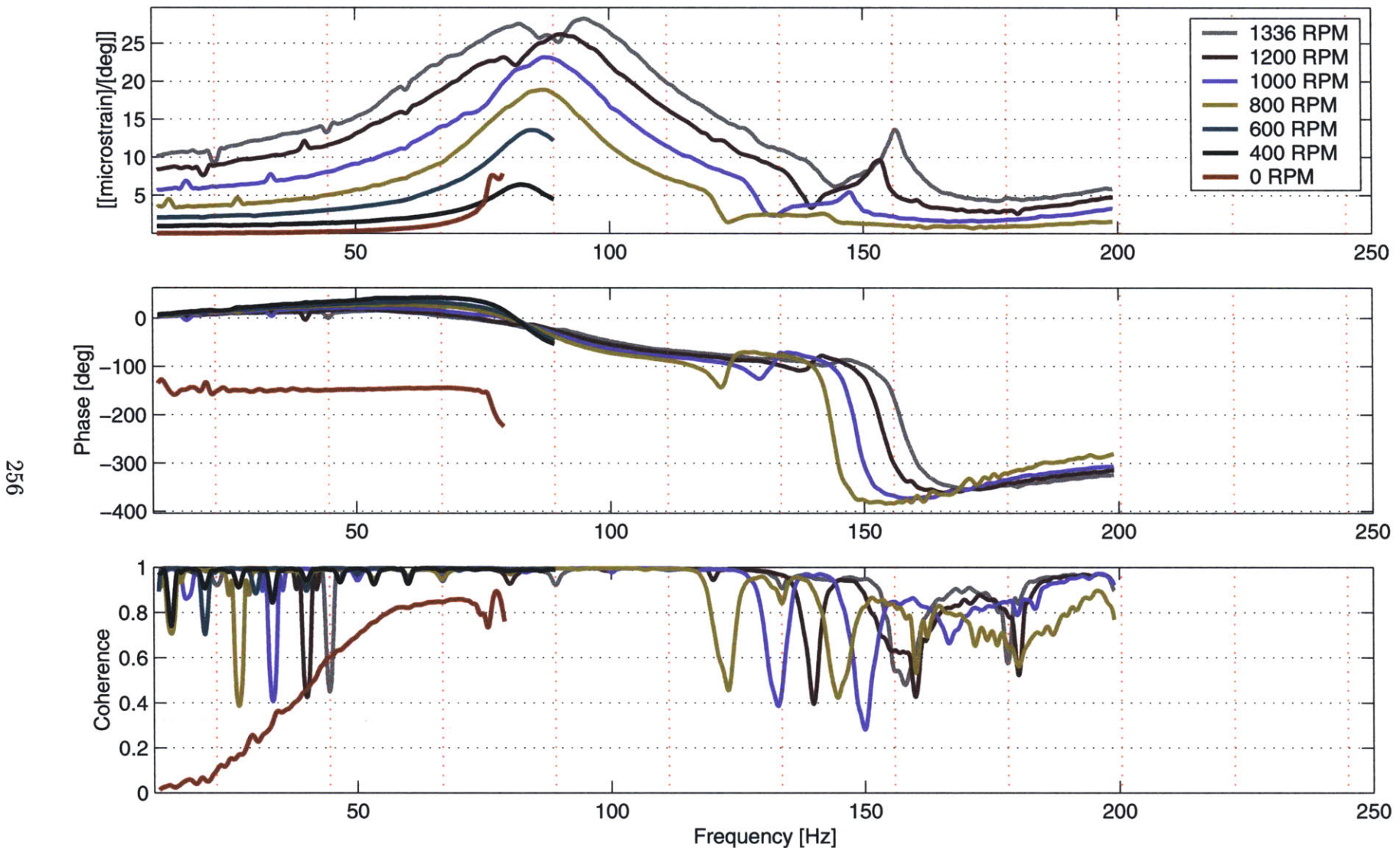


Figure C-33: Transfer function from flap deflection to torsional strain at 63%R with rotor speed

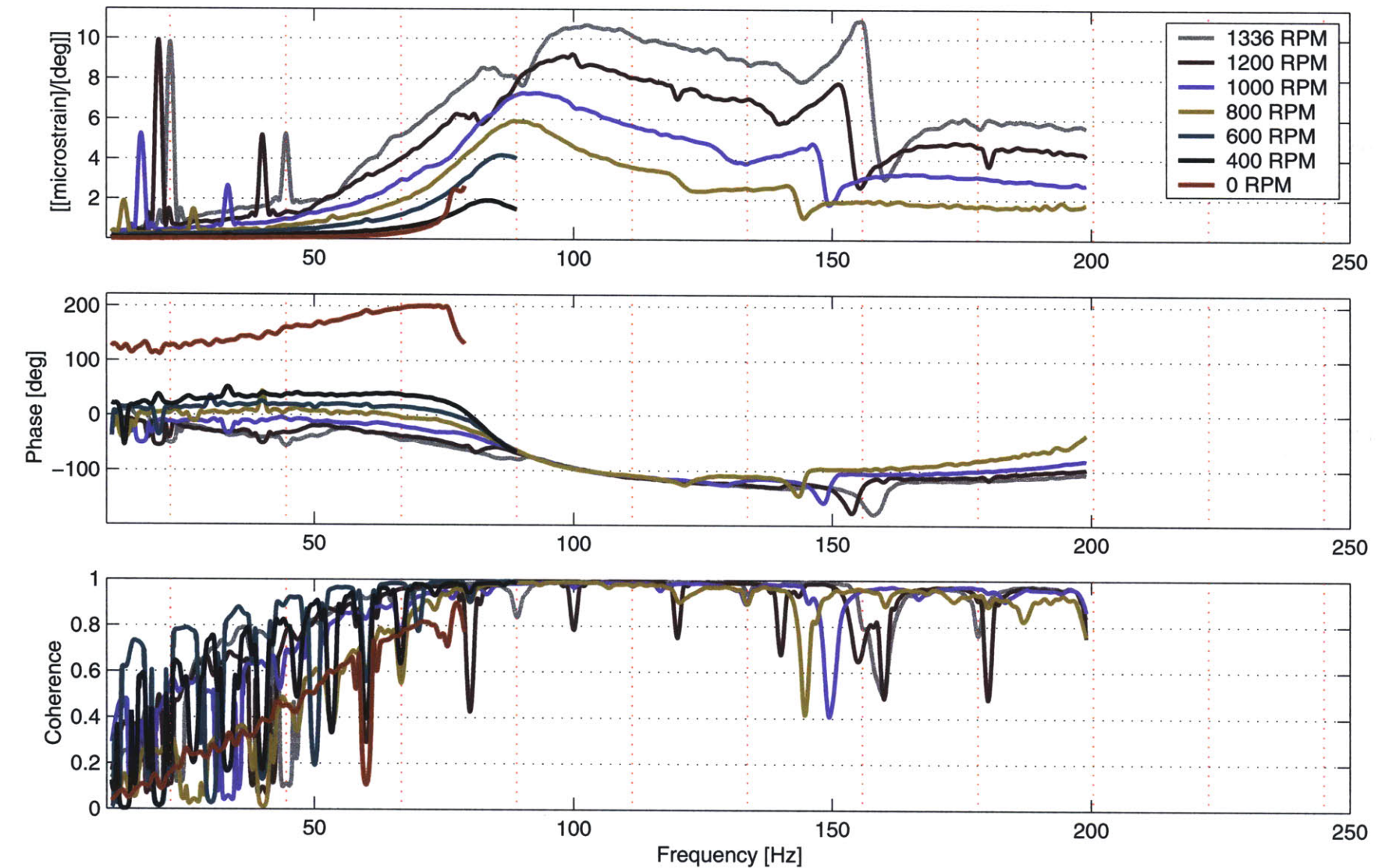


Figure C-34: Transfer function from flap deflection to torsional strain at 87%R with rotor speed

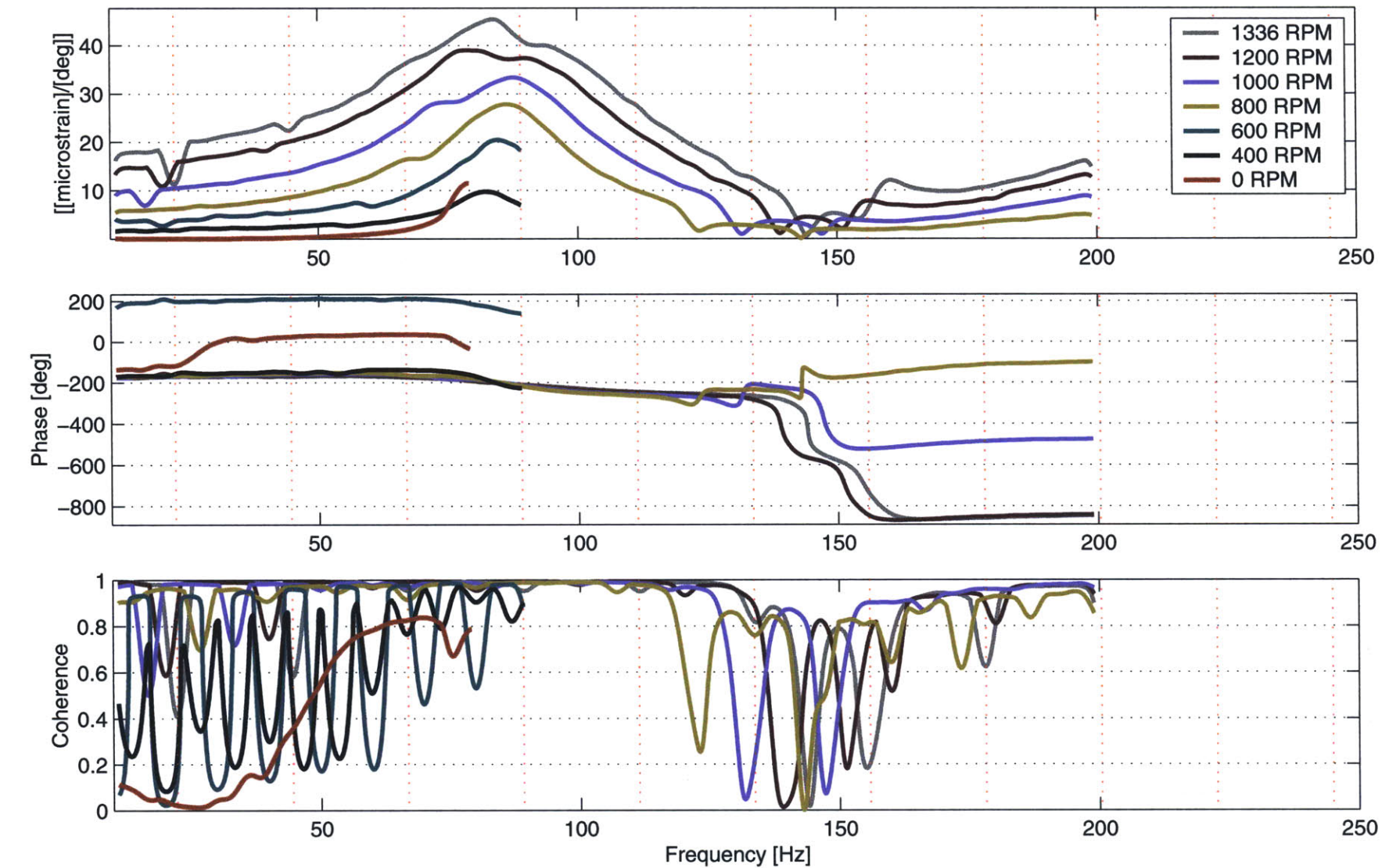


Figure C-35: Transfer function from flap deflection to shear strain just inboard of actuator bay (top surface) with rotor speed

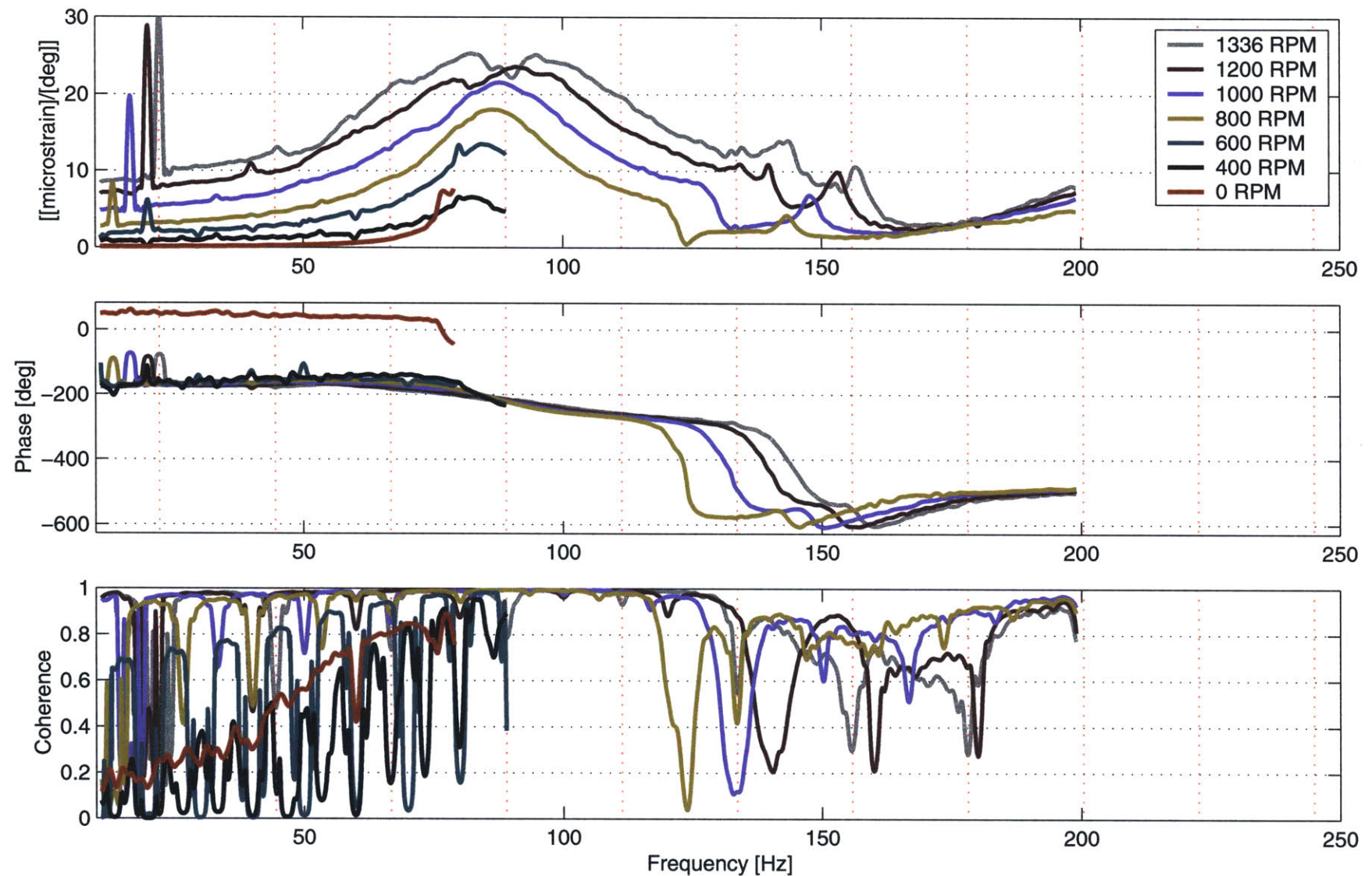


Figure C-36: Transfer function from flap deflection to shear strain just outboard of actuator bay (top surface) with rotor speed

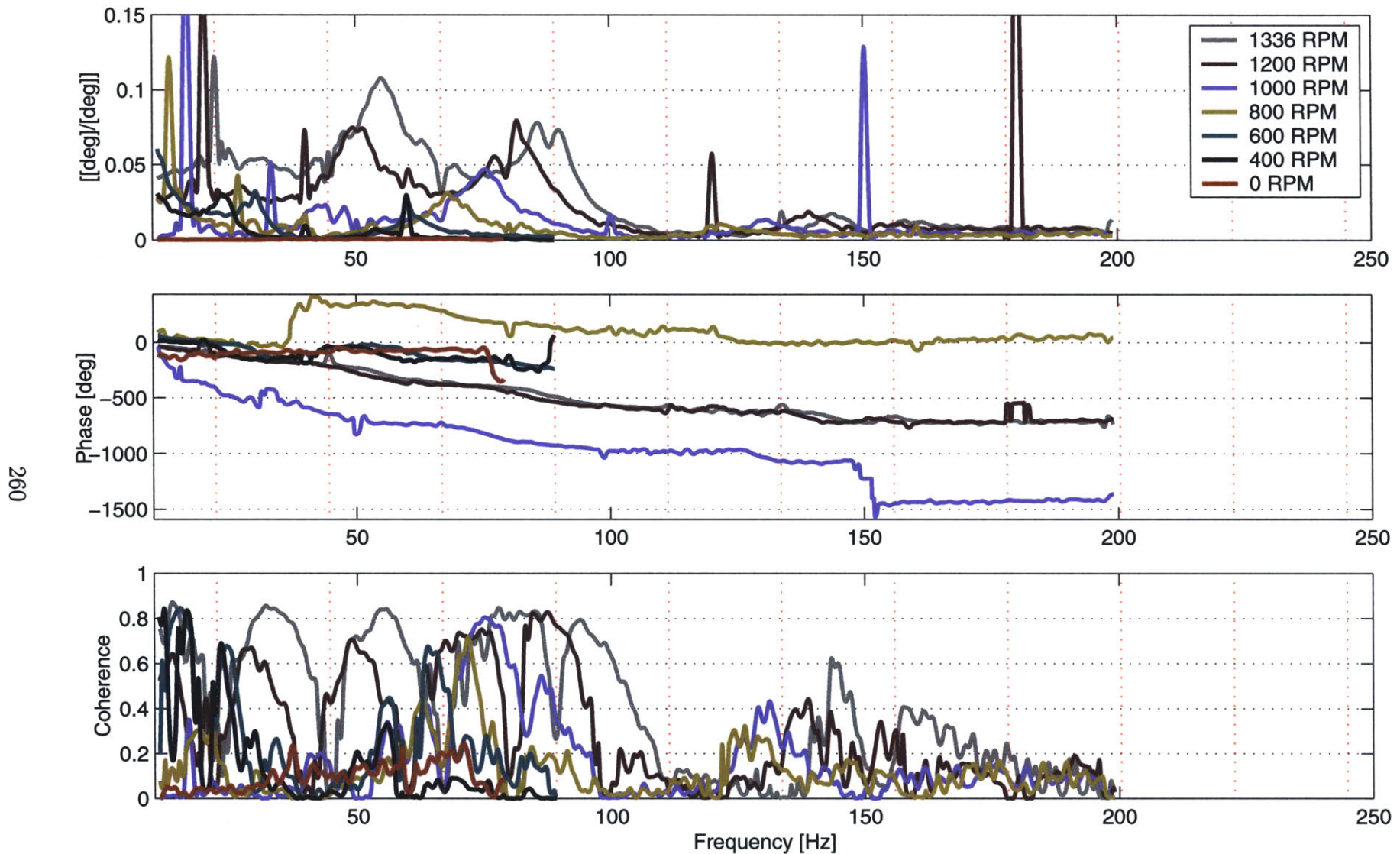


Figure C-37: Transfer function from flap deflection to blade flapping angle with rotor speed

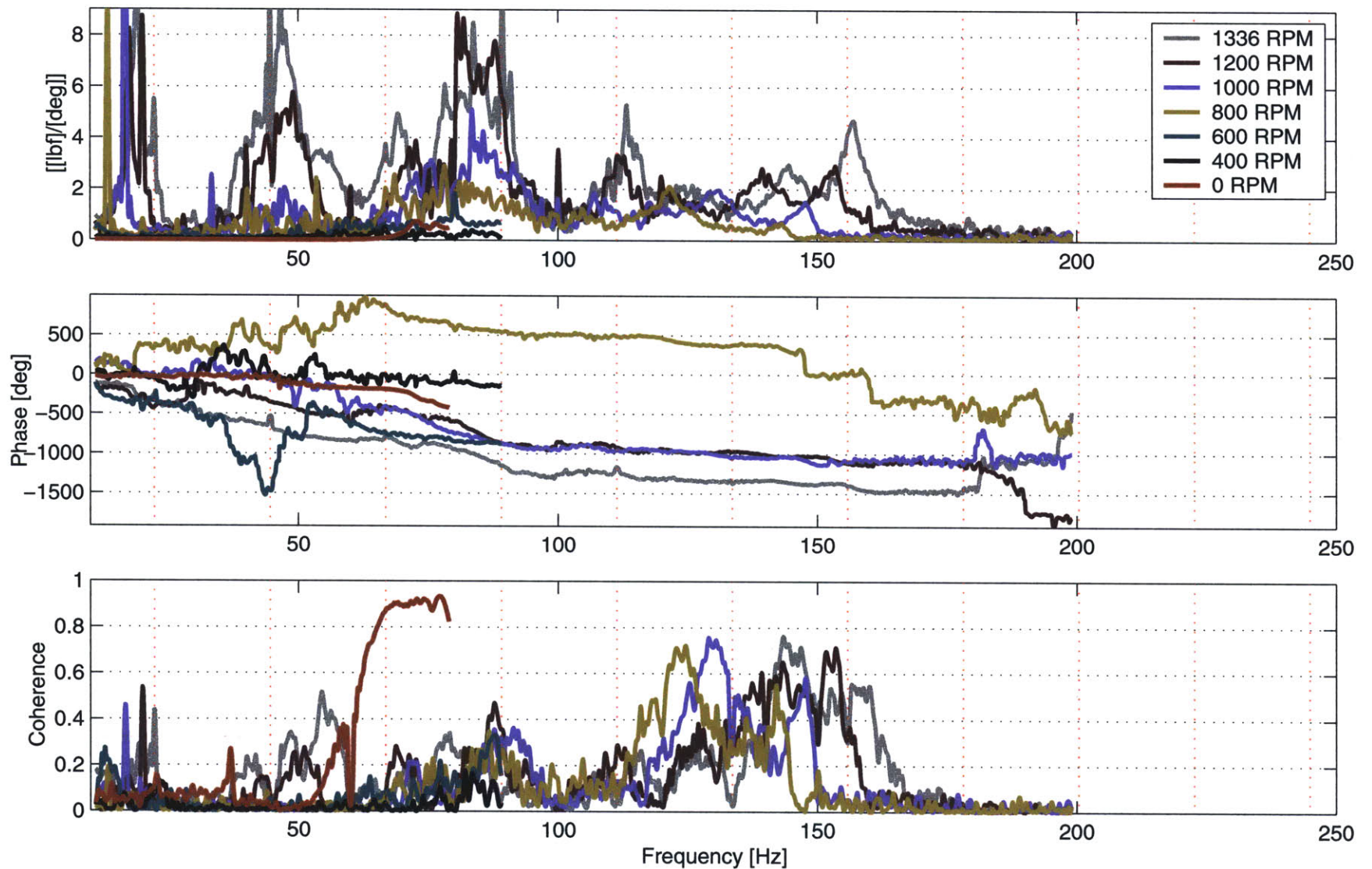


Figure C-38: Transfer function from flap deflection to  $F_x$  at hub with rotor speed

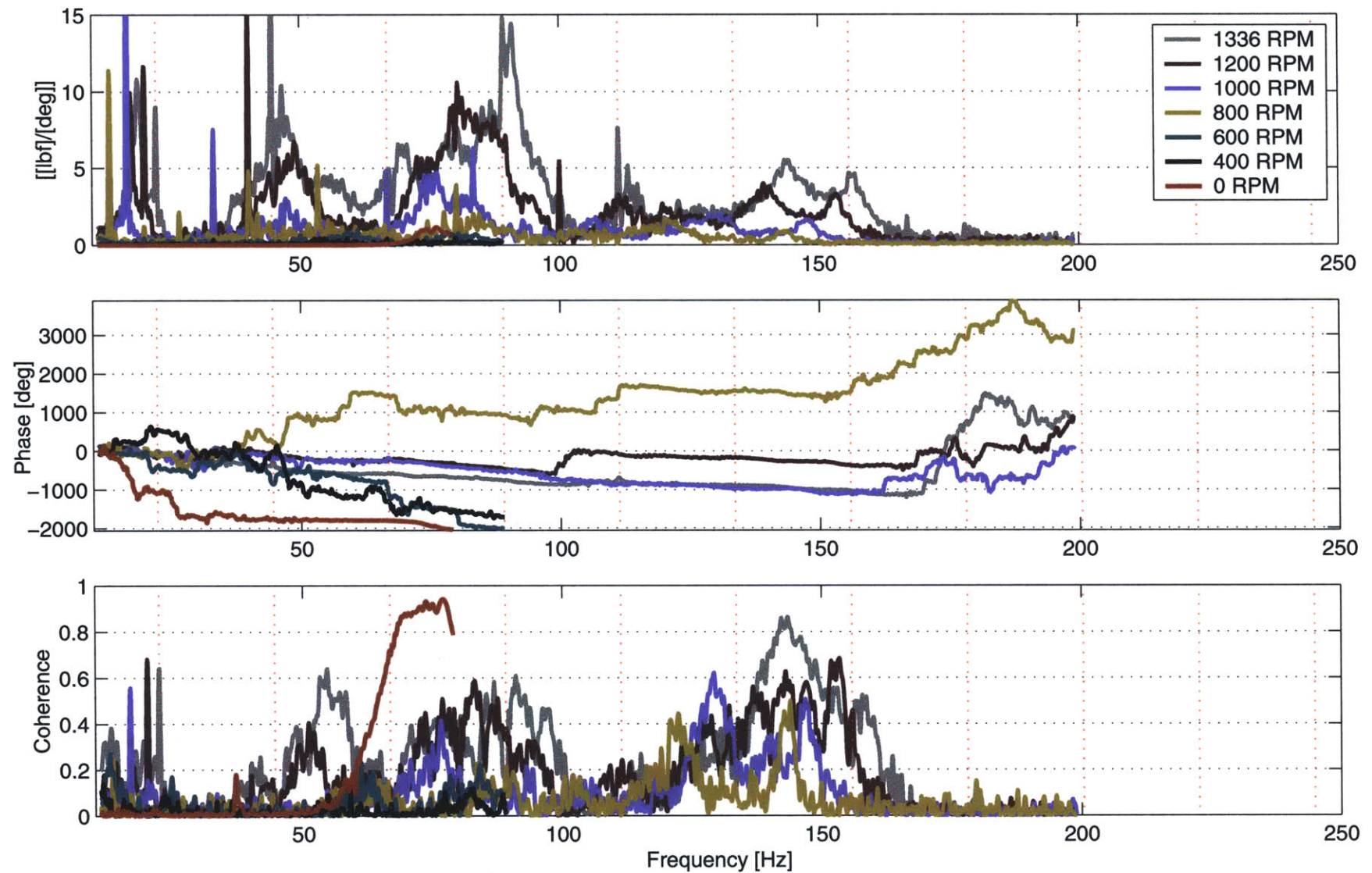


Figure C-39: Transfer function from flap deflection to  $F_y$  at hub with rotor speed

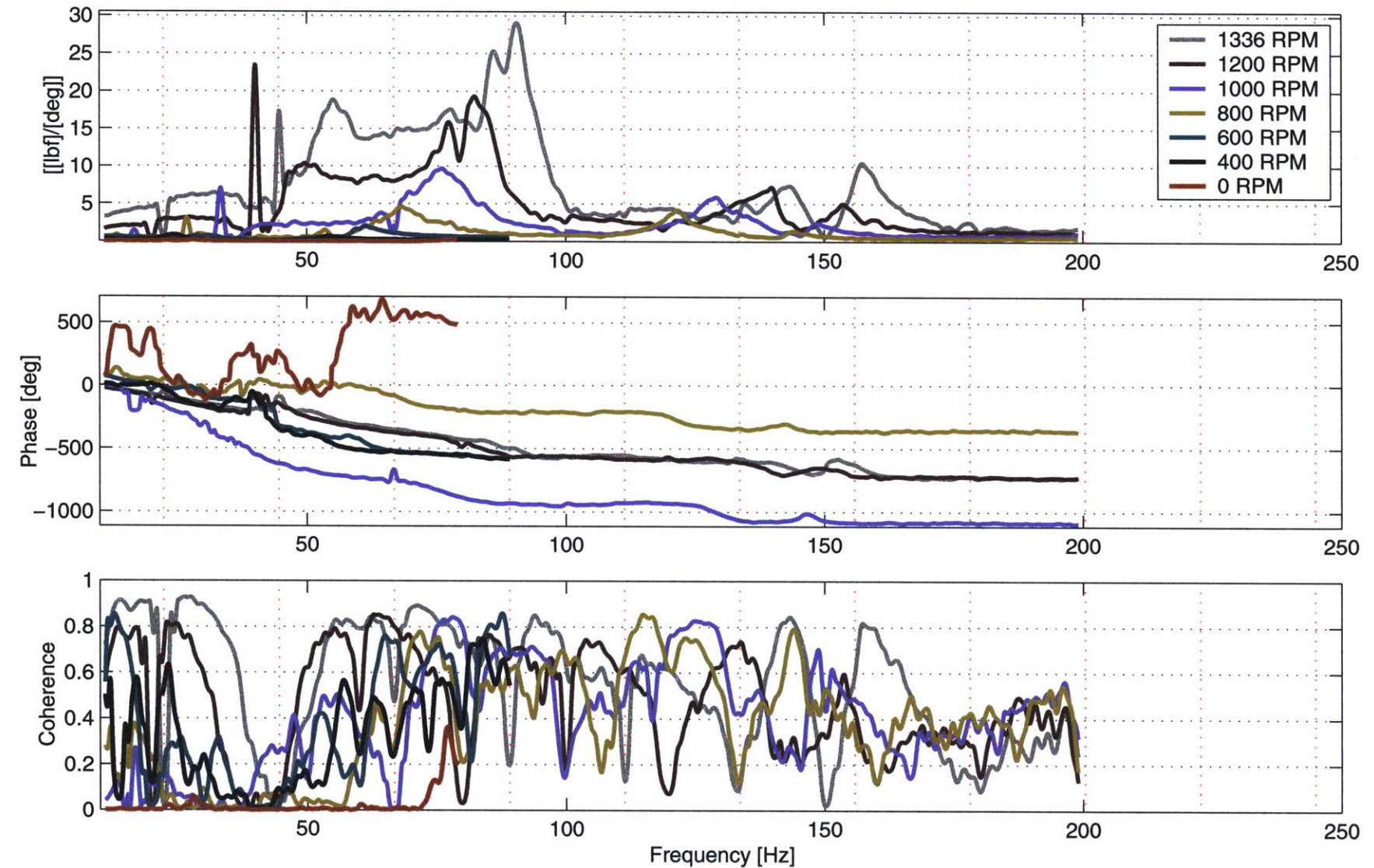


Figure C-40: Transfer function from flap deflection to  $F_z$  at hub with rotor speed

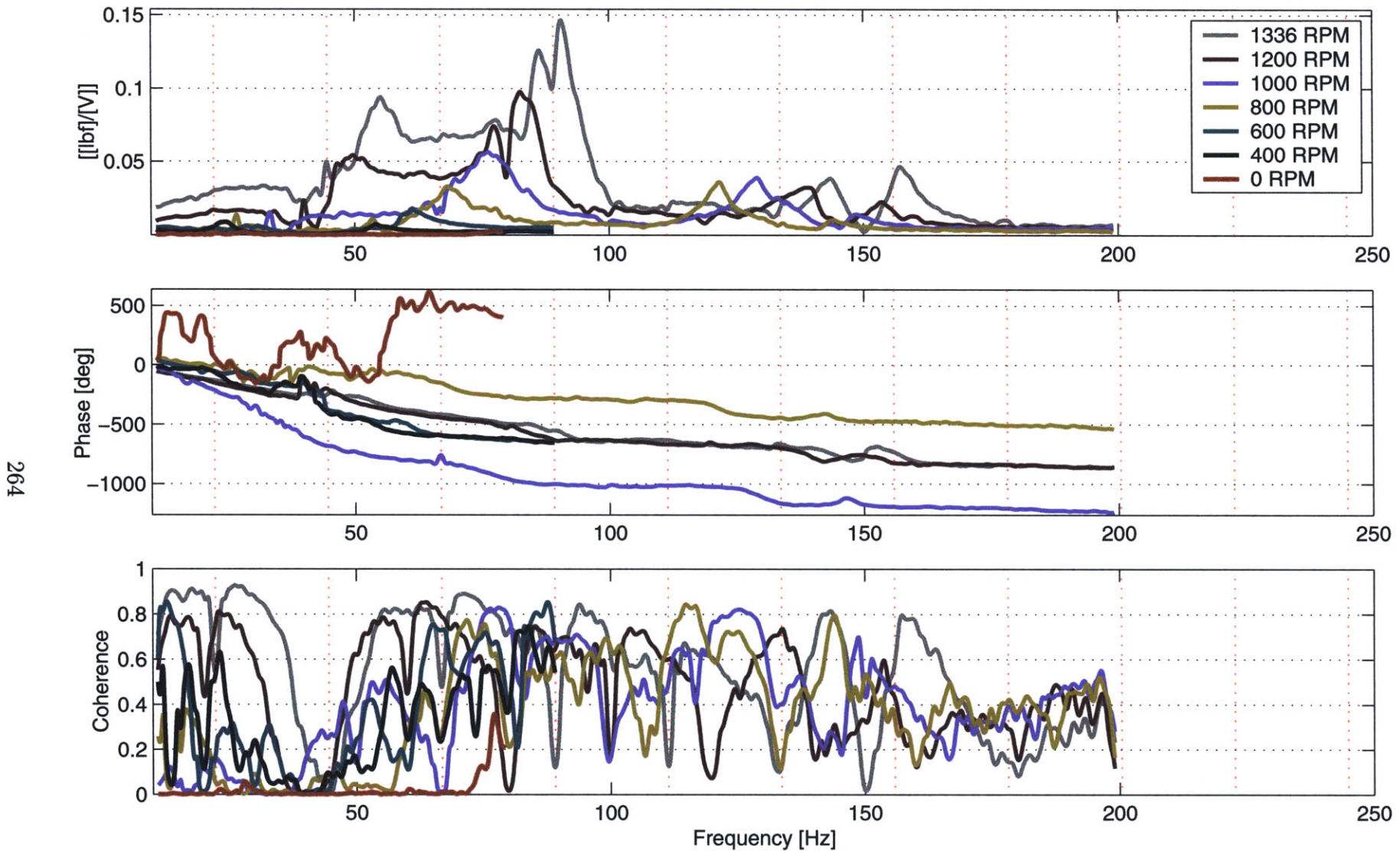


Figure C-41: Transfer function from applied voltage to  $F_z$  at hub with rotor speed

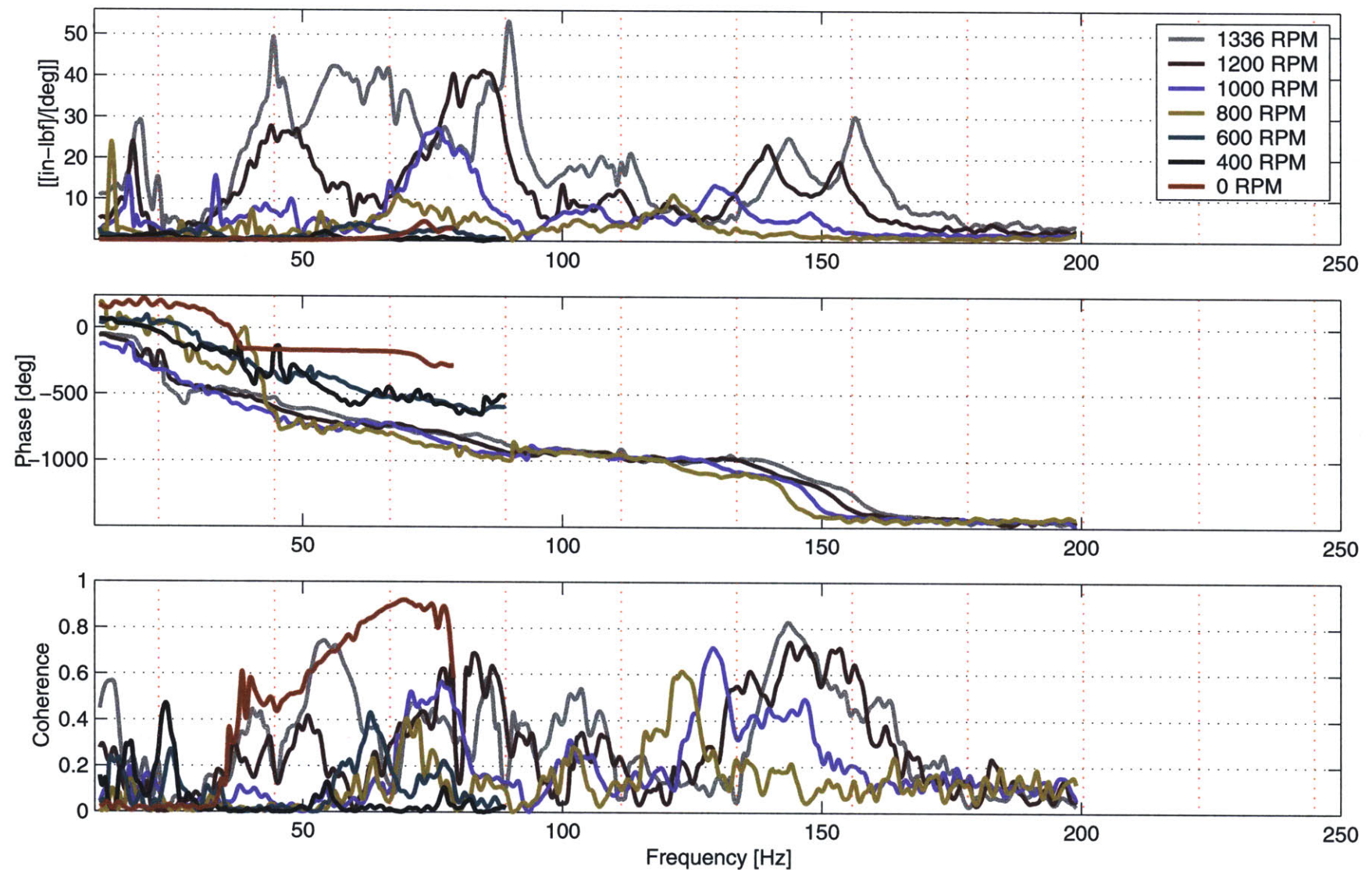


Figure C-42: Transfer function from flap deflection to  $M_x$  at hub with rotor speed

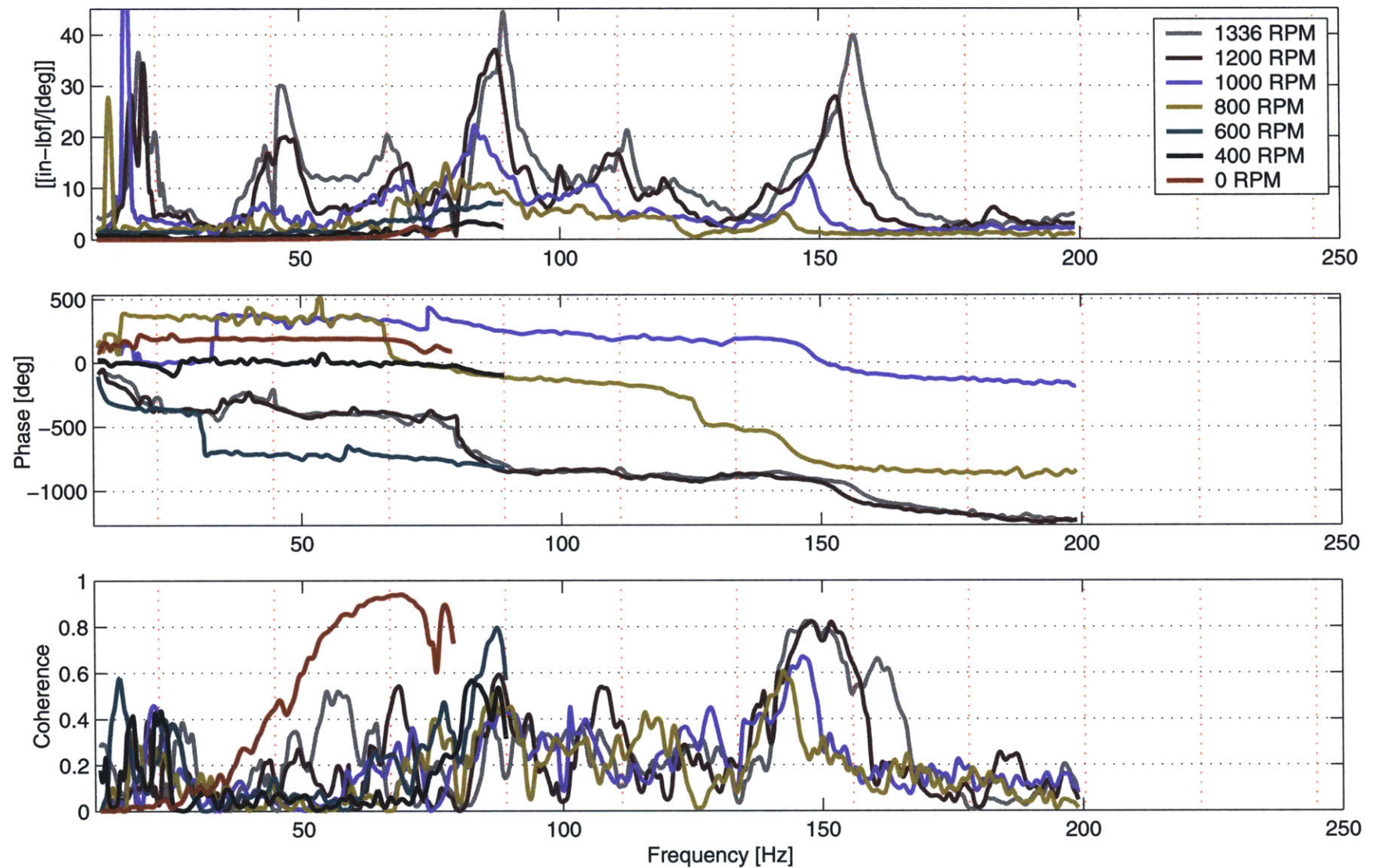


Figure C-43: Transfer function from flap deflection to  $M_y$  at hub with rotor speed

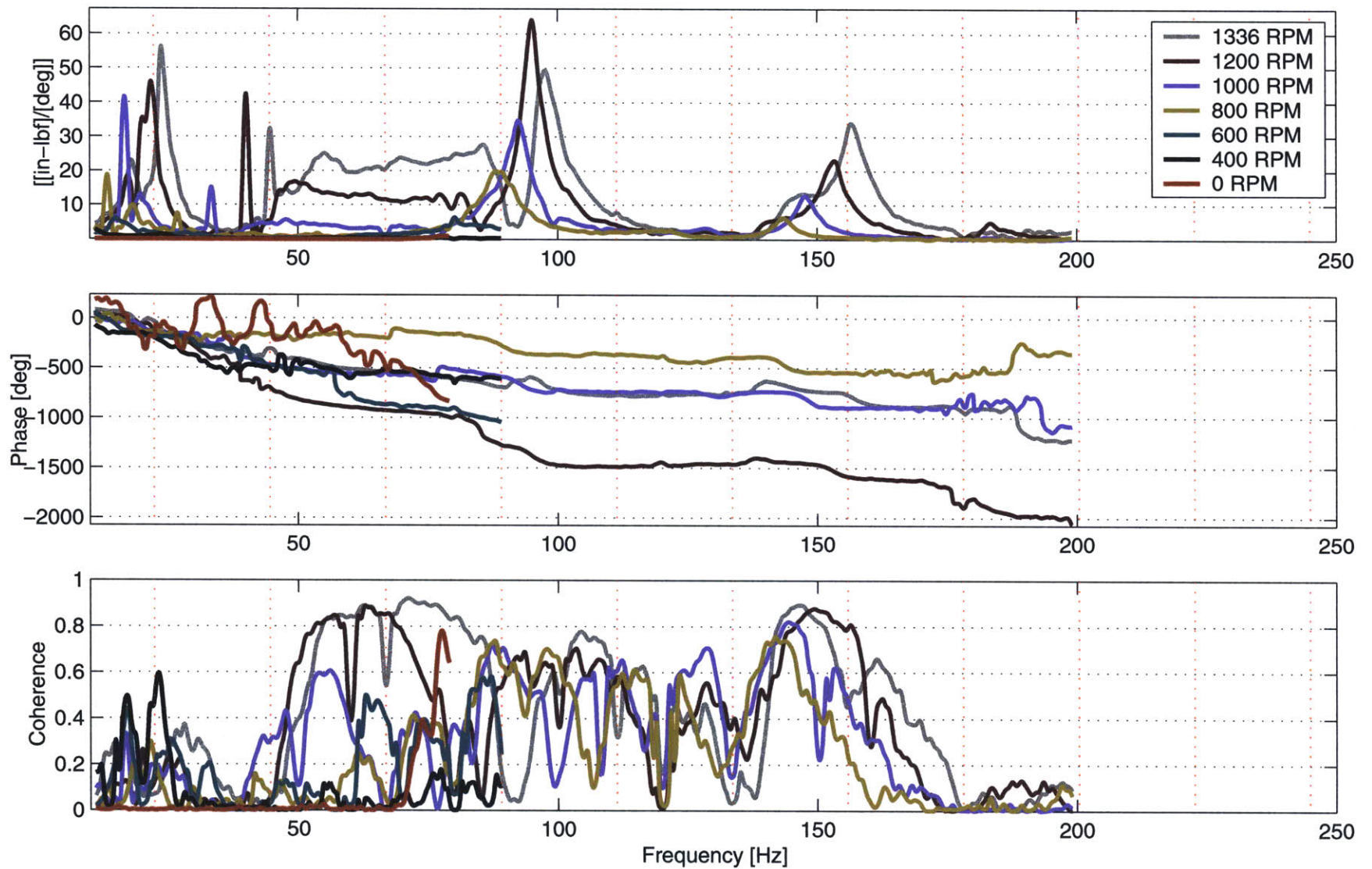


Figure C-44: Transfer function from flap deflection to  $M_z$  at hub with rotor speed



# Appendix D

## Closed-Loop Rotor Control Plots

This appendix contains, for each continuous time controller implemented, the Bode and Nichols plots as well as a comparison of the open and closed loop vibration spectra for six components of force/moment measured at the rotor hub. In addition, a comparison of the open and closed loop vibration spectra for the hub forces/moments for the discrete time controllers is presented. This appendix complements the discussions in Chapter 5.

The results from ten different controllers are presented in this appendix. As discussed in Chapter 5, the gain and phase of each individual controller was adjusted to maximize stability margins. The gain and phase adjustments to each of the controllers presented in this appendix were given originally in Tables 5.4, 5.1, and 5.3.

270

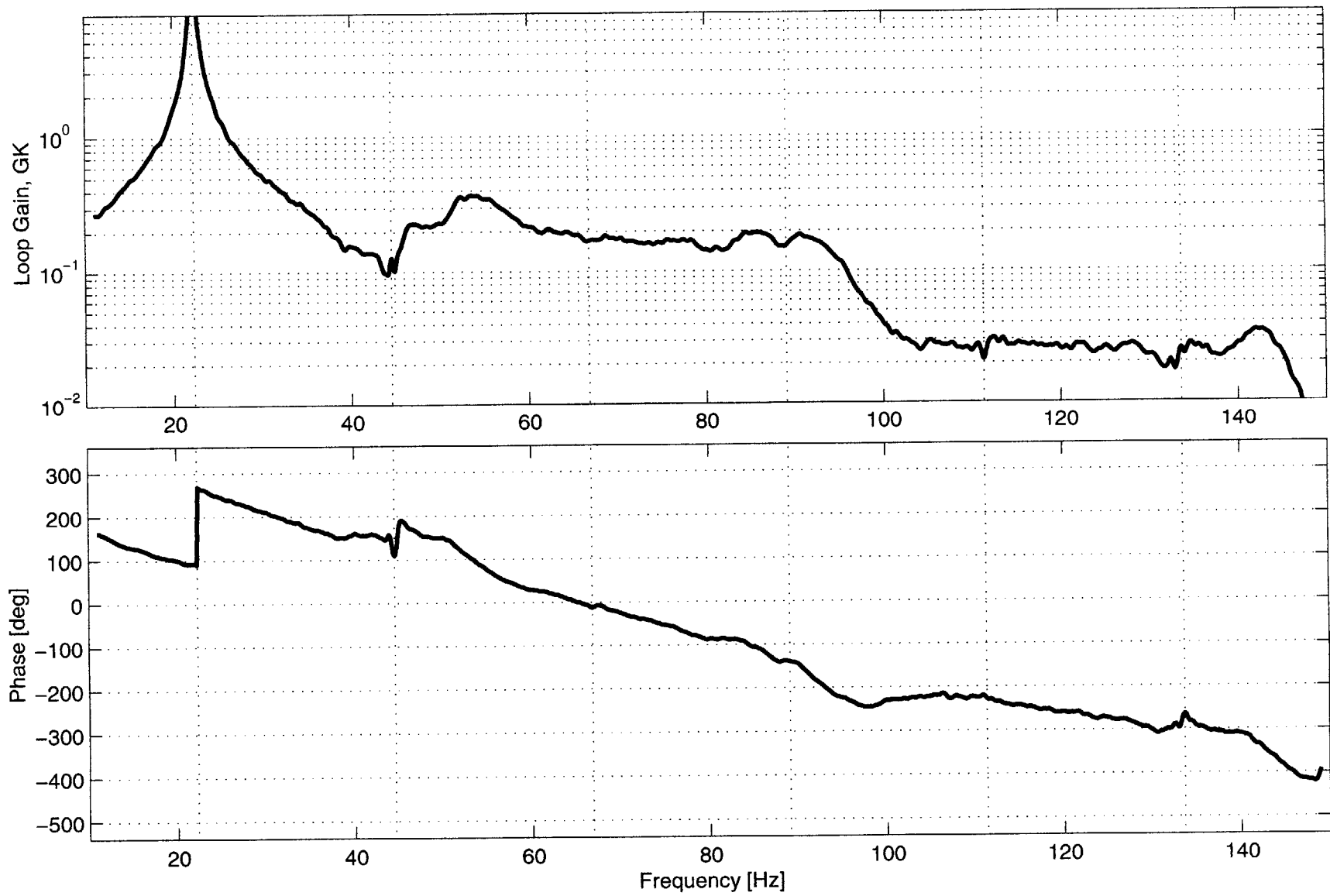


Figure D-1: Loop transfer bode plot of the 1/rev controller

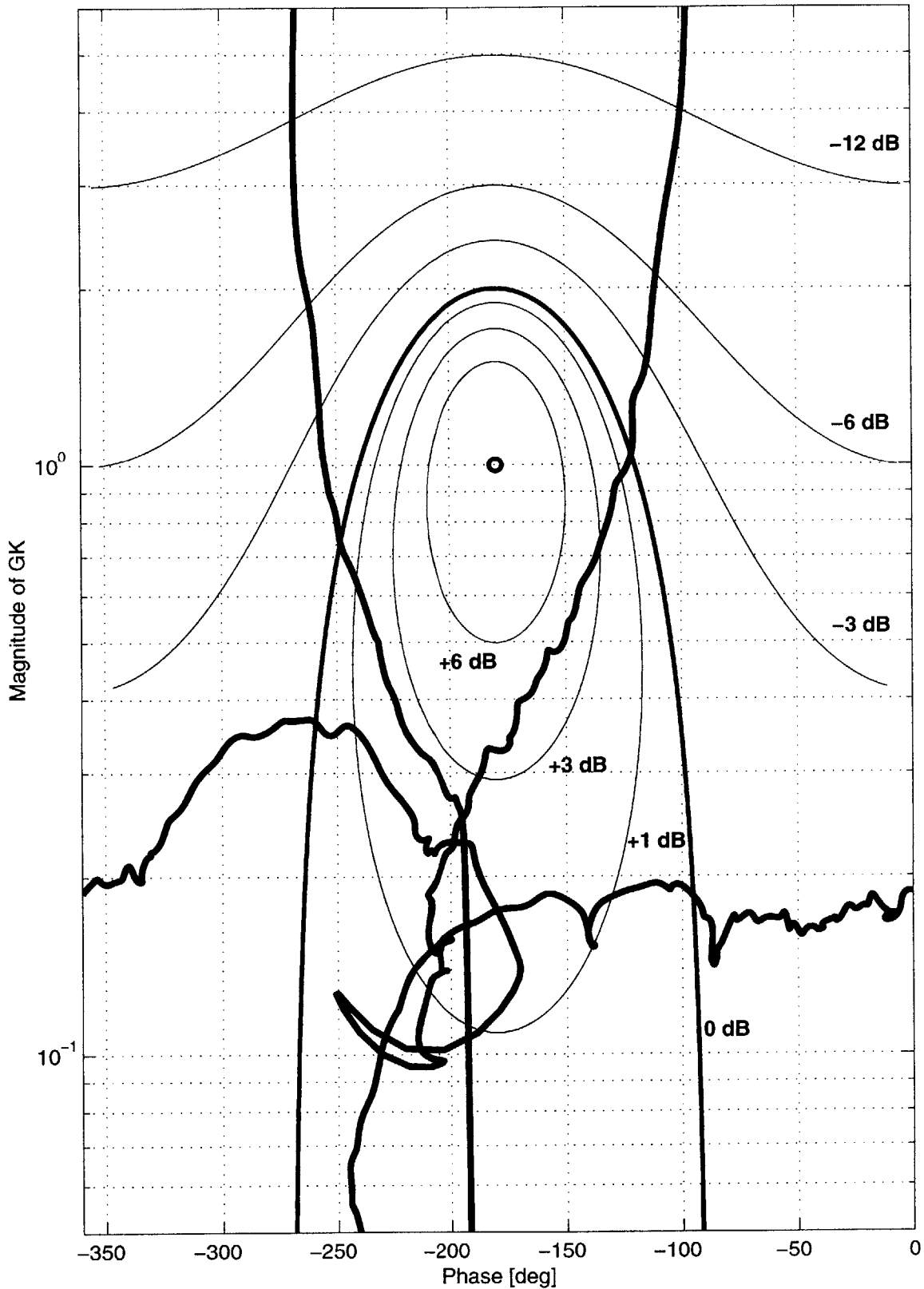


Figure D-2: Nichols plot of the 1/rev controller

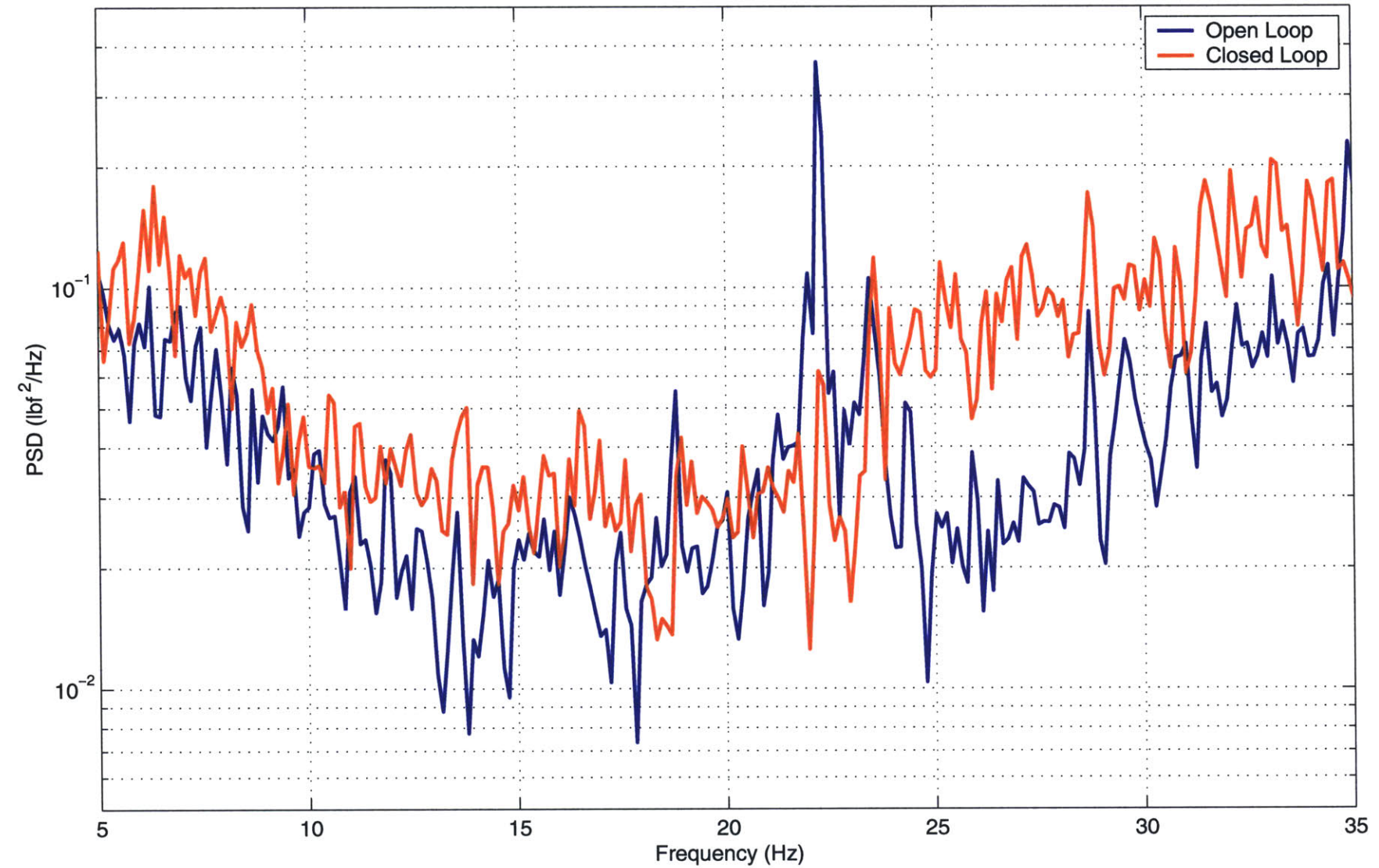


Figure D-3: Comparison of the open and closed loop vertical hub shear for the 1/rev controller

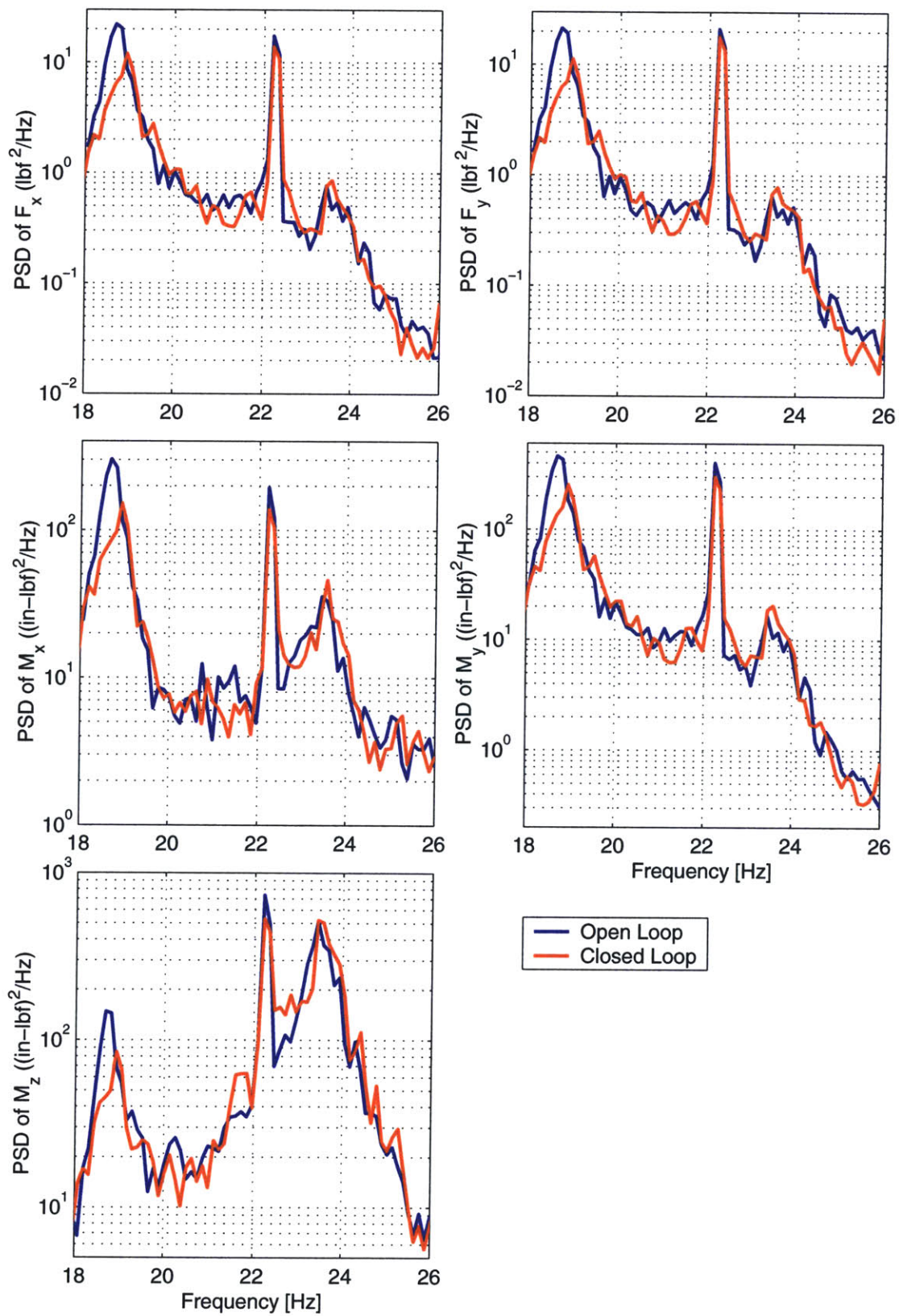


Figure D-4: Comparison of the open and closed loop measurements of the uncontrolled hub forces and moments for the 1/rev controller

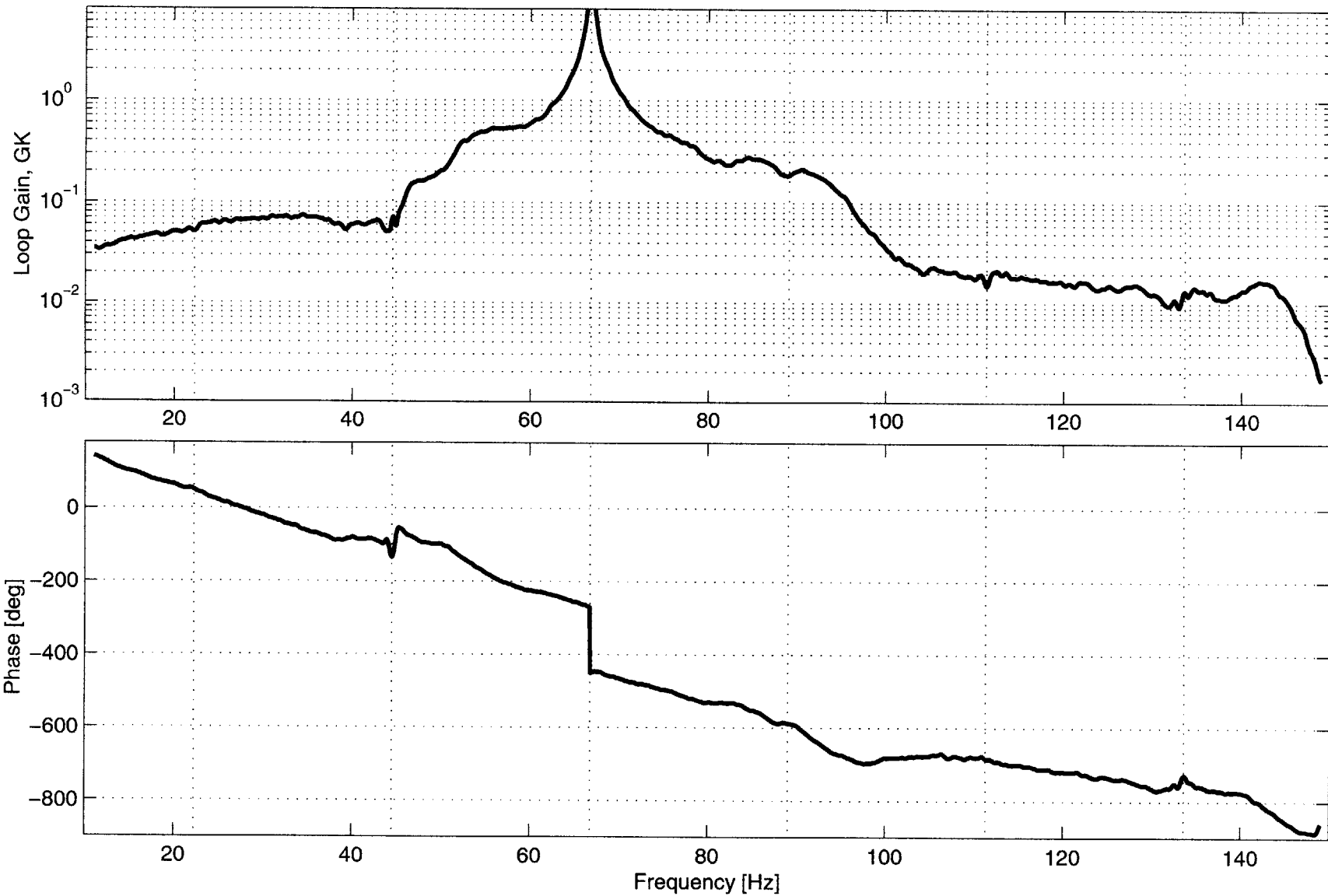


Figure D-5: Loop transfer bode plot of the 3/rev controller

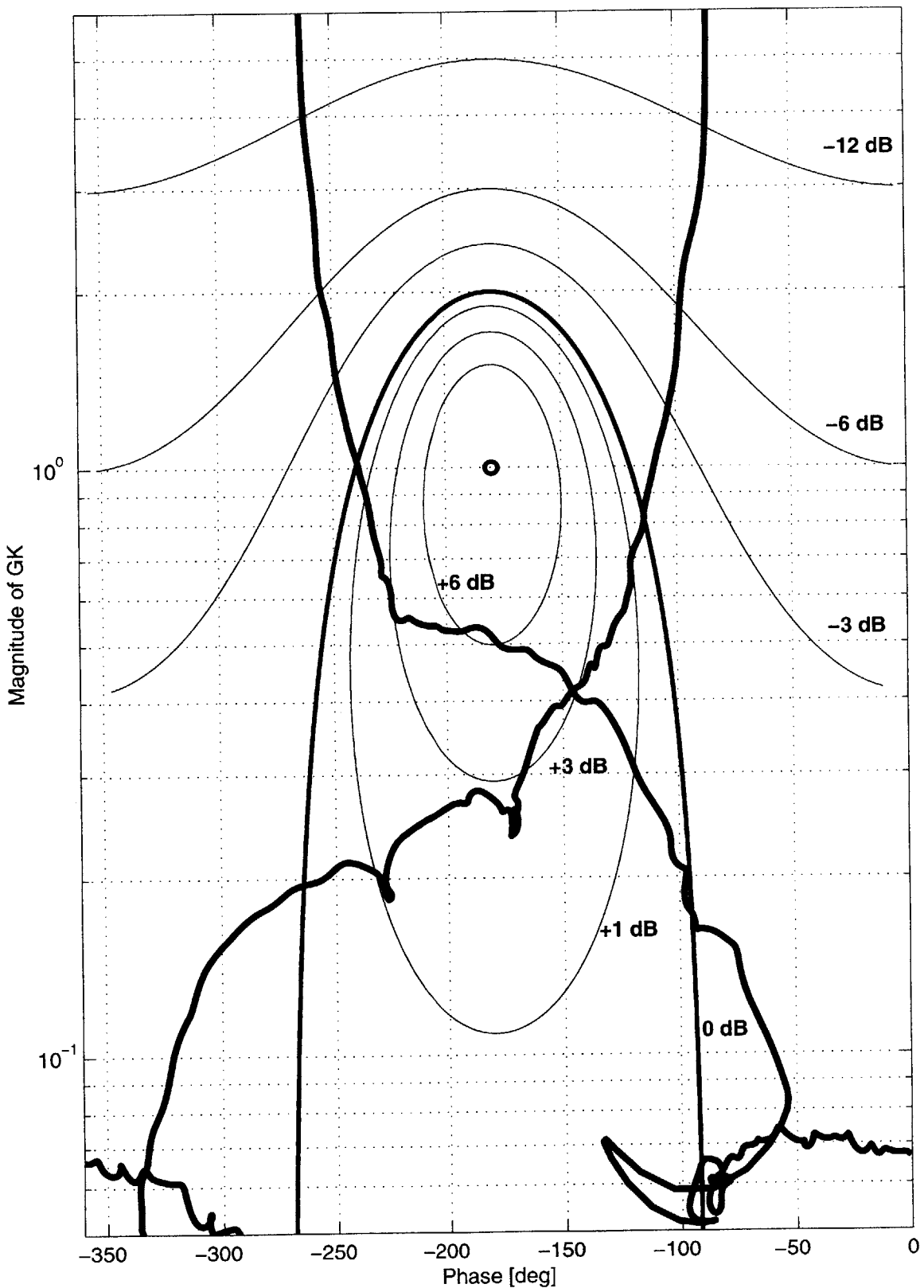


Figure D-6: Nichols plot of the 3/rev controller

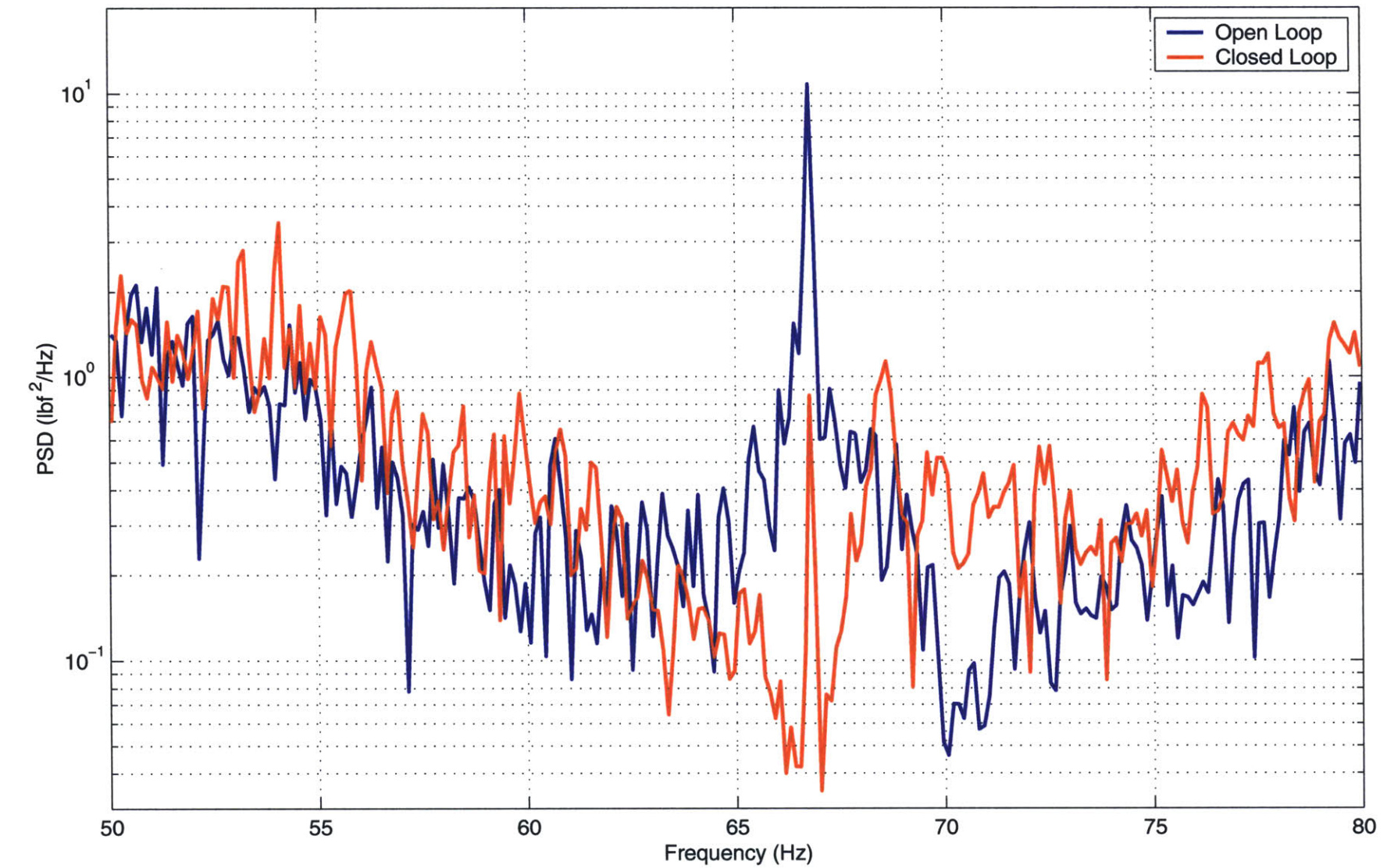


Figure D-7: Comparison of the open and closed loop vertical hub shear for the 3/rev controller

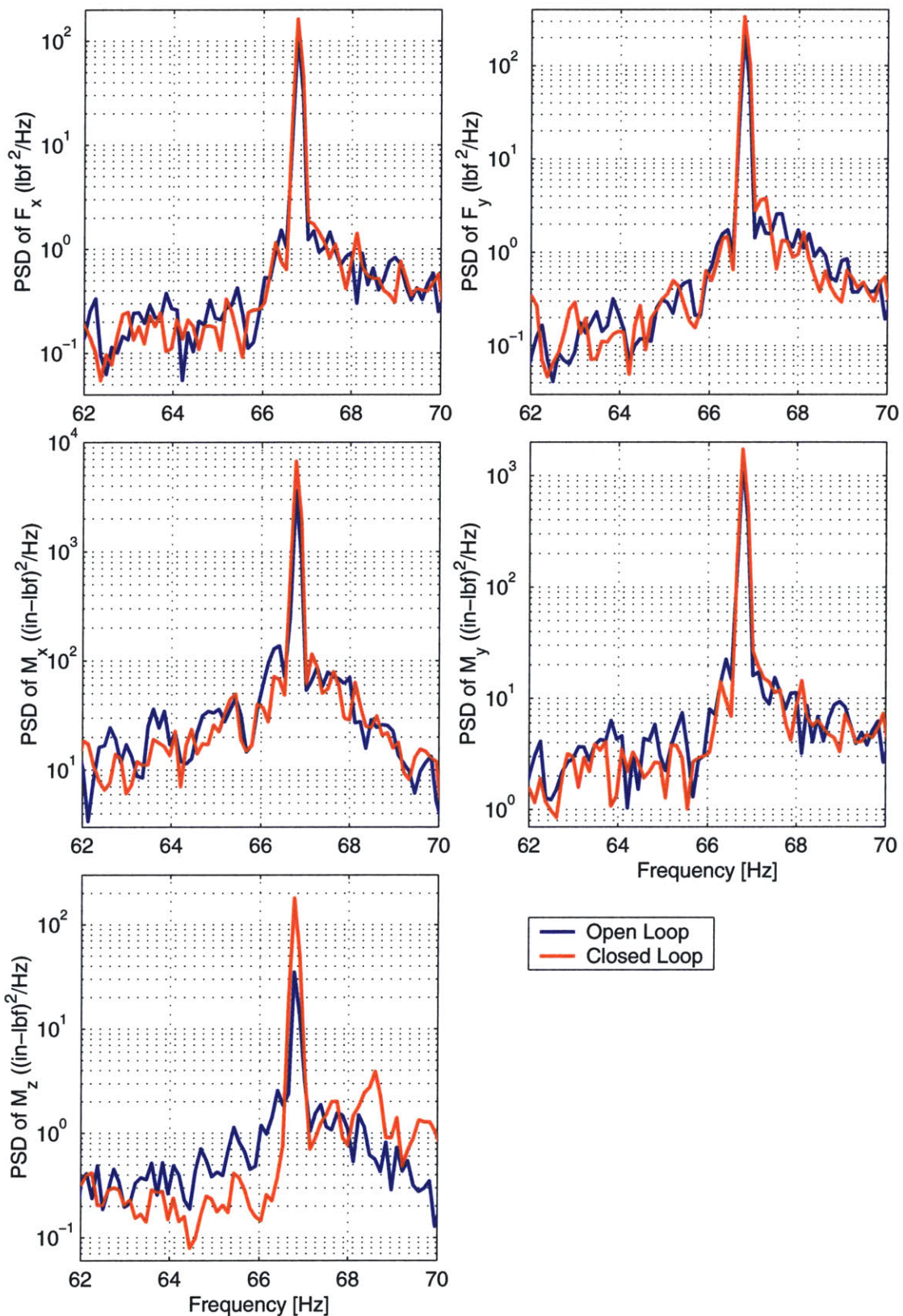


Figure D-8: Comparison of the open and closed loop measurements of the uncontrolled hub forces and moments for the 3/rev controller

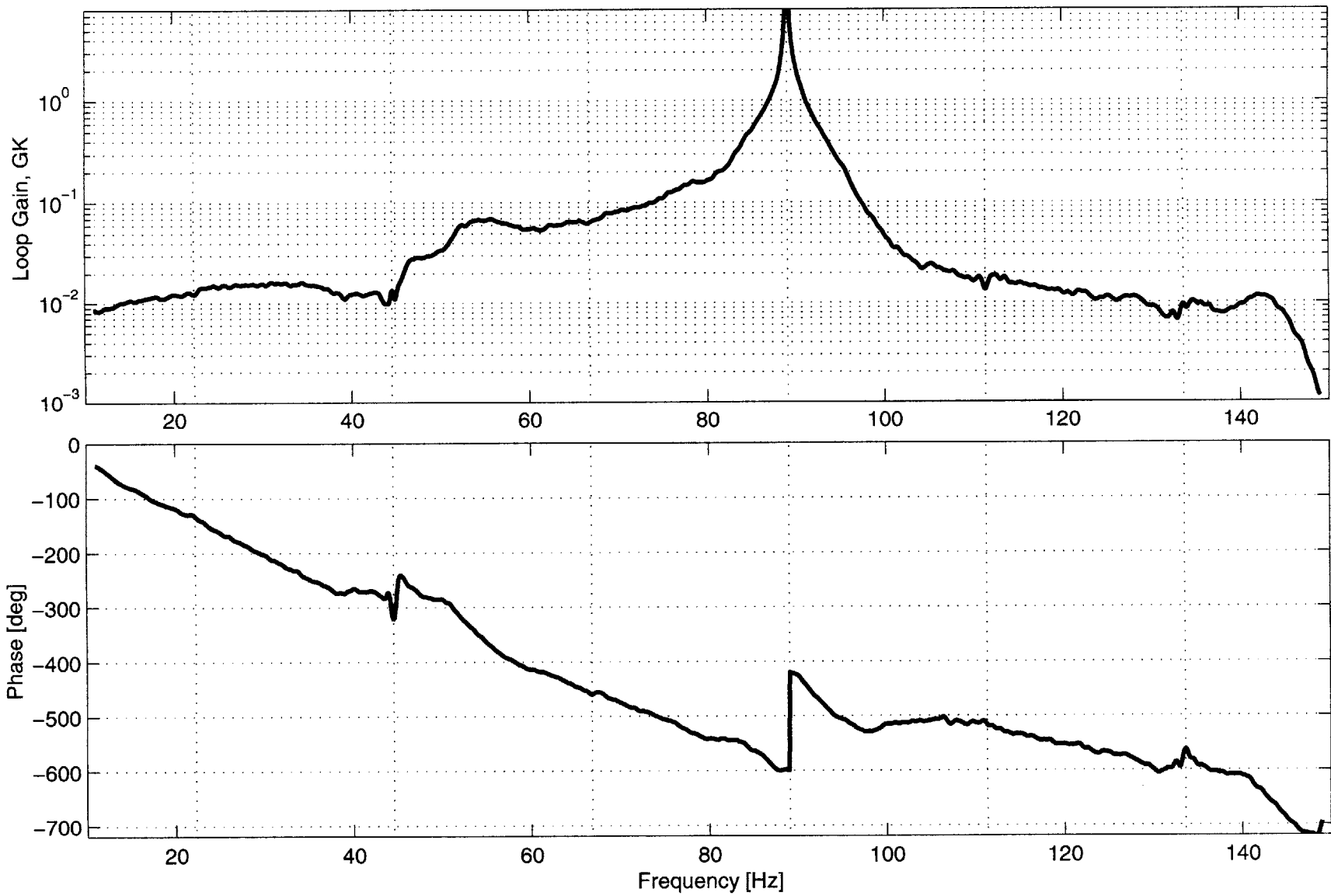


Figure D-9: Loop transfer bode plot of the 4/rev controller

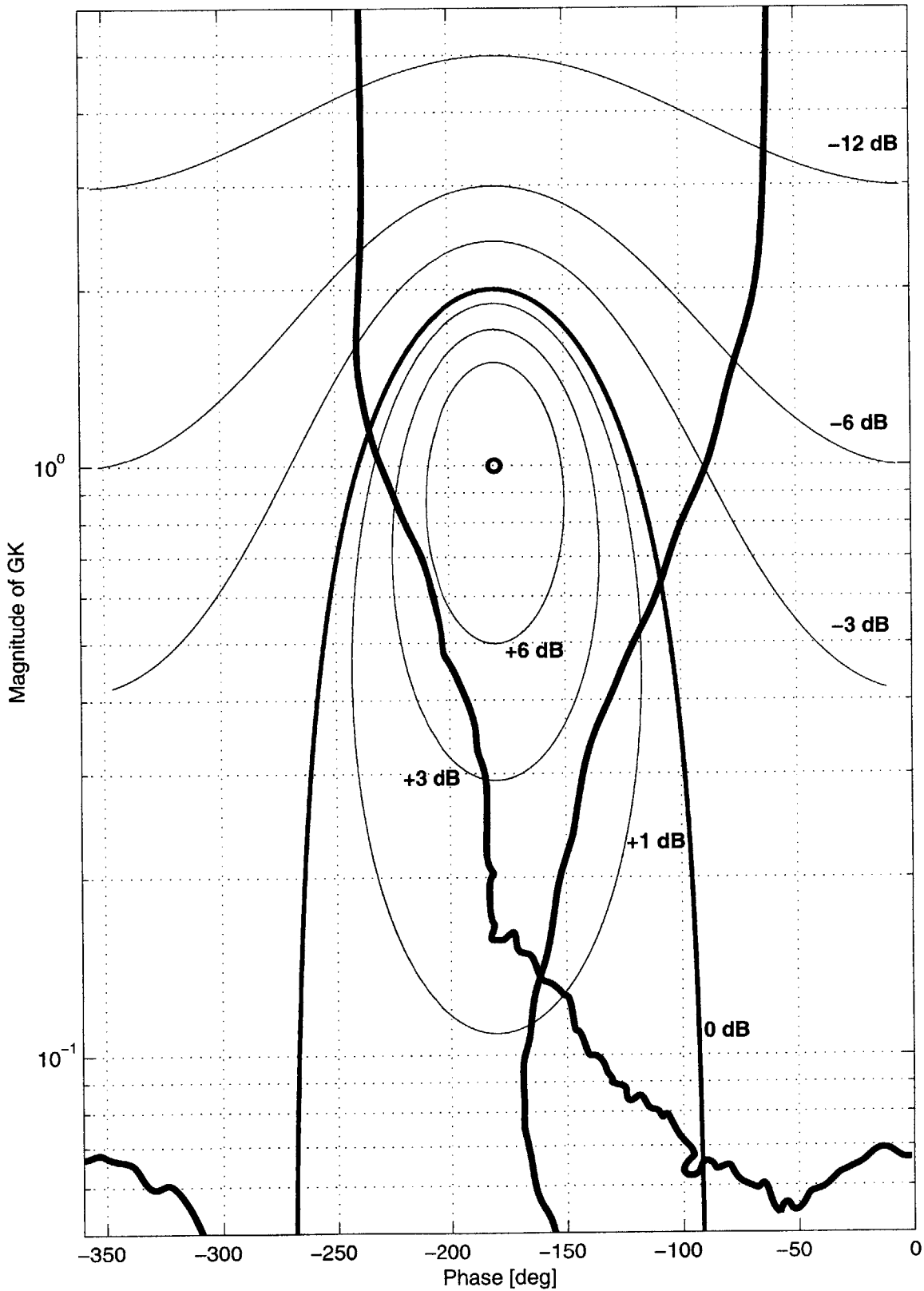


Figure D-10: Nichols plot of the 4/rev controller

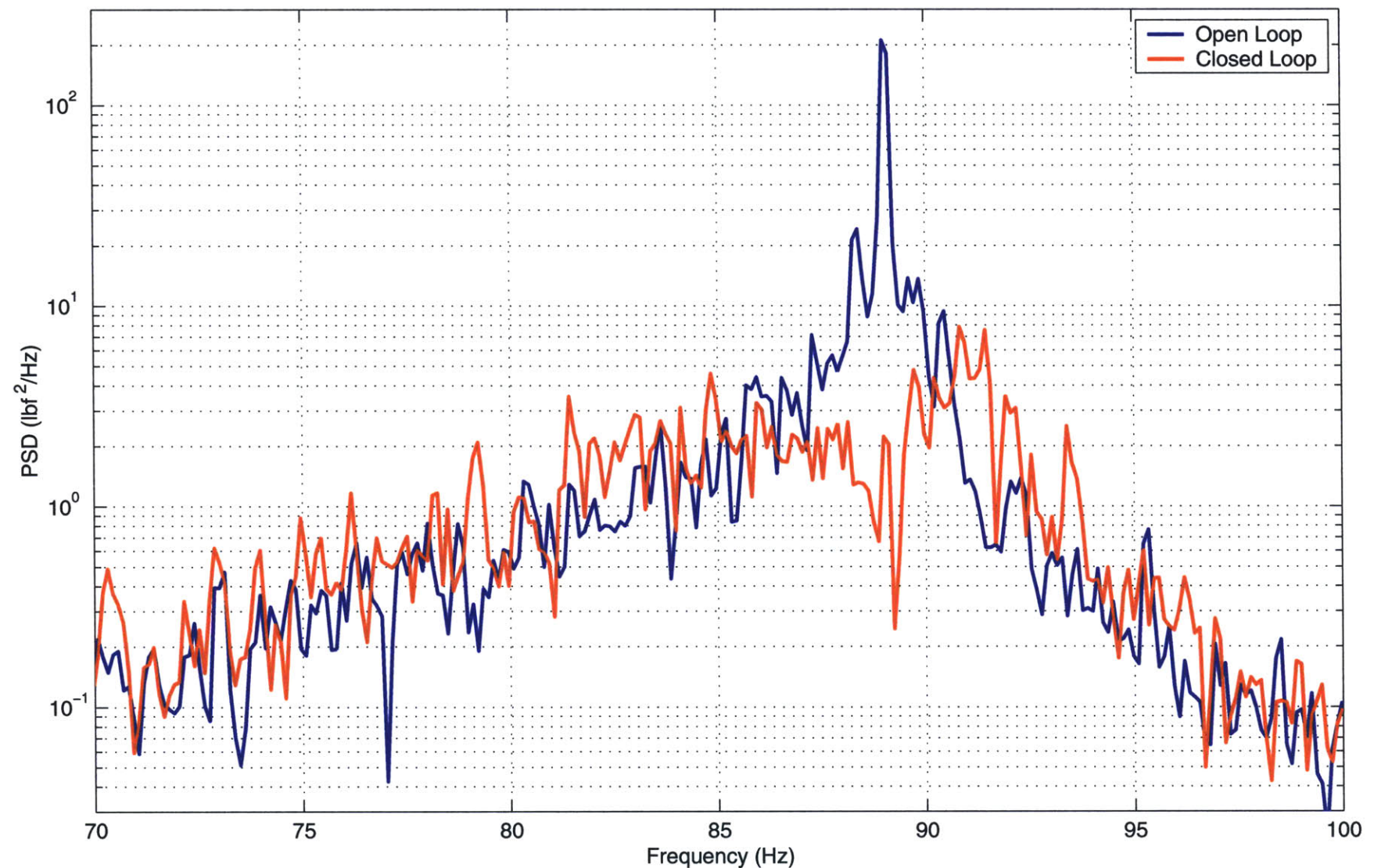


Figure D-11: Comparison of the open and closed loop vertical hub shear for the 4/rev controller

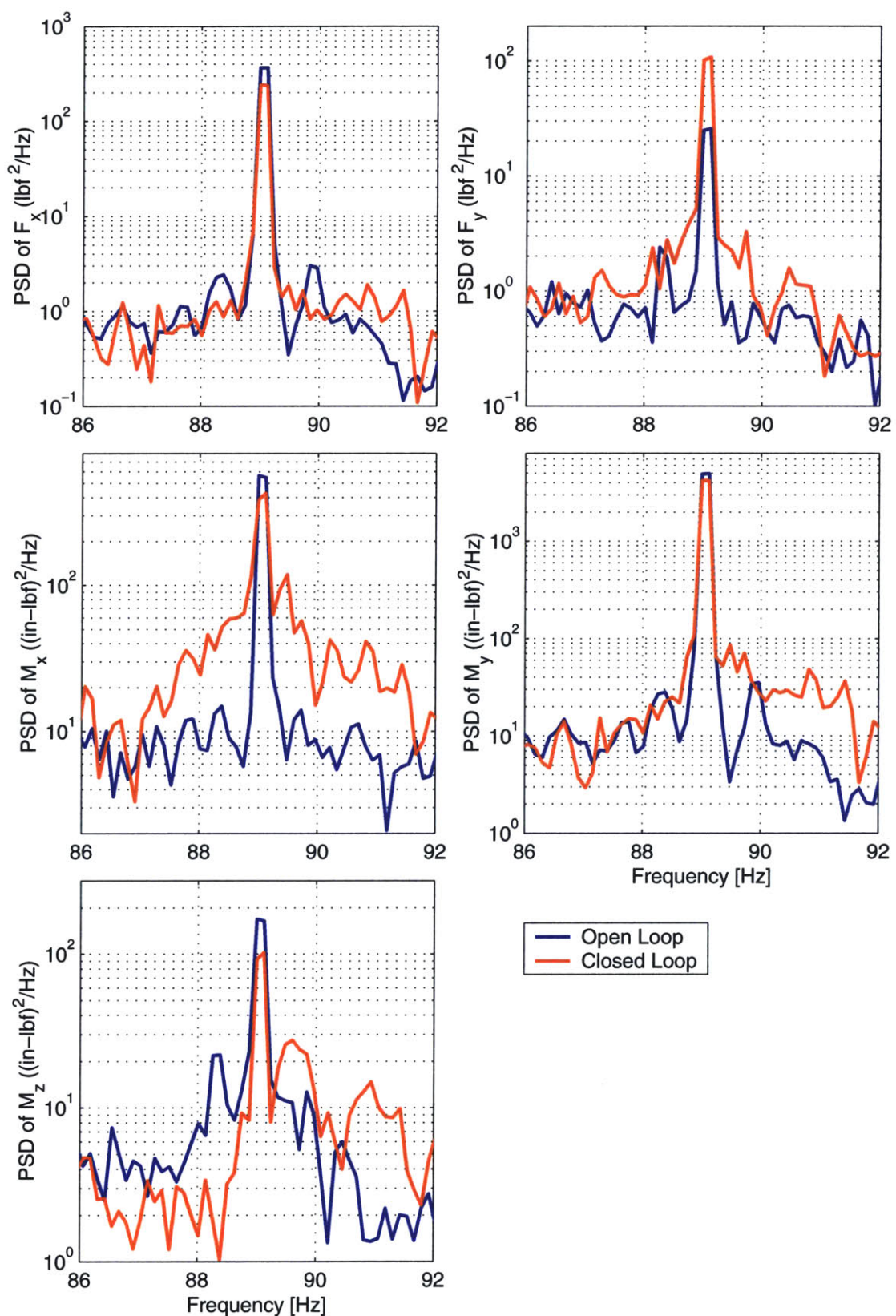


Figure D-12: Comparison of the open and closed loop measurements of the uncontrolled hub forces and moments for the 4/rev controller

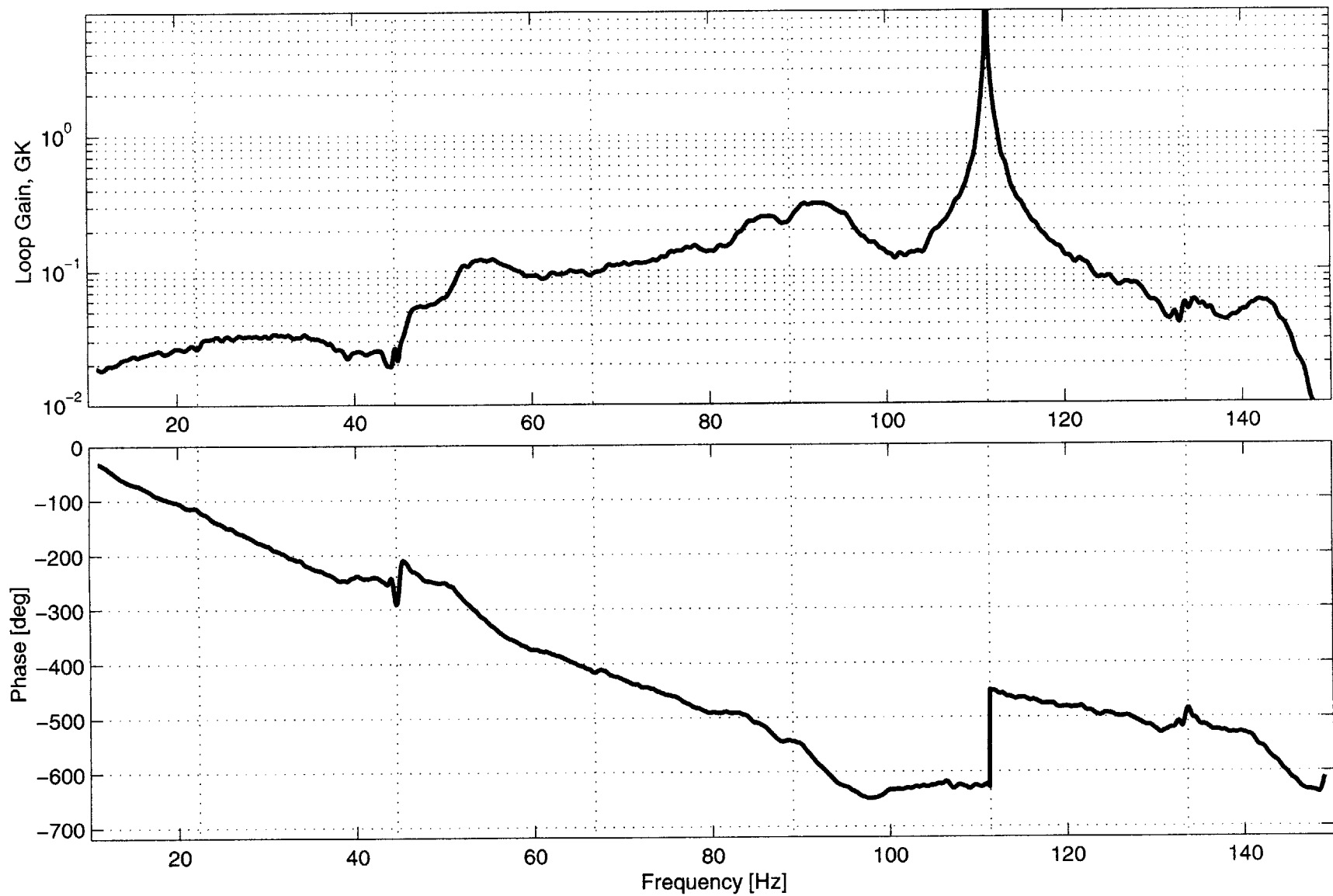


Figure D-13: Loop transfer bode plot of the 5/rev controller

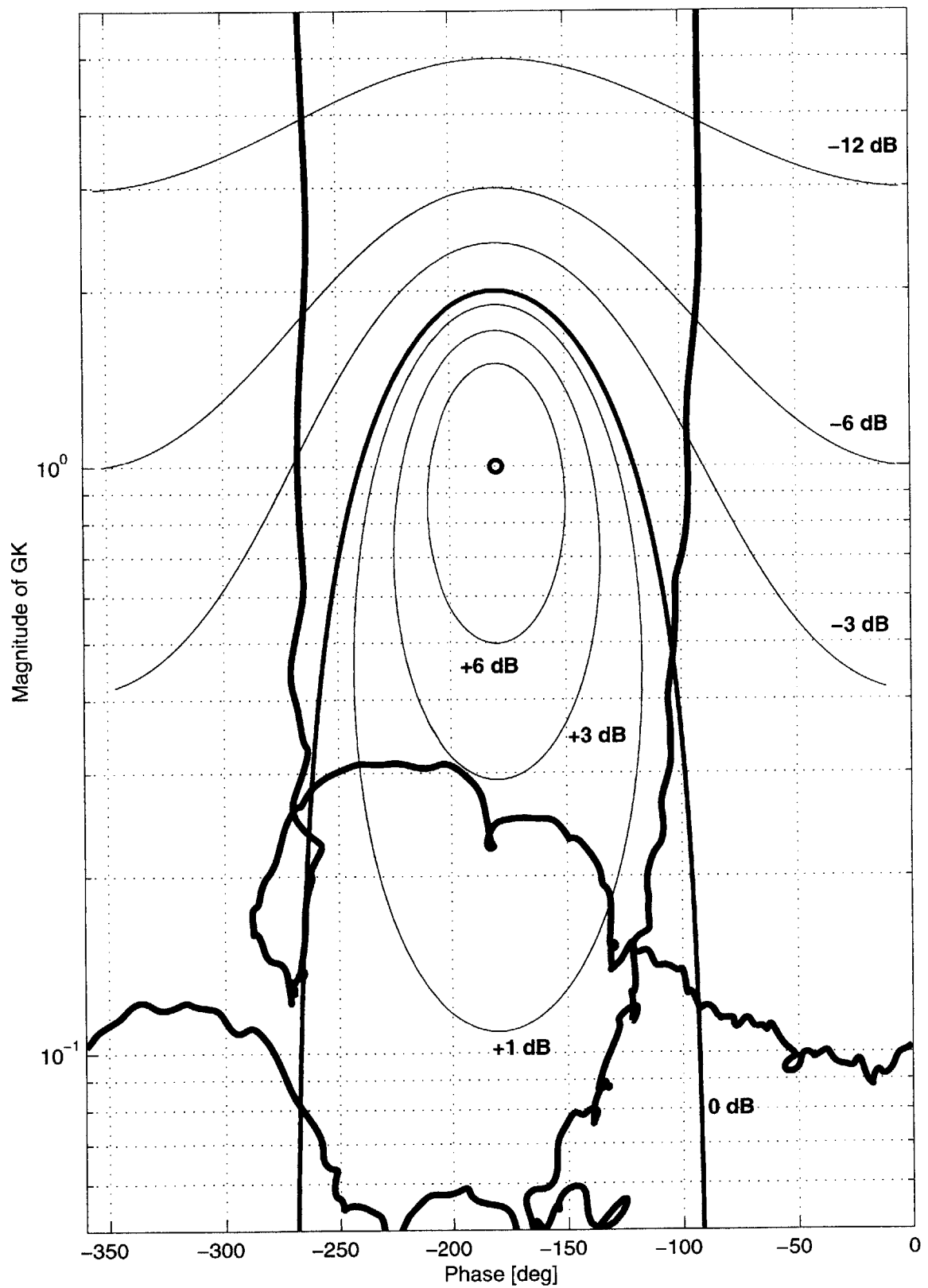


Figure D-14: Nichols plot of the 5/rev controller

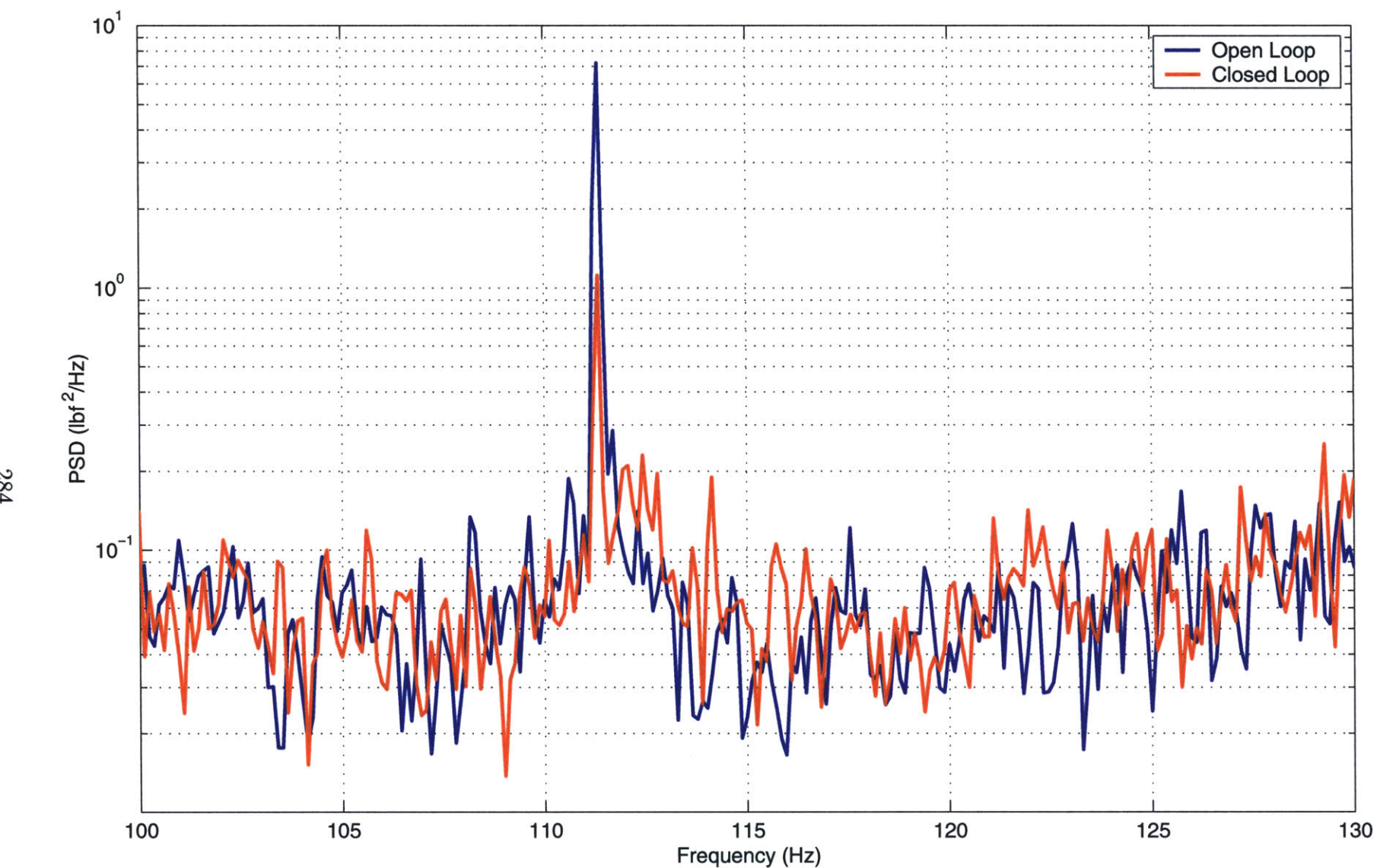


Figure D-15: Comparison of the open and closed loop vertical hub shear for the 5/rev controller

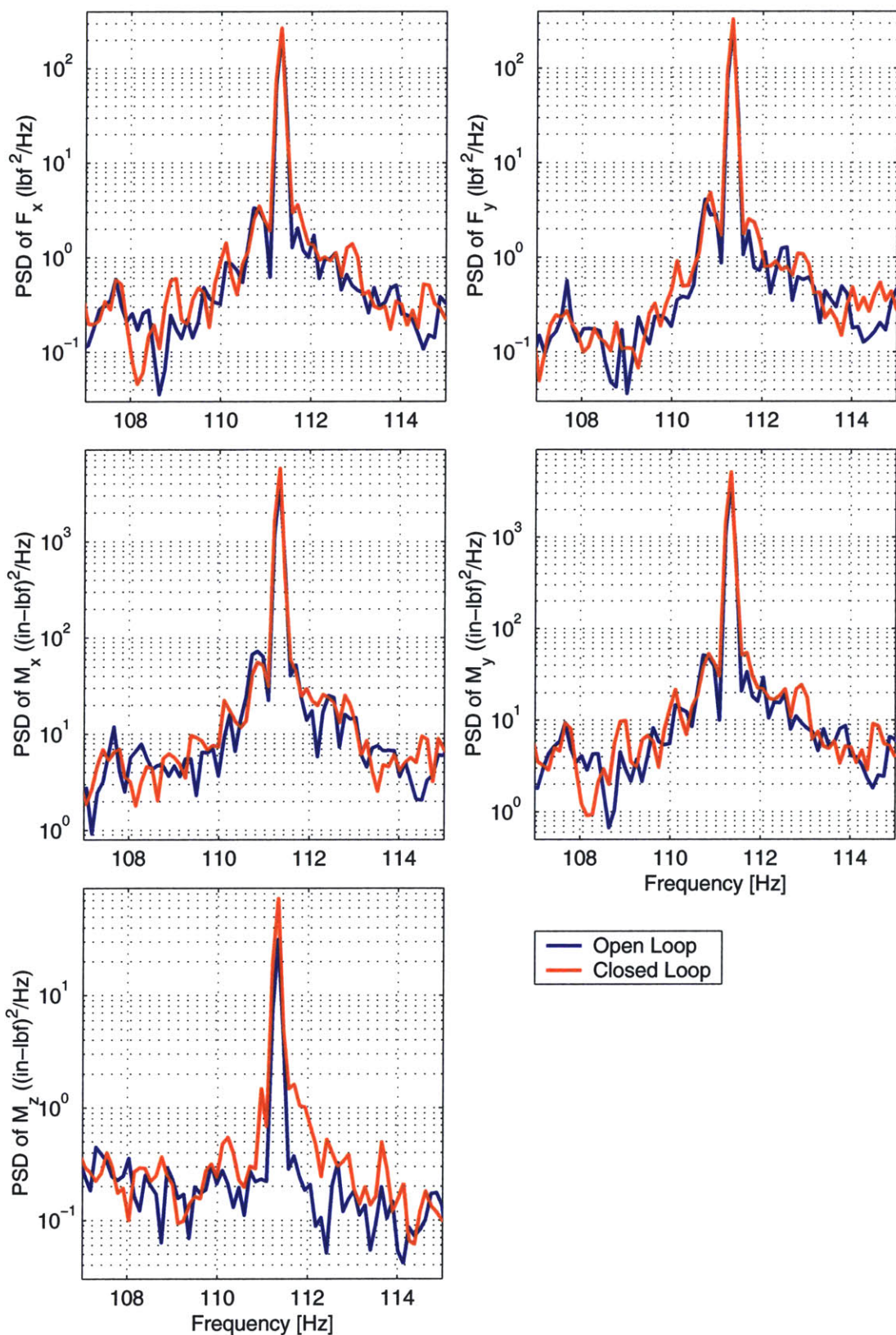


Figure D-16: Comparison of the open and closed loop measurements of the uncontrolled hub forces and moments for the 5/rev controller

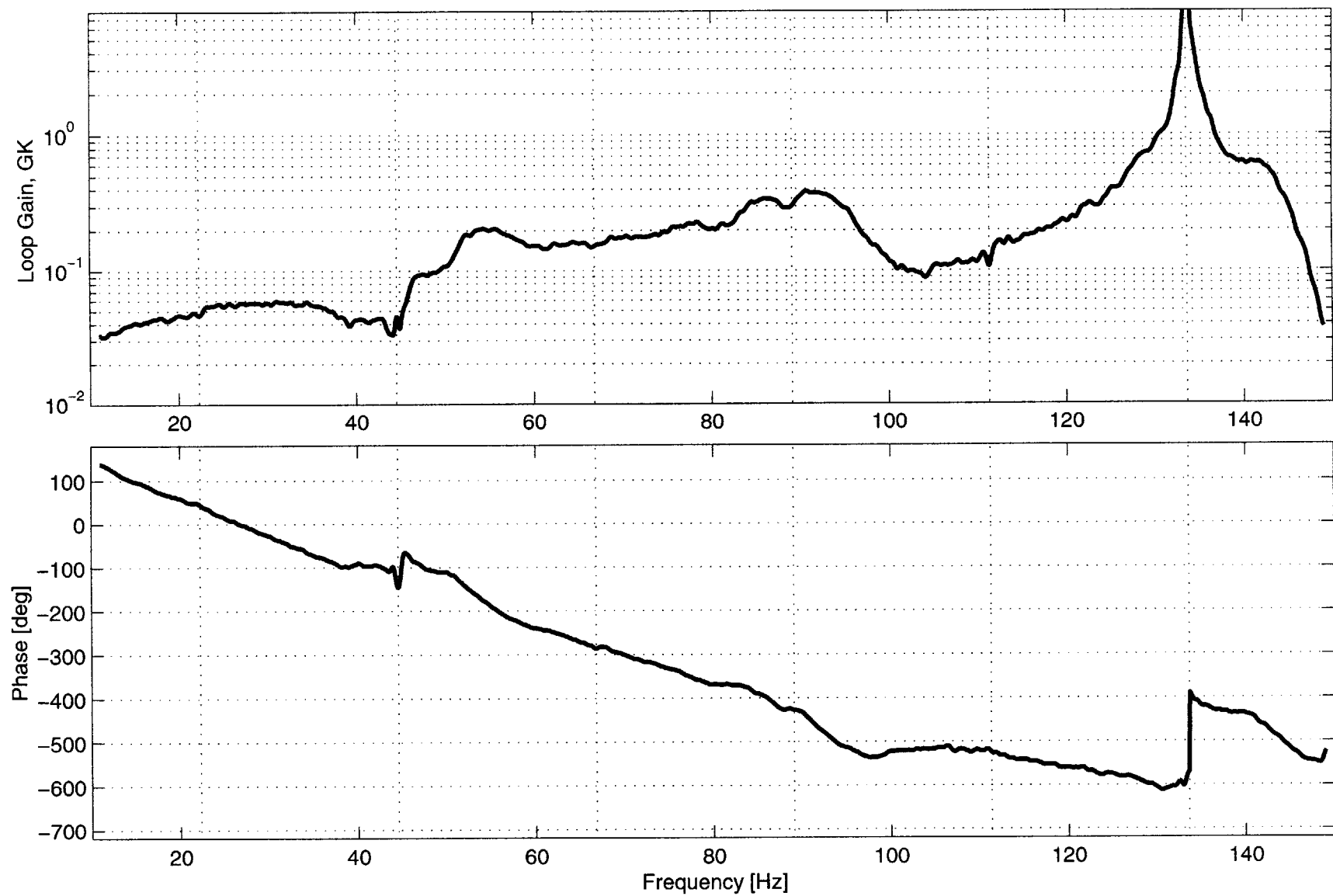


Figure D-17: Loop transfer bode plot of the 6/rev controller

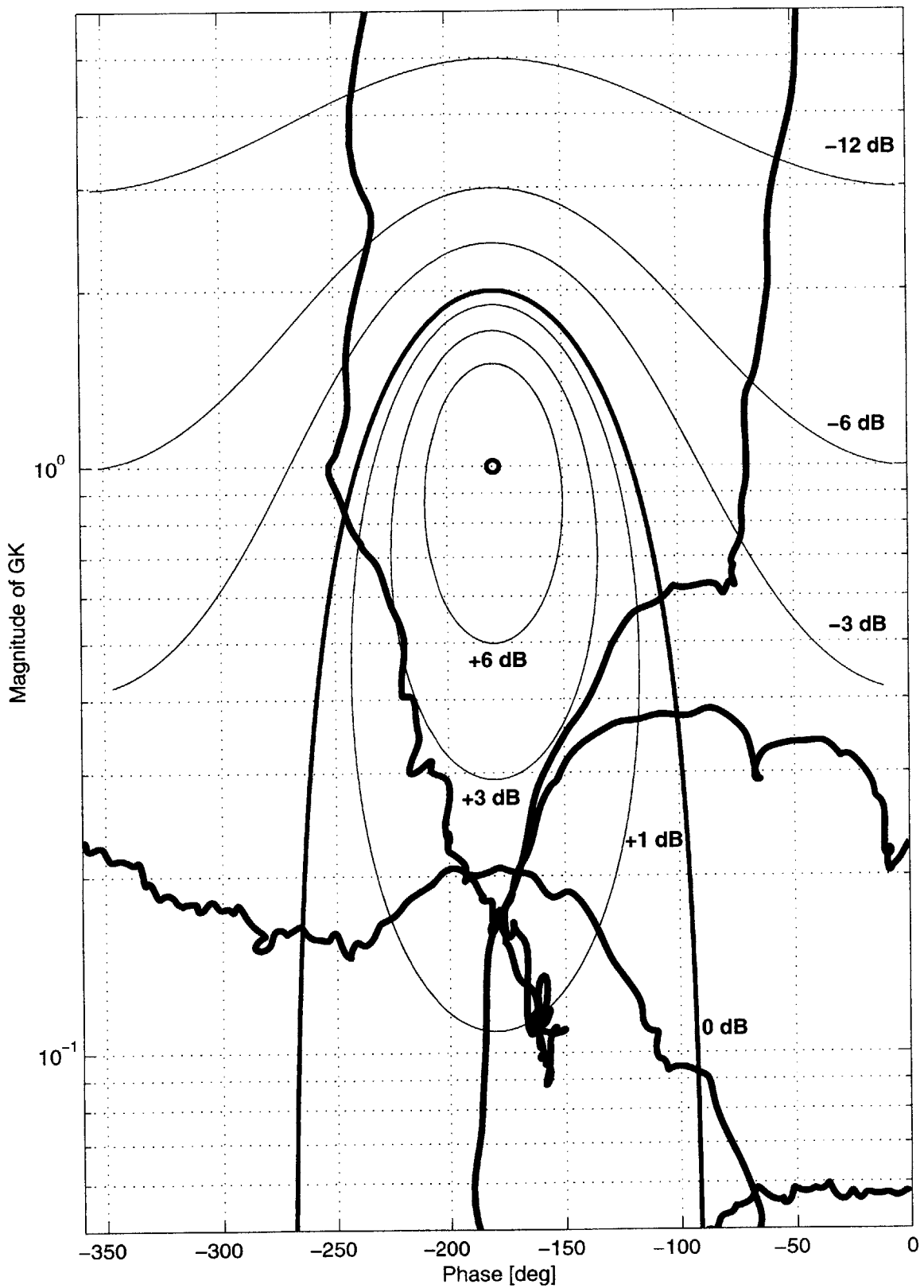


Figure D-18: Nichols plot of the 6/rev controller

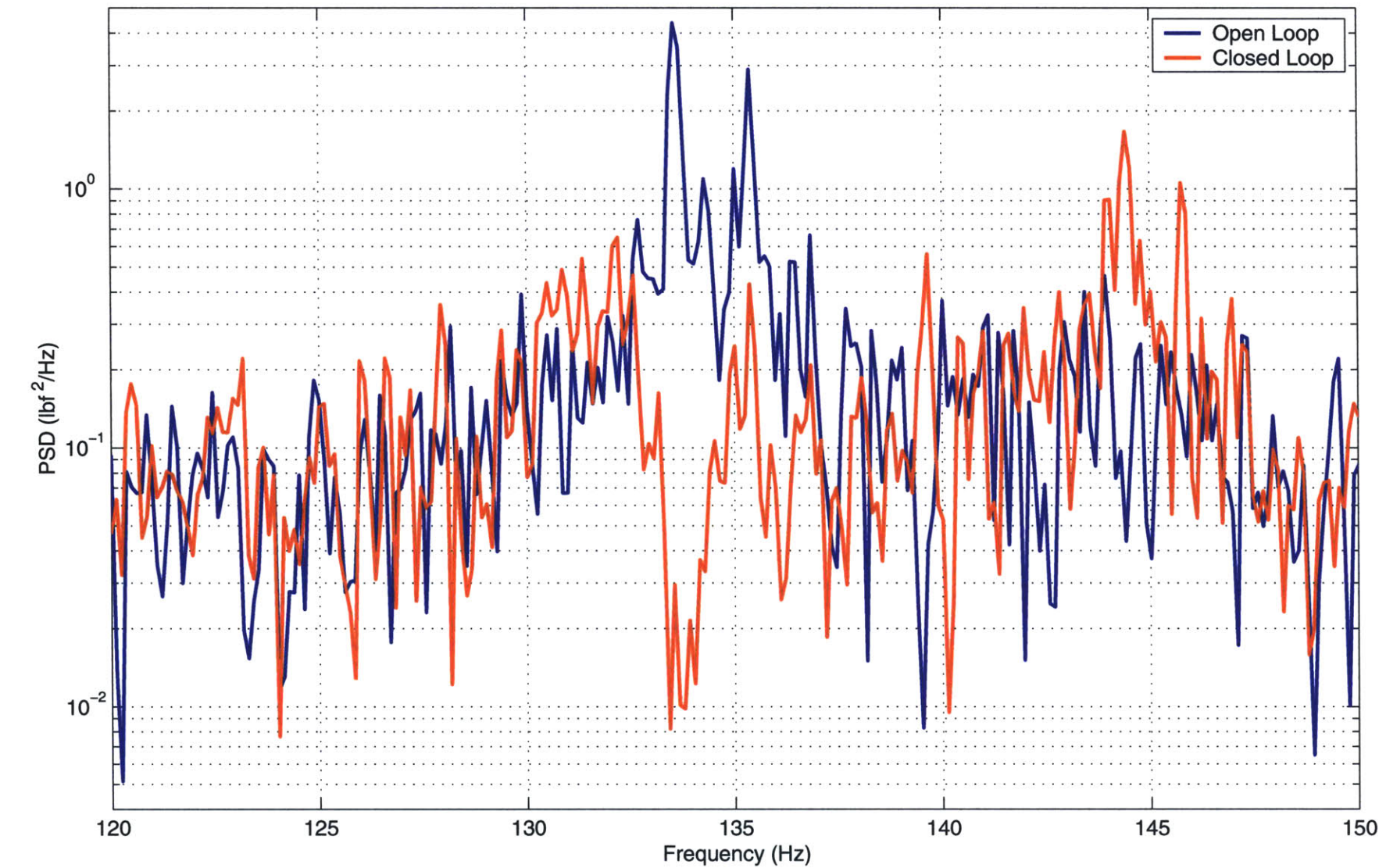


Figure D-19: Comparison of the open and closed loop vertical hub shear for the 6/rev controller

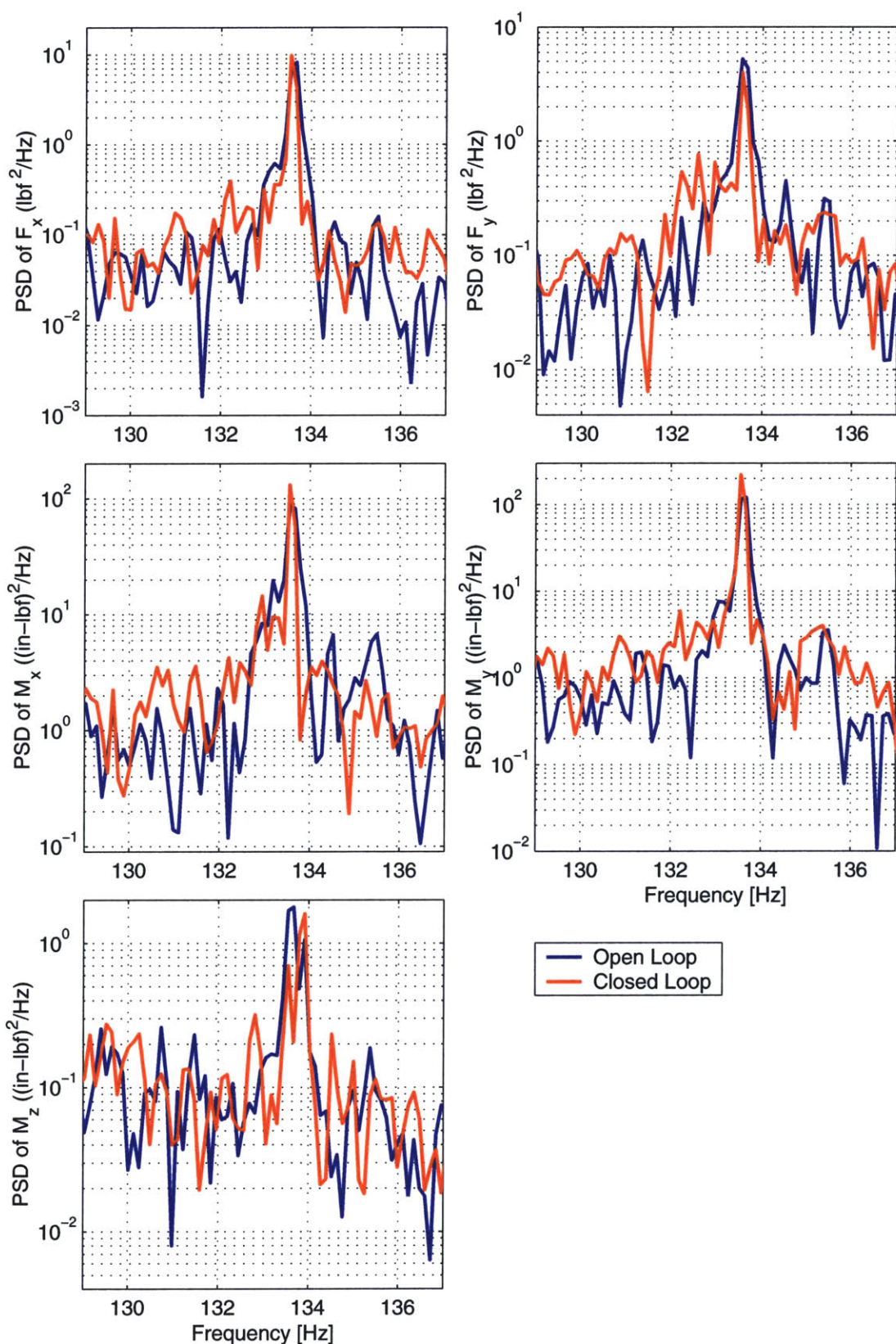


Figure D-20: Comparison of the open and closed loop measurements of the uncontrolled hub forces and moments for the 6/rev controller

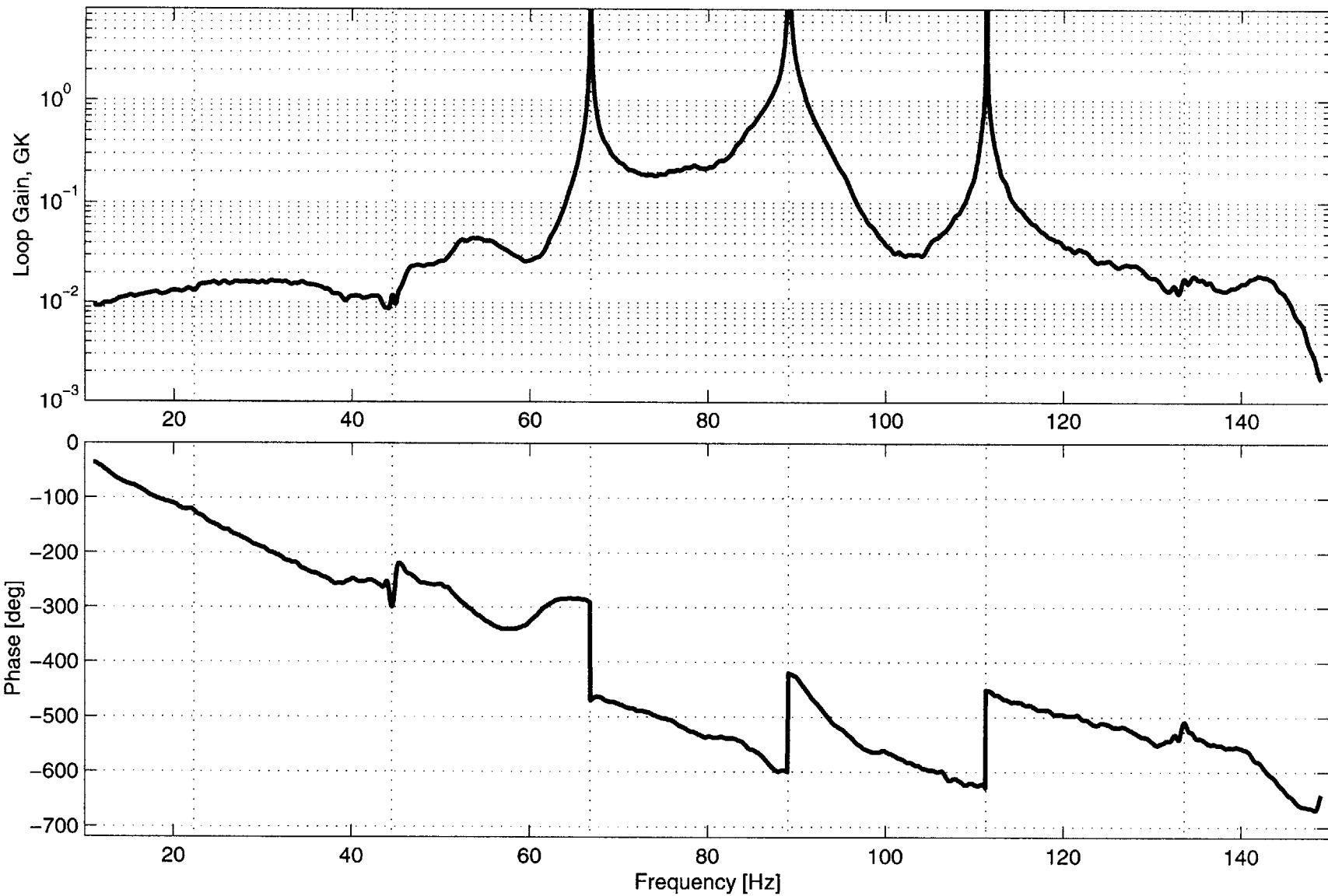


Figure D-21: Loop transfer bode plot of the multiharmonic 3,4, and 5/rev controller

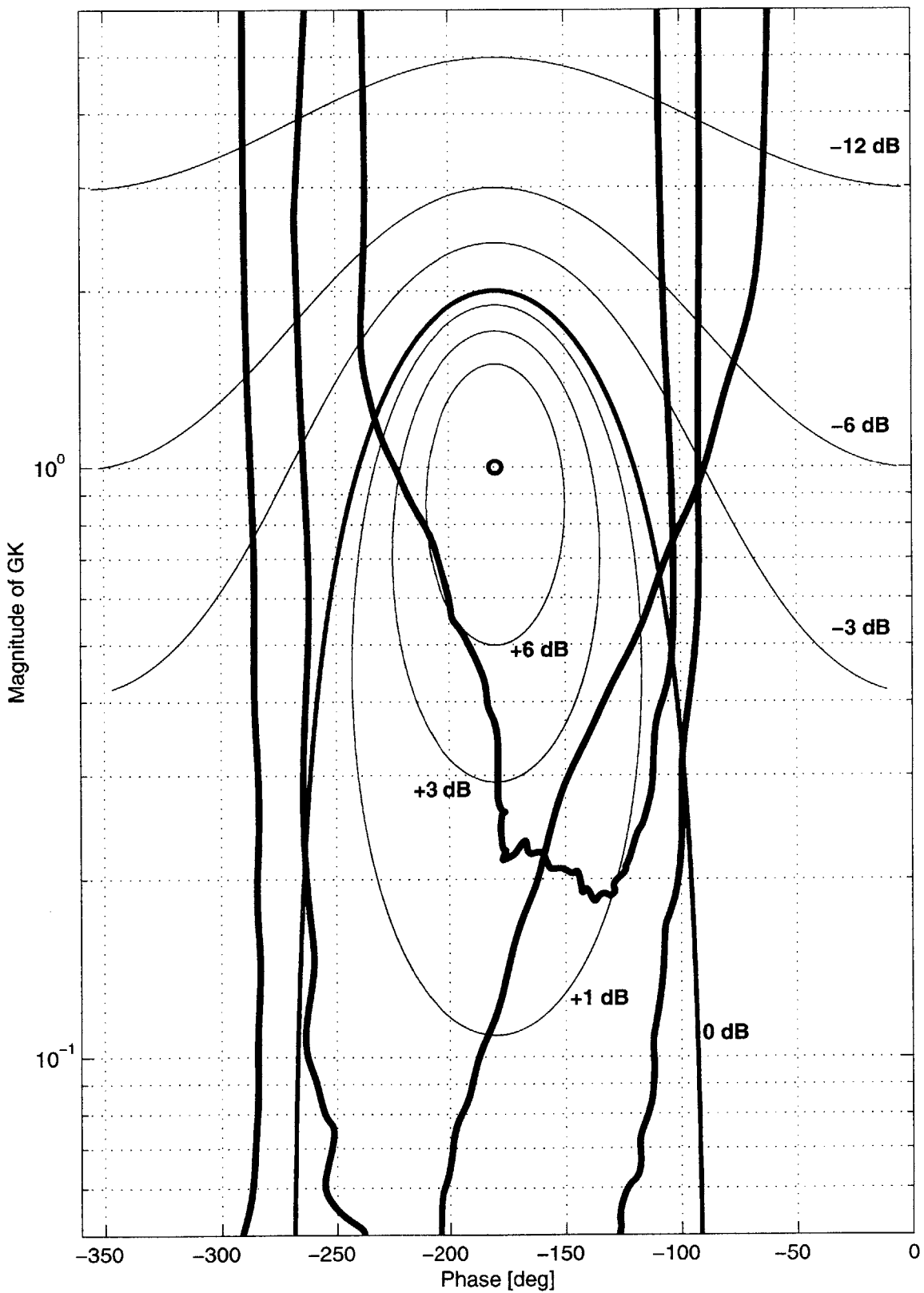


Figure D-22: Nichols plot of the multiharmonic 3,4, and 5/rev controller

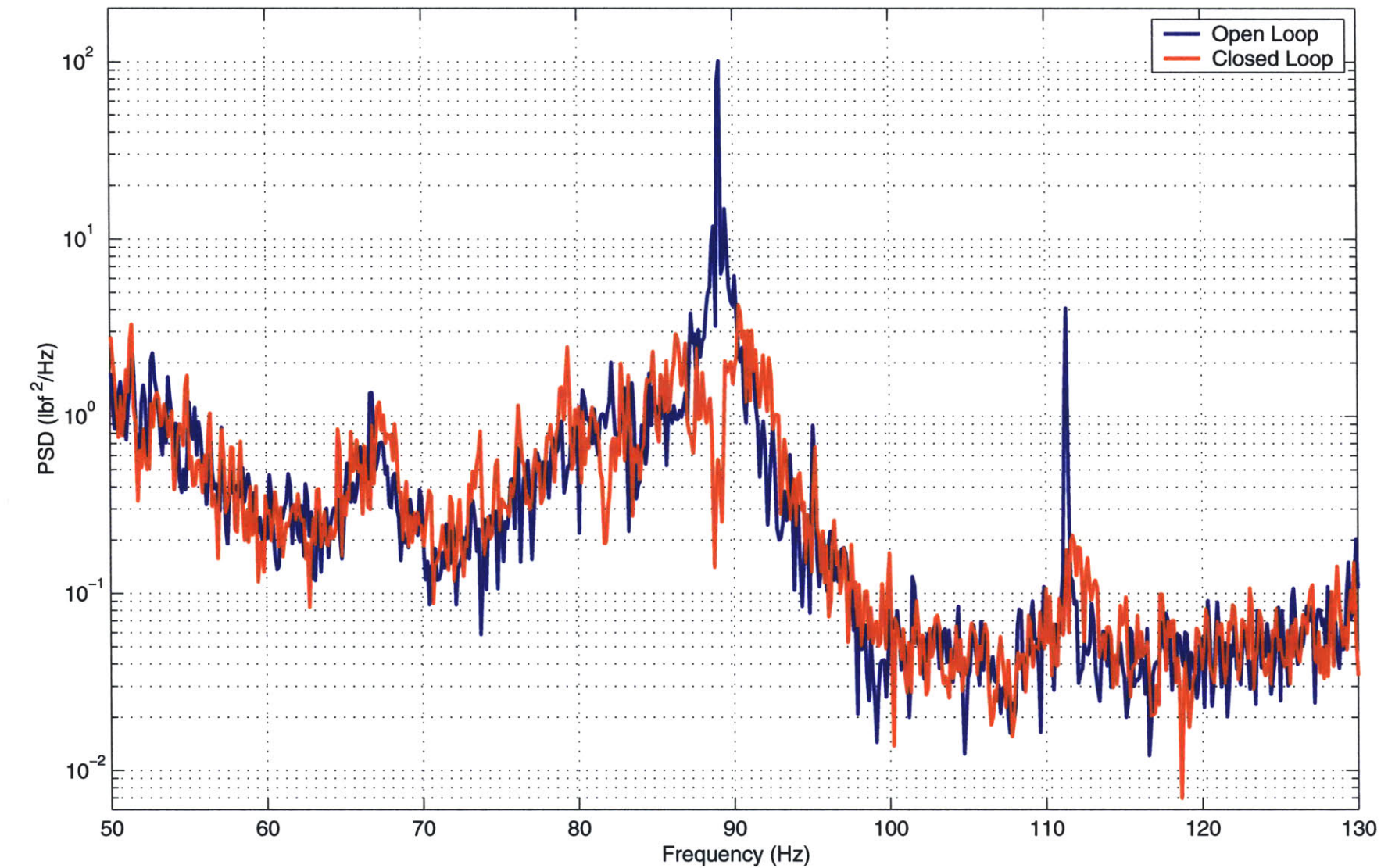


Figure D-23: Comparison of the open and closed loop vertical hub shear for the multiharmonic 3,4, and 5/rev controller

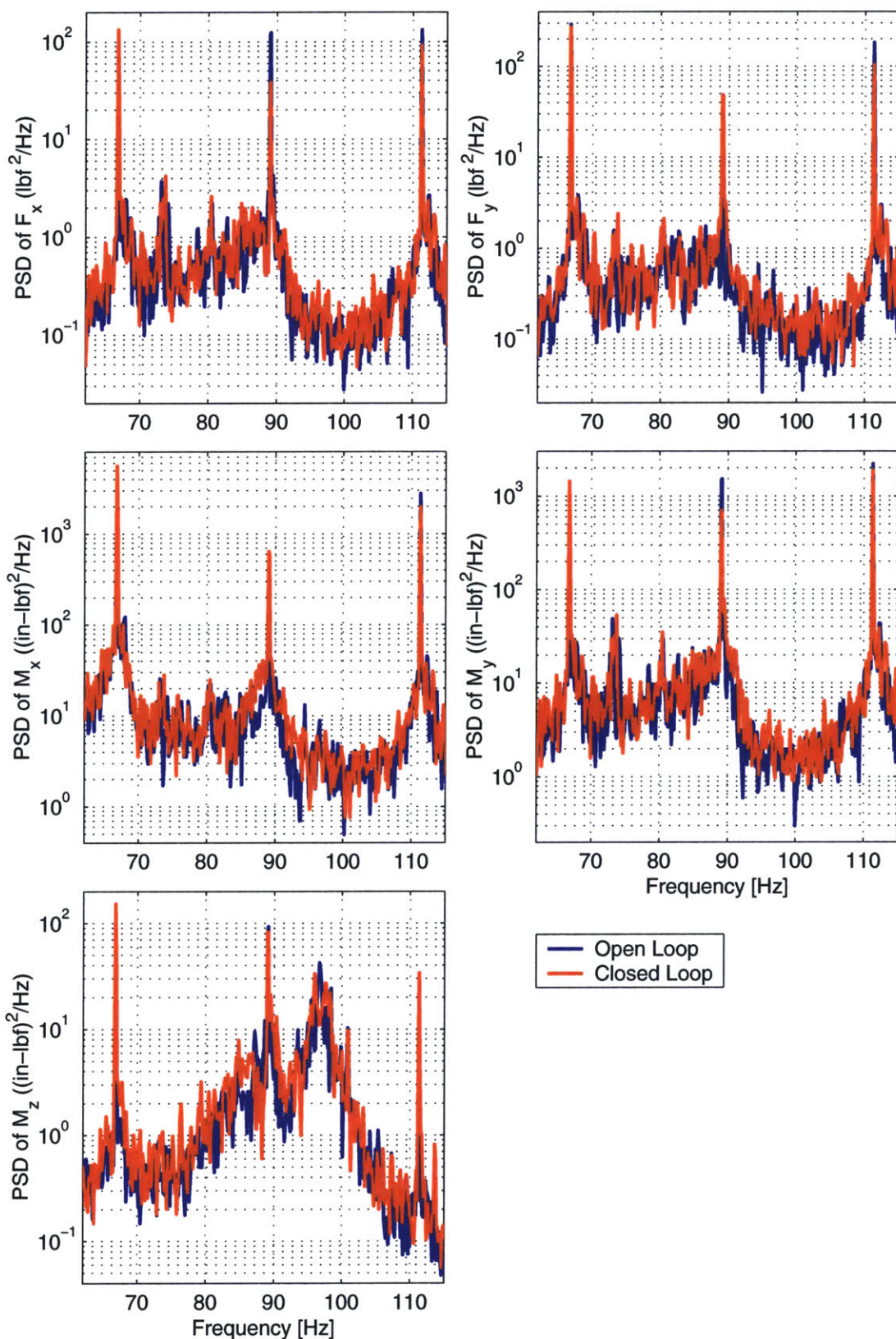


Figure D-24: Comparison of the open and closed loop measurements of the uncontrolled hub forces and moments for the multiharmonic 3,4, and 5/rev controller

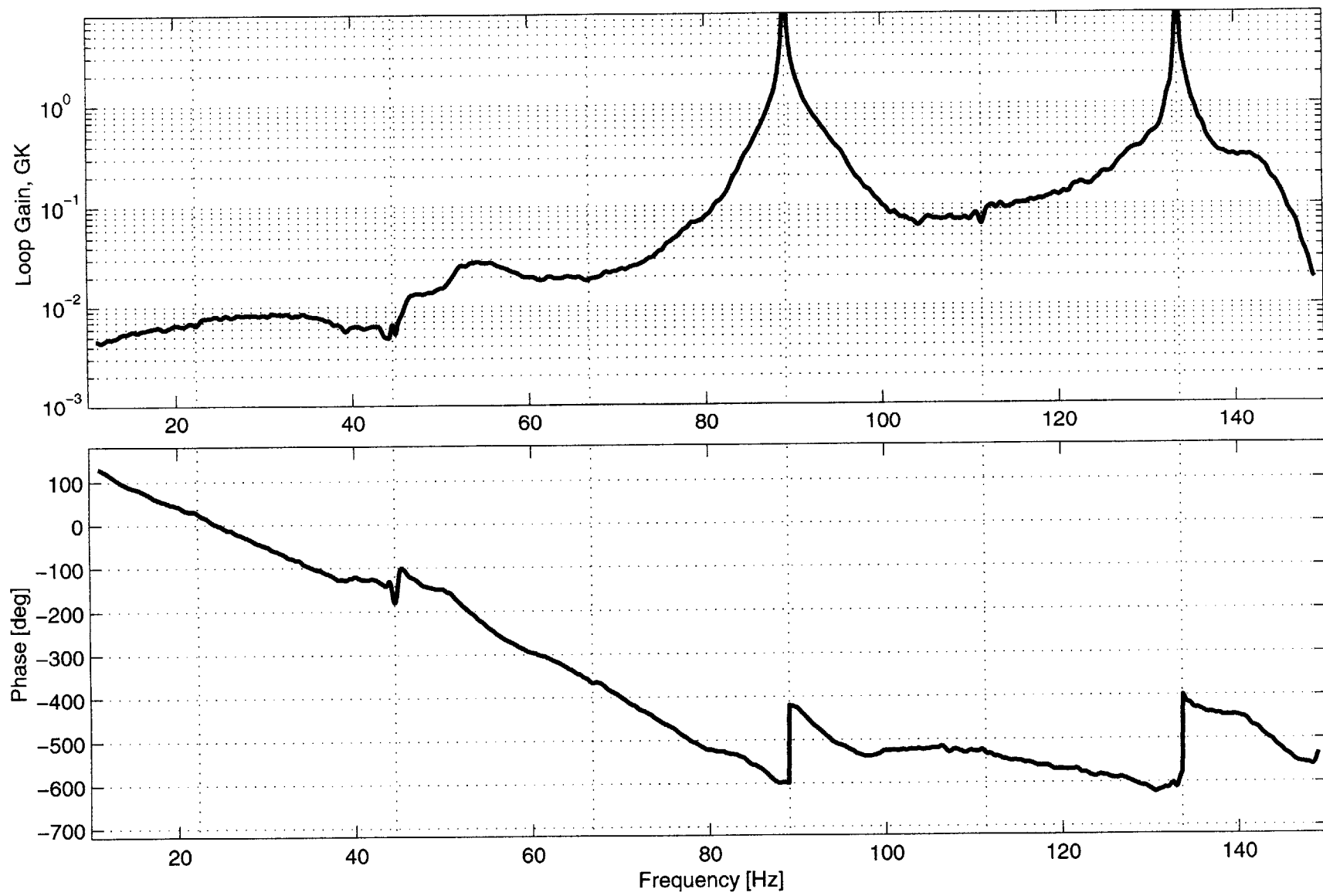


Figure D-25: Loop transfer bode plot of the multiharmonic 4 and 6/rev controller

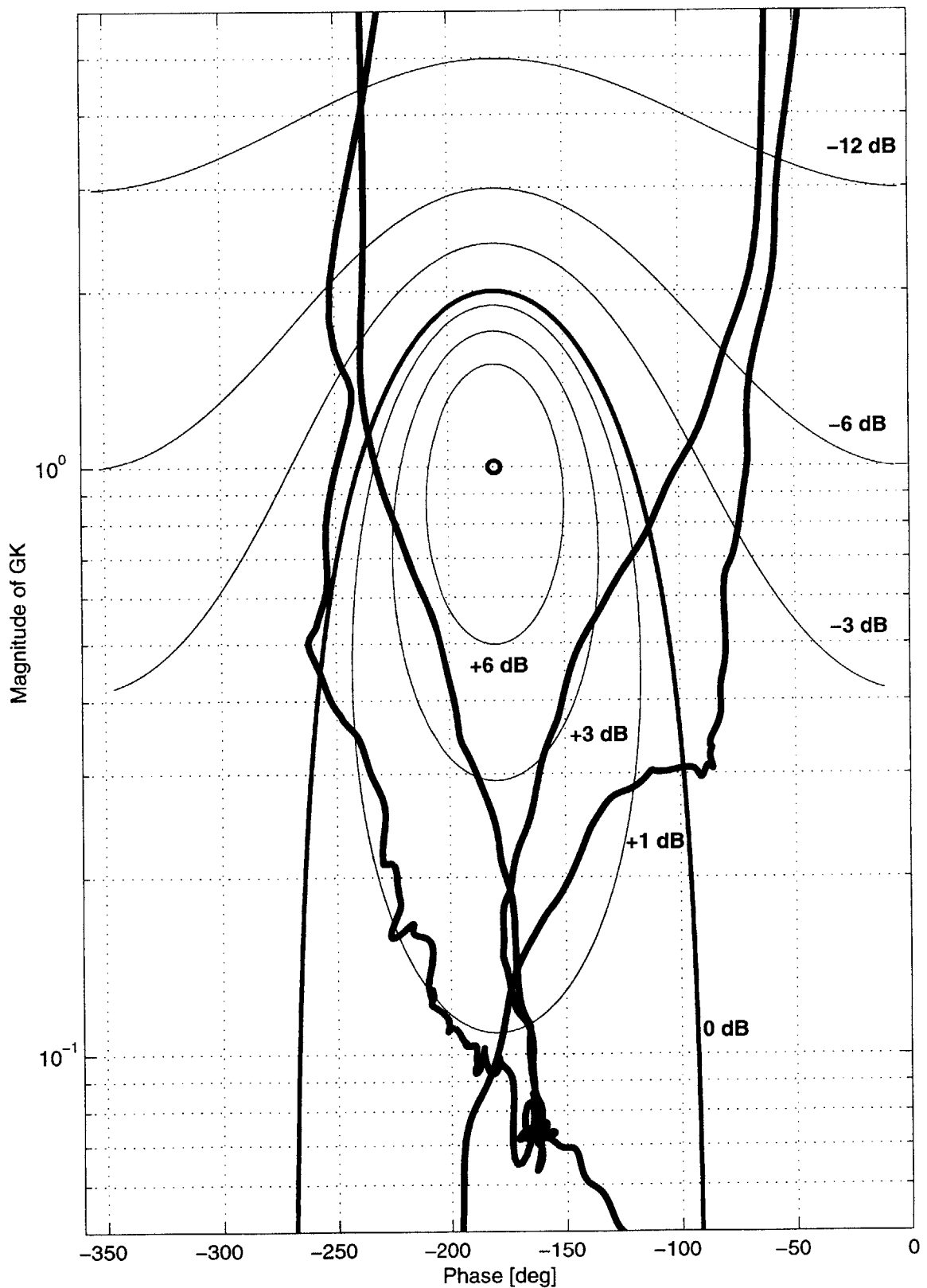


Figure D-26: Nichols plot of the multiharmonic 4 and 6/rev controller

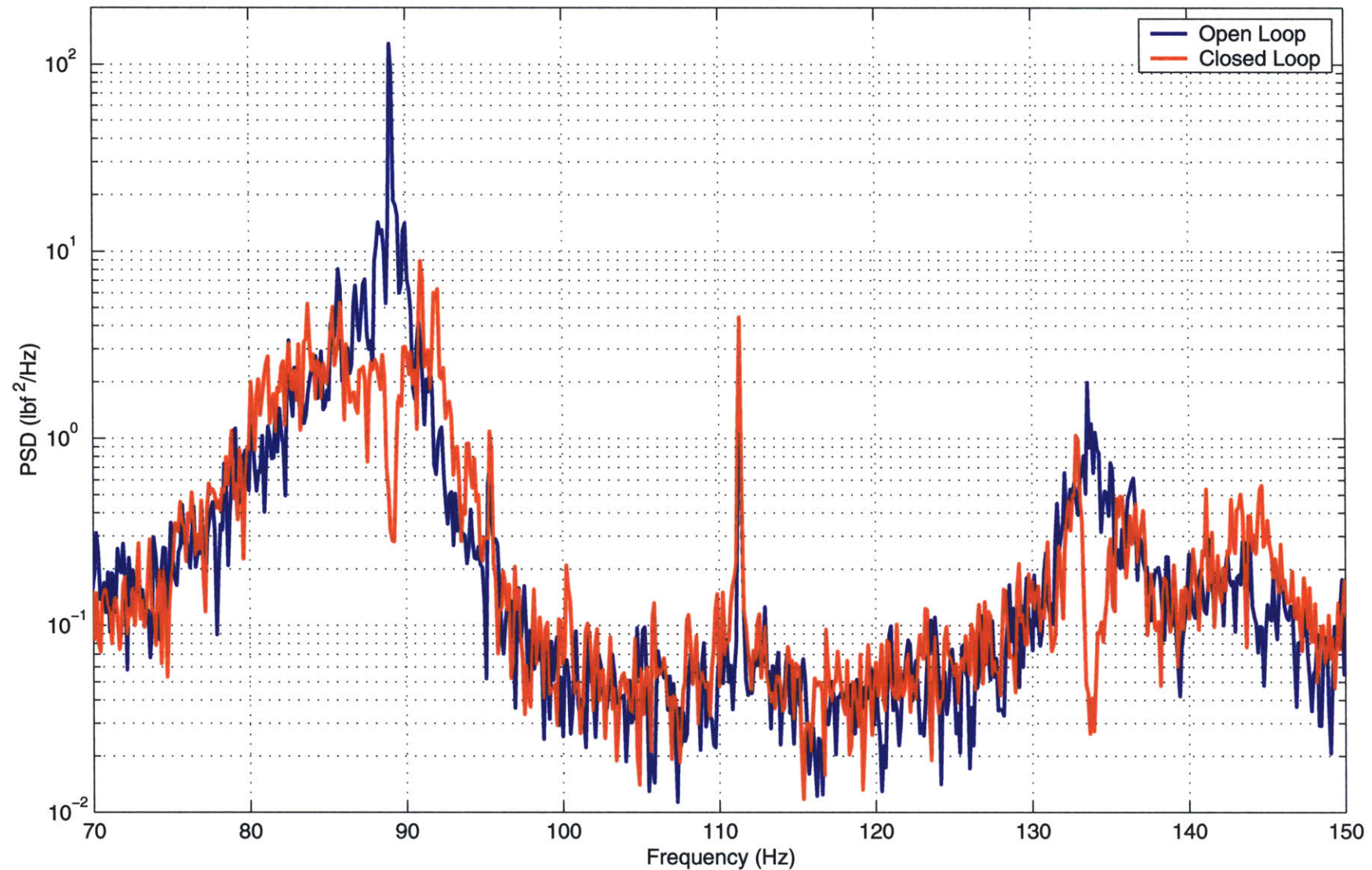


Figure D-27: Comparison of the open and closed loop vertical hub shear for the multiharmonic 4 and 6/rev controller

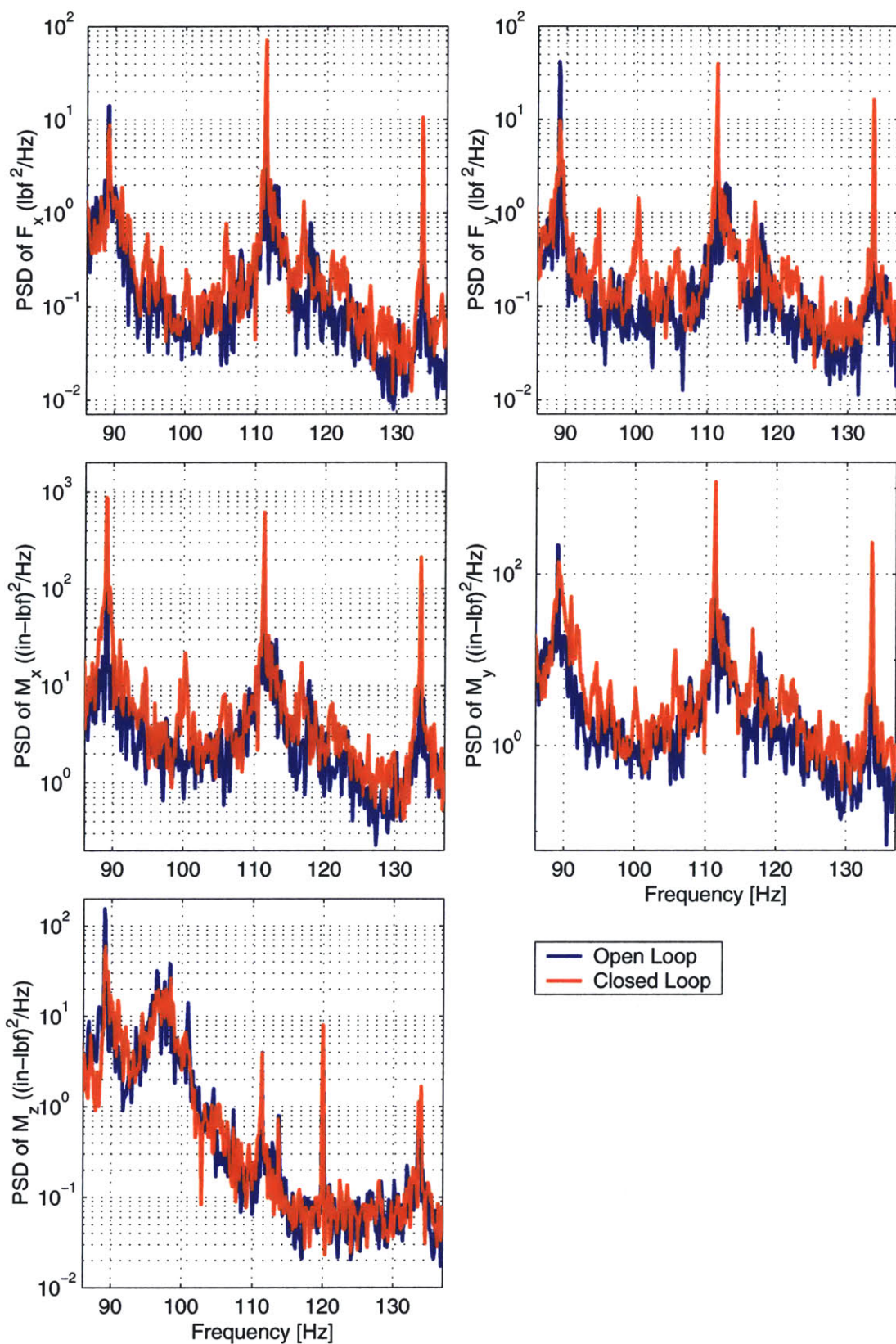


Figure D-28: Comparison of the open and closed loop measurements of the uncontrolled hub forces and moments for the multiharmonic 4 and 6/rev controller

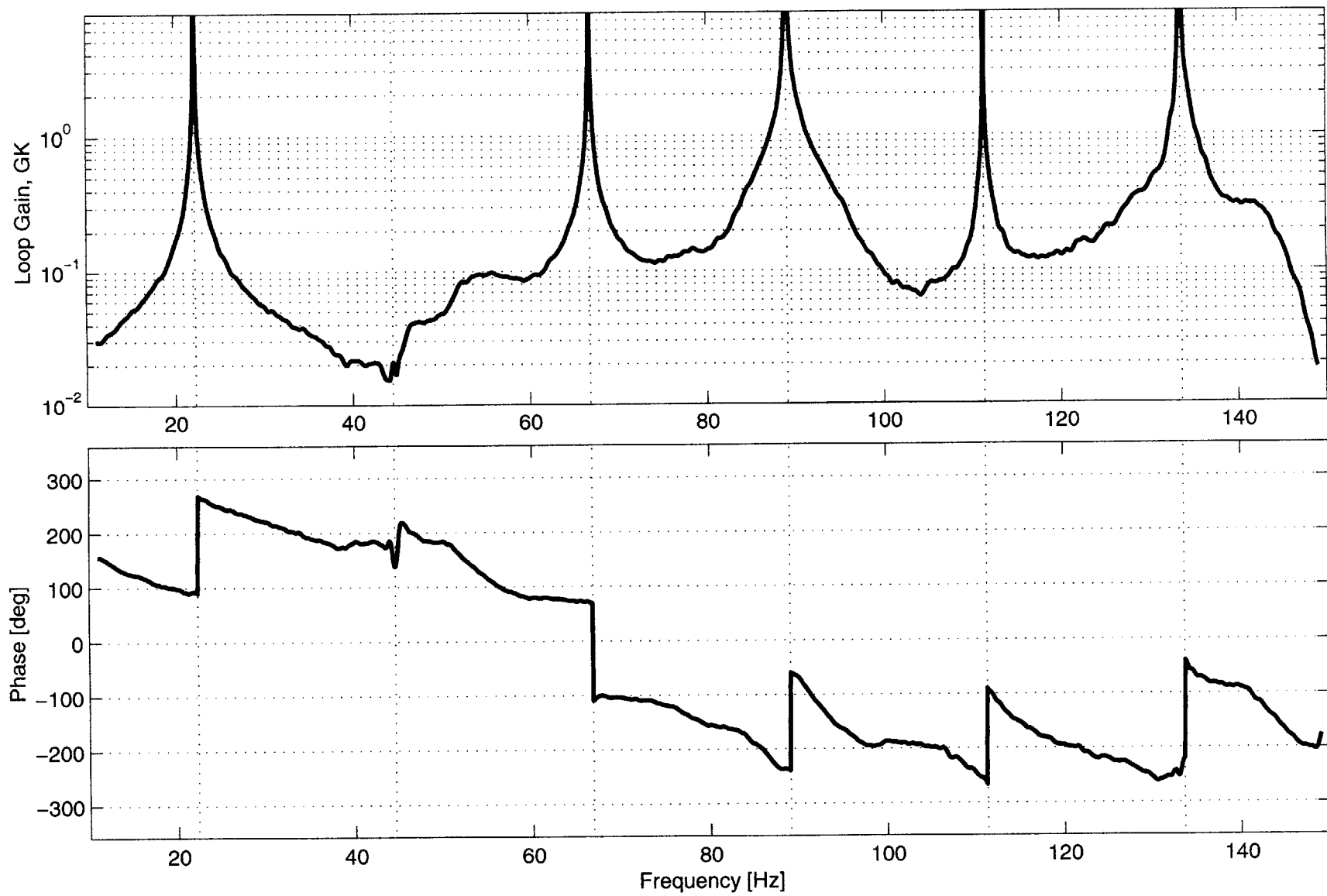


Figure D-29: Loop transfer bode plot of the multiharmonic 1,3,4,5, and 6/rev controller

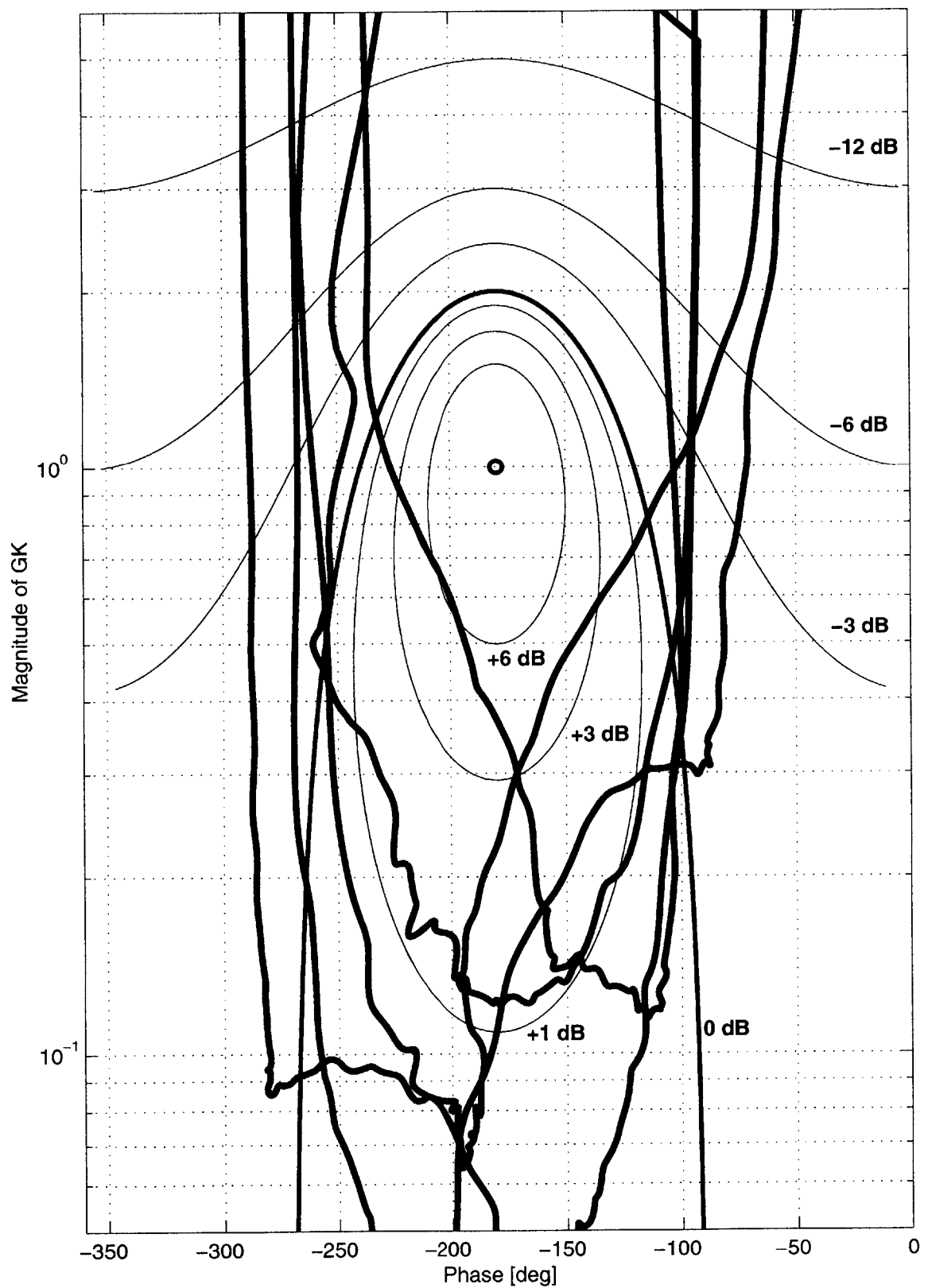


Figure D-30: Nichols plot of the multiharmonic 1,3,4,5, and 6/rev controller

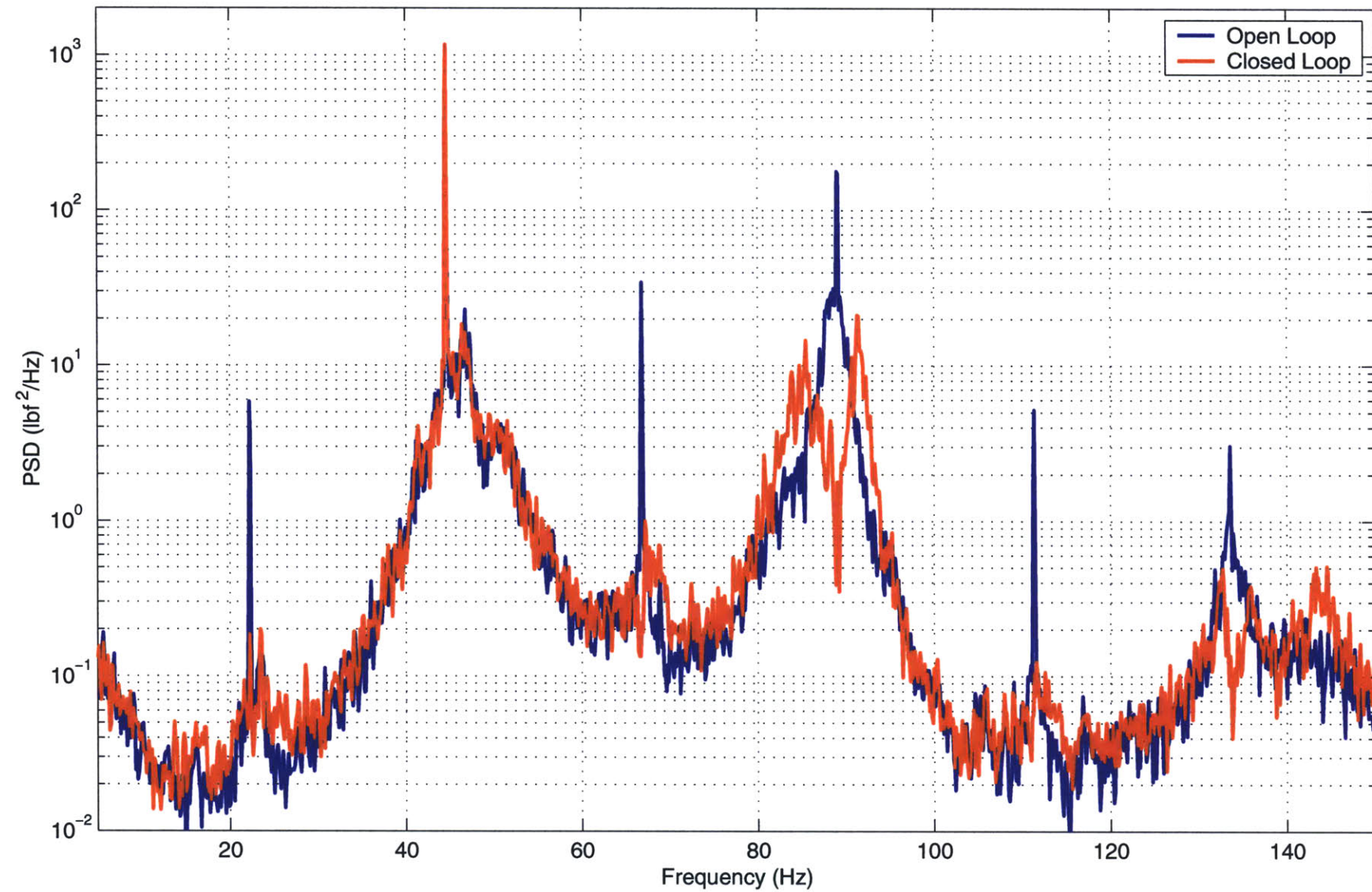


Figure D-31: Comparison of the open and closed loop vertical hub shear for the multiharmonic 1,3,4,5, and 6/rev controller

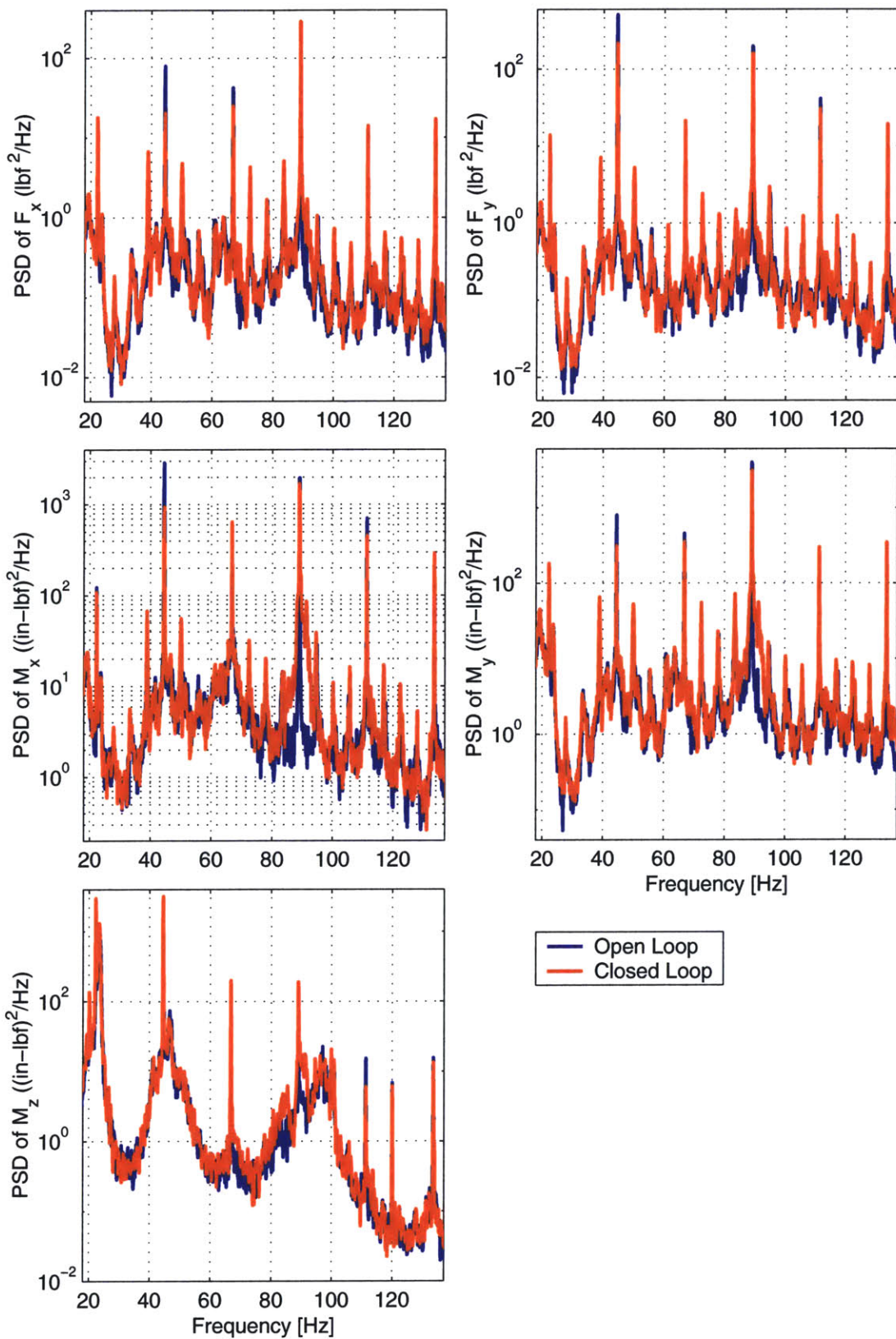


Figure D-32: Comparison of the open and closed loop measurements of the uncontrolled hub forces and moments for the multiharmonic 1,3,4,5, and 6/rev controller

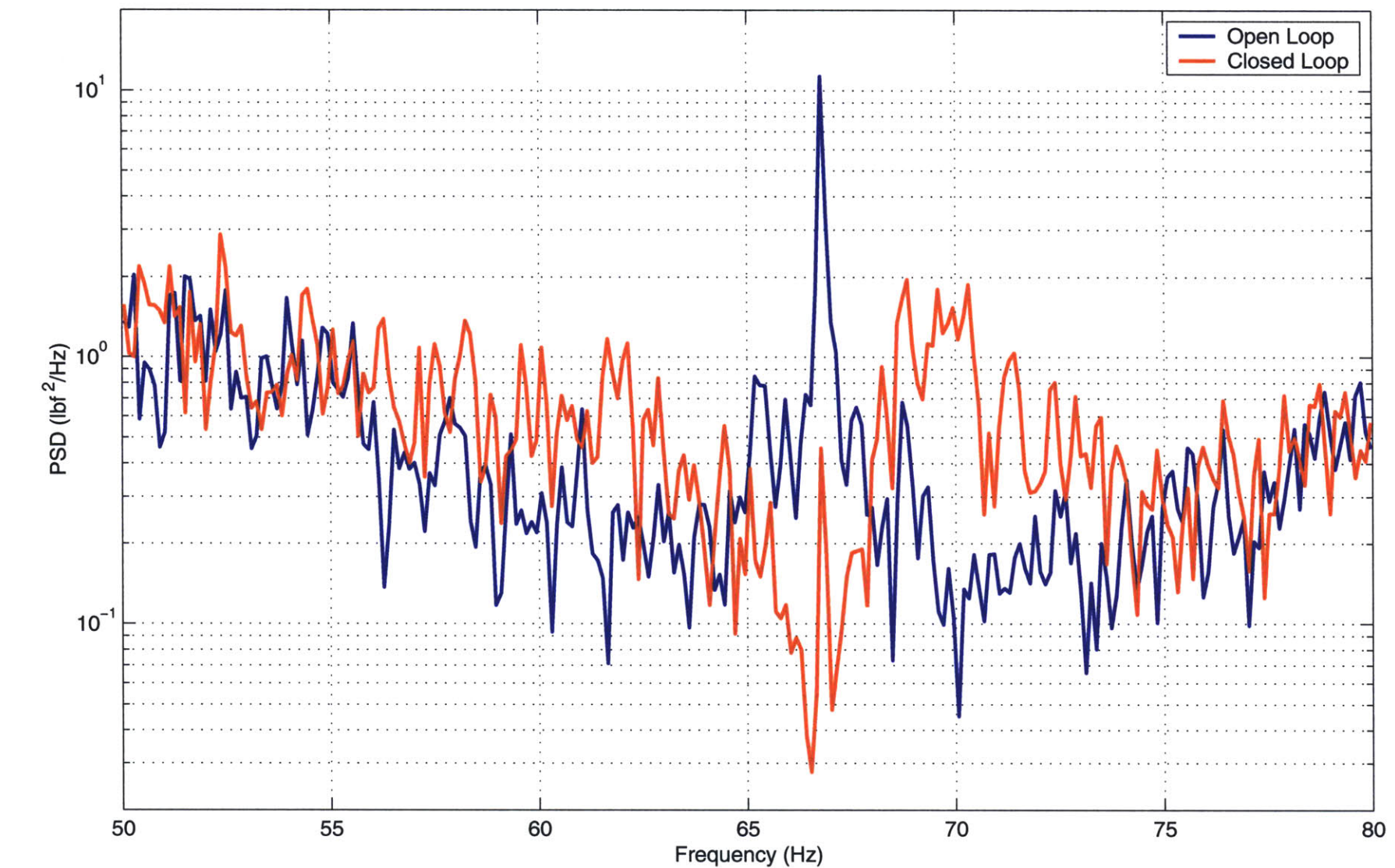


Figure D-33: Comparison of the open and closed loop vertical hub shear for the 3/rev discrete controller

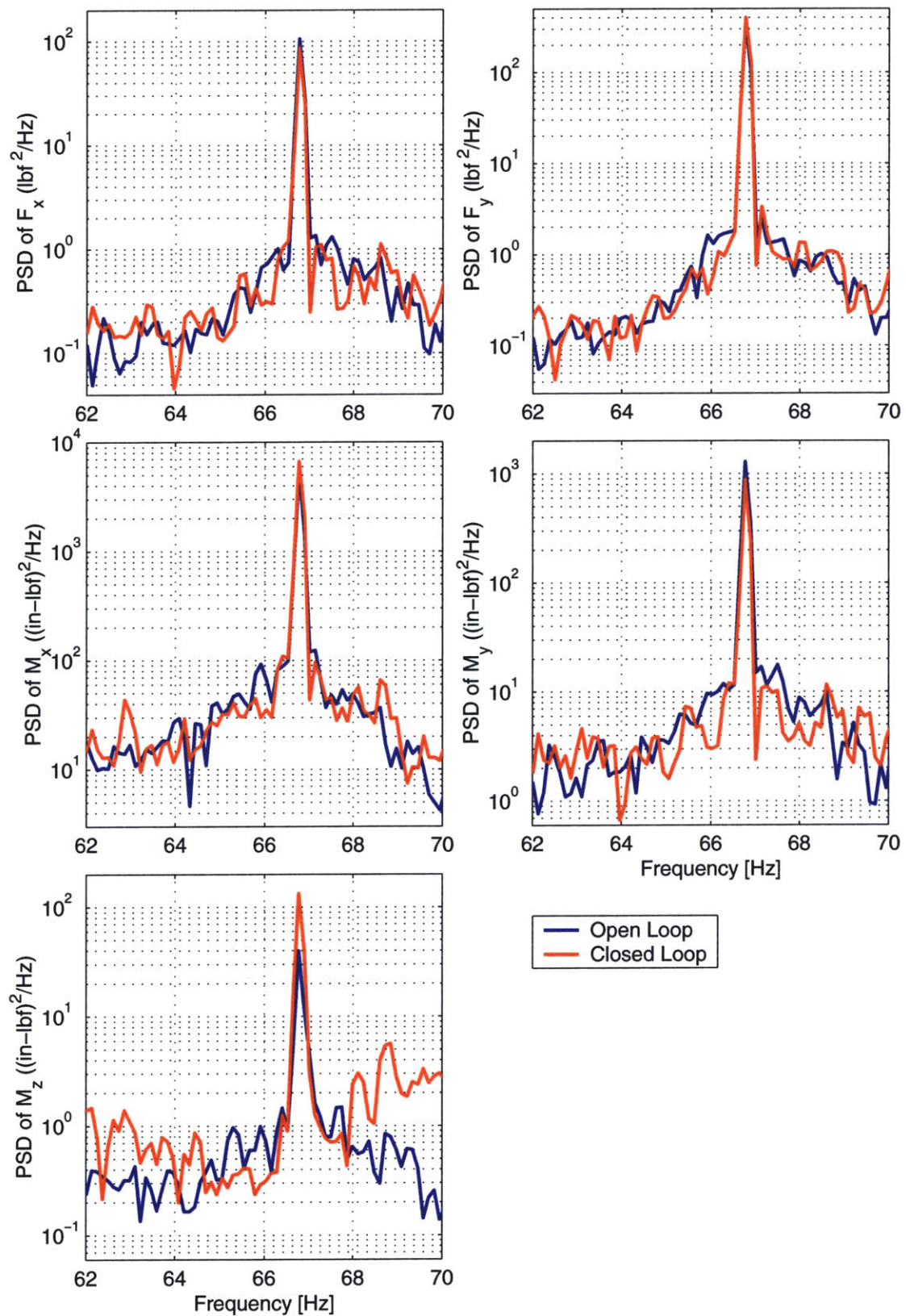


Figure D-34: Comparison of the open and closed loop measurements of the uncontrolled hub forces and moments for the 3/rev discrete controller

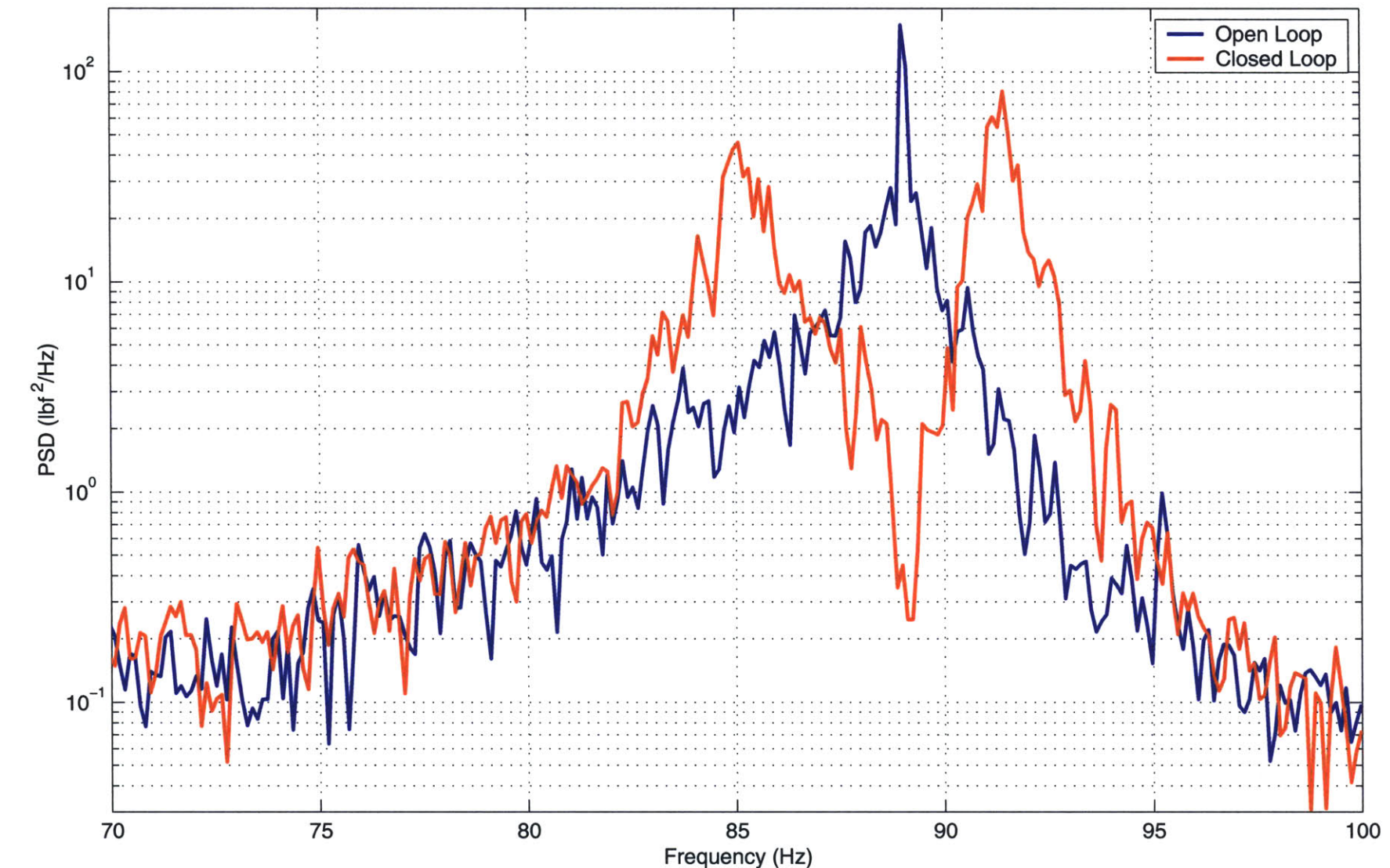


Figure D-35: Comparison of the open and closed loop vertical hub shear for the 4/rev discrete controller

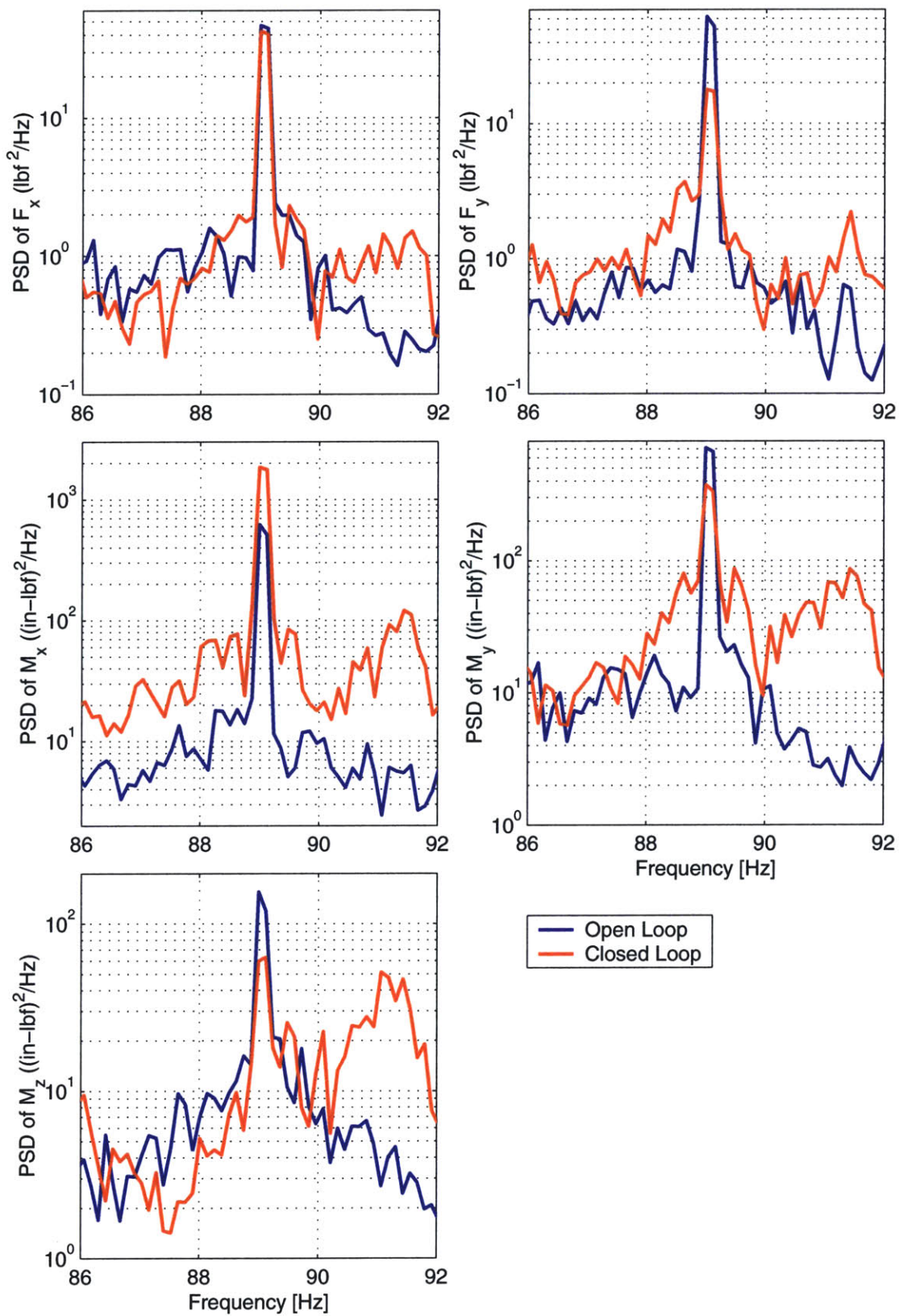


Figure D-36: Comparison of the open and closed loop measurements of the uncontrolled hub forces and moments for the 4/rev discrete controller



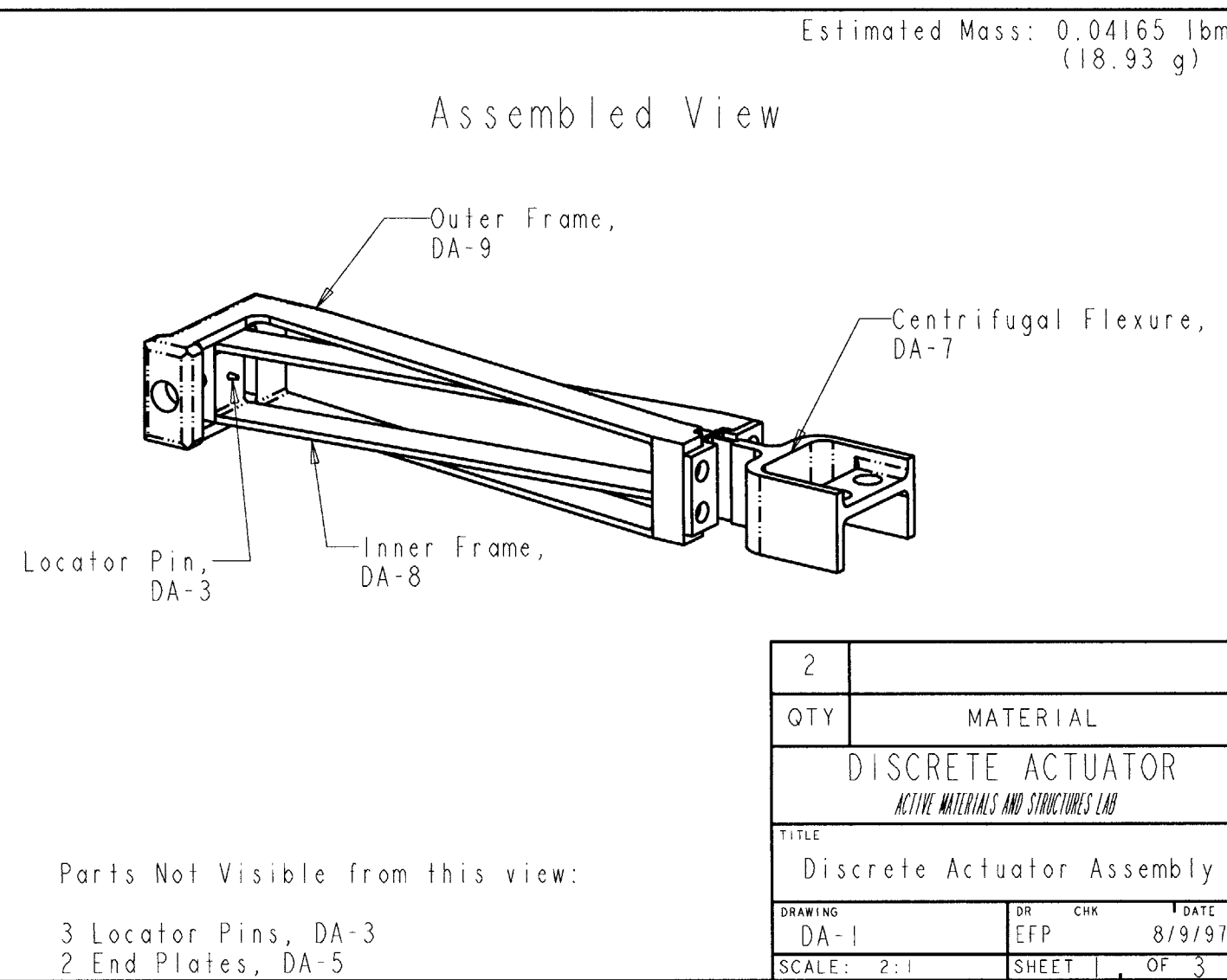
# **Appendix E**

## **Active Rotor Blade Fabrication**

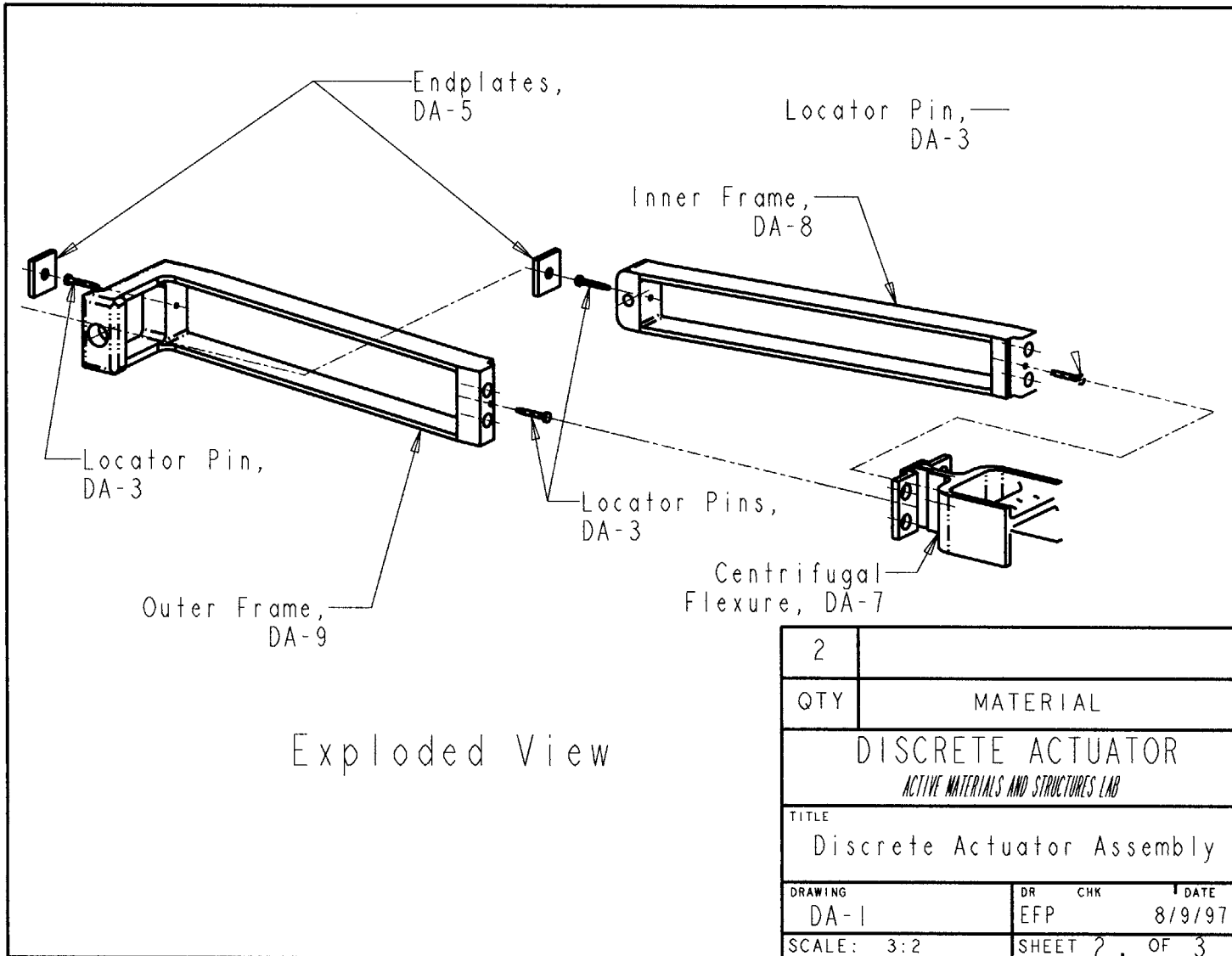
This appendix provides information related to the fabrication of the active blade. Section E.1 provides some basic engineering drawings of the actuator components in the rotor blade. Section E.2 presents a stepwise description of the composite manufacturing of the active blade.

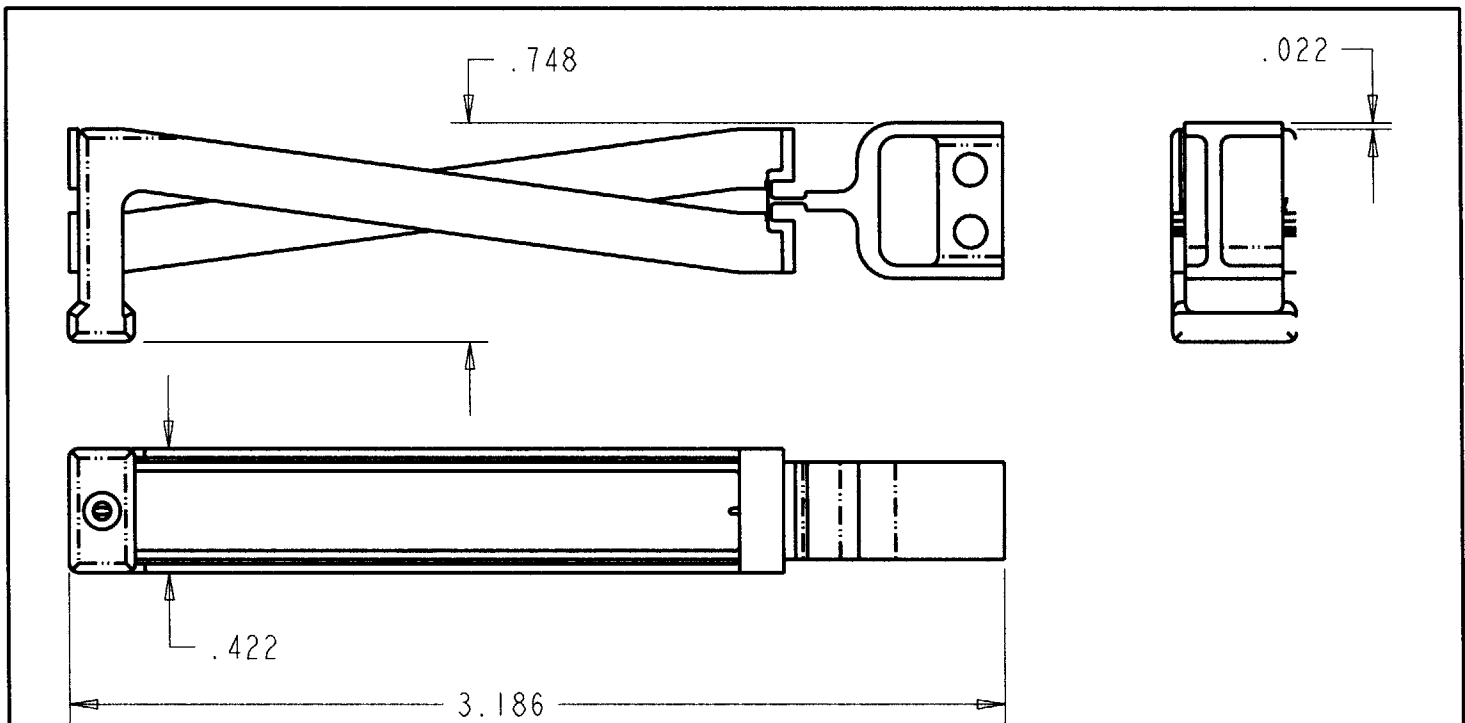
### **E.1 X-Frame Actuator Drawings**

This section contains engineering drawings of the model scale X-Frame actuator used in the active rotor blade. These drawings are protected, in part, by United States patent number 5,907,211 [34].



609

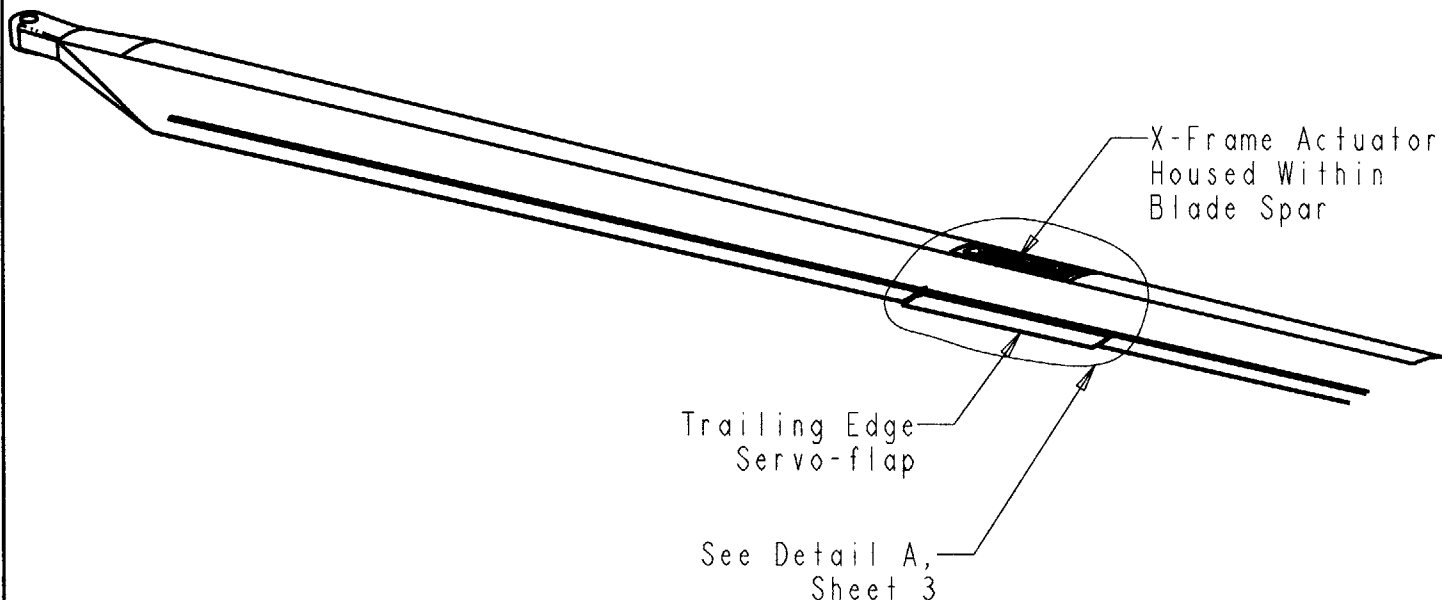


**Notes:**

1. All dimensions in inches
2. Unless otherwise specified, tolerances are:  
Angle +/- 1/4 deg  
Length +/- 0.005
3. All dimensions are post surface treatment specs.
4. Remove burrs and break sharp edges
5. 80 microinch max machine surface  
✓ roughness, unless otherwise specified

2		
QTY	MATERIAL	
<b>DISCRETE ACTUATOR</b> <i>ACTIVE MATERIALS AND STRUCTURES LAB</i>		
TITLE		
Discrete Actuator Assembly		
DRAWING	DR	CHK
DA-1	EFP	DATE 8/9/97
SCALE: 2:1	SHEET 3	OF 3

Active Rotorblade  
Assembled View



Active Rotor Blade  
ACTIVE MATERIALS AND STRUCTURES LAB

TITLE

Active Rotorblade

DRAWING

ARB-1

DR

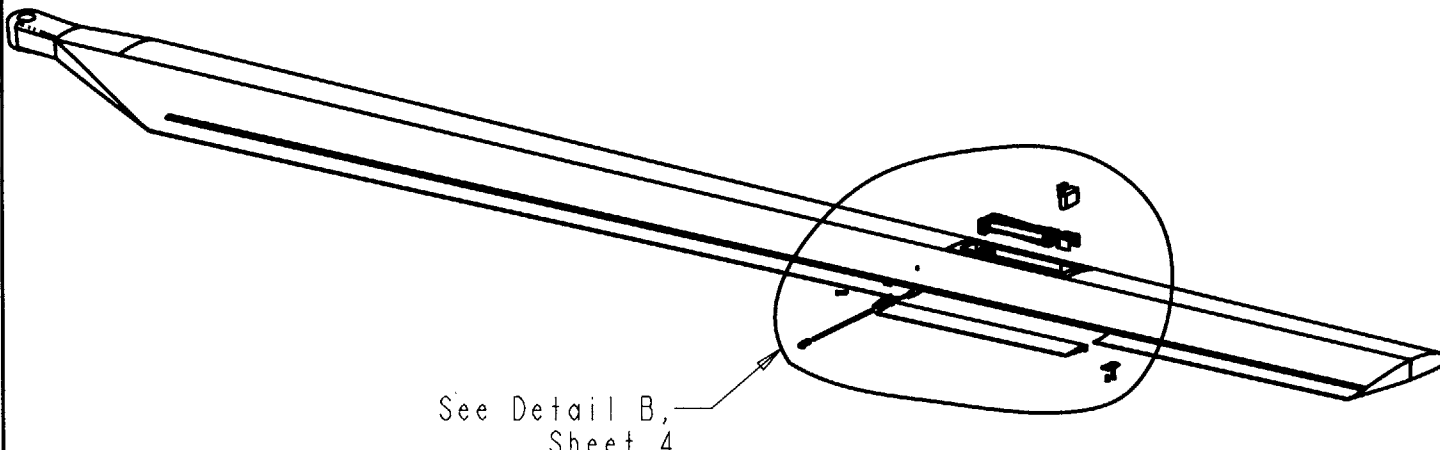
CHK

EFP 8/17/98

SCALE: 0.2250

SHEET 1 OF 5

Active Rotorblade  
Exploded View



Active Rotor Blade  
ACTIVE MATERIALS AND STRUCTURES LAB

TITLE  
Active Rotorblade

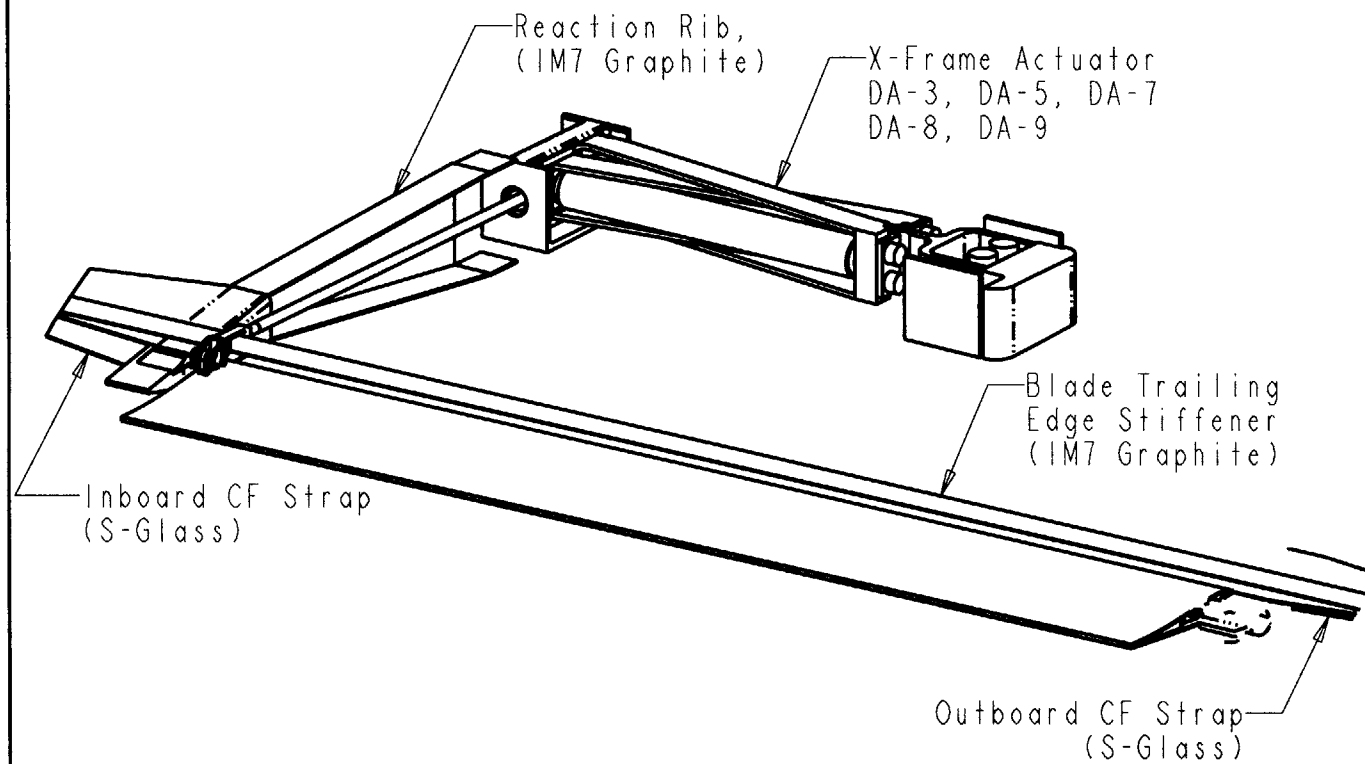
DRAWING  
ARB-1

SCALE: 0.2250

DR CHK DATE  
EFP 8/17/98

SHEET 2 OF 5

Detail A, Active Rotorblade  
Close-up, Assembled View  
(Blade Spar and Fairing Not Shown)



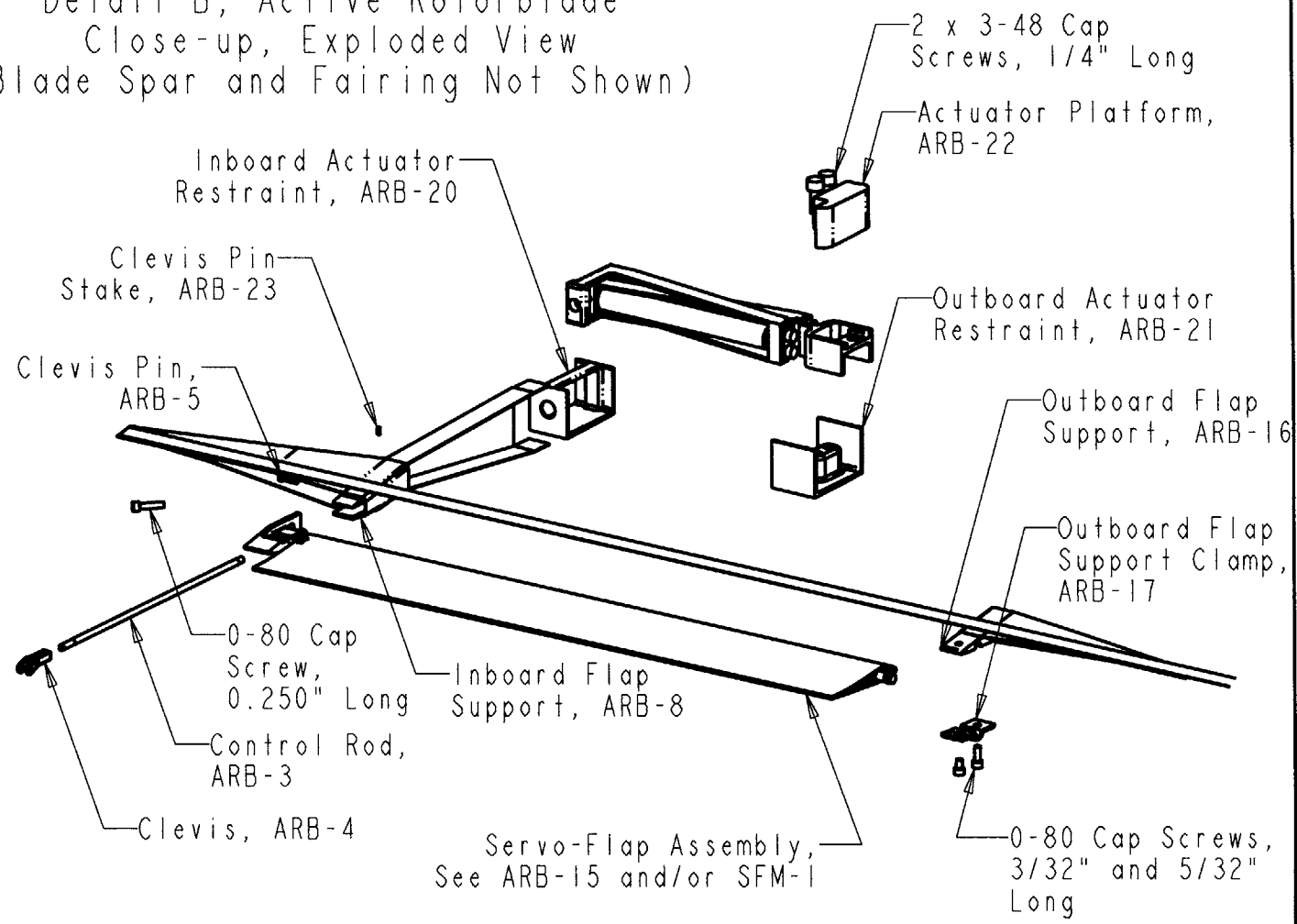
Active Rotor Blade  
ACTIVE MATERIALS AND STRUCTURES LAB

TITLE  
Active Rotorblade

DRAWING  
ARB-1  
SCALE: 1.2000

DR CHK DATE  
EFP 8/17/98  
SHEET 3 OF 5

Detail B, Active Rotorblade  
 Close-up, Exploded View  
 (Blade Spar and Fairing Not Shown)



Active Rotor Blade  
 ACTIVE MATERIALS AND STRUCTURES LAB

TITLE

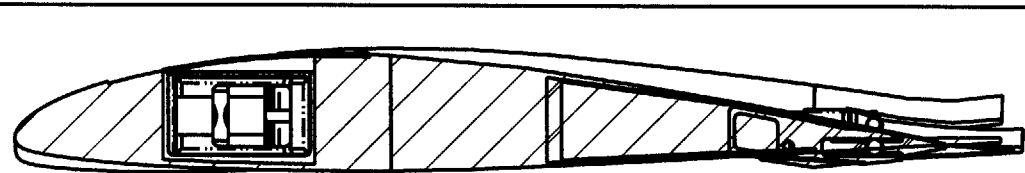
Active Rotorblade

DRAWING  
ARB-1

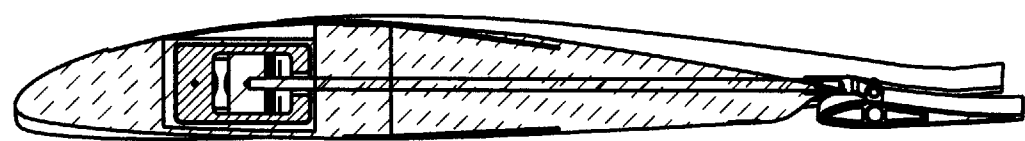
DR EFP  
CHK  
DATE  
8/17/98

SCALE: 0.7500

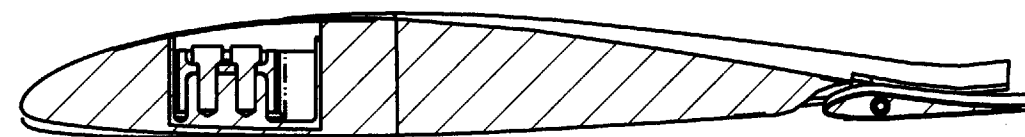
SHEET 4 OF 5



BS 43.947, 0.725R  
Scale 1.250  
Cross-Section at the  
Spanwise Center of  
PS-Wire Flange.



RBS 44.199, 0.729R  
Scale 1.250  
Cross-section at the  
Reference Blade  
Station.



BS 47.1625, 0.778R  
Scale 1.250  
Cross-section at the  
Outboard Restraint  
Bolt Hole Blade  
Station.



BS 51.110, 0.843R  
Scale 0.750

Cross-section at the  
Spanwise Center of  
PS Wire Keys.



BS 51.401, 0.848R  
Scale 0.750

Cross-section at the  
Spanwire Center of the  
Outboard Flap Support.

I	Varies
QTY	MATERIAL
Active Rotor Blade	
<i>ACTIVE MATERIALS AND STRUCTURES LAB</i>	
TITLE	Active Rotorblade
DRAWING	DR      CHK      DATE
ARB-1	EFP      8/17/98
SCALE: varies	SHEET 5, OF 5

## E.2 Manufacturing Steps

The active rotor blade is a composite structure that was built at MIT. The manufacturing procedure was based heavily on the process used by Boeing Helicopters to fabricate their model-scale rotor blades. Modifications were made to the process to incorporate the actuation system components while satisfying the design requirements of Section 3.1.1. The detailed manufacturing procedure is presented in this section.

### E.2.1 Main Blade Manufacture

The rotor blade consists of a Rohacell foam core with an external composite skin. The main body of the rotor blade is manufactured in two cures, a spar cure and then a fairing cure. Each cure is performed by wrapping composite plies around the foam core and curing the laminate in an aluminum blade mold. Most of the structural material is included in the spar of the blade. Thus, the spar manufacturing step is a critical factor in determining the dominant strength and stiffness properties of the blade. In the second cure, the fairing is attached to the spar through a lap bond between the fairing skin and the heel of the spar. In traditional passive rotor blades, the fairing is used mostly for aerodynamic purposes, but slight increases in the chordwise bending and torsional stiffnesses are attributed to its presence. Because of the addition of a trailing edge servo-flap in this active blade, the role and manufacturing of the fairing is of great importance towards successful performance of the blade.

The blade molds used were supplied by Boeing Helicopters. They have 16 embedded heaters and a thermocouple at each end of the blade. The thermocouple and heaters are integrated into a feedback control system to regulate the curing temperature. The curing cycle for all composites used in the blade is 250° F for 90 minutes. Pressure in the composite during the cure is achieved by using an oversized foam core and eight large steel clamps on the exterior of the molds.

The following sections describe the process used to shape the foam mandrel, add the instrumentation, and perform the spar and fairing cures. The final sections de-

scribe the post-cure operations on the blade.

### Foam Core Preparation

The interior of the rotor blade is composed of Rohacell foam. Rohacell 71 is used for the spar foam outboard of BS 10.608, and for the fairing foam inboard of BS 16.406. Less dense Rohacell 31 is used for the rest of the fairing. At the very root of the blade, from BS 9.093 to BS 10.608, higher density Rohacell 300 is used for strength purposes.

The foam mandrel is fabricated by sanding a number of short segments and joining them with 5-minute epoxy. Rectangular blocks of Rohacell were shaped on a belt sander by fixing them to steel templates of the desired shape. Figure E-1 shows the sanding process for one of the spar foam sections. After belt-sanding, special contours,



Figure E-1: Foam shaping on belt sander

shaped to accommodate leading edge weights and extra composite, were sanded into the foam by hand. A completed spar foam section is shown in Figure E-2.



Figure E-2: Rohacell spar foam section after sanding

The foam shape was determined by taking the outer mold line of the blade and subtracting out the thickness of the composite plies. Calipers were used to check the foam to ensure proper sizing. Figure E-3 shows the entire collection of spar and fairing foam. Figure E-4 shows a close-up of the spar and fairing foam at the root. As shown, the foam cross-section at the root differs significantly from the main blade section.

At the blade stations where the actuator was located, the foam was modified to account for the inclusion of the actuator bay and slotted profile at the trailing edge. The foam near the actuator location is shown in Figure E-5. Because the inboard flap support protrudes below the standard fairing contour, foam was added to the bottom surface, just inboard of the support location to provide a smooth contour for the composite as it transitions from the standard contour to the support. A cut-out was machined into the blade molds to account for this protrusion.

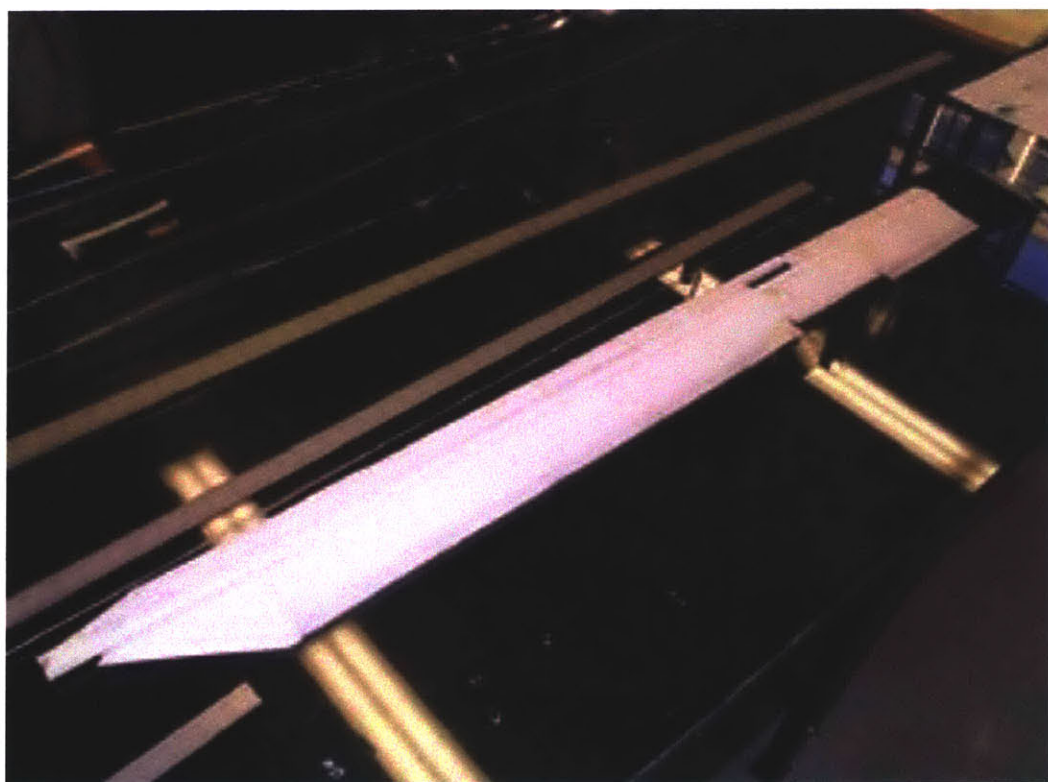


Figure E-3: Entire collection of spar and fairing foam for the active rotor blade

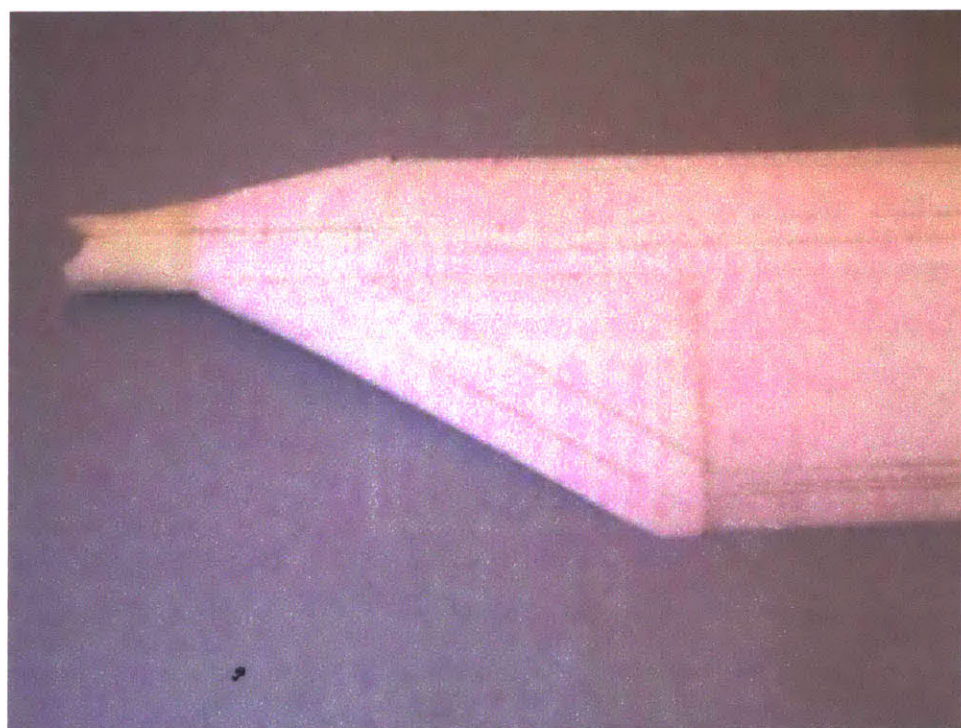


Figure E-4: Close-up view of the top surface of the spar and fairing foam at the blade root



Figure E-5: Close-up view of bottom surface of the spar and fairing foam at the actuator and servo-flap blade stations

### Instrumentation

The sensors used in the rotor blade include strain gages, Hall effect transducers (HETs), and a resistive thermal device (RTD), as discussed in Section 3.1.6. In addition, high voltage wires were needed to power the piezoelectric stacks. One high voltage and one ground wire is required to power each stack. Thus, four wires are needed to power the actuator. But for redundancy, eight high voltage wires were used to supply the high voltage signal.

The sensor and high voltage wires were run from the root of the blade to the desired blade station through a number of canals located within the foam core. To form these cavities, the prepared foam core was cut open with a razor and shallow troughs in the foam were cleared out. There were three primary wire harness cavities in the blade. One is located along the pitch axis of the blade, *i.e.*, at the blade 1/4 chord, which houses the majority of the sensor wires. One cavity is located in the web of the fairing foam to hold eight wires that are used for the trailing edge hall effect

sensor and axial strain gage bridge. And one cavity is located in the web of the spar foam. This cavity holds the eight high voltage wires used to power the actuator. To accommodate the two sensors located outboard of the actuator bay, seven wires were routed around the front of the bay. These wires traveled through a smaller cavity that branches off of the pitch axis cavity inboard of the bay.

All of the wires exit the blade at the aft side of the root near BS 10.608. The pitch axis wire harness cavity is curved aft at the root to allow the wires to exit, as shown in Figure E-6.

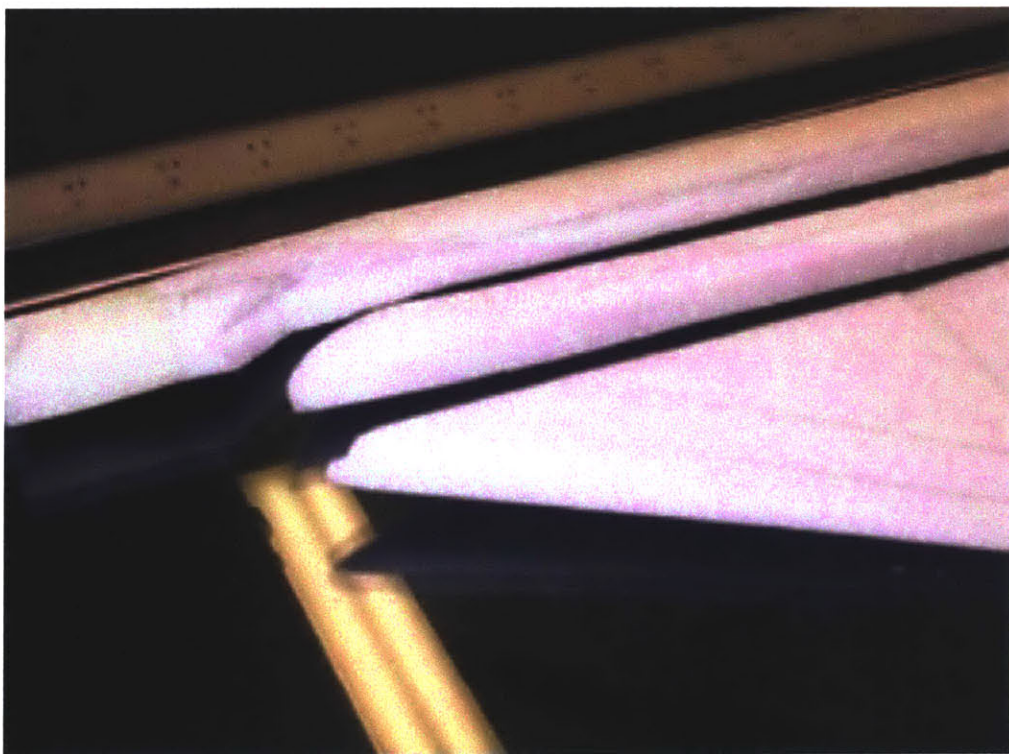


Figure E-6: Details of the cut at the root of the spar foam made to accommodate the wire harness

Each of the various groups of wires was placed into its foam cavity. Rectangular strips of aluminum foil were placed between the instrumentation wire groups and the spar web, where the high voltage wires reside. To shield the instrumentation wire harnesses from the high voltage signals, these aluminum strips were grounded electrically during testing. To support the wire harnesses in the centrifugal field of the blade, the wires and cavities are filled with 9309 epoxy and, in the case of the

spar foam, the two spar halves are joined together.

## Spar Manufacture

The general make-up of the rotor blade spar consists of a solid foam core (with the exception of the embedded wires) surrounded by a composite skin. To allow access to the actuator bay, a hatch in the blade spar at the actuator location must be incorporated. Structurally, the hatch represents a large hole in the spar structure, raising the stresses in the surrounding composite, and lowering the torsional stiffness. To offset the loss in torsional stiffness from the hatch, ribs and webs were added to the interior walls of the actuator bay. Each web and rib is composed of two plies of S-Glass, running at +45 and -45 degree orientations. The ribs run approximately two inches chordwise, from the leading edge over the entire width of the spar. The webs run spanwise from BS 43.749 to BS 47.572.

The ribs are the first composite plies applied. Care must be taken upon attaching these plies to allow for the instrumentation wires to poke through the ribs, as shown in Figure E-7. The wires (and aluminum foil shielding) for the outboard instrumentation are seen running near the leading edge of the foam in Figure E-7. After the ribs are in place, two pieces of spar foam are used to sandwich these wires. 9309 epoxy is used to pot the wires in this cavity using a procedure similar to that used for the main spar foam, described above.

The front web ply is attached to the cured foam section. All of the instrumentation wires and four of the high voltage wires are run along the inboard rib and front web and connected to small solder pads. Scotch tape strips were used to aid in holding these wires in place against the bay walls during the soldering process. After the wires were correctly located, they were tacked to the walls with 5 minute epoxy to hold them in place. Figure E-8 shows the front web and the logistics of how these wires are routed.

A spar mandrel assembly was used to create the actuator bay. The function of the assembly is to provide a spacer around which the composite can cure. After the cure, the mandrel is removed leaving a void in the structure of a desired shape. Successful

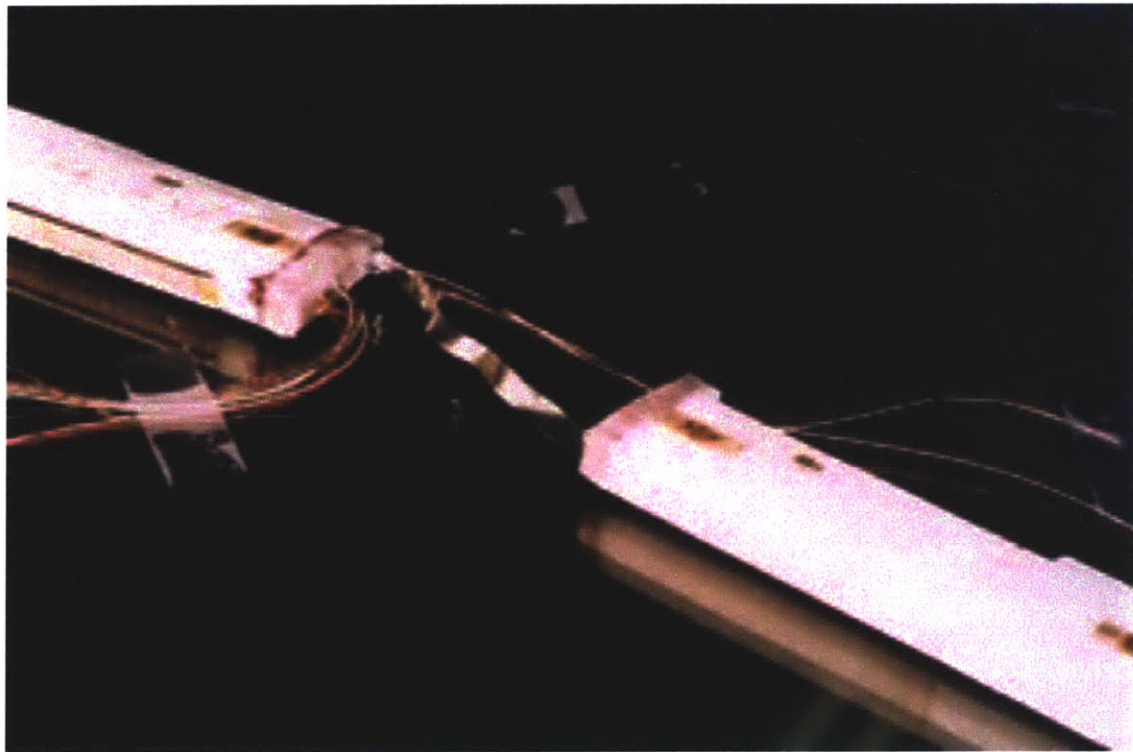


Figure E-7: View of inboard and outboard S-Glass ribs and wiring logistics at the actuator bay section

design of a mandrel is dependent on satisfying two main requirements. Firstly, the mandrels must hold the spar restraints in the proper orientation during the cure. Secondly, it must be possible to easily remove the mandrels after the cure without damaging the composite structure.

The parts that make up the spar mandrel assembly are shown in an exploded view in Figure E-9. An assembled view of the components (with the exception of the mating bolts and locator pins) is shown in Figure E-10. The outboard spar restraint is bolted against the outboard spar mandrel. A cut-out on the bottom side of the mandrel accommodates the platform on the spar restraint. The middle spar mandrel slides underneath the cross-member in the inboard spar restraint to support that member during the cure. The inboard end of the outboard spar mandrel interfaces with the outboard side of the inboard spar restraint/middle spar mandrel. The two mandrels are joined together using a bolt and threaded hole oriented at 45 degrees. The interface of these two mandrels determines the relative positions and orientations

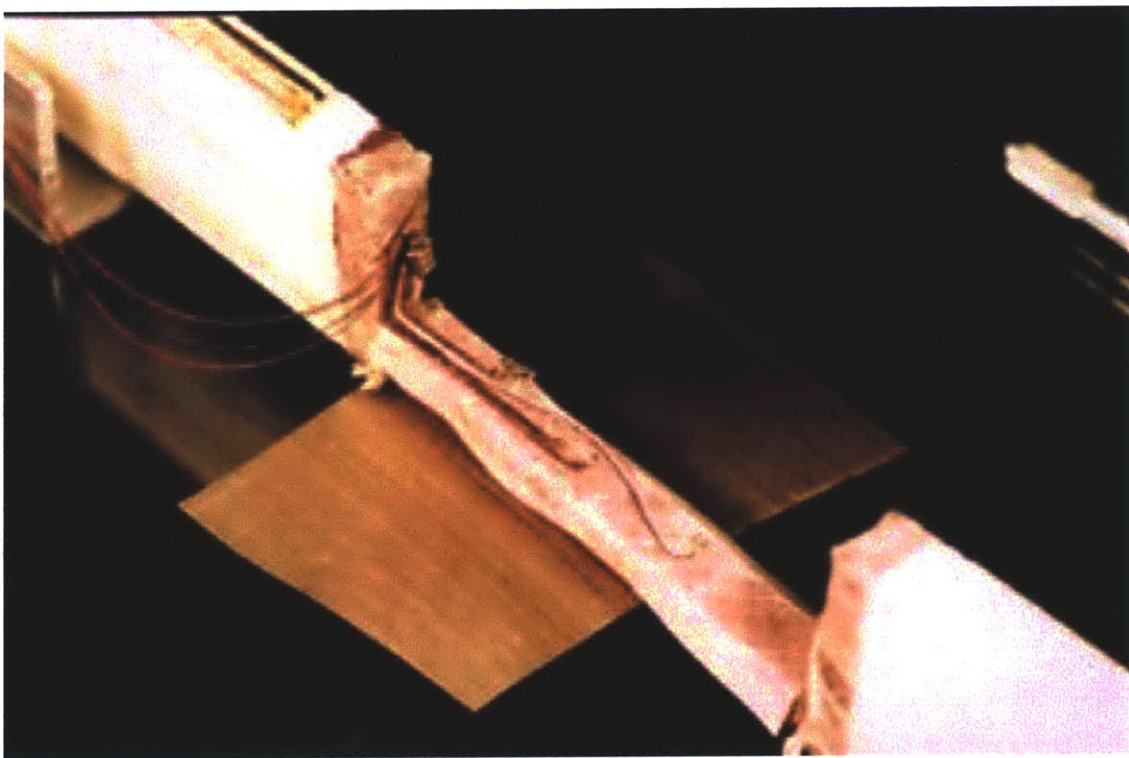


Figure E-8: Logistics of the bay instrumentation wires and solder pads (held down to the front web with scotch tape) and the high voltage actuation wires

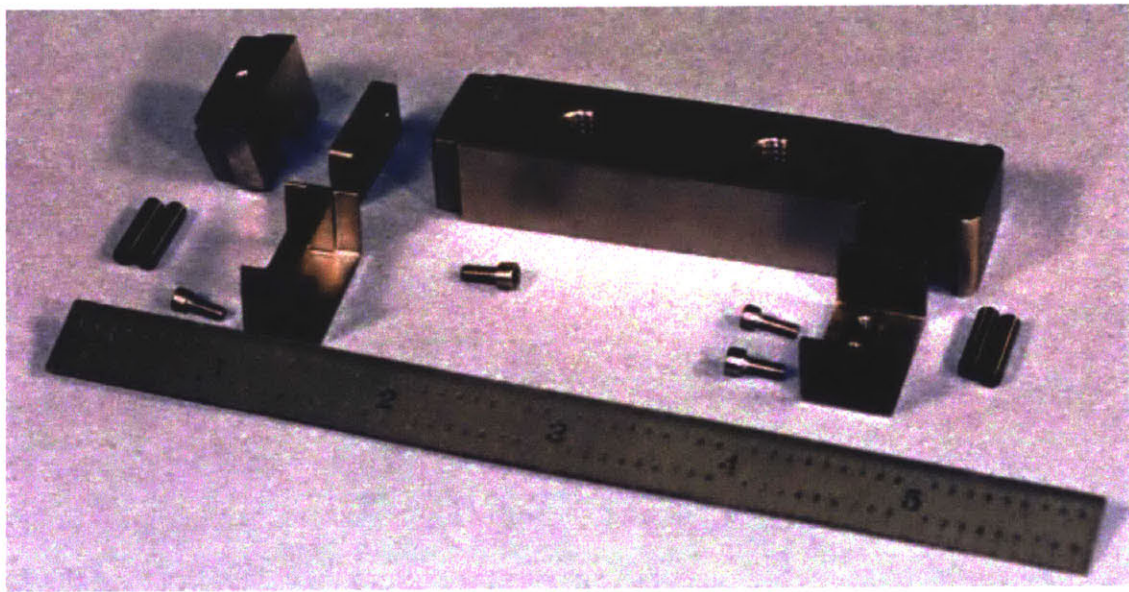


Figure E-9: Exploded view of the components making up the spar mandrel assembly

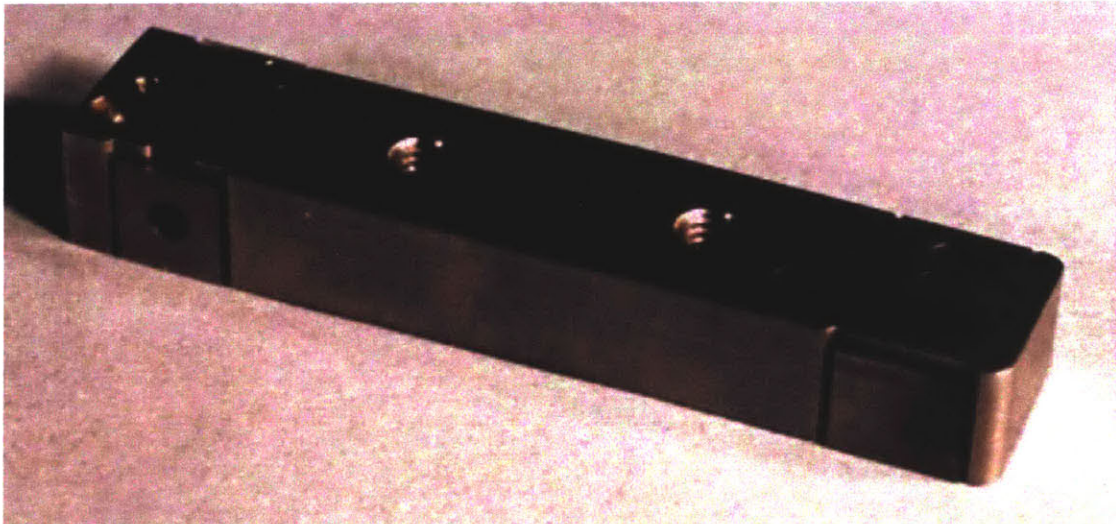


Figure E-10: Assembled view of the spar mandrel assembly prior to surface prep

of the two spar restraints. Precise positioning of these restraints is necessary to ensure that the actuator fits within the blade properly.

To create a space inboard of the actuator, the inboard spar mandrel interfaces with the inboard side of the inner spar restraint/middle spar mandrel in a manner identical to that for the outboard spar mandrel. Counter-bored holes are included in the inboard and outboard spar mandrels to isolate the bolts from the blade mold line surface.

Two 1/4-20 threaded holes are added to the top surface of the outboard spar mandrel and one 2-56 threaded hole is added to the top surface of the inboard spar mandrel. These holes are used as grip points to aid in pulling the mandrels directly up and out of the actuator cavity after the spar cure. Gauze is inserted into these holes, as shown in Figure E-11, and they are covered with GNPT tape to protect the threads from flowing epoxy during the cure.

To maintain the orientation of the restraints during the cure, four 1/4 inch diameter dowel locator pins are pressed into the inboard and outboard spar mandrels and mate with holes machined into the blade molds. These pins are lying along-side the spar restraints in Figure E-9. Figure E-13 shows the spar mandrel assembly, prepared for the spar cure, with the locator pins pressed into place.

The spar mandrels are designed so that, after the cure, they can be unbolted



Figure E-11: Preparation of the outboard spar mandrel. Placing gauze in the threaded holes to absorb flowing epoxy during cure

from each other and the outboard spar restraint so that the inboard and outboard spar mandrels can slide vertically out of the formed actuator bay. The middle spar mandrel is then removed from under the inboard spar restraint cross-member.

In order to succeed in sliding these mandrels out of the bay, without damaging the composite structure, all surfaces of both the mandrels and restraints were prepared by coating the bare metal with frekote, applying GNPT tape, and coating the exterior of the tape with frekote, again. Furthermore, to ensure that the two restraints are held tightly in place, the outer surfaces of the restraints, that form the lap joint surface, are sanded with 220 grit sandpaper, coated with BR-127 Primer (made by Cytec Industries), and covered with two layers of film adhesive. The application of the primer to the lap-joint surfaces is shown in Figure E-12. Once all parts were suitably prepared, they were joined into the assembly shown in Figure E-13, and the spar mandrel assembly was slid into place between the bay webs and ribs.

Film adhesive was applied to all spar foam surfaces in preparation for adding the



Figure E-12: Application of primer to the lap joint surfaces of the inboard and outboard spar mandrels



Figure E-13: Assembled and surface prepped spar mandrel assembly, including GNPT tape on sliding surfaces and film adhesive on lap joint surfaces

main spar skin plies, as shown in Figure E-14. A specific distribution of tungsten



Figure E-14: The blade spar foam with film adhesive applied

leading edge weights is used to properly balance the rotor blade. The weights include both long, thin rods and short segmented weights. The various weights are distributed spanwise and rolled up in a 0° S-Glass uni-directional ply. The S-Glass is used to properly restrain the weights in the centrifugal field. The segmented weights are also wrapped in film adhesive to aid in bonding them to the S-Glass. This leading edge weight assembly, referred to as the *nose block*, and the E-Glass web plies are attached to the fore and aft edges of the prepared foam, respectively.

The blade skin consists of five layers of composite as shown in Figure E-15. This is the make-up of the spar composite laminate over the majority of the blade span. With the exception of the uni-directional IM7 layer, a rectangular cut-out was made in the top surface of the plies to form the actuator bay hatch. Figure E-16 shows the process used to lay-up and trim the S-Glass 45 degree spar ply number 4. On the bottom side of the spar, small holes are cut into the different composite layers to allow the locator pins to poke through, as shown in Figure E-17.

Spar Ply 1	E120 Fabric	$0^\circ$
Spar Ply 2	IM7/SP381 Tape	$0^\circ$
Spar Ply 3	S2/SP381 Tape	$+45^\circ$
Spar Ply 4	S2/SP381 Tape	$-45^\circ$
Spar Ply 5	S2/SP381 Tape	$0^\circ$

Figure E-15: Main blade skin lay-up

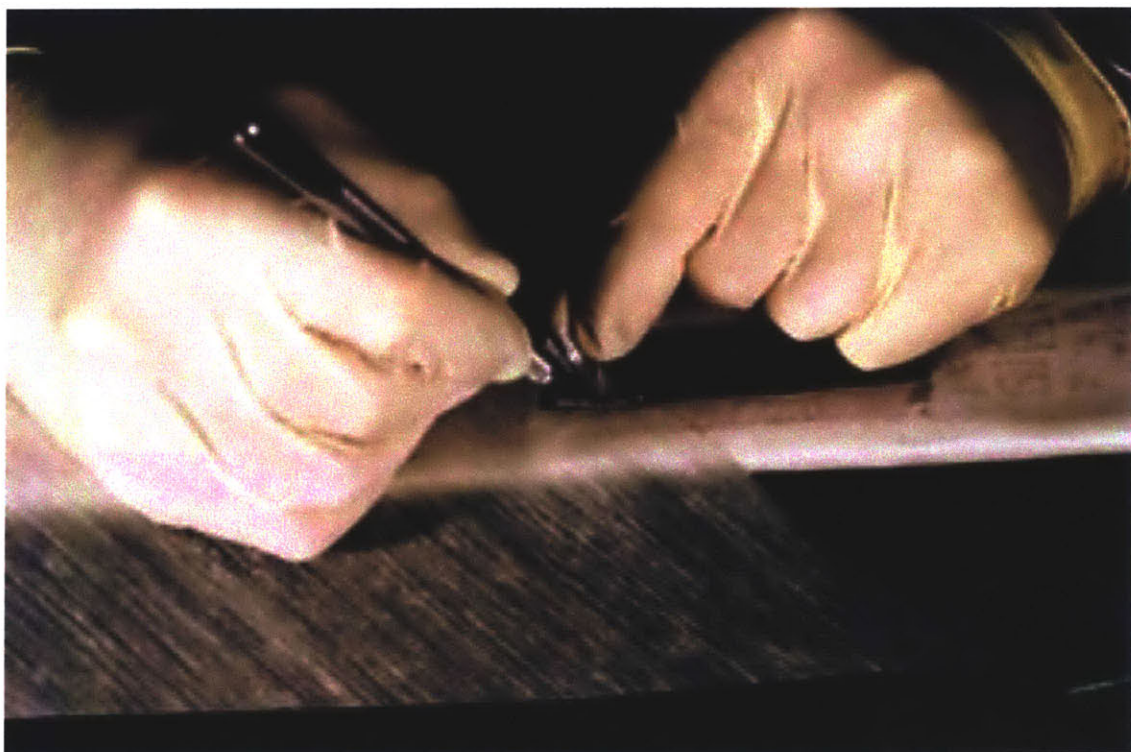


Figure E-16: Trimming the S-Glass  $45^\circ$  spar plies around the top surface of the actuator bay

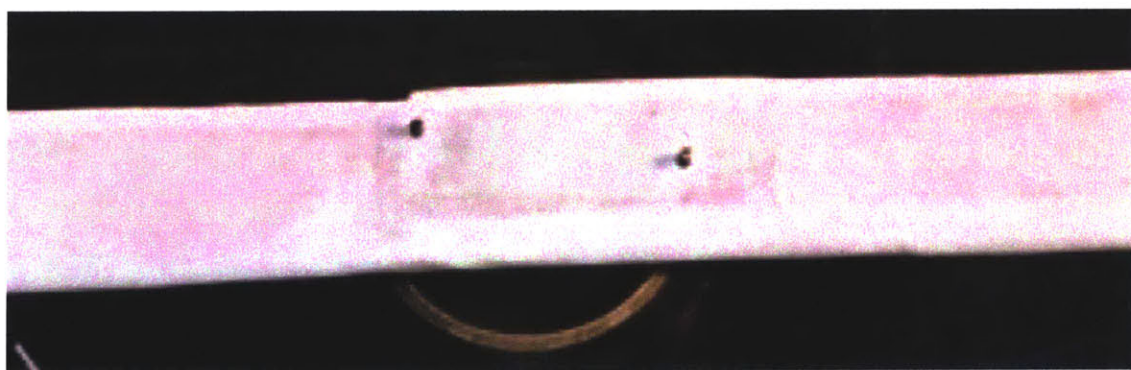


Figure E-17: Lower surface locator pins poking through S-Glass spar plies

The 0° IM7 graphite uni-directional plies are layed down in a manner identical to that for the spar doublers. However, the presence of the actuator hatch on the top surface complicated the process. If this ply is cut to allow for the hatch, a great deal of the centrifugal strength of the blade would be lost outboard of the hatch. To avoid trimming this ply, as the strips are layed down on the top surface, they are diverted to the sides of the actuator bay. The diversion begins about four inches from either end of the actuator bay. Thin strips are cut into the plies in the fiber direction to make the ply easier to shear during this diversion process. The diversion process and the completed logistics of the IM7 ply are shown in Figures E-18 and E-19.



Figure E-18: Diversion of IM7 unis around the actuator bay on the top surface

Secondary bonds are applied to the blade spar during the fairing cure at the blade root and along the spar web. In addition, the hatch gets bonded to the top surface, covering the actuator just before hover tests. Aluminum tape is used to indent the spar during the cure to make room for this hatch. For the secondary bonds at the blade root, aluminum tape is applied directly to the blade mold to make space for the future plies, as shown in Figure E-20. After applying this tape, the molds are

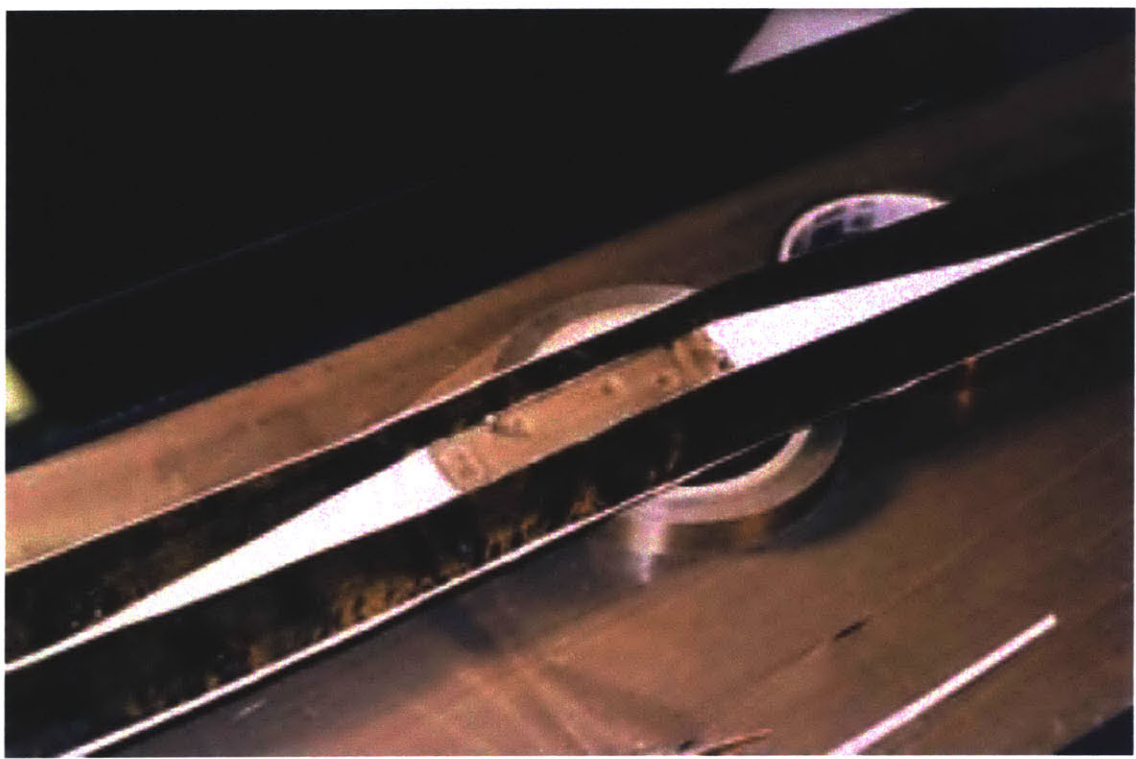


Figure E-19: Top surface IM7 logistics after uni diversion

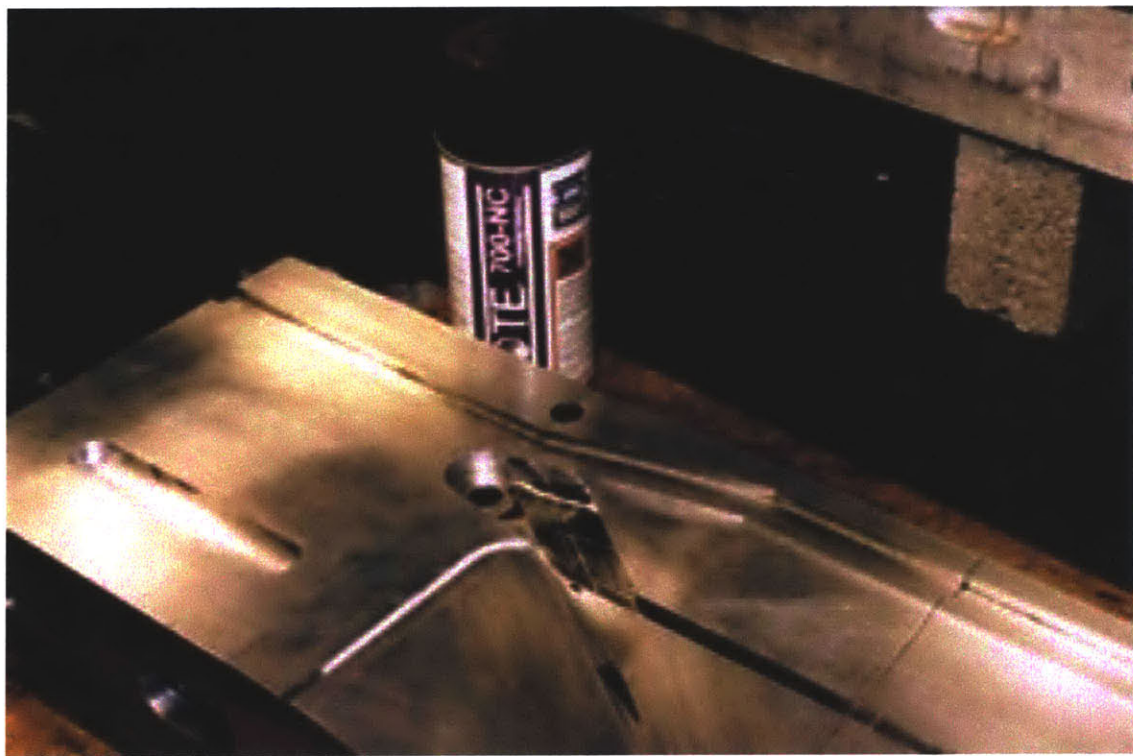


Figure E-20: Aluminum tape applied to the blade root to make room for the secondary bonds during the fairing cure

frekoted three times in preparation for the spar cure.

One of the greatest challenges in the spar manufacture was getting the spar laminate, which is oversized, into the blade mold. This was especially difficult at the blade root. With some effort the root was fit into the mold. The instrumentation and high voltage wire bundles were taped into pre-machined channels in the blade spar. In addition, an S-Glass hard-back is fixed in the aft side of the mold to provide back-pressure on the spar during the cure. With the root in place, the tip of the blade was pushed in toward the root until the two top alignment pins in the spar mandrel assembly dropped into the mating holes in the mold.

After all the alignment pins were in place, the composite at the very root of the blade was pressed and shaped by hand and with various tools to get the composite to fit within the mold lines. The strategy used was to re-distribute as much composite as possible toward the outboard side of the root pin. To check the fit of the root, a piece of GNPT was placed over the blade and the bottom mold was lowered into place and clamped lightly at the root. The molds were separated, and any pinched material was reshaped and pushed tighter against the root pin. The appearance of the root just prior to closing the molds for the final cure is shown in Figure E-21. As shown, most of the composite was successfully within the blade root boundaries. A slight pinch of the composite material is evident along the aft side of the root. However, a determination was made that this was an acceptable distribution of plies to warrant the closing of the molds.

The molds were closed and clamped together using eight heavy duty steel C-clamps (and one, smaller C-Clamp), as shown in Figure E-22. The spar was cured at 250 deg F for 90 minutes and the molds were allowed to cool fully.

A picture of the blade root just after the molds were opened is shown in Figure E-23. As shown, a small amount of the composite at the root was pinched during the cure. However, this represents only a small percentage of the composite located there.

The composite cures fully after 90 minutes at 250° F. Because of the root pin and the spar mandrel assembly alignment pins, the blade is held fixed at these two spanwise positions while the blade and mold cool. Because the coefficient of thermal

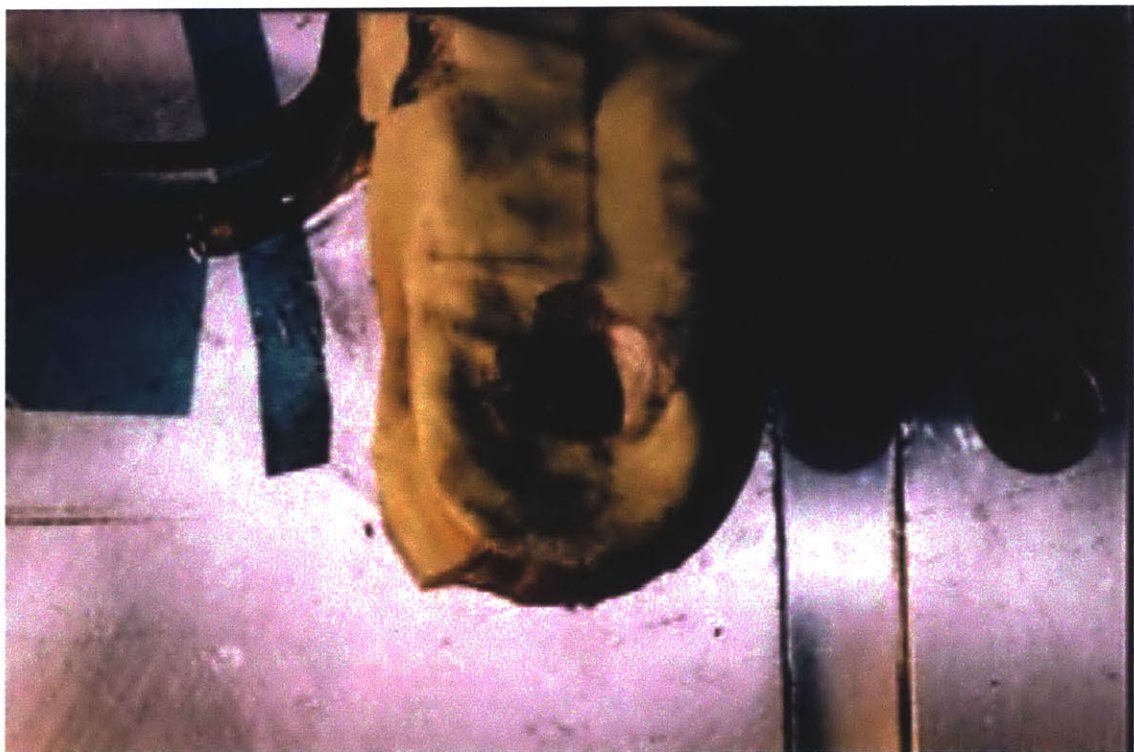


Figure E-21: Bottom surface of the root, shaped as tight as possible (with slight pinch on aft side) just prior to final closing of molds



Figure E-22: Rotor blade molds, closed and clamped together for the spar cure



Figure E-23: Post-cure view of root bottom surface just after opening molds

expansion of the aluminum is much greater than that of the composite, a compressive stress is created in the composite rotor blade during cooling. Upon removing the blade, this residual compressive stress releases and the blade extends a small amount. This prohibited re-insertion of the blade into the cooled mold while both the root pin and locator pins were in place.

A view of the blade root after trimming the composite flash around the root is shown in Figure E-24. Some pinching of the graphite ply on the lower, aft edge of the root is evident in this figure.

Figure E-25 shows the top surface of the blade spar after the cure with the hatch spacer still in place. There is some slight non-uniformity of the composite at the web around this blade station. This was due to the fact that the spar mandrel assembly did not lie flush with the bay walls at the beginning of the lay-up. The large pressures used to close the mold compacted this composite, causing the non-uniformity. This non-uniformity represented a small level of damage to the blade structure and was not of great concern.



Figure E-24: Aft edge of root after trimming off the composite flash

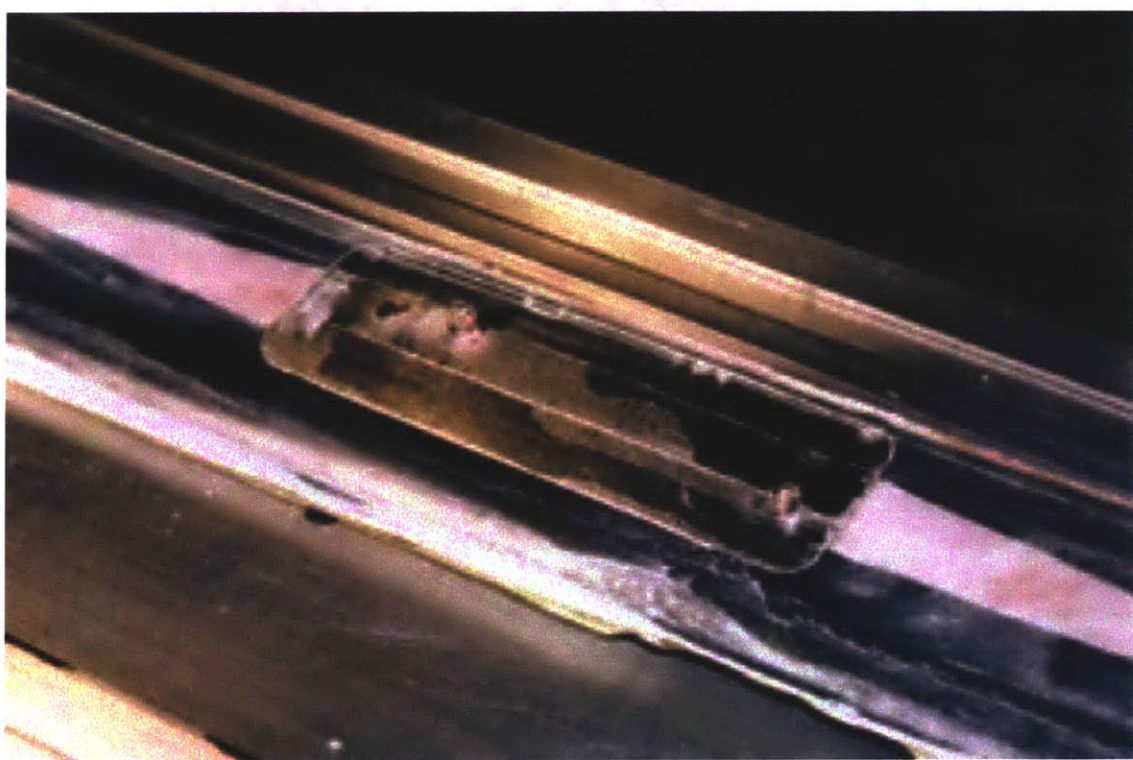


Figure E-25: Post-cure view of the top spar surface at the actuator bay just prior to removal of the peel-ply/aluminum tape spacer

The next step in the manufacturing process was to remove the spar mandrels and ream the clearance hole through the web to allow for the control rod to pass freely. A view of the spar mandrel assembly in the cured blade spar from the aft side is shown in Figure E-26.

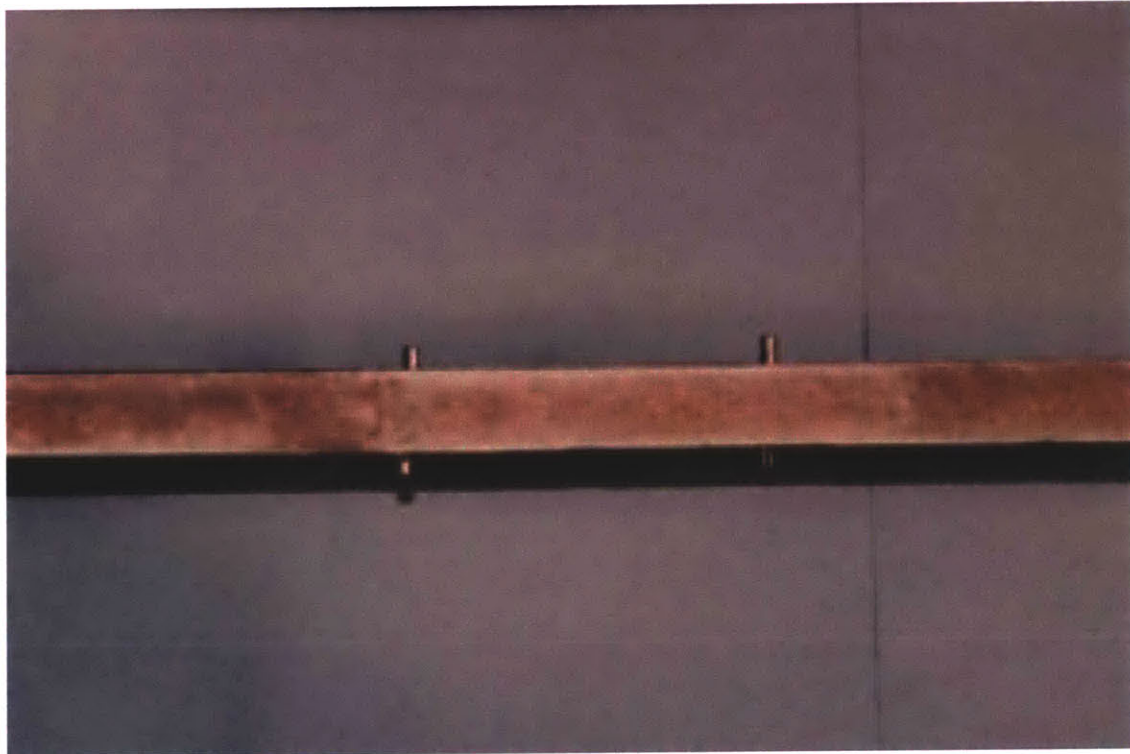


Figure E-26: Aft view of the web at the actuator bay location, highlighting the spar mandrel assembly locator pins

The control rod hole was machined into the blade by orienting the spar at the proper angle on a milling machine and performing drilling and reaming operations through the blade web, as shown in Figure E-27. The hole was located using reference points off of the inboard spar restraint.

While mounted to the milling machine, the locator pins were pulled out of the spar mandrels using a vice-grip, as shown in Figure E-28.

The inboard and outboard spar mandrels were designed to be removed by pulling them vertically out of the blade spar. Before they could be removed, the composite material around the mandrel had to be trimmed away with a hobby knife.

The 2-56 threaded hole in the center of the inboard spar mandrel was used to

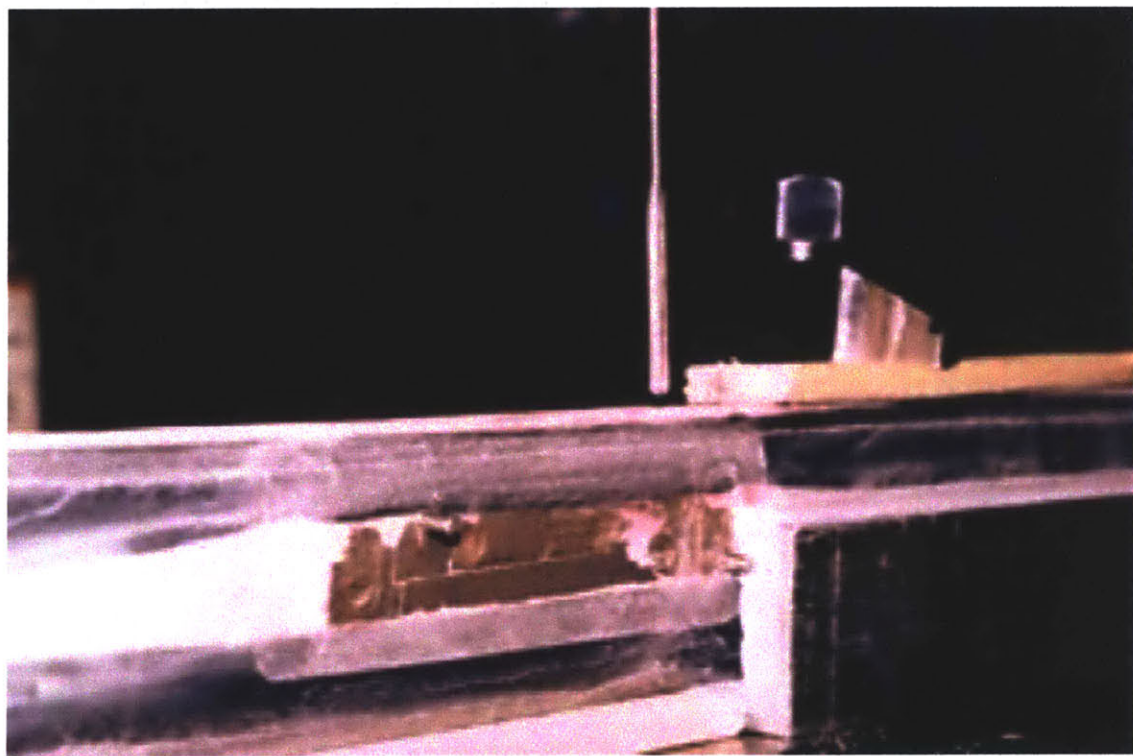


Figure E-27: Reaming of the control rod clearance hole through the web

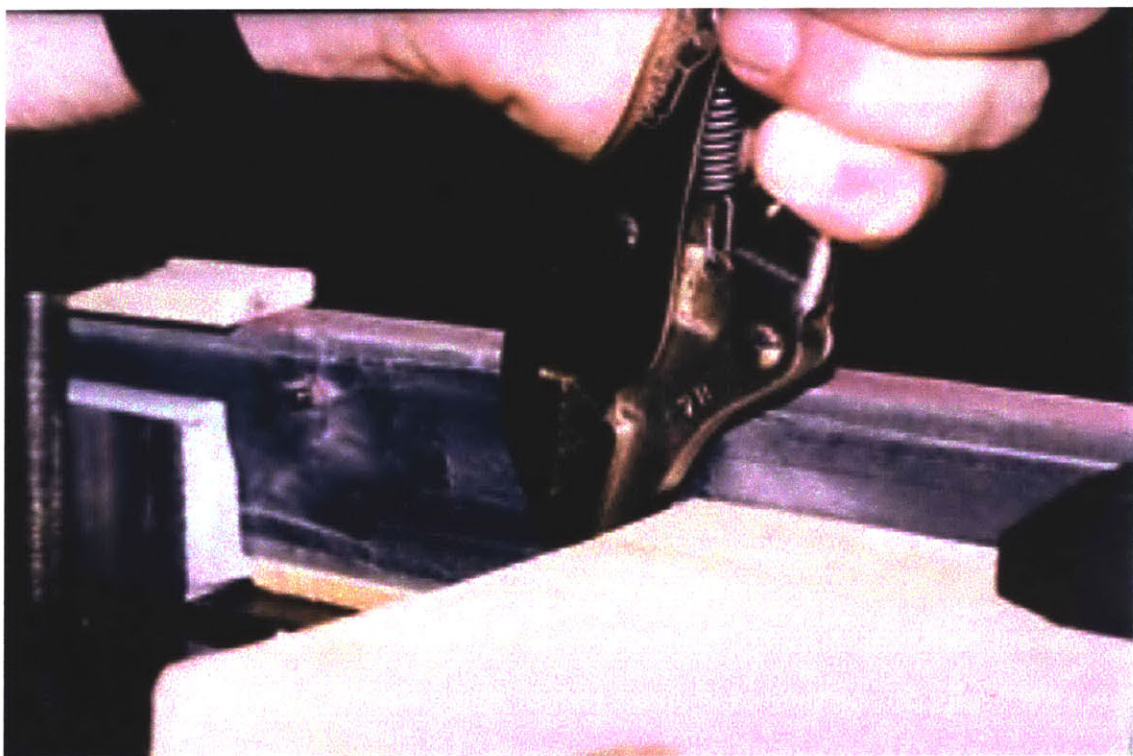


Figure E-28: Removal of the locator pins from the spar mandrel assembly

attach a make-shift grip to aid in pulling the mandrel out, as shown in Figure E-29. The inboard spar mandrel was able to be pulled out by hand part-way, into the

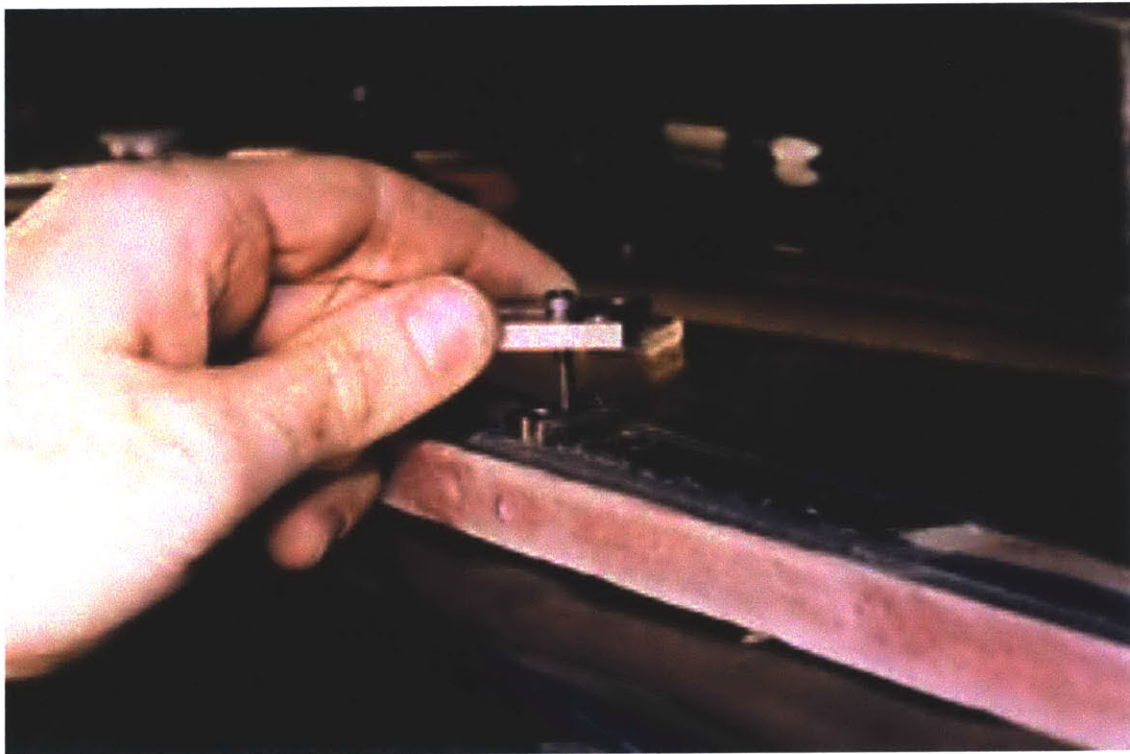


Figure E-29: View of the inboard spar mandrel pulled out halfway

orientation shown in the figure. A hammer (with a supporting piece of wood) was used to pry the mandrel out the rest of the way.

In a similar fashion, the composite around the outboard spar mandrel was trimmed away and the mandrel pulled out, as shown in Figures E-30 and E-31. Because the outboard spar mandrel has much greater surface area in contact with the composite, some mechanical advantage was needed to remove this mandrel, as shown in the figure.

A view of the completed spar is shown in Figure E-32 and Figure E-33 shows a close-up view of the actuator bay with the spar mandrels removed. Clearly seen in this figure are the wires and solder pads against the front web in the actuator bay. The GNPT tape is still covering these pads in the photograph.

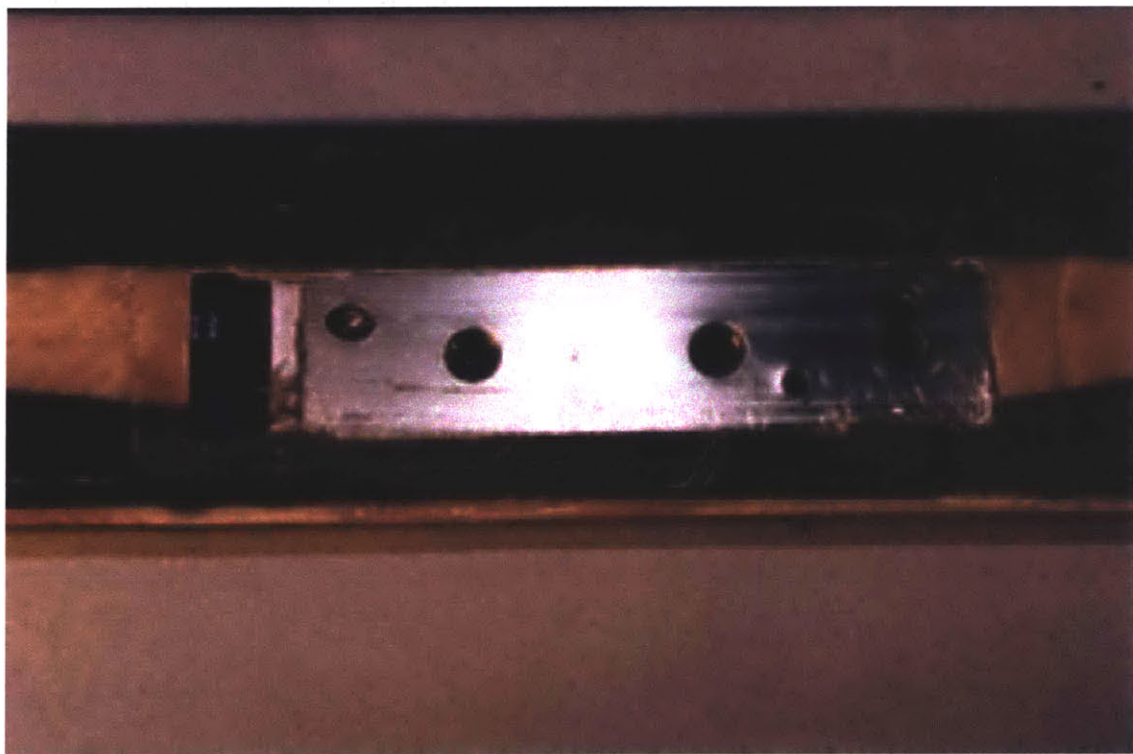


Figure E-30: Trimming of the composite from around the outboard spar mandrel

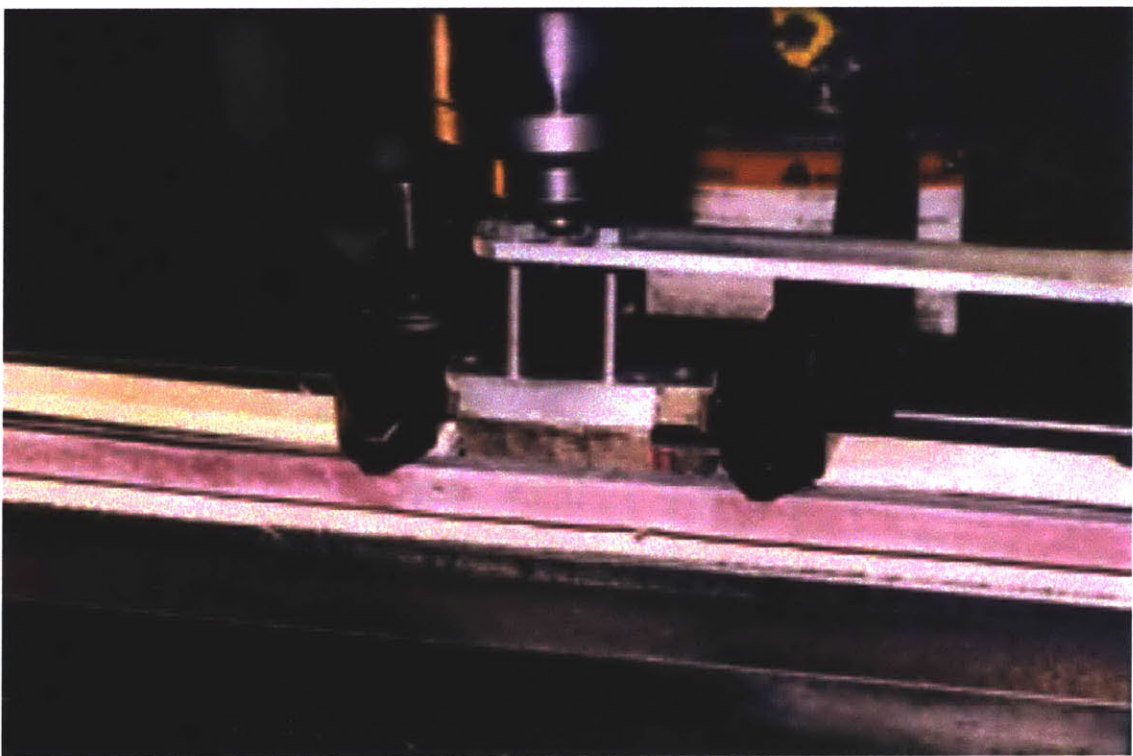


Figure E-31: Removal of outboard spar mandrel

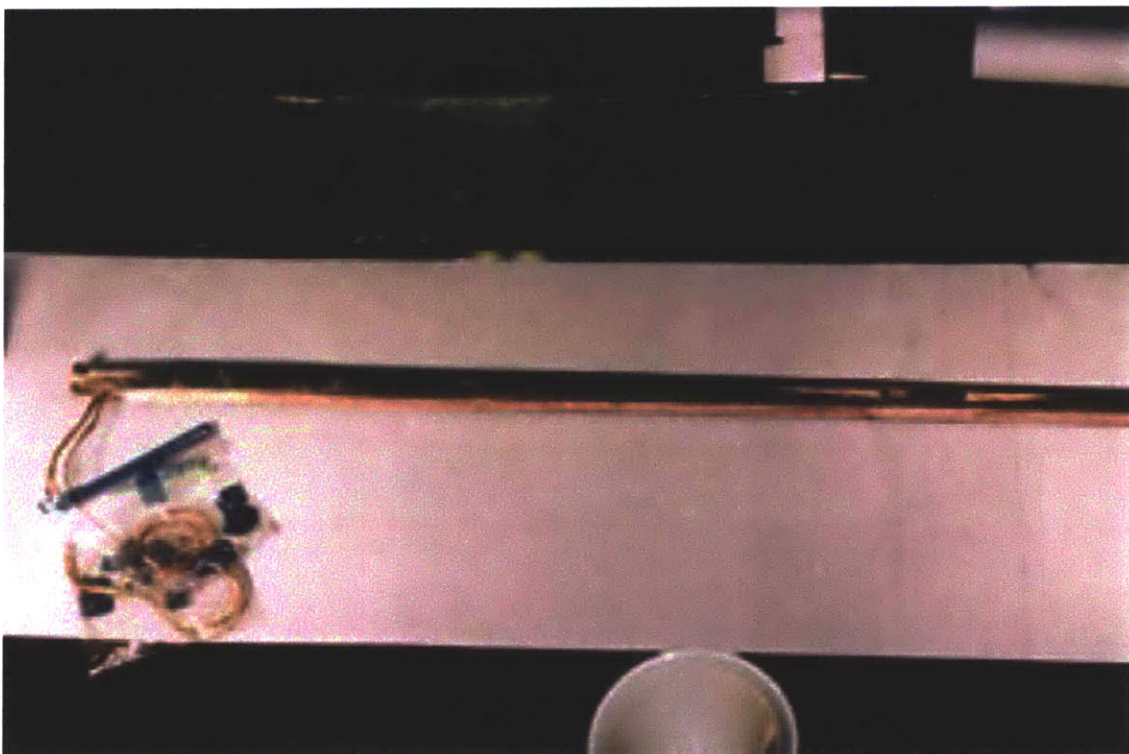


Figure E-32: View of the completed blade spar



Figure E-33: Close-up of actuator bay with solder pads against front wall, covered by GNPT tape

## Fairing Manufacture

The fairing on a passive blade consists primarily of a foam core and one E-Glass skin ply. The addition of the servo-flap complicates the fairing manufacturing for this blade. Referring to Figure 3-1, during the fairing cure, the inboard and outboard flap supports, the graphite reaction rib, and the supporting S-Glass plies must be incorporated into the blade fairing. In addition, the trailing edge of the fairing must take-on a slotted profile at the servo-flap blade stations. The process used to manufacture the fairing to include these features is described below.

As with the spar restraints, the two servo-flap supports are fixed within the blade fairing using lap bonds. The inboard flap support gets prepared just as with the spar restraints with respect to the use of sanding, primer, film adhesive, frekote, and GNPT tape. Figure E-34 shows the appearance of this part after surface preparations have been completed. The IM7 reaction rib is attached directly to the inboard flap support, as shown in Figure E-35.

The purpose of the S-Glass located around the two flap supports is to transfer the centrifugal loads of the servo-flap and the two supports into the trailing edge stiffener IM7 ply. These S-Glass plies are shaped to be wide as they wrap around the flap supports to maximize surface area (minimizing lap-bond stresses), but taper down to a 0.17 inch wide strip to interface with the upper and lower trailing edge stiffeners. These plies were made up of a number of smaller plies with varying lengths and widths no greater than 0.17 inches. These smaller S-Glass plies were layed into their designed shape before attaching them to the fairing components. They are referred to as superplies and are shown in Figure E-36. Because the centrifugal force carried by the inboard superply is much greater, it is the wider of the two superplies. The inboard superply is wrapped around the inboard flap support/rib part as shown in Figure E-37.

A trailing edge mandrel was used to position the flap supports with respect to each other and the blade structure as well as create the slotted profile of the blade at the flap blade stations. A view of the trailing edge mandrel is shown in Figure E-38.



Figure E-34: Inboard flap support, surface prepared for the fairing cure. Note the use of GNPT tape on the surface designed to slide against the trailing edge mandrel

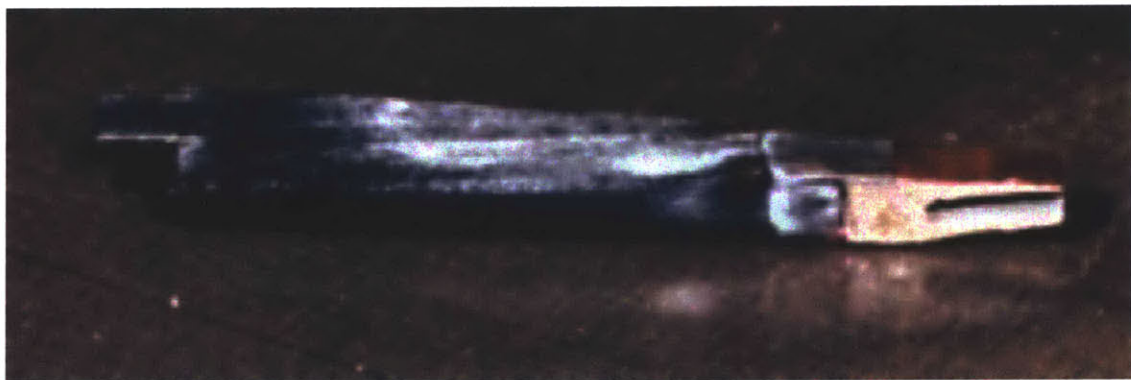


Figure E-35: Inboard flap support with the reaction rib in place

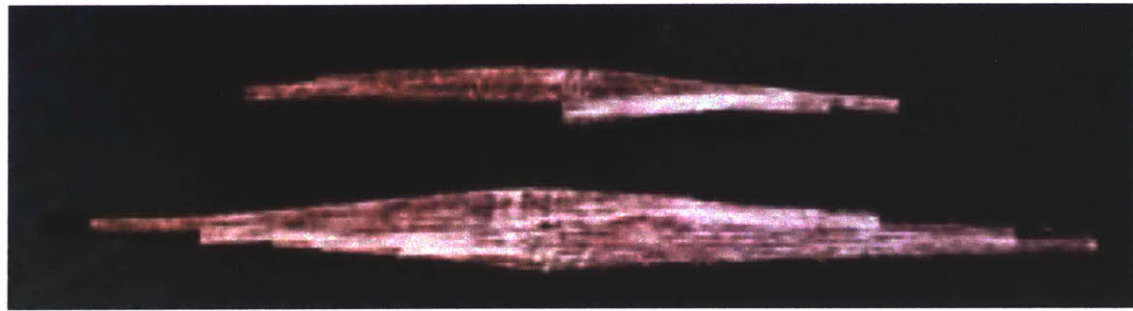


Figure E-36: Outboard and inboard S-Glass superplies



Figure E-37: Wrapping the inboard superply around the inboard flap support and reaction rib

Although not shown in the figure, the trailing edge mandrel used 1/4 inch diameter

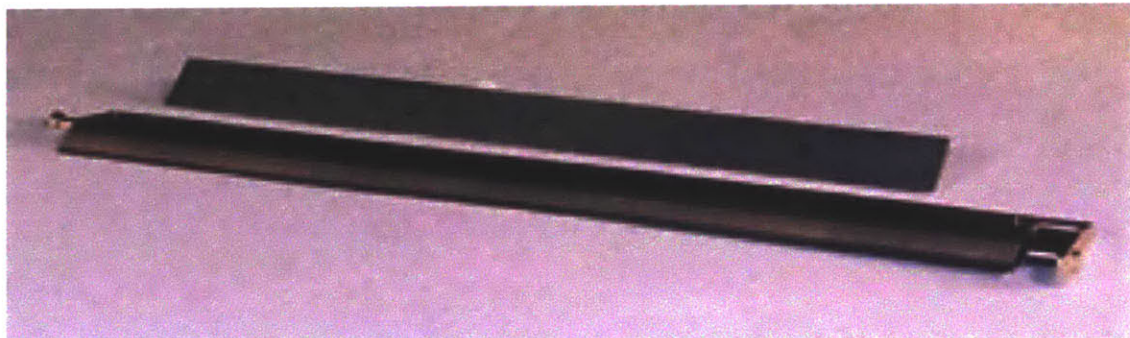


Figure E-38: View of the trailing edge mandrel prior to any surface treatment

locator pins and mating holes in the blade mold for positioning during the cures.

The orientation of the inboard flap support with respect to the trailing edge mandrel is important for proper servo-flap alignment. To facilitate this, an inboard flange of the mandrel is designed to slide onto the inboard flap support directly from the trailing edge (thus removal of the mandrel is done by sliding it directly aft after the cure). A close-up view of this flange is shown in Figure E-39. A small 1/32

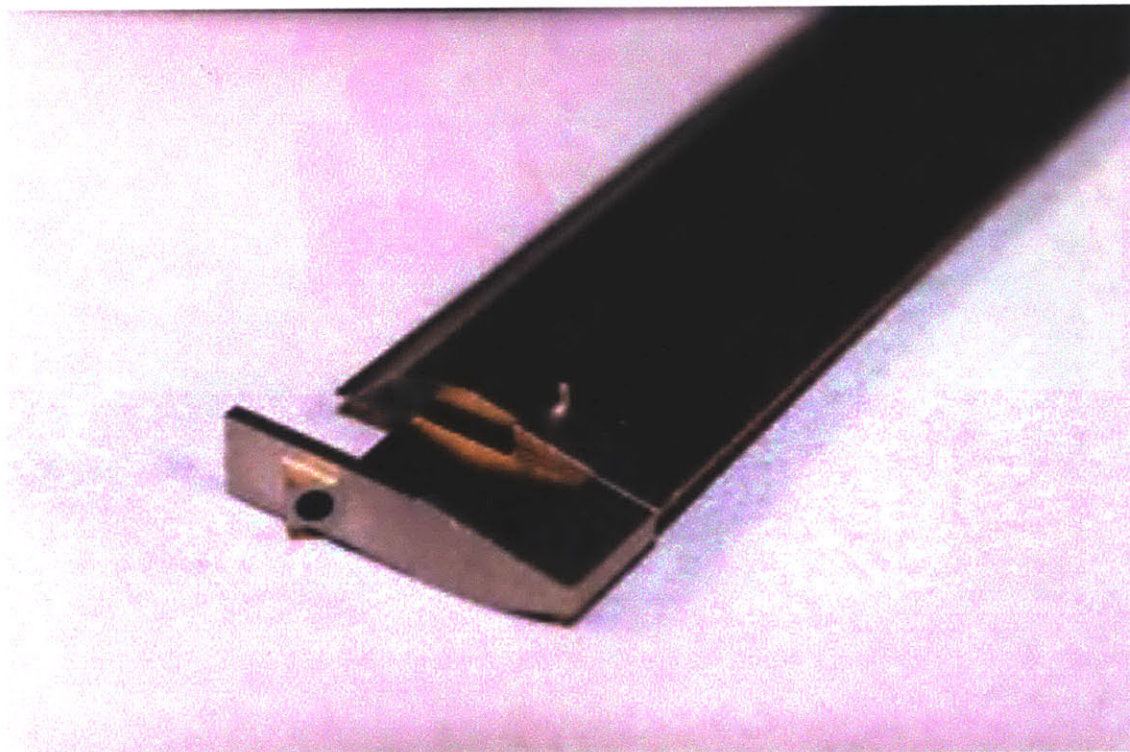


Figure E-39: Close-up view of the trailing edge mandrel flange

inch diameter pin is shown protruding from the mandrel upper surface in the figure. These smaller pins were originally designed to be the locator pins for the trailing edge mandrel. However, they were not strong enough to react the forces of the fairing cure. These pins were replaced before the final blade fairing cure with the 1/4 inch diameter dowel locator pins mentioned above.

The trailing edge mandrel is prepared in the same manner as the spar mandrels using the combination of frekote and GNPT tape. The mandrel is slid onto the inboard flap support/rib/S-Glass assembly with the aid of a piece of GNPT, as shown in Figure E-40. The fairing foam is cut with a razor blade and the entire trailing edge



Figure E-40: Use of GNPT to slide the inboard flap support/rib/superply assembly onto the trailing edge mandrel

mandrel and inboard flap support assembly is located within the fairing foam.

The surface of the outboard flap support is prepared in a similar fashion as for the inboard support. A view of the support before surface preparation is shown in Figures E-41. This support is attached to an outboard section of fairing foam with the outboard superply. This entire assembly is then glued with 5-Minute epoxy to the



Figure E-41: Close-up view of the outboard flap support with foam used to fill in the forward cut-out

inboard fairing foam and the outboard flap support is affixed to the outboard side of the trailing edge mandrel. Figure E-42 shows a top view of the trailing edge mandrel, flap supports, superplies and reaction rib, as they sit within the fairing foam on the bench-top.

The trailing edge stiffener plies are a layed onto the top and bottom surfaces of the fairing foam. Figure E-43 shows the top view of the entire fairing foam with this stiffener in place.

The next step is to attach the fairing to the blade spar through the application of the upper and lower skin plies. This is done in the lower blade mold. The lower skin is positioned in the mold and the spar, with film adhesive applied around its web, is lowered into place in the mold, as shown in Figure E-44. Figure E-45 provides a close-up view of the bottom skin and spar logistics at the blade root.

The fairing foam assembly is then lowered into place. The flange at the inboard side of the trailing edge mandrel and the inboard flap support are positioned within a mating cut-out machined into the lower blade mold. Slits were cut into the bottom skin at the edges of the slotted blade sections to form a flap of E-Glass skin. As the fairing foam assembly was lowered into place, the flap of skin was threaded between

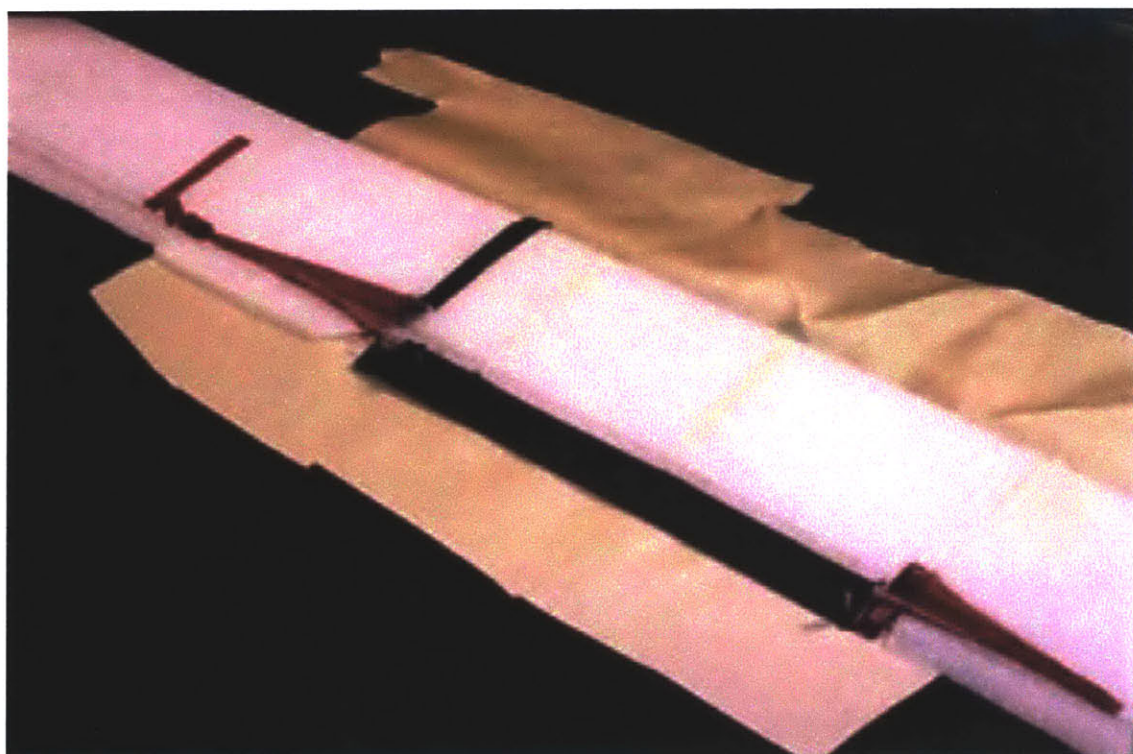


Figure E-42: Top surface of the servo-flap support components

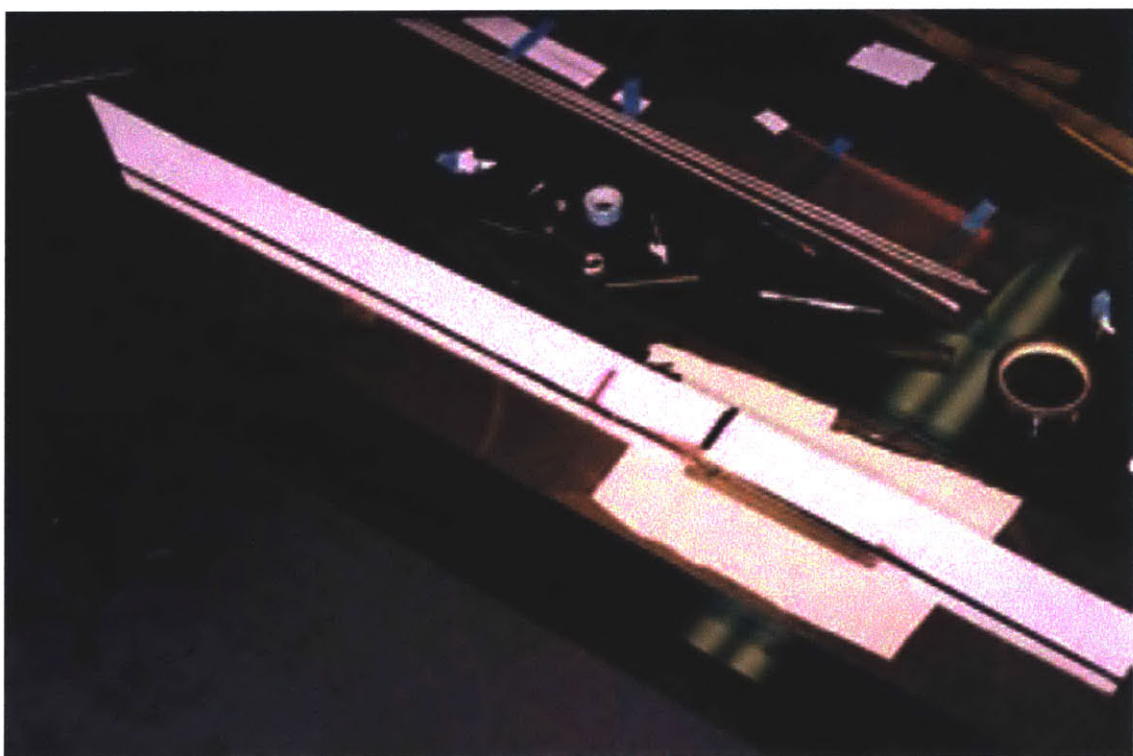


Figure E-43: Fairing foam with servo-flap support components in place and inclusion of the upper trailing edge stiffener

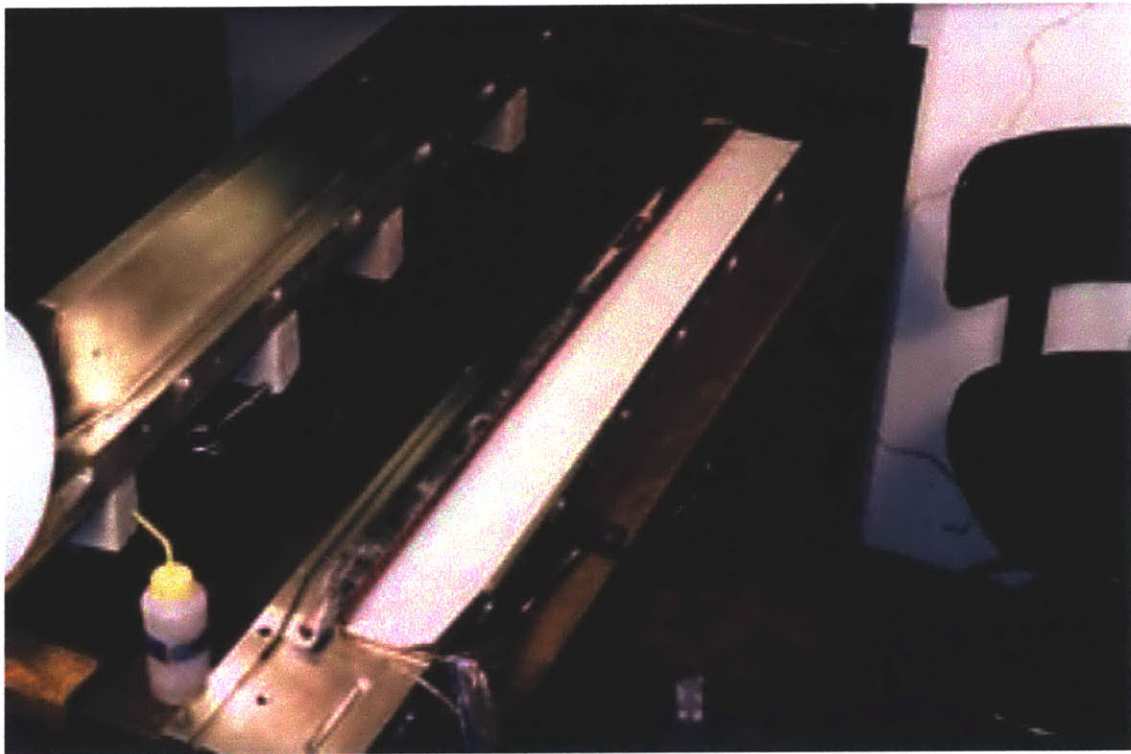


Figure E-44: View of the spar (with web film adhesive applied) positioned on top of the fairing skin in the lower mold

the front of the trailing edge mandrel and the fairing foam, as shown in Figure E-46. The top skin is then applied and both skin plies are cut back to expose the trailing edge alignment pins, as shown in Figure E-47.

After applying the fairing skin, the entire blade is pulled out of the mold and the root secondary bonds are applied. A picture of the blade root with these secondary bonds applied is shown in Figure E-48.

The blade is then placed into the top mold, the instrumentation and high voltage wires are taped down into the wire channels and the trailing edge mandrel locator pins are aligned. The bottom mold is clamped into place and the blade was cured at 250 degrees F for 90 minutes.

Just as in the spar cure, the use of alignment pins in the trailing edge mandrel, along with the cut-out in the lower mold surface for the inboard flap support/trailing edge mandrel flange cause compressive stresses to build up in the blade as it cools from its curing temperature. To guard against buckling the compliant fairing due to



Figure E-45: Close-up view of the root end of the lower fairing skin and the spar in mold

these compressive stresses, the molds were pulled apart slightly when they reached a temperature of 180 degrees F and the blade was lifted out of the locator pin holes and the inboard flap support cut-out. Then it was allowed to cool fully. A picture of the cured blade root just after opening the mold is shown in Figure E-49. A picture of the cured blade after being pulled out of the molds is shown in Figures E-50.

The post-cured appearance of the blade at the servo-flap location is shown in Figure E-51. A slight bend in the upper trailing edge stiffener is evident near the outboard side of the servo-flap cut-out. But the overall appearance is acceptable.

Some damage occurred to the blade fairing during the cure. The most noticeable damage was the appearance of delaminations between the fairing skin and the foam. Figure E-52 shows a view of some delaminations on the upper fairing surface. The cause of these delaminations is most likely due to poor resin content in the E-Glass used for the fairing skin. These delaminations were repaired by injecting 828 epoxy below the skin with a hypodermic needle, placing the blade back into the molds and

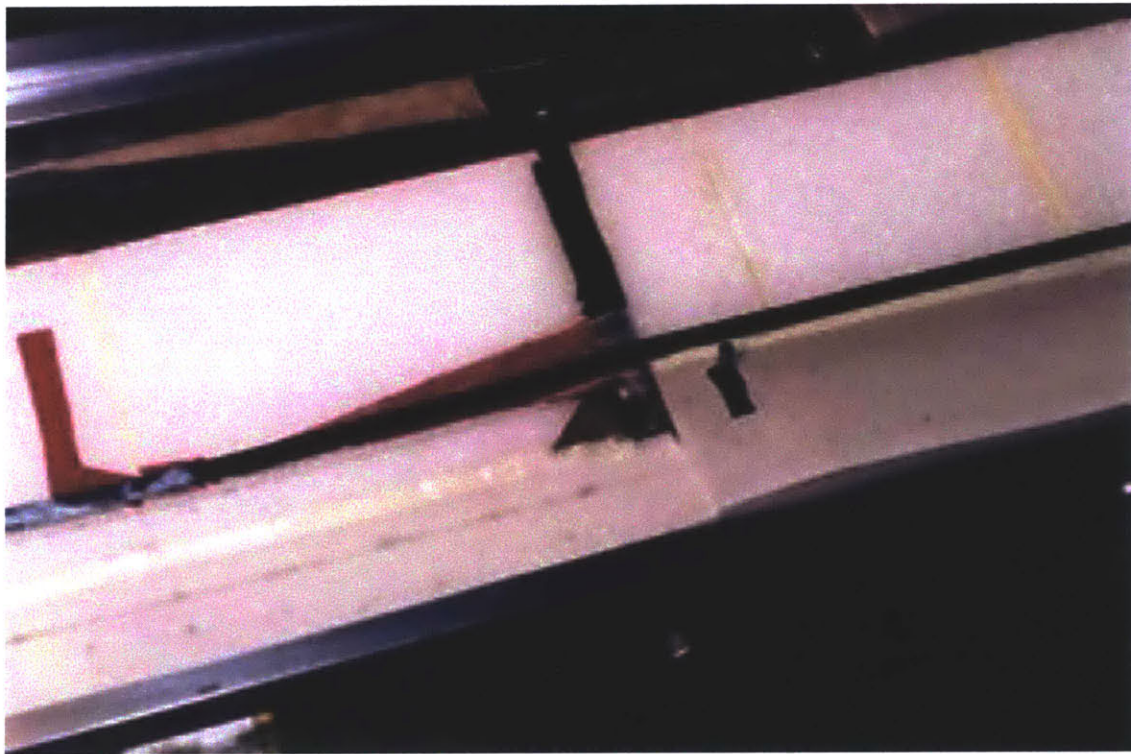


Figure E-46: Threading of the lower skin up to the top surface of the trailing edge mandrel at the servo-flap section

curing the epoxy with the molds closed.

Some dents were also created in the blade surface while extracting it from the molds and due to various flaws in the composite cure. To fill these various dents, a mixture of 9309 epoxy and cab-o-sil cotton flox was created as a lightweight filler material, as shown in Figure E-53. A template was used that matched the blade profile to fill in these dents using this light weight epoxy, as shown in Figure E-54.

Finally, the trailing edge developed a small crack between the trailing edge stiffener and trailing edge tab. This crack was repaired by bonding a 1/4 inch wide piece of dry E-Glass fabric on top of the crack with 828 epoxy. The epoxy was applied sparingly by a series of small drops along the doubler length.

The epoxy used for the repairs to the delaminations, dents, and crack in the composite were all cured with the blade mounted inside the molds. As with the spar, because of the difference in coefficients of thermal expansion between the mold and the composite, the blade did not fit in the cooled mold at both the root and the

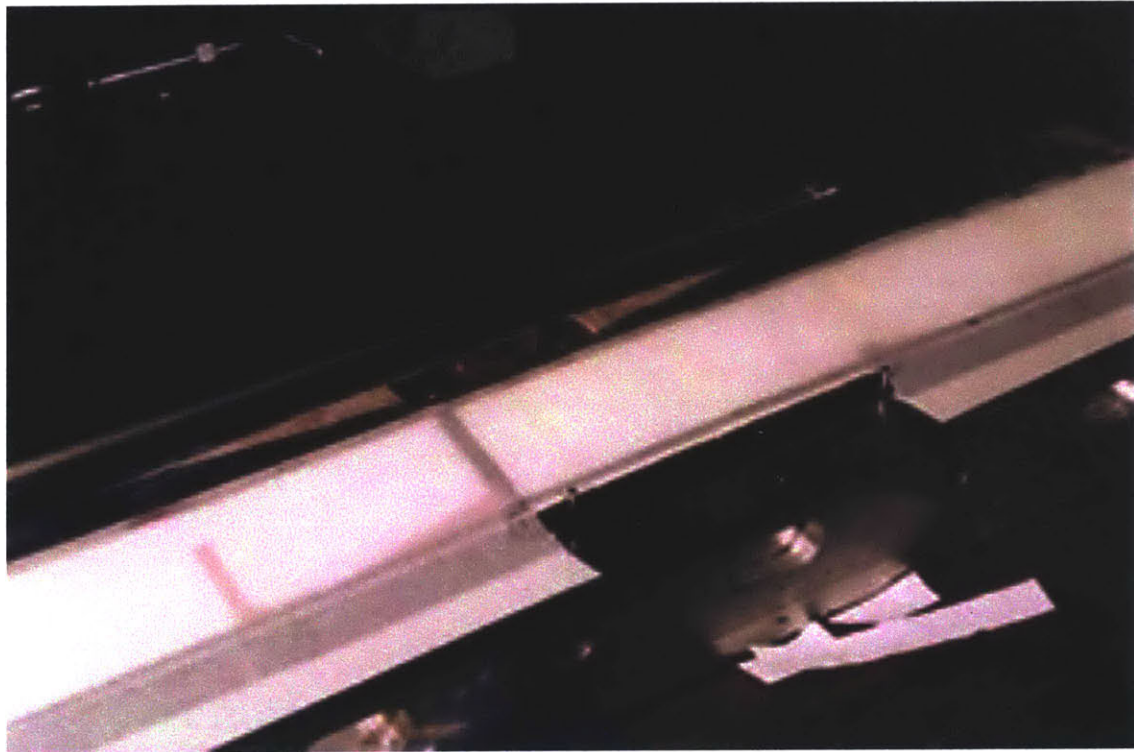


Figure E-47: View of the fairing foam and top fairing skin in place and trimmed around the trailing edge mandrel location

inboard flap support cut-out. To allow the blade to fit into the mold for the surface repairs, the inboard section of the mold was removed from the blades. The logistics of the blade root, hanging outside the mold, during these blade repairs is shown in Figure E-55.

Unfortunately, during the repair of the original blade damage, a mold heater came into contact with the bottom fairing surface and the instrumentation wire bundle at the blade root. The damage from this contact is shown in Figure E-56. The damage to the fairing was repaired by adding an S-Glass doubler to the damaged surface and curing the section in the inboard blade molds. The S-Glass used to enact this repair is shown before the cure in Figure E-57.

When the heater landed on the instrumentation wire bundle, it melted all of the insulation from the wires together. To repair the damage, each of the wires was separated out using a soldering iron, tweezers and a stereo microscope. After the wires were separated, thin, micro-bore teflon tubing was slid over the exposed wire

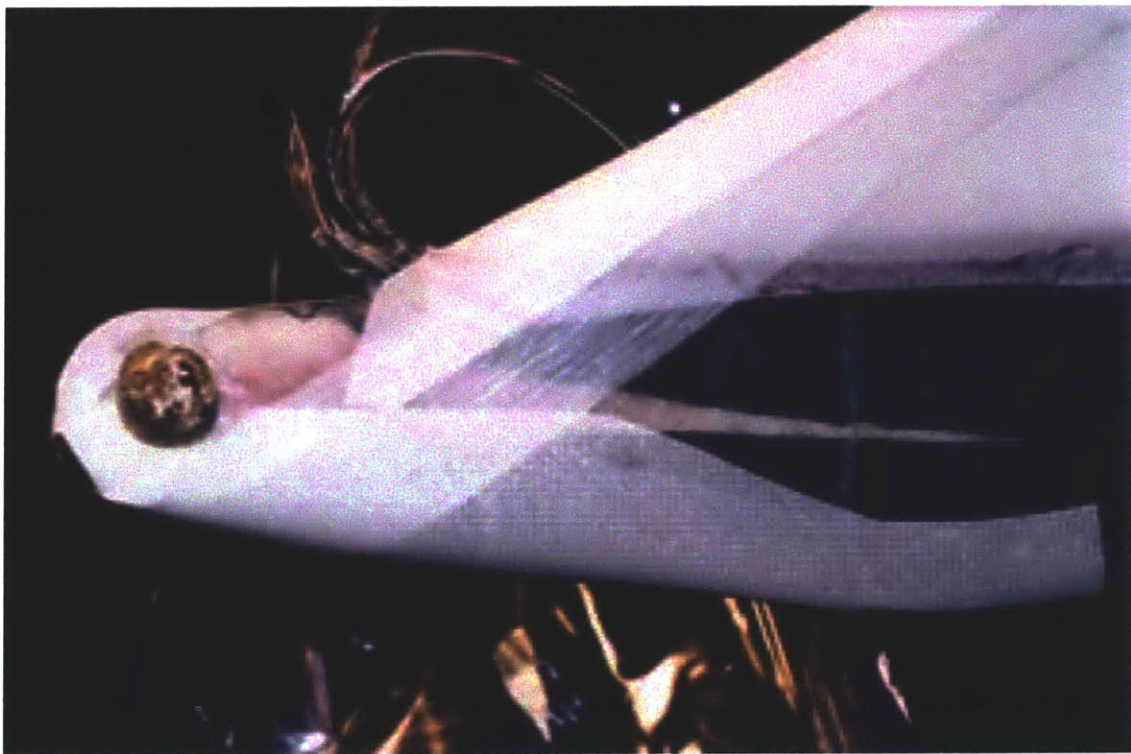


Figure E-48: Secondary root plies. View of the lower root doubler as well as the leading edge and trailing edge shear ties



Figure E-49: View of the bottom surface of the blade root after fairing cure

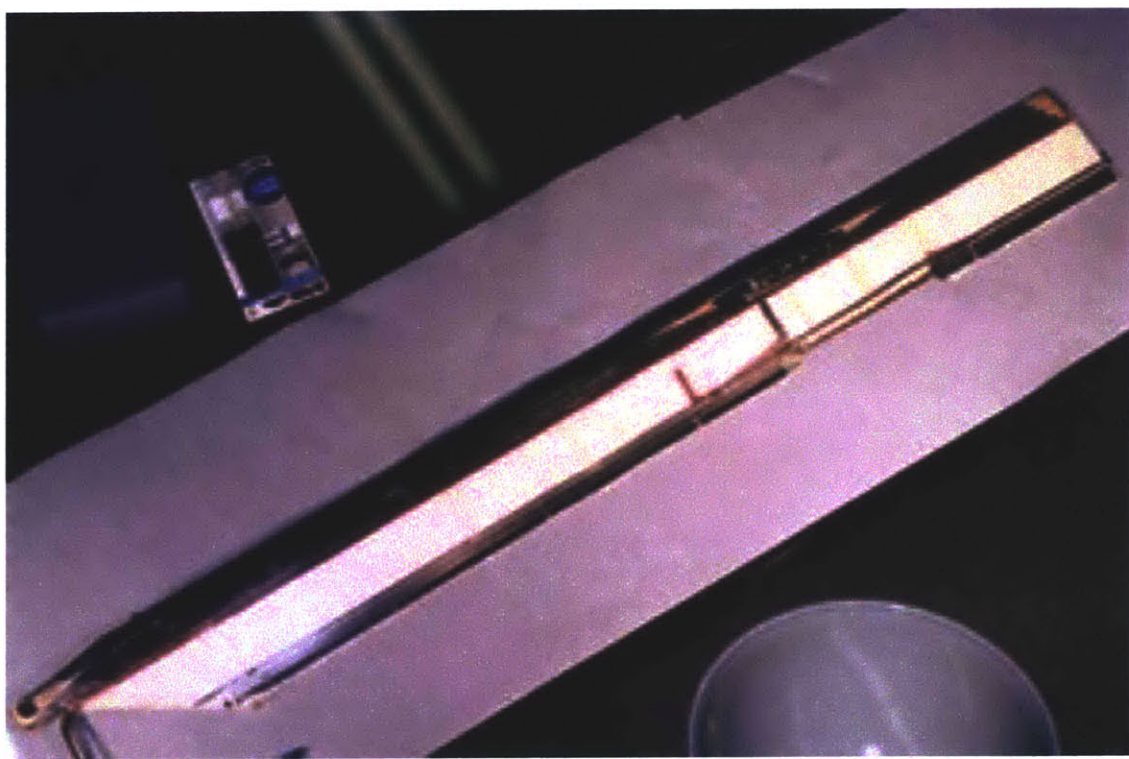


Figure E-50: The blade after both cures

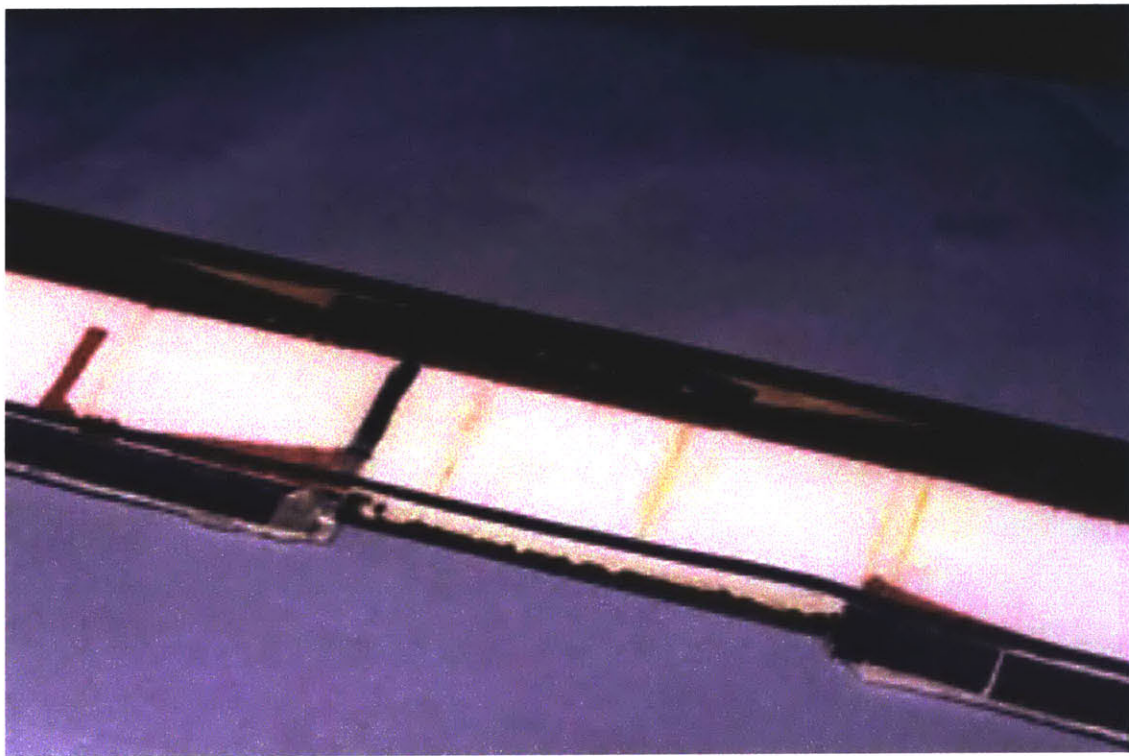


Figure E-51: Close-up view of the top surface of the blade at the actuator bay/servo-flap location after the fairing cure



Figure E-52: View of delaminations in the fairing skin that were due to low resin content in the composite pre-preg

and a dot of 5-minute epoxy was used to hold the insulating patch tube in place. This technique was successful in repairing the damage to most of the wires, however, the leads to the chordwise bending gage, the root torsion gage, and two of the high voltage ground wires could not be repaired. An exterior root torsion gage was attached to the blade skin to replace the lost sensor.

After completing the fairing cure, some additional operations were performed on the blade. The lag pin hole was machined using a boring bar operation. The diameter of this hole was machined so that the lag pin fit snugly within the hole. A piece of ruslon fabric was bonded to the upper and lower root surfaces. This ruslon provides a low friction surface to reduce the friction between the blade and the pitch shaft assemblies. A bonding apparatus was used to apply this ruslon, as shown in Figure E-58, so that the final thickness of the blade with the ruslon matched the mating cut-out in the pitch shaft assemblies. A clearance hole for the control rod was machined into the blade from the trailing edge of the fairing. An additional fiberglass



Figure E-53: Application of cab-o-sil cotton flox to 9309 epoxy to make a low-weight filler adhesive

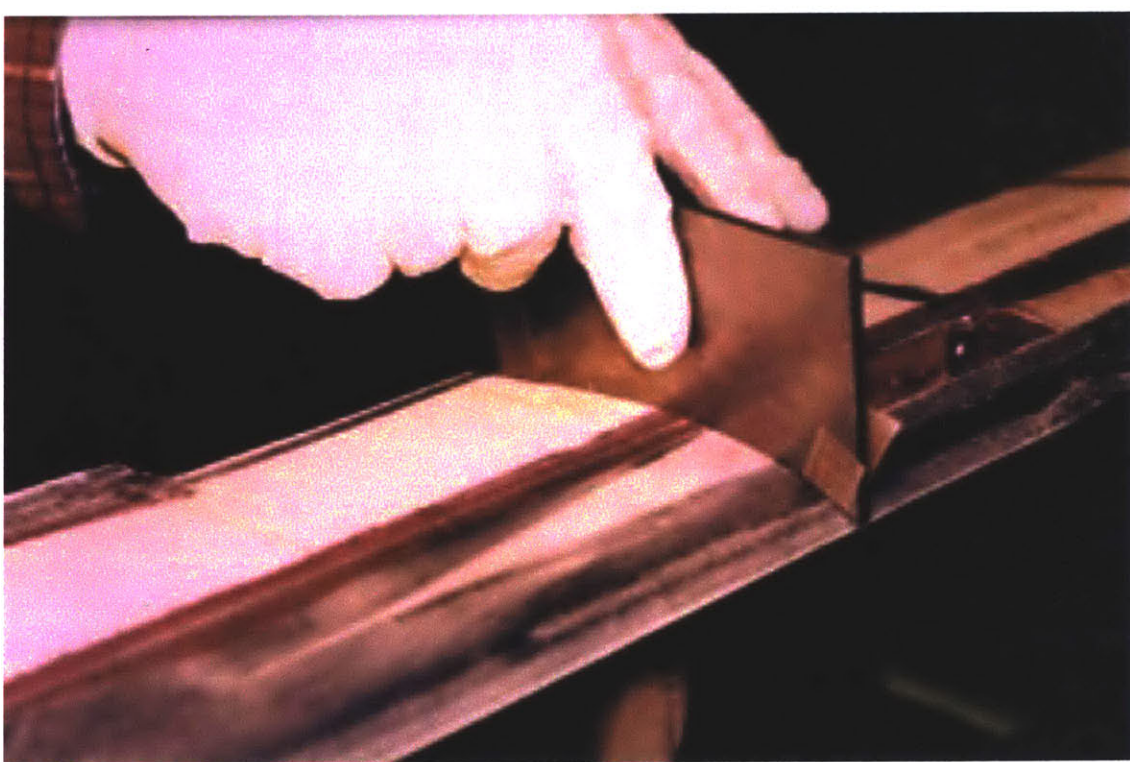


Figure E-54: Use of surface template to fill dents in blade surface



Figure E-55: The position of the blade root during the re-cures to fix damage

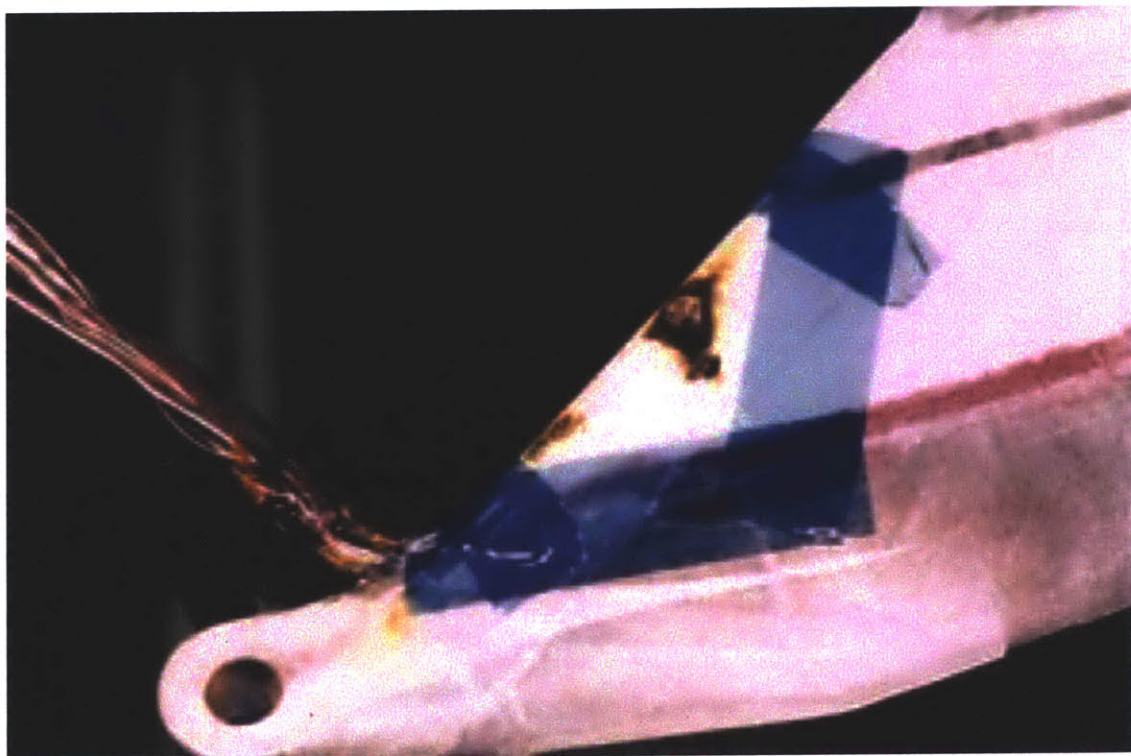


Figure E-56: Burn in lower root doubler and instrumentation wires due to inadvertent contact with mold heater



Figure E-57: Application of an S-Glass patch used to repair the burnt root doubler

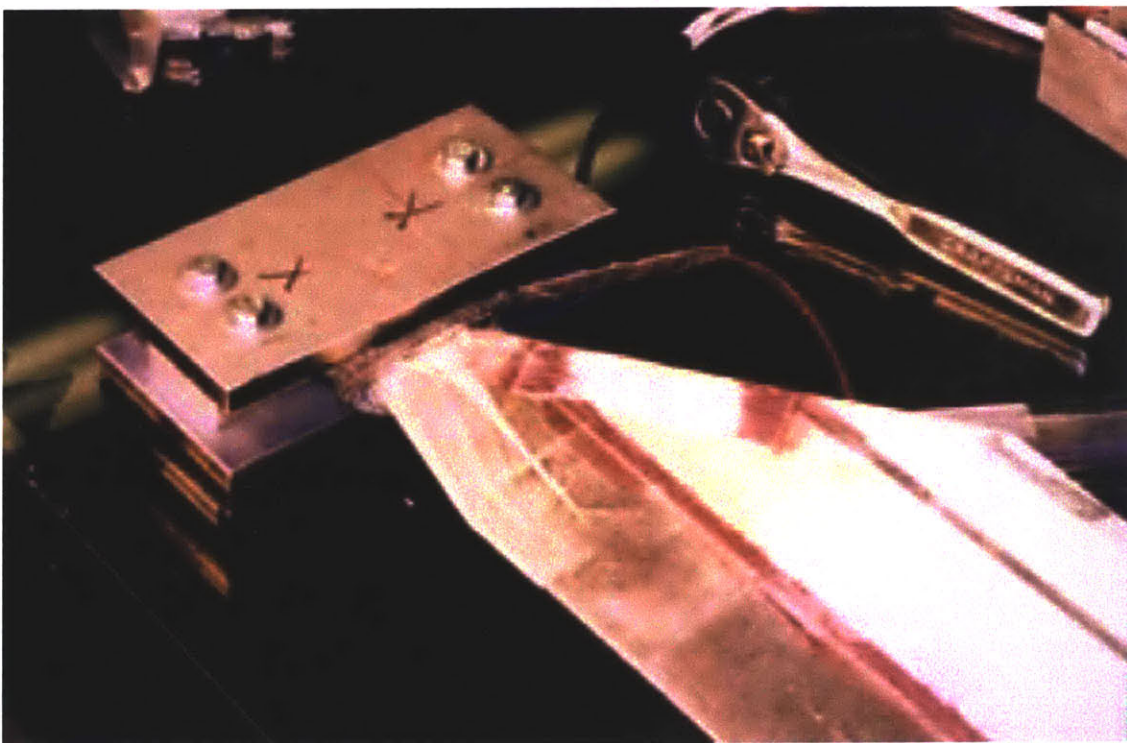


Figure E-58: Bonding of ruslon to top and bottom surface of blade root for interface with pitch shaft assemblies

doubler was bonded to the fairing surface over a circular area extending about 0.5 inches radially out from the hole for extra support.

In assembling the active blade, the servo-flap slides into place from the trailing edge, and a bolt oriented at a 45 degree angle is used to fix the pre-stress wire flange to the inboard flap support. To allow the pre-stress wire flange to slide into place from the trailing edge and to be able to tighten this bolt, a triangular cut-out was made in the bottom surface of the composite, as shown in Figure E-59.

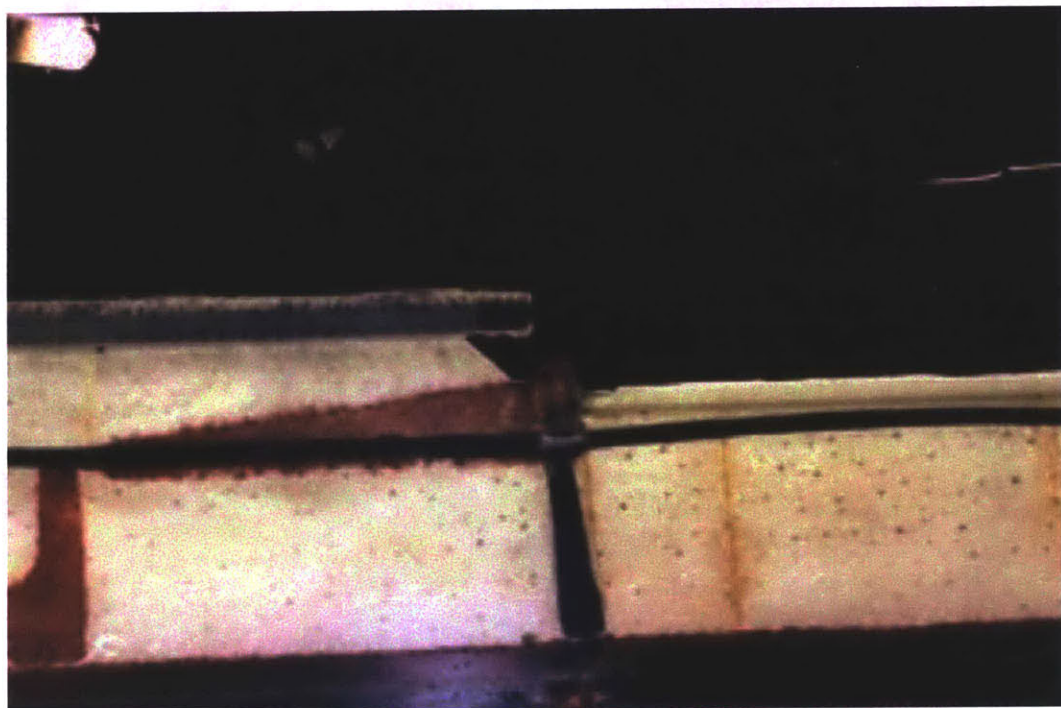


Figure E-59: View of the lower blade surface just inboard of the flap cut-out, highlighting the triangular cut in the fairing skin made to aid in fixing the servo-flap to the inboard flap support

Some instrumentation was added to the interior of the actuator bay. A resistive thermal device (RTD) was mounted to the center of the front bay wall to measure the thermal environment in the bay during operation. A full strain gage bridge was attached to the outer frame of the actuator to measure the actuated force. Finally, a Hall effect sensor was mounted to the aft wall just inboard of the inboard spar restraint, along with three Samarium-Cobalt magnets bonded to the inner frame. This hall effect sensor/magnet combination was used as the primary measure of actuator

deflection.

The solder pads in the bay were used to connect these additional sensors. In addition to the instrumentation wires, the leads to the actuator stacks were also soldered to high voltage pads on the fore and aft walls of the bay. To aid in performing these soldering operations, the blade was propped up at an angle and a stereo microscope was used for visualization.

### Hatch Cure

The hatch is composed of two layers of  $\pm 45^\circ$  E-Glass fabric. The boundaries of the hatch were created by placing GNPT tape into the molds at the proper spanwise and chordwise locations to create ledges in the cured E-Glass, as shown in Figure E-60



Figure E-60: Tape used in mold for hatch cure

The two composite plies were layed down and thermocouples inserted at either end. Peel ply was applied to the inside surface to create a rough bonding surface. Tape was used to hold the layers in place. One layer of GNPT was layed on top of

the peel ply and then compliant rubber and a steel plate were layed on top of that. The plate was clamped to the mold and the rubber served to distribute loads to the composite material. The mold was heated to 250 degrees F for 90 minutes.

After the cure, the hatch was cut to the proper width and height according to the lines left by the GNPT tape and the corners of the hatch were rounded using sandpaper to fit the contour on the top surface of the blade spar. The completed hatch is shown in Figure E-61.



Figure E-61: The cured hatch

### E.2.2 Servo-Flap Manufacture

The servo-flap is also composed of a Rohacell 31 foam core with a composite skin. The skin consists primarily of two layers of  $\pm 45^\circ$  E-Glass. However, one layer of  $0^\circ$  uni-directional IM7 composite was added to the front 55% of the servo-flap to improve its flapwise bending stiffness. Aluminum molds used to cure the servo-flaps were machined in-house.

As with the main blade section, the servo-flap has a foam core. A close up of the foam cross-section before the lay-up is shown in Figure E-62.

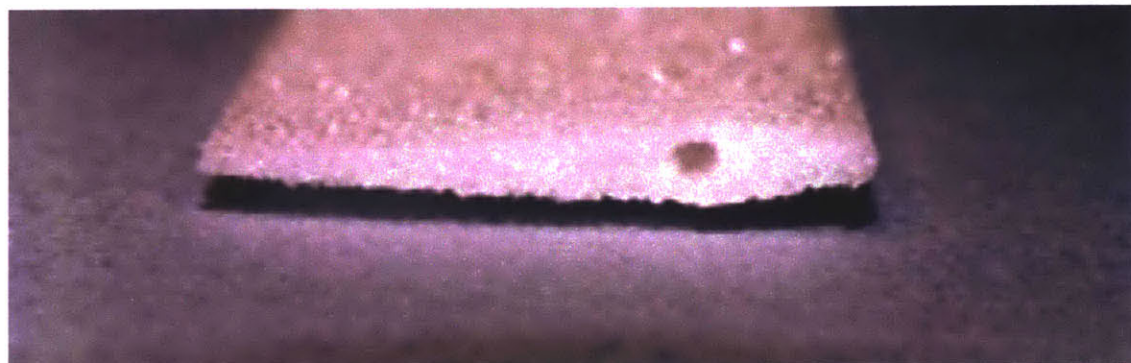


Figure E-62: Close-up view of one end of the flap foam

The horn is bonded to the inboard end of the flap skin through a lap joint. Similarly, the keymount, magnet housing, and a small Samarium-Cobalt magnet are bonded to the outboard side of the flap skin through a lap joint. To hold these components in place during the flap cure, four mandrels were used. The lay-out of the inboard and outboard flap cure components are shown in Figures E-63 and E-64, respectively. Three epoxy end-pieces are used at the flap ends to help react the spanwise pressures during the flap cure. These end-pieces are also shown in the figures. The horn alignment pin slides through the upper hole in the horn during the cure to help maintain horn position during the flap cure. The inboard flap axis mandrel slides through the main bore hole of the horn and screws onto the middle flap axis mandrel, which runs down the entire length of the flap along its rotational axis. This mandrel interfaces with the keymount mandrel at the outboard end via a sliding attachment. The middle spar mandrel keeps the bore holes for the horn and keymount aligned with each other. The keymount mandrel interfaces with the keyway in the keymount and a rectangular cut-out in the molds is used to hold these parts at the appropriate orientation during the cure.

The lap-joint and mandrel surfaces were prepared in a manner similar to those for the spar and fairing cures with respect to the use of sanding, primer, film adhesive, frekote, and GNPT tape.

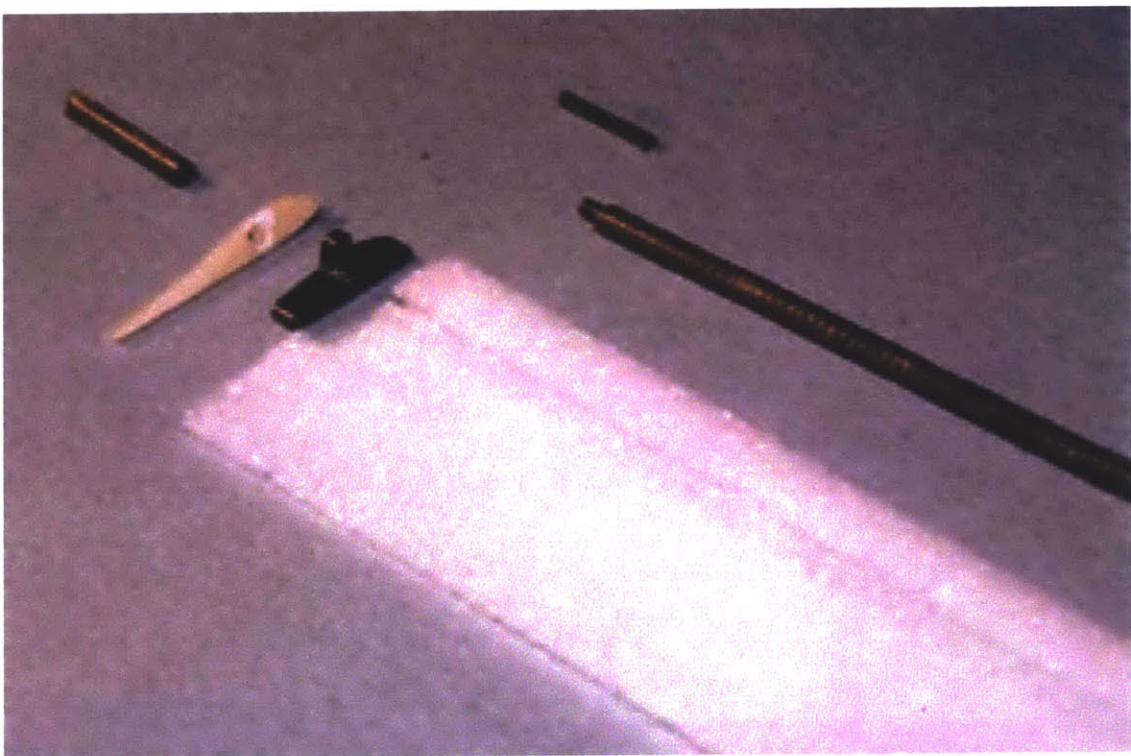


Figure E-63: Parts used at the inboard side of the flap during the cure

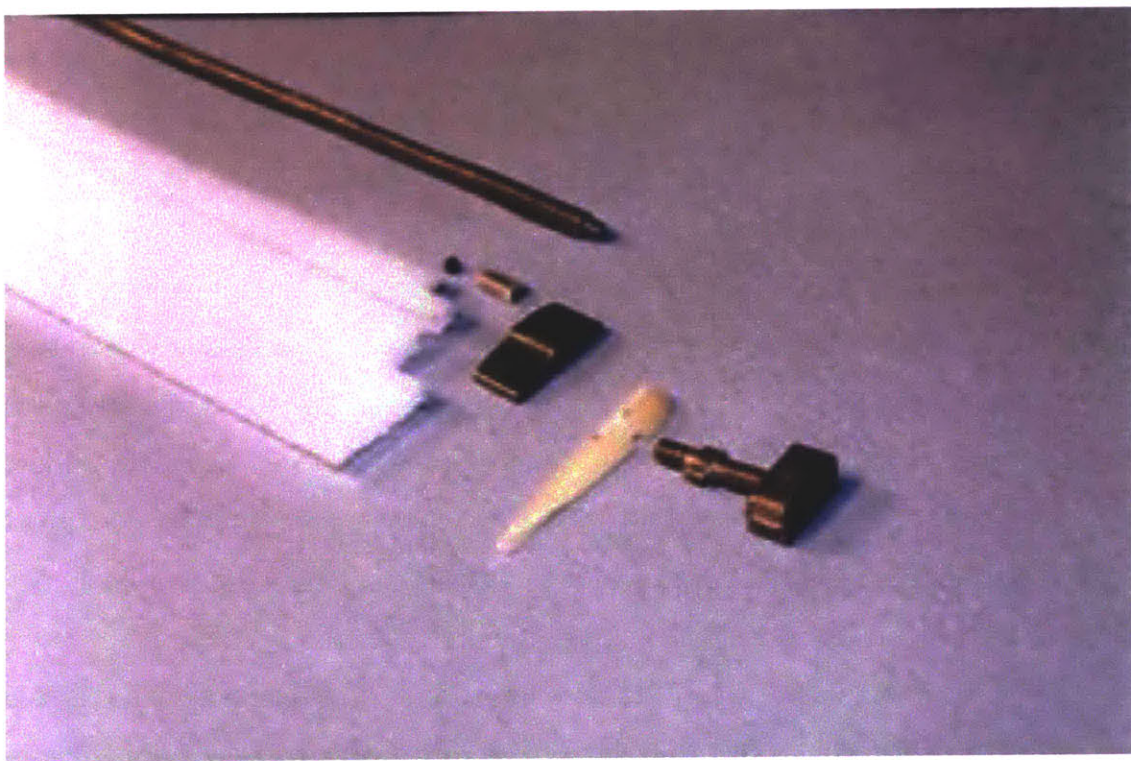


Figure E-64: Parts used at the outboard side of the flap during the cure

The E-Glass plies are applied first. Special shaping of the ply is needed to account for the presence of the horn. The E-Glass ply is wrapped around the inboard and outboard ends of the servo-flap. Special trimming of the ply is also done to keep the key-ways in the keymount clear, as shown in Figure E-65. The graphite uni ply is



Figure E-65: Close-up view of the keymount with E-glass, trimmed before cure

applied to the flap last.

After the lay-up, the mandrels are attached to the laminate as shown in Figure E-66. The flap is placed into the lower mold and positioned for the cure, as shown in Figure E-67. The mold is heated a bit to soften the composite enough to allow the oversized laminate to fit in the mold.

Thermocouples are inserted at each end of the flap. The top mold is lowered in place and a number of C-Clamps are used to press the molds together. The molds are placed in an oven and heated to hold the composite at 250° F for 90 minutes.

After the cure, the flap is pulled out and has the appearance shown in Figure E-68. The mandrels are removed. Special trimming is needed at the keymount key-ways to remove the keymount mandrel, as shown in Figure E-69.

The removal of the middle flap axis mandrel was difficult and required the use of a fairly large amount of force. During the removal, the flap skin delaminated a bit near the trailing edge. This delamination was repaired by curing some 828 epoxy at the delamination.



Figure E-66: View of the flap lay-up with mandrels in place just prior to placing in molds

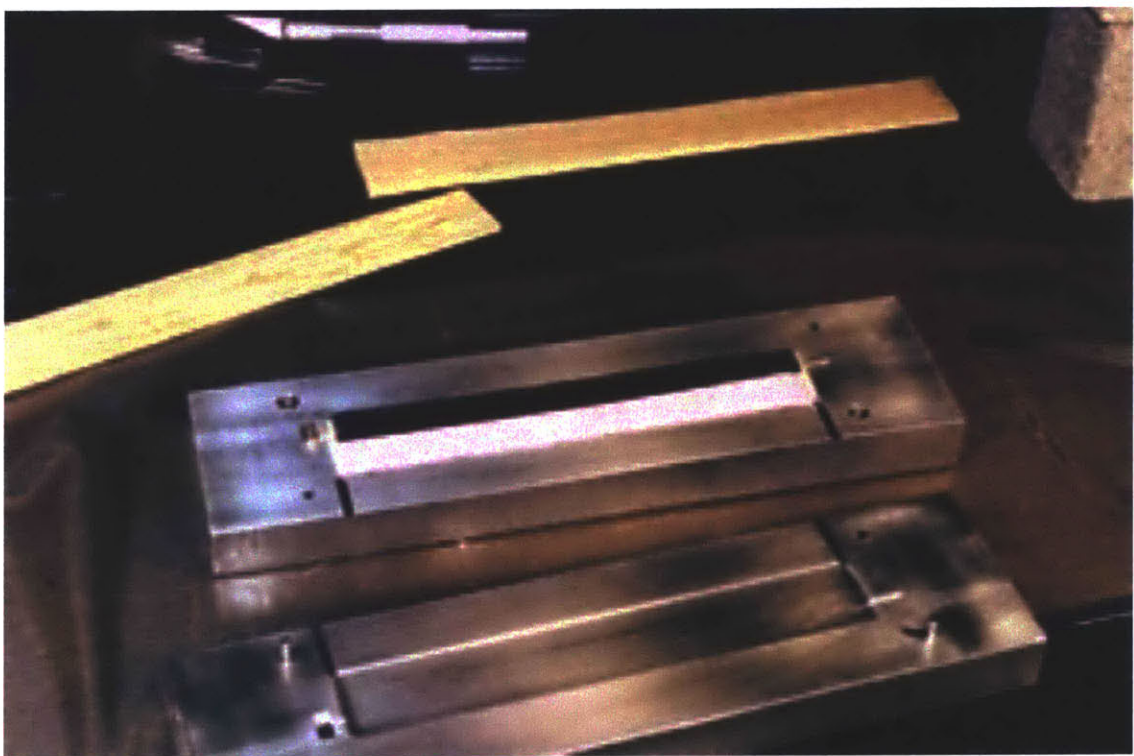


Figure E-67: Flap lay-up in mold before cure

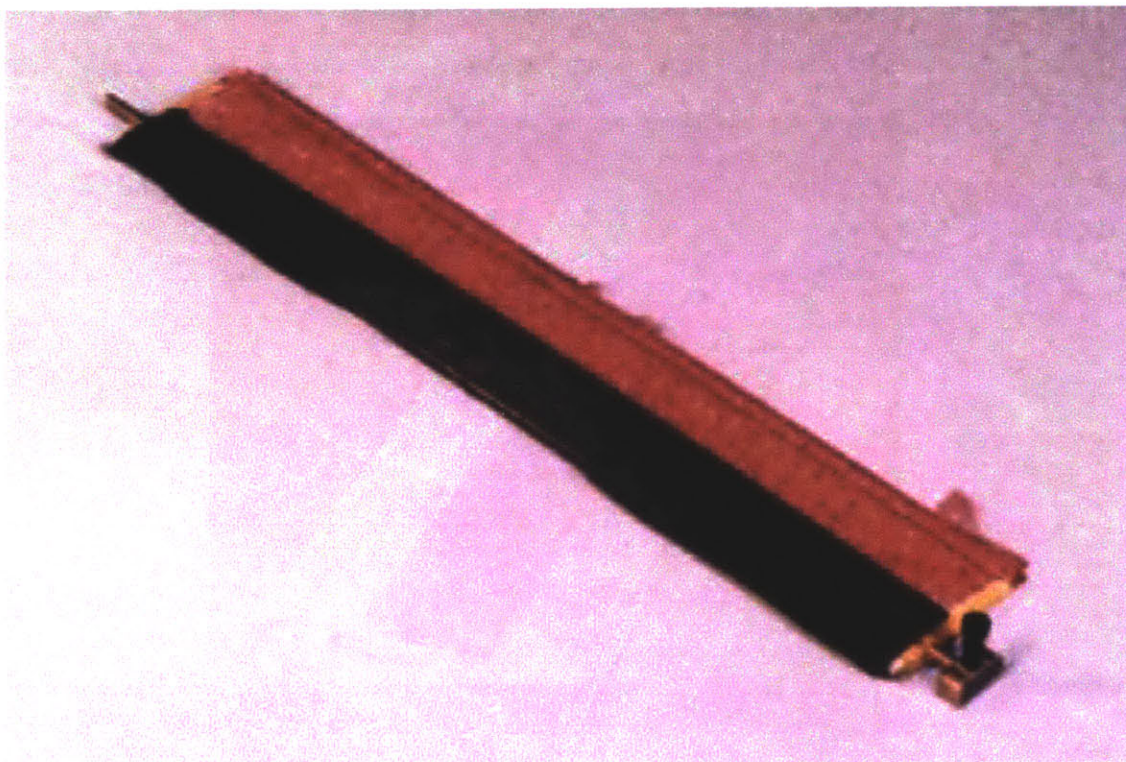


Figure E-68: Appearance of the flap just after cure



Figure E-69: Close-up view of the keymount, trimmed after cure

The pre-stress wire was threaded through the flap axis cavity in preparation of its laser-beam weld to the pre-stress wire flange. Pictures of the flap and pre-stress wire in different configurations are shown in Figure E-70 and E-71. The flap and

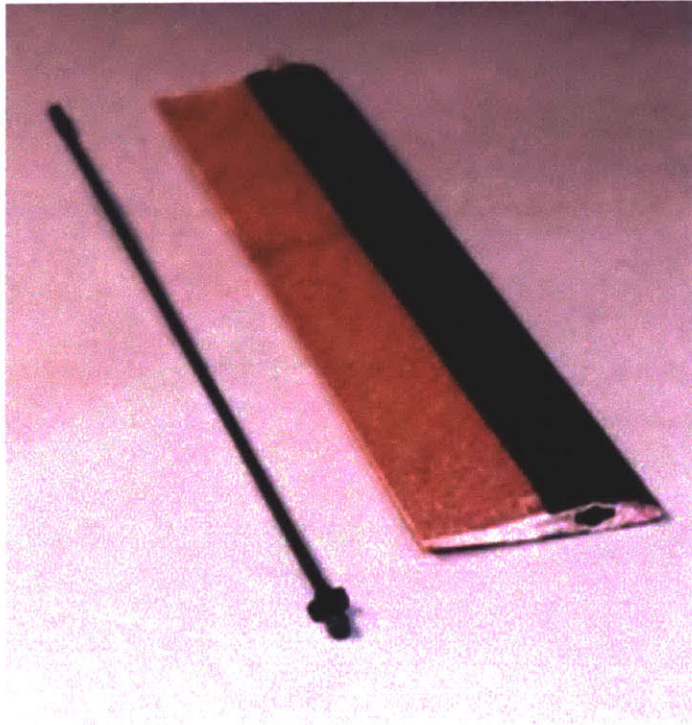


Figure E-70: View of the keymount keyway and outboard end of the pre-stress wire, highlighting the keyed interface between these parts at the outboard end of the flap

pre-stress wire was sent to a vendor for the laser beam weld of the inboard end of the pre-stress wire to the pre-stress wire flange.

### E.2.3 Active Rotor Blade Assembly

After the manufacturing of all the parts, the active blade was assembled. All screws in the active blade were applied using lock-washers and Loctite Threadlocker 242. The components included in the blade assembly are shown in Figure E-72. The actuator was placed into and bolted down in the actuator bay. The actuator platform was located at the outboard end of the bay. The clevis was threaded onto the aft end of the control rod and the control rod was run from the trailing edge through the bored hole and threaded onto the inner frame.

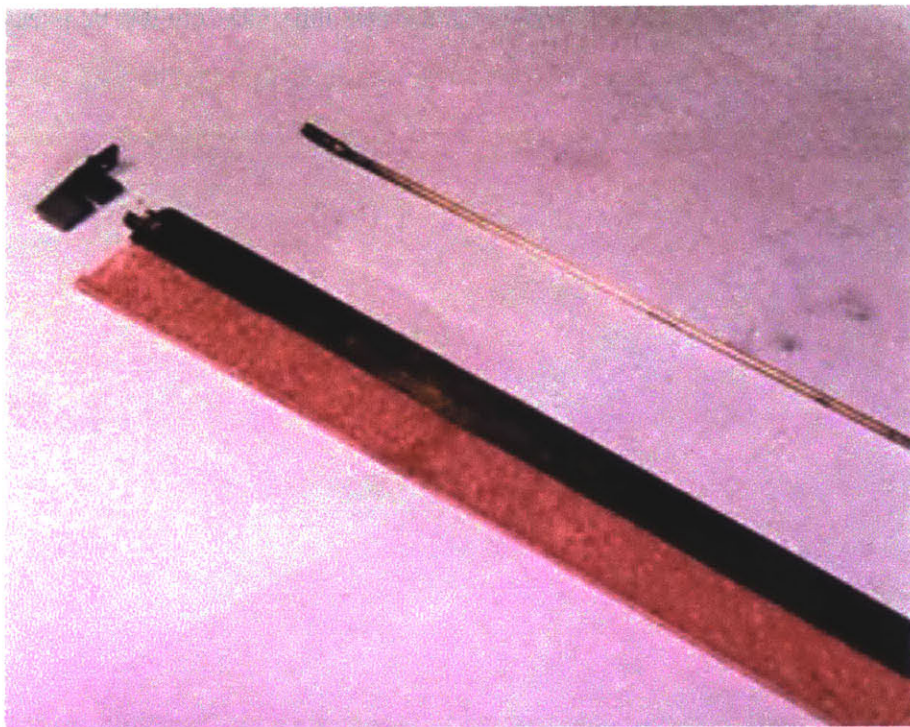


Figure E-71: Inboard end of servo-flap with pre-stress wire threaded through (an additional pre-stress wire is just in front of the flap for reference) and the pre-stress wire flange, just prior to weld

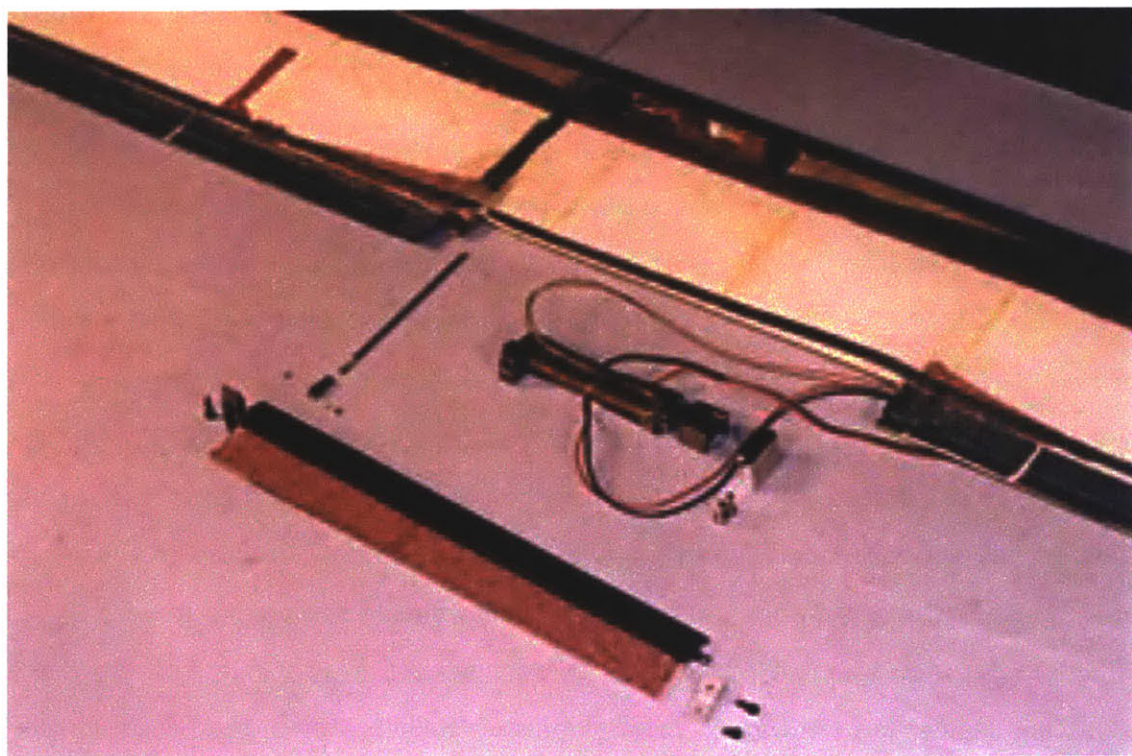


Figure E-72: Active blade components just prior to assembly

The unstressed position of the pre-stress wire flange in relation to the flap chordline is shown in Figure E-73. To place the servo-flap in position, the flap had to be rotated

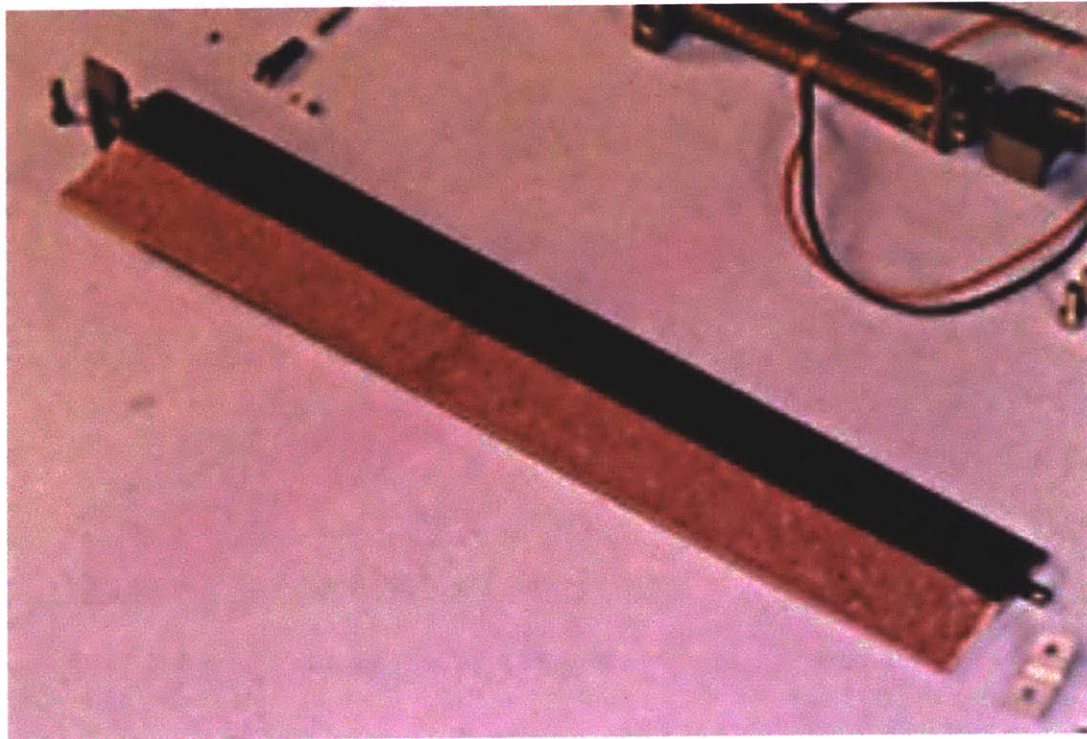


Figure E-73: Close-up of the servo-flap just after the laser-beam weld, showing the almost 90° rotation of the pre-stress wire flange with respect to the flap chordline

approximately 90 degrees nose down to allow the pre-stress wire flange to slide into place with the inboard flap support. Two people are needed to attach the flap. As one person twists the flap and places it into position, a second person attaches the clevis to the flap horn with the clevis pin. The assembled active rotor blade is shown in Figure E-74. A small teflon washer is also included on the inboard surface of the horn for a low friction sliding interface between the horn and clevis. This washer is seen clearly in Figure E-75. Once in place, the pre-stress wire flange is bolted to the inboard flap support, and the outboard flap support clamp is bolted to the bottom of the outboard flap support around the outboard end of the pre-stress wire.

Some iteration was needed in this assembly process to properly trim the flap by adjusting the clevis position. A close-up view of the actuator in the bay is shown in Figure E-76. This view of the actuator in the bay shows the strain gage attached to

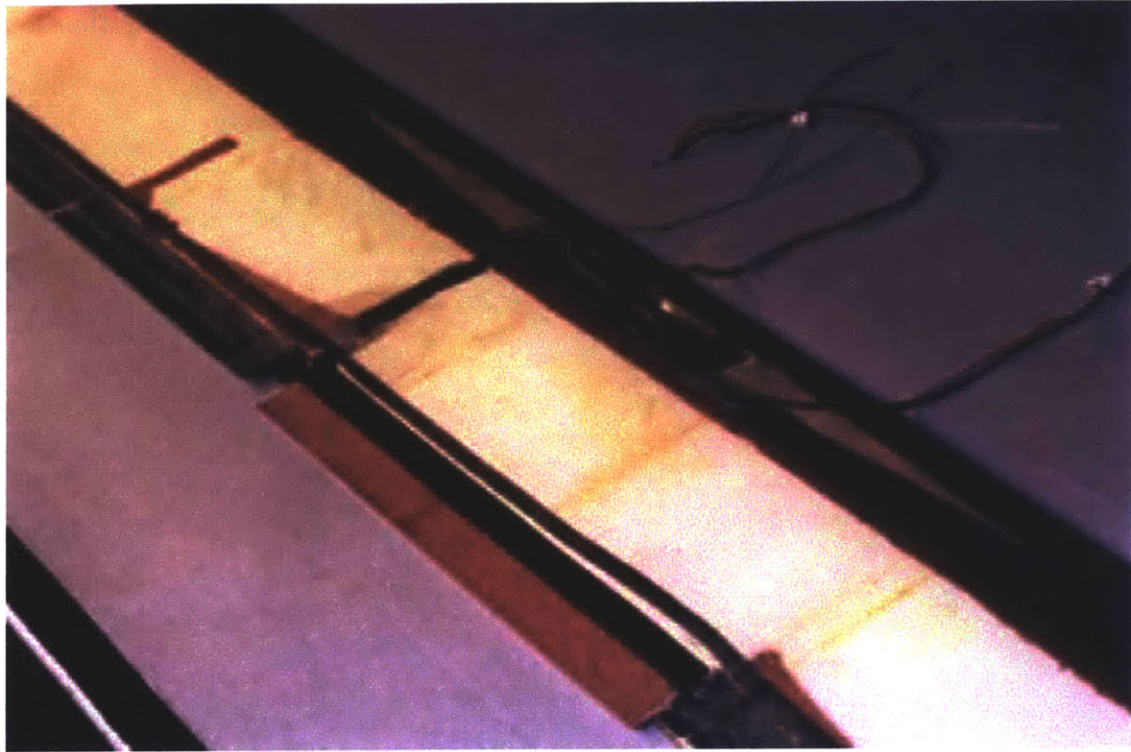


Figure E-74: Assembled active blade. Note that the stack wires have not been soldered in yet

the actuator frame and the magnets bonded to the inboard end of the inner frame used for primary actuator deflection measurement.

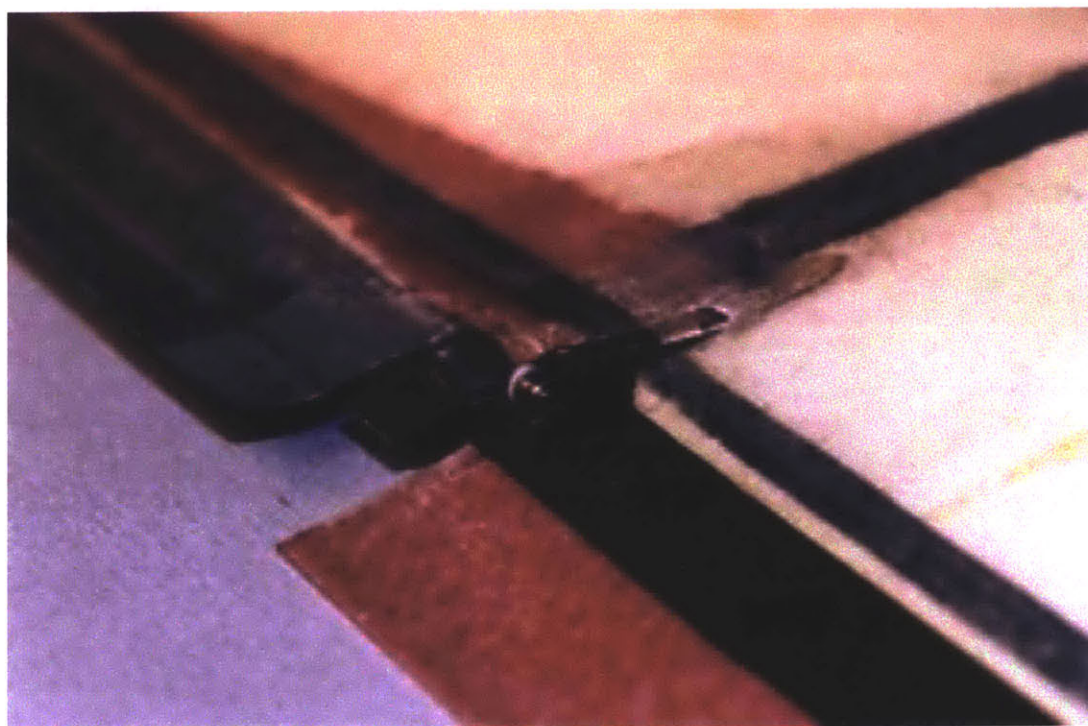


Figure E-75: Close-up view of the interface between the control rod, clevis and servo-flap horn. Note the small, white teflon washer located just inboard of the horn surface.

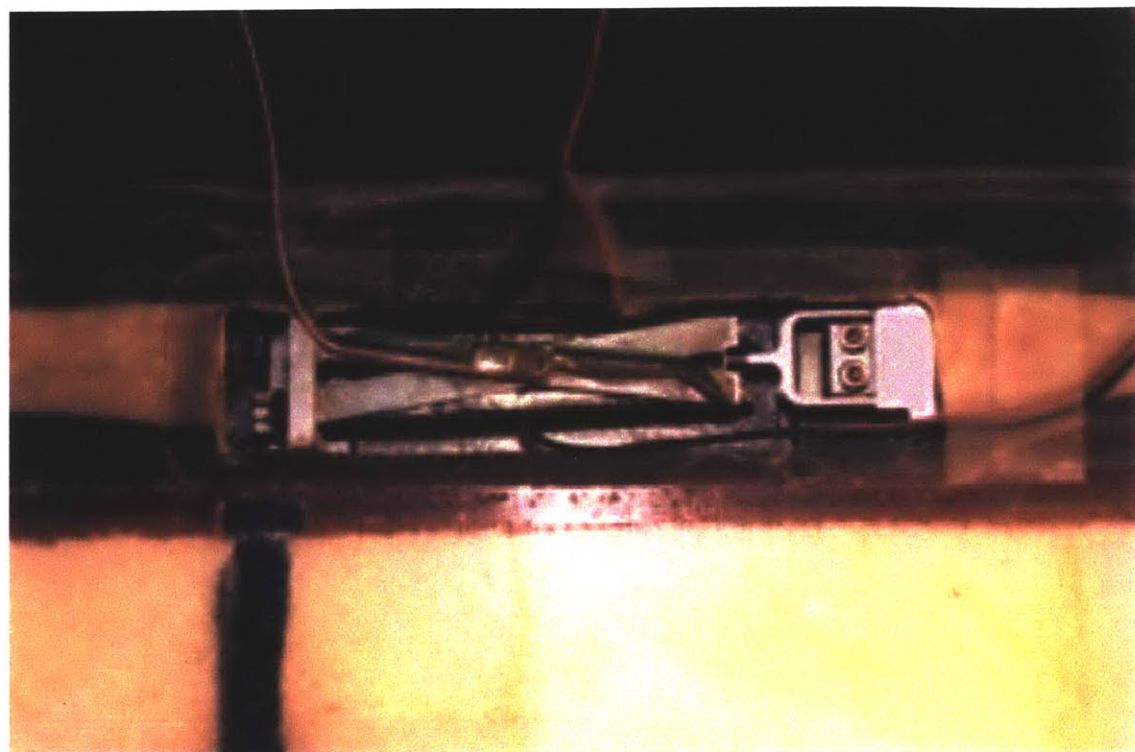


Figure E-76: Top view of the actuator in the bay with strain gage attached to the outer frame and magnets epoxied to the inner frame at its output end